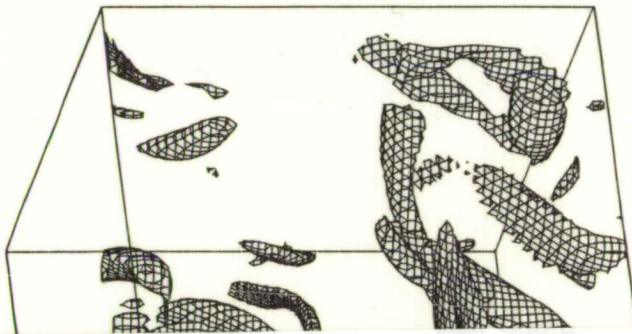


Studying Turbulence Using Numerical Simulation Databases - IV

Proceedings of the 1992 Summer Program



(NASA-CR-194556) STUDYING
TURBULENCE USING NUMERICAL
SIMULATION DATABASES. 4:
PROCEEDINGS OF THE 1992 SUMMER
PROGRAM (Stanford Univ.) 421 p

445329

N94-14745
--THRU--
N94-14768
Unclas

G3/34 0189660

Center for Turbulence Research

November 1992



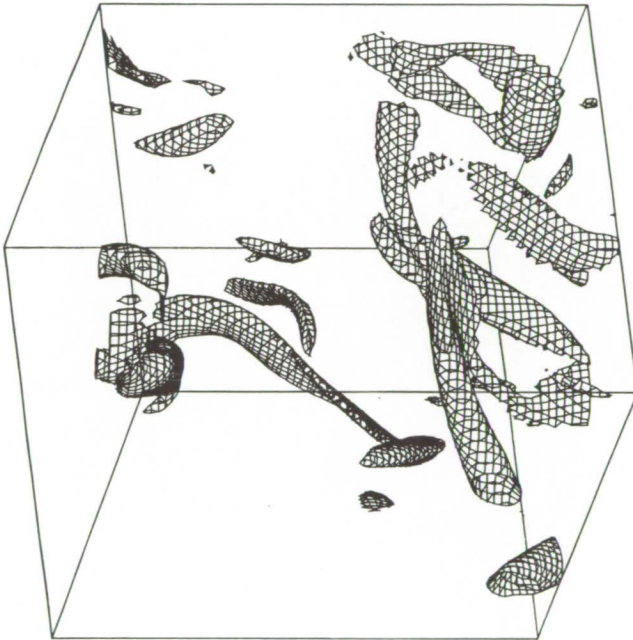
Ames Research Center



Stanford University

Studying Turbulence Using Numerical Simulation Databases - IV

Proceedings of the 1992 Summer Program



Center for Turbulence Research

November 1992



Ames Research Center



Stanford University

ORIGINAL PAGE
BLACK AND WHITE PHOTOGRAPH



CONTENTS

ORIGINAL CONTAINS
COLOR ILLUSTRATIONS

Preface	1-0
I. Small Scales	
Overview	3-0
A small-scale turbulence model. T. S LUNDRÉN	5-1
The structure of intense vorticity inhomogeneous isotropic turbulence. J. JIMÉNEZ, A. A. WRAY, P. G. SAFFMAN and R. S. ROGALLO	21-2
On the local nature of the energy cascade. C. MENEVEAU, T. S. LUND and J. CHASNOV	47-3
Search for subgrid scale parameterization by projection pursuit regression. C. MENEVEAU and T. S. LUND	61-4
Triad interactions in the dissipation range. S. KIDA, R. KRAICHNAN, R. ROGALLO, F. WALEFFE and A. WRAY	83-5
A study of the fine scale motions of incompressible time-developing mixing layers. J. SORIA, M. S. CHONG, R. SONDEGAARD, A. E. PERRY and B. J. CANTWELL	101-6
Isotropy of small scale turbulence. R. A. ANTONIA and J. KIM	123-7
LES versus DNS: a comparative study. L. SHTILMAN and J. R. CHASNOV	137-8
II. Turbulence Physics	
Overview	145-0
Behavior of streamwise rib vortices in a three-dimensional mixing layer. J. LOPEZ and J. BULBECK	147-9
Direct simulation of polymer drag reduction in free shear flow and vortex dipoles. P. ORLANDI, G. M. HOMSY and J. AZAIEZ	165-10
Estimation of the vortex length scale and intensity from two-dimensional samples. D. L. REUSS and W. P. CHENG	175-11
III. Compressible Flow and Modeling	
Overview	197-0
Rapid distortion analysis and direct simulation of compressible homogeneous turbulence at finite Mach number. C. CAMBON, G. N. COLEMAN and N. N. MANSOUR	199-12
Investigation of the dilatational dissipation in compressible homogeneous shear flow. G. A. BLAISDELL and O. ZEMAN	231-13

Response of a supersonic boundary layer to a compression corner. D. VANDROMME and O. ZEMAN	247-14
Vortex-induced disturbance field in a compressible shear layer. D. PAMOSCHOU and S. K. LELE	259-15
Evolution of the shock front and turbulence structures in the shock/turbulence interaction. N. KEVLAHAN, K. MAHESH and S. LEE	277-16
A transport equation for eddy viscosity. P. A. DURBIN and Z. YANG	293-17
IV. Reacting Flows and Combustion	
Overview	305-0
DNS and modeling of the interaction between turbulent premixed flames and walls. T. J. POINSOT and D. C. HAWORTH	307-18
The evolution equation for the flame surface density in turbulent premixed combustion. A. TROUVÉ and T. POINSOT	325-19
Numerical simulations of turbulent premixed $H_2/O_2/N_2$ flames with complex chemistry. M. BAUM, T. J. POINSOT and D. C. HAWORTH	345-20
Effect of finite-rate chemistry and unequal Schmidt numbers on turbulent non-premixed flames modeled with single-step chemistry. J. H. CHEN, S. MAHALINGAM, I. K. PURI and L. VERVISCH	367-21
Structure of turbulent non-premixed flames modeled with two-step chemistry. J. H. CHEN, S. MAHALINGAM, I. K. PURI and L. VERVISCH	389-22
Stochastic modeling of turbulent reacting flows. R. O. FOX, F. GAO, R. D. MOSER, M. M. ROGERS, and J. C. HILL	403-23
Panel discussion on computational combustion. J. C. HILL	425-0

omit to
P5

Preface

The fourth Summer Program of the Center for Turbulence Research was held during the four-week period July 13 to August 7, 1992. As in the past summer programs, direct numerical simulation databases were used to study turbulence physics and modeling issues. Twenty-seven participants from seven countries were selected based on their research proposals. They joined twenty-three local participants from Stanford and NASA-Ames Research Center who devoted virtually all of their time during the Program to this activity.

The Program included a special emphasis on the physics of small scale turbulence which was, in part, motivated by the recent advances in subgrid scale modeling for large eddy simulations. A relatively large effort was also devoted to turbulent reacting flows. Direct numerical simulation of turbulent reacting flows has been an integral part of CTR's summer and core programs. A panel of experts (Thierry Poinsot, Stephen B. Pope, and Forman A. Williams) were invited to discuss application of these simulations (which due to computer limitations are performed with limited ranges of parameters) to turbulence combustion. A summary of the panel's deliberations was prepared by James Hill and is included in this report.

As part of the program, four review tutorials were given on *Vortical States, Vortex Filaments, and Turbulence* (Philip G. Saffman), *PDF Modeling* (Stephen B. Pope), *Energy Transfer Mechanism* (Shigeo Kida), and *Experimental Studies of Local Isotropy in high Reynolds Number Flows* (Seyed G. Saddoughi).

The databases consisted of a turbulent mixing layer, turbulent channel flow with passive scalar, forced homogeneous isotropic turbulence, compressible homogeneous turbulence, compressible free-shear flows, and reacting flows. Additional calculations were made when time series of the flow fields were needed. In particular, very large simulations of forced isotropic turbulence with 512^3 degrees of freedom were made on the massively parallel Intel/Delta computer at Caltech.

This report contains twenty-four papers that resulted from the 1992 Summer Program. The papers are divided into four groups and are preceded by an overview written by each group coordinator. Early reporting of some of the projects occurred at the Forty-Fifth Meeting of the Fluid Dynamics Division of the American Physical Society in Tallahassee, Florida, November 22-24, 1992. Fifteen abstracts based on the work accomplished during the Summer Program were presented at this meeting.

We are grateful to Ms. Debra Spinks for the compilation of this report and her invaluable assistance in the organization of the Summer Program.

Parviz Moin
William C. Reynolds
John Kim

I. Small turbulence scales group

Inclusion of the study of small scales in the 1992 Summer program was, in part, motivated by the recent resurgence of interest in large eddy simulation of turbulent flows which in turn was brought about by the development of the dynamic subgrid scale model during the 1990 Summer Program. In contrast to the 1990 Program where several models were developed and tested, this year's studies mostly focused on fundamental questions about the small scales. The eight papers in this group can be divided into three parts: structure and kinematic properties of small scales (Lundgren; Jimenez *et al.*; Soria *et al.*; Antonia & Kim), nature of energy cascade and interaction among scales (Meneveau, Lund & Chasnov; Kida *et al.*), and parameterization and predictability (Meneveau, Lund & Moin; Shtilman & Chasnov).

Lundgren revisited his earlier theory in which he had shown that a model of small scale turbulence consisting of randomly orientated axially strained spiral vortices generates Kolmogorov's $k^{-5/3}$ spectrum. A numerical formulation of his model provided some flexibility for experimentation with parameters of the model that was not possible in his earlier analytical work. For example, he showed that the results are insensitive to the time dependence of the strain rate imposed on the vortices. Lundgren also gained new insight into his original model by noting that, in the inviscid limit, it gives a self similar enstrophy spectrum which is the key for obtaining the Kolmogorov energy spectrum.

Jimenez, Wray, Saffman & Rogallo conducted a comprehensive study of the celebrated tube-like intense vortical structures in homogeneous turbulence at several Reynolds numbers. The diameter of the tubes scale with the Kolmogorov scale and their lengths with the integral scale. Since these structures, also known as "worms", have been observed only in forced isotropic turbulence calculations, there was some concern that they may be artifacts of the forcing. Jimenez *et al.* present evidence that the worms are robust and occur without forcing. The worms apparently form from the roll-up of vortex sheets in the regions where two large scale structures come in contact. They occupy a smaller fraction of the flow volume with increasing Reynolds number and are not significant contributors to the flow dynamics. The worms are the primary contributors to the intense events manifested in the tails of the probability distributions of functions of velocity gradients. The tails get longer with increasing Reynolds number with no apparent sign of convergence, a result which supports multifractal models of turbulence.

Soria *et al.*, in a continuation of their study during the 1990 Summer Program, investigated the topology of the dissipating motions in turbulent mixing layers. Three incompressible mixing layers with different initial conditions were considered. The objective was to study the effect of initial conditions and Reynolds number on flow scaling and the topology of dissipating motions. Interesting observations were made on the evolutionary changes of structures in different flow regimes, but the underlying mechanisms remain for future investigations.

The concept of local isotropy in turbulent flows with mean strain or shear has been contested in some recent studies. Antonia & Kim investigated this issue using fully developed turbulent channel data at relatively low Reynolds numbers. They demonstrated that the isotropic relation for temperature derivatives and vorticity (both of which have significant contributions from small scales) is approximately satisfied as the channel centerline is approached. It was found that the criterion for local isotropy suggested by Corrsin (and Uberoi) is too restrictive although the parameter involved, which is the ratio of the Kolmogorov time scale to the time scale of mean shear, is appropriate. As long as this parameter is less than about 0.1, local isotropy is satisfied independent of Reynolds number.

The nature of interactions among different scales of turbulence has been a central one to turbulence research due to its fundamental role in the cascade of energy from large to small scales. Kida *et al.* studied the locality of the interactions using quasi-normal theories and data from highly resolved numerical simulations of forced isotropic turbulence. Whereas in the inertial range local triad interactions are dominant, in the dissipation range nonlocal triad interactions are dominant. Moreover, the nonlocality of the interaction was related to the form of the energy spectrum in the far-dissipation range.

The locality of the energy cascade was also studied by Meneveau, Lund & Chasnov in both physical and Fourier spaces. A novel Lagrangian space-time analysis of isotropic turbulence data provided evidence that fluid elements in a given energy band are better correlated with smaller eddies of nearly the same energy content at a later time than with eddies of the same spatial scale. This of course, supports the classical energy cascade phenomenology that large eddies break into smaller eddies as they decay.

The practical problem of parameterization of subgrid scale stresses in terms of the large scale data was considered by Meneveau, Lund & Moin using the projection pursuit algorithm. This is a powerful regression technique for many-dimensional parameter spaces which was originally developed to analyze experimental data in particle physics. The objective was to identify large-scale flow quantities that could be used in the modeling of subgrid-scale stresses. For isotropic turbulence, the search algorithm led to the strain rate tensor which is used in eddy viscosity models. For homogeneous shear flow and channel flow, more complex relationships in terms of other tensors were identified which resulted in some improvement of the correlation between the model and modeled terms. Overall, the improvements were not as high as expected, and it's unclear whether the new models will impact future large eddy simulations.

Shtilman & Chasnov performed a detailed study of the statistical predictability of LES calculations. They found good agreement between several statistics of an LES field and the corresponding statistics of a filtered DNS field in forced isotropic turbulence. These results are encouraging, providing evidence for the accuracy of large eddy simulations.

Parviz Moin

445336 51-34
189661

p-10 5
N94-14746

A small-scale turbulence model

By T. S. Lundgren¹

A model for the small-scale structure of turbulence is reformulated in such a way that it may be conveniently computed. The model is an ensemble of randomly oriented structured two dimensional vortices stretched by an axially symmetric strain flow. The energy spectrum of the resulting flow may be expressed as a time integral involving only the enstrophy spectrum of the time evolving two-dimensional cross section flow, which may be obtained numerically. Examples are given in which a $k^{-5/3}$ spectrum is obtained by this method without using large wavenumber asymptotic analysis. The $k^{-5/3}$ inertial range spectrum is shown to be related to the existence of a self-similar enstrophy preserving range in the two-dimensional enstrophy spectrum. The results are insensitive to time dependence of the strain-rate, including even intermittent on-or-off strains.

1. Introduction

One of the issues in turbulence theory is to understand what kinds of elementary flow structures are responsible for the part of the turbulent energy spectrum described by Kolmogorov's celebrated $k^{-5/3}$ law. A number of years ago, Lundgren (1982) proposed a model of the small scale structure of turbulence which gives this spectrum. The model was put together as an ensemble of randomly oriented vortices with spiral structure, each vortex being subjected to an axially symmetric irrotational straining field. The strain was made constant and axially symmetric for analytical reasons and this should be thought of as a representation of much more complicated strains. The idea was to model the most important property of turbulence, namely the mixing property which causes fluid particles to rapidly separate, stretching vortex blobs into elongated tubes. This model generalizes an earlier model by Townsend (1951) which assumed randomly oriented Burgers vortices and gave a k^{-1} spectrum.

Differential rotation in the vortices (the inner part has higher angular velocity therefore winds faster) causes the vortex layers in the spiral to tighten, and the axial straining decreases the cross section of the structure. These mechanisms cause a cascade to smaller scales which differs from the traditional concept of a cascade through eddies of different sizes induced by instabilities.

Many turbulent flows have distinct two dimensional vortices, and often flow visualization by laser-induced-fluorescence or smoke shows vortex cross sections with some spiral structure. Such structures may be seen in sections 4 and 6 of Van

¹ Department of Aerospace Engineering and Mechanics, University of Minnesota

Dyke's (1982) book. Schwarz (1990) identified intermittently occurring layered vortex sheets (apparently spirals) in oscillating grid turbulence by flow visualization with small suspended crystalline platelets. On the other hand, the numerically simulated periodic box turbulence of Vincent and Meneguzzi (1991) contains very pronounced two-dimensional vortices in which very little internal structure can be seen. (However, there is *some* spiral structure in their figure 15.) Perhaps the Reynolds number is too small in this kind of flow.

A number of authors have made further studies based on the original paper by Lundgren. In particular, Lundgren (1985) applied the model to the calculation of the scalar spectrum of the product of a fast chemical reaction. Gilbert (1988) used similar ideas for the study of two-dimensional turbulence. Buntine and Pullin (1988) and Pullin and Buntine (1989) used the model as a basis for computations of spectra produced by the merger of vortices. Pullin and Saffman (1992) used it to calculate vorticity and velocity derivative moments for homogeneous isotropic turbulence. Recently, Gilbert (1992) has produced a qualitative cascade argument based on the model to explain the Kolmogorov spectrum.

In section 2, the model is reformulated in such a way that the two-dimensional part of the model, the spiral flow or some more general two-dimensional vortical flow, may be conveniently carried out numerically.

In section 3 numerical computations of two-dimensional flows are used to generate three-dimensional energy spectra.

2. Reformulation of the spiral vortex model

It will be useful to separate the strictly two-dimensional part of the model, the flow in the cross section of the vortex, from the straining part of the model which is performed by a transformation. The 1982 paper will be referred to as L and equations from that paper will be referred to by L:(). It was shown in L that if a two-dimensional flow with vorticity given by $\omega_2(x, y, t)$ is placed in an axially symmetric strain flow with velocity components $(-.5ax, -.5ay, az)$ where the strain-rate a may be a function of time, then the vorticity in the resulting three-dimensional flow (which has the same initial vorticity as the two-dimensional flow) is given by

$$\omega(x, y, t) = S(t) \omega_2 \left(S(t)^{1/2} x, S(t)^{1/2} y, T(t) \right) \quad (2.1)$$

where

$$S(t) = \exp \left(\int_0^t a(t') dt' \right) \quad (2.2)$$

is the amount the flow is stretched and

$$T(t) = \int_0^t S(t') dt' \quad (2.3)$$

is a strained time. The energy spectrum of an ensemble of strained vortices of all ages, accounting for the greater length of the older vortices, may be deduced from L:(58), L:(75) and L:(76) and expressed, in a new form, by

$$E(k) = \frac{C}{k^2} \int_0^{T_c} S(T)^{1/2} F_2 \left(S(T)^{-1/2} k, T \right) dT \quad (2.4)$$

where $C = 2\pi^2 l_0 N_c / L^3$ is a constant. The function F_2 is the enstrophy spectrum (the vorticity power spectrum) of the strictly two-dimensional flow. This is defined by

$$F_2(k, t) = k \int_0^{2\pi} |\bar{\omega}_2(k \cos \theta_k, k \sin \theta_k, t)|^2 d\theta_k \quad (2.5)$$

where

$$\bar{\omega}_2 = \frac{1}{(2\pi)^2} \int \int \exp[-i(k_x x + k_y y)] \omega_2(x, y, t) dx dy \quad (2.6)$$

and represents the enstrophy in a circular shell in wavenumber space, divided by the width of the shell. The integration variable in Eq.(2.4) is the strained time and the stretching function S must be expressed as a function of this strained time. When the strain-rate is constant, the usual case considered, $S = \exp(at)$ and $T = (\exp(at) - 1)/a$ and hence

$$S = 1 + aT \quad (2.7)$$

is the appropriate function. In appendix A, it is shown by example that, even when the strain-rate is variable and quite different from constant, the stretching function is roughly a linear function of the strained time and the energy spectrum computed from Eq.(2.4) is insensitive to these modest deviations from linearity.

In Eq.(2.4), the function F_2 is all that is needed from the two-dimensional flow, and it may be specified numerically or analytically. The time integral represents the effect of stretching. The finite time cut-off on the integral is to prevent the vortices from being stretched indefinitely. It was assumed in L that they ultimately coalesce into shorter vortices and renew the spiral structure.

In L an analytical spiral vortex solution was developed. An approximate solution of the two-dimensional Navier-Stokes equation was given in the form of a Fourier series in the cylindrical angle variable θ ,

$$\omega(r, \theta, t) = \sum_{n=-\infty}^{\infty} \omega_n(r, t) \exp(in\theta) \quad (2.8)$$

$$\omega_n(r, t) = f_n(r) \exp \left[-in\Omega(r)t - \frac{1}{3}n^2 \left(\frac{d\Omega}{dr} \right)^2 \nu t^3 \right] \quad (2.9)$$

where the functions f_n are arbitrary and the angular velocity $\Omega(r)$ is related to the average vorticity ω_0 by

$$r\omega_0 = \frac{d}{dr} r^2 \Omega(r). \quad (2.10)$$

The function $\Omega(r)$ must be monotone decreasing – the property which gives differential rotation. If the functions f_n are all the same (independent of n) the solution looks like a spiraling vortex sheet in the inviscid limit. The approximations in Eq.(2.8) require that t must be large, i.e., the error becomes small as $t \rightarrow \infty$. However, it will be seen numerically that it is quite good even for fairly small t .

By using this analytical solution, the enstrophy function F_2 may be expressed as a series of integrals which involve Bessel functions. These may be evaluated by the method of stationary phase, which requires both k and t to be large, an asymptotic result which may be written

$$F_2 = t^{-1} G(k/t) \exp(-2\nu k^2 t/3) \quad (2.11)$$

where

$$G(k/t) = \frac{1}{\pi} \sum_{n=1}^{\infty} \frac{r_n}{n\Omega''(r_n)} |f_n(r_n)|^2 \quad (2.12)$$

with

$$k + n\Omega'(r_n)t = 0. \quad (2.13)$$

The last equation results from the method of stationary phase. One is supposed to solve this for r_n and substitute it into Eq.(2.12). Note that r_n is a function of k/t , hence the form of the argument of the function G . In writing this result, the contribution from the $n = 0$ term has been omitted. This term has a different functional dependence and was shown in L to contribute little at high wavenumber. Equation (2.11) does not appear in L but may be deduced from L:(66) and L:(64) (with $S \equiv 1$ and $P \equiv t$).

It is the functional form of Eq.(2.11) which is important. First note that the functions f_n are assumed to be of limited extent so that the spiral is restricted to a halo around a central vortex. Then the function F_2 looks like a localized hump when plotted versus wavenumber (this will be clear when some computations are seen). If the viscous factor can be neglected, the area under the hump stays constant because

$$\int_0^{\infty} t^{-1} G(k/t) dk \equiv \text{constant}. \quad (2.14)$$

The similarity form of the function shows that the top of the hump moves to higher wavenumber with constant speed, while the width broadens and the peak decreases in such a way that the area stays constant. This is an enstrophy preserving temporal cascade. The physics is clear: as the spiral turns tighten due to differential rotation, the enstrophy shifts to higher wavenumber while being conserved.

The function F_2 given by Eq.(2.11) is only part of the enstrophy spectrum. There is an additional large part at low wave number (the $n = 0$ term which was omitted). If viscosity is neglected, the *total* enstrophy is preserved, i.e., $\int \omega_2^2 dA = \int F_2 dk \equiv \text{constant}$. What has been shown here is that the spiral solution has scale separation of the enstrophy spectrum into two distinct peaks, and the enstrophy of each of these parts is independently preserved.

The energy spectrum expression given by Eq.(2.4) could also have been cast in terms of the two-dimensional energy spectrum, E_2 say. For the spiral solution, E_2 also has scale separation into a large low wavenumber peak and a secondary smaller (much smaller because of the k^{-2} factor) high wave number peak with a similarity structure. While the total energy is conserved (in the absence of viscosity), the

energy in the separate peaks is not. The energy in the high wavenumber peak decreases like t^{-2} , giving up this energy to the low wavenumber peak.

This enstrophy preserving similarity form is responsible for the $k^{-5/3}$ part of the three-dimensional energy spectrum. When Eq.(2.11) is substituted into Eq.(2.4), the result

$$E(k) = Ak^{-5/3} \exp(-2\nu k^2/3a) \quad (2.15)$$

is obtained if one takes the upper limit to be infinite and approximates Eq.(2.7) by $S \simeq aT$, i.e., most of the contribution to the integral comes from large values of S . Equation (2.15) results from a simple change of the integration variable to $T/k^{2/3}$ and doesn't depend at all on the specific form of G . This generalizes the model since there could be other kinds of flows with scale-separated self-similar conservative enstrophy spectra, although none are presently known.

The following qualitative derivation of the functional form of the enstrophy spectrum was motivated by a discussion with Javier Jimenez. Assume that the enstrophy spectrum has a self-similar form $t^{-\alpha}G(k/t^\beta)$, then it is easy to see that conservation of enstrophy implies $\alpha = \beta$. One may argue that in a fairly steady shear flow the length of an element of a vortex sheet increases linearly with t ; its thickness, therefore, decreases like t^{-1} . The largest wavenumber in a system of such vortex sheets behaves like the reciprocal of the thickness. Therefore, $k \sim t$ and $\alpha = \beta = 1$, as desired.

It can also be noted that if there is no axial straining, so that $S \equiv 1$, Eq.(2.4) and Eq.(2.11) (without the viscous part) gives

$$E(k) \sim k^{-2}. \quad (2.16)$$

This was also noted by Gilbert (1988) and is consistent with Townsend's (1951) observation that a k^{-2} spectrum results from random arrays of vortex sheets. The conclusion to be drawn is that the axial straining gives the extra $k^{1/3}$.

The integration in Eq.(2.4) may be understood as follows. Imagine a K, T plane with $S^{1/2}F_2(K, T)$ plotted in a third dimension. This function looks like a ridge centered along a ray from the origin of the K, T plane, decreasing in height and spreading for increasing T . The argument $K = S^{-1/2}k$ required in Eq.(2.4) is a curve in the K, T plane starting from $K = k$ at $T = 0$ and moving to smaller K for larger T . The integrand in Eq.(2.4) is the height of the ridge seen as one traverses this curve. In order to get $k^{-5/3}$ for a band of k -values, the integration must extend through the ridge into the small values on the far side, for all k -values in this band.

3. Computations

The formula expressed by Eq.(2.4) makes it possible to test some of the analytical limitations of the spiral vortex model, since the two-dimensional enstrophy spectrum may be computed from numerical solutions of the two-dimensional Navier-Stokes equations rather than depending entirely on asymptotic methods. Further, one can use more general two-dimensional solutions. Buntine and Pullin (1988) and Pullin and Buntine (1989) used numerical analysis in a similar context. Their

approach was somewhat different than that described here. They expanded the two-dimensional vorticity in a Fourier series, as in Eq.(2.8), and solved numerically for the coefficients $\omega_n(r, t)$. These functions were then used to evaluate the Bessel function integrals required for L:(60), and finally the energy spectrum was obtained through the appropriate time integration. The advantage of the present approach is flexibility. Having identified the required physical quantity as the two-dimensional enstrophy spectrum, it may be computed by *any* method and processed through Eq.(2.4) without further reference to the detailed analytical expansions of Lundgren (1982).

In the computations reported below, a pseudo-spectral method was employed in a vorticity/streamfunction formulation in a square region with periodic boundary conditions. Aliasing errors were removed by the 2/3 rule and most of the computations were done with 240^2 resolution. The computations were performed at the Center for Turbulence Research at NASA Ames Research Center on a Cray YMP.

The characteristic length in the flows was taken such that the sides of the box have dimensionless length equal 2π units; this makes the wavenumbers be integers. The actual *unit* of length was related to some measure of the initial radius of the vorticity distribution, thus the vortex is quite a bit smaller than the box. The characteristic velocity was selected such that the dimensionless circulation of the vortex was unity. This makes the Reynolds number of the flows be Γ/ν where Γ is the dimensional circulation of the vortex. The Reynolds number would be about an order of magnitude smaller if an average swirling velocity at unit radius were used for the characteristic velocity. The dimensionless turn around time is about 40 units.

The enstrophy spectrum, given by Eq.(2.5), was approximated by summing all values of the squared magnitudes of the discrete Fourier coefficients with x, y wavenumbers in a cylindrical shell of unit wavelength in wave space. This value is then assigned to a wavenumber which is the midradius of the shell.

Two series of computations were done with the spiral vortex solution. In the first, the two-dimensional enstrophy spectrum was computed from the analytical spiral solution by a fast Fourier transform algorithm. The second computes the enstrophy spectrum from a numerical solution of the spectral equations with the spiral solution as an initial condition. Comparison thus tests the integrity of the spiral solution.

The spiral solution was taken in the form of a two-sided rollup with two halo spirals of amplitude f , with 180° separation, plus an additional central core. The specific functions used here are expressed as

$$\omega_2(r, \theta, t) = \omega_0(r) + 2f(r) \sum_{n=1}^{\infty} \cos[2n(\theta - \Omega(r)t)] \exp(-4n^2\Omega'(r)^2\nu t^3/3), \quad (3.1)$$

$$\omega_0(r) = \Gamma \frac{\exp[-(r/a)^2]}{(1+h)\pi a^2} + 2f(r), \quad (3.2)$$

$$f(r) = \Gamma \frac{h(r/a)^2 \exp[-(r/a)^2]}{2(1+h)\pi a^2}, \quad (3.3)$$

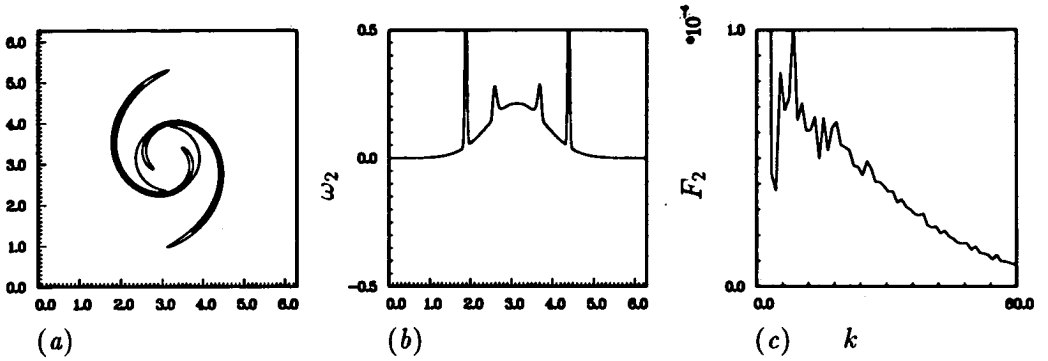


FIGURE 1.1. $t=0, t_{\text{spiral}}=50$. See caption below.

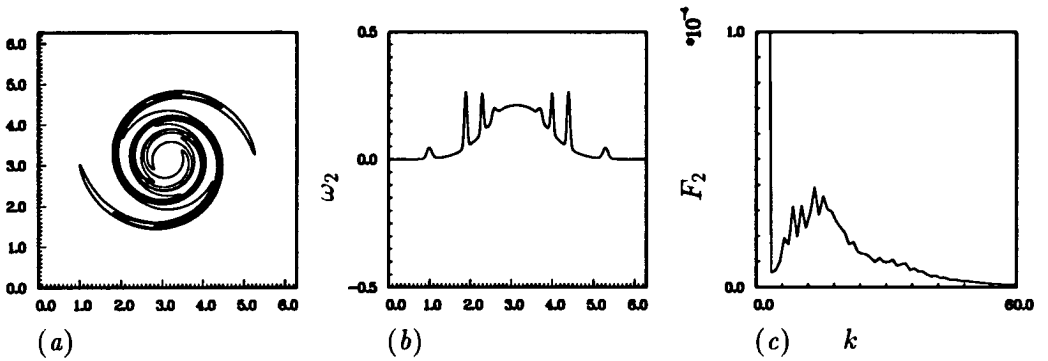


FIGURE 1.2. $t=50, t_{\text{spiral}}=100$. See caption below.

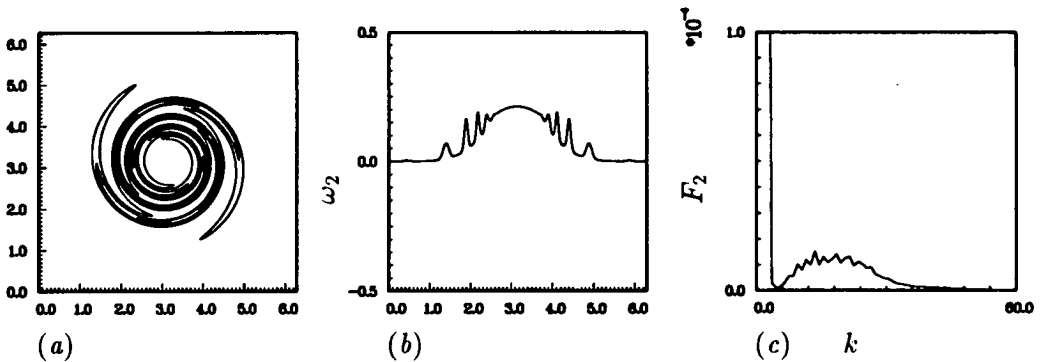


FIGURE 1.3. $t=100, t_{\text{spiral}}=150$. See caption below.

$$\Omega(r) = \Gamma \frac{[1 + h - (1 + h + h(r/a)^2) \exp(-(r/a)^2)]}{2(1 + h)\pi a^2}, \quad (3.4)$$

$$\Omega'(r) = \frac{[\omega_0(r) - 2\Omega(r)]}{r}, \quad (3.5)$$

where Γ is the circulation of the vortex, a is a radial dimension and h is a constant. If $0 < h < 1$, $\Omega(r)$ will be monotone decreasing. In dimensionless form $\Gamma = 1, a = 1$, ν is the reciprocal of the Reynolds number and in these computations $h = 1/2$.

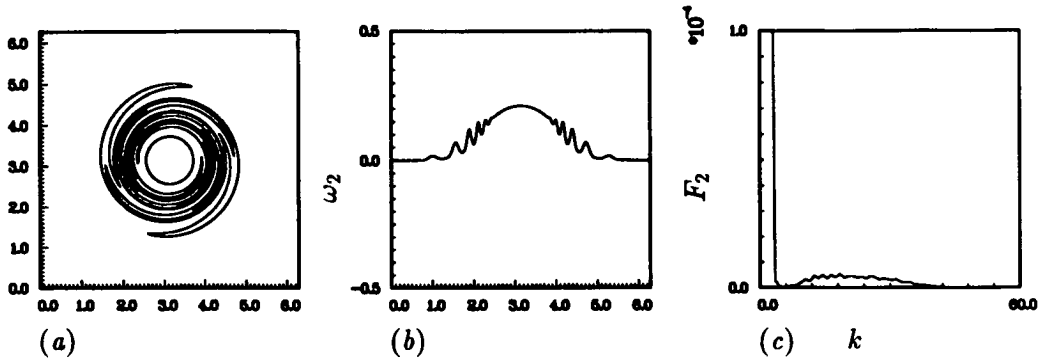


FIGURE 1.4. $t=150$, $t_{\text{spiral}}=200$. See caption below.

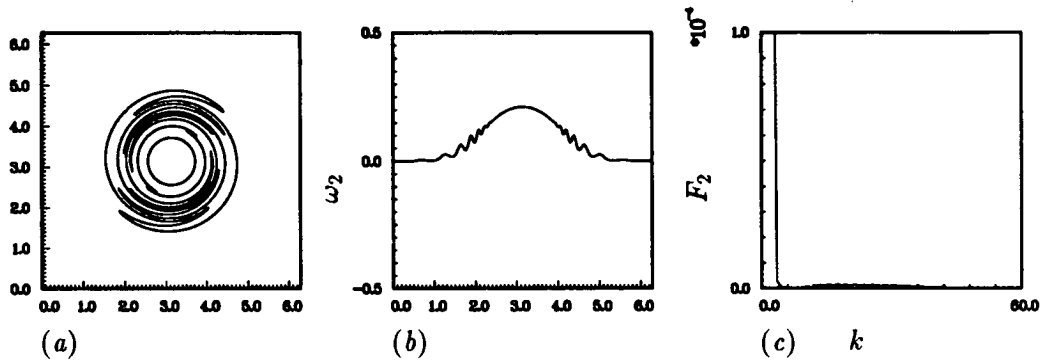


FIGURE 1.5. $t=200$, $t_{\text{spiral}}=250$. See caption below.

FIGURE 1.1–1.5. Analytical spiral solution at selected times. t_{spiral} is the time in Eq.(3.1), t is for comparison with figures (2.1)–(2.5) which have the same initial condition. $\Gamma/\nu = 25,000$. (a) vorticity contours. (b) vorticity along a horizontal cut through the middle of (a). (c) Enstrophy spectrum versus wavenumber.

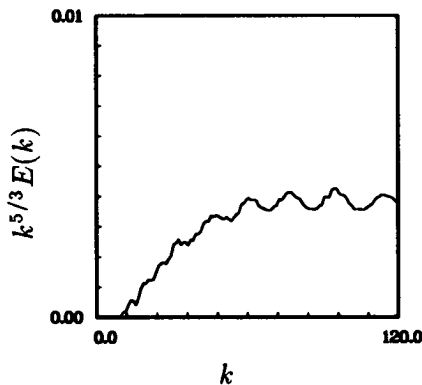


FIGURE 1.6. $k^{5/3}$ times the three-dimensional energy spectrum calculated by using Eq.(2.4) with the analytical spiral solution.

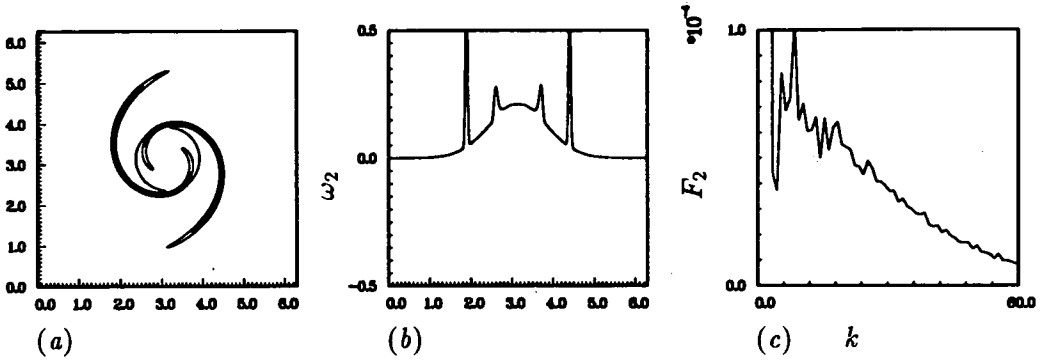


FIGURE 2.1. $t=0$. See caption below.

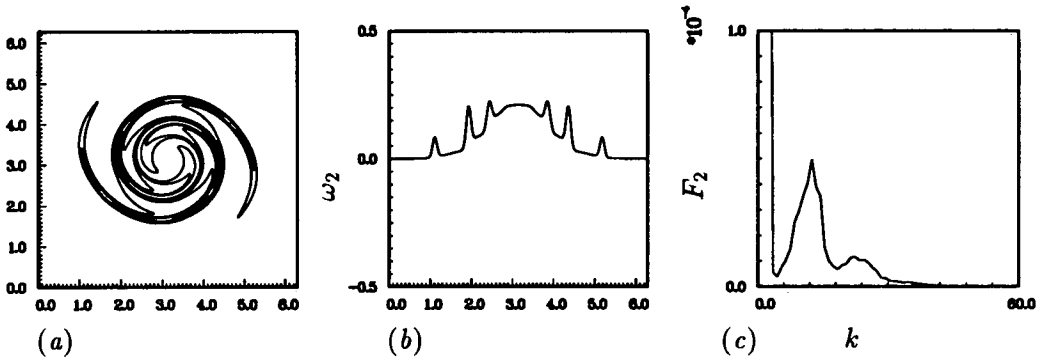


FIGURE 2.2. $t=50$. See caption below.

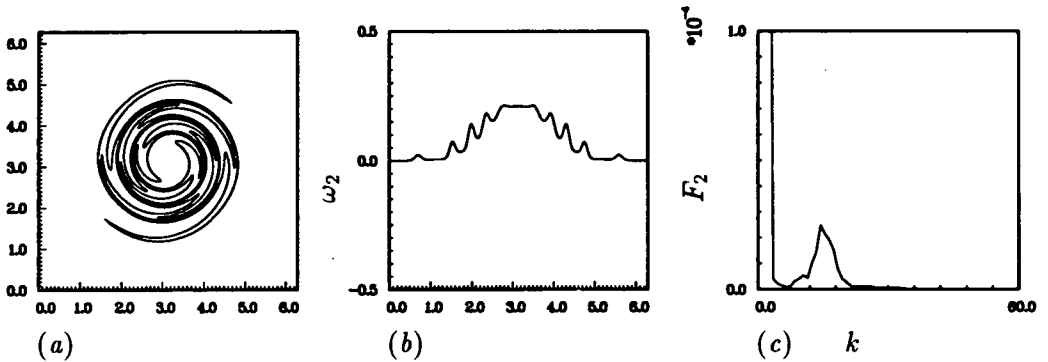


FIGURE 2.3. $t=100$. See caption below.

The first series, displayed in figures 1.1-1.6, is computed from the analytical solution with $\Gamma/\nu = 25,000$. The required discrete Fourier series were computed by means of Temperton's fast Fourier transform algorithms. The figures labeled (a) are vorticity contours at 5 times starting with the partially wound state corresponding to a dimensionless time $t_{\text{spiral}} = 50$; the figures labeled (b) show the vorticity along a horizontal cut through the middle of the contour figures. The figures labeled (c) are of the enstrophy spectrum. There is a huge peak at low wavenumber which is off scale in these figures. Enstrophy similarity, which was found asymptotically,

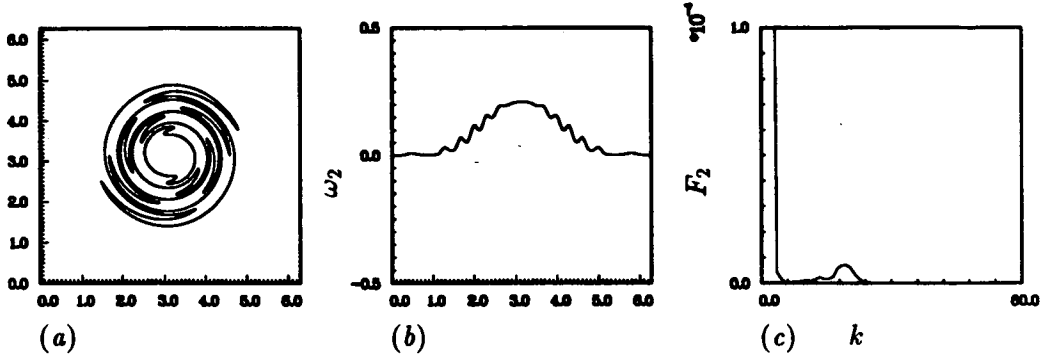
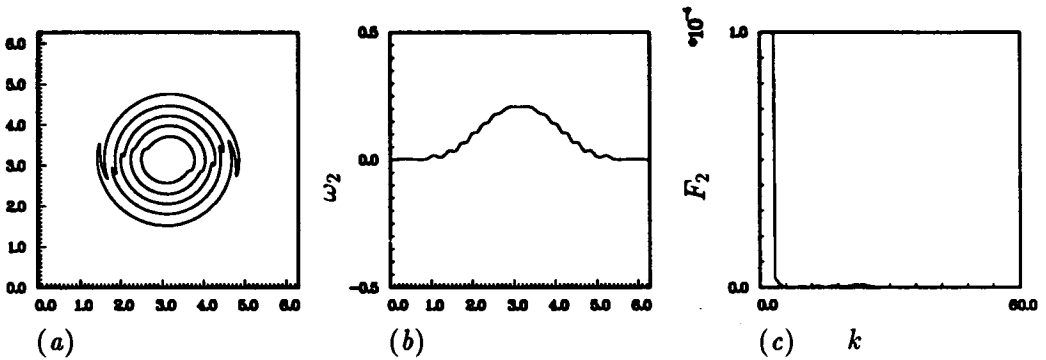
FIGURE 2.4. $t=150$. See caption below.FIGURE 2.5. $t=200$. See caption below.

FIGURE 2.1–2.5. Computed spiral solution at selected times. $\Gamma/\nu = 25,000$.

(a) vorticity contours. (b) vorticity along a horizontal cut through the middle of (a). (c) Enstrophy spectrum versus wavenumber.

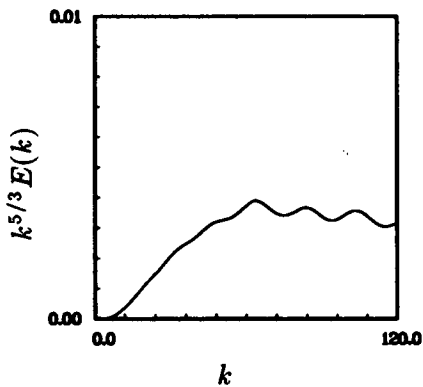
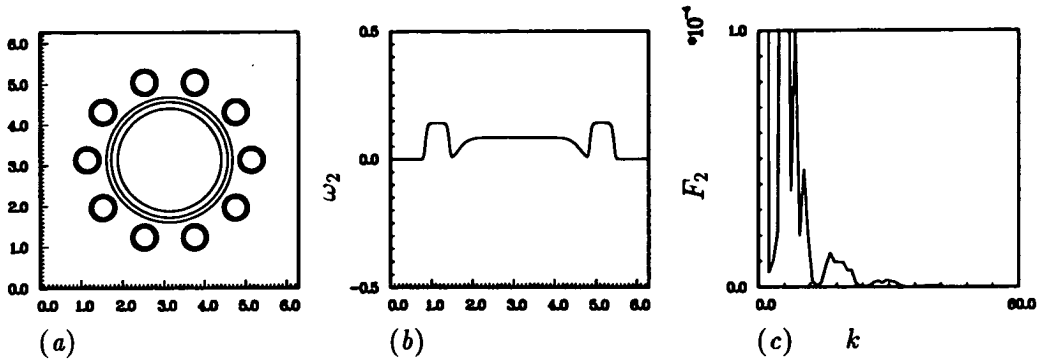
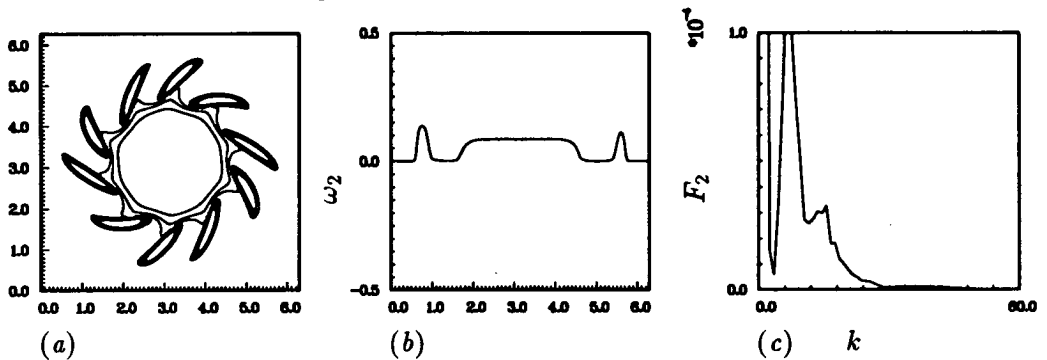
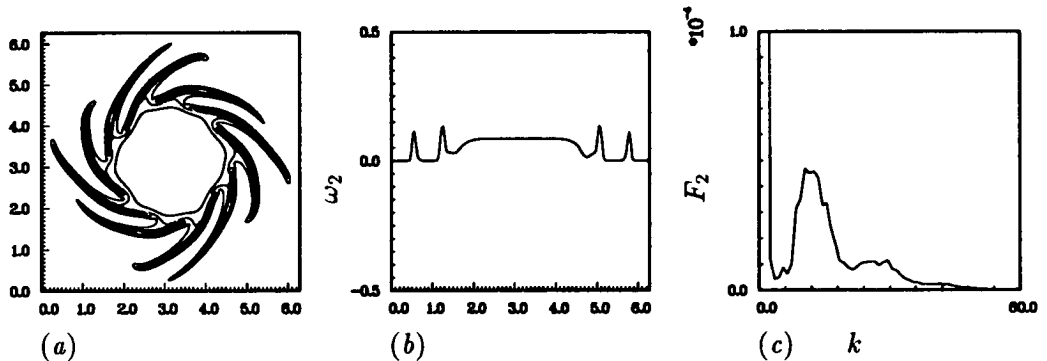


FIGURE 2.6. $k^{5/3}$ times the three-dimensional energy spectrum calculated by using Eq.(2.4) with solution computed using the analytical spiral solution as initial condition.

FIGURE 3.1. $t=0$. See caption below.FIGURE 3.2. $t=50$. See caption below.FIGURE 3.3. $t=100$. See caption below.

is not perfect but is qualitatively recognizable. As time increases, one can see the number of turns in the spiral increase due to differential rotation and the peak in the enstrophy spectrum move outward to larger wavenumber as the spatial scale in the spiral decreases.

Figure 1.6 shows the three-dimensional energy spectrum computed from Eq.(2.4). The integration was carried out from $T = 0$ to $T = 250$ with a coarse integration time interval of $\Delta T = 5$, which was adequate here. (In computations where the Navier-Stokes equations were solved numerically, ΔT was taken the same as the

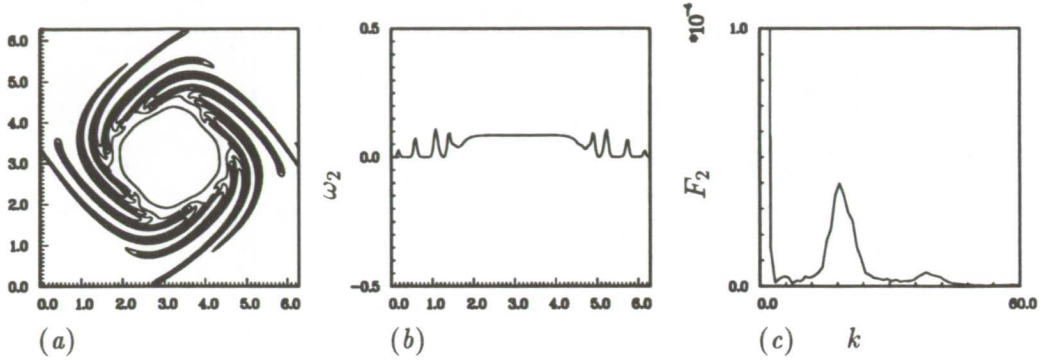
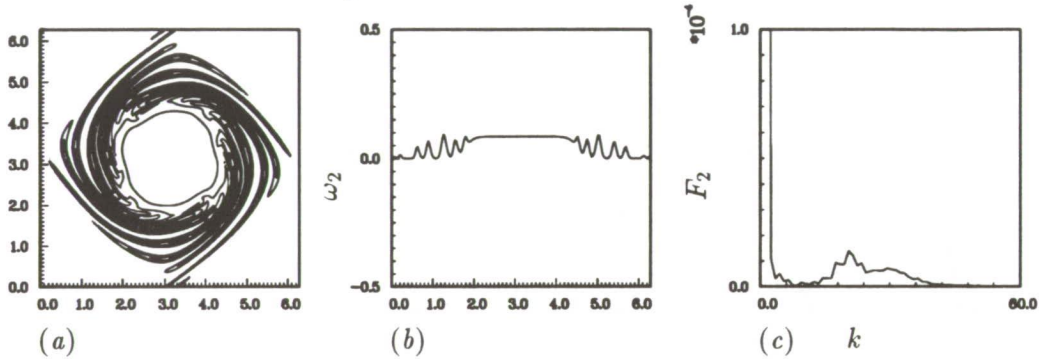
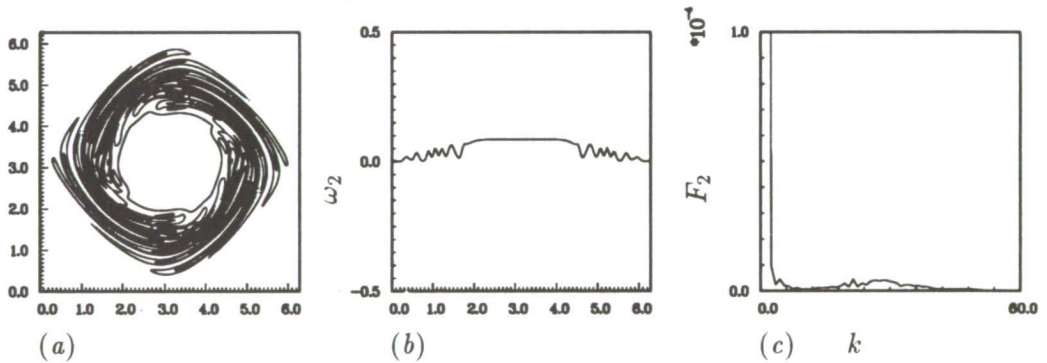
FIGURE 3.4. $t=150$. See caption below.FIGURE 3.5. $t=200$. See caption below.FIGURE 3.6. $t=250$. See caption below.

FIGURE 3.1—3.6. Computed spiral solution at selected times. $\Gamma/\nu = 100,000$. (a) vorticity contours. (b) vorticity along a horizontal cut through the middle of (a). (c) Enstrophy spectrum versus wavenumber.

updating time step, namely $\Delta T = .05$.) The strain-rate was taken to be unity. The low wavenumber end of the spectrum was suppressed by cutting off the integration when $S(T)^{-1/2}k$ is less than 5, thus avoiding the large low wavenumber enstrophy peak. The result in figure 1.6 has a wavenumber range from about 60 to 120 where

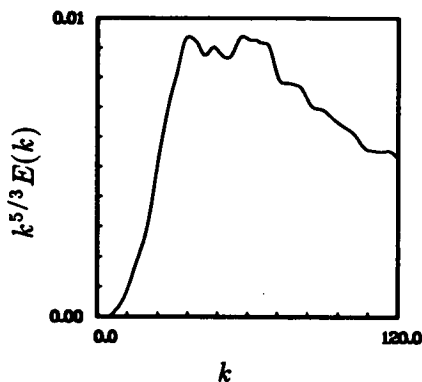


FIGURE 3.7. $k^{5/3}$ times the three dimensional energy spectrum calculated by using Eq.(2.4) with the solution depicted in figures 3.1– 3.6.

the spectrum is approximately $k^{-5/3}$. Note that since $2^{1/3} \simeq 1.26$, one should be able to tell the difference between $k^{-5/3}$ and k^{-2} on this figure.

The second series of computations, seen in figures 2.1–2.6, are presented in the same format as the first series. The Navier-Stokes equations were solved numerically with initial conditions the same as the initial frame of the first series. Here the object is to show that the analytical spiral solution is a good approximation to the Navier-Stokes equations even though time (t_{spiral}) is not large enough at the beginning for the spiral to have many turns. Comparing the two series of computations, one can see that the results are quite close but not identical. In particular the enstrophy spectrum of the second series is smoother and more compact. The energy spectrum is very similar but perhaps slightly tipped toward k^{-2} .

A third series of computations has been carried out with quite different initial conditions with the objective of producing a spiral solution without actually starting with one. The vorticity distribution at the initial time is shown in figure 3.1. One large vortex, with radius 1.5, almost uniform vorticity and circulation .6 is surrounded by 10 smaller vortices with centers 2 units from the center of the large vortex. Each of these smaller vortices have radii .3 units and circulation .04 so that the total circulation of the configuration is unity. The Reynolds number was $\Gamma/\nu = 100,000$. The smaller vortices get sheared into bands of vorticity which continue to tighten in the differential rotation of the combined vorticity. The result is a multilayered spiral vortex with a decent enstrophy cascade. Similarity is approximately satisfied; comparing the enstrophy spectrum at $t = 50$ with that at $t = 100$, the amplitude is almost half and the peaks have moved approximately to twice the wavenumbers as required by similarity. However, comparison of $t = 100$ with $t = 200$ is not quite as satisfactory.

The energy spectrum in figure 3.7 has a short $k^{-5/3}$ range from about $k = 36$ to $k = 72$ and then falls off faster. The viscous factor in Eq.(2.15), which is about .9 when $k = 120$, is not small enough to account for all of the observed decrease.

4. Conclusions

The original 1982 spiral vortex model was reformulated in a form where the effect of the two-dimensional flow in the vortex cross section was more clearly separated from the axial stretching. While this was done in order to be able to use computational methods more effectively, the new formulation has allowed greater insight into the workings of the model. It was shown in section 1 that, in the inviscid limit, the analytical spiral vortex solution gives an asymptotic time-dependent enstrophy spectrum in a self-similar form which conserves enstrophy. It is this self-similar form which leads to the $k^{-5/3}$ energy spectrum.

Computations with flows which develop spiral structure showed, qualitatively correct, but imperfect, self-similar enstrophy spectra. The resulting three-dimensional energy spectra nevertheless showed short ranges with the $k^{-5/3}$ power law. These results seem quite rugged and verify results which were previously obtained asymptotically.

The integral which processes the computed two-dimensional enstrophy spectrum to produce the three-dimensional energy spectrum requires integrations over a very long times, of the order of 6 turn-around-times, during which the vortex is stretched by a factor of about 250. The result from appendix A, which shows that the strain may be applied intermittently, make this seem more reasonable.

Acknowledgements

I would like to thank P. G. Saffman, J. Jimenez, and N. N. Mansour for fruitful discussions during the 1992 CTR Summer Program. I am especially grateful to N. N. M. for providing the pseudo-spectral code and showing me how to run it.

Appendix A. Insensitivity to time dependent strain-rate

The strain-rate which a real vortex feels is generated by the presence of other nearby vortices and is unlikely to be constant for very long; therefore, it is important to see if the results are sensitive to time dependence of the strain-rate function.

Equation (2.4) calls for the stretching function S to be expressed as a function of the strained time T . When the strain-rate $a(t)$ is constant this leads to the simple linear relationship given by Eq.(2.7). When the strain-rate is not constant, S and T are defined by

$$S(t) = \exp \left(\int_0^t a(t') dt' \right) \quad (A1)$$

$$T(t) = \int_0^t S(t') dt' \quad (A2)$$

and it is not simple to relate them analytically, though it is clear that since S is positive, T is a strictly increasing function of time which can be inverted in principle. It is easy to get the relationship numerically in special cases. As an example, the strain-rate function

$$a(t) = 1 + .5 \sin(2\pi t) \quad (A3)$$

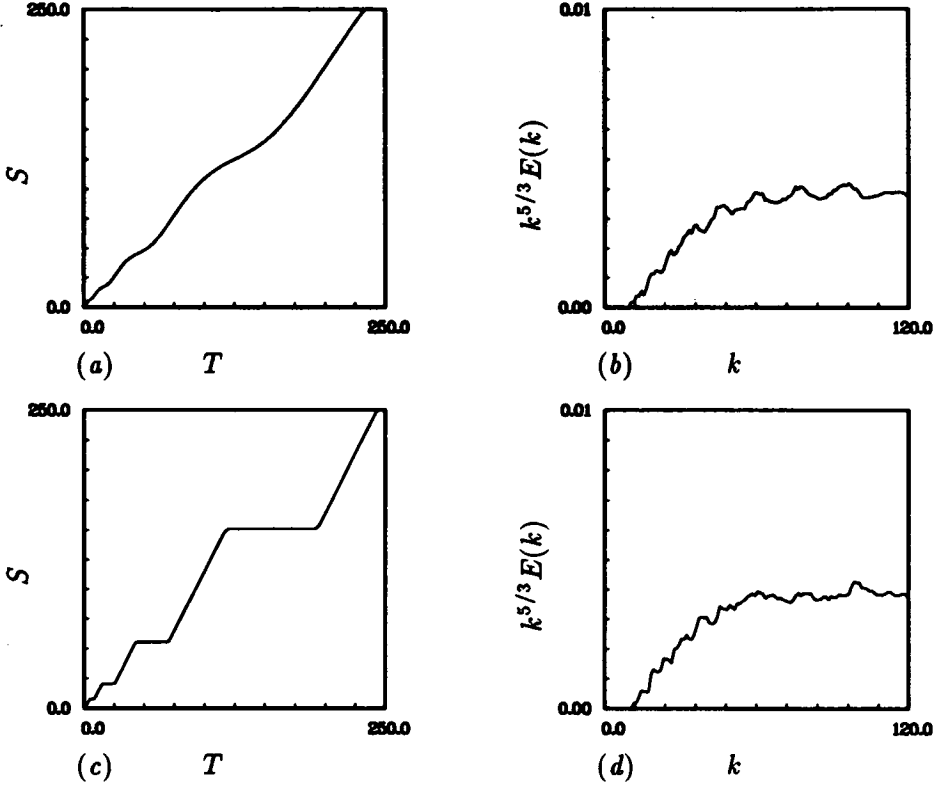


FIGURE 4. Time dependent strain-rate. (a),(b) generated with sinusoidal strain-rate, $a(t) = 1 + .5 \sin(2\pi t)$; (c),(d) generated with on-off strain-rate of same period, $a(t) = 1 + (-1)^{\text{int}(2t)}$.

has average value unity and periodic variations of $\pm 50\%$. During each successive period, the stretch increases by a factor e . These functions have been computed (by solving the pair of differential equations $dS/dt = aS$, $dT/dt = S$) and presented as S vs. T in figure 4a. The relationship is roughly linear. This function was used in Eq.(2.4) to compute the energy spectrum using the analytical spiral solution with the same set-up as for the “series one” computations. The resulting energy spectrum in figure 4b is almost identical with that in figure 1.6 which had constant strain-rate. Therefore, it appears that the spectral results are insensitive to moderate variations in strain-rate.

A more extreme intermittent case was tried in which there are alternating periods of positive strain-rate and zero strain-rate. The function used was

$$a(t) = 1 + (-1)^{\text{int}(2t)} \quad (A4)$$

where the function “int” truncates the decimal part of a number. This strain-rate function has the same period as Eq.(A3) and the same average value. Alternating half-periods have $a = 2$ or $a = 0$. The S vs. T result in figure 4c is still very roughly linear, and the energy spectrum still has the same range of $k^{-5/3}$.

As one increases the frequency of the strain-rate function, the relationship between S and T will become more nearly linear and will have little effect on the spectral result. Lower frequencies could have an effect. In the extreme case of very long on and off periods, one would get either $k^{-5/3}$ or k^{-2} , depending on which period comes first.

REFERENCES

- BUNTINE, J. D. & PULLIN, D. I. 1988 Merger and cancellation of strained vortices. *J. Fluid Mech.* **205**, 263.
- GILBERT, A. D. 1988 Spiral structures and spectra in two-dimensional turbulence. *J. Fluid Mech.* **193**, 475.
- GILBERT, A. D. 1992 A cascade interpretation of Lundgren's stretched spiral vortex model for turbulent fine structure. Private communication.
- LUNDGREN, T. S. 1982 Strained spiral vortex model for turbulent fine structure. *Phys. Fluids* **25**, 2193.
- LUNDGREN, T. S. 1985 The concentration spectrum of the product of a fast bimolecular reaction. *Chem. Eng. Sci.* **40**, 1641.
- PULLIN, D. I. & BUNTINE, J. D. 1989 Interactive dynamics of strained vortices. *Tenth Australian Fluid Mechanics Conference—University of Melbourne*, 9.5.
- PULLIN, D. I. & SAFFMAN, P. G. 1992 On the Lundgren-Townsend model of turbulent fine scales. Submitted for publication.
- SCHWARZ, K. W. 1990 Evidence for organized small-scale structure in fully developed turbulence. *Phys. Rev. Lett.* **64**, 415.
- TOWNSEND, A. A. 1951 On the fine-scale structure of turbulence. *Proc. Roy. Soc. Lond. A* **208**, 534.
- VAN DYKE, M. 1982 *An Album of Fluid Motion*. Stanford, Parabolic Press.
- VINCENT, A. & MENEGUZZI, M. 1991 The spatial structure and statistical properties of homogeneous turbulence. *J. Fluid Mech.* **225**, 1.

52-34 445339
189662

- p. 25
N94-14747

The structure of intense vorticity in homogeneous isotropic turbulence

By J. Jiménez¹, A. A. Wray², P. G. Saffman³ AND R. S. Rogallo²

The structure of the intense vorticity regions is studied in numerically simulated homogeneous, isotropic, equilibrium turbulent flow fields at four different Reynolds numbers in the range $Re_\lambda = 36-171$. In accordance with previous investigators, this vorticity is found to be organized in coherent, cylindrical or ribbon-like, vortices ("worms"). A statistical study suggests that they are just especially intense features of the background, $O(\omega')$, vorticity. Their radii scale with the Kolmogorov microscale and their lengths with the integral scale of the flow. An interesting observation is that the Reynolds number based on the circulation of the intense vortices, γ/ν , increases monotonically with Re_λ , raising the question of the stability of the structures in the limit of $Re_\lambda \rightarrow \infty$. One and two-dimensional statistics of vorticity and strain are presented; they are non-gaussian, and the behavior of their tails depends strongly on the Reynolds number. There is no evidence of convergence to a limiting distribution in our range of Re_λ , even though the energy spectra and the energy dissipation rate show good asymptotic properties in the higher Reynolds number cases. Evidence is presented to show that worms are natural features of the flow and that they do not depend on the particular forcing scheme.

1. Introduction

It is generally agreed that homogeneous isotropic turbulence is approximately described by the Kolmogorov (1941) cascade theory. In particular, the $k^{-5/3}$ energy spectrum and the almost universal scaling of the dissipation range in Kolmogorov variables stand as two of the most successful predictions in fluid mechanics. It has also been known for a long time that this description is incomplete. It was first shown by Batchelor & Townsend (1949) that the statistics of the velocity derivatives are incompatible with an uncorrelated random behavior of the velocity field at scales comparable to the Kolmogorov dissipation limit. This intermittent behavior becomes more pronounced as the Reynolds number increases, and flatness factors ~ 50 have been reported in the atmospheric boundary layer (Van Atta & Antonia, 1980), suggesting that any theory based on uncorrelated gaussian fields might be seriously deficient in the limit $Re \rightarrow \infty$. It has to be stressed that, even in these cases, the energy spectrum remains self similar and agrees reasonably well with Kolmogorov's predictions. Energy, and even energy transfer, are large scale or

1 Center for Turbulence Research

2 NASA Ames Research Center

3 California Institute of Technology, Pasadena

inertial range phenomena and do not seem to be strongly affected by intermittency, while the higher moments are associated with rare, intense, small scale events which do not influence the low order statistics.

It is not a priori clear whether this state of affairs will persist for large Re . Moreover, since experiments at much higher Reynolds numbers than those presently available from geophysical flows cannot be expected in the near future, some sort of theoretical understanding of the intermittent small scales is clearly desirable. In this paper we present new data from numerical isotropic homogeneous turbulence at several Reynolds numbers. Even if numerical constraints restrict our experiments to $Re \leq 200$, it may be expected that the exceptional level of detail that can be derived from numerical simulations might help in the theoretical study of the phenomena.

It was discovered recently that strong coherent elongated vortices (“worms”) are present among the small scales of many turbulent flows (Siggia, 1981, Kerr, 1985, Hosokawa & Yamamoto, 1990, She *et al.*, 1990, Ruesch & Maxey, 1991, Vincent & Meneguzzi, 1991, Douady *et al.*, 1991), and this discovery generated considerable excitement in the turbulence community. One reason for this interest is that, being strong and therefore presumably decoupled from the influence of other flow components, the behavior of the worms should be relatively easy to understand. Should these vortices be found to form an important part of the turbulence phenomenon, their relative simplicity would give us a tool for the analysis of at least some part of the flow. Failing that, if it could be shown that they are nothing but extreme cases of a more general population of weaker vorticity structures, it might still be true that their study contains some clues as to the behavior of those background vortices, which in turn would constitute an important part of the flow. Even if none of these possibilities turns out to be true, the strong vortices are still relatively simple objects submerged in a turbulent flow, and they may be used as probes for the flow structure.

We will show below that, of these three possibilities, the second seems to be the correct one. In terms of integrated quantities, the strong structures constitute a negligible part of homogeneous isotropic turbulent flows, although they are made conspicuous in flow visualizations by their local high intensities. Moreover, their statistical properties are generally similar to those of the background vorticity, and they seem to be just especially intense realizations of the latter. On the other hand, since they are easy to identify and relatively few in number for any given simulation, their behavior can be studied easily and can be extrapolated to a description of the behavior of the background.

2. The numerical experiments

Our observations are made on direct numerical simulations of isotropic homogeneous turbulence in triply periodic boxes at four different Reynolds numbers ranging from $Re_\lambda = 36$ to 170. It is surprising that we are able to find similarity laws spanning the whole range of Reynolds numbers, and that even the lowest Re_λ flow seems to be essentially turbulent. This gives us some confidence that our observations may represent asymptotic trends for high Reynolds number turbulence.

Line	Re_λ	N	L	L/λ	L/η	$\epsilon L/u'^3$	$\omega'T$	t/T	$-S_k$
Chaindot	35.8	64	2.02	2.59	31	1.08	10.0	12.8	0.496
Dotted	62.8	128	1.87	3.54	56	0.83	13.0	5.3	0.503
Dashed	94.5	256	1.31	4.21	80	0.66	16.2	7.6	0.518
Solid	171.5	256	1.62	7.50	193	0.65	29.0	5.9	0.500

TABLE 1. Numerical and flow parameters for the four basic cases analyzed in this paper. t/T is the total run time in eddy turnover units, and S_k is the skewness coefficient. Line types are used consistently in later figures.

The numerical method is fully spectral, using primitive variables \mathbf{u} , p , with dealiasing achieved by a spherical mask and phase shifting (Canuto et al., 1987). The resolution N , given in Table 1, reflects the number of real Fourier modes in each direction before dealiasing. The time stepping procedure is a second order Runge-Kutta for the nonlinear terms and an analytic integrating factor for the viscous ones. The time step is automatically controlled to satisfy the numerical stability condition. Unless stated otherwise, all experiments are forced to achieve a statistically stationary steady state. Forcing is achieved by introducing a negative viscosity coefficient for all the modes with wave numbers $k = |\mathbf{k}| \leq 2$. The Fourier expansion functions are $\exp(ik_j x_j)$, $k_j = 0, 1, \dots, K = N/2$, so that the length of the box side is always 2π . The magnitude of the negative viscosity is adjusted every few time steps so as to keep constant the product $K\eta$, where $\eta = (\nu^3/\epsilon)^{1/4}$ is the Kolmogorov scale. The instantaneous energy dissipation rate, ϵ , is computed in terms of the three dimensional energy spectrum $E(k)$, as

$$\epsilon = \nu\omega'^2 = 2\nu \int_0^\infty k^2 E(k) dk.$$

Other scales used in this paper are the r.m.s. velocity, defined by

$$u'^2 = \frac{2}{3} \int_0^\infty E(k) dk,$$

the integral scale,

$$L = \frac{\pi}{2u'^2} \int_0^\infty k^{-1} E(k) dk,$$

and the Taylor microscale, defined by $\lambda^2 = 15\nu u'^2/\epsilon$. The microscale Reynolds number is defined as $Re_\lambda = u'\lambda/\nu$, and the large eddy turnover time as $T = L/u'$ (Batchelor, 1953).

Table 1 summarizes the characteristics of the different runs. Each of them was continued sufficiently long for the instantaneous spectra and other integral characteristics to become statistically steady. This typically took a few large eddy times,

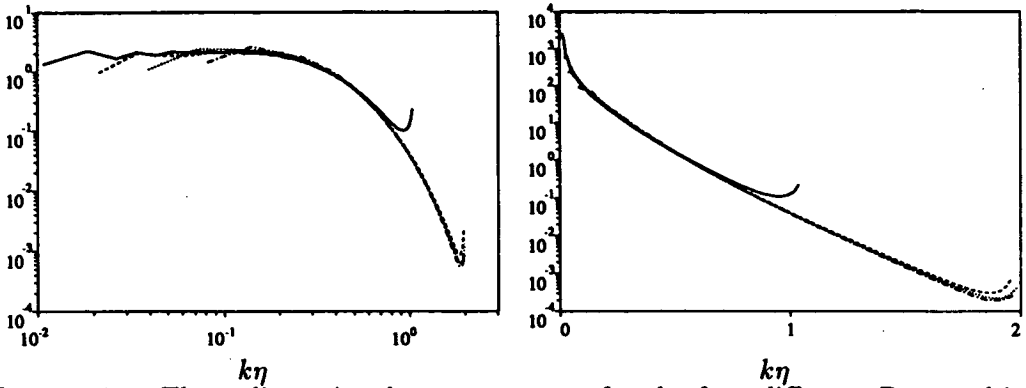


FIGURE 1. Three dimensional energy spectra for the four different Re_λ used in this paper. Left: $\epsilon^{-2/3} k^{5/3} E(k)$, to enhance inertial range. Right: $\epsilon^{-2/3} \eta^{-5/3} E(k)$, to display the dissipation range. For symbols see table 1.

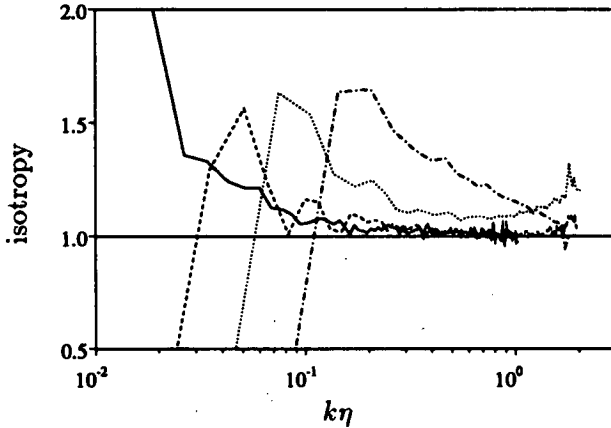


FIGURE 2. Isotropy coefficient for different Reynolds numbers, defined in eq. (1) in text. Symbols as in table 1.

which may not be long enough to guarantee absolute statistical steadiness for the large scales, but which should be enough for the small scales to reach equilibrium. The quantities in table 1 and the spectra in the following pages are averages over whole flow fields and over periods of time that vary between 0.25 and 6 large eddy turnover times. The shorter averaging times correspond to the highest Reynolds numbers. The histograms presented later in the paper are spatial statistics, further averaged over 3 to 5 different moments in time. The variation between the averaged spectra and their instantaneous values was smaller than 1%, but larger deviations were observed in the extreme tails of the histograms.

Note that the dimensionless energy dissipation $\epsilon L/u^3$ decays slowly with Re_λ but stabilizes around 0.65 in the last two cases. This is consistent with the behavior observed by Sreenivasan (1984) in a compilation of data from grid turbulence, in which the dissipation stabilizes above approximately $Re_\lambda > 60$. His asymptotic value of the dissipation, $\epsilon L/u^3 \approx 1$, is different from ours, but this is not too surprising since

the integral scale is dominated by the large eddies, which are presumably different in the two cases.

The statistics of the small scale intense regions are sensitive to the numerical resolution. After some experimentation, it was found that $K\eta = 1$ was the absolute minimum needed for convergence of the velocity gradients histograms, and that $K\eta = 2$ was very desirable. We tried to maintain this latter resolution uniformly, but it was not possible to do so for the highest Reynolds number case during the time limits of the summer school. In the experiments presented here, this case is only resolved to $K\eta = 1$.

Three dimensional, shell averaged, energy spectra for the three cases are presented in figure 1. The two cases with the highest Re_λ show a short "inertial" range with a power decay close to $k^{-5/3}$. No such interval is present at the lowest Re_λ , but the collapse of the dissipation range is satisfactory. Figure 2 displays an isotropy coefficient, defined by

$$\frac{E_{11}(k_1) - k_1 \partial E_{11}(k_1) / \partial k_1}{2E_{22}(k_1)}, \quad (1)$$

where E_{11} and E_{22} are the longitudinal and transverse one dimensional spectra. This quantity should become equal to 1.0 for an isotropic field (Batchelor, 1953), and it does so approximately for the small scales in the two high Re_λ cases, suggesting that they have attained equilibrium. The two cases with lower Reynolds numbers do not satisfy isotropy, and this is true as much for individual realizations as for averages over fairly long times, although the direction of the deviation is different for different realizations. This lack of isotropy is probably due to the relatively low number of structures contained in such low Reynolds number flows.

In summary, the flows used in this paper seem to be typical of experimental approximations to homogeneous isotropic turbulence. It is particularly important to note that the two highest Reynolds numbers display a short $k^{-5/3}$ inertial range and appear to have reached the asymptotic regime in which energy dissipation becomes independent of the Reynolds number.

3. Worms

Implicit in the Kolmogorov (1941) model for the turbulent cascade is the idea that the small scales of turbulence are fully controlled by the viscosity ν and by the energy dissipation rate $\epsilon = \nu\omega'^2$. This and the dimensional arguments of the original theory imply that the velocity gradients should reach some asymptotic statistical distribution as $Re \rightarrow \infty$, whose single scale should be ω' . Evidence that this is not so has accumulated over the years, starting with the measurements of higher statistical moments mentioned earlier and more recently in the form of increasingly non-gaussian histograms obtained from numerical experiments at increasing Reynolds number (Siggia, 1981, She *et al.*, 1990, Vincent and Meneguzzi, 1991, Ruetsch & Maxey, 1991). We will concentrate here on the statistics of the quantities appearing directly in the vorticity equation,

$$\frac{d|\omega|^2/2}{dt} = \omega_i S_{ij} \omega_j + \nu \omega_i \nabla^2 \omega_i, \quad (2)$$

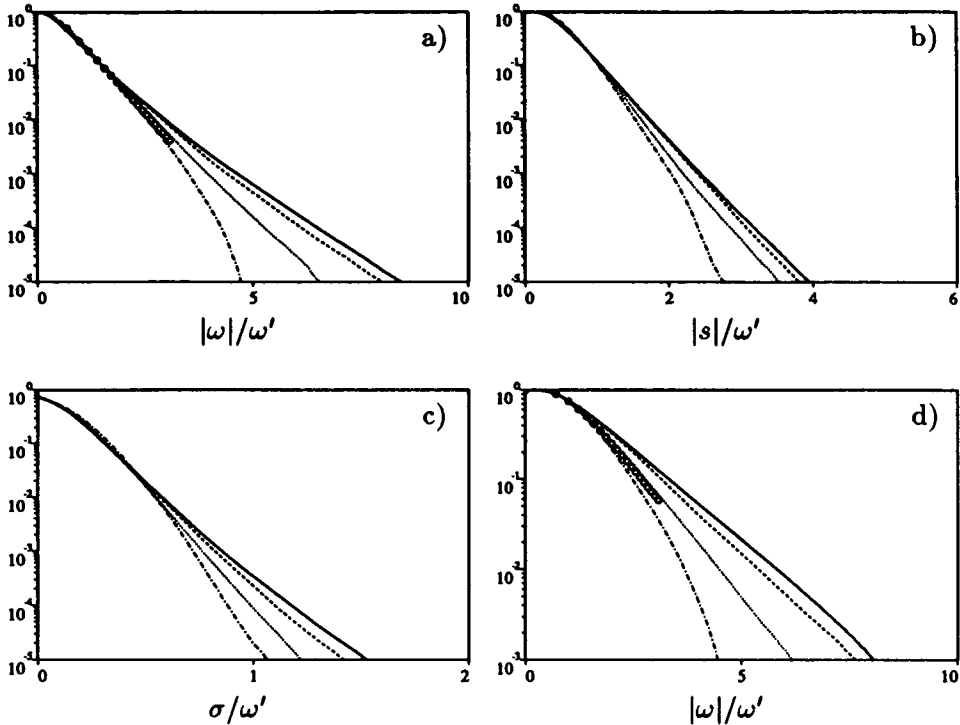


FIGURE 3. One dimensional histograms of the volume fraction occupied by points above a certain threshold. (a) Vorticity, (b) Strain, (c) Stretching. (d) Fraction of total enstrophy associated with points above a given vorticity magnitude. Lines as in table 1. Open circles are from (Ruetsch & Maxey, 1991) at $Re_\lambda = 62$.

where $|\omega| = (\omega_i \omega_i)^{1/2}$ is the vorticity magnitude, and $S_{ij} = (\partial u_i / \partial x_j + \partial u_j / \partial x_i) / 2$ is the rate of strain tensor. In particular, we will be interested in the statistics for $|\omega|$, $|s| = (S_{ij} S_{ij})^{1/2}$, and

$$\sigma = \frac{\omega_i S_{ij} \omega_j}{|\omega|^2}.$$

The square of the total rate of strain, $|s|$, is proportional to the local dissipation, but it does not appear explicitly in equation (2). It is probably more a consequence of the events that lead to turbulence than their cause. The quantity σ is the part of the strain which is aligned to the local vorticity, and it is the one doing the stretching of the vortex lines in equation (2). Its mean value is related to the skewness of the velocity derivatives.

One dimensional histograms for the volume fraction occupied by values of these three variables above a given threshold are given in figure 3. They are all far from gaussian, except perhaps for the lowest Reynolds number, and show few signs of converging to a limit distribution for large Re_λ . Note, however, that the variable tails involve only relatively small fractions of the total volume. The figure also contains a histogram for the fraction of the total enstrophy contributed by points with a vorticity magnitude above a given threshold. Even if the decay of this



FIGURE 4. Vortex lines for homogeneous isotropic turbulence, $Re_\lambda = 209$. Length of z -axis $\approx 100\eta$. Left: Only $0.2\omega' < |\omega| < \omega'$; Right: Only $|\omega| > \omega'$; Vortex lines are the same in both sets.

histogram is slower than that of the volume fraction, most of the enstrophy is still contained in a relatively “weak” background where $|\omega| \approx O(\omega')$. In fact, for the Reynolds numbers of our simulations, the contribution of the intense tails to the integrated value of any of the low order statistics of the flow is only a few percent, although they would clearly dominate sufficiently high order moments. Similar results were obtained by Ruetsch and Maxey (1991) at $Re_\lambda \approx 60$ (see fig. 3).

The conclusion from these histograms is that most of the volume in the flow is occupied by relatively “weak” vorticity with strong vortices filling only a small fraction of the space. The structures of the weak and strong vorticities are also very different. Figure 4 shows a collection of vortex lines passing through randomly chosen points on the middle plane of a subset of a high Re_λ simulation and continuing until they leave the cube. The vortex lines are exactly the same in both cases, but in the left hand side of the figure they are only displayed where $0.2\omega' \leq |\omega| \leq \omega'$, while in the right hand side they are displayed where $|\omega| \geq \omega'$. While there is little apparent structure in the low intensity component of the flow, the strong vorticity tends to be organized in tubes or ribbons, which are the “worms” reported in previous experiments. It is remarkable that this seems to be true even at a threshold, ω' , which is much lower than the one used in most previous reports, and which still contains most of the total enstrophy.

For the rest of the paper, we will arbitrarily define *weak* vorticity as that having

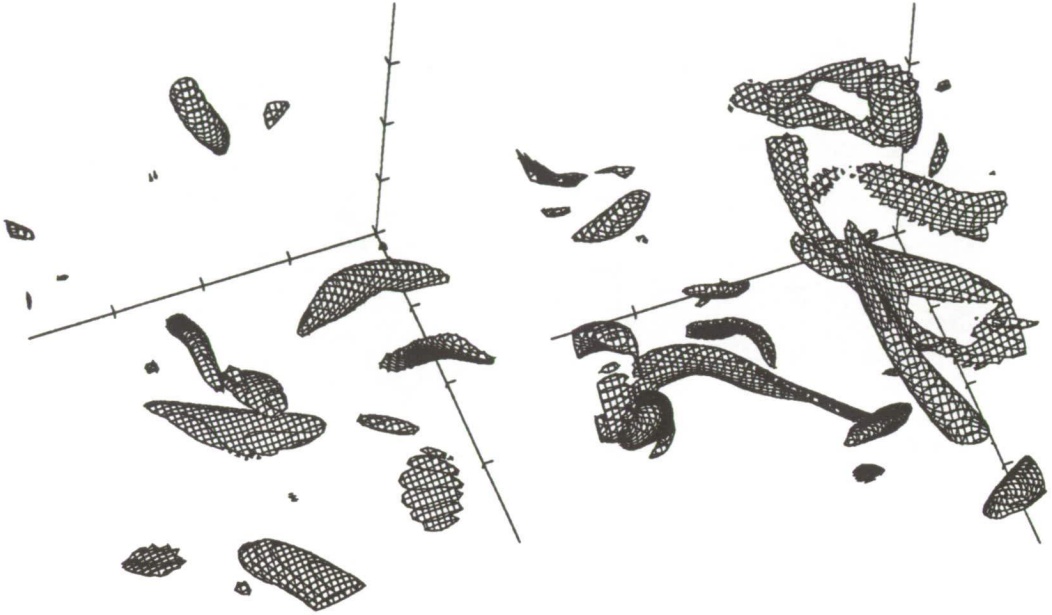


FIGURE 5. Intense vorticity isosurfaces, $|\omega|/\omega' \geq 2.5$, at two different Reynolds numbers. Resolution is similar in both subsets, with the length of each axis $\approx 100\eta$. Left: $Re_\lambda = 63$, integral scale $L = 56\eta$. Right: $Re_\lambda = 95$, $L = 80\eta$. Thresholds are chosen so that worms contain about 1% of total flow volume.

$|\omega| < \omega'$, *intense* vorticity, or *worms*, as that above a threshold covering 1% of the total volume, and *background* vorticity as that above ω' but weaker than the intense threshold. This definition of worms results in pictures roughly comparable to those of previous experimenters and is about as low as the threshold can be taken before the visual complication becomes overwhelming. Figure 4 shows that the organization in coherent structures is still present at the background level. At the Reynolds number of the figure, the vorticity above ω' fills 25% of the volume and accounts for 80% of the total enstrophy, while intense vorticity fills 1% of the volume and accounts for 15% of the enstrophy.

The length of the horizontal (z) axis in figure 4 is one eighth of that of the whole cube and one half of the integral scale of the flow. Some ribbons are seen to span the whole subset, although not with uniform intensity, and they may appear disconnected in plots of the high enstrophy worms. Long intense worms, comparable to the integral scale, are found occasionally.

The shape of the regions of highest vorticity (1%) is displayed in figure 5 at two different Reynolds numbers. In agreement with previous reports, they are shown to be either cylindrical vortices or ribbons of various widths. Although no real statistical analysis was made, the impression from different fields is that sheets and ribbons are predominant at low Reynolds numbers, while cylindrical vortices dominate at high Re_λ . This is apparent in figure 5 and is consistent with the idea that the worms are the result of stretching by strains which are generally not axisymmetric.

If a generic strain is applied to a weak vorticity blob, the vorticity component along the most extensional eigenvector is amplified most, but the other two principal strains remain active and try to stretch or compress the vortex unequally along the two equatorial axes. As the axial vorticity becomes stronger, it dominates the local flow and its rotation tends to make the vortex axisymmetric. The result is a vortex of elliptical cross section whose eccentricity becomes smaller as the ratio of the axial vorticity to the driving strain becomes larger. It will be shown later that the strain is generally $O(\omega')$, while it is clear from figure 3 that vortices in higher Reynolds number flows attain larger vorticities. This, together with the previous argument, explains their more circular cross sections.

The spatial distribution of the worms is not uniform, although this is difficult to see in graphical representations of large subsets. Figure 6 displays a thin slab across a complete flow field. The worms are seen to lie on the borders of large scale velocity eddies, the energy containing scales, which are themselves relatively free from vorticity. This is even clearer in figure 7, which represents the mid-plane of the slab in the previous one. The light colored regions in this figure mark the background vorticity, $|\omega| > \omega'$. The darker regions are the worms, which are seen to be embedded in the background of which they constitute the local maxima. The large eddies themselves are mostly free even from background vorticity.

4. Truncated fields

Even if the results in the previous section suggest that, at least at these Reynolds numbers, the worms contribute relatively little to the turbulent statistics, it is conceivable that they may be important indirectly in some other respect. There is also the possibility that the worms themselves may be spurious effects of the forcing method and that they would not be present in "natural", decaying turbulence.

To clarify these points, we have carried out a series of experiments in which the worms are artificially removed from a flow and in which both the properties of the truncated field and those of the isolated worms are studied independently. Consider a flow field given by a velocity $\mathbf{u}(\mathbf{x})$ and a vorticity $\omega = \text{rot } \mathbf{u}$. We wish to generate a new field $\mathbf{u}_>$, associated just with the worms, by eliminating the vorticity at points where its magnitude is smaller than a given threshold, $|\omega| \leq \Omega$. This field cannot be constructed by just zeroing the vorticity of the original flow at the desired points. The resulting vortex lines would not be closed, and no velocity could be constructed. Consider the naively truncated field

$$\omega_o = \omega \quad \text{if } |\omega| > \Omega, \quad \omega_o = 0 \quad \text{otherwise.} \quad (3)$$

This field is generally not solenoidal, $\text{div } \omega_o \neq 0$. We define the worms as the field $\omega_> = \omega_o + \Delta$ such that $\text{div } \omega_> = 0$ and such that the extra enstrophy $\int |\Delta|^2 d\mathbf{x}$ is as small as possible. Note that vorticity of this field is not strictly zero outside the worms, but that the construction guarantees that the undesired residual is a minimum. It follows from straightforward variational analysis that $\Delta = -\nabla\lambda$, where the scalar λ satisfies $\nabla^2\lambda = \text{div } \omega_o$.

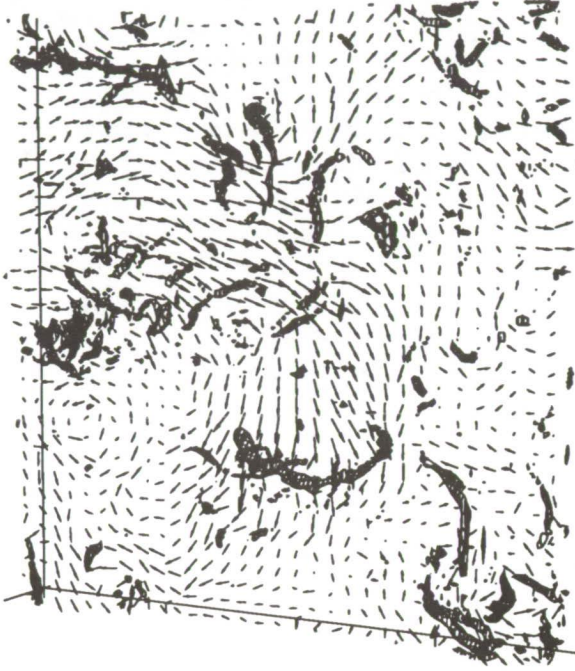


FIGURE 6. Intense vorticity regions $|\omega| > 2.7\omega'$, and velocity field, $Re_\lambda = 209$. Size of the display domain, $(800^2 \times 50)\eta$, periodic in the two long directions. Velocity vectors correspond to points in the mid plane.

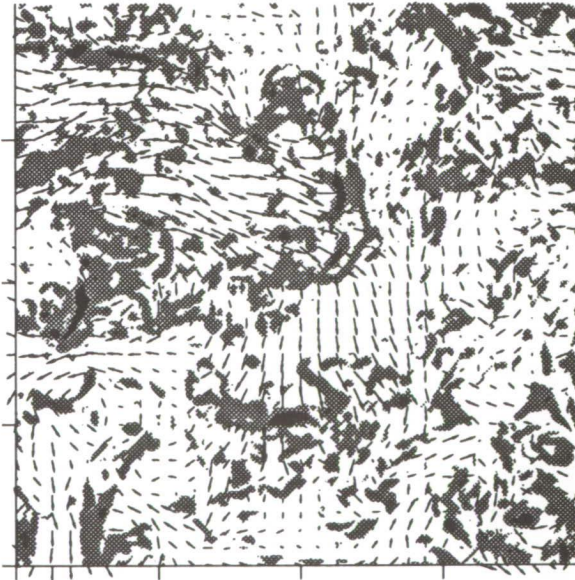


FIGURE 7. Background vorticity $|\omega| > \omega'$ (light gray), at center plane in figure 6, in relation to darker intense regions, $|\omega| > 2.7\omega'$. Vectors are velocity.

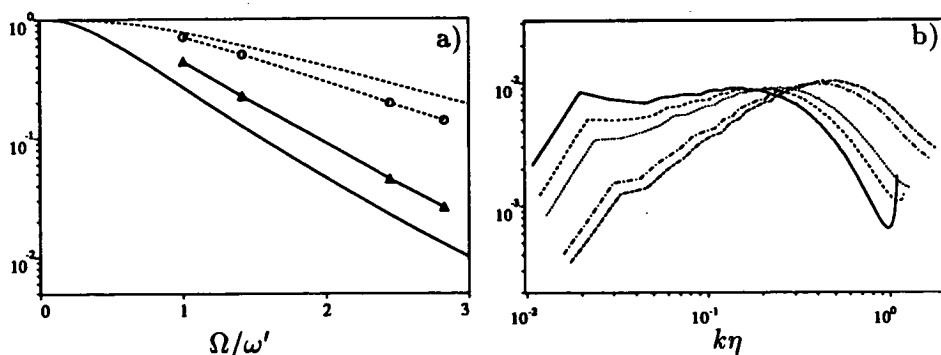


FIGURE 8. Effect of the truncation threshold on the worm fields truncated to $|\omega| > \Omega$ as described in text. (a) Simple solid line: volume fraction above vorticity threshold in original field. Dashed: enstrophy above threshold. Dashed with circles: Enstrophy of truncated field, as fraction of original. Solid with triangles: Kinetic energy of truncated field. (b) Enstrophy spectra. Threshold in order of decreasing enstrophy at low wave numbers: Ω/ω' : 0., 1., 1.41, 2.45, 2.83. $Re_\lambda = 209$.

Note that the new field is nothing but the solenoidal projection of ω_0 and that a velocity can be computed from it.

The effect of this truncation is shown in figure 8a, which displays both the enstrophy and kinetic energy of the truncated worm fields as a function of the threshold as well as the volume and enstrophy associated to regions of the original field whose vorticity is above that threshold. It is seen that the effect of the projection is to decrease only slightly the enstrophy contained in the worms. A visual check of the corresponding enstrophy isosurfaces confirms that the intense regions in the truncated field correspond to those of the original one but that the vorticity in the background has been mostly eliminated. The energy of the truncated flow is always small, roughly proportional to the volume occupied by the worms themselves. There seems to be no appreciable local enhancement of the kinetic energy because of the presence of the worms. This is confirmed by inspection of the velocity fields in figures 6 and 7.

Similar experiments on the truncated background fields, resulting from the removal of the vorticity above a given threshold, reveal a complementary effect. The effect of removing the worms is small, both on the enstrophy and on the energy, and it only becomes appreciable when the truncation threshold is made comparable to ω' .

In addition, no particular part of the energy spectrum seems to be especially associated with the worms. Figure 8b displays enstrophy spectra, $2k^2 E(k)$, for the high vorticity component at different truncation thresholds, each of them normalized by its own Kolmogorov scaling. The spectrum of the original field is consistent with an inertial range, $E(k) \sim k^{-5/3}$, while that of the high intensity worms is close to $E(k) \sim k^{-1}$, but the effect is gradual, proportional to the removal of the total kinetic energy. The latter spectrum was shown by Townsend (1951) to be that of a random array of vortex tubes of uniform radii and is, therefore, consistent with the

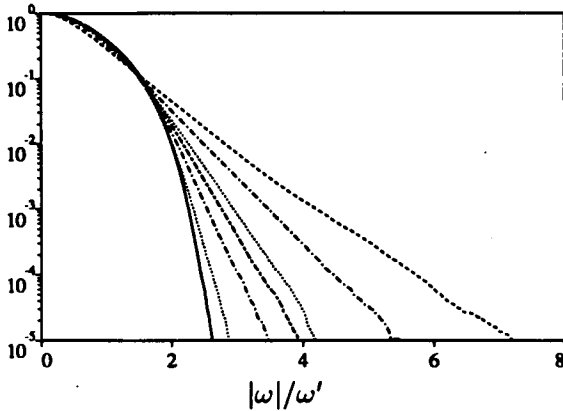


FIGURE 9. Time evolution of the histograms of volume fraction above a given vorticity threshold, during decay of a flow field initially truncated to $|\omega| < 1.5\omega'$. $Re_\lambda = 96$. Decay time, left to right: $u't/L = 0, 0.019, 0.037, 0.056, 0.073, 0.158$. All normalizations refer to the initial field before truncation.

general structure of the worms.

Since the integral of the dissipation is proportional to that of the enstrophy, the effect of removing the worms, which contain only a small percentage of the latter, is not expected to have a large effect on the decay of the kinetic energy of a turbulent field. This was tested directly by comparing the evolution of the decay of identical initial conditions with and without the worms removed. An equilibrium field was generated ($Re_\lambda = 96$), and the forcing was removed to initiate a decay. The same initial conditions were truncated to $|\omega| < 2.5\omega'$ and left to decay. The behavior of the energy in both cases was almost identical when normalized with the initial enstrophy of each field. The enstrophy of the truncated field decayed initially faster but, after a short transient during which it decayed by about 7%, it also behaved similarly to that of the equilibrium initial condition. The difference in the total enstrophy of the initial fields at this truncation level was 20%.

A more severe truncation was applied to check whether the presence of the worms could be somehow associated with the forcing scheme. The same flow field as in the previous experiment was truncated to $|\omega| < 1.5\omega'$ and left to decay. Figure 9 shows the time evolution of the volume fraction histograms. It is clear that, after a short time, the worms reappear even in the absence of forcing. This was checked directly by visualization.

It follows from these experiments that the worms are a natural product of the evolution of turbulent flows, both forced and decaying, and that their importance in the dynamics of turbulence is only proportional to the magnitude of their integrated quantities with respect to those of the whole flow. They do not seem to play any special role besides that which corresponds to the energy and enstrophy that they contain. At the Reynolds numbers of our experiments, both are small fractions of the total.

An interesting observation is that the skewness coefficient of the truncated worm

fields, those formed only by the high intensity regions, was always negative and roughly of the same order as that of the full turbulent field ($S_k = -0.5$ to -1.0). The high intensity regions are still straining each other, and they would be capable of generating new enstrophy, although the relatively low kinetic energy that they contain means that the Reynolds number of the truncated flow is low and that the viscous diffusion would dominate before any appreciable evolution is possible.

5. The dynamics of worm formation

Even if the worms do not seem to have a special function in the overall dynamics of turbulent flows, the process by which they are formed is interesting in itself. Moreover, since they appear to be part of the general $O(\omega')$ background vorticity, we may look at them as particular cases of the evolution of that component, which is responsible for most of the turbulent dissipation. Finally, since they do not scale correctly in Kolmogorov variables (i.e. the histograms do not scale with ω'), their generation mechanisms might point to some deficiency in the standard cascade theory, especially as $Re_\lambda \rightarrow \infty$.

Qualitatively, it is clear that strong vortex regions have to be formed by straining of weaker vorticity. No other mechanism is available, away from no-slip walls, for the production of enstrophy. Strain itself is generated by the vorticity, and the process may become nonlinear. It has been realized for some time that nonlinear self interaction of vorticity can, in principle, lead to a singularity of the inviscid equations in finite time and that it may therefore be invoked to explain the generation of vorticity of almost any magnitude.

Some orders of magnitude might be relevant at this point. If we apply a strain α to a viscous fluid, the smallest flow features that we may expect to generate are of the order of the Burgers' radius, $\delta = (\nu/\alpha)^{1/2}$. There are two "natural" straining scales in turbulence: the strain generated by the large eddies, $1/T = u'/L$, and the inverse of the Kolmogorov time scale, which is equal to the r.m.s. vorticity $\omega' = (\epsilon/\nu)^{1/2}$. The Burgers' radius for the former is the Taylor microscale λ , while that for the latter is the Kolmogorov η . Moreover, if we think of a cylindrical equilibrium Burgers' vortex generated by a strain α , its peak vorticity would be $\omega_{\max} \sim Re_\gamma \alpha$, where $Re_\gamma = \gamma/\nu$ is a vortex Reynolds number based on its total circulation. If we assume, e.g. on stability grounds, that Re_γ cannot be larger than a given limit independent of the applied strain, the peak vorticity should never be more than a fixed multiple of the strain.

We have evidence in the histograms in figure 3 that some component of the turbulent flow contains peak vorticities that increase with Reynolds number faster than ω' . From the previous discussion, this implies either that there exist stretching motions which are stronger than ω' or that there exist vortices whose Re_γ grows larger as Re_λ increases. The first possibility implies that we should find structures whose transverse scale is smaller than η and that this discrepancy should increase with increasing Re_λ . This contradicts the relatively good collapse of the energy spectra in the dissipation range, expressed in Kolmogorov variables, although some weak effect can not be ruled out from the experiments. The second possibility raises

Re_λ	ℓ/L	R/η	$Re_\gamma/Re_\lambda^{1/2}$	N_w
35.8	3.16	4.22	21.1	26
62.8	2.60	4.16	17.0	32
94.5	3.15	4.16	18.1	14
171.5	2.88	4.61	21.1	15

TABLE 2. Average worm parameters as identified by the tracking algorithm defined in the text. N_w is the number of worms in each sample, ℓ their average length, and R their radius.

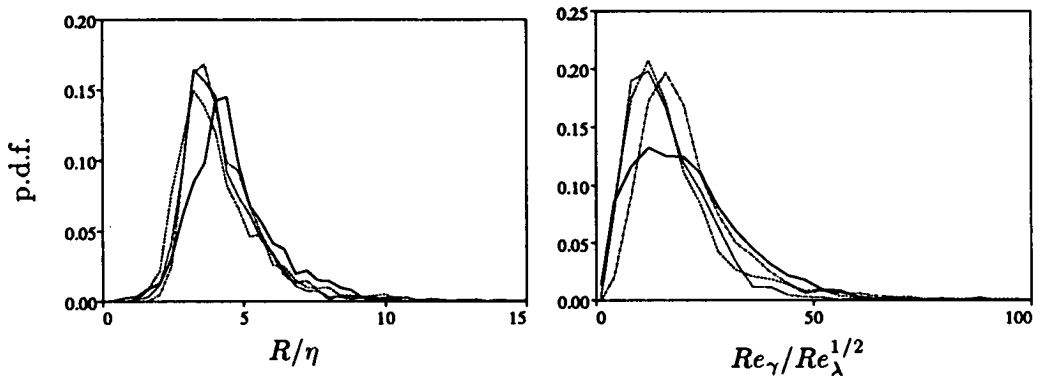


FIGURE 10. Probability density functions for worm radii and circulations at four different Reynolds numbers. Symbols as in table 1. Normalization has been chosen so as to optimize collapse.

the question of how such high Reynolds number vortices remain stable long enough to form.

To answer this question, we undertook a statistical investigation of the dimensions and circulation of the intense vorticity structures. Most of the previous investigators who have treated this subject give their radii as a few Kolmogorov scales and their lengths as being of the order of the integral scale. A survey including some new measurements of radii and intensity is contained in Jiménez (1991). It was concluded that, for the available flow fields, the average radius was approximately $3-5\eta$, and $Re_\gamma \approx 150-400$. It was noted, however, that most of the data had $Re_\lambda \approx 100$ and that no reliable scaling trend could be deduced. We believe that the present investigation is the first one in which enough data sets with uniform resolution and overall quality have been collected over a wide enough range of Reynolds numbers to allow for some scaling information.

An automatic tracking algorithm, described in detail in the appendix, was implemented and applied uniformly to all the data fields. Briefly, a point in the worm axis is identified as a vorticity maximum, and the axis is followed until either its

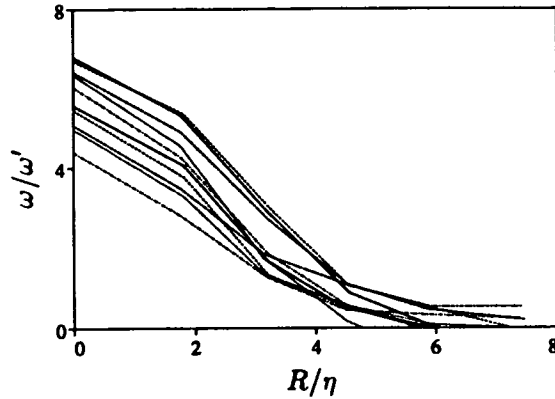


FIGURE 11. Radial vorticity distribution for different cross sections along a typical worm. $Re_\lambda = 62.8$.

peak vorticity falls below ω' or until the worm closes into itself or intersects a previously known one. At each point in the axis, the vorticity in a normal plane is averaged azimuthally, and the resulting radial distribution is fitted to a gaussian. The local radius of the worm is defined as the $1/e$ radius of the gaussian, and the circulation as that of the fitted distribution. It was, unfortunately, impractical to continue this process until no more worms could be found, and the samples used here represent what could be achieved in a fixed amount of computer time (3 hours). A rough estimate of the total volume of the worms in the sample compared to the volume occupied by vorticity above ω' suggests that the sample contains most of the worms in the lowest Reynolds number case, but only about 1% of them in the highest one. Average values of worm length, radius, and circulation are given in table 2. A comparison with the range of scales in table 1 is enough to show that the normalizations chosen here are fairly robust, at least in this range of Re_λ , and that other choices would lead to significant trends. In particular, the worms radii scale with η and their lengths with the integral scale L , and their circulation increases as $Re_\lambda^{1/2}$.

The trends of the radii and circulations are consistent with those observed in Jiménez (1991) for the intense longitudinal vortices in the wall region of a turbulent channel. It was shown there on the basis of rather limited data that the radii of the vortices scale well in wall units, within a range of Reynolds numbers $Re_\tau = 100$ –200. The circulations, however, do not remain constant, and increase by almost a factor of two in the same range. Since wall units are the near wall equivalent of Kolmogorov scaling, those trends are equivalent to the ones observed here. In the same spirit, the recently established tendency of turbulent fluctuations to increase with Re_τ beyond their dependence in wall units (Wei & Willmarth, 1989) can be considered as related to the failure of Kolmogorov scaling in figure 3.

Actual probability density distributions of radii and circulations are given in figure 10 and a sample of azimuthally averaged vorticity profiles across a typical worm is given in figure 11, showing that the gaussian model is at least reasonable. This

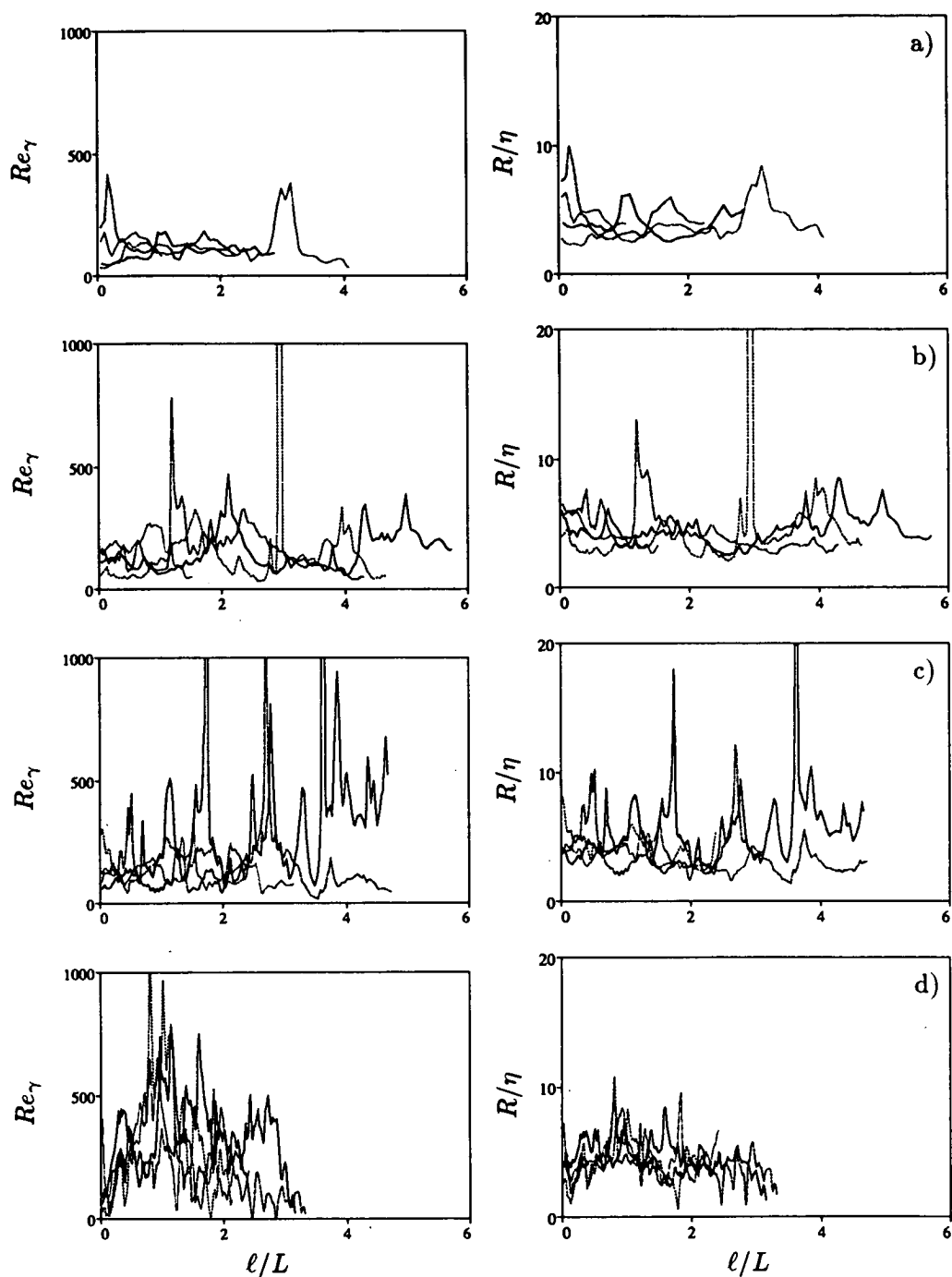


FIGURE 12. Distribution of normalized radii and circulations along worm axes as function of arc length ℓ . Each figure contains four worms chosen at random. (a) $Re_\lambda = 35.8$, (b) 62.8 , (c) 94.5 , (d) 171.5 .

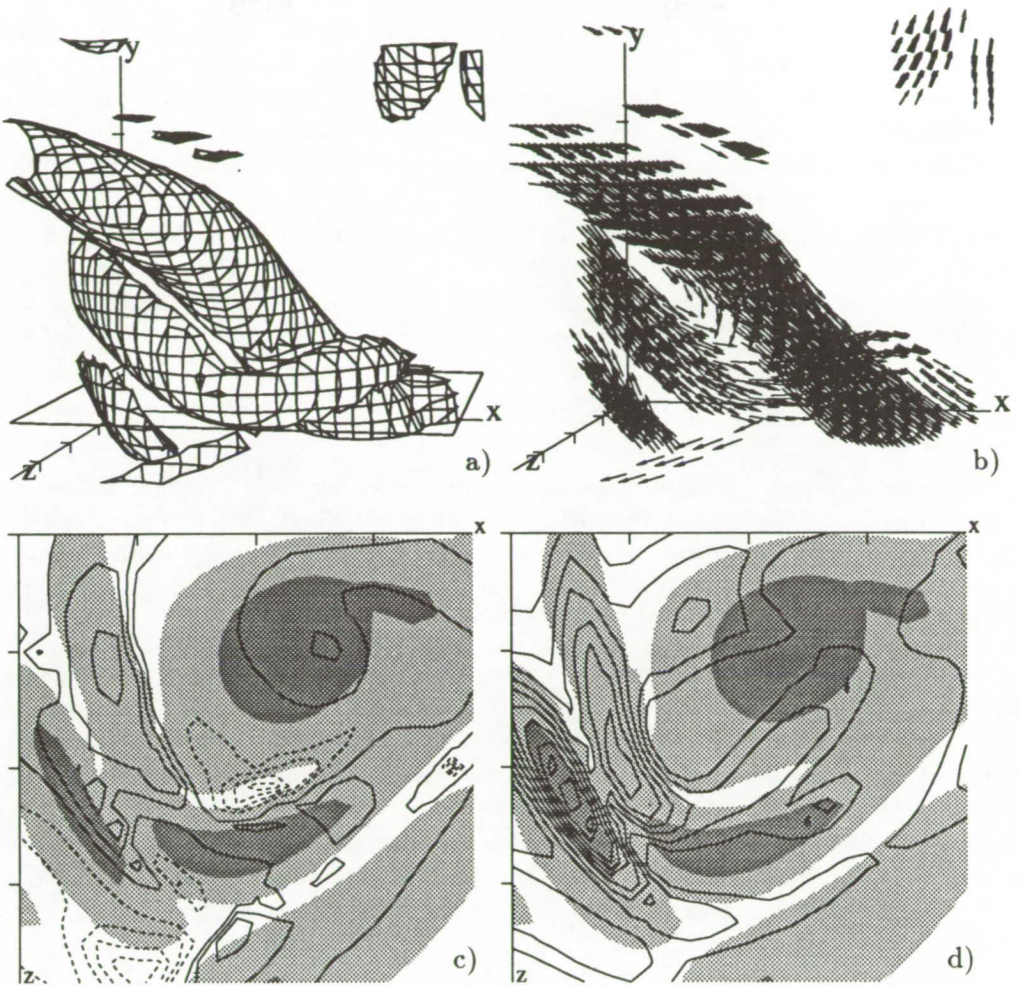


FIGURE 13. Portrait of a worm interaction, identified by a local maximum of the stretching term σ . $Re_\lambda = 94.5$. Length of axes, approximately 40η . (a) Intense vorticity isosurfaces, $|\omega| = 2.8\omega'$. (b) Vorticity vectors within the surfaces in (a). Vector lengths are proportional to vorticity. (c) Stretching and vorticity magnitude in the horizontal plane outlined in (a). Isolines are σ at $0.2\omega'$ increments; negative contours, dashed; zero contour not shown. Light gray, $\omega' < |\omega| < 2.8\omega'$. Dark grey, $|\omega| > 2.8\omega'$. (d) Same as (c), but isolines are strain magnitude $|s| > \omega'$ at $0.2\omega'$ intervals.

model is consistent with that of an axially stretched equilibrium Burgers' vortex. The distributions of radii and circulation along the length of a few typical worms is given in figure 12 for the four different Reynolds numbers. It is difficult to extract general trends from this figure and the number of actual coherent worms in each field is not enough to allow for rigorous statistics, but the most striking feature in these traces is the increase in complication as the Reynolds number increases.

Since we know from the previous analysis that an increase in Re_λ implies an increase in the Reynolds number of the vortices themselves, this is not surprising. It just means that, as their Reynolds number increases, the worms themselves are becoming turbulent, and it is an interesting question whether at high enough Re_λ they would retain enough coherence to be identified as separate objects. This question can not be answered directly here, but some analysis is possible on the type of complexity which is being added by increasing the Reynolds number. It is clear from figure 12 that the circulation traces are noisier than those of the radii. Part of the noise is doubtlessly due to detection problems, but the difference between the two sets of measurements is probably true. Since the circulation of a coherent vortex, defined as a fixed set of vortex lines, is constant along its length, the peaks in the circulation traces can be interpreted as interactions with other vortices, and it is the number of interactions that appears to increase with Re_λ .

Interactions between adjacent worms are indeed common in the flow fields and can often be found by looking for "active" spots in which either the vorticity or the stretching are especially large (see figure 13). Interactions between strong vortices and weaker vorticity are still more common, and they do not usually result in the destruction of the stronger partner.

The question of what is the origin of the stretching that generates the worms has still not been addressed. Figures 14 and 15 show two dimensional joint probability density functions for vorticity magnitude and strain. Figure 14a compares total strain $|s| = (S_{ij}S_{ij})^{1/2}$ with vorticity magnitude. It is clear from the figure that there is a correlation between these quantities, even if a rather weak one. Strong vorticity coexists with strong strain either because strong vortices generate high strains or because they are generated by them. That alternative is addressed in figure 14b, which compares vorticity magnitude with the stretching term σ . This histogram shows that the highest stretching rates are not associated with regions of high enstrophy, but with the background vorticity $O(\omega')$. In fact, the stretching associated with the highest enstrophy regions is fairly low and seems to scale well with ω' , with little evidence of self stretching by the strongest structures. This apparent lack of correspondence between the behavior of the total strain and of the stretching component is also clear in figure 15, which compares both quantities. Although there is clearly a correspondence between strong strain and large stretching in the sense that strong stretching or compression is associated more often with strong strains than with weak ones, the correspondence is only moderate, and the distribution of the ratio $\sigma/|s|$ is broad, peaking at low values rather than near the extremes. This ratio can be shown to be kinematically limited to the interval $\pm(2/3)^{1/2}$, which accounts for the sharp lateral cutoffs in the histograms in figure 15, but, within those limits, σ and $|s|$ are only weakly correlated. Strong strain does not necessarily mean strong compression or stretching, and the direction of the principal axis of the strain tensor seems to be relatively independent of the local vorticity direction. This is also seen in figures 13c-d, in which the total strain and the stretching terms are plotted independently. The total strain (fig. 13d) is relatively well correlated with the presence of strong vorticity, but the stretching

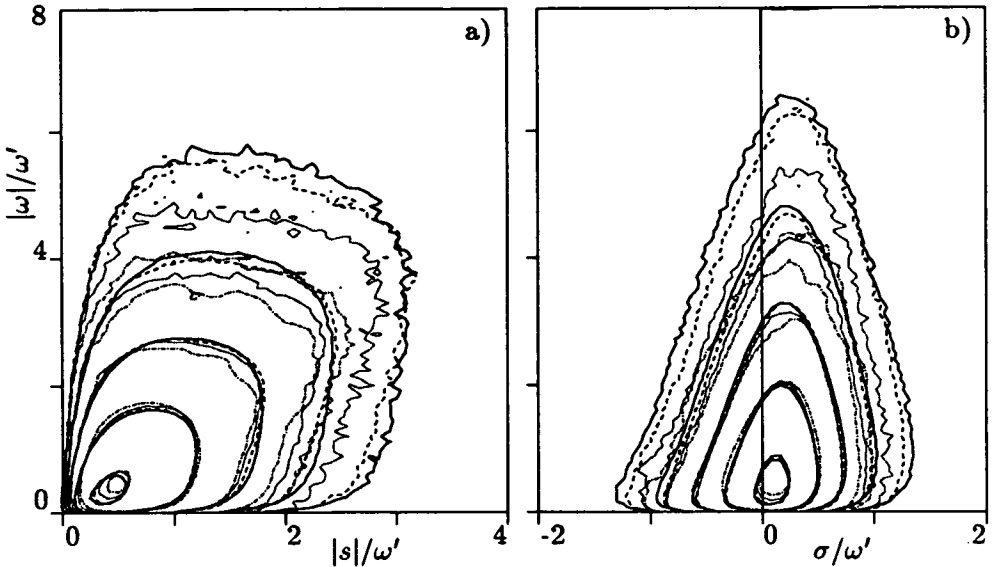


FIGURE 14. Joint probability density functions of strain magnitude and stretching versus vorticity magnitude. All values are normalized with ω' . Density contours are logarithmic and spaced by a factor of 10. Lines as in table 1.

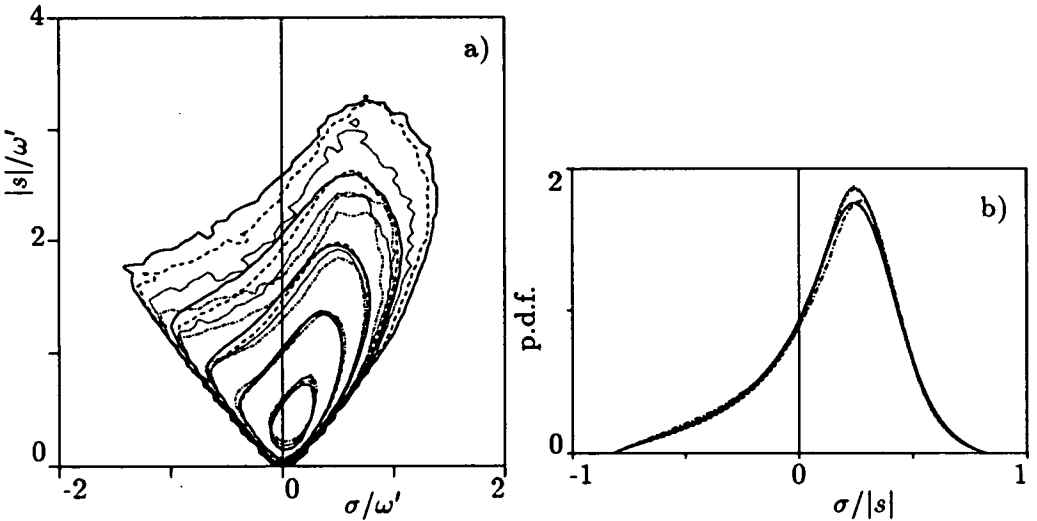


FIGURE 15. (a) Joint probability density functions of stretching versus strain magnitude. (b) Univariate probability density function of $\sigma/|s|$.

is much more randomly distributed, and both strong compressions and extensions are present close to each other. Plots of σ over larger sections of the flow field reveal a spotty distribution with a tendency to concentrate on the periphery of background (or intense) vorticity but not on its interior. Apparently, once vorticity gets stretched to a high enough amplitude, it decouples from the original strain field

and loses its orientation relative to it.

All this is consistent with the result obtained by previous investigators that there is little preferential alignment of the vorticity with the strongest strain axis at low vorticity magnitudes and that the alignment is to the intermediate (weakest) strain eigenvector in the intense regions (Ashurt *et al.*, 1987).

It is interesting to note that there seems to be a fairly good collapse of the distribution of $\sigma/|s|$ for different Re_λ and that this distribution is tilted both in figures 15 and 14b towards positive values of σ . This asymmetry corresponds to the negative skewness of the velocity derivatives in the flow field and is what makes possible the net amplification of vorticity.

One of the most striking features of these probability distributions is the similarity of their shape at different levels. The probability distributions, scaled on ω' , collapse closely near the origin, corresponding to the good collapse of the one dimensional histograms in that range. Even away from that point where the higher Reynolds number cases display much stronger tails, the *shape* of the distributions are very similar for the high and for the low Reynolds flows. The outer, low probability isolines of the low Reynolds number distributions coincide almost exactly with the inner, high probability ones at high Re_λ . This suggest again that, whatever mechanism is responsible for the generation of high enstrophy or of high strain regions, it is independent of Reynolds number and that the only difference is that it becomes more common as the Reynolds number increases. The correspondence of inner and outer contours also suggests that the dynamics of the intense regions is not fundamentally different from that of the $O(\omega')$ background.

6. Discussion and conclusions

We have presented results on the structure of the intense vorticity regions in numerical turbulent flow fields at four different Reynolds numbers ranging from $Re_\lambda = 36$ to 171. Numerical resolution in terms of η and running time in large eddy turnover units were kept as constant as possible. The fields themselves are in statistical equilibrium with a suitable forcing, and the two higher Reynolds numbers are already in the "asymptotic" range in which dissipation becomes independent of Re_λ . In this sense, we are dealing with true turbulent flows. These last two fields also exhibit an inertial $k^{-5/3}$ spectral range that, in the highest Reynolds number case, spans almost a decade. The collapse of all the spectra in the dissipation range when expressed in Kolmogorov units is excellent, although there is a suggestion of a weak trend to slightly fuller spectra at higher Reynolds numbers (Fig. 1). The energy spectra in this range are exponential with an algebraic prefactor.

We give univariate histograms for several quantities related to the velocity gradients, especially for those related to the terms of the vorticity production equation. They are not gaussian, and they do not collapse in Kolmogorov units (ω'). There is a strong trend to longer tails of intense events at higher Reynolds numbers, which show no signs of converging to an asymptotic distribution within our experimental range.

We have confirmed in accordance with previous investigators that the physical

structure of these intense events is that of long coherent vortices of more or less elliptical cross section (“worms”). Although we lack adequate statistical confirmation, the eccentricity of the cross section appears to decrease as the Reynolds number increases. We have offered an explanation in terms of the relative strength of the strain and vorticity in those regions.

By means of an automatic tracking algorithm, we have computed the scaling laws for the kinematic properties of the worms. Their radii scale with the Kolmogorov microscale and their lengths with the integral scale of the flow, and their circulations increase with the Reynolds number as $Re_\gamma = \gamma/\nu \sim Re_\lambda^{1/2}$. With respect to this latter scaling, the data might be consistent with a slightly higher or lower exponent, but they are not consistent with the obvious guess that Re_γ should remain constant.

We have tried to clarify the dynamics of worm formation by means of joint probability densities of strain and vorticity. As expected, high enstrophy and high strain are associated with one another, although rather loosely, but, surprisingly, strong vorticity is not associated with high values of the stretching term, $\sigma = \omega S\omega/|\omega|^2$. In fact, the stretching of the high intensity worms is low and seems to scale well with the background vorticity ω' . Since the Burgers' length for a strain ω' is $(\nu/\omega')^{1/2} = \eta$, this is consistent with the scaling of the radius quoted above but strongly suggests that self stretching is not an important factor in the evolution of the intense vorticity.

An interesting observation is that the *shapes* of the probability isolines in the tails of the joint distributions are essentially similar to those in their central parts and that they are quite independent of the Reynolds number. This, together with the previous observation on the lack of self stretching, suggests that the worms are only particularly intense realizations of the background vorticity field, $|\omega| > \omega'$. This background component is responsible for most of the turbulent dissipation (80%) but fills a much smaller percentage of the volume (25%). We have presented some indications that it is concentrated in large scale, turbulent, vortex sheets separating the energy containing eddies at the integral scales. The worms are imbedded within this background (Figs. 6-7).

We have also shown by removing the worms artificially from an equilibrium turbulent field and studying its further development that worms are not especially important in the overall dynamics of turbulence and that they are only responsible for a fraction of the kinetic energy proportional to the volume that they occupy and for a fraction of the dissipation proportional to their integrated enstrophy. Both are small numbers at the Reynolds numbers of our simulations but could become bigger in the limit $Re_\lambda \gg 1$. We have also shown that worms are not artifacts of forced turbulence. If they are removed from a decaying field, they reappear within a small fraction of a turnover time.

The lack of convergence of the probability distributions appears to support the multifractal models of turbulence in which cascades of increasing intensities are concentrated on increasingly small regions of space. The way in which this local concentration is implemented is, however, somewhat surprising, although consistent with previous indications from the near wall region of turbulent channels. Instead

of having vortices of fixed circulation being stretched more at higher Reynolds numbers, our data imply increasingly stronger vortices being stretched by a fixed amount.

The question of how these vortices are formed will not be addressed here and will be the subject of coming publications. The purpose of this paper is to present a data base that can be used to constrain any such future model. It may still be of some interest to discuss briefly the nature of some of these constraints. There are three basic problems: how the large vorticities are generated, why Re_γ increases with Re_λ , and how a small scale structure can maintain a length of the order of the macroscale.

The first question presents no qualitative difficulty, although its quantitative answer lies at the heart of turbulence theory. High vorticity is generated by stretching, and stretching is generated by the integrated effect of the rest of the vorticity in the flow. We have seen that the highest vorticity has transverse dimensions of the order of η . This is already implicit in Kolmogorov theory and implies that the prevailing rate of strain is $O(\omega')$. Since we know from the histograms in figure 3 that the predominant vorticity is also $O(\omega')$, this implies that the Reynolds number of a typical dissipative eddy, Re_γ , is $O(1)$ and independent of Re_λ . This is in agreement with intuitive stability arguments.

A relatively small percentage of dissipative eddies (at our Re_λ) seems to be strained while maintaining a much larger Re_γ . Large Reynolds number vortex sheets are subject to inviscid instabilities and will quickly roll into individual vortices, but columnar vortices are linearly stable, although they are subject to inertial waves and will probably break up if perturbed hard enough. There is little doubt that a sufficiently high Reynolds number vortex will eventually become internally turbulent, but it may survive long enough to be observed in rare situations. We have seen in figure 12 that worms become "noisier" as Re_λ increases, in general agreement with this argument. Note also that the evidence suggests that the strong vortices are subject to rates of strain that are much weaker than their own vorticity. Under those circumstances, they would behave as essentially unstrained and they could only be appreciably perturbed by self, or mutual, interaction.

It might even be possible to shed some light on the scaling law $Re_\gamma \sim Re_\lambda^{1/2}$. The relation that comes to mind is

$$u'\eta/\nu \sim Re_\lambda^{1/2},$$

which implies that the velocity increment across an intense worm is of the same order as the characteristic velocity of the energy containing eddies. A simple model is that of large eddies straining vorticity at the interfaces in which they meet (see figures 6 and 7). On most occasions, the vortex sheets generated in that way become unstable and break into smaller eddies that strain each other into the $O(\omega')$ vorticity background. Occasionally, however, a small part of the vortex sheet survives the instability and is strained to thickness η while still retaining across itself the full velocity difference u' . The eventual roll-up of this sheet generates worms.

Note that this model does not predict the conditions for the formation of worms, but that it singles out the observed scaling law as an upper limit for Re_γ , since

strong intermittency of the velocity itself is not observed. Note also that it suggests that the initial stretching takes the form of sheets since the velocity increment across a stretched sheet is maintained while that of a cylindrical vortex increases in inverse proportion to its diameter.

Finally, the problem of the long lengths of the worms is harder. It is inconceivable that a rate of strain $O(\omega')$ remains coherent over a region of space of size $O(L)$. Since we know that velocities are only $O(u')$, the largest possible coherence length for a strain ω' is $u'/\omega' \sim \lambda$. This suggests that worms are not formed in a single stage, but that they grow or coalesce along their lifetimes. Several possible mechanisms come to mind, but they are beyond the scope of this paper.

Acknowledgements

We have benefitted from fruitful discussions with R. Kraichnan. We are especially indebted to J. Soria for early work in the generation of figure 14. The simulations were carried out on the NAS 128-node Intel hypercube.

REFERENCES

- ASHURST, W. T., KERSTEIN, A. R., KERR, R. M. & GIBSON, C. H. 1987 Alignment of vorticity and scalar gradient with strain in simulated Navier Stokes turbulence. *Phys. Fluids*. **30**, 3243-3253.
- BATCHELOR, G. K. 1953 *The theory of homogeneous turbulence*. Cambridge Univ. Press.
- BATCHELOR G. K. & TOWNSEND, A. A. 1949 The nature of turbulent motion at large wave numbers. *Proc. Roy. Soc. London*. **A 199**, 238-255.
- BETCHOV, R. 1956 An inequality concerning the production of vorticity in isotropic turbulence. *J. Fluid Mech.* **1**, 497-504.
- CANUTO, C., HUSSAINI, M. Y., QUARTERONI, A. & ZANG, T. A. 1987 *Spectral methods in fluid dynamics*. Springer, pp. 85-86.
- DOUADY, S., COUDER, Y. & BRACHET, M. E. 1991 Direct observation of the intermittency of intense vorticity filaments in turbulence. *Phys. Rev. Lett.* **67**, 983-986.
- HOSOKAWA, I. & YAMAMOTO, K. 1990 Intermittency of dissipation in directly simulated fully developed turbulence. *J. Phys. Soc. Japan*. **59**, 401-404.
- JIMÉNEZ, J. 1991 On small scale vortices in turbulent flows. *CTR Annual Res. Briefs.* , 45-56 (see also *Phys. Fluids*, **A 4**, 652-654).
- KERR, R. M. 1985 Higher order derivative correlation and the alignment of small-scale structures in isotropic numerical turbulence. *J. Fluid Mech.* **153**, 31-58.
- KOLMOGOROV, A. N. 1941 The local structure of turbulence in incompressible viscous fluids a very large Reynolds numbers. *Dokl. Nauk. SSSR.* **30**, 301-305 (see e.g. L.D. Landau & E.M. Lifshitz, 1959, *Fluid mechanics*, Pergamon, pp. 116-123).

- RUETSCH, G. R. & MAXEY, M. R. 1991 Small scale features of vorticity and passive scalar fields in homogeneous isotropic turbulence. *Phys. Fluids. A* **3**, 1587-1597.
- SHE, Z-S., JACKSON, E. & ORSZAG, S. A. 1990 Intermittent vortex structures in homogeneous isotropic turbulence. *Nature*. **344**, 226-228.
- SIGGIA, E. D. 1981 Numerical study of small scale intermittency in three dimensional turbulence. *J. Fluid Mech.* **107**, 375-406.
- SREENIVASAN, K. R. 1984 On the scaling of the turbulence energy dissipation rate. *Phys. Fluids*. **27**, 1048-1051.
- TOWNSEND, A. A. 1951 On the fine scale structure of turbulence. *Proc. Roy. Soc. London. A* **208**, 534-542.
- VAN ATTA, C. W. & ANTONIA, R. A. 1980 Reynolds number dependence of skewness and flatness factors of turbulent velocity derivatives. *Phys. Fluids*. **23**, 252-257.
- VINCENT, A. & MENEGUZZI, M. 1991 The spatial structure and statistical properties of homogeneous turbulence. *J. Fluid Mech.* **225**, 1-25.
- WEI, T. & WILLMARTH, W. W. 1989 Reynolds-number effects on the structure of a turbulent channel flow. *J. Fluid Mech.* **204**, 57-95.

Appendix I: Data processing for vortex radii and circulations.

In order to elucidate the geometric structure of the worms, an algorithmic definition is needed for the set of points in space which will be taken to constitute a single worm. Such definitions necessarily contain some degree of arbitrariness, and the one used here is certainly no more than one among many possibilities.

We are interested in the strong vortical regions, and we take maxima of enstrophy as starting points. We define a worm axis and core starting with:

(1) Find the point of maximum enstrophy not yet included in any worm core. This is the first worm-axis point of a new worm.

From that point one could reasonably proceed along the vortex line through the point to define a worm centerline. However, an elongated region of high enstrophy, which we take intuitively as a worm, does not have vorticity perfectly aligned along its axis, nor does a given vortex line necessarily remain within it over its entire length. Therefore, to increase the chances of staying within the high-vorticity structure, the worm-core definition is taken as:

(2) Follow the local vorticity vector from the current worm-axis point until it intersects the next grid plane, then choose as worm-core points the four grid points in this plane which surround the point of intersection. The new worm-axis point is the one with the maximum enstrophy.

This is done in both directions from the first worm-axis point until:

(3) The worm is taken to end when the new maximum enstrophy is below the global mean value, ω'^2 , or when the worm axis intersects its own or another worm's core.

From the set of worm-axis points we compile radial distributions of axial vorticity in the next two steps:

(4) Define the radial plane around a given worm-axis point as that set of points for which the given axis point is the closest point on the worm axis.

(5) Average the component of vorticity parallel to the worm axis (at the given axis point) over these radial-plane points. The averaging is done into radial bins of width Δx .

With the distributions of axial vorticity as a function of distance from and position along the axis, we can compute approximations to the worm radius and circulation as functions of axial position. The radial distribution is fitted to a gaussian shape, with the measured value of ω_0 the axial vorticity at the axis. The $1/e$ radius, R , of the distribution is estimated from the distance r_q at which the vorticity falls to a fraction q of its value at the axis:

$$R = r_q / (-\ln(q))^{\frac{1}{2}}.$$

This estimation is repeated for several $q \in (0.25 - 0.75)$, and the average of the different estimations is taken as the final radius. The circulation γ at this section is then approximated by integrating the gaussian, assuming axisymmetry:

$$\gamma = \omega_0 \pi R^2$$

We have found this procedure to give clearer results than computing the circulation directly from the radial distribution. The latter is hampered by the difficulty of doing the circulation integral over a quite noisy distribution containing vorticity from other worms and the background.

Steps (1)-(5) are repeated to obtain a database containing a few tens of worms. Statistics of radius and circulation are collected over this database.

On the local nature of the energy cascade

By C. Meneveau¹, T. S. Lund² AND J. Chasnov²

The local nature of the energy cascade in space and time is studied using direct numerical simulation of decaying and forced isotropic turbulence. To examine the concept that large scales evolve into smaller ones, we compute the Lagrangian correlation coefficient between local kinetic energy at different scales. This correlation is found to peak at a Lagrangian time-delay that increases with scale separation. The results show that, on average, the flow of energy to smaller scales is predominantly local in physical space and that the view of eddies decaying into smaller ones while transferring their kinetic energy appears to be, on average, quite realistic. To examine the spectral characteristics of the cascade under unsteady conditions, a pulse of large-scale energy is added to the large-eddy simulation of forced isotropic turbulence. As time progresses, the evolution of this pulse through bands of increasing wavenumbers is studied.

1. Introduction

The theoretical framework underlying most turbulence modeling hypotheses is the Kolmogorov phenomenology, in which the cascade of energy from large to small scales occupies the central stage. It is postulated that the rate at which energy is dissipated is dictated by the large-scales and that the transfer of energy is mainly local in wave-number space. The $-5/3$ decay exponent in the inertial range, its extent, isotropy of small-scales, and so on, follow directly from these assumptions. This spatially averaged view is of importance for modeling at the Reynolds averaged level and is consistent with the 1941 version of Kolmogorov's theory. In the realm of sub-grid scale modeling for Large Eddy Simulations (LES), a slightly stronger version of the Kolmogorov phenomenology is at work. Spatial features of the energy cascade have to be taken into account, and the equilibrium between the *local* energy flux (or subgrid-scale energy production) and rate of dissipation is used to derive the popular Smagorinsky model. A spatially local version of the energy cascade is also invoked in models for small-scale intermittency (Kolmogorov, 1962; Meneveau & Sreenivasan 1991). In spite of the wide use of these ideas, the hypothesis that kinetic energy originally associated with some large-scale structure gets transferred to smaller flow structures that have evolved from the bigger one has never been directly tested. The purpose of the present work is to perform such an explicit test using direct numerical simulations. Several issues complicate this task. To properly account for the time needed for the energy transfer between scales as well as to take sweeping by the large scales properly into consideration, the flow structures

1 Johns Hopkins University

2 Center for Turbulence Research

have to be followed in time in a Lagrangian fashion. Also, proper statistical means have to be employed to ensure that the observed trends are robust. The calculation methods and results are presented in section 2.

The Kolmogorov phenomenology can also be used to make predictions about how the cascade should react to overall unsteadiness at the large scales. In a recent article, Lumley (1992) used the Kolmogorov phenomenology to predict that an energy pulse at largest scales will tend to 'propagate' along the spectrum, only to 'arrive' at small scales at some later time. This hypothesis is tested using simulations of forced isotropic turbulence. The results of these tests are reported in section 3. Conclusions are presented in Section 4.

2. Spatial structure of the energy cascade

Let the local kinetic energy of the flow-field composed of scales smaller than r' , at location \mathbf{x} and time t be denoted by $e_{r'}(\mathbf{x}, t)$. As defined more precisely below, the effect of advection by scales larger than r' is excluded from $e_{r'}(\mathbf{x}, t)$. Let us assume that at a certain instant and position this local energy is larger than the corresponding spatial average. The question we wish to address is how such a pulse will evolve in time if the underlying turbulent structure is followed as it is advected through space. The simplistic view of the energy cascade as consisting of large eddies breaking down to form smaller ones would suggest that if we follow a fluid element initially located at (\mathbf{x}, t) in a Lagrangian fashion, this pulse should become associated with local kinetic energy at decreasing scales as time progresses. In other words, we would expect that after following a fluid element with excess energy at scale r' for some time, we would find an excess of energy not at scale r' , but at some smaller scale, say $r = r'/2$. To quantify such an effect statistically, it is useful to compute the correlation coefficient between local kinetic energies at different scales.

Several alternative definitions for the local kinetic energy will be used. The first is the trace of the subgrid-scale stress tensor (minus the Leonard term),

$$e_{r'}(\mathbf{x}, t) = \widehat{u_k u_k} - \widehat{u_k} \widehat{u_k}. \quad (1)$$

The hat represents low-pass spatial filtering at scale r' ;

$$\widehat{a}_{r'}(\mathbf{x}, t) \equiv \int a(\mathbf{x}', t) G_{r'}(\mathbf{x} - \mathbf{x}') d^3 \mathbf{x}', \quad (2)$$

where $G_{r'}$ is a filter of characteristic scale r' . $e_{r'}(\mathbf{x}, t)$ as defined according to Eq. (1) is the total kinetic energy minus the resolvable portion of the large scale kinetic energy. Decomposing the original velocity u_k into $u_k = \widehat{u_k} + u'_k$ shows that this definition also includes cross-terms of the form $\widehat{u'_k u'_k}$. We shall also consider the kinetic energy of the small scales only, defined as

$$e_{r'}(\mathbf{x}, t) = \widehat{u'_k u'_k}. \quad (3)$$

Notice that these definitions of local kinetic energy differ from the local wavelet spectrum (Meneveau, 1991) in the sense that they include the energy of all scales

smaller than the characteristic scale r' rather than just that of a particular spectral band.

The spatial filtering to be used can be of several forms. First, a spectral cut-off filter is considered, i.e.

$$G_{r'}(\mathbf{k}) = 1 \text{ if } |\mathbf{k}| < \frac{\pi}{r'}, \quad (4)$$

and zero otherwise. $G_{r'}(\mathbf{k})$ is the Fourier transform of $G_{r'}(\mathbf{x} - \mathbf{x}')$. We shall also consider Gaussian filter,

$$G_{r'}(\mathbf{x} - \mathbf{x}') = \left(\sqrt{\frac{6}{\pi}} \frac{1}{r'} \right)^3 \exp \left[-\frac{6(\mathbf{x} - \mathbf{x}')^2}{r'^2} \right], \quad (5)$$

and top-hat filter,

$$G_{r'}(\mathbf{x} - \mathbf{x}') = \frac{1}{r'} \text{ if } |\mathbf{x} - \mathbf{x}'| < \frac{r'}{2}. \quad (6)$$

At instant t_0 , we compute the local energy at scale r' , at some position \mathbf{x}_0 . At later times, the local kinetic energy at a smaller scale $r < r'$ is computed at position displaced from \mathbf{x}_0 along the trajectory of a particle moving with velocity \tilde{u}_i ;

$$\mathbf{x} = \mathbf{x}_0 + \int_0^t \tilde{\mathbf{u}}(\mathbf{x}, t) dt, \quad (7)$$

where tilde now represents filtering at a smaller scale r . This posterior and smaller-scale local kinetic energy is defined either as

$$e_r(\mathbf{x}, t_0 + t) = \widetilde{u_k u_k} - \widetilde{\widetilde{u_k u_k}}, \quad (8)$$

or as in Eq. (3), by replacing the filtering at scale r' (hat) by filtering at scale r (tilde).

Finally, the correlation coefficient between the two local kinetic energies depending on the Lagrangian time delay t and the scale ratio $b = r'/r$ is defined as

$$\rho(b, t) = \frac{\langle e_{br}(\mathbf{x}_0, t_0) e_r(\mathbf{x}, t_0 + t) \rangle - \langle e_{br}(\mathbf{x}_0, t_0) \rangle \langle e_r(\mathbf{x}, t_0 + t) \rangle}{\sqrt{\sigma_{e_{br}}^2 \sigma_{e_r}^2}}. \quad (9)$$

Here $\sigma_{e_{br}}^2$ and $\sigma_{e_r}^2$ are the variances of the local kinetic energies at scale br and r , respectively. Figure 1 illustrates the variables to be computed.

The correlation coefficient $\rho(b, t)$ will be used as a measure of how fluctuations of local energy propagate between different scales of motion as the underlying turbulent structures evolve in space and time. It can be measured for different definitions of local energy as well as different types of filters.

The next section describes the direct numerical simulations from which $\rho(b, t)$ is measured.

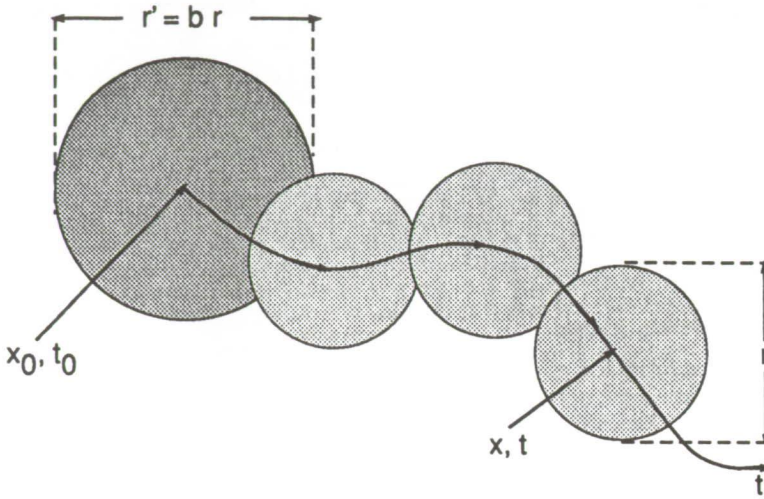


FIGURE 1. Sketch of local energy at 'large' scale $r' = br$, and at 'smaller' scale r after following a fluid particle for some time t .

2.1 Description of flow fields

Both forced and decaying isotropic turbulent fields were considered. They were generated with a pseudo-spectral code (Rogallo, 1981) on a 128 cubed mesh. The initial phases for the complex velocity field were chosen randomly but in such a way that the divergence-free condition was satisfied (see Rogallo, 1981 for more details on the initial conditions). Forcing was achieved by adding an anti-diffusion term (negative diffusion coefficient) to the Navier-stokes equations. The diffusion coefficient was wavenumber dependent and non-zero only for modes within wavenumber shells less than 3. The value of the coefficient for low wavenumbers was chosen so that the maximum wavenumber, scaled in Kolmogorov units, was unity (i.e. $k_{max}/\eta = 1$). To generate realistic steady-state turbulence, the flow was evolved for approximately 2 large scale eddy turn-over times. The Reynolds number, R_λ , settled at 95.8, while the velocity derivative skewness settled at -0.486 . The energy spectrum is shown in Figure 2, where the vertical lines indicate the cut-off wavenumber at scale r (4 mesh spacings) and the maximum value of r' , equal to $2.6r$. Note the tail-up in the energy spectrum at high wavenumbers. This results from the desire to achieve maximal Reynolds number for the given resolution. The dissipation range is not fully resolved, and, as a result, energy piles up there. It is generally believed (Rogallo, 1992) that the tail-up at high wavenumber will not adversely affect the data in the central portion of the spectrum used here. To generate data for the Lagrangian test, the simulation was run for approximately an additional 2 small scale eddy turnover times. In order to follow the evolution in time with sufficient accuracy, the entire velocity field was stored at 14 intermediate times, each separated by roughly $1/6$ th of the turn-over time associated with scales of size r (as estimated by $(\widetilde{S}_{ij}\widetilde{S}_{ij})^{-1/2}$).

For the decaying turbulence, the energy spectrum was initialized according to

$$E(k) = \frac{1}{32} \left(\frac{k}{2} \right)^4 \exp \left(-\frac{k}{2} \right). \quad (10)$$

This spectrum has its energy peak at wavenumber 8. In order to develop realistic turbulence from the random phase initial condition, the flow was allowed to evolve freely for 1.4 small scale eddy turnover times (based on quantities derived from the end of the initial run; $\tau_{t_0} = \frac{\lambda_0}{u'_0}$ where λ_0 and u'_0 are the Taylor microscale and the rms turbulence intensity, respectively). Over this period of time, the total turbulent kinetic energy decayed by 20%. The Taylor microscale Reynolds number ($u'\lambda/\nu$) was 56.1. The 3-D radial energy spectrum at the end of this initial run is plotted in Kolmogorov units in Figure 3. Also shown are the experimental data of Comte-Bellot and Corrsin (1971), as well as two additional spectra for the later times t_6 and t_{13} discussed below. The simulation spectra collapse reasonably well with the experimental data for wavenumbers beyond the energy peak (where the universal scaling is expected to hold). As in the forced simulation, there is a noticeable energy pile-up at the highest wavenumbers.

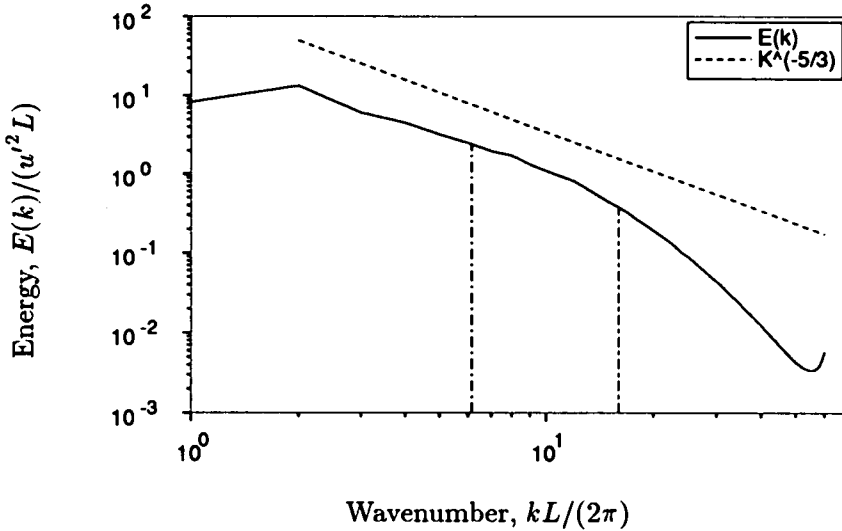


FIGURE 2. 3-D radial energy spectrum for the forced isotropic turbulence.

Data for the Lagrangian test was generated by evolving the flow approximately an additional two small scale eddy turn-over times, with 13 velocity fields saved at intervals of 1/6 of a turn-over time. Over this period of time, the kinetic energy decayed an additional 43%. The velocity derivative skewness changed from -0.382 to -0.302 in progressing from t_0 to t_{13} , while R_λ changed from 56.1 to 35.2. The vertical lines in Figure 3 correspond to the cut-off wavenumber of the scale r (4 mesh spacings in physical space) and the maximum $r' = 2.6r$ considered.

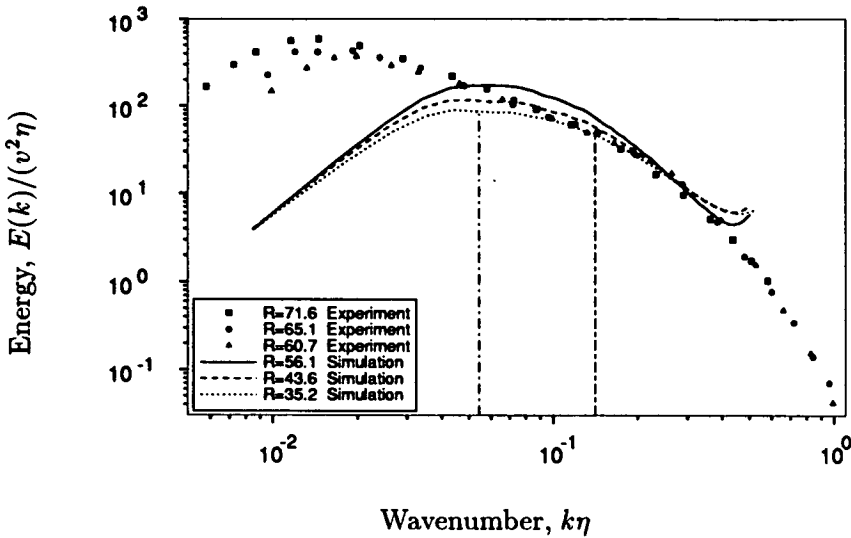


FIGURE 3. 3-D radial energy spectrum for the decaying isotropic turbulence, plotted in Kolmogorov units.

2.2 Calculations and results

The filtered velocity $\tilde{\mathbf{u}}$ was computed at scale r and sampled on a 32^3 mesh for each time t_0 to t_{13} . Also computed were the local energies e_{br} and e_r at every point of the coarse 32^3 mesh. For each grid-point on this mesh, Eq. (7) was integrated numerically using Euler's method with time increment $\Delta t = t_{n+1} - t_n$ and using multilinear interpolation to find the velocity between grid points. The local energy at $t = 0$ ($t_0 = 0$, say) of the larger scales (up to br) is computed for positions \mathbf{x}_0 corresponding to each grid point, and the final energy at scale r is obtained by multilinear interpolation of the field e_r at the end-points of the Lagrangian tracking, at all times t_1 to t_{13} . This calculation was repeated for different ratios $b = r'/r$ between the larger scale and smaller-scale energies, in a range $1 \leq b \leq 2.6$, where r is kept fixed and r' is increased.

First, we consider spectral cut-off filtering and the definition of local kinetic energy as the trace of the subgrid-scale tensor, according to Eq. (1). The results corresponding to the forced field are shown in Figure 4, and the results pertaining to the decaying field are shown in Figure 5. The time delay t has been normalized with the characteristic time-scale corresponding to the lower cut-off scale r at t_{13} :

$$|S| \equiv \sqrt{\langle \tilde{S}_{ij} \tilde{S}_{ij} \rangle}. \quad (11).$$

The upper curve corresponds to $b = 1$ and represents the Lagrangian autocorrelation function of the local kinetic energy. It exhibits the expected overall decorrelation time of the order of a few turn-over time scales of structures of size r .

The curves for $b > 1$, on the other hand, do not peak at $t = 0$, but at some later

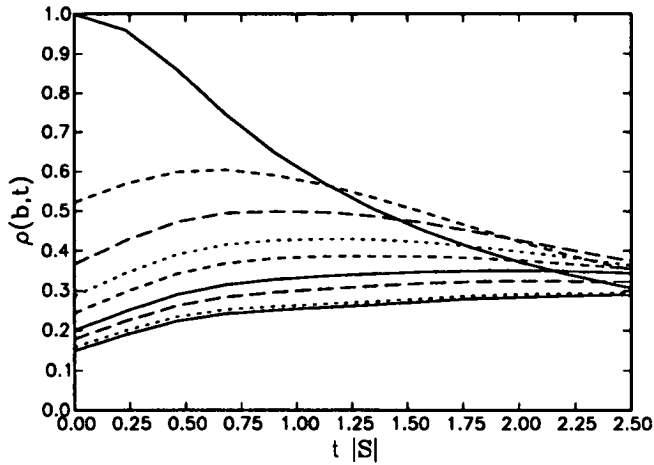


FIGURE 4. Correlation between local energies at different scales, as a function of Lagrangian time-delay. The flow is forced isotropic turbulence. The local energies are computed as the trace of the subgrid-scale stress tensor, using cut-off filtering. Different curves are for different scale separation; from top to bottom curve (at $t = 0$): $b = 1.0$,

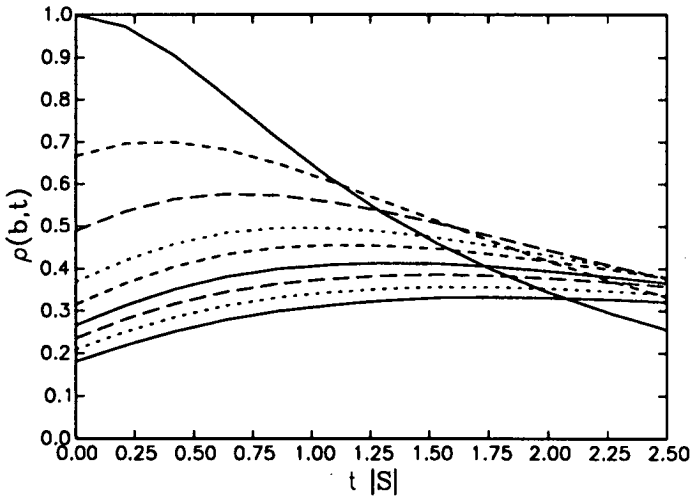


FIGURE 5. Same as Figure 4, but for the decaying isotropic turbulence simulation.

time. This time $(T_b)_{max}$ is an increasing function of the scale-ratio b . It implies that to exhibit maximum correlation between energy occurring at different scales some time must be allowed to pass. Pulses of higher local energy tend, on the average, to correlate better with pulses at smaller scales only after allowing the cascade to proceed for some time. As the ratio between scales becomes larger, this

time increases.

To verify that the approximate integration scheme to compute the Lagrangian path is sufficiently accurate for present purposes, the calculation is repeated using an even coarser resolution in time. This can be done by using every second field at $t_0, t_2, t_4 \dots t_{12}$. The symbols in Figure 6 show the resulting correlation (for the forced flow, for $b = 1, b = 1.4$ and $b = 2$) as compared to the lines corresponding to the higher temporal resolution employing all fields t_0, t_1, t_2, \dots etc. Only minor variations (less than 0.015 in the correlation coefficient) are visible, and we conclude that the procedure is sufficiently accurate.

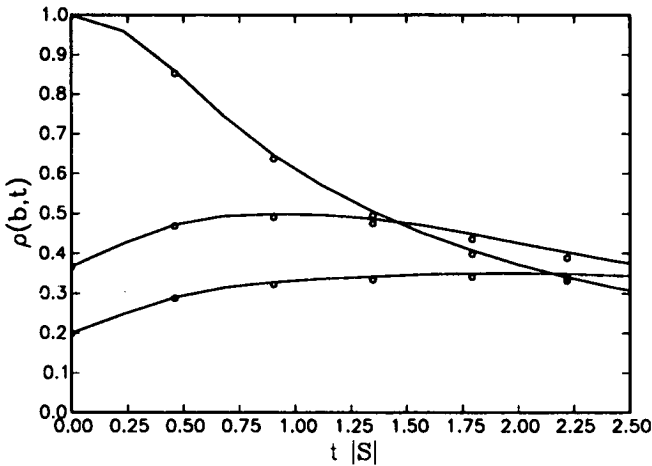


FIGURE 6. Test of sensitivity of results on accuracy of time integration, for the forced isotropic flow using the trace of the subgrid-scale tensor. Different solid curves are, from top to bottom: $b = 1, 1.4, 2.0$. The circles are obtained from a time-step that is twice as large, i.e. using every second of the stored fields only.

Next, we consider the second possible definition of local kinetic energy in terms of the product of small-scale velocities (Eq. (3)). Figure 7 shows the resulting correlations for the forced isotropic flow-field. The overall trend is the same as before, but the time at which the curves peak is slightly reduced.

The importance of different types of filtering is now quantified. Figures 8 and 9 show the correlation as a function of Lagrangian time for the Gaussian and top-hat filters. The local energy is now defined again according to Eq. (1). It is clear that considerable differences are present in terms of the peak time-delay as well as the magnitude of the correlation. Nevertheless, the basic trend of a time-delay that increases with scale separation is robust.

Finally, as an illustration of how the cascade of energy is associated with decreasing length-scales when following a fluid particle, we plot b^{-1} as a function of the peak time-delay $(T_b)_{max}$ in Figure 10. It contains all results pertaining to the cut-off filtering and the mean trend through the results pertaining to the Gaussian

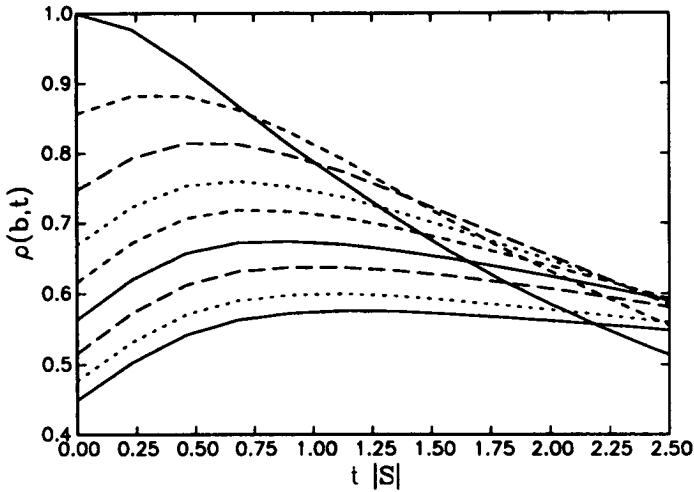


FIGURE 7. Same as Figure 4 but using Eq. to define local energy, and cut-off filtering applied to the forced isotropic flow.

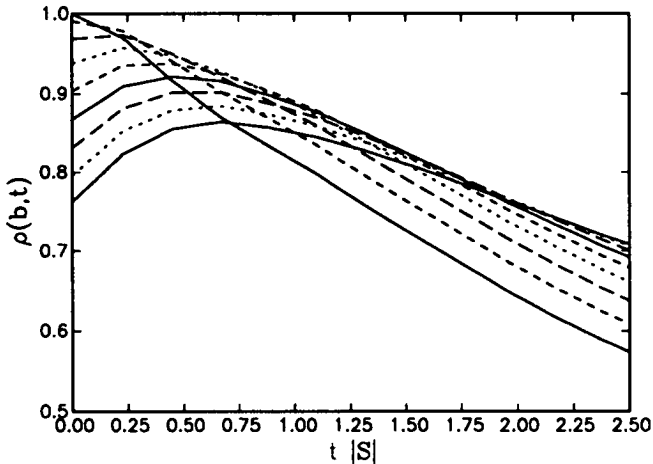


FIGURE 8. Same as Figure 4, but using a Gaussian filter.

and top-hat filter calculations. It can be seen that the data is consistent with a reduction in scale by a factor of 2, in a time that is of the order of $|S|^{-1}$.

Considerable scatter about this mean behavior is seen to exist. The largest variability is due to the filter type: The decrease in length-scale is considerably faster for the Gaussian or top-hat filter as compared to the spectral cut-off filter. The results for $b > 2.5$ are physically not very meaningful since the large-scale br already approaches the peak in the energy spectrum.

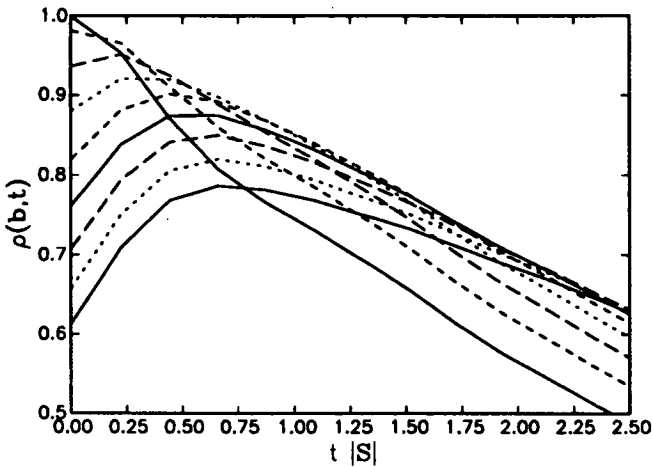


FIGURE 9. Same as Figure 4, but using a top-hat filter.

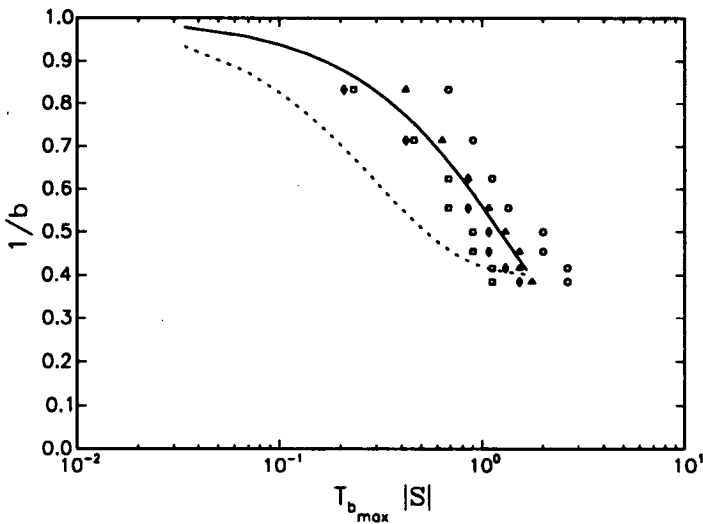


FIGURE 10. Plot of $1/b$ as a function of the corresponding time delay at which the two-point energy correlation peaks. It can be viewed as a decrease in length-scale of eddies as a function of time. Symbols are for the cut-off filtering. \triangle : decaying flow, local energy according to Eq. (1); \diamond : decaying flow, local energy according to Eq. (3); \circ : forced flow, local energy according to Eq. (1); \square : forced flow, local energy according to Eq. (3); — : mean trend through symbols; ---- : mean trend through all results corresponding to Gaussian and top-hat filtering.

3. Spectral evolution of sharp pulse of energy

In this section, we consider the temporal evolution of a sharp pulse of kinetic

energy originally present at low wavenumbers in the spectrum. To attain high Reynolds numbers, a large-eddy simulation was employed to study this case. We consider a high Reynolds number forced 128^3 LES using the subgrid-scale model described in Chasnov (1991). The method of forcing entails adjusting the energy of each Fourier mode in the first wavenumber shell $1 \leq k < 2$ to a fixed value. The component distribution of the energy and the Fourier phases in the first shell evolve according to the Navier-Stokes equations. A long-time evolution of this forced flow together with the subgrid scale model results in an approximate $k^{-5/3}$ energy spectrum over the entire range of computational wavenumbers. The spectral subgrid-scale model used here contains both an eddy-viscosity and a stochastic backscatter term, that effects most strongly the evolution of modes closest to the cut-off wavenumber.

Starting from this fully-developed statistically-stationary inertial subrange, we have doubled the energy in the first band of wavenumbers at an initial time $t = 0$ by a simple rescaling of the Fourier amplitudes and followed the cascade of this energy to higher wavenumbers as a function of time. Figure 11 shows the results of this calculation. We plot the time-evolution of the energy in logarithmic bands of wavenumbers from the initial instant of time. The n^{th} band plotted represents the energy in the Fourier modes with wavenumbers between $2^{n-1} \leq k < 2^n$. The energies are normalized by their values at $t = 0$. A plot of the energy in the first band would be a horizontal line at a value of two, and we expect that, for large-times, a statistically asymptotic state would develop where all the normalized energies approach a value of two.

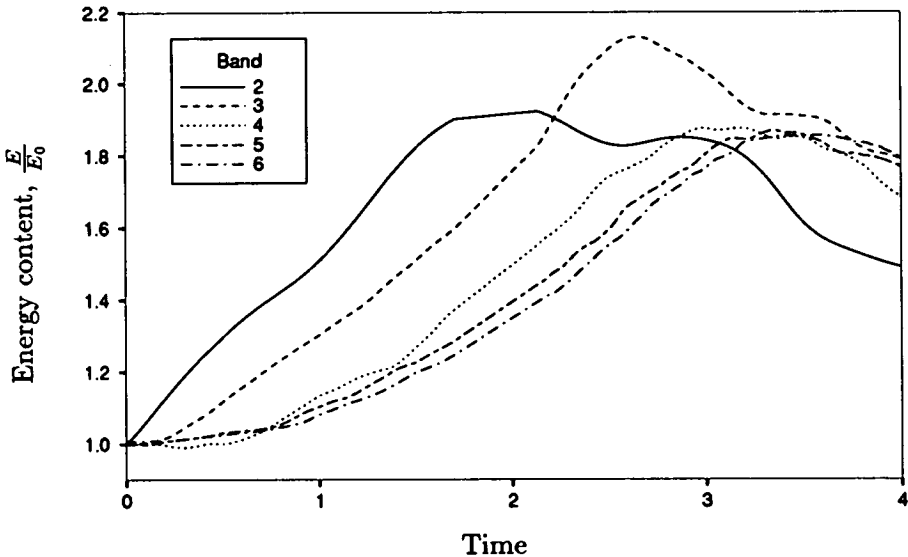


FIGURE 11. Time-evolution of the energy in logarithmic wavenumber bands after a pulse of energy was added to the first band. Band n represents the energy in wavenumbers $2^{n-1} \leq k < 2^n$ normalized to its value at $t = 0$. Band 1 would be represented by a horizontal line at a value of 2.

There is evidently a large amount of statistical fluctuation in the data so that we limit ourselves to qualitative observations based on this single realization. A large eddy-turnover time based on the length of the computational box and the initial root-mean-square velocity may be computed and corresponds to approximately $t = 3$. The initial pulse of energy is, therefore, seen to become distributed more-or-less evenly among all the wavenumber bands on the order of a large-eddy turnover time. Furthermore, the cascade appears to proceed in a manner such that most of the energy is passed locally in wavespace (for $1 \leq t \leq 2$, the normalized energy level of the bands are ordered consecutively), but some of the energy is passed to all higher wavenumber bands (the normalized energy levels do not rise in a delayed step-like fashion, but rather begin to rise early on). Also, the time difference between consecutive peaks in Figure 11 is seen to decrease for the bands corresponding to larger wavenumbers, implying shorter turn-over times-scales for the smaller scales of motion.

These results are in qualitative agreement with the scenario described in Lumley (1992), where at each step in the energy cascade most of the energy is passed to the next higher wavenumber band while a diminishing fraction of the energy is passed to all other higher-wavenumber bands.

4. Summary and conclusions

First, it was shown that 'pulses' of kinetic energy of flow-structures at a particular scale will propagate to smaller scale structures as fluid particles are followed in time. This effect leads to a peak in the correlation between local energy at different scales occurring after a time delay. It was also shown that the time needed for a length-scale reduction factor of $b = 2$ is of the order of the 'characteristic' time scale in the energy cascade. Although these important qualitative results were very robust, quantitatively they were strongly dependent on filter type and on the precise definition used to compute the local energy density. Also, the increase in correlation after a Lagrangian time-delay was typically not very large. This is to be expected since the 'forward' flow of energy to smaller scales is itself a weak effect, coming from the difference between local forward flux and backscatter.

Secondly, unsteadiness in the large-scales of the flow were studied from the spectral point of view. A pulse of energy added at low wavenumbers in a high Reynolds number forced isotropic turbulence was observed to propagate to higher wavenumbers such that the energy levels increased faster in wavenumber bands closest to the initial pulse and slower in wavenumber bands farther away. The energy of the initial pulse was seen to be more-or-less evenly distributed among all the wavenumber bands in a time on the order of one large-eddy turnover time.

Acknowledgements

We thank P. Moin for stimulating discussions on this topic. This work was performed at the Center for Turbulence during the 1992 Summer Program. CM also acknowledges support from NSF CTS-9113048 and ONR N00014-92-J-1109.

REFERENCES

- CHASNOV, J. R. 1991 Simulation of the Kolmogorov inertial subrange using an improved subgrid model. *Phys. Fluids A*. **3**, 188-200.
- KOLMOGOROV A. N. 1941 Local structure of turbulence in an incompressible fluid at very high Reynolds number. *Dokl. AN SSSR*. **30**, 299
- KOLMOGOROV A. N. 1962 A refinement of previous hypotheses concerning the local structure of turbulence in a viscous incompressible fluid at high Reynolds number. *J. Fluid Mech.* **13**, 82.
- LUMLEY J. L. 1992 Some comments on turbulence. *Phys. Fluids A*. **4**, 203-211.
- MENEVEAU C. 1991 Analysis of turbulence in the orthonormal wavelet representation. *J. Fluid Mech.*. **232**, 469-520.
- MENEVEAU C. & SREENIVASAN 1991 The multifractal nature of the turbulent energy dissipation. *J. Fluid Mech.* **224**, 429-484.
- ROGALLO R. 1981 Numerical experiments in homogeneous turbulence. *NASA Tech. Mem.* 81315.
- ROGALLO R. 1992 private communication.

54-34 445343
189664

61
N94-14749

Search for subgrid scale parameterization by projection pursuit regression

By C. Meneveau¹, T. S. Lund² AND P. Moin²

The dependence of subgrid-scale stresses on variables of the resolved field is studied using direct numerical simulations of isotropic turbulence, homogeneous shear flow, and channel flow. The projection pursuit algorithm, a promising new regression tool for high-dimensional data, is used to systematically search through a large collection of resolved variables, such as components of the strain rate, vorticity, velocity gradients at neighboring grid points, etc. For the case of isotropic turbulence, the search algorithm recovers the linear dependence on the rate of strain (which is necessary to transfer energy to subgrid scales) but is unable to determine any other more complex relationship. For shear flows, however, new systematic relations beyond eddy viscosity are found. For the homogeneous shear flow, the results suggest that products of the mean rotation rate tensor with both the fluctuating strain rate and fluctuating rotation rate tensors are important quantities in parameterizing the subgrid-scale stresses. A model incorporating these terms is proposed. When evaluated with direct numerical simulation data, this model significantly increases the correlation between the modeled and exact stresses, as compared with the Smagorinsky model. In the case of channel flow, the stresses are found to correlate with products of the fluctuating strain and rotation rate tensors. The mean rates of rotation or strain do not appear to be important in this case, and the model determined for homogeneous shear flow does not perform well when tested with channel flow data. Many questions remain about the physical mechanisms underlying these findings, about possible Reynolds number dependence, and, given the low level of correlations, about their impact on modeling. Nevertheless, demonstration of the existence of causal relations between sgs stresses and large-scale characteristics of turbulent shear flows, in addition to those necessary for energy transfer, provides important insight into the relation between scales in turbulent flows.

1. Introduction

Of central importance to the numerical simulation of the large scales in turbulent flows is the proper parameterization of the subgrid-scale (sgs) stress deviator, defined as

$$\tau_{ij} \equiv \widetilde{u_i u_j} - \bar{u}_i \bar{u}_j - \frac{1}{3}(\widetilde{u_k u_k} - \bar{u}_k \bar{u}_k) \delta_{ij}, \quad (1)$$

¹ Johns Hopkins University

² Center for Turbulence Research

as a function of the resolved velocity field \tilde{u}_i . Here $\tilde{(\)}$ represents spatial filtering at a particular scale r . The most widely used model is Smagorinsky's (1963):

$$\tau_{ij} = -2 C_s^2 r^2 \sqrt{2\tilde{S}_{ij}\tilde{S}_{ij}}, \quad (2)$$

where

$$\tilde{S}_{ij} = \frac{1}{2} \left(\frac{\partial \tilde{u}_i}{\partial x_j} + \frac{\partial \tilde{u}_j}{\partial x_i} \right) \quad (3)$$

is the strain rate of the resolved motion. The model constant C_s can be prescribed or can be determined dynamically based on information provided by the resolved field, as in the recently developed dynamic model (Germano *et al.*, 1991).

Although the Smagorinsky model has been in use for nearly thirty years, for roughly half that period it has been known that the model provides only a very crude estimate for the stresses. This fact was first demonstrated by Clark *et al.* (1979), where direct numerical simulation (DNS) data for homogeneous isotropic turbulence was used to evaluate model predictions. Clark *et al.* found a correlation coefficient of approximately 0.2 when comparing predictions of the Smagorinsky model with the exact stresses. McMillan *et al.* (1979) found that the correlation coefficient was even lower in homogeneous shear flow, being of order 0.1. Later, Piomelli *et al.* (1988) found similar results in turbulent channel flow.

When contemplating these extremely low correlation coefficients, it may seem striking that the Smagorinsky model works at all. Of course, the resolution of this paradox is that, by construction, the Smagorinsky model insures that there will be a net drain of energy from the large scales to the subgrid-scale motions. This is the primary objective of a subgrid-scale model, and as long as this requirement is met, reasonable results may be expected. On the other hand, the Smagorinsky model provides poor predictions of the individual elements of the stress tensor. It is natural to expect that superior results could be obtained with a model that yields a more accurate prediction of the stress tensor. The objective of this work is to seek out potentially more accurate models.

The Smagorinsky model relates the subgrid-scale stress with only the resolved strain rate. It is reasonable to expect that the stresses might also depend on other resolved quantities such as the vorticity. If simple models based on a limited number of such quantities are postulated, conventional least-squares fitting techniques can be used to test the modeling hypothesis. Such a test was performed by Lund and Novikov (1992), where the stresses were assumed to depend on the anti-symmetric as well as the symmetric part of the velocity gradient tensor (rotation rate and strain rate tensors, respectively). It was shown that the stress tensor could be expanded in a series formed from products of these two tensors. Tests of this expansion in isotropic turbulence revealed that inclusion of rotation rate did not significantly improve the model prediction. The results of Lund and Novikov thus suggest that it is necessary to search for other quantities on which the stresses could depend. Velocity gradients taken at neighboring points or perhaps gradients filtered at different (larger) scales are possible candidates which would not violate Galilean invariance.

Unfortunately, as the list of possible independent variables increases, the task of finding statistically meaningful relations from the DNS data becomes unmanageable. In principal, if a multidimensional scatter-plot of τ_{ij} as a function of several independent variables is generated, a high-dimensional cloud of points would be obtained. This may (or may not) exhibit some clustering around a most probable behavior. If such a hypersurface exists about which the data appears preferentially clustered, it would constitute a clear basis for modeling. However, finding such a surface from the DNS data represents a difficult problem of regression in a high-dimensional space of variables. Parametric regression, such as least-square error fitting to some assumed functional form, is quite difficult because there is little indication as to what such a function should be. Finding the surface by dividing the high-dimensional space into small hypercubes and performing local smoothing of the data is impractical because even large amounts of data become extremely sparse in a high-dimensional setting (curse of dimensionality).

Although the challenges in performing a high-dimensional regression are apparent, recent advances in statistical science allow such problems to be tackled. An elegant method that circumvents many problems inherent to high-dimensional regression was proposed by Friedman & Stuetzle in 1981. Known as the Projection Pursuit Regression algorithm, this method was originally developed to analyze experimental data in particle physics involving a large number of variables. The algorithm consists of a numerical optimization routine that finds one dimensional projections of the original independent variables for which the best correlations with the dependent variable can be obtained. The dependent variable can then be written as a sum of empirically determined functions of the projections. We shall use the projection pursuit regression algorithm to investigate relationships between the subgrid-scale stresses and quantities in the resolved field.

In section 2, we briefly summarize the projection pursuit method, present an illustrative example, and comment on both its strengths and weaknesses. Section 3 describes applications to isotropic turbulence, both decaying and forced. Section 4 presents applications to homogeneous turbulent shear flow and section 5 to channel flow simulations. The results obtained from these anisotropic flows suggest possible modeling strategies that are explored at the end of sections 4 and 5. Section 6 summarizes this work and presents the conclusions.

2. Review of projection pursuit regression

The problem is to find the 'best' relation between a 'response' y and a set of predictor variables x_1, x_2, \dots, x_n . In our problem, y will be identified with each of the elements of the sgs stress tensor, and the x_i 's will be the elements of resolved rate of strain, vorticity, etc., i.e. all the variables that the stresses are assumed to depend upon. When performing tests with DNS data, there will be a large number of realizations (essentially at every grid-point) of the 'response variable' τ (y) and of the 'predictor variables' strain rate, vorticity, etc ($x_i, i = 1, 2, \dots, n$).

Friedman & Stuetzle (1981) summarize the inherent problems of traditional methods, such as parametric regression and regression based on local smoothing. With

the former, one has to assume a particular functional form and determine unknown coefficients or parameters by some method such as least-square error fitting. Since we do not wish to impose such relationships *a priori*, this is not a method of choice. Local smoothing consists of fitting a hypersurface in a small hypercube of data and repeating this in each cube. The regression surface is then the union of all these local fits. In high-dimensional settings, this is practically impossible. Consider the following example (Friedman & Stuetzle, 1981). Let $\mathbf{x} \in \mathbf{R}^{10}$, i.e. $n = 10$. If the width of the cube used for the local smoothing spans 10% of the range of each variable, each cube will contain typically only a fraction equal to 0.1^{10} of the data, which is too sparse. On the other hand, if one requires each hypercube to contain 10 % of the data, then the window has to span $0.1^{0.1} \sim 80\%$ of the range of the predictor variables, which is too large.

Projection pursuit regression (ppreg henceforth) circumvents these difficulties by projecting the high-dimensional data onto a single variable $z = \alpha_1 x_1 + \alpha_2 x_2 + \dots + \alpha_n x_n$. Local smoothing is then performed to obtain an empirically determined function $f(z)$ that follows the main trend of the data as a function of z . The smoothing algorithm is described in Friedman & Stuetzle (1981) and consists of several passes over the data (y as a function of z) to adjust the bandwidth of the smoothing to the local conditions. The variance $\sigma_\alpha^2 = \langle (y - f(z))^2 \rangle - \langle (y - f(z)) \rangle^2$ of the data around $f(z)$ is computed. The core of the algorithm is a numerical optimization procedure in which the coefficients α_i are selected so as to *minimize* the variance σ_α^2 . Let the α 's thus found be denoted by $\alpha_i^{(1)}$, and let $z^{(1)}$ and $f^{(1)}(z^{(1)})$ be the corresponding univariate projection and the empirical function giving a good fit for y as a function of $z^{(1)}$. The procedure is repeated for the residues, defined as $y - f^{(1)}(z^{(1)})$, and a new projection $\alpha_i^{(2)}$ and a smooth empirical function $f^{(2)}(z^{(2)})$ are found. This procedure is repeated until the variance stops to decrease appreciably by adding new projections. Finally, the model consists of the sum

$$y_{mod} = \sum_{m=1}^M f^{(m)}(\alpha_1^{(m)} x_1 + \alpha_2^{(m)} x_2 + \dots + \alpha_n^{(m)} x_n). \quad (4)$$

For the case that the response variable is a linear combination of x_i (i.e. $y = \beta_1 x_1 + \dots + \beta_n x_n$), ppreg reduces to the usual n -dimensional linear least-square error fit (where the α 's are the coefficients and $f^{(1)}$ is a linear function). In general however, the functions $f^{(m)}$ need not be linear. The fundamental advantage of this procedure is illustrated in the following example. If y is the product of x 's, say $y = x_1 x_2$, then this can be represented as a sum of two univariate functions according to $y = \frac{1}{4}(z^{(1)})^2 - \frac{1}{4}(z^{(2)})^2$, where $z^{(1)} = x_1 + x_2$ and $z^{(2)} = x_1 - x_2$. The ppreg algorithm is thus able to find some nonlinear relations without stipulating them *a priori*.

As an illustrative example, we consider 1000 realizations of a ten-dimensional random vector \mathbf{x} where each x_i is normally distributed with zero mean and unit variance. Then y is prescribed as follows:

$$y = x_3 x_4 + \tanh(x_6 + x_7) + \xi, \quad (5)$$

where ξ is another Gaussian random variable with zero mean and variance of 0.1. However, ξ is not included in the list of predictor variables x_i and, therefore, represents extraneous noise. Projection pursuit is applied to this artificially generated set of data. The projections found by pprog are, successively: $\alpha_6^{(1)} = 0.69$, $\alpha_7^{(1)} = 0.72$; $\alpha_3^{(2)} = 0.66$, $\alpha_4^{(2)} = 0.74$; and $\alpha_3^{(3)} = -0.67$, $\alpha_4^{(3)} = -0.73$; other α 's are negligible. The empirical functions (solid lines) resemble the tanh function in the first projection, parabolas in the latter two. The projected data are shown in Figures 1(a) to (c). If we least-square error fit a *tanh* profile through Figure 1(a), we obtain $y_1 = 1.1 \tanh[1.3(0.69x_6 + 0.72x_7)]$. The scatter plot in Figure 1(b) is then $y - y_1$ vs the second projection $z^{(2)} = 0.66x_3 + 0.74x_4$. Parabolic fits through Figures 1(b) and 1(c) give $y_2 = 0.4(0.66x_3 + 0.74x_4)^2$ and $y_3 = -0.4(-0.67x_3 + 0.73x_4)^2$. (These fits are not exactly equal to the empirical smoothing functions constructed by the algorithm, this being the reason why the scatter plot of Figure 1(c) falls below the smooth.) The final model then consists of $y_1 + y_2 + y_3$ which is plotted with the original y in Figure 1(d).

The residual noise is mainly due to the non-deterministic dependence of y with respect to ξ . The initial correlation coefficient between y and e.g. x_4 was 0.012, while the correlation coefficient between y and the model, y_{mod} , is now $\rho = 0.96$. Finding such a non-trivial dependence from few data points in a 10-dimensional space is quite remarkable.

Although impressive in the above example, pprog is not fool-proof. For cases when y depends on the x_i 's in ways that cannot be written as sums of functions of linear combinations of x_i 's (such as divisions), pprog is usually unable to find good projections. Therefore, while the method works remarkably well for an entire family of non-trivial relations, it cannot be considered entirely general.

In addition to application to sgs modeling to be reported in the following pages, we believe that the pprog method should be applicable to a host of other problems where large amounts of data need to be analyzed and functional dependencies established (Reynolds-stress modeling, reacting flows, control, etc.).

3. Isotropic turbulence

In this section, pprog is used to search for possible functional dependence between the residual stresses and a host of resolved variables in homogeneous isotropic turbulence. Both decaying and forced isotropic turbulent fields are considered.

3.1 Flow-fields and calculations

Both the forced and decaying isotropic turbulent fields were generated on a 128^3 mesh with the pseudo-spectral code of Rogallo (1981). For the decaying turbulence, the energy spectrum was initialized according to

$$E(k) = \frac{1}{32} \left(\frac{k}{2} \right)^4 \exp \left(-\frac{k}{2} \right).$$

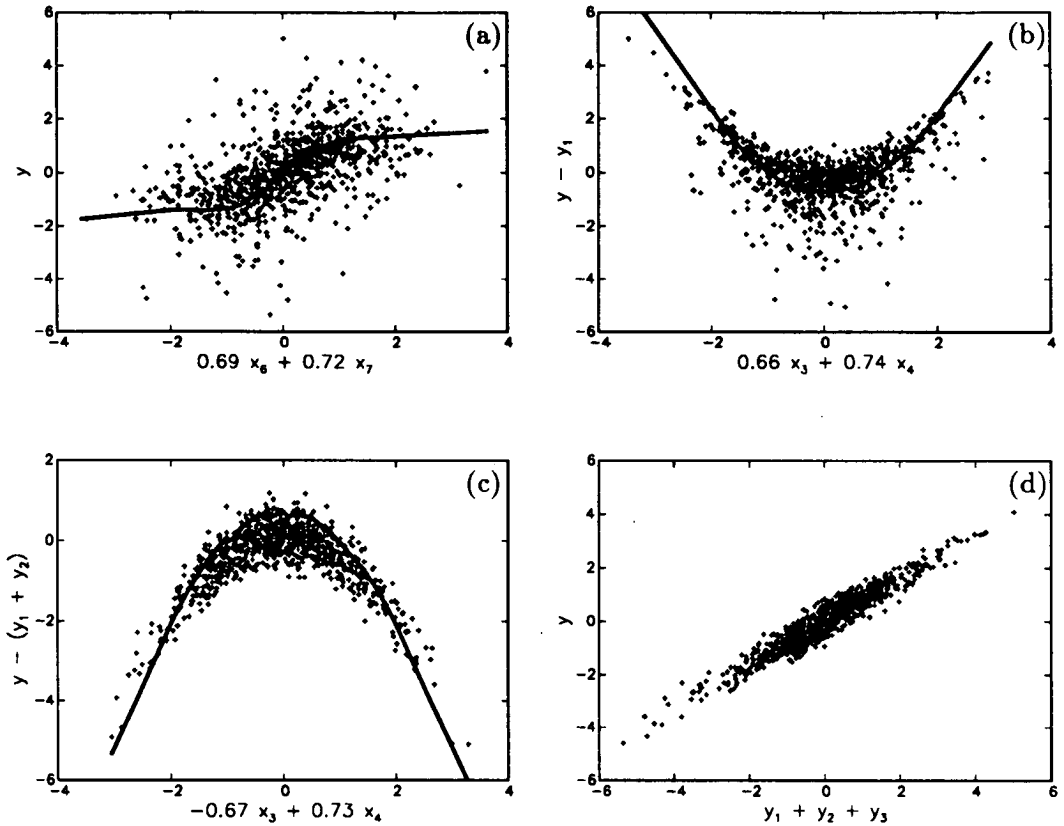


FIGURE 1. Illustrative application of pprog to a test case. (a) Response y as a function of first projection $z^{(1)} = 0.69x_6 + 0.72x_7$ (symbols) and mean trend $f^{(1)}(z^{(1)})$ found by local smoothing (solid line). (b) Second projection of $y - y_1$, where y_1 has been found by fitting a \tanh profile through Figure 1(a). Solid line: $f^{(2)}(z^{(2)})$ found by the algorithm. (c) Third projection and $f^{(3)}(z^{(3)})$. (d) Response variable y as a function of the sum of empirically determined fits in (a), (b) and (c).

This spectrum has its energy peak at wavenumber 8. The initial phases for the complex velocity field were chosen randomly but in such a way that the divergence-free condition was satisfied (see Rogallo, 1981 for more details on the initial conditions).

In order to develop realistic turbulence from the random phase initial condition, the flow was allowed to evolve freely for 2.9 small scale eddy turnover times, τ_{t_0} (based on quantities derived from the end of the initial run; $\tau_{t_0} = \frac{\lambda_0}{u'_0}$ where λ_0 and u'_0 are the Taylor microscale and the rms turbulence intensity, respectively). Over this period of time, the total turbulent kinetic energy decayed by 34%. The Taylor microscale Reynolds number ($u'\lambda/\nu$) was 45.3, and the velocity derivative skewness was -0.32 . The 3-D radial energy spectrum at the end of the run is plotted in

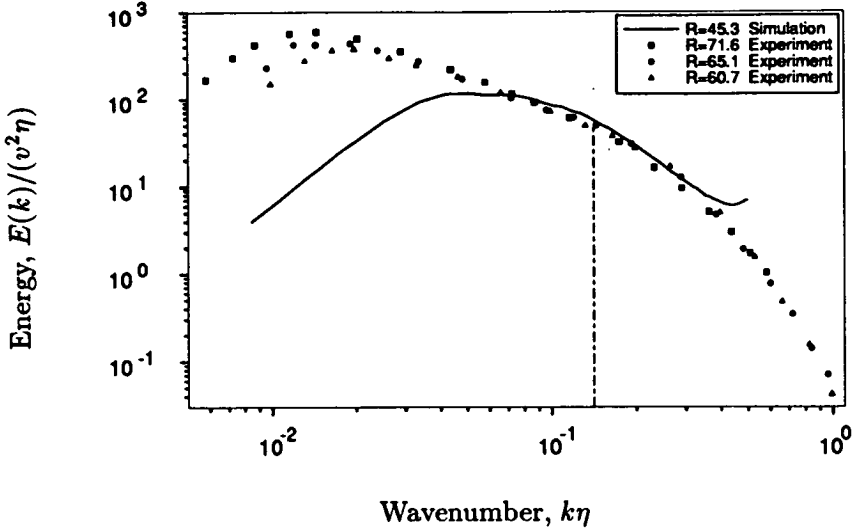


FIGURE 2. 3-D radial energy spectrum for the decaying isotropic turbulence, plotted in Kolmogorov units. The experimental data were taken from Comte-Bellot and Corrsin (1971). The vertical line indicates the scale at which the velocity field was filtered to obtain the synthetic large eddy field.

Kolmogorov units in Figure 2. Also shown are the experimental data of Comte-Bellot and Corrsin (1971) at somewhat higher Reynolds number. Agreement with the experimental data between $0.06 < k\eta < 0.4$ indicates that realistic turbulence has been achieved. The tail-up in the simulated spectrum at high wavenumbers indicates some lack of resolution. It is generally believed (Rogallo, 1992) that this will not adversely affect the data in the central portion of the spectrum used here. The vertical line in Figure 2 indicates the scale at which the DNS data was filtered in order to generate the synthetic large eddy field. This scale corresponds to four grid spacings.

For the forced simulation, energy was added to the large scales by including an anti-diffusion term (negative diffusion coefficient) in the Navier-stokes equations. The diffusion coefficient was wavenumber dependent and non-zero only for modes within wavenumber shells less than 3. The value of the coefficient for low wavenumbers was chosen such that the maximum wavenumber, scaled in Kolmogorov units, was unity (i.e. $k_{max}/\eta = 1$). To generate realistic statistically stationary turbulence, the flow was evolved from the random phase initial conditions for approximately 2 large scale eddy turn-over times. The Reynolds number, R_λ , settled at 95.8, while the velocity derivative skewness settled at -0.486 . The energy spectrum is shown in Figure 3, where again the vertical line indicates the scale used to generate the large eddy field.

The sgs stresses τ_{ij} and resolved rates of strain \tilde{S}_{ij} and vorticity $\tilde{\omega}_k$ were computed using a spectral cut-off filter with scale r corresponding to 4 grid points. The data

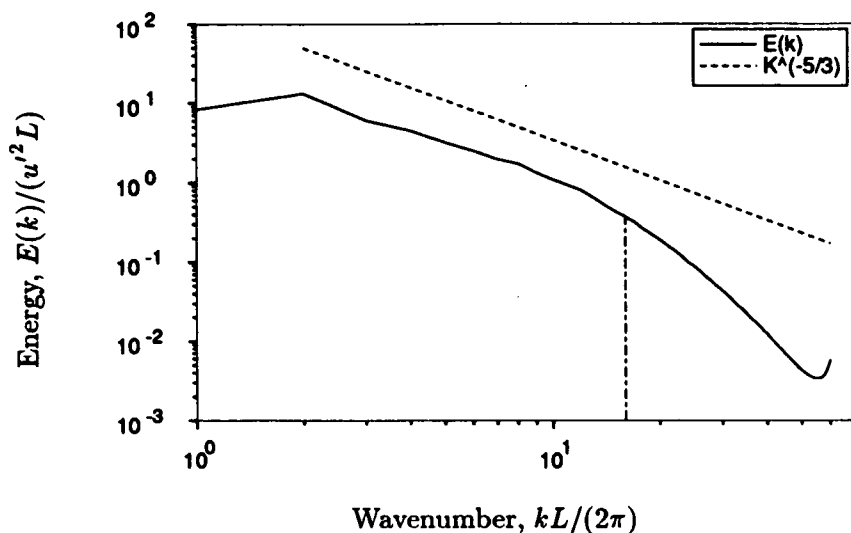


FIGURE 3. 3-D radial energy spectrum for the forced isotropic turbulence. The vertical line indicates the scale at which the velocity field was filtered to obtain the synthetic large eddy field.

was sampled on every 8th grid point, producing a total of 16^3 realizations. Also computed at each 16^3 point were resolved variables at a scale twice as large as r , \widehat{S}_{ij} and $\widehat{\omega}_k$. The invariants of the tensors were computed as follows:

$$II_{\tilde{S}} = \sqrt{\tilde{S}_{mn}\tilde{S}_{nm}}, \quad (6)$$

$$III_{\tilde{S}} = (\tilde{S}_{mn}\tilde{S}_{np}\tilde{S}_{pm})^{\frac{1}{3}}, \quad (7)$$

$$II_{\tilde{R}} = \sqrt{\tilde{\omega}_k\tilde{\omega}_k}, \quad (8)$$

and a similar list of invariants for the larger scale rates-of-strain and vorticity.

The search procedure consisted of considering separately each element of the tensor τ as the response variable. Each element of τ , in turn, was assumed to depend on *all* 24 of the predictor variables mentioned above (each element of the tensors plus all invariants). The search is thus a high dimensional one indeed.

It is important to note that when performing independent searches for each element of τ , the resulting model expressions are not expected to be tensorially correct. This weakness stems from the fact that the projection pursuit regression operates most effectively on scalar data. The findings of projection pursuit are still quite valuable, however, since they may be used to guide the construction of tensorially correct models. Such a procedure will be followed here.

3.2 Results

We begin with the decaying field and consider first the normal stress element τ_{11} . To limit the scope of the search, we initially restrict the predictor variables to quantities filtered at scale r . Furthermore, since $\tilde{S}_{ii} = 0$, we eliminate \tilde{S}_{33} from the search, reducing the list to 11 variables.

The main result is the following. The pprog algorithm finds only one projection (in which the variance of the data around a mean trend is reduced), namely that corresponding to \tilde{S}_{11} . The coefficient α corresponding to \tilde{S}_{11} is close to unity, while all others are less than 0.1. The same is true for all other tensor elements, i.e. the only causal dependence appears to be between corresponding elements of τ_{ij} and \tilde{S}_{ij} . The smoothed dependence is approximately linear, but the variance about it is still very large. The correlation coefficient between each element of the stress and rate-of-strain tensors is, averaging over all 6 elements, about $\rho = 0.26$. Notice that the Smagorinsky model requires the product between each rate-of-strain element and the second invariant $II_{\tilde{S}}$. Given the discussion in section 2, this could have been detected by the present approach by yielding pairs of projections with similar $|\alpha|$'s for both $II_{\tilde{S}}$ and \tilde{S}_{ij} and canceling parabolic dependences. However, such projections were found to produce more variance than the ones corresponding to constant eddy viscosity. This was checked *a posteriori* by computing the correlation coefficient between each element τ_{ij} and the corresponding term $-II_{\tilde{S}}\tilde{S}_{ij}$. The correlation was marginally smaller than for \tilde{S}_{ij} alone, about $\rho = 0.25$ on average.

The same procedure was repeated for the forced isotropic flow, and the same observations were made. The correlation between τ_{ij} and \tilde{S}_{ij} was even lower (about 0.12 instead of 0.26), but this was again the only causal dependence captured by the algorithm. All other projections did not reduce the variance in any fashion, and correlations with $-II_{\tilde{S}}\tilde{S}_{ij}$ were again smaller than with \tilde{S}_{ij} alone.

Inclusion of the velocity gradients filtered at a larger scale yielded projections that include a weak linear dependence on these gradients but again in terms of the same tensor elements only. In other words, for τ_{11} the 'best' (and only) projection is onto $\tilde{S}_{11} + 0.2\hat{S}_{11}$. Nevertheless, this leaves the correlation virtually unchanged since \tilde{S}_{11} and \hat{S}_{11} are themselves correlated. Similar results were obtained for other tensor elements.

We also considered the possibility that the sgs stresses depend not only on the resolved velocity gradients at the point in question, but at the 26 closest neighboring grid-points as well. To do this, the 6 elements of \tilde{S}_{ij} at each point $\tilde{S}_{ij}(x + i_x r, y + i_y r, z + i_z r)$; $i_x, i_y, i_z = -1, 0, 1$, as well as 3 vorticity components at each of these points was considered. The dimensionality of the space of these predictor variables is 243. It appears unrealistic to expect pprog to perform adequately in such extreme circumstances. In order to at least explore this direction, we considered $\tau_{11}(x, y, z)$ and investigated how it depends on the first element of the rate-of-strain tensor at all 27 neighboring points on the coarse grid, i.e. the predictor variables were $\tilde{S}_{11}(x + i_x r, y + i_y r, z + i_z r)$, $i_x, i_y, i_z = -1, 0, 1$. The projection pursuit projected again most strongly on $\tilde{S}_{11}(x, y, z)$ ($\alpha = 0.8$), while the α 's corresponding to neighboring points were below 0.25. Inclusion of these weak dependencies left the correlation

coefficient virtually unchanged. Since this test is incomplete (one should include all 243 elements in the test) the conclusion that the neighboring velocity gradient does not affect the sgs stresses is somewhat premature. Nevertheless, the partial results obtained here give no indication of any substantial influence.

3.3 The model of Bardina *et al.*

The only model which has been reported to yield high correlations when tested with DNS data is the model of Bardina *et al.* (1983). The correlation between τ_{ij} and $B_{ij} = \tilde{u}_i \tilde{u}_j - \widehat{\tilde{u}_i \tilde{u}_j}$ can be as high as 0.7 to 0.8 when the filter used in creating the synthetic large eddy field from the DNS data is Gaussian. In spite of this, experience shows that when the model is implemented in actual simulations, it dissipates almost no energy, and a Smagorinsky term has to be added (giving the mixed model, Bardina *et al.* 1983). This is puzzling since a high correlation implies at least some alignment between the modeled stress and rate of strain tensor required for dissipation. This issue is addressed below.

Using a Gaussian filter on the decaying isotropic data, we reproduced the quoted correlation of 0.8. We found this result to be misleading, however, since the Gaussian filter produces a 'large-scale' field that contains considerable contributions from the 'small scales', as viewed from a spectral analysis. This 'small scale' information is, of course, not available in an actual large eddy simulation if a spectral method is used. The model of Bardina *et al.* can be viewed as a procedure for extracting the 'small scale' component of the synthetic large eddy velocity field generated from the DNS data. While this procedure yields impressive correlations in tests with DNS data, lack of the 'small scale' component in an actual large eddy simulation field results in a model that may yield a very poor estimate for the real stresses. The near lack of dissipation is probably symptomatic of this.

This hypothesis was tested by experimenting with different filters. We feel that the cut-off filter is the most appropriate for generating the synthetic large eddy field since it completely eliminates the 'small scale' information that will never be present in a spectral large eddy simulation. We have repeated the tests of the model of Bardina *et al.* using a cut-off filter to determine \tilde{u}_i . The second filtering, $\widehat{\tilde{u}_i}$, was chosen either to be Gaussian or a second cutoff at a scale twice as large as r . Using this scheme, the model of Bardina *et al.* is written as

$$B_{ij}^* = \tilde{u}_i \tilde{u}_j - \widehat{\tilde{u}_i \tilde{u}_j}, \quad (9)$$

As expected, the correlation between the sgs stress and the Bardina model dropped to nearly zero when the cut-off filter was used to generate \tilde{u}_i . This was true independent of the second filter type ($\widehat{\tilde{u}_i}$). As a consistency check, we found that when B_{ij}^* was included in the projection pursuit as predictor variable, no dependence on this tensor was found.

4. Homogeneous sheared turbulence

In this section, we search for correlations between sgs stresses and resolved variables in homogeneous shear flow. The data was generated by Rogers (1987) on a

128^3 mesh using a variant of the Rogallo code. We considered three different realizations, corresponding to times 10, 12, and 14, in units of the inverse imposed mean shear, $S = \langle du_1/dx_2 \rangle$. The mean velocity is in the x_1 direction and the mean rotation in the x_3 direction. Cutoff filtering was performed on a scale $r = 4$ grid-points, and every eighth grid point was sampled, as in section 3. The list of predictor variables was again \tilde{S}_{11} , \tilde{S}_{22} , \tilde{S}_{12} , \tilde{S}_{23} , \tilde{S}_{13} , $\tilde{\omega}_1$, $\tilde{\omega}_2$, $\tilde{\omega}_3$, $II_{\tilde{S}}$, $III_{\tilde{S}}$ and $II_{\tilde{\omega}} = |\omega|$. Ppreg was repeated 6 times for each element of the sgs stress tensor.

4.1 Results

In contrast to the tests performed in isotropic turbulence, ppreg was able to find several interesting projections in the case of homogeneous shear flow. Table 1 shows the individual tensor elements and the linear combination of predictor variables $z = \alpha_i x_i$ that dominate the projections (chosen as those whose $\alpha > 0.15$). The functional dependence on each projection (f vs z) was found to be fairly linear. The correlation coefficients between τ_{ij} and $-II_{\tilde{S}}\tilde{S}_{ij}$ (Smagorinsky model) are contrasted in the same table with those between τ_{ij} and the dominant elements of the linear combinations found. On average, there is about a 100% improvement above the Smagorinsky model.

Stress	z , (best projection)	$\rho_{[\tau_{ij}, -II\tilde{S}_{ij}]}$	$\rho_{[\tau_{ij}, z]}$
τ_{11}	$-0.39\tilde{S}_{11} + 0.41\tilde{S}_{22} + 0.73\tilde{S}_{12} + 0.28\tilde{S}_{13} + 0.17\tilde{\omega}_2 + 0.15\tilde{\omega}_3$	0.23	0.36
τ_{22}	$-0.21\tilde{S}_{11} - 0.28\tilde{S}_{22} - 0.89\tilde{S}_{12} - 0.17\tilde{S}_{13}$	0.14	0.23
τ_{33}	$0.76\tilde{S}_{11} - 0.2\tilde{S}_{22} + 0.24\tilde{S}_{12} - 0.23\tilde{S}_{13} - 0.157\tilde{\omega}_2 - 0.44\tilde{\omega}_3$	0.07	0.29
τ_{12}	$-0.66\tilde{S}_{11} - 0.2\tilde{S}_{22} - 0.7\tilde{S}_{12}$	0.13	0.21
τ_{23}	$0.25\tilde{S}_{11} - 0.69\tilde{S}_{23} - 0.62\tilde{S}_{13} + 0.23\tilde{\omega}_2$	0.06	0.27
τ_{13}	$0.15\tilde{S}_{12} - 0.2\tilde{S}_{23} - 0.56\tilde{S}_{13} + 0.68\tilde{\omega}_1 + 0.29\tilde{\omega}_2 - 0.17\tilde{\omega}_3$	0.21	0.34

TABLE 1. Results of projection pursuit for homogeneous shear flow.

It can be appreciated that causal relations exist that are significantly different from the Smagorinsky model. The coefficients showed only minor variations for the other two times considered ($St=10$ and $St=14$). This robustness suggests that there is a physical mechanism by which the large-scale field consistently influences the sgs stresses, in addition to what is required energy transfer (i.e. alignment between τ_{ij} and \tilde{S}_{ij}). Since the relations tabulated above cannot by themselves provide an adequate relation between tensors, it could be that dependence on other quantities has been omitted. The next section explores the dependence on other quantities that may provide possible mechanisms for the observed degree of causality.

4.2 Dependence on mean shear and modeling

An important consideration when developing a model for the sgs stress is that the resulting model be in the form of a frame invariant tensor. Clearly, the individual terms found in the previous subsection are not invariant under rotations of the coordinate system. A tensorial relation must be found that is consistent with the findings of pprog on each tensor element. We attempt to find such a tensorial relation in this section. To do this, we first observe that \tilde{S}_{12} and $\tilde{\omega}_3$ are important contributors in the model for τ_{11} . These tensor elements of \tilde{S}_{ij} and $\tilde{R}_{ij} = -\frac{1}{2}\varepsilon_{ijk}\tilde{\omega}_k$ also correspond to the only non-zero elements in the mean strain-rate and mean rotation tensors. This fact suggests that tensor products of the mean strain rate and mean rotation with the fluctuating strain rate and fluctuating rotation would reproduce some of the dependence found by pprog for τ_{11} . Analogous reasoning holds for most of the other elements of τ .

To proceed further, we define the mean strain and rotation rate tensors as

$$\Sigma_{ij} = \begin{pmatrix} 0 & \frac{S}{2} & 0 \\ \frac{S}{2} & 0 & 0 \\ 0 & 0 & 0 \end{pmatrix} \quad (10)$$

$$\Omega_{ij} = \begin{pmatrix} 0 & \frac{S}{2} & 0 \\ -\frac{S}{2} & 0 & 0 \\ 0 & 0 & 0 \end{pmatrix} \quad (11)$$

and postulate a model of the following form:

$$\begin{aligned} \tau_{ij}^* = & -2c_1 r^2 II_{\tilde{S}} \tilde{S}_{ij} + \\ & c_2 r^2 (\tilde{S}_{ik} \Sigma_{kj} + \Sigma_{ik} \tilde{S}_{kj})^* + c_3 r^2 (\tilde{R}_{ik} \Omega_{kj} + \Omega_{ik} \tilde{R}_{kj})^* + \\ & c_4 r^2 (\tilde{S}_{ik} \Omega_{kj} - \Omega_{ik} \tilde{S}_{kj}) + c_5 r^2 (\tilde{R}_{ik} \Sigma_{kj} - \Sigma_{ik} \tilde{R}_{kj}), \end{aligned} \quad (12)$$

where (*) indicates trace-free part (note that some of the terms are naturally trace-free). The first (Smagorinsky) term is also present in the pprog results and thus is included here. To see more clearly how this model reproduces some of the trends of Table 1, note, for instance, that the [11] element of the product between \tilde{S}_{ij} and Σ_{ij} is linear in \tilde{S}_{12} and that between \tilde{R}_{ij} and Ω_{ij} will be linear in ω_3 . Again, similar correspondences can be found for other elements of τ .

Since Eq. (12) is linear in the coefficients c_i , these can be determined by the usual least-squares technique. This procedure is easily derived as follows. Write Eq. (12) symbolically as

$$\tau_{ij} = c_k (m_k)_{ij}, \quad (13)$$

where $(m_k)_{ij}$ is the k th trace-free model tensor in Eq (12). When the DNS data is used, the above expression can be compared with the exact trace-free part of the subgrid-scale stress, $(\tau_{ex}^*)_{ij}$. The error in representing the stress via Eq. (13) is given by

$$e_{ij} = (\tau_{ex}^*)_{ij} - c_k(m_k)_{ij}. \quad (14)$$

Assuming the c_k to be constant in space, the global square error is minimized with respect to the c_k by enforcing the following condition

$$\frac{\partial}{\partial c_k} \langle e_{ij}e_{ij} \rangle = 0, \quad (15)$$

where $\langle \rangle$ indicates an average over space. This operation leads to the following matrix equation for the c_k

$$c_k = \langle (m_l)_{ij}(m_k)_{ij} \rangle^{-1} \langle (m_l)_{ij}(\tau_{ex}^*)_{ij} \rangle \quad (16)$$

Note that this procedure is rather general and does not require that all five terms in Eq (12) be included. Any subset of the five terms can be used as a basis and corresponding coefficients solved for via Eq. (16). This feature will be used to determine which combinations of the five terms are most effective in maximizing the correlation between the modeled and exact subgrid-scale stresses.

The quality of the fit is measured in terms of the tensorial correlation coefficient

$$\eta = \frac{\langle (\tau_{ex}^*)_{ij}M_{ij} \rangle}{\sqrt{\langle (\tau_{ex}^*)_{ij}(\tau_{ex}^*)_{ij} \rangle \langle M_{ij}M_{ij} \rangle}}, \quad (17)$$

where $M_{ij} = c_k(m_k)_{ij}$ is the composite model tensor.

The procedure developed above was applied to the homogeneous shear flow data base. Correlation coefficients were determined for all possible combinations of one to five model components. Figure 4 shows the results of this study where the highest correlation coefficient obtained for a given number of model tensors is plotted against the number of tensors used.

The correlation increases as more model tensors are included. The increment in improved correlation, however, decreases as more terms are added. In fact, the correlation coefficient when just three terms are used is nearly identical to that when all five terms are included. This fact suggests that at least two of the terms in Eq. (12) are not particularly useful. The relative importance of the various terms are summarized in Table 2, where the optimal combinations of terms that give rise to the correlations in Figure 4 are listed.

Note that when only one term is used, the optimal choice is not the Smagorinsky model (term 1), but rather term 4, $r^2(\tilde{S}_{ik}\Omega_{kj} - \Omega_{ik}\tilde{S}_{kj})$. For reference, the correlation produced by the Smagorinsky model alone is shown as the square symbol in Figure 4. The Smagorinsky model is seen to be only slightly inferior to term 4. When two or more terms are included, the Smagorinsky model is always present. Terms 2 and 5 enter the list in the last two positions and do not significantly improve the correlation. It is interesting to note that both of these terms contain the mean shear. It is also interesting that terms 3 and 4 are proportional to the mean rotation, and it is these terms that are most effective in increasing the correlation. This point will be discussed further in the following section.

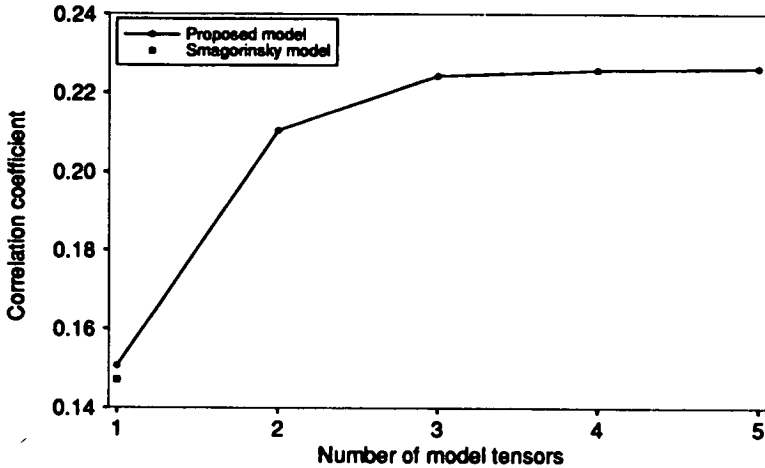


FIGURE 4. Correlation coefficient between the exact homogeneous shear flow sgs stress and subsets of the terms in the model of Eq. (12). For a given number of model tensors, the correlation coefficient plotted is the highest one obtained when all possible combinations of the five terms was considered.

Number of terms	Best combination
1	4
2	1, 4
3	1, 3, 4
4	1, 2, 3, 4
5	1, 2, 3, 4, 5

TABLE 2. Optimal subsets of the model terms in Eq. (12) applied to homogeneous shear flow.

When terms 1, 3, and 4 are used, there is slightly more than a 50% improvement over the Smagorinsky model. This compares with roughly 100% improvement for the tensorially incorrect model listed in Table 1. This discrepancy is due to the fact that not all of the terms contained in Table 1 can be reproduced by the model of Eq. (12). Nevertheless, a simple tensorially correct model was found that captures some of the trends found by projection pursuit.

The coefficients of terms 1, 3, and 4 are 8.52×10^{-3} , -3.03×10^{-2} , and 4.16×10^{-2} respectively.

5. Channel flow

In this section we consider DNS of channel flow. The data were generated with a pseudo-spectral code as detailed in Kim *et al.* (1987). The Reynolds number based on the wall friction velocity was 395, and $256 \times 193 \times 192$ grid points were used. The data was cutoff filtered in the streamwise and spanwise directions only, with a filter size of four grid cells. All results presented here were generated on a single plane of data at $\frac{y}{h} = 0.126$ ($y^+ = 49.8$) where h is the channel half width.

5.1 Results

As a starting point, the correlation between the exact stresses and the Smagorinsky model was investigated. Individual correlation coefficients were computed for each of the tensor elements, and these were found to be very low ($\rho \simeq 0.07$ on average). This trend is shown in Figure 5 in the form of a scatter plot of τ_{12} vs $-\tilde{S}_{12}$.

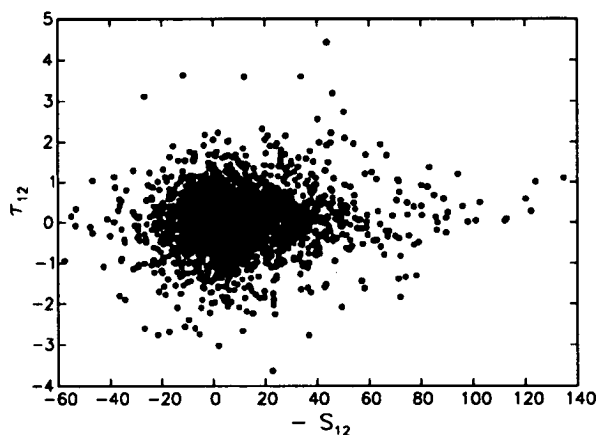


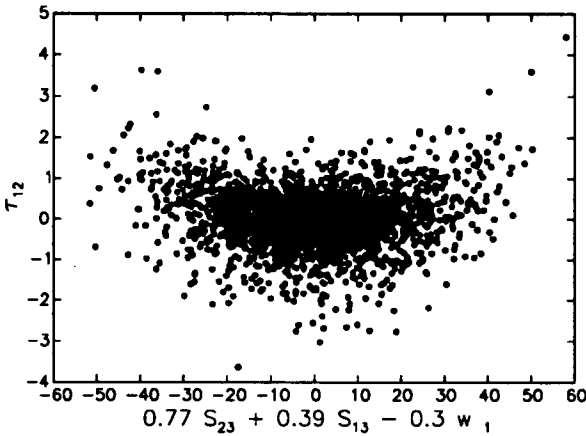
FIGURE 5. Scatter plot of sgs stress τ_{12} as a function of rate-of-strain element \tilde{S}_{12} in DNS of channel flow, at $y/h = 0.126$.

No causal dependence appears to exist between the two variables. The pprog algorithm was then applied to the data using all elements of \tilde{S}_{ij} , $\tilde{\omega}_k$ and the invariants as 11 predictor variables. A sequence of several projections was found for each element of τ_{ij} . This list of projections was reduced to a single one for each element of τ_{ij} by retaining the one that reduced the variance most strongly in each case. These optimal projections are listed in Table 3.

As opposed to the results for homogeneous shear flow, the functional form between τ_{ij} and these projections was found to be non-linear. As an illustration, a scatter plot between τ_{12} and the projection $z_{12} = 0.77\tilde{S}_{23} + 0.39\tilde{S}_{13} - 0.3\tilde{\omega}_1$ is shown in Figure 6. The main trend of τ_{12} as a function of z_{12} appears to be quadratic.

Stress	z , (best projection)	$\rho_{\{\tau_{ij}, -II\tilde{S}_{ij}\}}$	$\rho_{\{\tau_{ij}, z^2\}}$
τ_{11}	$-0.8\tilde{S}_{13} + 0.51\tilde{\omega}_2$	0.12	0.44
τ_{22}	$-0.4\tilde{S}_{22} - 0.86II\tilde{S}$	0.10	0.21
τ_{33}	$0.45\tilde{S}_{23} + 0.85\tilde{S}_{13} + 0.17\tilde{\omega}_2$	0.02	0.36
τ_{12}	$0.77\tilde{S}_{23} + 0.39\tilde{S}_{13} - 0.3\tilde{\omega}_1$	0.10	0.34
τ_{23}	$-0.51\tilde{S}_{11} - 0.43\tilde{S}_{22} + 0.35\tilde{S}_{12} +$ $0.47\tilde{S}_{23} - 0.29\tilde{S}_{13} - 0.17(\tilde{\omega}_1 - \tilde{\omega}_2 + \tilde{\omega}_3)$	0.05	0.27
τ_{13}	$0.82\tilde{S}_{11} + 0.48\tilde{S}_{22} - 0.23\tilde{\omega}_2$	0.05	0.31

TABLE 3. Results of projection pursuit for channel flow.

FIGURE 6. Scatter plot of sgs stress τ_{12} as a function of best projection onto elements of filtered velocity gradient tensor, found by pprog. Same data as in Figure 5.

Similar behavior was found for all other tensor elements, the trend being strongest for the [11], [33], [12], and [13] components. To quantify the causality between the stresses and the corresponding z 's, the correlation coefficients between individual elements of τ and the corresponding z^2 were computed. Since each of the observed quadratic trends had a minimum close to the origin, it is sufficient to consider the single term z^2 . These correlation coefficients appear in the last column of Table 3. Notice that when compared with the correlation produced by the Smagorinsky model, more than a four-fold increase is detected. This trend can also be observed

by comparing Figure 5 to Figure 6.

5.2 Modeling

As in section 4.2, the expressions in Table 3 are by themselves not valid relations between tensors. Unlike the linear relationship found in shear flow, the elements of τ depend quadratically on the projections in channel flow. For example, the model for τ_{12} is $(0.77\tilde{S}_{23} + 0.39\tilde{S}_{13} - 0.3\tilde{\omega}_1)^2$. The tensor model found for homogeneous shear flow may not be of much use in this case since it is not able to produce the non-linear products that result from squaring the projection. The quadratic non-linearities suggest that it may be possible to model the stresses in terms of various tensor products of the strain and rotation rates. Such a model is

$$\begin{aligned} \tau_{ij}^* = & -2c_1 r^2 II_{\tilde{S}} \tilde{S}_{ij} + \\ & c_2 r^2 (\tilde{S}_{ik} \tilde{S}_{kj})^* + c_3 r^2 (\tilde{R}_{ik} \tilde{R}_{kj})^* + \\ & c_4 r^2 (\tilde{S}_{ik} \tilde{R}_{kj} - \tilde{R}_{ik} \tilde{S}_{kj}) + c_5 r^2 (\tilde{S}_{ik} \tilde{S}_{kl} \tilde{R}_{lj} - \tilde{R}_{ik} \tilde{S}_{kl} \tilde{S}_{lj}) / II_{\tilde{S}}, \end{aligned} \quad (18)$$

where (*) again indicates trace-free part. This model was studied by Lund and Novikov (1992) and represents the most general relation between the subgrid-scale stress and the strain and rotation rate tensors.

The least-squares fitting procedure was applied to the above model as well as the model of Eq. (12). The resulting correlation coefficients are shown in Figure 7.

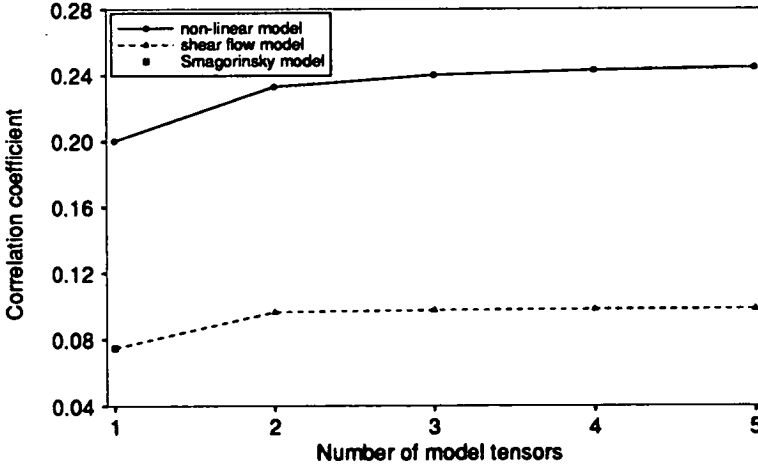


FIGURE 7. Correlation coefficients for the terms in the models of Eqs (12) and (18) applied to channel flow data.

As expected, the model developed for shear flow (Eq. (12)) does not offer much improvement here. The non-linear model of Eq (18), on the other hand, considerably

Number of terms	Best combination
1	4
2	3, 4
3	1, 3, 4
4	1, 3, 4, 5
5	1, 2, 3, 4, 5

TABLE 4. Optimal subsets of the model terms in Eq. (18) applied to channel flow.

increases the correlation relative to the Smagorinsky model. As in the shear flow case, only two or three terms contribute significantly to the increase in correlation coefficient. The ranking of terms in Eq. (18) is summarized in Table 4.

As in the shear flow, the Smagorinsky model does not produce the highest correlation when used in isolation. In fact, it produces the lowest correlation of any single term, while term 4, the best one, produces a correlation coefficient that is roughly 2.7 times higher! Furthermore, the Smagorinsky model does not enter the list until three or more terms are included and adds little to the correlation at that point. When three terms are included, the correlation coefficient is about 3.2 times higher than that provided by the Smagorinsky model. This compares with an average of improvement of a factor of 4.4 obtained by the projection pursuit algorithm. Thus the model of Eq. (18) incorporates quite well the findings of projection pursuit into a tensorially correct model.

As in the shear flow, the rotation rate enters as an important parameter. In both the shear and channel flow, the best single term is the product of strain and rotation rate (actually, it is the mean rotation in the shear flow and the local rotation in the channel flow). The observed strong dependence on this term is perhaps not too surprising since it is representative of vortex stretching. Although there is a connection with vortex stretching, the strain, rotation product does not remove energy from the large scales (*i.e.* $(\tilde{S}_{ik}\tilde{R}_{k,j} - \tilde{R}_{ik}\tilde{S}_{k,j})\tilde{S}_{ij} = 0$). Thus, by itself, this term would not be a useful model, and a term that has a non-zero projection on the strain rate (such as the Smagorinsky model) must be added.

The coefficients of terms 1, 3, and 4 are 1.13×10^{-3} , -1.38×10^{-2} , and -8.71×10^{-3} respectively.

The above collection of predictor variables is by no means exhaustive. Examples of other dependencies that could have been included are the mean velocity gradients Σ_{ij} and Ω_{ij} and the distance from the wall λ_i (a vector).

6. Summary and conclusions

A novel regression algorithm has been used to explore DNS data in an effort to determine improved models that parameterize the sgs stresses for large eddy

simulation. In addition to the rate of strain, several other variables have been considered. These include rotation, velocity gradients filtered at larger scales, and velocity gradients at neighboring points as well as the invariants of the strain and rotation rate tensors. DNS data from isotropic turbulence, homogeneous shear flow, and turbulent channel flow have been considered.

For isotropic turbulence, no statistically robust relations were found other than the small correlation between the stress and rate-of-strain tensor required for energy transfer. This finding may imply that, other than the weak relation between the stress and rate of strain, the large-scale velocity gradients in isotropic flow do not dictate the behavior of the small scales giving rise to the sgs stresses. Given that the pprog algorithm is not guaranteed to find *all* existing trends, we can not state this conclusion with absolute certainty. Nevertheless, it is very likely that for the Reynolds number range considered, there is no strong, simple connection between large scale velocity gradients and sgs stresses in isotropic turbulence.

Entirely different behavior was observed in turbulent shear flows. Individual components of the stress tensor were found to depend on several elements of the fluctuating strain and rotation rate tensors. The dependence was found to be linear in the case of homogeneous shear flow and quadratic in the case of channel flow. In the case of homogeneous shear flow, the observed dependence was used to guide the construction of a model that involved tensor products of the mean strain and rotation rate with their fluctuating counterparts. This model was shown to produce a correlation between modeled and exact stresses that was 50% higher than that given by the Smagorinsky model. The proposed model for homogeneous shear flow did not carry over to channel flow, and only marginal improvement over the Smagorinsky model was observed. The results of projection pursuit were again used to guide the construction of a model for channel flow. This model was considerably more successful, yielding more than a 200% improvement over the Smagorinsky model. Whereas the shear flow model did not extend well to channel flow, the channel flow model did perform reasonably well in shear flow, yielding correlations that were roughly 90% of those achieved with the shear flow model.

One interesting finding of this work is that mean strain and rotation rates enter in the parameterization of the subgrid-scale stresses, at least in the case of homogeneous shear flow. This is at variance with the view that at large Reynolds numbers the small scales should be nearly isotropic and unaligned with the large-scale motions (Kolmogorov, 1941). Indeed, recent experimental measurements of Saddoughi (1992) confirm small-scale isotropy at high Re . Of course, the low Reynolds number data used here does not provide a sufficient range of scales to realize small scale isotropy, and, consequently, the subgrid scales have some residual alignment with the mean gradients. It is thus conceivable that the observed dependence on the mean quantities would disappear if the Reynolds number and hence the scale separation were increased.

On the other hand, it is not clear that traditional measures of isotropy (spectra, structure functions etc.) have a direct connection with the behavior of the sgs stresses. Alternately, the observed dependence on the mean quantities could also

be present in a slightly different form at higher Reynolds number. In this view, the shear and rotation produced by large scales of size, say, br (where r is the filter size and $b > 2$) may take on the role of mean shear and rotation as far as the small scales are concerned. We did not find such trends in the isotropic flow using $b = 2$, but it is possible that such a trend requires large separation ($b \gg 2$) and higher Re . Unfortunately, this issue cannot be addressed using DNS data at low Reynolds numbers.

Acknowledgements

This work was performed at the Center for Turbulence Research during the 1992 Summer Program. We are thankful to Dr. M. Rogers for making the homogeneous shear calculations available and to Dr. W. Cabot for valuable help with the channel flow data base. CM thanks Prof. J. Friedman (Statistics Dept., Stanford U. & SLAC) for sending him the pprog program, and Profs. D. Naiman and C. Wu (Dept. of Math. Sciences, Johns Hopkins U.) for their initial help in the use of the Splus (©Statistical Sciences Inc.) software, which was ultimately used for this project. CM also acknowledges financial support from NSF CTS-9113048 and ONR N00014-92-J-1109.

REFERENCES

- BARDINA G. 1983 Improved turbulence models based on large eddy simulation of homogeneous, incompressible, turbulent flows, Ph.D. thesis, report TF-19, Mechanical Engineering, Stanford Univ.
- CLARK R. A., FERZIGER J. H., & REYNOLDS W. C. 1979 Evaluation of subgrid-scale models using an accurately simulated turbulent flow. *J. Fluid Mech.* **91**, 1.
- COMTE-BELLOT, G., & CORRSIN, S. 1971 Simple Eulerian time correlation of full and narrow-band velocity signals in grid-generated 'isotropic' turbulence. *J. Fluid Mech.* **48**, 273-337.
- FRIEDMAN J.H. & STUETZLE W. 1981 Projection pursuit regression. *J. Amer. Stat. Assoc.* **76**, 817.
- GERMANO M., PIOMELLI, U., CABOT, W., AND MOIN, P., 1991 A dynamic subgrid-scale eddy viscosity model. *Phys. Fluids A*, **3**, 1760-1765.
- KIM, J., MOIN, P., AND MOSER, R. D., 1987 Turbulence statistics in fully developed channel flow at low Reynolds number. *J. Fluid Mech.* **177**, 133.
- KOLMOGOROV A. N. 1941 Local structure of turbulence in an incompressible fluid at very high Reynolds number. *Dokl. AN SSSR*. **30**, 299.
- LUND T. & NOVIKOV E.A. 1992 Parameterization of subgrid-scale stresses by the velocity gradient tensor, in preparation.
- MCMILLAN O.J. & FERZIGER J.H. 1979 Direct testing of subgrid-scale models. *AIAA J.* **17**, 1340.

- PIOMELLI U., MOIN P. & FERZIGER J.H. 1988 Model consistency in large eddy simulation of turbulent channel flows. *Phys. Fluids*. **31**, 1884.
- ROGALLO R. 1981 Numerical experiments in homogeneous turbulence. *NASA Tech. Mem.* 81315.
- ROGERS, M. M. & MOIN, P. 1987 The structure of the vorticity field in homogeneous turbulent flows. *J Fluid Mech.* **176**, 33-66.
- ROGALLO R. 1992 private communication.
- SADDOUGHI, S. G., 1992 Experimental investigation of local isotropy in high Reynolds number turbulence. *CTR Annual Research Briefs*, Stanford Univ./NASA Ames.

Triad interactions in the dissipation range

By S. Kida¹, R. H. Kraichnan², R. S. Rogallo³, F. Waleffe⁴, and Y. Zhou⁴

Nonlocality of the triad interactions in the dissipation range of developed turbulence is investigated by numerical simulation and the quasi-normal theories. It is found that the energy transfer is dominated by nonlocal triad interactions over the wavenumber range $0.1 < k/k_d < 4$, where k_d is the Kolmogorov wavenumber. The nonlocality of the interaction has a close relation with the power of an algebraic prefactor of the exponential decay of the energy spectrum in the far-dissipation range.

1. Introduction

The triad interaction is the fundamental coupling among the various Fourier components of a turbulent velocity field and transfers energy predominantly from lower to higher wavenumbers. Properties of the triad interactions were studied by Kraichnan (1971) and have recently been analyzed numerically using data from numerical simulations (Domaradzki 1988; Yeung & Brasseur 1991; Domaradzki & Rogallo 1990; Ohkitani & Kida 1992) and by an analysis of interactions among helical waves (Waleffe 1992).

In the inertial range where the energy spectrum obeys the Kolmogorov $-5/3$ power form,

$$E(k) = C_K \epsilon^{2/3} k^{-5/3}, \quad (1.1)$$

where ϵ is the energy dissipation rate and C_K is the Kolmogorov constant (Kolmogorov 1941), the interaction is local in the sense that triad interactions of scale disparity (see (3.4) for definition) greater than 10 (100) contribute only 15% (1%) of the energy flux (Kraichnan 1971; Ohkitani & Kida 1992). Although the locality of the triad interaction is very weak, it is compatible with Kolmogorov's (1941) concept of local energy cascade.

The nature of triad interactions in the dissipation range is expected to be different from that in the inertial range because the energy spectrum decreases very rapidly (exponentially) in the dissipation range. In this paper, we investigate the interactions by analyzing numerical turbulence and by its comparison with the prediction of the quasi-normal closure theories.

1 Kyoto University - RIMS

2 Santa Fe, NM

3 NASA Ames Research Center

4 Center for Turbulence Research

2. Fundamentals

We consider the energy dynamics of the motion of an incompressible viscous fluid in an infinite domain. The equation of motion is written in the Fourier representation as

$$\frac{\partial}{\partial t} \tilde{u}_j(\mathbf{k}) = -\frac{i}{2} P_{jkl}(\mathbf{k}) \sum_{\mathbf{p}+\mathbf{q}+\mathbf{k}=0} \tilde{u}_k^*(\mathbf{p}) \tilde{u}_l^*(\mathbf{q}) - \nu k^2 \tilde{u}_j(\mathbf{k}) + \tilde{f}_j(\mathbf{k}) \quad (2.1)$$

with the continuity equation

$$k_j \tilde{u}_j(\mathbf{k}) = 0, \quad (2.2)$$

where $\tilde{u}_j(\mathbf{k})$ is the x_j ($j = 1, 2, 3$) component of the Fourier coefficient of velocity at wavevector \mathbf{k} ,

$$P_{jkl}(\mathbf{k}) = k_k \left(\delta_{jl} - \frac{k_j k_l}{k^2} \right) + k_l \left(\delta_{jk} - \frac{k_j k_k}{k^2} \right) \quad (2.3)$$

is a third order tensor, ν is the kinematic viscosity, and $\tilde{f}_j(\mathbf{k})$ is the external forcing. Here the time argument t is omitted for brevity, the asterisk denotes the complex conjugate, and repeated subscripts are summed over 1 to 3.

The energy spectral density at wavevector \mathbf{k} ,

$$E(\mathbf{k}) = \frac{1}{2} |\tilde{\mathbf{u}}(\mathbf{k})|^2 \quad (2.4)$$

evolves according to

$$\frac{\partial}{\partial t} E(\mathbf{k}) = T(\mathbf{k}) - 2\nu k^2 E(\mathbf{k}) + \text{Re} \left\{ \tilde{u}_j^*(\mathbf{k}) \tilde{f}_j(\mathbf{k}) \right\}, \quad (2.5)$$

which is derived by multiplying (2.1) by \tilde{u}_j^* and taking the real part.

The first term on the r.h.s. of (2.5) represents the rate of energy transfer to the Fourier mode \mathbf{k} through the nonlinear interactions with all the other modes, the second the energy dissipation by the viscosity, and the third the energy input by the external force.

The energy transfer function $T(\mathbf{k})$ is written as

$$T(\mathbf{k}) = \sum_{\mathbf{p}, \mathbf{q}} T(\mathbf{k}|\mathbf{p}, \mathbf{q}), \quad (2.6)$$

where

$$T(\mathbf{k}|\mathbf{p}, \mathbf{q}) = -\frac{1}{2} \text{Im} \left\{ P_{jkl}(\mathbf{k}) \tilde{u}_j(\mathbf{k}) \tilde{u}_k(\mathbf{p}) \tilde{u}_l(\mathbf{q}) \right\} \delta_{\mathbf{k}+\mathbf{p}+\mathbf{q}} \quad (2.7)$$

is the triad energy transfer due to the interaction among three wavevectors \mathbf{k} , \mathbf{p} , and \mathbf{q} that constitute a triangle ($\mathbf{k} + \mathbf{p} + \mathbf{q} = 0$). Through a triad interaction, energy is exchanged among the three modes involved, with the total energy being conserved. That is, the following detailed balance of energy holds;

$$T(\mathbf{k}|\mathbf{p}, \mathbf{q}) + T(\mathbf{p}|\mathbf{q}, \mathbf{k}) + T(\mathbf{q}|\mathbf{k}, \mathbf{p}) = 0. \quad (2.8)$$

Consequently, the sum of the energy transfer function over all the wavevectors vanishes,

$$\sum_{\mathbf{k}} T(\mathbf{k}) = \sum_{\mathbf{k}, \mathbf{p}, \mathbf{q}} T(\mathbf{k}|\mathbf{p}, \mathbf{q}) = 0. \quad (2.9)$$

Since the flow field is statistically isotropic, it is convenient to average each term in (2.5) over spherical cells in the wavevector space. We introduce the band-averaged energy spectrum

$$\hat{E}(k)\Delta k = \sum_{k-\frac{1}{2}\Delta k \leq |\mathbf{k}'| < k+\frac{1}{2}\Delta k} E(\mathbf{k}'), \quad (2.10)$$

the band-averaged energy transfer function

$$\hat{T}(k)\Delta k = \sum_{k-\frac{1}{2}\Delta k \leq |\mathbf{k}'| < k+\frac{1}{2}\Delta k} T(\mathbf{k}'), \quad (2.11)$$

and the band-averaged forcing spectrum

$$\hat{F}(k)\Delta k = \sum_{k-\frac{1}{2}\Delta k \leq |\mathbf{k}'| < k+\frac{1}{2}\Delta k} \text{Re} \left\{ \tilde{u}_j^*(\mathbf{k}') \tilde{f}_j(\mathbf{k}') \right\}. \quad (2.12)$$

The energy spectrum equation (2.5) is then written for the band-averaged quantities as

$$\frac{\partial}{\partial t} \hat{E}(k) = \hat{T}(k) - 2\nu k^2 \hat{E}(k) + \hat{F}(k). \quad (2.13)$$

The triad energy transfer function $T(\mathbf{k}|\mathbf{p}, \mathbf{q})$ is also averaged over a spherical cell as

$$\hat{T}(k|p, q)(\Delta k)^3 = \sum_{\substack{k-\frac{1}{2}\Delta k \leq |\mathbf{k}'| < k+\frac{1}{2}\Delta k \\ p-\frac{1}{2}\Delta k \leq |\mathbf{p}'| < p+\frac{1}{2}\Delta k \\ q-\frac{1}{2}\Delta k \leq |\mathbf{q}'| < q+\frac{1}{2}\Delta k}} T(\mathbf{k}'|\mathbf{p}', \mathbf{q}'). \quad (2.14)$$

The energy transfer function is then written as

$$\hat{T}(k) = (\Delta k)^2 \sum_{p, q} \hat{T}(k|p, q). \quad (2.15)$$

The detailed balance of energy (2.8) and the conservation of total energy by all the triad interactions (2.9) are written respectively as

$$\hat{T}(k|p, q) + \hat{T}(p|q, k) + \hat{T}(q|k, p) = 0 \quad (2.16)$$

and

$$\sum_{\mathbf{k}} \hat{T}(k) = 0. \quad (2.17)$$

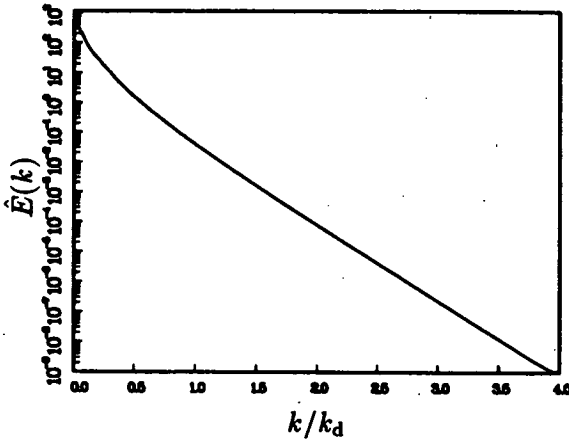


FIGURE 1. Energy Spectrum in the dissipation range. The decay with wavenumber is essentially exponential.

3. Numerical Simulation

The equations of motion (2.1) and (2.2) are solved numerically in a periodic cube with an instability forcing,

$$\tilde{f}_j(\mathbf{k}) = C\tilde{u}_j(\mathbf{k}) \quad \text{for } |\mathbf{k}| \leq k_0. \quad (3.1)$$

The constant C is chosen to force the flow field to equilibrium with a specified range of forced scales $k_0 = 3$ and a specified range of resolved scales, in Kolmogorov units, $k_{\max}/k_d = 4$. The Fourier-spectral method (Rogallo 1981) is employed for the spatial resolution, and time is advanced with a second-order Runge-Kutta procedure. The alias errors arising in the nonlinear terms is removed by a combination of coordinate shifting and spectral truncation. The computational mesh (in physical space) is 256^3 . The initial flow field is taken after over five large-scale turnover times from forced turbulence created at a lower resolution (128^3) at about the same Reynolds number ($R_\lambda \approx 65$). The 256^3 field was then advanced until an equilibrium between transfer, and dissipation was achieved at the higher wavenumbers. We will study that transfer here in some detail. The Kolmogorov dissipation wavenumber,

$$k_d = (\nu^3/\epsilon)^{1/4} \quad (3.2)$$

is about 30, so that the maximum resolved wavenumber $k_{\max} = 121$ retained in the simulation is about four times the Kolmogorov wavenumber.

3.1 Energy spectrum

The energy spectrum at the final time of the simulation is shown in a semi-logarithmic plot in figure 1. The nearly straight line indicates that the energy spectrum decays essentially exponentially with wavenumber. In order to examine

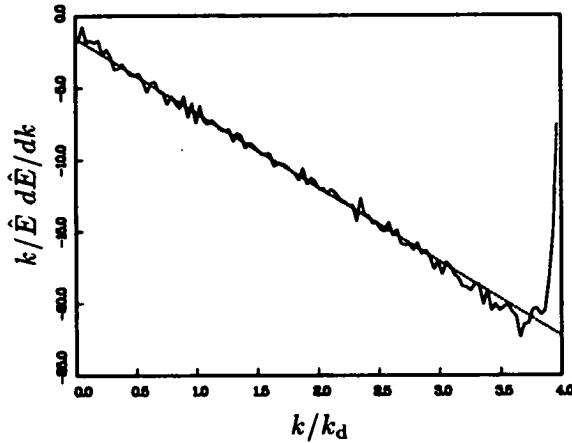


FIGURE 2. Logarithmic derivative of the energy spectrum function. For $E(k) = A(k/k_d)^\alpha \exp[-\beta k/k_d]$ the slope of the curve gives $-\beta$ and the intersection on the vertical axis gives α . —, simulation data; ----, least-square fit over $.5 \leq k/k_d \leq 3$ gives $\alpha = -1.6$, $\beta = 5.2$.

the shape of the spectrum more precisely, we compare it with an exponential form with an algebraic prefactor

$$E(k) = A(k/k_d)^\alpha \exp[-\beta k/k_d]. \quad (3.3)$$

In figure 2, we plot the logarithmic derivative of the energy spectrum. If the spectrum has the form (3.3), the slope of the line and its intersection with the vertical axis give the values of β and α , respectively. Since this is an instantaneous spectrum, the fluctuations are quite large. Nevertheless, the least squares fit over $0.5 \leq k/k_d \leq 3$ gives $\alpha = -1.6$ and $\beta = 5.2$, which are consistent with those observed before in numerical simulations by other researchers (Kida & Murakami 1987; Kida *et al.* 1990; Kerr 1990; Sanada 1992). More recently however, Chen (1992 private communication) has simulated the dissipation range at $R_\lambda \approx 15$ to much higher k/k_d . He finds $\alpha = 2.16$ and $\beta = 7.35$ by a least-square fit over the range $5.2 \leq k/k_d \leq 10.4$. The data from the present simulations do not coincide with Chen's for $k/k_d \leq 4$, suggesting that the results are sensitive to Reynolds number. There may also be some effect due to the method of forcing. Incidentally, the exponential shape of the energy spectrum in the far-dissipation range has also been observed in experiments (Sreenivasan 1985).

There is a theoretical prediction of the power in the algebraic correction. The quasi-normal theories of turbulence (Kraichnan 1959; Tatsumi 1980; Lesieur 1987), which will be discussed in some detail in the next section, predict $\alpha = 3$ in the far-dissipation range. This value of α is quite different from those observed in the numerical simulations. But it should be remembered that the dissipation range is restricted to $k/k_d < 2 \sim 3$ in the simulations mentioned above so that it is not clear whether this discrepancy results from a failure of the quasi-normal theories

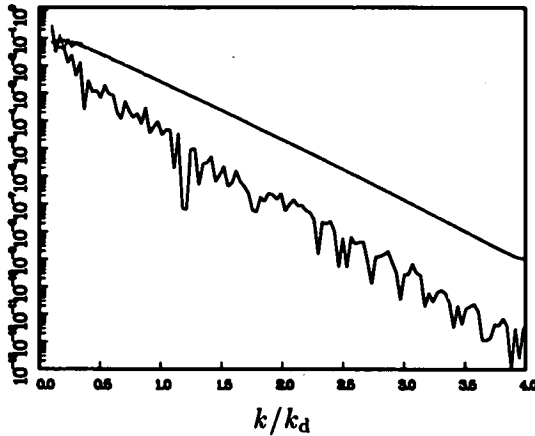


FIGURE 3. The energy-spectrum balance: ----, transfer $\hat{T}(k)$; - · -, dissipation $2\nu k^2 \hat{E}(k)$; —, departure from equilibrium $|\hat{T}(k) - 2\nu k^2 \hat{E}(k)|$. The equilibrium between transfer and dissipation is apparent over most of the wavenumber range.

or from the low wavenumbers considered. As a matter of fact, there is a numerical suggestion that the spectrum may be consistent with positive values of α less than 3 over the wavenumber range $4 < k/k_d < 10$ for a low Reynolds number ($R_\lambda \approx 15$) flow (Domaradzki 1992 private communication).

In order to see the dominant terms of (2.13), we plot $\hat{T}(k)$ and $2\nu k^2 \hat{E}(k)$ in figure 3. Recall that the forcing term $\hat{F}(k)$ in (2.13) is restricted to low wavenumbers ($k/k_d \leq 0.1$). We see that both $2\nu k^2 \hat{E}(k)$ and $\hat{T}(k)$ vary exponentially with wavenumber and that they are in equilibrium. Their difference is less than their magnitude by more than two orders of magnitude over most of the wavenumber range ($k/k_d > 1$, say).

3.2 Triad energy transfer

The triad energy transfer function $\hat{T}(k|p, q)$ is most efficiently calculated by an alias-free spectral method applied to filtered fields (Domaradzki & Rogallo 1990). In figure 4, we plot $\hat{T}(k|p, q)$ for $k/k_d = 2$ and $k/k_d = 3$. The finest band-width is employed, i.e. $\Delta k = 1$. The solid and broken curves denote the positive and negative values, respectively. We recognize the following characteristics in $\hat{T}(k|p, q)$. First, there are strong dipoles at the corners $q \ll p \approx k$ and $p \ll q \approx k$ of the boundary. The signs of the dipoles are positive (negative) on the smaller (larger) side of wavenumber p/k or q/k . Second, the most significant part of $\hat{T}(k|p, q)$ is localized near the boundary $p + q = k$, and the thickness of this part decreases as k/k_d increases. The magnitude of $\hat{T}(k|p, q)$ decreases exponentially with wavenumber away from this boundary. The value of $\hat{T}(k|p, q)$ in the blank region is too low to draw clear curves.

The first characteristic was also observed in the inertial range (Kida & Ohkitani 1992) and represents the energy transferred to larger wavenumbers by nonlocal interactions. The second characteristic, on the other hand, is peculiar to the dissipation

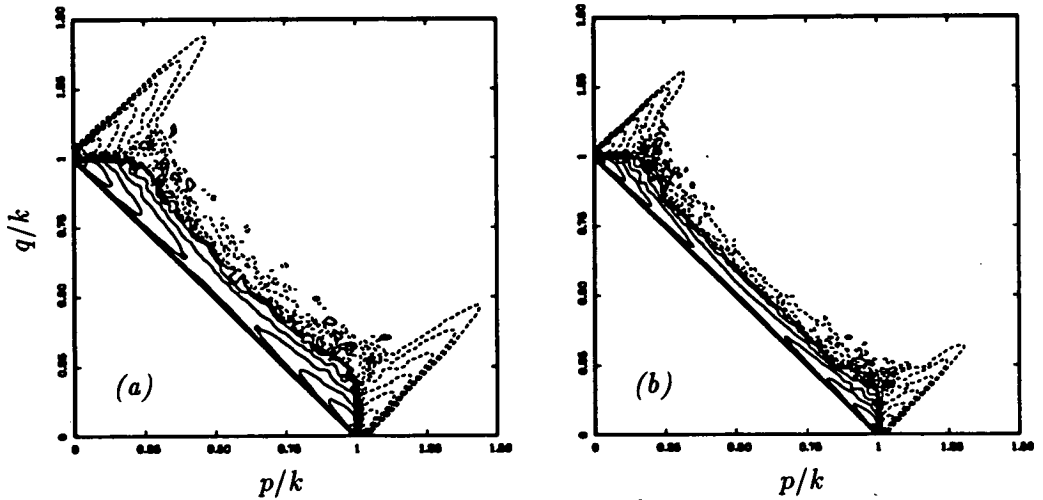


FIGURE 4. The triad energy transfer function $\hat{T}(k|p, q)$ for the numerical turbulence. (a) $k/k_d = 2$, (b) $k/k_d = 3$. The solid and broken curves represent the positive and negative parts, respectively. The contour levels are logarithmic, rather than linear, and are separated by a factor of 4.

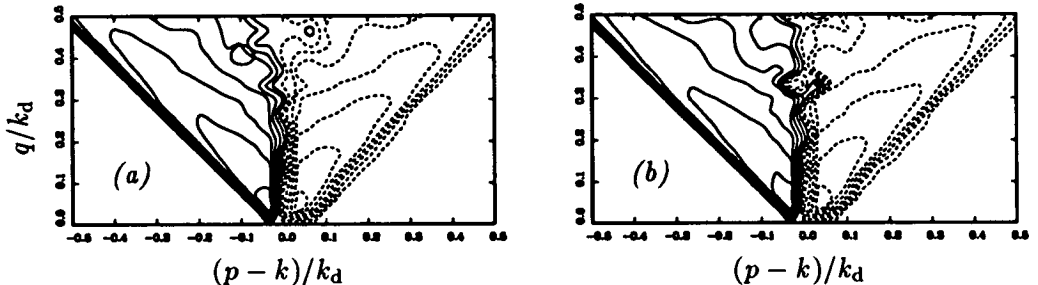


FIGURE 5. The triad energy transfer function $\hat{T}(k|p, q)$ for the numerical turbulence. (a) $k/k_d = 2$, (b) $k/k_d = 3$. The solid and broken curves represent the positive and negative parts, respectively. The contour levels are logarithmic, rather than linear, and are separated by a factor of 4.

range. This arises from the rapid (exponential) decay of the energy spectrum with wavenumber in the dissipation range in contrast with the slow (algebraic) decay in the inertial range.

Similarity in the contours evidently is not obtained over the whole domain of $\hat{T}(k|p, q)$ plotted in figure 4. Since, however, the dipole parts are very similar in figures 4(a) and (b), we enlarge the corner region and replot the contours in figures 5(a) and (b), respectively, with wavenumbers normalized by the Kolmogorov wavenumber k_d instead of k . This scaling of the wavenumber is suggested by the closure theory (see (4.12)).

The close resemblance of figures 5(a) and (b) implies that the shape of the dipoles of $\hat{T}(k|p, q)$ is similar near the corners if the wavenumber is scaled by the Kolmogorov wavenumber.

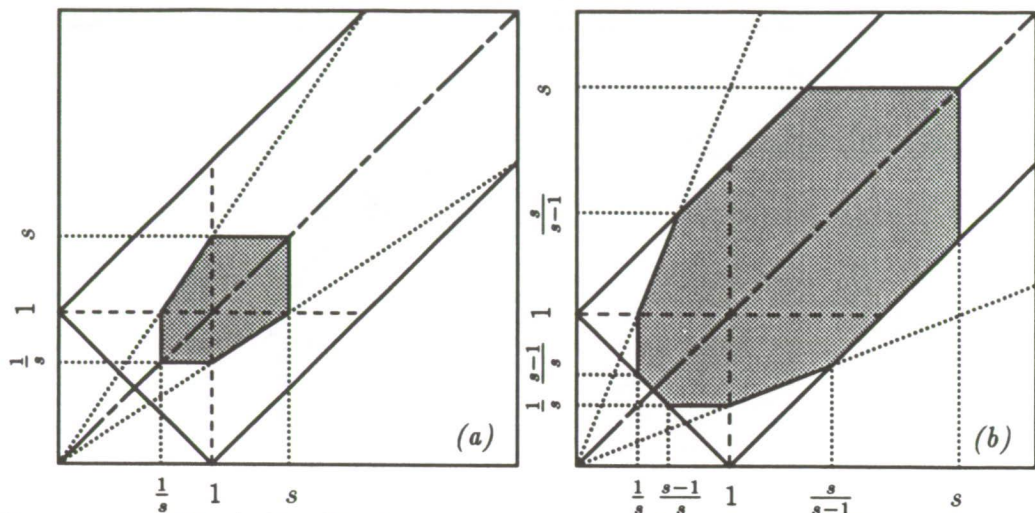


FIGURE 6. The $(p/k, q/k)$ domain of integration for $T(k|p, q)$. The measure of scale disparity is $s = \max(k, p, q)/\min(k, p, q)$. (a) $s \leq 2$, (b) $s \geq 2$.

3.3 Nonlocality of triad interaction

The triad energy transfer function $\hat{T}(k|p, q)$ represents the energy exchange among three wavenumbers with magnitudes k , p , and q . In order to express the scale locality of the triad interaction, we introduce the scale disparity parameter (Zhou 1992), the ratio of the maximum to the minimum of the triad wavenumbers,

$$s = \frac{\max(k, p, q)}{\min(k, p, q)}. \tag{3.4}$$

It follows by definition that $s \geq 1$. This scale disparity parameter measures the scale locality of the triad interaction. If s is smaller, the interaction is more local, and vice versa. In figure 6, we indicate the (k, p, q) domains for relatively local ($s \leq 2$) and relatively non-local ($s \geq 2$) triad interactions.

Let us denote by $\hat{T}(k|s)\Delta k$ the contribution to the energy transfer from triad interactions with scale disparity parameter between $s - \frac{1}{2}\Delta s$ and $s + \frac{1}{2}\Delta s$. Then, we have

$$\hat{T}(k|s) = (\Delta k)^2 \sum_{\substack{p, q \\ s - \frac{1}{2}\Delta s \leq \frac{\max(k, p, q)}{\min(k, p, q)} < s + \frac{1}{2}\Delta s}} \hat{T}(k|p, q). \tag{3.5}$$

In figure 7, we plot $\hat{T}(k|s)$, obtained by summing up the terms in the r.h.s. of (3.5) numerically for $k/k_d = 2$ and $k/k_d = 3$. It is seen that $\hat{T}(k|s)$ may have a scale similarity with sk_d/k .

4. Closure Theory

In the quasi-normal closure theories (see Tatsumi 1980; Lesieur 1987), the energy transfer term in the energy spectrum equation (2.13) is expressed in terms of the

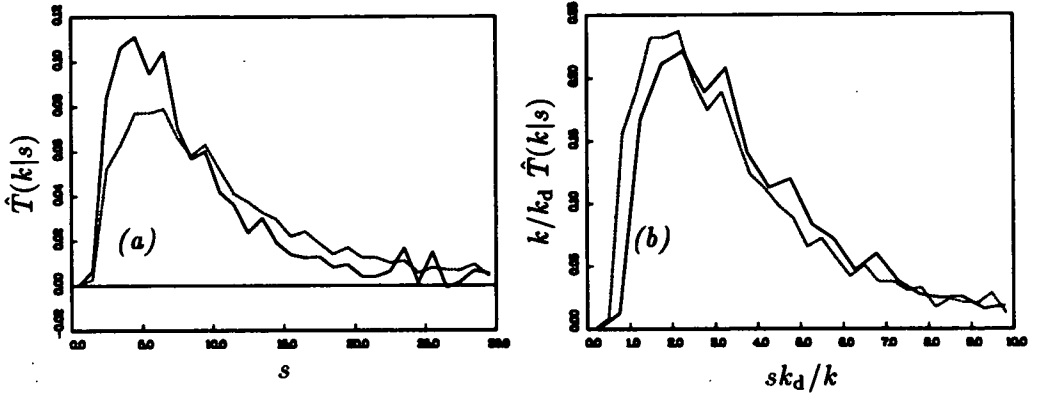


FIGURE 7. The scale disparity of energy transfer $\hat{T}(k|s)$: —, $k/k_d = 2$; ----, $k/k_d = 3$. (a) local scaling: s , (b) non-local scaling sk_d/k .

energy spectrum function under the assumption that the fourth-order cumulants of the velocity are negligible:

$$T(k|p, q) = \theta_{kpq} \frac{Q^2}{16kpq} \left((B_{kpq} + B_{kqp}) \frac{E(p)E(q)}{p^2q^2} - B_{kpq} \frac{E(k)E(q)}{k^2q^2} - B_{kqp} \frac{E(k)E(p)}{k^2p^2} \right), \quad (4.1)$$

where

$$B_{kqp} = (k^2 - q^2)(p^2 - q^2) + k^2p^2 \quad (4.2)$$

and

$$Q^2 = 2k^2p^2 + 2k^2q^2 + 2p^2q^2 - k^4 - p^4 - q^4. \quad (4.3)$$

Here θ_{kpq} , the relaxation time of the triple moments of velocity, takes different forms in the various theories. In the far-dissipation range ($k, p, q \gg k_d$), however, it has the common expression

$$\theta_{kpq} = \frac{1}{\nu(k^2 + p^2 + q^2)}. \quad (4.4)$$

In the far-dissipation range of statistically stationary turbulence, the first two terms balance in (2.13),

$$T(k) = 2\nu k^2 E(k). \quad (4.5)$$

In this section, we omit the hat ($\hat{}$) because we are considering the continuous limit (infinite size of the periodic cube). The summation in (2.15) of the energy transfer function converts into the integral

$$T(k) = \int \int_{\Delta_k} T(k|p, q) dp dq, \quad (4.6)$$

where the integration is carried out under the condition that the three wavenumbers k , p , and q constitute a triangle.

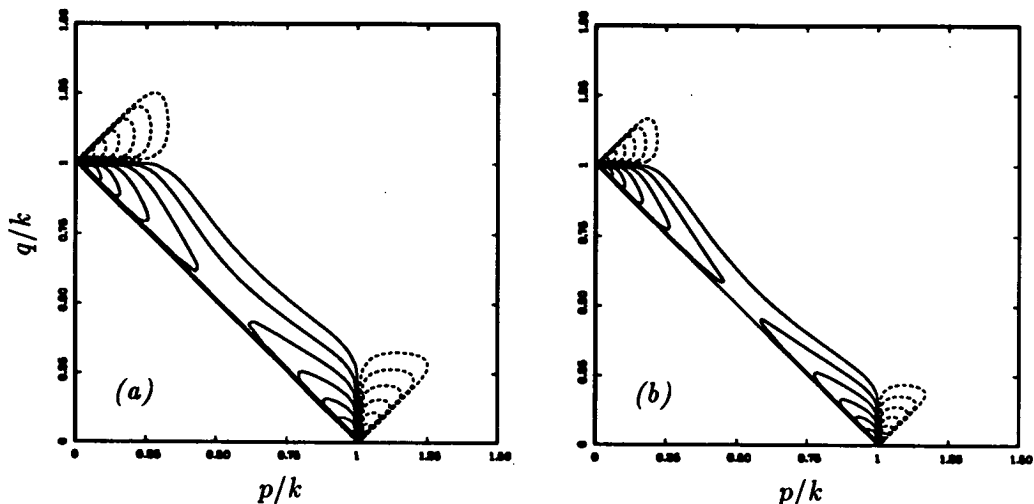


FIGURE 8. The triad energy transfer function $T(k|p, q)$ for the quasi-normal closure theory with $E(k) \propto (k/k_d)^{-1.6} \exp[-4.9k/k_d]$. (a) $k/k_d = 2$ and (b) $k/k_d = 3$. The solid and broken curves represent the positive and negative parts, respectively. The contour levels are logarithmic, rather than linear, and are separated by a factor of 4.

By substituting (4.6) with (4.1)-(4.4) and (3.3) into (4.5) and taking the leading terms in the limit of large wavenumber $k \gg k_d$, we obtain $\alpha = 3$ (Tatsumi 1980). This value of α is not consistent with the results of the numerical simulation as mentioned in section 3. The reason for this discrepancy is not known at present. As will be discussed in the next section, other values are consistent with the theory if the relaxation time θ_{kpp} is suitably modified (see (5.1)). We therefore proceed to examine the behavior of the triad energy transfer function expressed as (4.1) for the spectrum (3.3) with $\alpha = -1.6$.

In figure 8, we show the contours of $T(k|p, q)$ expressed by (4.1) with the spectrum (3.3) with $\alpha = -1.6$ and $\beta = 4.9$ for both $k/k_d = 2$ and $k/k_d = 3$. Contrary to the simulation data (figure 4), we can see contour lines at very low levels clearly. The same characteristics of $T(k|p, q)$ observed in figure 4 are also observed here. That is, (i) there are strong dipoles at the corners of the boundary of the triangle condition, (ii) $T(k|p, q)$ is positive where either p or q is less than k and negative otherwise, (iii) the magnitude of $T(k|p, q)$ decreases rapidly as point (p, q) moves away from the boundary $p + q = k$, and (iv) it decreases more rapidly as k/k_d increases. Moreover, the shape of the contours in figures 4 and 8 is very similar. The agreement is better for positive contours than for negative ones.

The difference in the shape of the contours can be seen more clearly in figure 9, which is an enlargement of figure 8 near $q \ll p \approx k$. As will be discussed in the next subsection, the slight difference in the shape of contours seems to be the main reason for the discrepancy in the behavior of $T(k|s)$ between the numerical simulation and the closure theory.

It should be mentioned here that the influence of the forcing term may not be

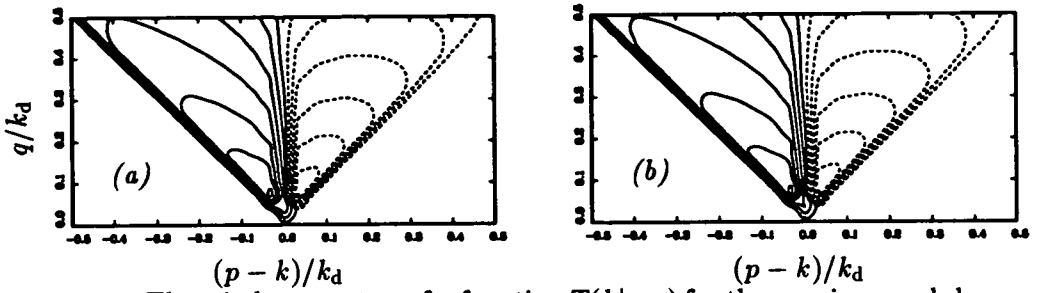


FIGURE 9. The triad energy transfer function $T(k|p, q)$ for the quasi-normal closure theory with $E(k) \propto (k/k_d)^{-1.6} \exp[-4.9k/k_d]$. (a) $k/k_d = 2$ and (b) $k/k_d = 3$. The solid and broken curves represent the positive and negative parts, respectively. The contour levels are logarithmic, rather than linear, and are separated by a factor of 4.

negligibly small. Since the fluid is forced at wavenumbers less than 3, the contours at $q/k_d < 0.1$ are directly affected by the forcing term.

So far, we have examined only the case of $\alpha = -1.6$. In order to see the dependence of $T(k|p, q)$ on the value of α , we plot in figure 10 the contours of $T(k|p, q)$ for various values of α ranging from 3 to -2. It is seen that the domains of the positive and negative parts are insensitive to the value of α , but the shape of the contours other than the zero level changes depending on the value of α . For a large value of α , the positive and negative peaks of $T(k|p, q)$ are far from the corners. They move toward the corner as α decreases. For $\alpha > 0$, the peaks are away from the corner, but for $\alpha < 0$, a positive and a negative peak merge into a dipole at the corner (see (4.12)). As will be shown in the next subsection, the dominant interactions in the energy transfer are local for $\alpha > 1$ and nonlocal for $\alpha < 1$.

4.1 Scale Disparity of Energy Transfer

Let $T(k|s)ds$ be the contribution to the energy transfer to Fourier modes at wavenumber k due to triad interactions for which the scale disparity parameter lies between s and $s + ds$. The contribution from all the triad interactions of scale disparity less than s is then written as

$$\int_1^s T(k|s')ds' = \int \int_{\substack{\Delta_k \\ \frac{\max(k,p,q)}{\min(k,p,q)} \leq s}} T(k|p, q)dpdq. \tag{4.7}$$

The derivative of (4.7) gives the scale disparity of energy transfer

$$T(k|s) = \frac{d}{ds} \int \int_{\substack{\Delta_k \\ \frac{\max(k,p,q)}{\min(k,p,q)} \leq s}} T(k|p, q)dpdq. \tag{4.8}$$

The integration of $T(k|s)$ over all s gives the energy transfer $T(k)$, i.e.

$$T(k) = \int_1^\infty T(k|s)ds. \tag{4.9}$$

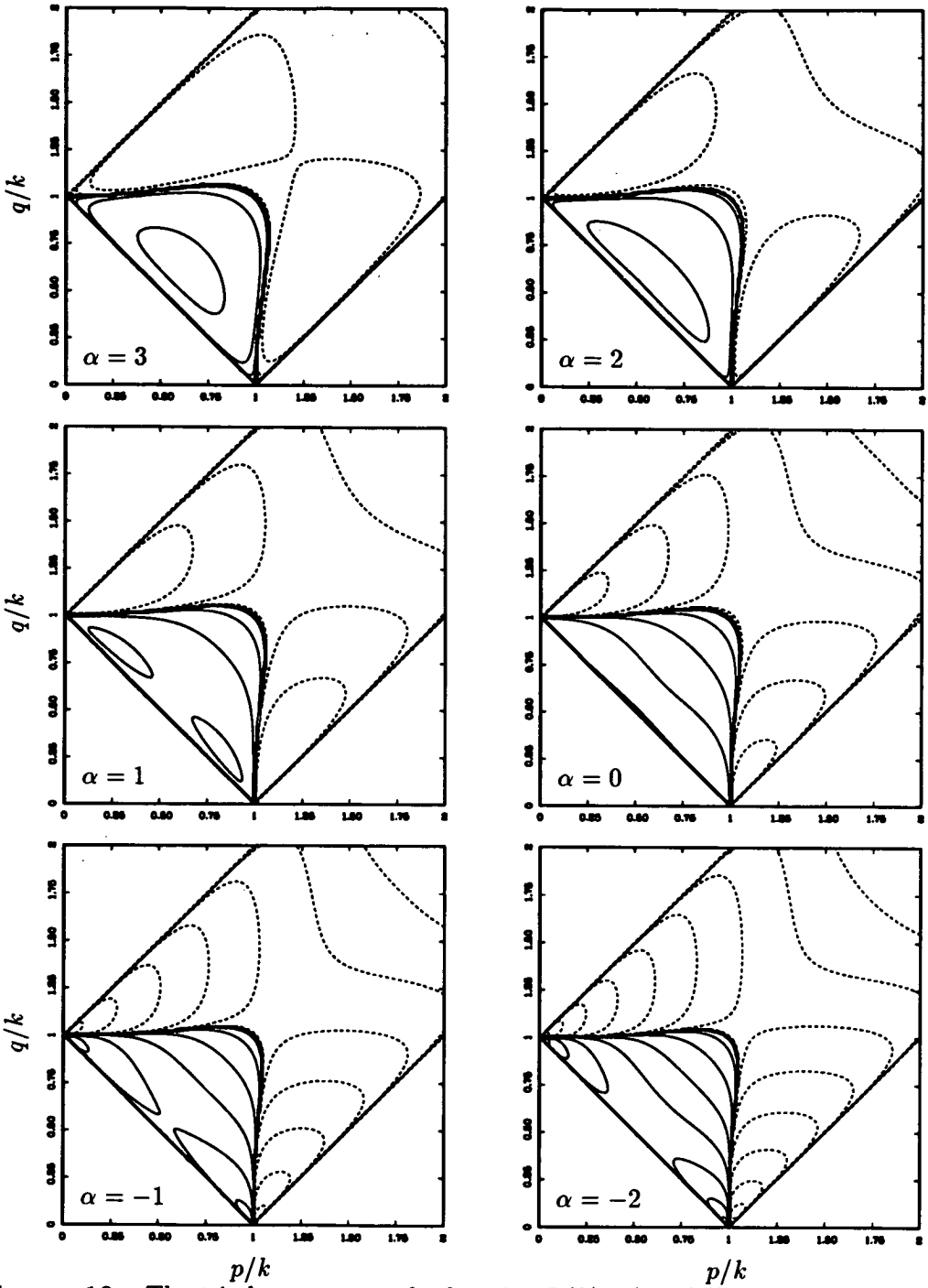


FIGURE 10. The triad energy transfer function $T(k|p, q)$ at $k/k_d = 1$ given by the quasi-normal closure theory for $E(k) \propto (k/k_d)^\alpha \exp[-4.9k/k_d]$, $-2 \leq \alpha \leq 3$

The integral (4.7) is written explicitly for $s \leq 2$ as (see figure 6)

$$\int_1^s T(k|s') ds' = 2 \left\{ \int_{k/s}^k dp \int_{k/s}^p dq + \int_k^{sk} dp \int_{p/s}^p dq \right\} T(k|p, q) \quad (4.10a)$$

and for $s \geq 2$ as

$$\begin{aligned} \int_1^s T(k|s') ds' = 2 \left\{ \int_{k/2}^{(s-1)k/s} dp \int_{k-p}^p dq + \int_{(s-1)k/s}^k dp \int_{k/s}^p dq \right. \\ \left. + \int_k^{sk/(s-1)} dp \int_{p/s}^p dq + \int_{sk/(s-1)}^{sk} dp \int_{p-k}^p dq \right\} T(k|p, q) \end{aligned} \quad (4.10b)$$

Differentiating (4.10a) and (4.10b) with respect to s we obtain

$$\begin{aligned} T(k|s) = 2 \left\{ \frac{k}{s^2} \int_{k/s}^k T(k|p, k/s) dp + k \int_k^{sk} T(k|sk, q) dq \right. \\ \left. + \frac{1}{s^2} \int_k^{sk} p T(k|p, p/s) dp \right\} \quad (s \leq 2) \end{aligned} \quad (4.11a)$$

$$\begin{aligned} = 2 \left\{ \frac{k}{s^2} \int_{(s-1)k/s}^k T(k|p, k/s) dp + k \int_{(s-1)k}^{sk} T(k|sk, q) dq \right. \\ \left. + \frac{1}{s^2} \int_k^{sk/(s-1)} p T(k|p, p/s) dp \right\} \quad (s \geq 2) \end{aligned} \quad (4.11b)$$

By substituting the expression (4.1) for $T(k|p, q)$ from the quasi-normal closure theory with the energy spectrum (3.3) into (4.11a) and (4.11b), we can calculate $T(k|s)$ explicitly. The scale disparity transfer function behaves differently depending on the values of α and k/k_d . In figure 11(a), we plot $T(k|s)$ for $k/k_d = 1, 2,$ and 3 with $\alpha = 3$. The interaction is localized around $s = 2$. The peak of the scale disparity parameter moves little as k/k_d increases. In figure 11(b), we plot $T(k|s)$ for $k/k_d = 1, 2,$ and 3 with $\alpha = -1.5$. The interaction becomes more nonlocal as k/k_d increases, and the peak of the scale disparity parameter moves linearly with k/k_d for large k/k_d .

In order to examine the wavenumber dependence of the transfer function, we replot it in figure 11(c) against sk_d/k for $k/k_d = 2, 3,$ and ∞ (see below for $k/k_d = \infty$). The scale disparity of the energy transfer seems to approach a universal form for large values of k/k_d . The approach is faster for large values of s .

As demonstrated in figure 10, the triad energy transfer function $T(k|p, q)$ for small α (see below (4.12) for the critical value) has a double peak at the corners $q \ll p \approx k$ and $p \ll q \approx k$. This peak becomes steeper for larger values of k/k_d because of the exponential decay of the energy spectrum. This enables us to make

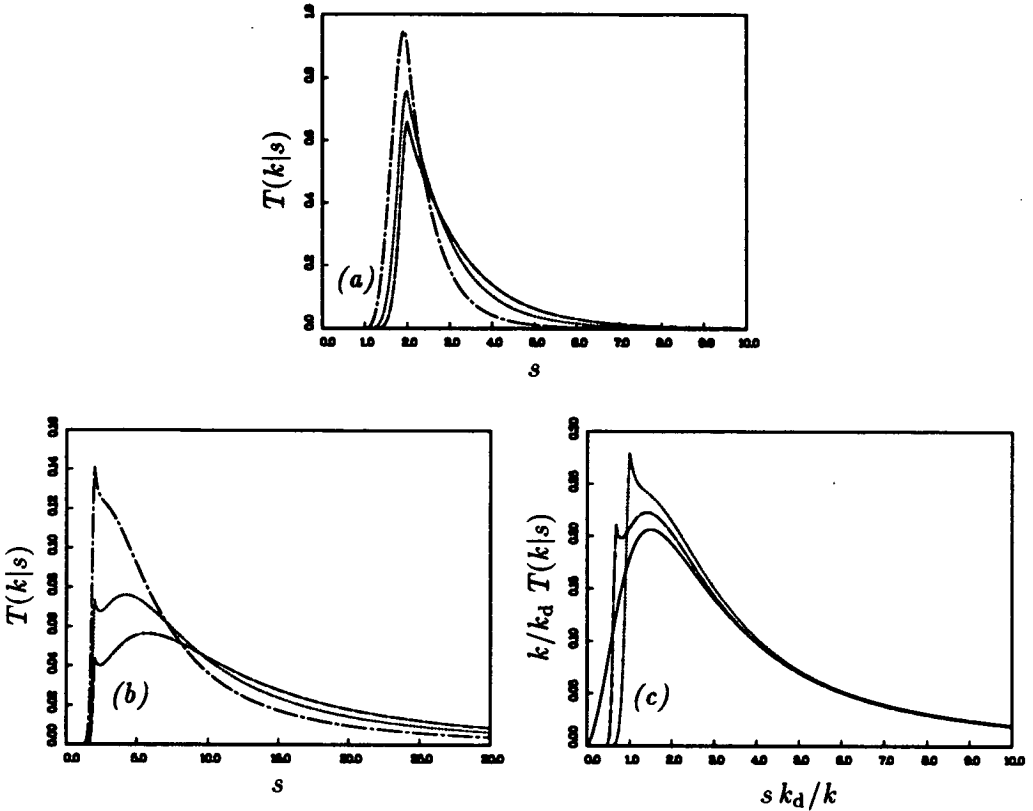


FIGURE 11. The scale disparity of energy transfer $T(k|s)$ in the quasi-normal closure theory with $E(k) \propto (k/k_d)^\alpha \exp[-4.9k/k_d]$. (a) $\alpha = 3$, (b,c) $\alpha = -1.5$. ----, $k/k_d = 1$; - - - -, $k/k_d = 2$; - · - ·, $k/k_d = 3$; ———, $k/k_d = \infty$.

a local analysis around the corner to estimate the asymptotic behavior of $T(k|s)$ for large values of k/k_d . The triad energy transfer function (4.1) with the energy spectrum (3.3) behaves around $q \ll p \approx k$ as

$$T(k|p, q) = \frac{A^2}{4\nu} \left(\frac{k}{k_d}\right)^\alpha e^{-\beta k/k_d} \left(\frac{q}{k_d}\right)^\alpha q^{-3} (q^2 - (p-k)^2) e^{-\beta q/k_d} \left(e^{\beta(k-p)/k_d} - 1\right). \quad (4.12)$$

The energy transfer function $T(k)$ is calculated by integrating $T(k|p, q)$ with respect to p and q over the whole range. When $\alpha < 1$, the integral is localized at the corners $q \ll p \approx k$ and $p \ll q \approx k$ so that the asymptotic expression (4.12) can be used. The result is

$$\begin{aligned} T(k) &= 2 \int_0^\infty \int_{k-q}^{k+q} T(k|p, q) dp \\ &= \frac{2A^2 k_d}{\nu \beta^{\alpha+1}} \left(\frac{2^{-2}}{(\alpha-2)(\alpha-1)} - \frac{1}{3} \right) \Gamma(\alpha+1) \left(\frac{k}{k_d}\right)^\alpha e^{-\beta k/k_d} \end{aligned} \quad (4.13)$$

for $-2 < \alpha < 1$, where Γ is the Gamma function. Note that the integral is localized at the corners and converges only when $-2 < \alpha < 1$.

Substituting (4.12) into (4.11b), we obtain

$$T(k|s) = \frac{A^2 k_d}{2\nu\beta^{\alpha+2}} \left(\frac{k}{k_d}\right)^{\alpha-1} e^{-\beta k/k_d} \times \sigma^{-(\alpha+2)} \left(2\sigma^2(1-\sigma) - \frac{4}{3}e^{-1/\sigma} + 2\sigma^2(1+\sigma)e^{2/\sigma}\right), \quad (4.14)$$

where

$$\sigma = \frac{k_d}{\beta k} s. \quad (4.15)$$

Note that we consider here the case $k/k_d \gg 1$ so that $s \gg 1$ for a finite value of σ . The asymptotic form (4.14) of $T(k|s)$ for large values of k/k_d is drawn for $\alpha = -1.5$ and $\beta = 4.9$ in figure 11(c).

5. Discussion

The triad interaction in the dissipation range has been investigated by analysis of numerical turbulence data and the quasi-normal closure theory of turbulence. The results of the numerical simulation suggest that the motion at the Kolmogorov dissipation scale couples directly with the smaller scales and that the triad interaction is nonlocal in scale, at least in the wavenumber range $0.1 < k/k_d < 4$ investigated here. The closure theory, on the other hand, suggests that the locality of the triad interaction depends crucially on the power α of an algebraic prefactor of the exponential decay of the energy spectrum at large wavenumbers. It is local or nonlocal for $\alpha > 1$ or $\alpha < 1$, respectively.

In the EDQNM and related quasi-normal closure theories, the triad energy transfer function is expressed by (4.1). The form of the relaxation time θ_{kpq} differs from theory to theory but has the common asymptotic form (4.4) in the far-dissipation range where a balance between energy transfer and dissipation requires $\alpha = 3$ instead of the value $\alpha \approx -1.6$ found in the numerical simulation.

It is interesting, however, to note that if the relaxation time is assumed to be independent of the wavenumber in the far dissipation range, say equal to the Kolmogorov time scale

$$\theta_{kpq} \propto \sqrt{\nu/\epsilon} = \frac{1}{\nu k_d^2}, \quad (5.1)$$

then any value of α (including $\alpha = -1.6$) is compatible with the energy balance equation (4.4). As shown below, however, this is not the case in the EDQNM theory.

In the EDQNM theory, the relaxation time takes the form

$$\theta_{kpq} = \frac{1}{\nu(k^2 + p^2 + q^2) + \mu(k) + \mu(p) + \mu(q)}, \quad (5.2)$$

where $\mu(k) = \lambda(\int_0^k r^2 E(r) dr)^{1/2}$ is the eddy damping rate and λ is an adjustable constant which may be related to the Kolmogorov constant C_K as $\lambda = 0.154 C_K^{3/2}$

(André & Lesieur 1977). Note that $\lambda = 0.37$ for $C_K = 1.8$. The first term in the denominator in (5.2) represents viscous damping and the second the relaxation by straining motions of comparable and larger scales. The relaxation time has the following asymptotic forms for small and large wavenumbers for $C_K = 1.8$:

$$\theta_{kpq} = \frac{2.3}{k^{2/3} + p^{2/3} + q^{2/3}} \quad (k, p, q \ll k_d) \quad (5.3a)$$

$$= \frac{1}{\nu(k^2 + p^2 + q^2)} \quad (k, p, q \gg k_d) \quad (5.3b)$$

The integrals in (5.2) tend to the energy dissipation for large wavenumber,

$$\epsilon/2\nu = \int_0^\infty r^2 E(r) dr. \quad (5.4)$$

The peak of the integrand lies around $r = 0.15k_d$, and the majority of the integrand is covered in the wavenumber domain $r < 0.5k_d$ (see Kida & Murakami 1987). The two effects are comparable at wavenumber

$$k, p, q \approx \lambda^{1/2}/2^{1/4} k_d \approx 0.5k_d. \quad (5.5)$$

Around these wavenumbers the relaxation time is written as

$$\theta_{kpq} \approx \frac{1}{\nu(k^2 + p^2 + q^2) + 0.78(\epsilon/\nu)^{1/2}} = \frac{1}{\nu(k^2 + p^2 + q^2 + 0.78k_d^2)}. \quad (5.6)$$

We may conclude from (5.3) and (5.6) that there is no region of constant θ_{kpq} in the EDQNM theory.

It is possible that the value of $\alpha \approx -1.6$ observed in wavenumber range $0.1 < k/k_d < 4$ is simply a tangent and that it approaches 3 in the limit of large wavenumbers. If so, the transfer may be dominated there by local triad interactions.

REFERENCES

- ANDRÉ, J. C. & LESIEUR, M. 1977 Influence of helicity on the evolution of isotropic turbulence at high Reynolds number. *J. Fluid Mech.* **81**, 187.
- DOMARADZKI, J. A. 1988 Analysis of energy transfer in direct numerical simulations of isotropic turbulence. *Phys. Fluids.* **31**, 2747.
- DOMARADZKI, J. A. & ROGALLO, R. S. 1990 Local energy transfer and nonlocal interactions in homogeneous isotropic turbulence. *Phys. Fluids A.* **2**, 413.
- KERR, R. M. 1990 Velocity, scalar and transfer of spectra in numerical turbulence. *J. Fluid Mech.* **211**, 309.
- KIDA, S. & MURAKAMI, Y. 1987 Kolmogorov similarity in freely decaying turbulence. *Phys. Fluids.* **30**, 2030.

- KIDA, S., MURAKAMI, Y., OHKITANI, K. & YAMADA, M. 1990 Energy and flatness spectra in a forced turbulence. *J. Phys. Soc. Japan.* **59**, 4323.
- KOLMOGOROV, A. N. 1941 The local structure of turbulence in incompressible viscous fluid for very large Reynolds numbers. *C. R. (Dokl.) Acad. Sci. USSR.* **30**, 301.
- KRAICHNAN, R. H. 1959 The structure of isotropic turbulence at very high Reynolds numbers. *J. Fluid Mech.* **5**, 497.
- KRAICHNAN, R. H. 1971 Inertial-range transfer in two- and three-dimensional turbulence. *J. Fluid Mech.* **47**, 525.
- LESIEUR, M. 1987 *Turbulence in Fluids*. Martinus Nijhoff.
- OHKITANI, K. & KIDA, S. 1992 Triad interaction in a forced turbulence. *Phys. Fluids A.* **4**, 794.
- ROGALLO, R. S. 1981 Numerical experiments in homogeneous turbulence. *NASA TM-81315*.
- SANADA, T. 1992 Comment on the dissipation-range spectrum in turbulent flows. *Phys. Fluids A.* **4**, 1086.
- SREENIVASAN, K. R. 1985 On the fine-scale intermittency of turbulence. *J. Fluid Mech.* **151**, 81.
- TATSUMI, T. 1980 Theory of homogeneous turbulence. *Adv. Appl. Mech.* **20**, 39.
- WALEFFE, W. 1992 The nature of triad interactions in homogeneous turbulence. *Phys. Fluids A.* **4**, 350.
- YEUNG, P. K. & BRASSEUR, J. G. 1991 The response of isotropic turbulence to isotropic and anisotropic forcings at large scales. *Phys. Fluids A.* **3**, 884.
- ZHOU, Y. 1992 Interacting scales and energy transfer in isotropic turbulence. (Submitted for publication.)

A study of the fine scale motions of incompressible time-developing mixing layers

By J. Soria¹, M. S. Chong², R. Sondergaard³,
A. E. Perry⁴ AND B. J. Cantwell³

This work is an extension of a project conducted at the previous CTR summer program and was reported by Chen *et al.* (1990). In that program, the geometry and topology of the dissipating motions in a variety of shear flows was examined. All data was produced by direct numerical simulations (DNS). The partial derivatives of the velocity field were determined at every grid point in the flow and various invariants and related quantities were computed from the velocity gradient tensor. Motions characterized by high rates of kinetic energy dissipation and high enstrophy were of particular interest. Scatter diagrams of the invariants were mapped out and interesting and unexpected patterns were seen. Each type of shear layer produced its own characteristic scatter plot.

In the present project, attention is focused on the incompressible plane mixing layer, and the scatter diagrams are replaced with more useful joint probability density contours. Comparison of the topology of the dissipating motions of flows at different Reynolds numbers are made. Also, plane mixing layers at the same Reynolds number but with different initial conditions are compared.

1. Method of approach

The velocity gradient tensor may be broken up into a symmetric and an antisymmetric part $A_{ij} = \partial u_i / \partial x_j = S_{ij} + W_{ij}$ where $S_{ij} = (\partial u_i / \partial x_j + \partial u_j / \partial x_i) / 2$ and $W_{ij} = (\partial u_i / \partial x_j - \partial u_j / \partial x_i) / 2$ are the rate-of-strain and rate-of-rotation tensors, respectively. The eigenvalues of A_{ij} satisfy the characteristic equation

$$\lambda^3 + P\lambda^2 + Q\lambda + R = 0 \quad (1)$$

where the matrix invariants are:

$$P = -(A_{11} + A_{22} + A_{33}) = -\text{trace}[A] = -S_{ii} \quad (2)$$

1 C.S.I.R.O., Highett, Australia.

2 Dept. of Mechanical Engineering, University of Melbourne, Australia.

3 Department of Aeronautics and Astronautics, Stanford University

4 Currently GALCIT, California Institute of Technology.

$$\begin{aligned}
 Q &= \begin{vmatrix} A_{11} & A_{12} \\ A_{21} & A_{22} \end{vmatrix} + \begin{vmatrix} A_{11} & A_{13} \\ A_{31} & A_{33} \end{vmatrix} + \begin{vmatrix} A_{22} & A_{23} \\ A_{32} & a_{33} \end{vmatrix} \\
 &= \frac{1}{2} [P^2 - \text{trace}[A^2]] \\
 &= \frac{1}{2} [P^2 - S_{ij}S_{ji} - W_{ij}W_{ji}]
 \end{aligned} \tag{3}$$

and

$$\begin{aligned}
 R &= - \begin{vmatrix} A_{11} & A_{12} & A_{13} \\ A_{21} & A_{22} & A_{23} \\ A_{31} & A_{32} & a_{33} \end{vmatrix} = -\det[A] \\
 &= \frac{1}{3} (-P^3 + 3PQ - \text{trace}[A^3]) \\
 &= \frac{1}{3} (-P^3 + 3PQ - S_{ij}S_{jk}S_{ki} - 3W_{ij}W_{jk}S_{ki}).
 \end{aligned} \tag{4}$$

It can be shown that, in the $P - Q - R$ space of matrix invariants, the surface which divides characteristic equations with three real solutions for the eigenvalues from characteristic equations with one real and two complex solutions is

$$27R^2 + (4P^3 - 18PQ)R + (4Q^3 - P^2Q^2) = 0. \tag{5}$$

A detailed discussion of the properties of this surface is given in Chong, Perry & Cantwell (1990) along with a guide to the various possible elementary flow patterns which can occur in different domains.

Much of the discussion in this report concerns the symmetric part of the velocity gradient tensor, the second invariant of which is proportional to the negative of the kinetic energy dissipation. The invariants of the rate-of-strain tensor, P_S , Q_S and R_S , are generated by setting the components of W_{ij} to zero in the above relations. The flows considered are, with one exception, incompressible hence $P = P_S = 0$. Thus the local geometry of the flow is completely described by the second and third invariants (Q, R) and (Q_S, R_S). The second invariant of the rate-of-rotation tensor, Q_W , is non-zero and is proportional to the enstrophy. The first and third invariants of the rate-of-rotation tensor are identically zero.

The method for classifying the flow structure was first developed at the 1990 CTR summer program by Chen *et al.* (1990) and is described as follows:

- (i) Evaluate the nine partial derivatives of the velocity gradient tensor at every point in the computed field.
- (ii) Evaluate Q, R, Q_S, R_S and Q_W at every point.
- (iii) Create scatter plots of the results in the space of invariants, Q versus R, Q_S versus R_S , and $-Q_S$ versus Q_W .

Figure 1 illustrates the various flow topologies which can occur in the plane $P = 0$. The intersection of this plane with the surface (5) is given by

$$R = \pm \frac{2\sqrt{3}}{9} (-Q)^{3/2} \tag{6}$$

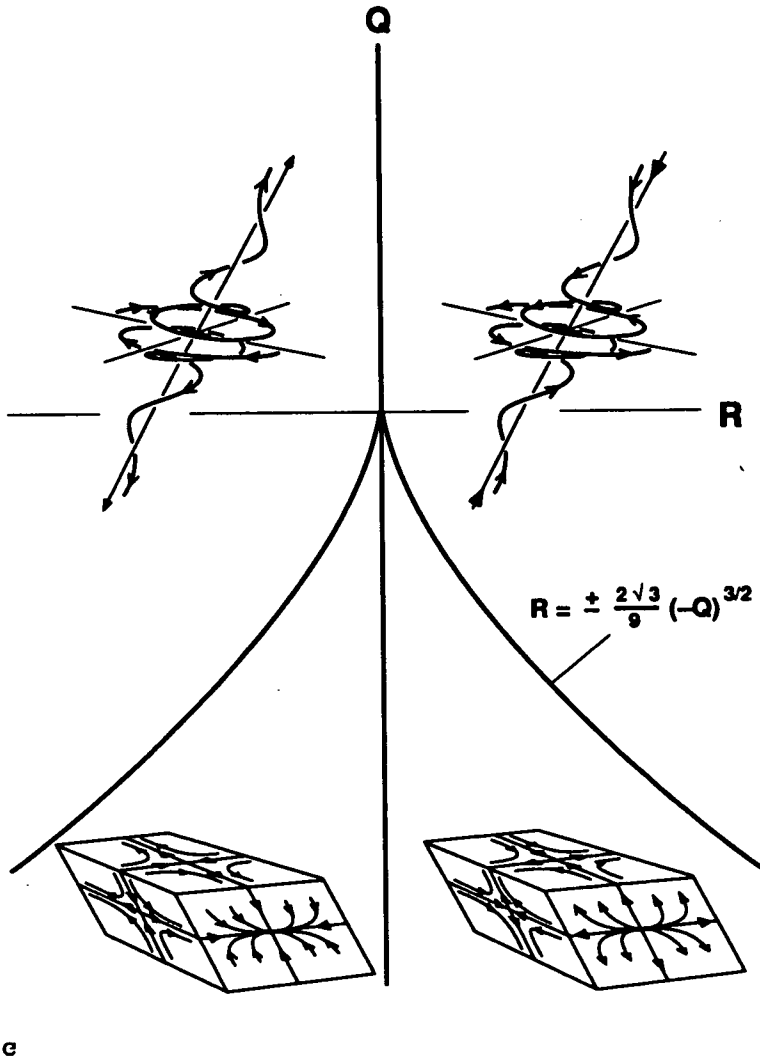


FIGURE 1. Three-dimensional topologies in the $Q - R$ ($P = 0$) plane.

which divides real solutions from complex solutions as indicated.

For the case $P = 0$, the second invariant is

$$Q = \frac{1}{2} [W_{ij}W_{ij} - S_{ij}S_{ij}] \tag{7}$$

where the indices have been switched to indicate explicitly that Q is formed from the difference of two terms, each of which is a positive sum of squares. The local topology has complex or real eigenvalues depending on whether the (Q, R) pair evaluated at a given point in the flow lies above or below (6).

The mechanical dissipation of kinetic energy due to viscous friction is

$$\phi = 2\nu S_{ij}S_{ij} = -4\nu Q_S. \tag{8}$$

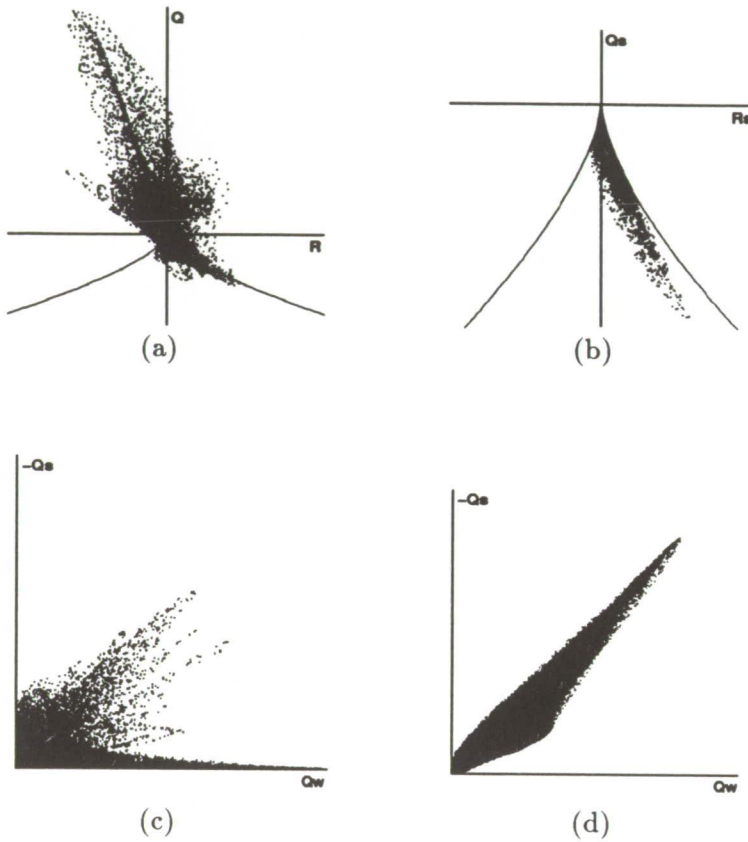


FIGURE 2. Scatter plots of (a) Q vs. R , (b) Q_s vs. R_s , (c) $-Q_s$ vs. Q_w for *hipairex* at $tU/\delta_0 = 29.8$, and (d) Q_s vs. Q_w for a compressible mixing layer computed by Chen (1991) at $tU/\delta_0 = 72.0$.

Large negative values of Q_s correspond to large rates of dissipation of kinetic energy. Large negative values of Q indicate regions where the strain is both large and strongly dominant over the enstrophy. Large positive values of Q indicate the reverse.

2. Results

We will consider in this paper the incompressible ($P = 0$) plane mixing layers computed by Rogers and Moser at NASA Ames. Three direct numerical simulations (DNS) are considered, namely, *hipairex*, *mega*, and *tbl*. The cases *hipairex* and *mega* were initiated from laminar error function profiles, and *tbl* was initiated with two turbulent boundary layer realizations with equal and opposite free stream velocities placed on opposite sides of a dividing plate which was dissolved at time $t = 0$. The initial turbulent boundary layers were DNS computations of Spalart (1988).

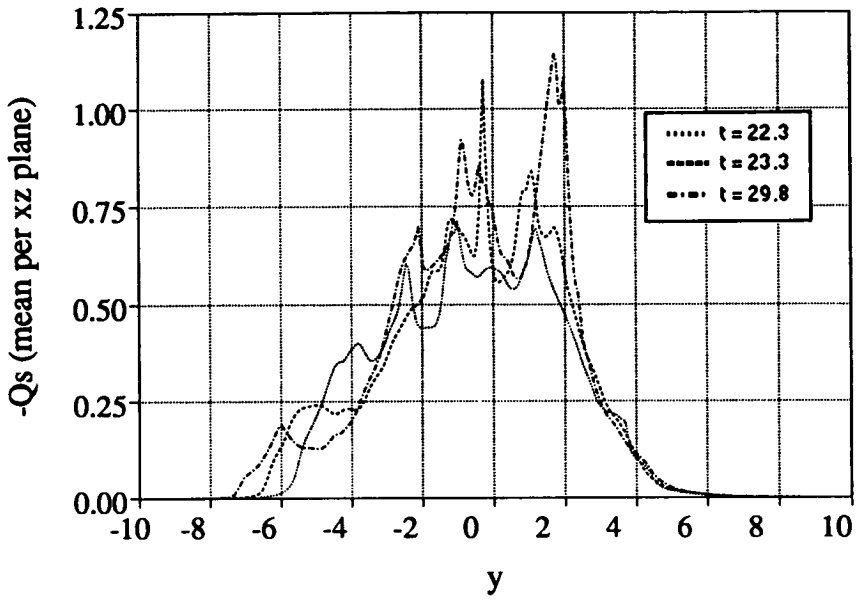


FIGURE 3. Planar x-z average $\overline{Q_s}$ vs. cross-stream direction y for *hipairex* at $tU/\delta_0 = 22.3, 25.3, 29.8$.

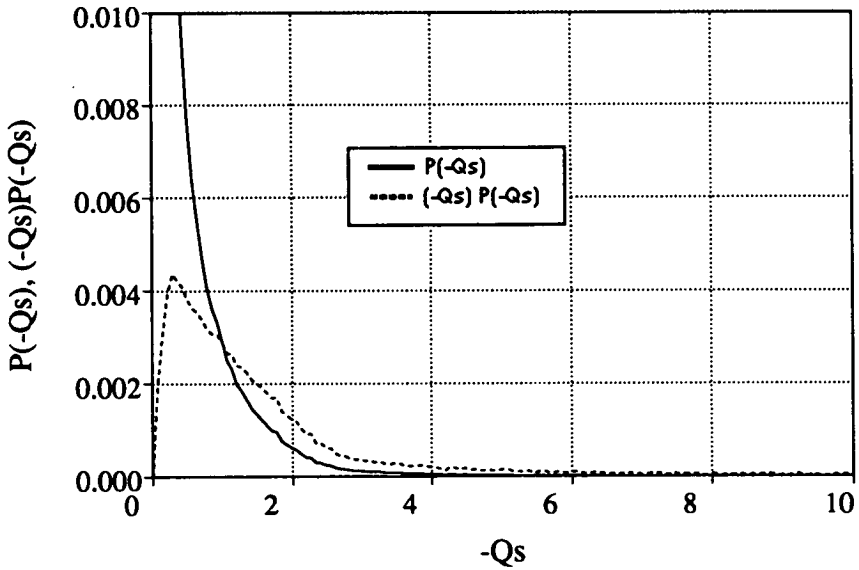


FIGURE 4. Weighted Probability Density Functions $P(-Q_s)$ and $(-Q_s)P(-Q_s)$ vs. $-Q_s$ for *hipairex* at $tU/\delta_0 = 29.8$.

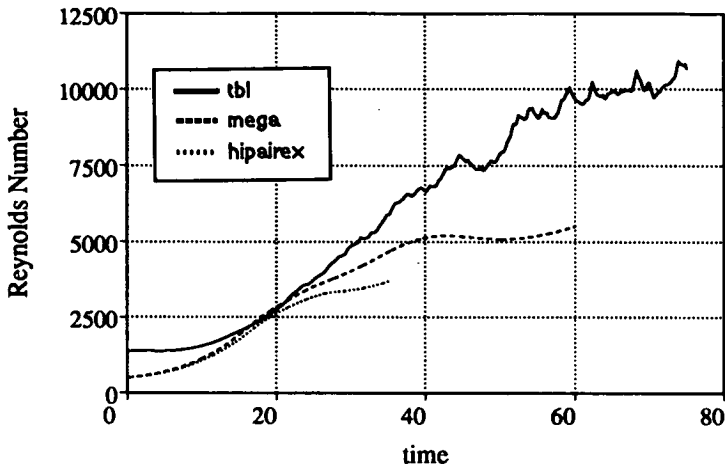


FIGURE 5. Vorticity thickness Reynolds number R_δ vs. non-dimensional time for the incompressible mixing layers.

Table I

	<i>hipairex</i>	<i>mega</i>	<i>tbl</i>
$\Delta U = U_2 - U_1$	2	2	2
Initial vorticity thickness, δ_0	1	1	1.4
Viscosity, ν	1/250	1/250	1/500
Initial $Re = \Delta U \delta_0 / 2\nu$	250	250	700

All cases were computed as time developing layers and Table I shows the properties of the layers. Details of the *hipairex* results have been reported by Moser & Rogers (1990) and Rogers & Moser (1992). Unless otherwise stated, all results are normalized by half the velocity difference across the layer, U , and the initial vorticity thickness δ_0 . Figures 2(a), 2(b) and 2(c) show scatter diagrams taken from Chen *et al.* (1990). These diagrams are made up of the entire data set for a given time. Figure 2(a) shows that most of the high gradient motions belong to the topology of stable focus stretching. Figure 2(c) is most informative. Data which falls on the line of 45° through the origin represents high dissipation accompanied by high enstrophy. It can be shown that such points come from vortex sheets where most of the rate-of-strain is dominated by the velocity gradient within the sheet. Data which lies along the horizontal axis represents high enstrophy with little dissipation as would occur in solid body rotation in vortex tubes. As a matter of interest, Figure 2(d) shows a plot from a compressible mixing layer computation by Chen (1990), and, according to the figure, the data could be described as primarily sheet-like. The reason for this is a mystery at this stage.

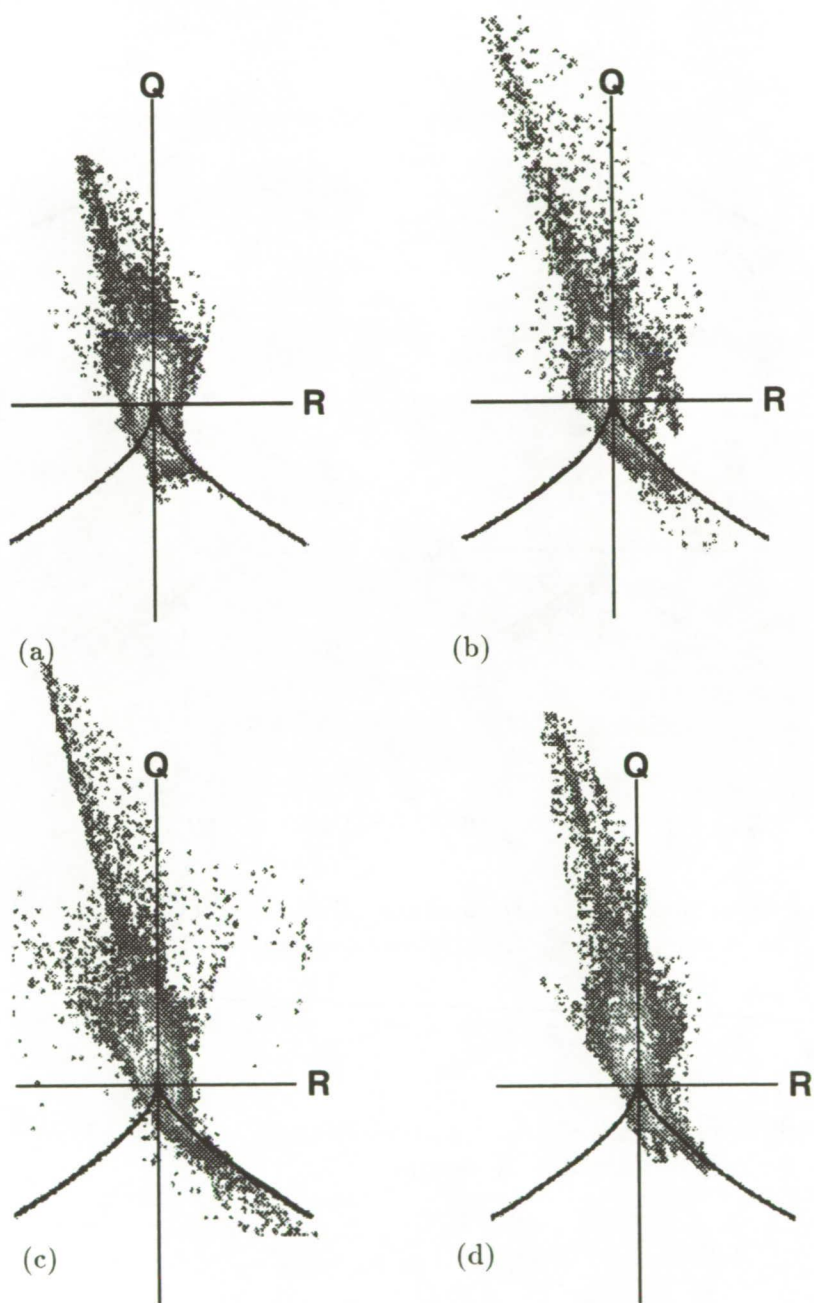


FIGURE 6. Q vs R for *hipairex*. $tU/\delta =$ (a) 19.3, (b) 22.3, (c) 25.3, (d) 29.8.

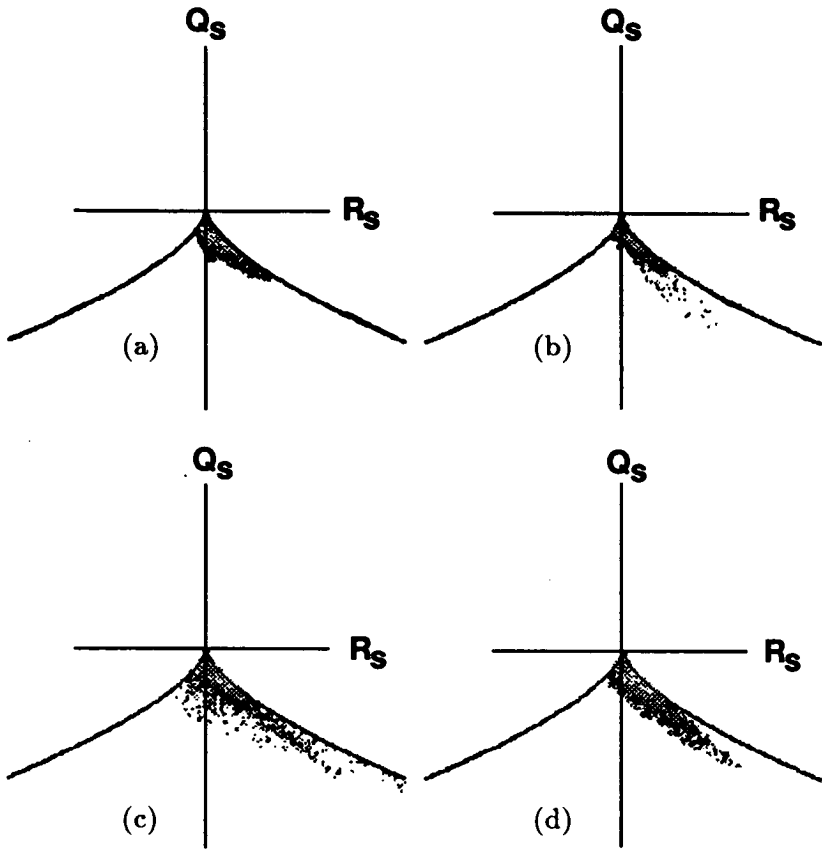


FIGURE 7. Q_s vs R_s for *hipair ex.* $tU/\delta =$ (a) 19.3, (b) 22.3, (c) 25.3, (d) 29.8.

Classical arguments, based on the idea that dissipation of turbulent kinetic energy scales with production, lead to the following estimates:

$$\epsilon = 2\nu \overline{S'_{ij} S'_{ij}} = -\overline{u'v'} \frac{\partial \overline{U}}{\partial y} \tag{9}$$

where the S'_{ij} are fluctuating non-normalized strain rates. Results from experiment show that for fully developed shear layers

$$-\overline{u'v'}/(\Delta U)^2 \simeq .012 = \frac{-\overline{u'v'}}{4U^2}. \tag{10}$$

From (9) and (10) it can be shown that

$$\epsilon = 2\nu \overline{S'_{ij} S'_{ij}} = .096U^3/\delta \tag{11}$$

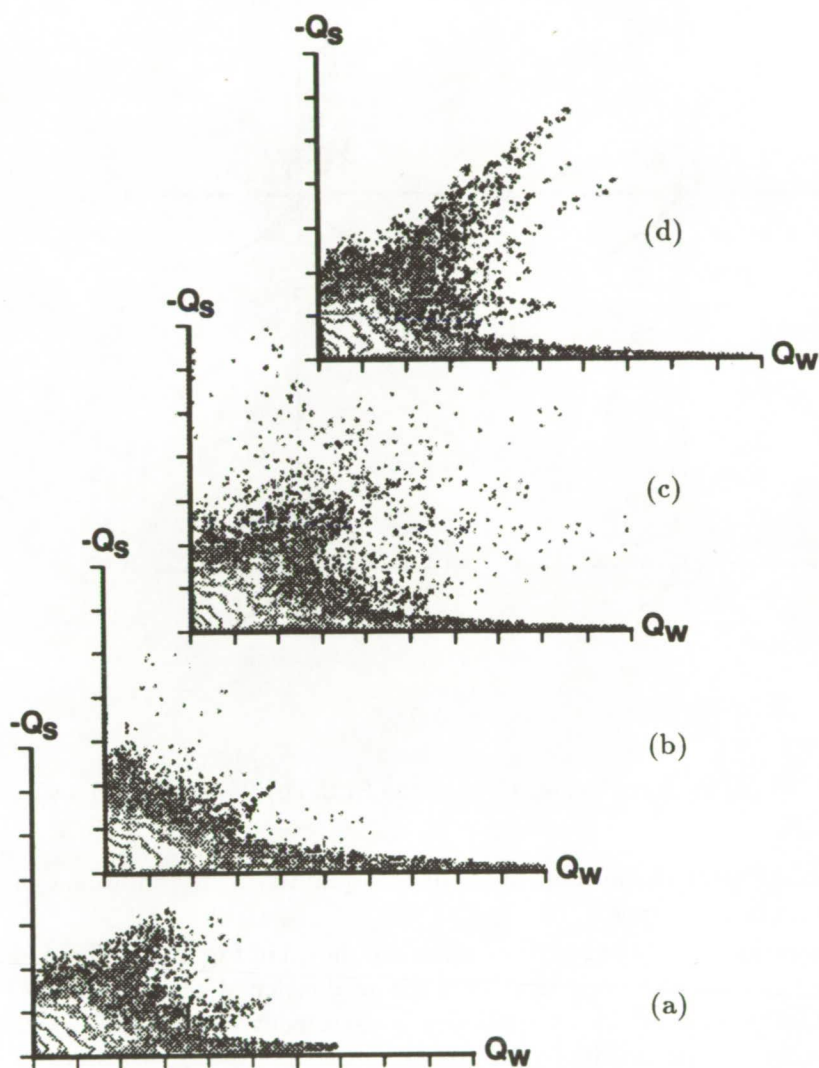


FIGURE 8. $-Q_s$ vs Q_w for *hipairex*. $tU/\delta =$ (a) 19.3, (b) 22.3, (c) 25.3, (d) 29.8.

For time $tU/\delta_0 = 29.8$ in *hipairex* where the vorticity thickness has increased by a factor of 6.5 over the initial thickness, the Reynolds number R_δ based on the current vorticity thickness, δ , and the velocity difference across the layer is 3000. Hence

$$\frac{\overline{S'_{ij} S'_{ij} \delta_0^2}}{U^2} \approx \frac{.096}{4} R_\delta \left(\frac{\delta_0}{\delta} \right)^2 = 1.704. \quad (12)$$

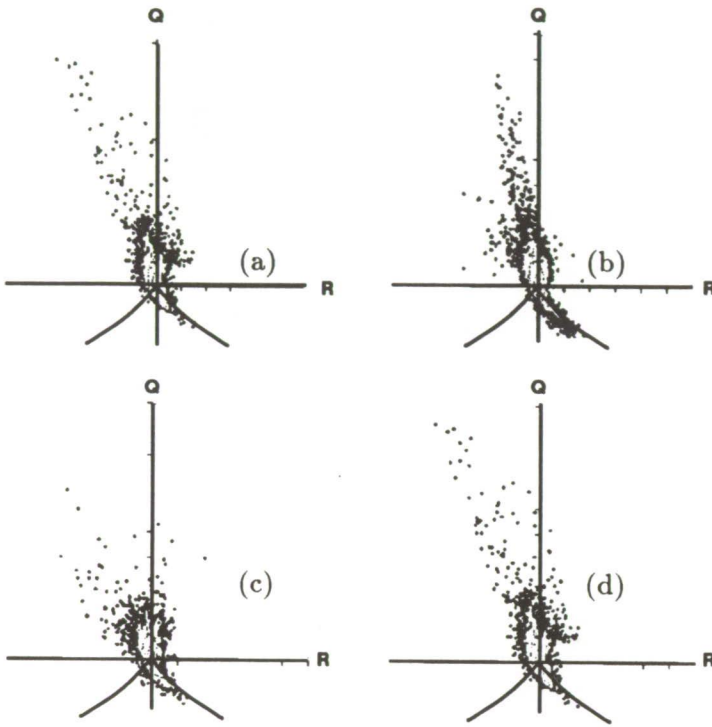


FIGURE 9. Q vs R for *mega*. $tU/\delta =$ (a) 21.0, (b) 25.0, (c) 35.0, (d) 49.0.

One would expect the average value of this quantity at the midplane of the mixing layer to be of this order.

Mean profiles of $-Q_S$ at various times are shown in Figure 3 and are half the value indicated by (12) which is indicative of the production of kinetic energy. This ratio of about 2 for production to dissipation is in agreement with the fully developed value obtained from experiments by Bradshaw & Ferriss (1967). An order of magnitude analysis similar to (12) reported by Chen *et al.* (1990) giving the value of 18.2 was in error due to incorrect normalization of the variables.

Figure 4 shows the weighted probability density function of $-Q_S$ over the entire volume of the mixing layer, and most of the contribution comes from $-Q_S$ between 0 and 3. Although the far flung values of $-Q_S$ on the scatter diagram tend to follow interesting patterns, they contribute only of order 10% to the total energy dissipation. For this reason, it was felt that scatter diagrams should be replaced by joint probability density diagrams with contours corresponding to the logarithm of the probability density function so that possible ridges could be seen in regions which are highly darkened in the scatter plots.

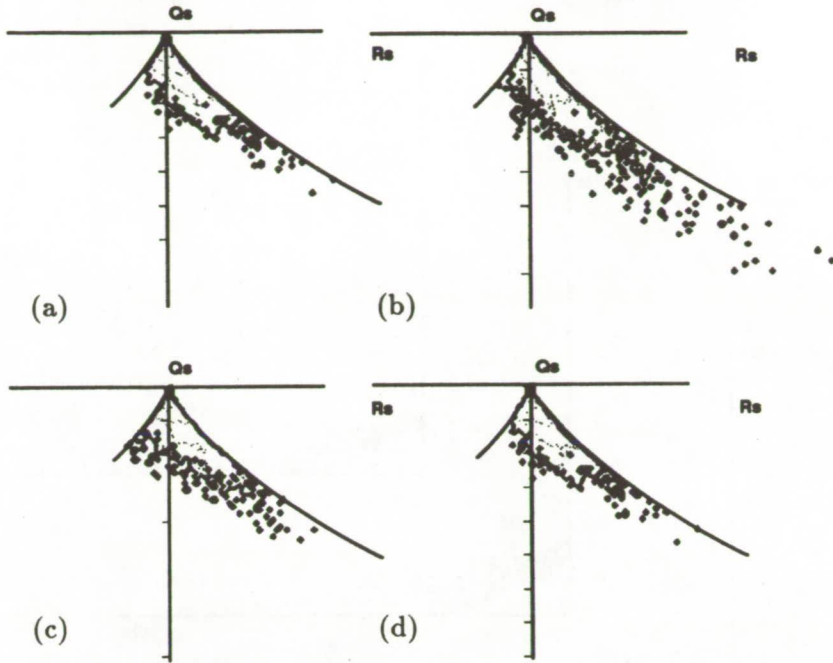


FIGURE 10. Q_s vs R_s for *mega*. $tU/\delta =$ (a) 21.0, (b) 25.0, (c) 35.0, (d) 49.0.

From (11) and (12) it can be seen that Q_S normalized by the current vorticity thickness scales with R_δ , and, therefore, it seems likely that R_S should scale with $R_\delta^{3/2}$. This would imply that the data should follow a curve

$$|R_s| \propto (|Q_s|)^{2/3} \tag{13}$$

This relationship is what one might expect purely on dimensional grounds, but there is no rigorous proof. It is interesting to note that such a curve on the Q_S versus R_S plot represents a rate of strain geometry where the principal rates of strain α , β and γ are in a constant ratio to one another. For the data set *hipairex*, points of high dissipation follow closely the curve corresponding to the ratio of $\alpha:\beta:\gamma = 3:1:-4$, which was observed by Ashurst *et al.* (1987) in studies of forced isotropic turbulence. In addition, as noted by Sondergaard *et al.* (1991), the vorticity vector tends to align itself with the second principle rate of strain β . It should be noted that while other data sets analyzed by Sondergaard *et al.* (1991) show the same vorticity alignment, the 3:1:-4 ratio of rates of strain is not always observed.

The result depicted in 2(b) is that motions characterized by very high rates of dissipation (large negative Q_S) clearly show a preference for the right half plane of Figure 2(b) corresponding to a local topology of the rate of strain tensor which is

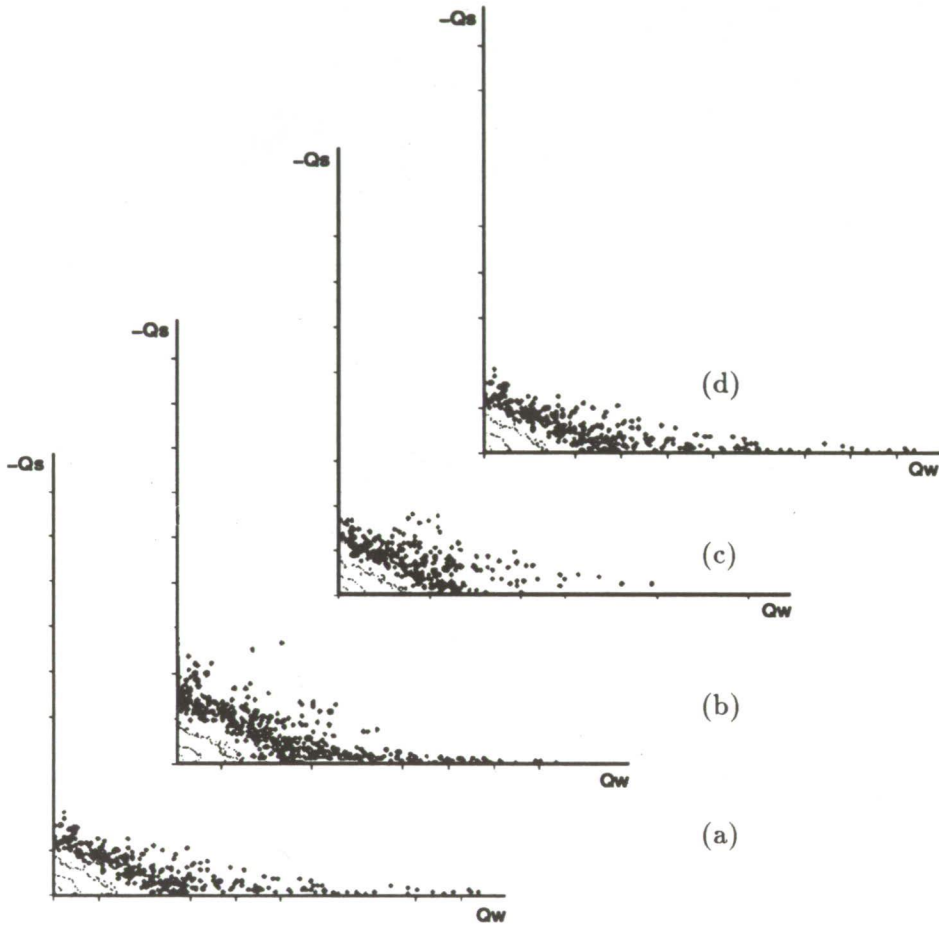


FIGURE 11. $-Q_s$ vs Q_w for *mega*. $tU/\delta =$ (a) 21.0, (b) 25.0, (c) 35.0, (d) 49.0.

of the type saddle-saddle-unstable node (cf. Figure 1). From Figure 2(a), it can be seen that the velocity gradient tensor admits all possible incompressible topologies although there is, nevertheless, a great deal of structure in Figure 2(a). Not only is the basic scaling (12) observed, but it appears that, with a modest amount of scatter, the fine scale motions follow a relation of the form

$$R_s \cong K(-Q_s)^{\frac{3}{2}}. \tag{13}$$

The positive quantity K is expected to be a function of the Reynolds number with an upper limit of $K = 2\sqrt{3}/9$ corresponding to locally axisymmetric flow (cf. Figure 1).

3. Comparison with high Reynolds number flows

Figure 5 shows a plot of Reynolds number based on current vorticity thickness for the three cases mentioned earlier. Figures 6, 7, and 8 show the invariant plots

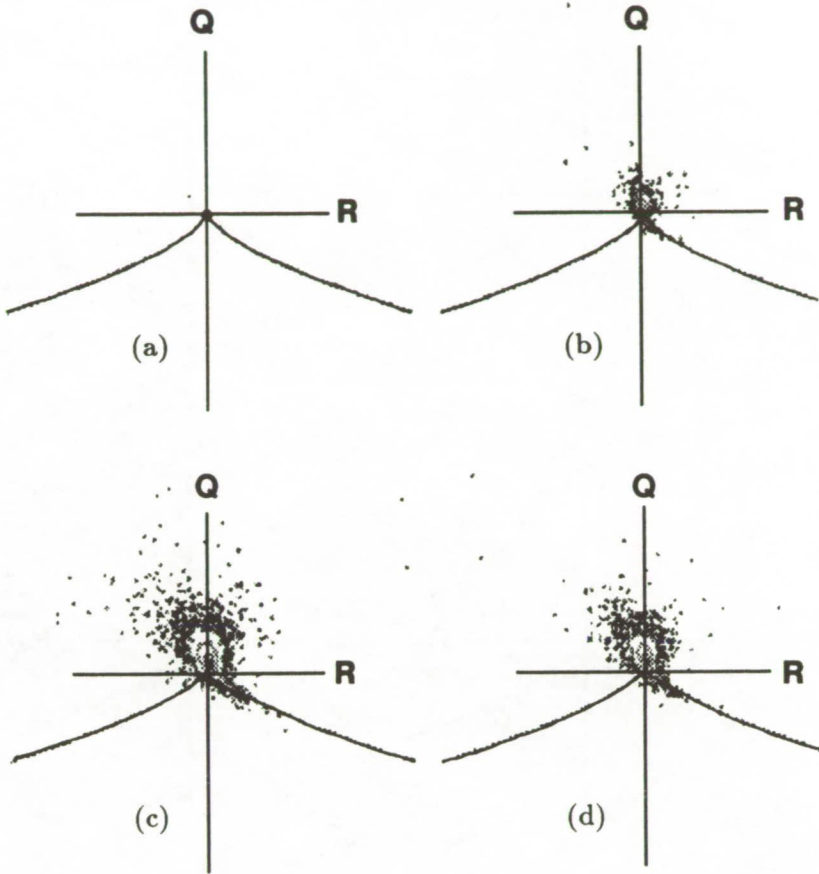


FIGURE 12. Q vs R for tbl . $tU/\delta =$ (a) 0.0, (b) 26.25, (c) 47.5, (d) 76.25.

for *hipairex* in contour plot form for the joint probability density distributions. Figures 9, 10, and 11 show the results for *mega*. These results are similar to the scatter diagrams given in Figure 2 but are corrected for nonuniform grid spacing. More structural features are apparent, and an interesting feature in Figures 6 to 8 is that velocity gradients tend to increase with time and at the latest time show a decrease. In fully developed turbulent plane mixing layers, if dissipation scales with production, then according to the Kolmogorov scaling, the velocity gradients should decrease with time. According to this reasoning, *hipairex* is under-developed for most if not all of the times shown. It is unclear whether, at the latest time, the gradients are beginning to decrease because the flow is reaching a fully developed state or because of constraining by the grid. Figures 9, 10, and 11 show the results for *mega*, and there appears less pronounced sheet-like structures but more tube-like patterns for the higher Reynolds numbers.

Figures 12, 13, and 14 show similar results for *tbl*. which started out as two

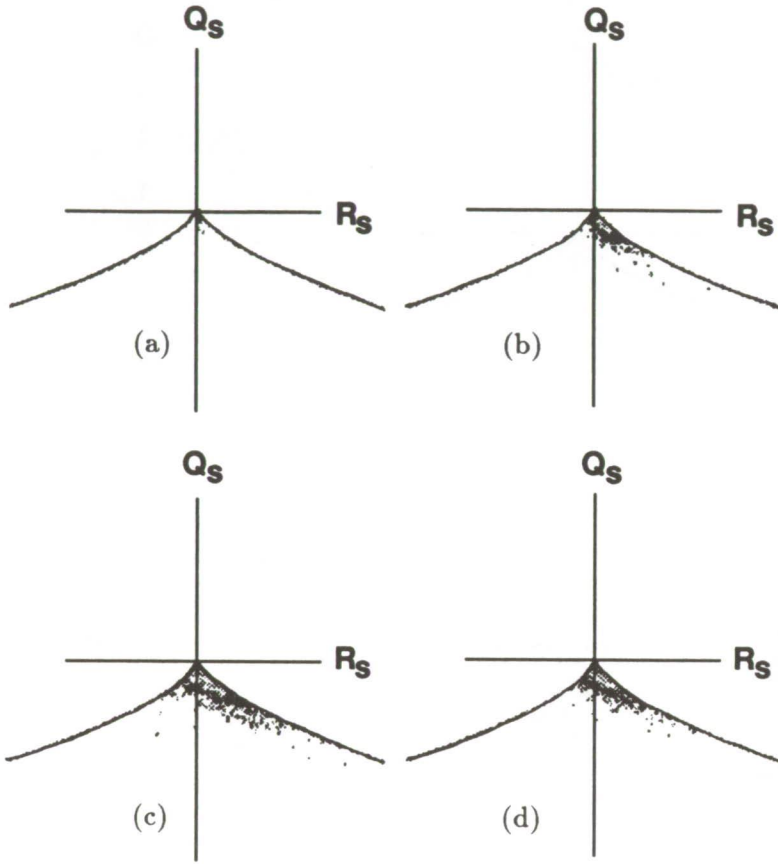


FIGURE 13. Q_s vs R_s for *tbl*. $tU/\delta =$ (a) 0.0, (b) 26.25, (c) 47.5, (d) 76.25.

turbulent boundary layers and then developed to a much higher Reynolds number than *hipairex*. Figure 12 is most interesting. It shows that all data points for the turbulent boundary layer cluster near the origin of the Q versus R plot and suddenly explode to much higher gradients in the plane mixing layer. These pictures graphically illustrate how much greater velocity gradients become when the wall constraint of a turbulent boundary layer is removed. It should be noted that near the wall, the Q and R of a turbulent boundary layer are small even when the gradients aren't. A better measure of the relative magnitudes of the velocity gradients can be inferred from figure 14. Again, the gradients tend to grow and then diminish at late times. The Q_S versus R_S plot shows that the strain rates tend to follow a different curve, closer to the real-imaginary dividing surface (6). Hence, this aspect of the fine scale motion appears to be Reynolds number dependent. The plots in Figure 14 show that the turbulent boundary layer structures at $t' = 0$ are sheet-like, but, in contrast to *hipairex*, there are no preferred structures revealed by the $-Q_S$ versus Q_W plot for later times (cf. Figure 8). As with *hipairex* the Q versus R plot

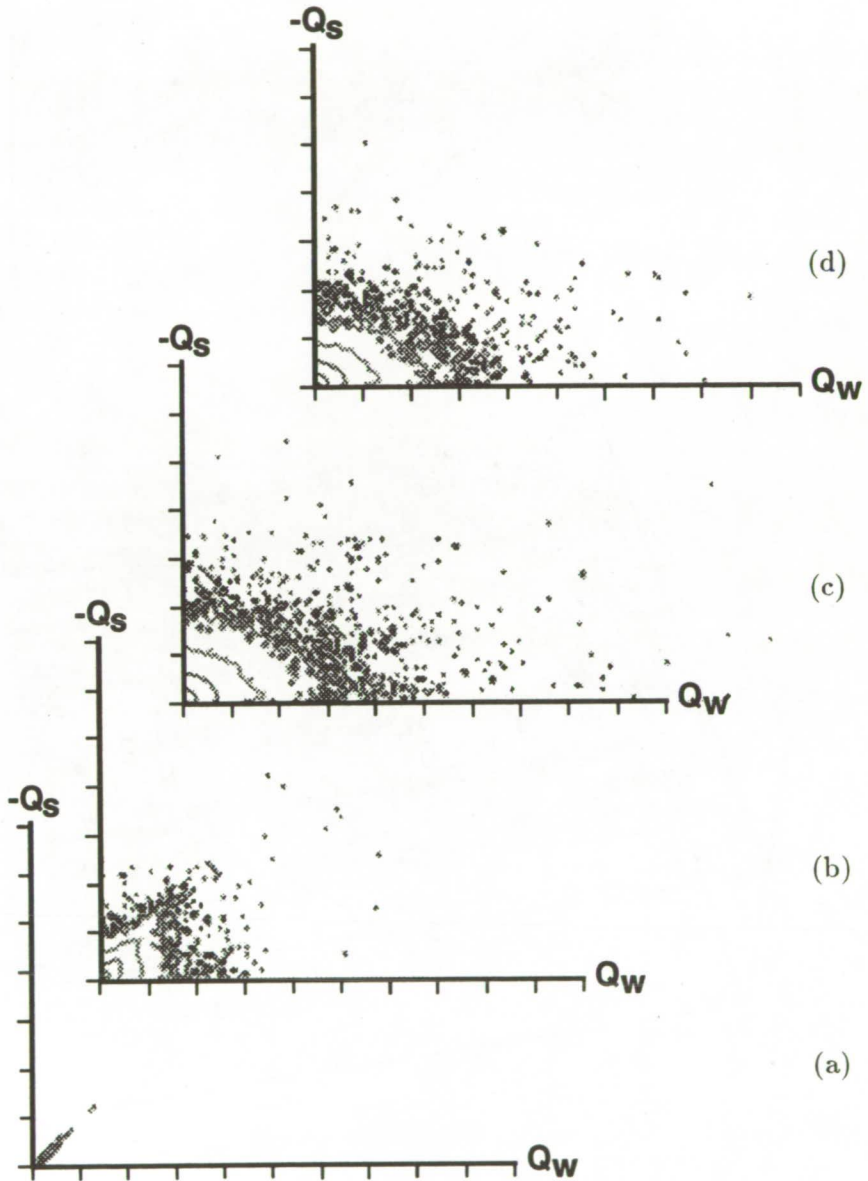


FIGURE 14. $-Q_s$ vs Q_w for *tbl.* $tU/\delta =$ (a) 0.0, (b) 26.25, (c) 47.5, (d) 76.25.

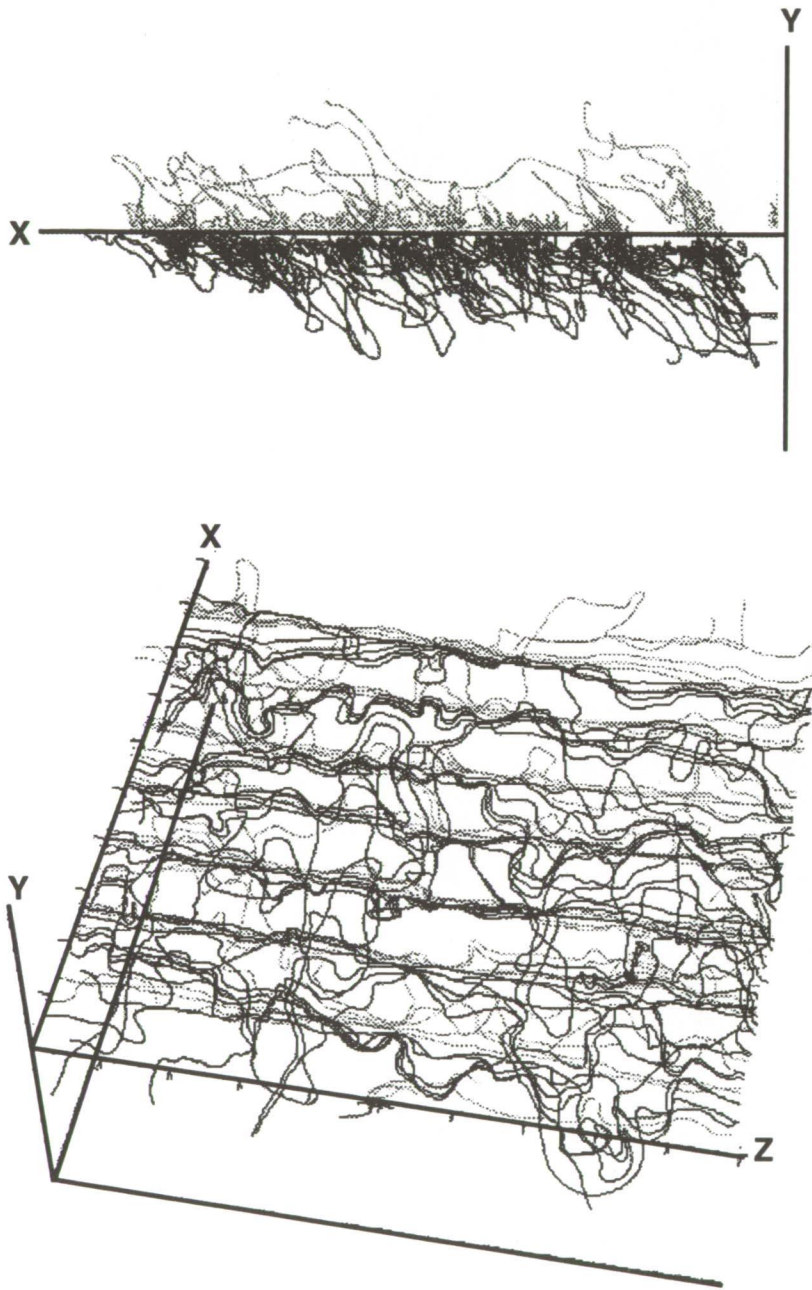


FIGURE 15. Vortex lines for *tbl* at $tU/\delta = 0.0$.

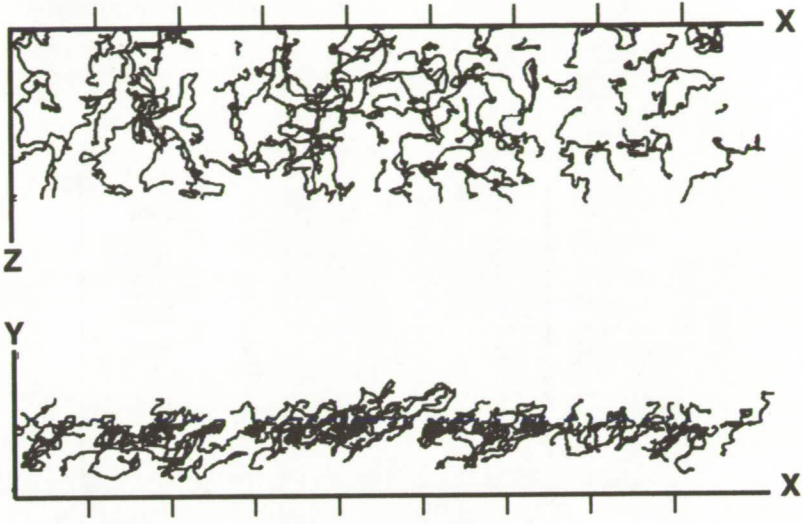


FIGURE 16. Vortex lines for *tbl* at $tU/\delta = 76.3$.



FIGURE 17. Streamlines for *tbl* at $tU/\delta = 76.3$.

shows that most of the gradients belong to the topology of stable focus stretching.

The highly organized patterns seen in Chen *et al.* (1990) for *hipairex* are replaced by most complex structures in *tbl*. Vortex lines for *tbl* are shown in Figures 15 and 16. Shown in Figure 15 is the initial turbulent boundary layer, and the attached eddies which lean approximately 45° to the mean flow direction are apparent. In Figure 16 are shown vortex lines of the plane mixing layer after some development. Although no clear spanwise rollups are apparent from this vorticity plot, Figure 17 shows instantaneous streamline patterns which indicate possible large scale spanwise roll-ups.

4. Comparison of two initial conditions at the same Reynolds number

From Figure 5, it can be seen that there is an overlap of Reynolds numbers for *mega* and *tbl*. In fact, they both share a Reynolds number of 5000 as indicated in the

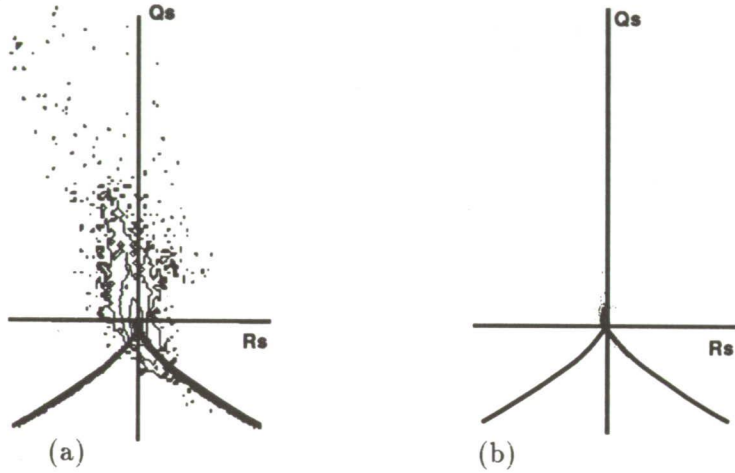


FIGURE 18. Rescaled Q vs. R plots for (a) *mega* at $tU/\delta = 49.0$; (b) *tbl* at $tU/\delta = 61.0$.

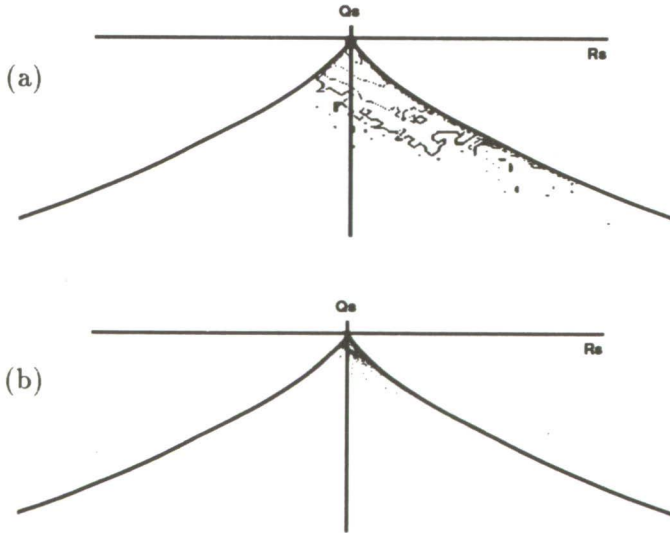


FIGURE 19. Rescaled Q_s vs. R_s plots for (a) *mega* at $tU/\delta = 49.0$; (b) *tbl* at $tU/\delta = 61.0$.

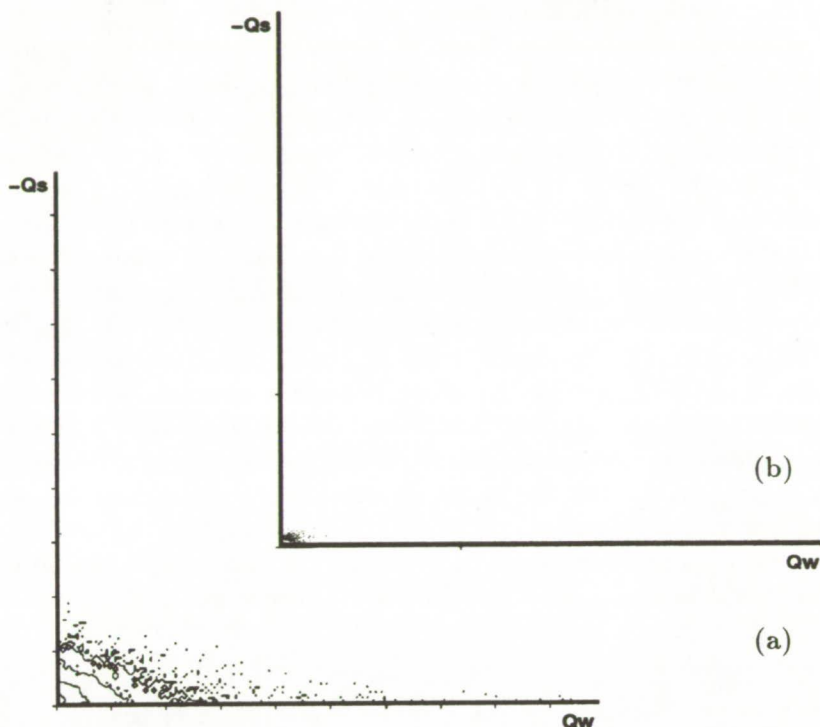


FIGURE 20. Rescaled $-Q_s$ vs. Q_w plots for (a) *mega* at $tU/\delta = 49.0$, (b) *tbl* at $tU/\delta = 61.0$.

figure. Figures 18(a) and (b) show Q versus R plots of *tbl* and *mega*, each scaled with the current vorticity thickness and appropriate velocity U . The joint probability density contours have been rescaled to account for the different population density of points. Figures 19 (a) and (b) show the corresponding $-Q_s$ versus Q_w plots for comparison. Although the shape of the plots are roughly the same, there appears to be a major difference in the scaling, indicating that the velocity gradients in *tbl* are considerably lower than in *mega* for the same Reynolds number. The reasons for this difference need to be pursued in future work.

5. Conclusions

In all flow cases considered here, motions with the highest dissipation of kinetic energy per unit volume were of the topological classification stable focus with stretching as found from $Q - R$ plots.

In the case designated as *hipairex*, the flow was initiated from a laminar layer with an error function profile and the maximum Reynolds number R_δ to which the flow evolved was 3000. Here, the highly dissipative motions were usually accompanied by a high enstrophy indicating a vortex sheet-like structure. From Q_s versus R_s plots, the rate of strain tensor for dissipating points had a topology of unstable node saddle-saddle with the rate of strains being of a given ratio and with the vorticity

vector tending to align with the intermediate strain β .

In the case of *tbl*, which was initiated from two turbulent boundary layers placed back to back, the highest local Reynolds number considered was $R_\delta = 9000$. Here, the $-Q_S$ versus Q_W plots indicated no preferred structure for the highly dissipating motions although the $Q - R$ plots indicated a strong preference for stable focus stretching. Also, the Q_S versus R_S plots showed that the highly dissipating motions tend toward $\alpha:\beta:\gamma = 1:1:-2$. No vorticity alignment checks were made, but it is expected that the vorticity vectors will tend to align with the β axis (cf. Sondergaard *et al.*, 1991).

Comparison of two flows at the same local Reynolds number but with two entirely different initial conditions was made using flow cases designated *mega* and *tbl*. Plots of Q versus R and $-Q_S$ versus Q_W when nondimensionalized appropriately show essentially the same topological structure and scaling from $R_\delta = 5000$ even though *mega* was initiated from a laminar error function profile layer and *tbl* from turbulent boundary layers. Although the shape of the plots are roughly the same, there appears to be a major difference in the scaling, indicating that the velocity gradients in *tbl* are considerably lower than in *mega* for the same Reynolds number. The reasons for this difference need to be pursued in future work.

Acknowledgements

We would like to acknowledge the invaluable assistance of Drs. Michael Rogers and Robert Moser of NASA-Ames Research Center in obtaining and understanding the data sets upon which this study is based. We would also like to acknowledge support from ONR Grant N00014-90-J-1976, the Center of Turbulence Research, and C.S.I.R.O.

REFERENCES

- ASHURST, W. T., KERSTEIN, A. R., KERR, R. M., & GIBSON, C. H. 1987 Alignment of vorticity and scalar gradients with strain rate in simulated Navier-Stokes turbulence. *Physics of Fluids*, **30**, 2343.
- BRADSHAW, P. B. & FERRISS, D. H. 1967 *The Spectral Energy Balance in a Turbulent Mixing Layer*. Aero Res. Council Current Paper No. 899.
- CHEN, J. 1991 *The Effect of Compressibility on Conserved Scalar Entrainment in a Plane Free Shear Layer*. Eighth Symposium on Turbulent Shear Flows, Munich K-1, 1-6.
- CHEN, J. H., CHONG, M. S., SORIA, J., SONDERGAARD, R., PERRY, A. E., ROGERS, M., MOSER, R., & CANTWELL, B. J. 1990 *A study of the topology of dissipating motions in direct numerical simulations of time-developing compressible and incompressible mixing layers*. Center for Turbulence Research Report CTR-S90.
- CHONG, M. S., PERRY, A. E., & CANTWELL, B. J. 1990 A general classification of three-dimensional flow fields. *Physics of Fluids*, **A.2(5)**, 765-777.

- MOSER, R. & ROGERS, M. 1990 *Mixing transition and the cascade to small scales in a plane mixing layer*. IUTAM Symposium on Stirring and Mixing, La Jolla, CA 20-24 August 1990.
- ROGERS, M. & MOSER, R. 1992 The three-dimensional evolution of a plane mixing layer: The Kelvin-Helmholtz Rollup. *J. Fluid Mech.*, *To appear*.
- SONDERGAARD, R., CHEN, J., SORIA, J., & CANTWELL, B. 1991 *Local topology of small scale motions in turbulent shear flows*. Eighth Symposium on Turbulent Shear Flows, Munich K-1, 1-6.
- SPALART, P. R. 1988 Direct simulation of a turbulent boundary layer up to $Re_\theta = 1410$. *J. Fluid Mech.* **187**, 61-98.

445348
57-34
189667
123
N9A-14752

Isotropy of small scale turbulence

By R. A. Antonia¹ AND J. Kim²

The degree to which local isotropy is satisfied has been examined using direct numerical simulations for a fully developed channel flow. Attention is mainly given to the high wavenumber part of vorticity and temperature derivative spectra. The ratio of these spectra and their isotropic values depends on the particular quantity considered, the departure from isotropy being more pronounced for the temperature derivative than for the vorticity. When the Kolmogorov-normalized wavenumber is sufficiently large, isotropy is satisfied provided the (Kolmogorov-normalized) mean strain rate is sufficiently small. This result appears to be independent of the quantity considered and of the Reynolds number.

1. Introduction

The concept of local isotropy has been of central importance to the theory of turbulence and continues to attract significant attention in turbulence, as can be gleaned, for example, from the compendium of papers in the A. N. Kolmogorov commemorative issue of the *Proceedings of the Royal Society* (1991). The concept implies that the small scales become statistically independent from the large scales or, perhaps more pertinently, from any orientation effects or bias introduced by the mean shear. This implication and related questions, for example, "is local isotropy achievable only at large Reynolds numbers?" or "do departures from local isotropy persist irrespectively of the Reynolds number?", are issues which continue to preoccupy, perhaps fascinate, turbulence researchers.

Before the previous questions can be adequately addressed, there is first the need to decide how best to measure "local isotropy". This is not a straightforward task given that there is a plethora of tests which can be applied (e.g. Monin and Yaglom, 1975; Mestayer, 1982) and that different tests may have different levels of sensitivity (e.g. Antonia *et al.*, 1986). Not unrelated to these difficulties is the issue of whether the word "local" is interpreted to signify "in physical space", as originally intended by Kolmogorov (1941) or whether it is given a spectral interpretation. If the first of these interpretations is adopted, the available evidence, which includes atmospheric data at quite large turbulence Reynolds numbers, appears to point fairly unambiguously to a departure from local isotropy (e.g. Antonia *et al.*, 1986; Sreenivasan, 1991). This departure appears to be especially emphasized in statistics, e.g. mean squared values and skewnesses of spatial derivatives of the temperature fluctuation

1 Department of Mechanical Engineering, University of Newcastle, N.S.W., 2308, Australia

2 NASA-Ames Research Center, Moffett Field, CA, 94035

(e.g. Sreenivasan et al., 1979; Sreenivasan and Tavoularis, 1980). The second interpretation allows the focus to be on high wavenumbers or small scales (e.g. Van Atta, 1991; Antonia *et al.*, 1986); with the caveat that there must be non-local interactions between small and large wavenumbers (e.g. Domaradzky and Rogallo, 1991; Brasseur, 1991). This arguably provides a better framework for testing local isotropy than seems possible under the first interpretation. It is worth underlining that while the practical applications which follow from the first interpretation of the concept are well known, the spectral interpretation is not without practical significance. For example, the measurement of spatial velocity and temperature derivatives with parallel hot wires requires their separation to be selected appropriately. This is not straightforward and the analysis (Wyngaard, 1969) which provides a possible correction for the spectral attenuation of the derivative spectrum relies on local isotropy.

Regardless of which interpretation is chosen, it is important to select turbulence quantities which are representative of the small scale structure when testing for local isotropy. In this context, velocity and temperature fluctuations could be less effective than their derivatives. Direct numerical simulations (DNS) can provide more reliable data for spatial derivatives than measurements. DNS data in a turbulent channel flow have been used (Antonia *et al.*, 1991; Antonia and Kim, 1992) to test for local isotropy using both the physical space and spectral interpretations of the concept. The first paper (Antonia *et al.*, 1991) showed that mean squared velocity derivative values approximately satisfied isotropy only as the channel centerline is approached, a result which appears consistent with Durbin and Speziale's (1991) conclusion that the dissipation rate tensor cannot be isotropic when the mean strain rate is not zero. The second paper (Antonia and Kim, 1992) focused mainly on the high wavenumber part of velocity and pressure spectra; the results adequately supported local isotropy in a flow region characterized by relatively small mean strain rates. There was no attempt, however, to quantify the dependence on the mean strain rate. The present investigation extends the previous work in two important ways. It focuses on quantities (the three spatial temperature derivatives and the three components of the vorticity vector) which may have stronger contributions from the small scale structure than simply velocity and scalar fluctuations. It also attempts to relate the degree of local isotropy to the mean strain rate.

In this paper, u_i , θ , and ω_i denote the velocity, temperature, and vorticity fluctuations, respectively, the subscript i ($i = 1, 2, 3$) denoting the streamwise ($i = 1$), wall-normal ($i = 2$), and spanwise ($i = 3$) directions.

2 Distributions of $\overline{\theta_{,i}^2}$ and $\overline{\omega_i^2}$

Isotropy requires that the three components of $\overline{\theta_{,i}^2}$, where $\theta_{,i} \equiv \partial\theta/\partial x_i$, and $\overline{\omega_i^2}$ are equal. Figure 1 shows that this is approximately satisfied as the centerline of the channel is approached. The presentation in Figure 1 clearly highlights the strong anisotropy which exists in the wall region. Note that $\overline{\theta_{,2}^2}$ and $\overline{\omega_3^2}$ clearly dominate near the wall. There is also reasonable similarity in the shapes of the component distributions of $\overline{\theta_{,i}^2}$ and those of $\overline{\omega_i^2}$ except for the near-wall increase of $\overline{\omega_1^2}$, the mean

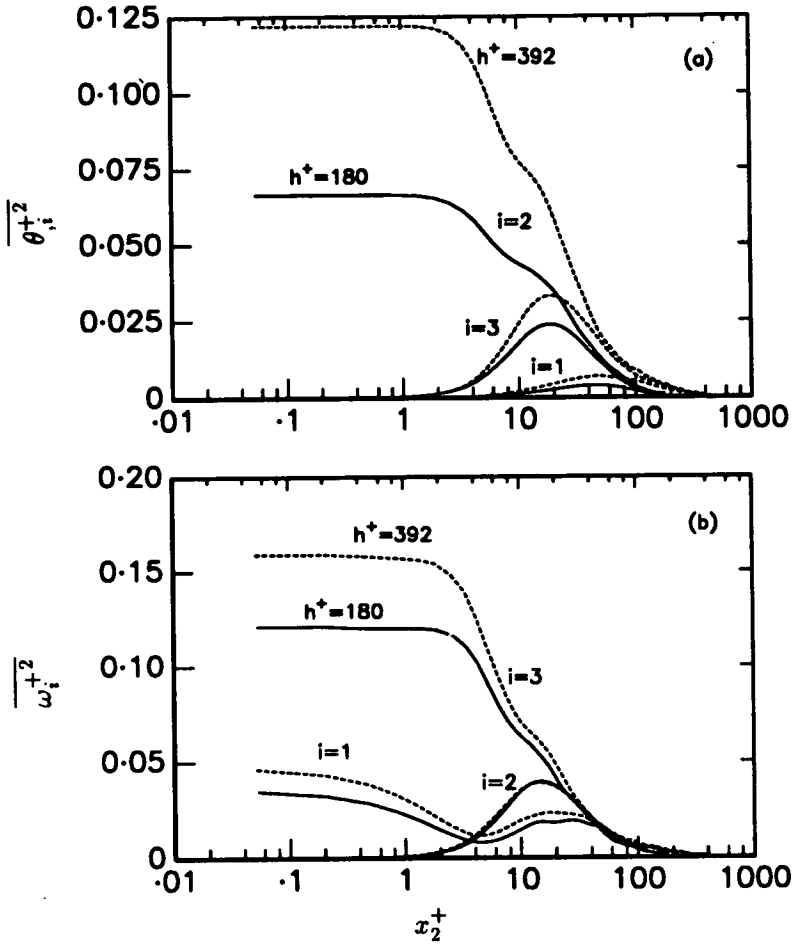


FIGURE 1. Distributions across the channel of the mean square values of the temperature derivatives and vorticity components. (a) $\overline{\theta_{i,i}^{+2}}$; (b) $\overline{\omega_{i,i}^{+2}}$.

square longitudinal vorticity. The transport equation for $\overline{\theta_{i,i}^{+2}}$ was first written by Corrsin (1953) who compared it with the transport equation for $\overline{\omega_2^2}$; while the two equations can be cast in similar forms, Corrsin noted that there are apparently significant differences (due mainly to the solenoidal nature of ω_i , viz. $\nabla \cdot \omega_i \equiv 0$ or $\omega_{i,i} \equiv 0$ and the lamellar nature of $\theta_{i,i}$, viz. $\nabla \times \theta_{i,i} \equiv 0$).

Figure 1 also underlines the significant Reynolds number dependence in the wall region of almost all the quantities that are plotted. Apart from $\overline{\omega_2^2}$, which is virtually unaffected, the remaining quantities are increased as h^+ increases. In the sublayer, the major increases are exhibited by $\overline{\omega_3^{+2}}$ (15%), $\overline{\omega_1^{+2}}$ (32%) and $\overline{\theta_2^{+2}}$ (92%). The increases in $\overline{\omega_1^{+2}}$ and $\overline{\omega_3^{+2}}$ reflect the increased stretching of the streamwise and spanwise vortices; speculatively, this stretching may increase the frequency (and amplitude) of excursions of hot fluid away from the wall and cold fluid towards the

wall, thus accounting for the increase in $\overline{\theta_2^{+2}}$.

An effective method of assessing the departure from isotropy of θ_i^2 or ω_i^2 is to examine invariant maps (Lumley and Newman, 1977; Lee and Reynolds, 1985) of the anisotropy tensors corresponding to these quantities, the information displayed on these maps being independent of the choice of co-ordinate axes. The temperature dissipation anisotropy tensor which corresponds to θ_i^2 may be defined as

$$t_{ij} = \alpha \frac{\overline{\theta_i \theta_j}}{\bar{\epsilon}_\theta} - \frac{1}{3} \delta_{ij} \quad (1)$$

where $\bar{\epsilon}_\theta = \alpha \overline{\theta_i \theta_i}$ is the average temperature dissipation (α is the thermal diffusivity). The second and third variants of t_{ij} are given by

$$II = -\frac{1}{2} t_{ij} t_{ji} \quad (2)$$

$$III = \frac{1}{3} t_{ij} t_{jk} t_{ki} \quad (3)$$

and all the states that characterize t_{ij} are identifiable on a plot of $-II$ vs III , as shown in Figure 2a. Similarly, the vorticity anisotropy tensor may be defined as

$$v_{ij} = \frac{\overline{\omega_i \omega_j}}{\bar{\omega}^2} - \frac{1}{3} \delta_{ij}, \quad (4)$$

and its second and third invariants are given by expressions analogous to (2) and (3). The AIM for v_{ij} was presented in Figure 7c of Antonia *et al.* (1991). It is reproduced in Figure 2b to allow comparison with the AIM (anisotropy invariant map) of Figure 2a.

At the wall, the only component of $\bar{\epsilon}_\theta$ is $\alpha \overline{\theta_2^2}$ so that the top right cusp of the AIM, with co-ordinates (2/27, 1/3), represents the one-component state of t_{ij} . As x_2^+ increases through the sublayer, the data points lie very close to the upper boundary of the AIM which represents the two-component state of t_{ij} (Figure 1 shows that $\overline{\theta_1^2}$ remains small by comparison to $\overline{\theta_2^2}$ and $\overline{\theta_3^2}$). In the buffer region, the invariants II_t and III_t approach the left "axisymmetric" boundary ($A_t \equiv -1$) of the AIM. In the outer part of the channel, the trend is towards the isotropic state ($II_t = III_t = 0$).

Figures 2a and 2b indicate a close similarity between the invariants of t_{ij} and v_{ij} in the buffer and outer regions of the channel. In particular, along the left axisymmetric boundary, which Lee and Reynolds (1985) describe as disk-like turbulence, two components are nearly equal ($\overline{\theta_2^2} \simeq \overline{\theta_3^2}$, $\overline{\omega_2^2} \simeq \overline{\omega_3^2}$) while the third ($\overline{\theta_1^2}$ or $\overline{\omega_1^2}$) is somewhat smaller than the other two. There are, however, marked differences between Figure 2a and Figure 2b in the near-wall region, reflecting the different boundary conditions for t_{ij} and v_{ij} . At the wall, the one-component t_{ij} state corresponds to the two-component v_{ij} state. The rod-like behavior of vorticity (right axisymmetric boundary in Figure 2b) appears to correspond to a two-component state for the temperature dissipation.

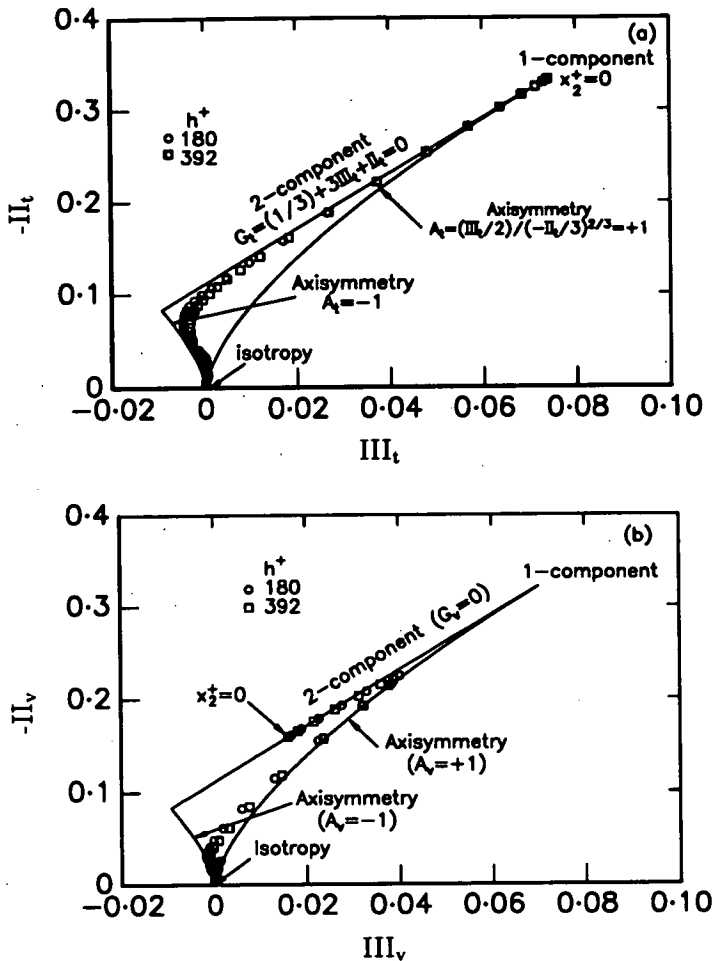


FIGURE 2. Anisotropy invariant map of temperature dissipation and vorticity. (a) $\overline{\theta^2}_{,i}$; (b) $\overline{\omega^2}_{,i}$.

3 Spectra of ω_i and θ_i

The comparison between the high wavenumber part of vorticity spectra and the corresponding isotropic calculation is a useful way of assessing the degree of isotropy of the small scale structure. Since vorticity is, like velocity, solenoidal ($\omega_{i,i} \equiv 0$, $u_{i,i} \equiv 0$), isotropic relations between two-point vorticity correlations are the same as the corresponding relations between two-point velocity correlations. Using Batchelor's (1953) notation,

$$g = f + \frac{r}{2} \frac{\partial f}{\partial r} \tag{5}$$

where g and f are the lateral and longitudinal correlations respectively and r is the magnitude of the separation between the two points, the Fourier transform of (5) obviously applies to both velocity and vorticity fields. It is convenient here to

consider spectra in terms of k_3 , the wavenumber in the spanwise direction. The isotropic relations for either the vorticity or velocity spectra may be written as follows

$$\phi_{\omega_1}(k_3) = \phi_{\omega_2}(k_3) = \frac{1}{2} \left(\phi_{\omega_3} - k_3 \frac{d\phi_{\omega_3}}{dk_3} \right) \quad (6)$$

$$\phi_{u_1}(k_3) = \phi_{u_2}(k_3) = \frac{1}{2} \left(\phi_{u_3} - k_3 \frac{d\phi_{u_3}}{dk_3} \right) \quad (7)$$

The spectra of ω_1 , ω_2 and ω_3 are shown in Figure 3 for two flow locations (data for $h^+ = 392$ only are presented). The asterisk denotes normalization by Kolmogorov scales (length $\eta = \nu^{3/4} \bar{\epsilon}^{-1/4}$ and velocity $u_\kappa = \nu^{1/4} \bar{\epsilon}^{1/4}$). At the channel centerline, ϕ_{ω_1} and ϕ_{ω_2} are virtually identical at all k_3^* , as required by the first equality in (6). They are also in close agreement with the calculation given by the right side of (6). By contrast to Figure 3a, the results at $x_2^+ = 15$ (Figure 3b) show that, except at the crossing point, ϕ_{ω_1} is significantly different from ϕ_{ω_2} . The latter distribution seems to asymptote towards the isotropic calculation, Eq. (6), at sufficiently large values of k_3^* .

It is possible that the logarithmic scale on the ordinate of Figure 3 may mask small departures from isotropy. To overcome this difficulty, the ratio of the DNS spectral density to that obtained from Eq. (6) has been calculated at several x_2^+ values and plotted using a linear scale in Figure 4. Note there is a significant region of the channel for which the ratio may be assumed to be close to 1. In the case of ω_1 , this approximation has an uncertainty of about $\pm 20\%$ when $x_2^+ \gtrsim 74$. For ω_2 , the approximation is satisfied to about $\pm 5\%$ for $x_2^+ \gtrsim 15$. The sharp increase in the ratio at the largest values of k_3^* is spurious and can be ignored. In order to ascertain whether the spectral ratio used in Figure 4 is sensitive to departures from isotropy, the ratio was computed, using DNS data for isotropic turbulence (Rogallo, private communication). The results in Figure 5 [shown for ϕ_{ω_2} and ϕ_{u_2} ; the isotropic calculations are based on $\phi_{\omega_1}(k_1)$ and $\phi_{u_1}(k_1)$] suggest that the sensitivity is adequate (better than $\pm 10\%$; the waviness in Figure 5 is a result of fitting to the ω_1 and u_1 spectra and is therefore artificial).

The isotropic relation between the temperature derivative spectra is given by (e.g. Van Atta, 1977; Browne *et al.*, 1983)

$$\phi_{\theta,1} = \phi_{\theta,2} = \int_{k_3}^{\infty} k^{-1} \phi_{\theta,3}(k) dk \quad (8)$$

The comparison between $\phi_{\theta,1}^*(k_3^*)$ and the isotropic calculation, based on Eq. (8), is shown in Figure 6. The good agreement, almost independently of k_3^* , at the centerline (Figure 6a) contrasts with the total lack of agreement at $x_2^+ = 15$. The ratio $\phi_{\theta,1}/(\phi_{\theta,1})_{iso}$, plotted in Figure 7, suggests that, in the wall region of the flow, the anisotropy of the temperature derivative field is more pronounced than that of the vorticity field (Figure 4). This increased anisotropy may be associated with the mean temperature gradient $\bar{T}_{,2}$, where \bar{T} is the mean temperature. For example, $\bar{T}_{,2}$ appears explicitly in the transport equation for the skewness of θ_1 . Sreenivasan

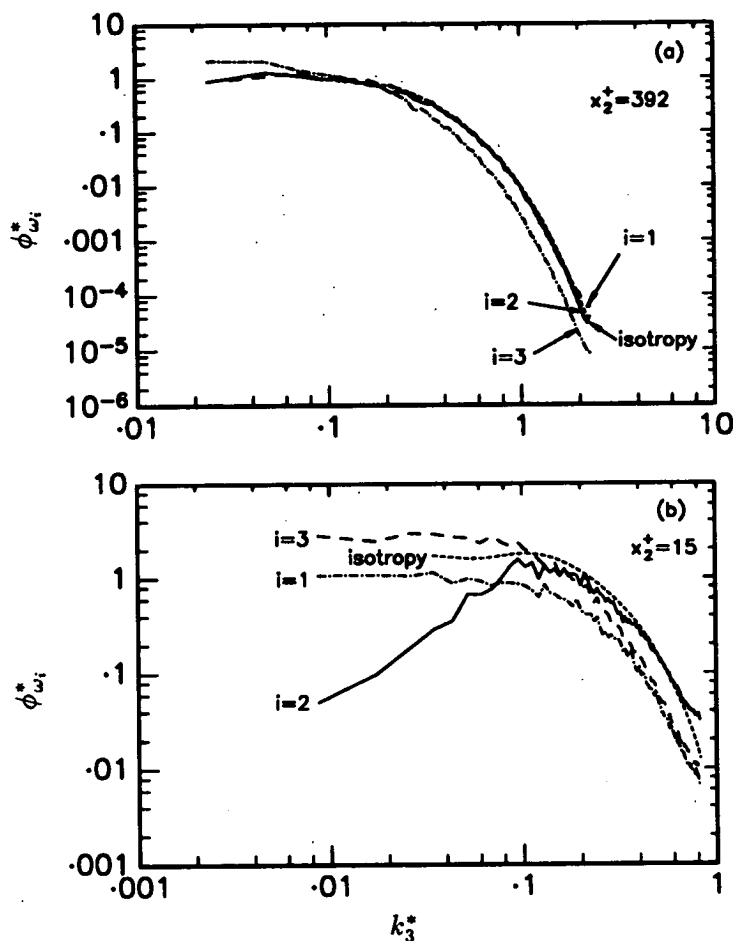


FIGURE 3. Vorticity spectra at two locations in the flow ($h^+ = 392$). (a) $x_2^+ = 392$ ($x_2 \simeq h$); (b) $x_2^+ = 15$.

and Tavoularis (1980) noted that this skewness is non-zero only when $\overline{U}_{1,2}$ and $\overline{T}_{,2}$ are both non-zero.

4 Dependence on the mean strain rate

Figures 5 and 7 suggest that the departure from isotropy may depend on the magnitude of the mean strain rate $\overline{U}_{1,2} (\equiv S)$. It is fairly common to normalize S by a time scale $(\overline{q^2}/2\overline{\epsilon})$ characteristic of the turbulence, e.g. Moin (1990) and Lee *et al.* (1990). Durbin and Speziale (1991) showed that the dissipation rate tensor deviates from isotropy if $S\overline{q^2}/\overline{\epsilon}$ is not zero. A disadvantage of using $S\overline{q^2}/\overline{\epsilon}$ is that it is zero at the wall where S is largest. There are other possibilities for non-dimensionalizing S . Uberoi (1957) used $S/\overline{u_{1,2}^2}^{1/2}$, with $\overline{u_{1,2}^2}^{1/2}$ representing a velocity gradient characteristic of the turbulence, for characterizing the anisotropy. Another possibility is to normalize S by the Kolmogorov time scale $(\nu/\overline{\epsilon})^{1/2}$; the ratio $S/(\overline{\epsilon}/\nu)^{1/2}$ will be

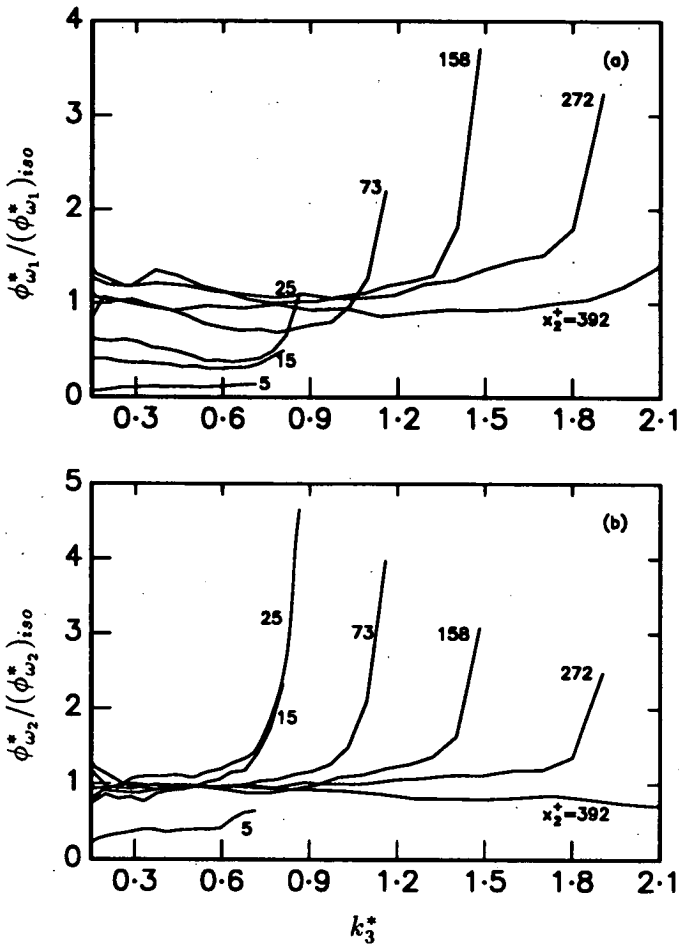


FIGURE 4. Wavenumber dependence of the ratio of the vorticity spectrum and the corresponding isotropic spectrum at different locations in the flow ($h^+ = 392$). (a) ω_1 ; (b) ω_2 .

denoted by S^* . Corrsin (1957, 1958) argued that the necessary condition for local isotropy to be a good approximation at a given wavenumber is that $(\nu/\bar{\epsilon})^{1/2}$, which may be identified with a time scale characteristic of the transfer of energy to higher wavenumbers, should be small compared with the inverse of the mean rate of strain, viz.

$$\left(\frac{\nu}{\bar{\epsilon}}\right)^{\frac{1}{2}} \ll \frac{1}{S}$$

or

$$S^* \ll 1 \quad (9)$$

The distribution of S^* is shown in Figure 8 together with $S/\overline{u_{1,2}^2}^{-1/2}$ and $Sq^2/2\bar{\epsilon}$ (the corresponding distributions at $h^+ = 180$ are almost the same as those at $h^+ = 400$ in the wall region; at the wall S^* is 2.6 at $h^+ = 180$ and 2.3 at $h^+ = 400$). Not

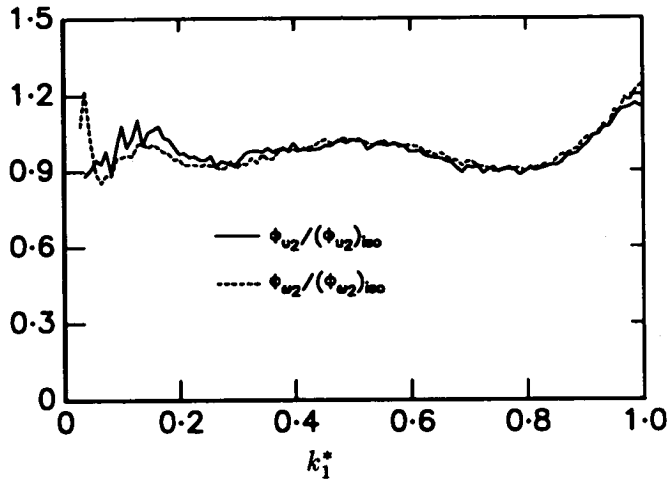


FIGURE 5. Wavenumber dependence of the ratios of spectra of u_2 and ω_2 and the corresponding isotropic spectra for a direct numerical simulation of isotropic turbulence.

unexpectedly, S^* and $S/u_{1,2}^2$ follow each other closely, the former being slightly smaller than the latter in magnitude. S^* or $S/u_{1,2}^2$ is clearly better behaved than $S(\overline{q^2}/2\bar{\epsilon})$, which increases from zero at the wall to a relatively large maximum near $x_2^+ = 10$.

The ratios of vorticity or temperature derivative spectra and the corresponding isotropic spectra are shown in Figure 9 in terms of S^* , for values of k_3^* in the range 0.1 to 0.7. One can identify a value of S^* , S_{min}^* say, for each of the three quantities in Figure 9 below which the ratio can be assumed to be approximately 1 (independently of k_3^*). The magnitude of S_{min}^* is about 0.3 for ω_1 while it is almost 1 for ω_2 . It is only 0.1 for θ_1 ; in this case, the departure from isotropy is more evident than for vorticity, especially at smaller values of k_3^* . It would appear that while Corrsin's inequality (9) has general validity, significant relaxation of this criterion is possible when the interest centers on specific quantities. For example, it seems that $S^* \leq S_{min}^* \approx 0.2$ may be sufficient for the small scale vorticity to be isotropic.

A comment about the possible effect of Reynolds number seems à propos here. The evidence we have gathered here and in a previous paper (Antonia *et al.*, 1991) strongly suggests that provided $S^* \lesssim S_{min}^*$, the magnitude of the Reynolds number should have little effect on the degree of isotropy that can be achieved at sufficiently large wavenumbers. The magnitude of the Reynolds number is, of course, important in determining the extent of the flow region in which $S^* \lesssim S_{min}^*$ is satisfied. This can be illustrated by reference to the logarithmic region for which energy equilibrium ($\bar{\epsilon} = -\overline{u_1 u_2} S$) is a reasonable approximation. At sufficiently high Reynolds numbers, $S \approx U_\tau / \kappa$ (κ is the von Kármán constant, U_τ is the friction velocity), $-\overline{u_1 u_2} \approx U_\tau^2$ and $S^* \approx (\kappa x_2^+)^{-1/2}$. For $S^* \approx 0.2$, this suggests that the region

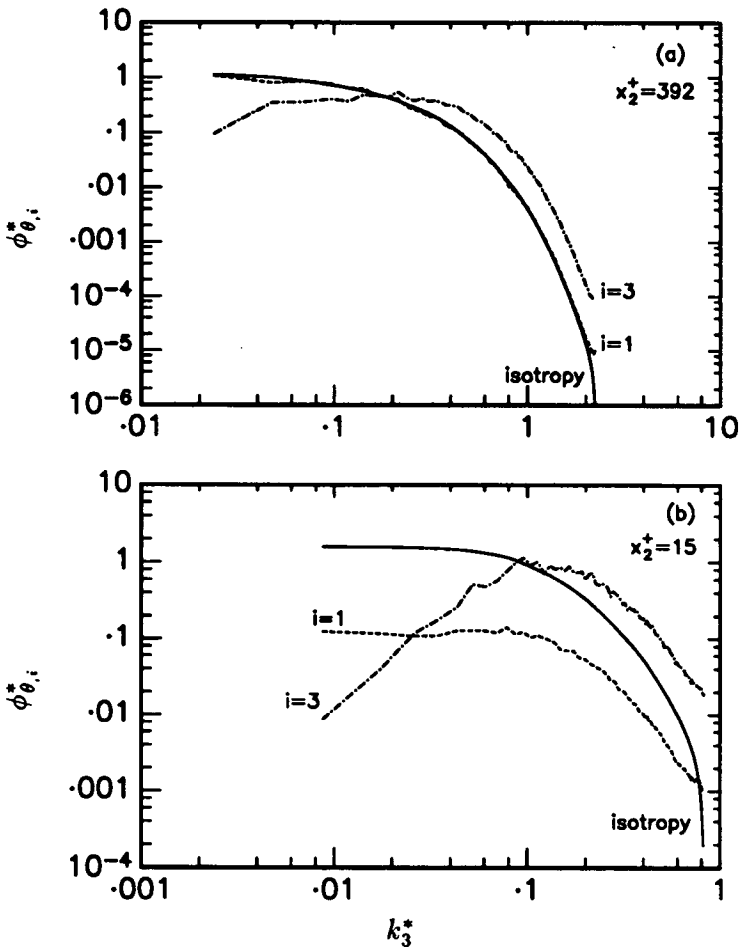


FIGURE 6. Temperature derivative spectra at two locations in the flow ($h^+ = 392$). (a) $x_2^+ = 392$; (b) $x_2^+ = 15$.

$x_2^+ \gtrsim 60$ should satisfy local isotropy; obviously, the physical extent of this region should increase with Reynolds number.

Corrsin (1957,1958) argued that a necessary condition for local isotropy is given by the inequality

$$\frac{1}{\eta} \gg \frac{S}{u_2'^2} \quad (10)$$

where the right side can be identified with a wavenumber, k_p say, corresponding to the turbulent energy production. The present data suggest that in the region where local isotropy is approximately satisfied, $k_p^* \lesssim 0.1$, suggesting that (10), like inequality (9), are unnecessarily restrictive and may be relaxed significantly.

5 Conclusions

Invariant maps of vorticity and temperature derivative anisotropy tensors in a

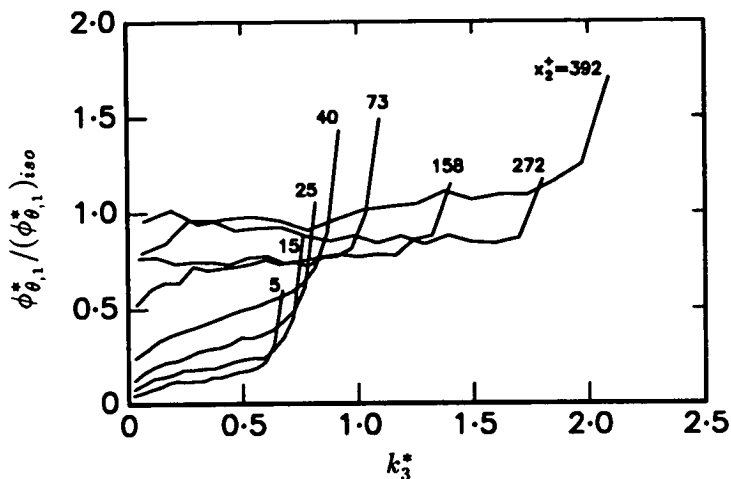


FIGURE 7. Wavenumber dependence of the ratio of the spectrum of $\theta_{1,1}$ and the corresponding isotropic spectrum at different flow locations ($h^+ = 392$).

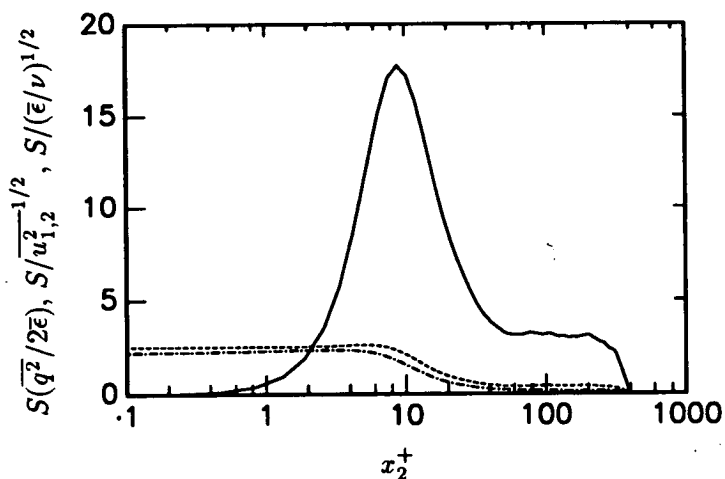


FIGURE 8. Local mean strain rate, using different normalizations ($h^+ = 392$).
 —, $S(\overline{q^2}/2\overline{\epsilon})^{1/2}$; ----, $S/\overline{u_{1,2}^2}^{1/2}$; - · - ·, $S/(\overline{\epsilon}/\nu)^{1/2}$.

fully developed turbulent channel flow indicate a similar approach towards isotropy as the channel centerline is approached. In the wall region, the nature of the anisotropy is different for these two quantities.

For sufficiently large wavenumbers, vorticity and temperature derivative spectra appear to satisfy isotropy provided the mean strain rates (suitably normalized) are sufficiently small. As far as we can ascertain, this conclusion appears to be independent of the Reynolds number. Using the Kolmogorov time scale to normalize the strain rate, the value of S^* at which the departure from isotropy is first observed

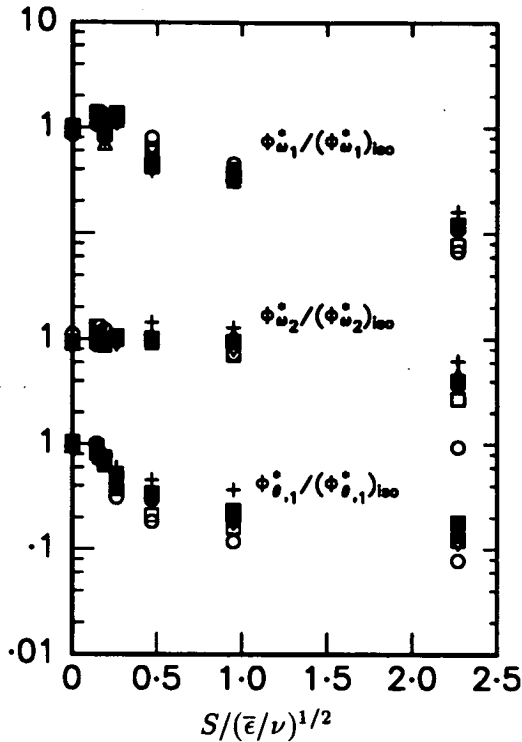


FIGURE 9. Dependence on the Kolmogorov normalized strain rate of the ratio of the vorticity or temperature derivative spectra and the corresponding isotropic spectra for different values of the wavenumber ($h^+ = 392$). (a) ω_1 ; (b) ω_2 ; (c) $\theta_{,1}$.

depends on the quantity under consideration. This value appears to be appreciably larger for the vorticity than for the temperature derivative. For given values of S^* and of the Kolmogorov normalized wavenumber, the temperature derivative spectrum exhibits a significantly larger degree of anisotropy than the vorticity spectrum. It is possible that the additional influence of the mean temperature gradient is reflected in the stronger anisotropy of the temperature derivatives, but further work would be needed to verify this possibility.

REFERENCES

- ANTONIA, R. A., ANSELMET, F. & CHAMBERS, A. J. 1986 Assessment of Local Isotropy Using Measurements in a Turbulent Plane Jet. *J. Fluid Mech.* **169**, 365-391.
- ANTONIA, R. A. & KIM, J. 1992 Isotropy of the Small-Scales of Turbulence at Low Reynolds Number. *J. Fluid Mech.*, *submitted for publication*.
- ANTONIA, R. A., KIM, J. & BROWNE L. W. B. 1991 Some Characteristics of Small Scale Turbulence in a Turbulent Duct Flow. *J. Fluid Mech.* **233**, 369-388.

- BATCHELOR, G. K. 1953 *The Theory of Homogeneous Turbulence*, Cambridge, Cambridge University Press.
- BRASSEUR, J. G. 1991 Comments on the Kolmogorov Hypothesis of Isotropy in the Small Scales. *Paper AIAA-91-0230, 29th Aerospace Sciences Meeting, January 7-10, 1991, Reno, Nevada.*
- CORRSIN, S. 1953 Remarks on Turbulent Heat Transfer: An Account of Some Features of the Phenomenon in Fully Turbulent Regions. *Proc. Iowa Thermodynamics Symposium.*
- CORRSIN, S. 1957 Some Current Problems in Turbulent Shear Flows. *Symposium on Naval Hydrodynamics, F. S. Sherman (ed.) 373-400.*
- CORRSIN, S. 1958 On Local Isotropy in Turbulent Shear Flow. *Report NACA R & M 58B11.*
- DOMARADZKY, J. A. & ROGALLO, R. S. 1991 Local Energy Transfer and Non-local Interactions in Homogeneous, Isotropic Turbulence. *Phys. Fluids A*, **2**, 413-426.
- DURBIN, P. A. & SPEZIALE, C. G. 1991 Local Anisotropy in Strained Turbulence at High Reynolds Numbers. *J. Fluids Eng.* **113**, 707-709.
- KOLMOGOROV, A. N. 1941 The Local Structure of Turbulence in an Incompressible Fluid with Very Large Reynolds Numbers. *Dokl. Akad. Nauk, SSSR*, **30**, 301-305.
- LEE, M. J., KIM, J. & MOIN, P. 1990 Structure of Turbulence at High Shear Rate. *J. Fluid Mech.* **216**, 561-583.
- LEE, M. J. & REYNOLDS, W.C. 1985 Numerical Experiments on the Structure of Homogeneous Turbulence. *Report TF-24, Thermosciences Division, Stanford University.*
- LUMLEY, J. L. & NEWMAN, G. R. 1977 The Return to Isotropy of Homogeneous Turbulence. *J. Fluid Mech.* **82**, 161-178.
- MESTAYER, P. 1982 Local Isotropy and Anisotropy in a High-Reynolds-Number Turbulent Boundary Layer. *J. Fluid Mech.* **125**, 475-503.
- MOIN, P. 1990 Similarity of Organized Structures in Turbulent Shear Flows. *Near-Wall Turbulence, S. J. Kline and N. H. Afgan (eds.), New York, Hemisphere, 2-6.*
- MONIN, A. S. & YAGLOM, A. M. 1975 Statistical Fluid Mechanics. *Mechanics of Turbulence, Vol. 2, J. L. Lumley (ed.) Cambridge, Mass., MIT Press.*
- SREENIVASAN, K. R. 1991 On Local Isotropy of Passive Scalars in Turbulent Shear Flows. *Proc. Roy. Soc. Lond.* **A434**, 165-182.
- SREENIVASAN, K. R., ANTONIA, R. A. & BRITZ, D. 1979 Local Isotropy and Large Structures in a Heated Turbulent Jet. *J. Fluid Mech.* **94**, 745-775.
- SREENIVASAN, K. R. & TAVOULARIS, S. 1980 On the Skewness of the Temperature Derivative in Turbulent Flows. *J. Fluid Mech.* **101**, 783-795.

- UBEROI, M. S. 1957 Equipartition of Energy and Local Isotropy in Turbulent Flows. *J. Appl. Phys.* **28**, 1165-1170.
- VAN ATTA, C. W. 1977 Second-Order Spectral Local Isotropy in Turbulent Scalar Fields. *J. Fluid Mech.* **80**, 609-615.
- VAN ATTA, C. W. 1991 Local Isotropy of the Smallest Scales of Turbulent Scalar and Velocity Fields. *Proc. Roy. Soc. Lond.* **A434**, 139-147.
- WYNGAARD, J. C. 1969 Spatial Resolution of the Vorticity Meter and Other Hot-Wire Arrays. *J. Sci. Instrum. (J. Phys. E)*. **2**, 983-987.

58-34 445349
189668 137
N947174753

LES versus DNS : a comparative study

By L. Shtilman¹ AND J. R. Chasnov²

We have performed Direct Numerical Simulations (DNS) and Large Eddy Simulations (LES) of forced isotropic turbulence at moderate Reynolds numbers. The subgrid scale model used in the LES is based on an eddy viscosity which adjusts instantaneously the energy spectrum of the LES to that of the DNS. The statistics of the large scales of the DNS (filtered DNS field or fDNS) are compared to that of the LES. We present results for the transfer spectra, the skewness and flatness factors of the velocity components, the PDF's of the angle between the vorticity and the eigenvectors of the rate of strain, and that between the vorticity and the vorticity stretching tensor. The above LES statistics are found to be in good agreement with those measured in the fDNS field. We further observe that in all the numerical measurements, the trend was for the LES field to be more gaussian than the fDNS field. Future research on this point is planned.

1. Introduction

Direct Numerical Simulation (DNS) of turbulent flows has become an indispensable tool in turbulence research. The importance of DNS was universally recognized when researchers started to obtain new qualitative results. While a DNS can reproduce basic turbulence constants or statistics determined previously from laboratory experiments, it is also able to provide statistical information difficult to obtain by experimental measurements. Among effects observed in the DNS prior to laboratory experiments are alignments of vorticity and velocity vectors (Pelz *et al.*, 1985), alignments of vorticity vector and the eigenvectors of the rate of strain (Ashurst *et al.*, 1987), and reduction of nonlinearity (Kraichnan & Panda, 1989). All of these effects are not present in gaussian fields. Some of the above observations can be qualitatively predicted in the framework of the DIA or the EDQNM closure approximations (see, for instance, Chen *et al.*, 1987). Others, such as the spottiness of the vorticity field that was observed in the DNS, have not yet been demonstrated by closures. Nevertheless, the DNS (with all its advantages) is still limited to relatively low Reynolds numbers. Attainment of a high Reynolds number simulation requires use of a subgrid scale model to represent the effects of the unresolved small-scale turbulence on the explicitly simulated large-scale flow.

The most important assumption in this Large Eddy Simulation (LES) approach is that the subgrid scale model may be parameterized in terms of the resolved large-scales and a relatively small set of additional parameters. The basis for such

1 Tel-Aviv University

2 Center for Turbulence Research

~~126~~

an assumption is the experimental evidence supporting the 1941 phenomenology of Kolmogorov that the low-order statistics of the small scales are self-similar in a high Reynolds number turbulence. The task of modeling is to find a subgrid scale model which can represent the effects of a strongly nongaussian, intermittent small scale field of turbulence on a large scale field. For homogeneous and isotropic turbulence, Kraichnan (1976) introduced an effective eddy viscosity $\nu_e(k|k_m, t)$ acting at time t on scales of wavenumber k due to the effects of scales with wavenumbers greater than k_m . In this model, the eddy viscosity is derived from the turbulence energy equation. Clearly, one should construct $\nu_e(k|k_m, t)$ (from analytical theories or the DNS) in such a way that, at a minimum, the low order statistics of the flow field (*e.g.*, the energy spectrum) is preserved. The major role played by a well-chosen eddy-viscosity is to "adjust" the spectrum to the value it is supposed to have from analytical or DNS considerations. Strict eddy-viscosity models, however, suffer from a lack of phase information and an eddy-viscosity model combined with a random gaussian force has been shown to somewhat better reproduce the inertial range energy spectrum (Chasnov, 1991). However, it is not clear if such eddy-viscosity subgrid models or their refinements are capable of reproducing higher-order statistical moments of the large scales. Ideally, an LES field should be statistically the same as the large-scales of a fully-resolved DNS, notwithstanding the inaccuracy in the representation of the small scales by a subgrid scale model.

2. The numerical experiment

Let us consider a DNS with resolution N^3 . One can filter (in k -space) the field resulting from this simulation. Then we obtain an M^3 field ($M \ll N$). Simultaneously we will perform an LES with resolution M^3 . We will use the same initial conditions and the same Reynolds number. Does the LES field remain the same as the filtered DNS field after a long time of evolution? To answer this question, we define a correlation coefficient for the filtered DNS and LES fields:

$$\eta = \frac{\langle \mathbf{u} \cdot \mathbf{u}' \rangle}{\langle \mathbf{u}^2 \rangle^{1/2} \langle \mathbf{u}'^2 \rangle^{1/2}}. \quad (1)$$

In the context of unpredictability studies using closure theories (Leith & Kraichnan, 1972), it was demonstrated that two turbulent fields which are identical in the large-scales but differ in the small scales at high Reynolds numbers will become decorrelated after a time on the order of a large-eddy turnover time. The implication is that an LES can not hope to follow a single realization of a turbulent flow. Although this may have some practical importance to problems such as weather prediction, most engineering applications only require an LES to obtain the correct statistics of the large scales. The more important question we will therefore address is: are the filtered DNS field and the LES field still statistically the same after a sufficiently long time evolution after which the fields themselves are completely different? We will check that commonly accepted effects associated with the non-gaussian nature of turbulence fields, such as the above mentioned alignments, are observed in an LES and are quantitatively similar to those measured in the filtered DNS field.

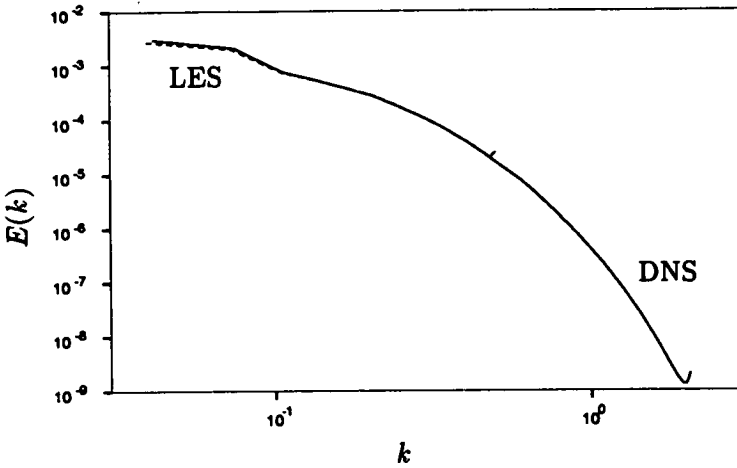


FIGURE 1. Final energy spectrum of the DNS and the LES.

Toward this end, we performed simulations of forced isotropic, homogeneous turbulence with $Re \approx 70$ and a resolution of 128^3 . A fully-developed field was used as the initial conditions for the DNS and LES comparison. Starting with this field, we have time-evolved a 128^3 DNS and a 32^3 LES. Our subgrid scale model for the LES consists of adjusting the shell-averaged spectrum of the LES to the value obtained from the DNS by a simple rescaling of the Fourier amplitudes within each shell without phase modification. Instead of the 128^3 DNS field, we therefore have a 32^3 LES field plus the energy spectrum of the truncated DNS (averaged in shells of unit thickness), which consists of 15 real numbers. Thus the LES preserves the instantaneous spectrum of the DNS, which is better than all existing subgrid scale models. Although such an LES is not realistic in practice since one needs to perform a fully-resolved DNS concurrently, the failure of this LES could very well imply the failing of the approach itself.

3. Results

In figure 1, we present the final energy spectrum for the DNS and the LES. The plot demonstrates that all the scales of the DNS are fully-resolved. The DNS has a maximum Kolmogorov wavenumber of 2 while the LES and the fDNS have a maximum Kolmogorov wavenumber of 0.5.

In figure 2, we present the time-evolution of the correlation coefficient η (eq. (1)). This plot demonstrates the impossibility of an LES to follow a particular realization of the DNS field. Indeed, after approximately two large-eddy turnover times, the filtered DNS field and the LES field are completely decorrelated. Clearly, this result should not discourage us since even two DNS fields having slightly different initial conditions will diverge exponentially with time. Our real goal is to check whether the LES field has the same statistics as the filtered DNS field.

Some statistics of turbulent fields (*e.g.*, the PDF of vorticity and dissipation) are

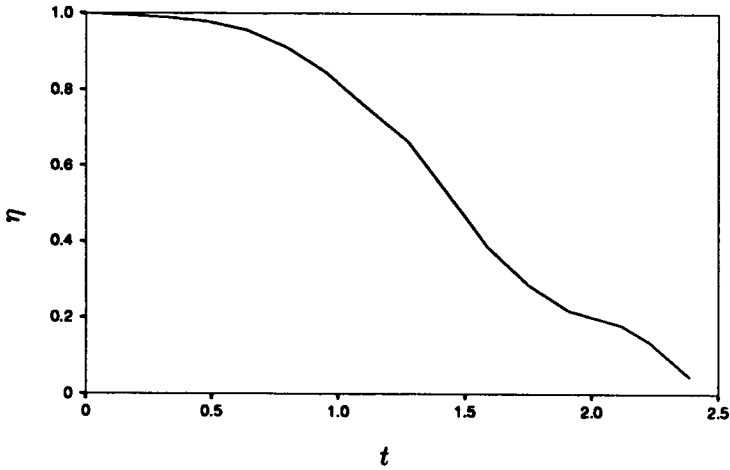


FIGURE 2. Time-evolution of the correlation coefficient $\eta(t)$, defined in eq. (1), between the LES and the fDNS fields. Time t is in units of a large-eddy turnover time.

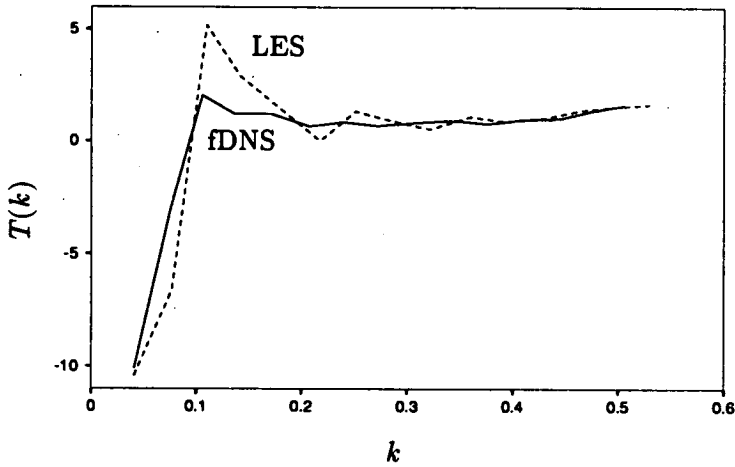


FIGURE 3. Energy transfer spectrum

close to those for gaussian fields (Shtilman *et al.*, 1992) while some statistics (*e.g.*, helicity fluctuations) require statistical averaging over realizations for accuracy. We exclude results related to these quantities in the present study. In figure 3, we present a comparison between the energy transfer spectrum for the LES and the fDNS. We note that the spectrum preservation in the LES does not necessarily imply that the fDNS and the LES have the same transfer spectrum in the large-scales. The energy equation for isotropic turbulence is

$$\frac{\partial E(k)}{\partial t} = T(k) - 2\nu k^2 E(k),$$

Statistic	DNS	fDNS	LES	Gaussian
S_3	-0.54	-0.44	-0.37	0
S_4	4.62	3.74	3.69	3
S_5	-8.52	-5.01	-4.18	0

Table 1. Derivative skewness, flatness and hyperflatness from the DNS, the filtered DNS, and the LES. The values for a gaussian field are shown for comparison.

where the transfer term $T(\mathbf{k})$ is defined as the shell integral of

$$T(\mathbf{k}) = \text{Re}[\lambda(\mathbf{k}) \cdot \mathbf{v}^*(\mathbf{k})],$$

where $\lambda(\mathbf{k})$ is the Fourier transform of the Lamb vector, $\lambda(\mathbf{x}) = (\mathbf{v} \times \boldsymbol{\omega})(\mathbf{x})$ and the asterisk denotes complex conjugate. Clearly $T(\mathbf{k})$ depends on the absolute value of $\mathbf{v}(\mathbf{k})$ and on its phase. While the mean-square Fourier amplitude in a shell is adjusted to its DNS value, the individual Fourier phases are determined by solution of the Navier-Stokes equations. Nevertheless, from figure 3 we learn that the transfer term of LES has values close to those of fDNS.

In Table 1, we present high-order derivative statistics of the flow fields – the skewness S_3 , flatness S_4 and hyperflatness S_5 , where

$$S_n = \frac{1}{3} \sum_{i=1,3} \left\langle \left(\frac{\partial u_i}{\partial x_i} \right)^n \right\rangle / \left\langle \left(\frac{\partial u_i}{\partial x_i} \right)^2 \right\rangle^{\frac{n}{2}}$$

It is seen from Table 1 that the fDNS and the LES values are both more gaussian than those values obtained from the full DNS, as one would expect for high-order statistics. We also note that the LES values are more gaussian than their fDNS counterparts, although we do not yet know if this is only a statistical fluctuation or if it is a shortcoming of LES. Additional numerical experiments which directly address this question are planned for the future.

In figure 4, the PDF of the cosine of the angle between $\boldsymbol{\omega}$ and the eigenvectors of the rate of strain S_{ij} is presented. The results for the LES and the fDNS are seen to be in good agreement. These PDF's are flat for a gaussian field and most authors relate this alignment to the tube-like nature of the vorticity field. A detailed examination of this plot demonstrates again that the LES field has a tendency to be more gaussian than the fDNS field.

Another quantity we consider is the statistics of the angle between the vorticity and the vorticity stretching vector

$$W_j = \omega_i S_{ij}.$$

It was shown in laboratory experiments (Dracos *et al.*, 1991) and numerical experiments (Shtilman *et al.*, 1992) that W_j has a strong tendency to be aligned with

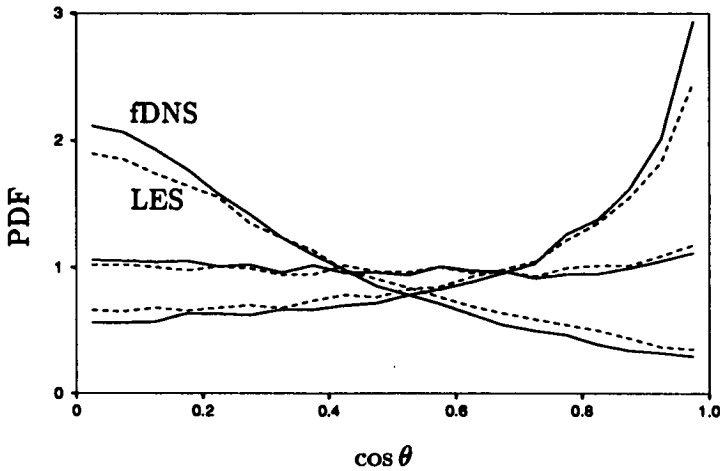


FIGURE 4. PDF of cosine of the angle between ω and the eigenvectors of the rate of strain tensor S_{ij} .

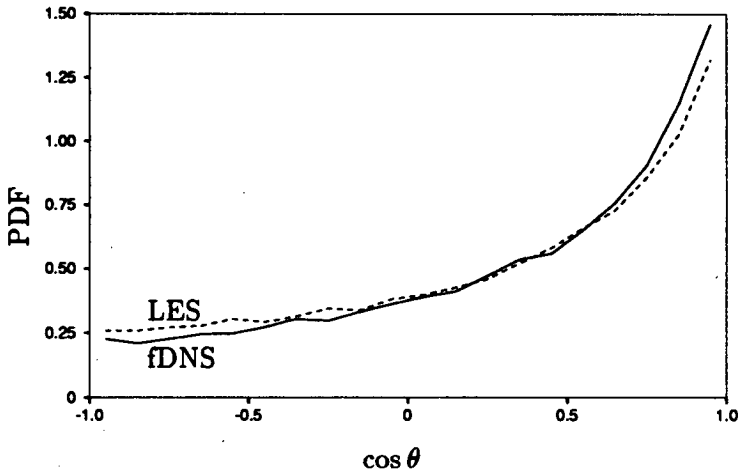


FIGURE 5. PDF of the cosine of the angle between ω and the vorticity stretching vector $W_j = \omega_i S_{ij}$.

vorticity. This alignment reflects the total positive production of enstrophy. In figure 5, we present the PDF of the cosine of the angle between \mathbf{W} and ω . While the LES and fDNS curves are in reasonable agreement, we again note the tendency of the LES curve to be more gaussian than the fDNS curve.

4. Conclusions

We have compared the statistics of the large scales of the DNS field with the LES field for forced isotropic turbulence at moderate Reynolds numbers. The subgrid

scale model used is based on an eddy viscosity which adjusts the instantaneous shell-averaged energy spectrum of the LES to that of the DNS at each time-step. After a couple of large-eddy turnover times, the LES field is uncorrelated with the fDNS field. Several statistical parameters of the large scales of the fDNS were compared to that of the LES. Among them were the transfer spectrum, skewness and flatness factors of velocity components, and PDF's of the angle between vorticity and eigenvectors of the rate of strain and that between the vorticity and vorticity stretching tensor. The overall agreement between the LES and the fDNS statistics was quite good, although we did observe a tendency for the LES field to be slightly more Gaussian than the fDNS field. Nevertheless, the preliminary results presented here point to the promising future of LES.

We thank R. Rogallo for use of his numerical codes and for many helpful discussions. LS would also like to thank E. Levich for discussions and the CTR for its hospitality during the Summer program.

REFERENCES

- ASHURST, W. T., KERSTEIN, A. R., KERR, R. M., & GIBSON, C. H. 1987 Alignment of vorticity and scalar gradient with strain rate in simulated Navier-Stokes turbulence. *Phys. Fluids*. **30**, 2343.
- CHASNOV, J. R. 1991 Simulation of the Kolmogorov inertial subrange using an improved subgrid model. *Phys. Fluids A*. **3**, 188-200.
- CHEN, H., HERRING, J. R., KERR, R. M., & KRAICHNAN, R. H. 1989 Nongaussian statistics in isotropic turbulence. *Phys. Fluids A*. **1**, 1844-1854.
- KRAICHNAN, R. H. 1976 Eddy viscosity in two and three dimensions. *J. Atmos. Sci.* **33**, 1521-1536.
- KRAICHNAN, R. H. & PANDA, R. 1988 Depression of nonlinearity in decaying isotropic turbulence. *Phys. Fluids*. **31**, 2395.
- LEITH, C. E., & KRAICHNAN, R. H. 1972 Predictability of turbulent flows. *J. Atmos. Sci.* **29**, 1041-1058.
- PELZ, R. B., YAKHOT, V., ORSZAG, S. A., SHTILMAN L. & LEVICH, E. 1985 Velocity-vorticity patterns in turbulent flow. *Phys. Rev. Lett.* **54**, 2505-2508.
- SHTILMAN, L., SPECTOR, M., & TSINOBER, A. 1993 On some kinematic versus dynamic properties of homogeneous turbulence. *J. Fluid Mech.* in press.
- TSINOBER, A., KIT, E., & DRACOS, T. 1990 Some experimental results on velocity-velocity gradients measurements in turbulent grid flows. *Topological Fluid Mechanics, Proc. of the IUTAM Symp.* edited by H. K. Moffatt and A. Tsinober. Cambridge University Press.

II. Turbulence physics group

Numerical simulation of turbulence has proven to be a powerful tool in studying the physics of turbulence. There are three papers in this group, each illustrating how numerical simulations are being used for this purpose. Lopez and Bulbeck analyzed an existing database to investigate vortex breakdown in a mixing layer. Orlandi, Homsy, and Azaiez reported preliminary results from modeling the effect of viscoelasticity on flow structures. The last paper by Reuss and Cheng was an attempt to develop new experimental techniques for characterizing vortices in a complex flow by exploring different approaches in a much simpler flow situation. Some highlights as well as critiques of these reports are given below:

Lopez and Bulbeck studied vortex breakdown in a time-developing plane mixing layer by analyzing the database obtained by Moser and Rogers. Vortex breakdown in large-scale flows has been observed frequently, from which much of our knowledge of vortex breakdown is derived. There exists some evidence that such breakdown may also occur in smaller scales over a wide range of flows and that vortex breakdown may play a role in characterizing a length scale for vortical structures in turbulent flows. The objective of this paper was to investigate whether vortex breakdown occurs in the rib vortices in the plane mixing layer, where a previous study indicated a rapid change in the local topology. If vortex breakdown were found here, they postulated that it would also exist in other turbulent flows. Using the criteria developed by Brown and Lopez for breakdown of an isolated vortex, i.e., the sudden acceleration of the axial flow and the helix angle of the velocity vector being larger than that of the vorticity vector, they found evidence that the rib vortex downstream of the mid-braid plane began vortex breakdown. There was no evidence, however, of sudden core expansion or intense mixing, phenomena nominally associated with large-scale vortex breakdown flows. There were some discussions during the final presentation of the Summer Program as to whether what they observed here in the temporally developing mixing layer could be regarded as a true vortex breakdown.

Orlandi *et al.* performed numerical simulations of a two-dimensional mixing layer and the interaction of vortex dipole with a wall in order to investigate the effect of viscoelastic fluids on flow structures. Three different viscoelastic models were used to account for the viscoelasticity. For some models, however, they could not obtain a converged solution. In the case of mixing layer, they found that the viscoelasticity enhanced the formation of small scales, which produced intense gradients in the braid region of the mixing layer. These intense gradients led to a faster and more intense roll-up of the layer. This is contrary to the linear stability analysis by Azaiez and Homsy, who showed that viscoelasticity reduced the instability of the flow. The second part of the paper concerned with the effect of viscoelasticity on vortex dipole impinging on a wall, a model of streamwise vortices in a turbulent

boundary layer. They considered both free-slip and no-slip walls but found that the effect of the viscoelasticity for both cases was small. The results presented in this paper appear to be preliminary and they should be interpreted as such. As the authors pointed out, further numerical studies as well as experimental verifications are deemed necessary to validate the present result.

Reuss and Cheng explored different methods for characterizing vortex structures by examining a turbulent flow field obtained from a simulation of turbulent channel. The senior author has been conducting experiments to investigate vortex structures that influence flame wrinkling in reciprocating internal combustion engine, and the objective of this project was to develop an experimentally suitable technique for identifying the turbulence properties associated with these structures. They applied two-dimensional spatial filtering to the instantaneous flow field to separate different scales present in the flow field. As expected, they were able to identify vortical structures which were not apparent from the unfiltered field, but the results were highly dependent on the filter size used. They proceeded to use a conditional-averaging procedure in which the detection was based on the local peak vorticity. They presented results obtained from this procedure as representative of the coherent parts of the flow field. It should be pointed, however, that these results might also depend on the threshold value used for the detection and, to a lesser extent, on how the alignment for the averaging process was conducted. I might add that in the past other investigators have used an iterative procedure using a correlation technique to minimize this problem.

John Kim

449352 59-34

189669 147

N94-1A754

Behavior of streamwise rib vortices in a three-dimensional mixing layer

By J. M. Lopez¹ AND C. J. Bulbeck¹

The structure and behavior of a streamwise rib vortex in a direct numerical simulation of a time-developing three-dimensional incompressible plane mixing layer is examined. Where the rib vortex is being stretched, the vorticity vector is primarily directed in the vortex axial direction and the radial and azimuthal velocity distribution is similar to that of a Burger's vortex. In the region where the vortex stretching is negative, there is a change in the local topology of the vortex. The axial flow is decelerated and a negative azimuthal component of vorticity is induced. These features are characteristic of vortex breakdown. The temporal evolution of the rib vortex is similar to the evolution of an axisymmetric vortex in the early stages of vortex breakdown. The effect of vortex breakdown on other parts of the flow is, however, not as significant as the interaction between the rib vortex and other vortices.

1. Introduction

In the main, the term vortex breakdown has been associated with large scale flows. In aeronautics, vortices generated by swept leading edges and the trailing vortices generated at wing tips are observed to undergo vortex breakdown. In such flows, vortex breakdown is characterized by the sudden deceleration of the axial flow, with an associated sudden expansion of the core. Downstream, the flow is unsteady and seemingly disorganized. With the exception of a few idealized flows designed to study vortex breakdown in isolation, our knowledge of vortex breakdown is based solely on such large scale flows.

Recently, there have been suggestions that vortex breakdown occurs naturally over a much wider range of flows and scales than has previously been expected. One example is the breakdown of the side vortices associated with a jet in cross-flow (Kelso 1991). Orszag (1991) has suggested that vortex breakdown may be present in the results of computations of homogeneous isotropic turbulence reported by She, Jackson and Orszag (1990). He observed that coherent structures in homogeneous isotropic turbulence (which are tube-like vortical structures recently referred to by the term 'worms') have characteristic flow features suggestive of vortex breakdown. He observed that the tangent of the helix angle (ratio of azimuthal to axial component) of the velocity vector is larger than that of the vorticity vector. This represents one of the necessary conditions for vortex breakdown developed by Brown

¹ Defence Science and Technology Organisation, Air Operations Division - Aeronautical Research Laboratory, Melbourne, Australia

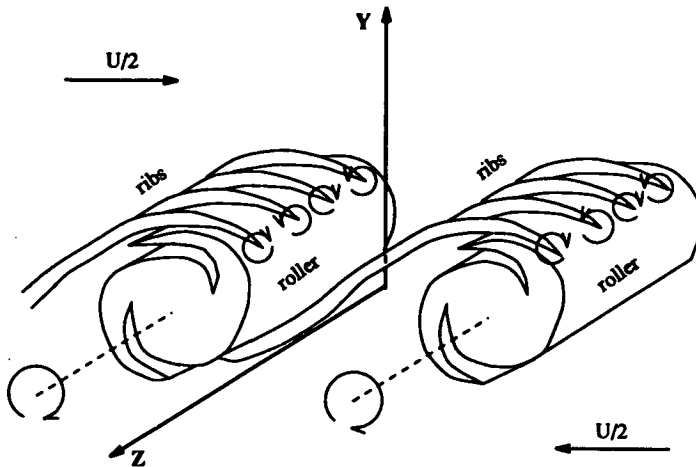


FIGURE 1. Diagram of the structures in a plane mixing layer.

and Lopez (1990) on the basis of steady, axisymmetric swirling flow theory. Chen *et al.* (1990) have also suggested that vortex breakdown may occur within the three-dimensional plane mixing layer flow computed by Moser and Rogers (1992). It is this latter suggestion that is the subject of investigation in this study.

The flow computed by Moser and Rogers (1992) is a three-dimensional, incompressible plane mixing layer formed between two streams moving at differing velocities. In such a plane mixing layer, spanwise vortices, called 'rollers', are generated by the Kelvin-Helmholtz instability of the layer. These rollers undergo 'pairing' whereby neighboring rollers co-rotate and amalgamate. Three-dimensional instability of the mixing layer also gives rise to counter-rotating 'rib' vortices which exist in the region between the rollers (the 'braid' region) and extend from the bottom of one roller to the top of the next (Figure 1). The vorticity in the rib vortices is predominantly perpendicular to that of the rollers. An observed change in the character of the local topology along a rib vortex, from stable focus/stretching to unstable focus/contracting, was taken by Chen *et al.* (1990) as evidence for vortex breakdown. We wish to determine whether the phenomenon of vortex breakdown is indeed responsible for the observed change in local topology.

The approach used in the present study to identify vortex breakdown is to project flow field quantities in the vicinity of the rib vortex onto a locally cylindrical polar co-ordinate system. The cylindrical polar co-ordinate system is constructed such that the axial direction corresponds to the axis of the rib vortex. Local topology (explained in detail in section 2), axial velocity, azimuthal vorticity, and enstrophy are all examined in this co-ordinate system. Comparisons are made with axisymmetric vortex breakdown in confined swirling flows as computed by Brown and Lopez (1990). Vortex-vortex interactions are also investigated to determine whether they

or the vortex breakdown are responsible for the observed spiralling of the rib vortex core.

The motivation behind the present research is twofold. Firstly, vortex breakdown can make a significant contribution to mixing. If it occurs in a flow such as the plane mixing layer, which is undergoing a transition to turbulence, mixing associated with vortex breakdown may provide a mechanism for transition. Secondly, if vortex breakdown can occur in a coherent structure in the mixing layer flow, it may also be occurring in coherent structures in other flows, such as in the worms found in homogenous isotropic turbulence.

2. Global and local classifications of flow field topologies

Complex flow fields can be interpreted by classifying their topology. This can either be done *globally* or *locally*. In the global approach, developed by Perry and Fairlie (1974) and extended by Chong, Perry, and Cantwell (1990), the critical points of the flow field are identified. The critical points in a flow field are those points where all three velocity components are simultaneously zero relative to a global observer. A local Taylor series expansion of the velocity field with respect to space co-ordinates is made at each of these critical points, and the invariants of the resulting 3×3 Jacobian matrix, the velocity gradient tensor A , are used to completely classify the topology of this critical point.

In the local approach, the co-ordinate system translates without rotation while following the fluid particle. That is, each point in the flow field is considered to be a critical point since the velocity of each point is zero relative to a local observer. The topology of each point in the flow is then classified, as in the global approach, by considering the local velocity gradient tensor at each point in the flow. Due to the Galilean invariant nature of the velocity gradient tensor and hence any property based on this tensor, the local topological classification of each fluid flow point is independent of the observer. This local classification of the flow field was first used by Chen *et al.* (1990) and is the approach used in this study.

The velocity gradient tensor can be decomposed into its symmetric and antisymmetric parts, i.e.

$$A_{ij} = \frac{\partial u_j}{\partial x_i} = S_{ij} + W_{ij},$$

where

$$S_{ij} = \left(\frac{\partial u_i}{\partial x_j} + \frac{\partial u_j}{\partial x_i} \right) / 2,$$

is the rate-of-strain tensor and

$$W_{ij} = \left(\frac{\partial u_i}{\partial x_j} - \frac{\partial u_j}{\partial x_i} \right) / 2,$$

is the rotation tensor. A_{ij} , S_{ij} and W_{ij} are all tensors of second order.

For a second order tensor, \mathbf{A} , where λ_1 , λ_2 , and λ_3 are the eigenvalues and e_1 , e_2 , and e_3 are the eigenvectors, then

$$(\mathbf{A} - \lambda \mathbf{I})e = \mathbf{0},$$

and the corresponding characteristic equation

$$\det[\mathbf{A} - \lambda\mathbf{I}] = 0,$$

may be written as

$$\lambda^3 + P\lambda^2 + Q\lambda + R = 0.$$

The invariants P , Q , and R are

$$P = -S_{ii},$$

$$Q = (P^2 - S_{ij}S_{ji} - W_{ij}W_{ji})/2,$$

$$R = (-P^3 + 3PQ - S_{ij}S_{jk}S_{ki} - 3W_{ij}W_{jk}S_{ki})/3.$$

For an incompressible flow as is being considered here, $P = 0$, and the topology of the flow is completely classified by Q and R .

The characteristic equation $\lambda^3 + Q\lambda + R = 0$ can have (i) all real distinct roots, (ii) all real roots with at least two equal, or (iii) one real root and a conjugate pair of complex roots. The curve $27R^2 + 4Q^3 = 0$ separates the regions of real and complex roots. Chong, Perry and Cantwell (1990) define regions where the velocity gradient tensor has complex eigenvalues as vortex cores, i.e. regions where $Q > -3(R/2)^{2/3}$ are vortical in nature. The eigenvalues of the velocity gradient tensor determine the local kinematics of the flow, and these are determined by the invariants Q and R . If $Q > -3(R/2)^{2/3}$, then a conjugate pair of complex eigenvalues result, and hence the trajectories will be spiralling locally. Whether the spirals are stable or unstable is determined by the sign of the real eigenvalue, which in turn is determined by the sign of R . If $R > 0$, then the spiral is unstable, and to conserve mass, the local topology is of the unstable focus/contracting (UFC) type. For $R < 0$, it is of the stable focus/stretching (SFS) type. For the degenerate case of $R = 0$, the trajectory is a closed loop rather than a spiral. For $Q < -3(R/2)^{2/3}$, the local flow is strain dominated, and for $R < 0$, the topology is of the stable node/saddle/saddle (SNSS) type, and for $R > 0$, it is of the unstable node/saddle/saddle (UNSS) type.

3. Determination of the rib vortex axis

The following discussion centers on the flow case 'HIGH1P' of Moser and Rogers (1992) in which the initial conditions of the calculation involved a high-strength three-dimensional perturbation. The structure of the vortex was determined at non-dimensional time $t = 28.5$, after a pairing of the main rollers had occurred. Chen *et al.* (1990) have suggested that vortex breakdown may be occurring at this time based on their observation of a subsequent change in the local topology along the vortex core.

In order to describe the structure of the vortex, its associated velocity and vorticity fields, a co-ordinate system that is peculiar to the vortex is required rather than one using the co-ordinate system in which the governing equations are cast. A local cylindrical polar co-ordinate system is chosen where the axial direction is tangent to the axis of the vortex. A difficulty arises in defining the axis of the vortex. Here,

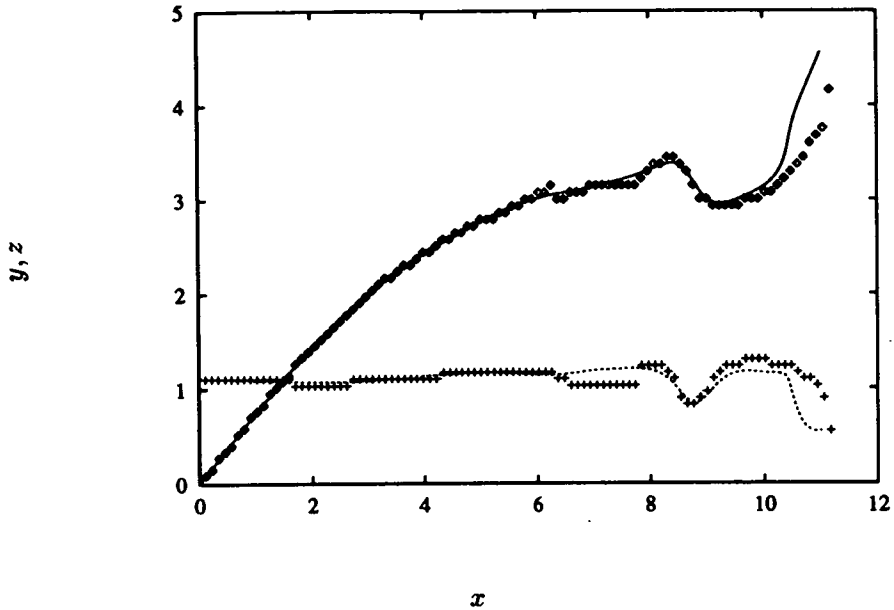


FIGURE 2. Location of the vortex axis projected onto x - y and x - z planes at time $t = 28.5$.

a distinction is made between the 'centerline' and the 'axis' of the vortex. If the modal decomposition of the azimuthal components of the vortex velocity and vorticity fields are dominated by even modes, then the centerline and the axis coincide. If, however, the odd modes dominate, then the centerline spirals around the vortex axis.

There has been much controversy over what constitutes the centerline of a vortex (e.g. Yates and Chapman 1992). In regions where the vortex is predominantly axisymmetric, its centerline can be reasonably approximated by either the loci of enstrophy local maxima, or a vortex line extending from a point of maximum enstrophy in the vortex core. The vortex core is taken to be the region enclosed by the maxima of the azimuthal component of velocity. The axis of the vortex has been determined by both methods and the location of the axis projected onto x - y and x - z planes are given for $t = 28.5$ in Figure 2. There is very little difference in the determined axis from either method for $x < 8$.

The structure of the rib vortex at $t = 28.5$ can be described in terms of three distinct regions. Region I extends from the mid-braid plane to the axial location where the local topology changes from stable focus/stretching to unstable focus/contracting. The mid-braid plane is the z - y plane mid way between two spanwise rollers (see Figure 1), and in the time-developing calculations of Moser and Rogers (1992), this plane is a symmetry plane. Region II extends downstream from the point of topology change. The structure of the vortex in regions I and II

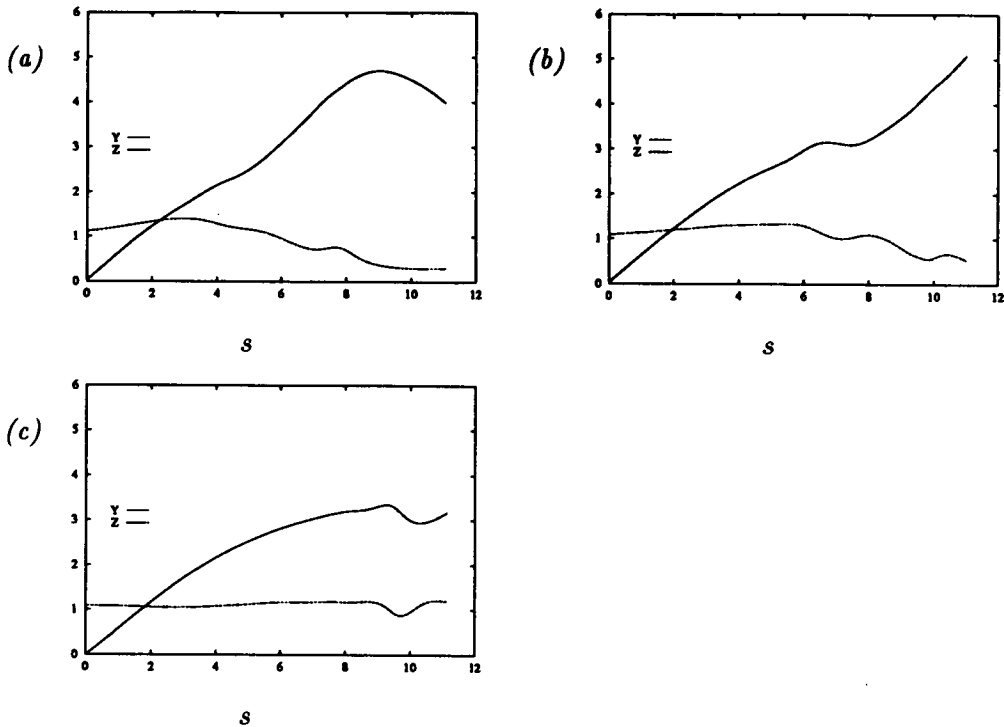


FIGURE 3. Spanwise Z , and vertical Y , locations of the vortex axis in terms of distance along the axis at times (a) $t = 22.3$, (b) $t = 25.3$ and (c) $t = 28.5$.

is dominated by the axisymmetric azimuthal mode. The rib vortex then evolves to a stage where it is no longer dominated by the axisymmetric mode. This region is denoted as region III. Region III does not appear at the earlier times considered since the centerline does not spiral about the axis at these times.

4. Temporal and spatial evolution of the streamwise rib vortex

The development of the rib vortex was investigated by analyzing the flow field at three non-dimensional times, $t = 22.3$, $t = 25.3$, and $t = 28.5$ (where the first pairing occurs at $t = 23.4$). At each time, the vortex axis was determined by the techniques outlined in section 3. The vortex axes are shown in Figure 3. The parameter s is the distance along the vortex axis from the mid-braid plane. Local cylindrical polar co-ordinates were determined at each of the three times. At any point on the vortex axis, the axial direction \mathbf{ax} is defined as being tangent to the vortex axis, positive downstream. The radial direction \mathbf{r} is defined in terms of the axial direction \mathbf{ax} and the vertical direction \mathbf{y} by $\mathbf{r} = \mathbf{ax} \times \mathbf{y}$. Figure 4 illustrates the local cylindrical polar co-ordinate system.

The distribution of azimuthal velocity across the vortex core at a streamwise location downstream of the mid-braid plane but upstream of the topology change

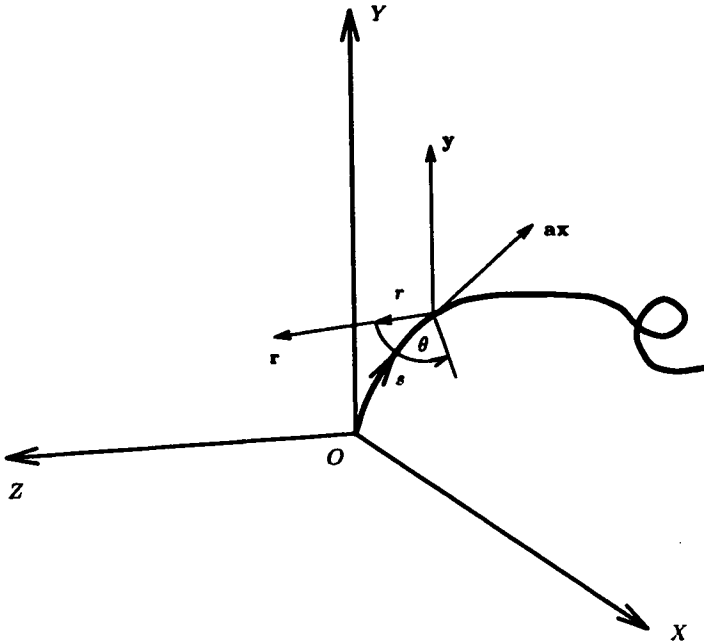


FIGURE 4. Local cylindrical polar co-ordinate system defined along the axis of the vortex.

($s = 1.0$) at time $t = 28.5$ is shown in Figure 5. The point $s = 1.0$ lies in region I. Also shown is the azimuthal velocity for a Burger's vortex given by

$$v_{\theta}(r) = \frac{\Gamma}{2\pi} \frac{(1 - \exp(-\alpha\gamma))}{\sqrt{2\gamma}},$$

where $\gamma = r^2/2$, $\Gamma = 2.2$ and $\alpha = 18$. Both Γ and α have been fitted to the data from the mixing layer calculation. Despite the highly three-dimensional nature of the flowfield, in region I the azimuthal velocity of the rib vortex is nearly axisymmetric and well described by the equation for a Burger's vortex.

Figure 6 shows the variation in the velocity gradient tensor invariants, Q and R , along the vortex axis as well as the vortex stretching, $\omega_i S_{ij} \omega_j$, at the three times considered. The instantaneous exponential stretching rate for a vortex element is given by

$$\zeta = \frac{d}{dt} \log \|\omega(t)\|,$$

where ω is the vorticity vector. In the inviscid limit (Dresselhaus and Tabor 1991),

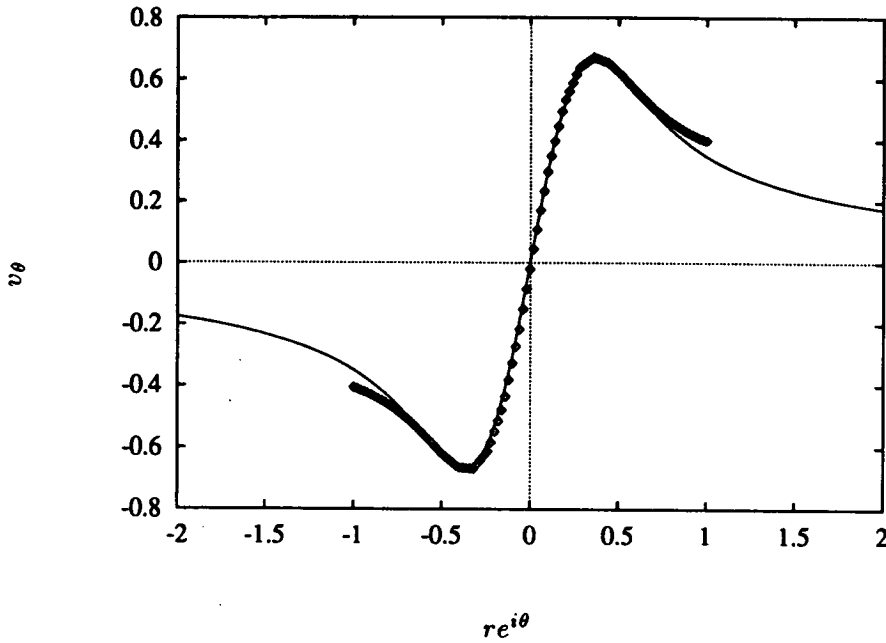


FIGURE 5. Radial distribution of azimuthal velocity at axial location $s = 1.0$ and azimuthal locations $\theta = 0$ and $\theta = \pi$, denoted by \diamond and compared with a Burger's vortex azimuthal velocity distribution for $\Gamma = 2.2$ and $\alpha = 18$.

this may be expressed as

$$\zeta = \sum_{i,j} S_{ij} \hat{\omega}_i \hat{\omega}_j,$$

where $\hat{\omega}$ is the unit vector in the direction of ω . A related term, $\omega_i S_{ij} \omega_j$ is referred to as 'vortex stretching'. A vortex intensifies if it is being stretched, i.e. $\omega_i S_{ij} \omega_j$ is positive. The imposed axial strain will cause a decrease in the cross-sectional area of the vortex, and to conserve angular momentum, the angular velocity, and hence vorticity, will increase. There is a strong negative correlation between the vortex stretching and the third invariant R , i.e. when one is positive, the other is negative. Since the second invariant is positive in the vortex core region, positive vortex stretching corresponds to a local topology of the stable focus/stretching type and negative vortex stretching to the unstable focus/contracting type.

Figure 7 shows the radial variation of the local topology along the vortex axis at $\theta = 0$ and π at the three different times. The light regions correspond to a stable focus/stretching type topology and the dark regions to an unstable focus/contracting type topology. Along the centerline, the local topology changes from stable focus/stretching to unstable focus/contracting, and this denotes the boundary between regions I and II. This boundary moves downstream at a non-dimensional speed 0.37.

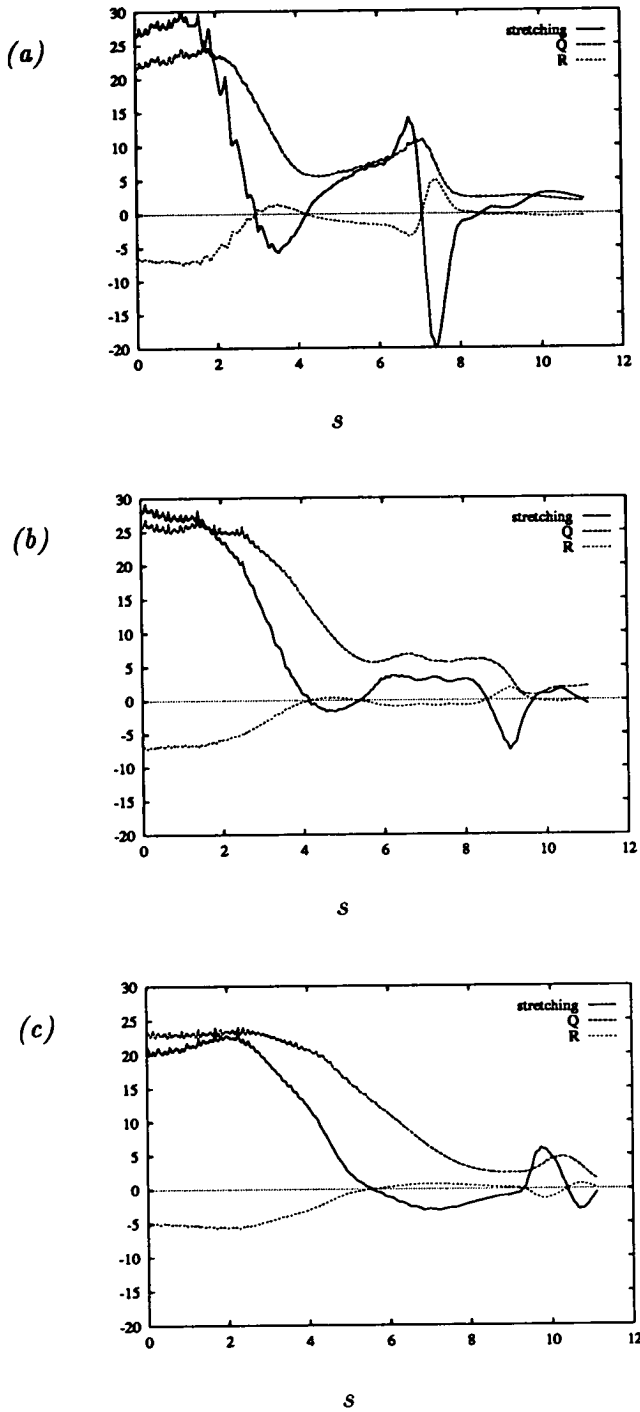


FIGURE 6. Variation of the vortex stretching term, $\omega_i S_{ij} \omega_j$, and the second and third invariants of the velocity gradient tensor, Q and R , with distance along the vortex axis s , at times (a) $t = 22.3$, (b) $t = 25.3$, and (c) $t = 28.5$.

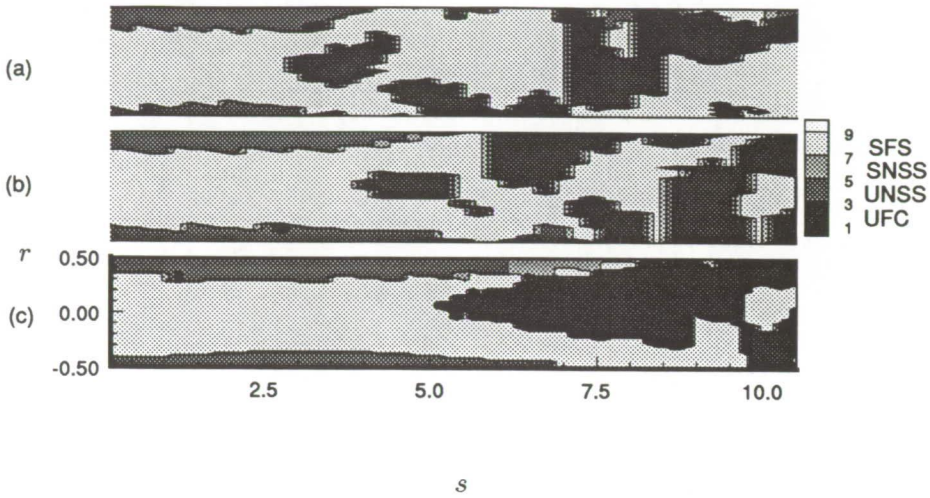


FIGURE 7. Local topology in the vortex core region of the streamwise rib vortex at times (a) $t = 22.3$, (b) $t = 25.3$ and (c) $t = 28.5$.

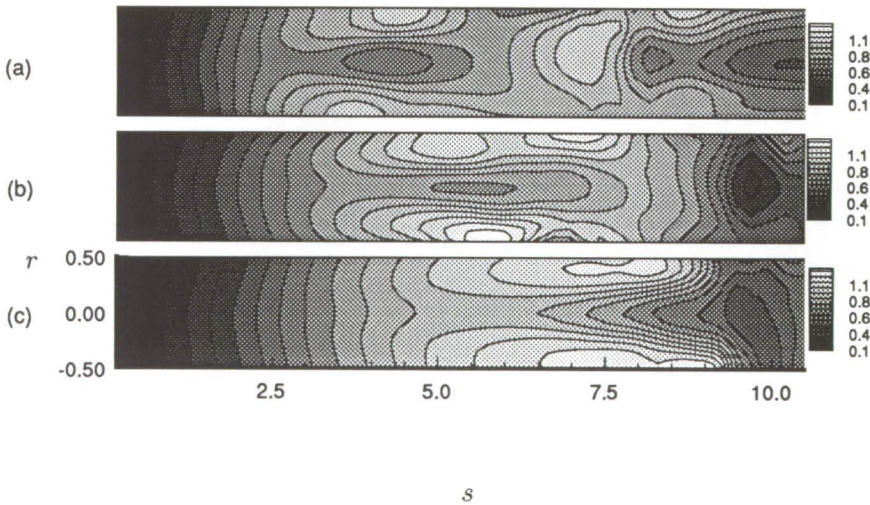
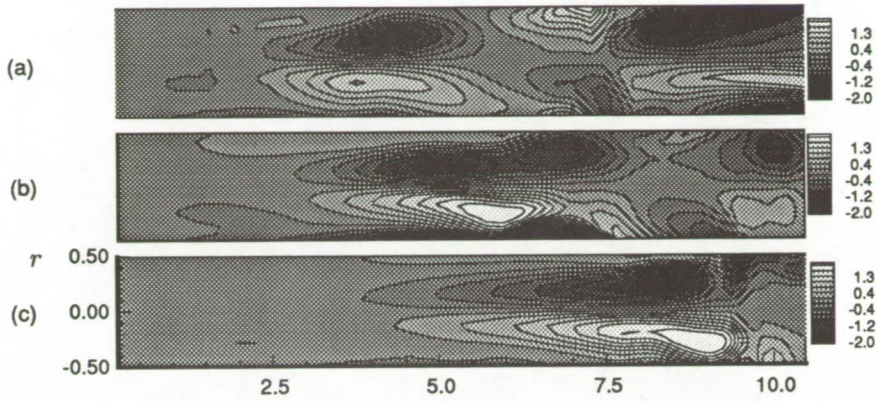


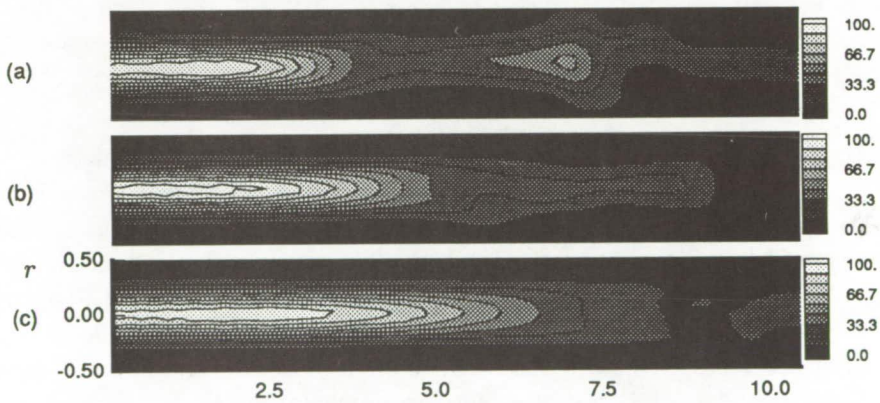
FIGURE 8. Axial velocity in the vortex core region of the streamwise rib vortex at times (a) $t = 22.3$, (b) $t = 25.3$ and (c) $t = 28.5$.

Figure 8 shows contours of axial velocity. It may be seen that deceleration of the axial flow is associated with the topology change. Furthermore, the axial velocity in the region of the topology change is approximately equal to, or perhaps a little greater than, the speed at which the boundary between regions I and II moves downstream, indicating that the boundary is advected downstream by the local velocity.



s

FIGURE 9. Azimuthal vorticity in the vortex core region of the streamwise rib vortex at times (a) $t = 22.3$, (b) $t = 25.3$ and (c) $t = 28.5$.



s

FIGURE 10. Enstrophy in the vortex core region of the streamwise rib vortex at times (a) $t = 22.3$, (b) $t = 25.3$ and (c) $t = 28.5$.

In Figure 9, the distribution of the azimuthal component of vorticity is shown. In region I, for all three times, the azimuthal vorticity is nearly zero. The vorticity vector is almost entirely directed in the axial direction. Just upstream of region II, a negative component of azimuthal vorticity appears. It has a local extremum off the axis. This negative component of azimuthal vorticity off the axis induces a retardation of the axial flow. This scenario is entirely consistent with the early

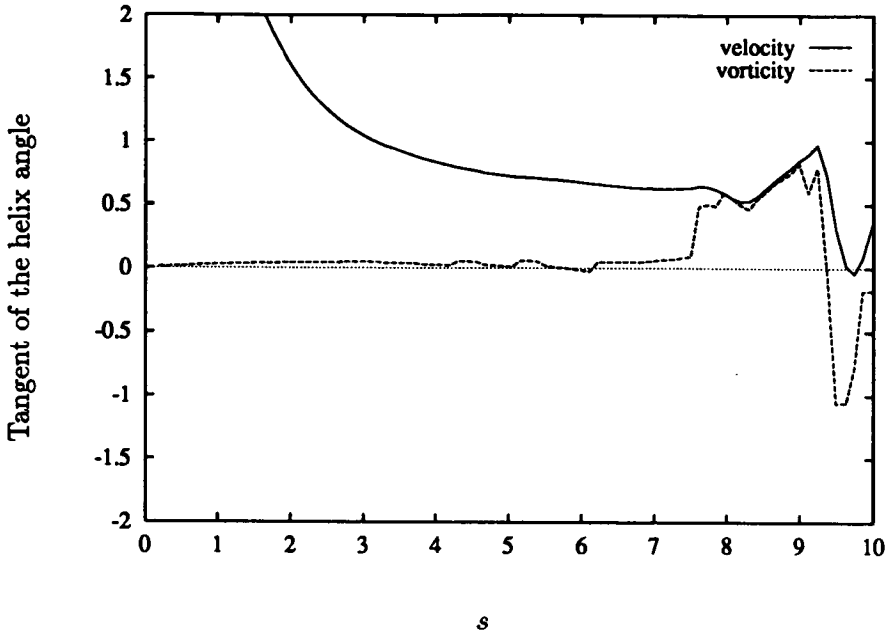


FIGURE 11. Axial distribution of the tangents of the helix angles of velocity and vorticity at the radius of maximum azimuthal velocity at time $t = 28.5$.

stages in the evolution of an axisymmetric vortex beginning to undergo vortex breakdown.

Figure 10 shows contours of enstrophy. The maximum enstrophy is at the center of the vortex and has diminished to about half its maximum value at the topology change. Where the azimuthal vorticity is at its maximum, the enstrophy has decreased to approximately one fifth of its maximum value.

The ratio of the tangents of the helix angles of the velocity and vorticity vectors in region I at the edge of the vortex core is much larger than one (see Figure 11). This indicates that the streamwise rib vortex, which is nearly axisymmetric in region I, has a structure which satisfies a necessary condition for an inviscid, axisymmetric vortex to undergo vortex breakdown. The primarily axially directed vorticity vector is locally turned into the negative azimuthal direction, and the corresponding induced velocity results in a deceleration of the axial flow as detailed in Brown and Lopez (1990). The temporal and spatial developments, particularly of azimuthal vorticity, are similar to those found by Brown and Lopez (1990) for an isolated axisymmetric vortex in the early stages of vortex breakdown. Contours of the azimuthal vorticity from that study are presented in Figure 12. Initially, the azimuthal vorticity close to the axis is positive with little axial variation. The inflow profile is time independent. Slow radial diffusion, due to the finite Reynolds number of this flow, results in a slight broadening of the vortex core and a slight slowing of the axial flow. Off the axis, the initially axially directed vorticity vector has been

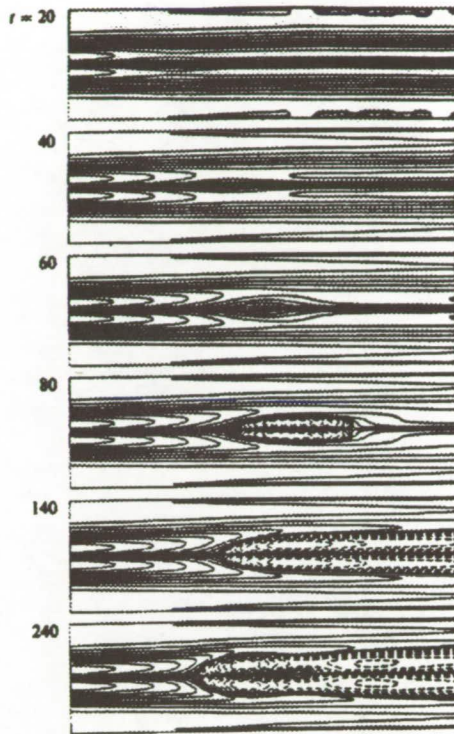


FIGURE 12. Azimuthal vorticity contours for an isolated axisymmetric vortex (reproduced from Brown and Lopez 1990).

turned into the negative azimuthal direction. This is enhanced locally by the non-linear feed-back mechanism detailed in Brown and Lopez (1990). By time $t = 80$, a local concentration of negative azimuthal vorticity has developed. This is advected downstream by the mean axial flow at the same time as it is growing in intensity through the non-linear process. By time $t = 240$, the negative azimuthal vorticity is large enough to induce a reversed axial flow and begins to propagate upstream under its own induced velocity. The major difference between the evolution of the rib vortex and the isolated axisymmetric vortex is the lack of a significant positive azimuthal component of vorticity in the rib vortex. Nevertheless, in both cases, the ratio of helix angles is greater than one, the region of negative azimuthal vorticity initially travels downstream, and there is an associated deceleration of the axial flow, underlining the similarities between the two cases.

5. Vortex-vortex interactions in region III

It is clear from the discussion in the previous section that the rib vortex, at the times considered, is in the early stages of axisymmetric vortex breakdown. However, the most striking aspect of the structural development of the rib vortex is not

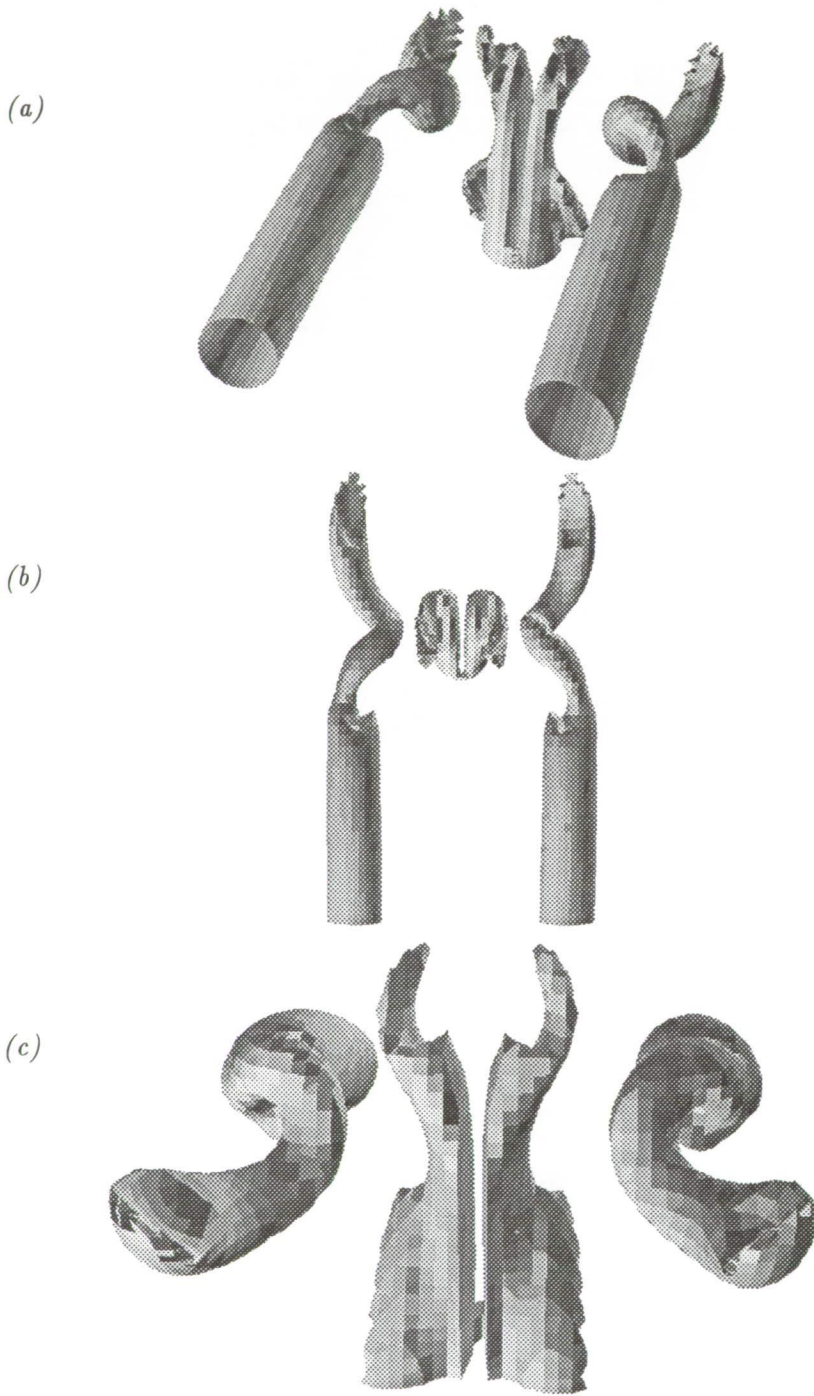


FIGURE 13. Counter rotating streamwise rib vortices visualized by an enstrophy isosurface of level 3.2: (a) perspective view looking downstream, (b) view from top, and (c) view looking upstream.

directly associated with the vortex breakdown process occurring in regions I and II. At the latest time considered, $t = 28.5$, the vortex has developed a very distinctive spiral in region III. Figure 13 gives three views of the structure as visualized by an isosurface of the enstrophy. Shown are a pair of counter rotating rib vortices and some concentrated vortical flow between them.

Due to the spanwise periodicity in the flow, the rib vortices are present as an array of vortices with alternating senses of rotation across the mixing layer. This arrangement results in their drawing vortical fluid from within the spanwise roller region to between the rib vortices, whose induced velocity in the plane between them is directed vertically outward from the spanwise roller region. Bernal and Roshko (1986) have demonstrated this effect visually using spanwise laser-light sheets illuminating fluorescent dye which has been introduced into the flow. The observed mushroom-like structures indicate the locations of the rib vortices.

At time $t = 22.3$, the rib vortex pairs have not yet drawn much vortical fluid out between them. By $t = 25.3$, the vortical flow between the rib vortex pair has begun to collapse into a vortex loop, following the scenario depicted by Corcos (1988). The enstrophy associated with this vortex loop is diffuse and of elliptic cross section. By $t = 28.5$, the vortex loop has been stretched by the induced velocity from the streamwise rib vortex pair. In the neighborhood of the rib pair, the vortex loop has been stretched and intensified into a vortex pair, which is connected by a loop. Three different views of these vortices are given in Figure 14, where vortex lines passing through the center of the vortices have been used as well as an isosurface of enstrophy. These figures clearly show the spiralling of the rib vortex pair. Note that the sense of the spiral is opposite to that of the sense of rotation of the vortex. The spiralling of the rib vortex pair occurs at the axial location closest to the intensified vortex loop, suggesting that the spiralling is due to a vortex-vortex interaction between the rib vortex and a leg of the vortex loop.

The ratio of enstrophy in the rib vortices to that in the spanwise rollers needed for the rib vortices to draw up vortical flow and intensify it by vortex stretching into a counter-rotating pair between a pair of streamwise rib vortices remains to be determined.

6. Conclusions

From this study of the streamwise rib vortices in a three-dimensional plane mixing layer, it is evident that these vortices evolve from an essentially axisymmetric state, well-described as a Burger's vortex. The vorticity vector, initially aligned with the axial direction, is susceptible to being turned into the negative azimuthal direction by the swirling flow. Brown and Lopez (1990) have shown that this inviscid process is possible when the tangent of the helix angle of the velocity vector is larger than that of the vorticity vector, as is the case for the rib vortices investigated. This structure is typical of the rib vortex downstream of the mid-braid plane and upstream of the topology change. Evidence has been found that it begins to undergo vortex breakdown. This is indicated by the change in the local topology, the development of a negative azimuthal component of vorticity, a deceleration of

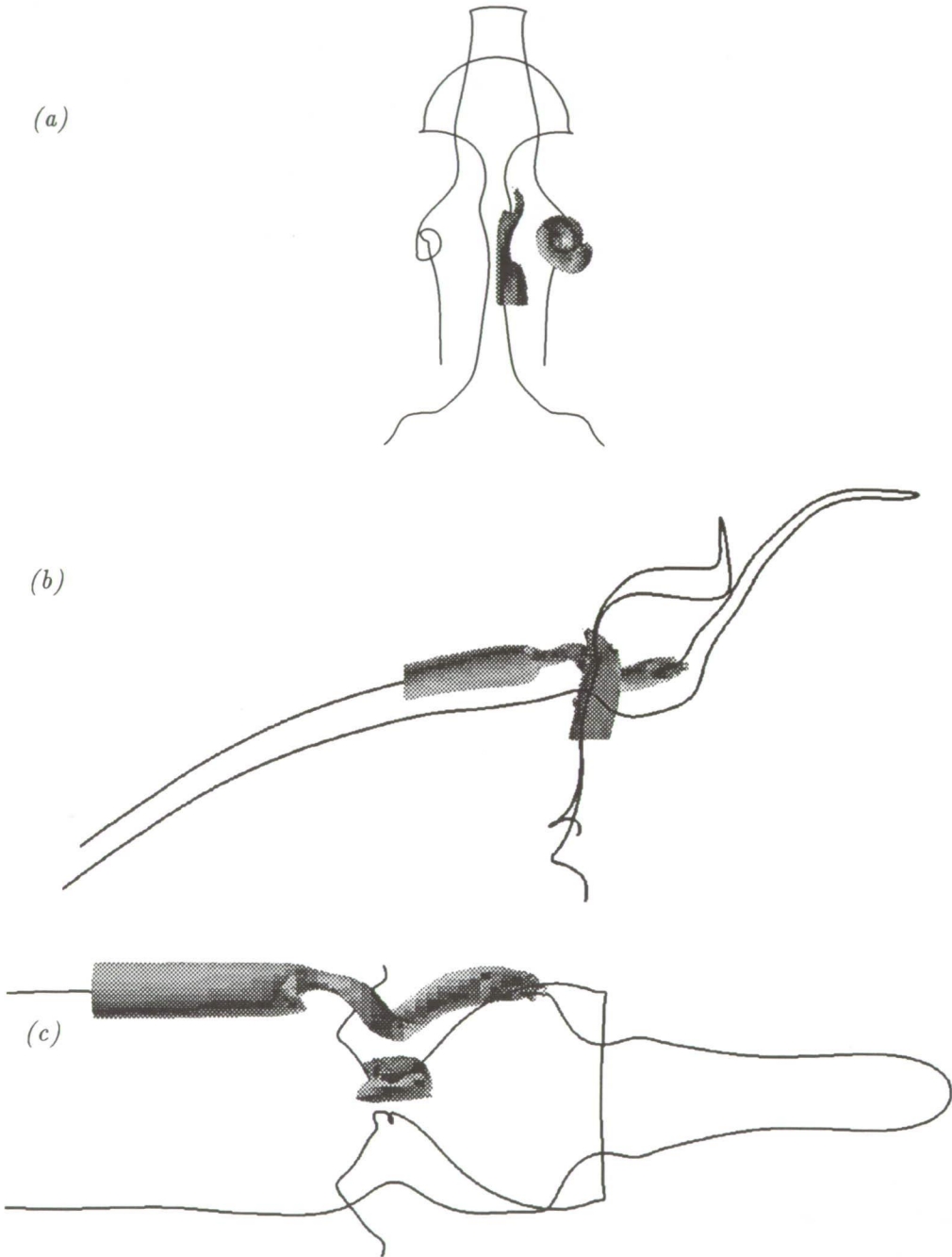


FIGURE 14. Counter rotating streamwise rib vortex pair and intensified vortex loop visualized by an enstrophy isosurface of level 3.2 and vortex lines: (a) view looking upstream, (b) spanwise view, and (c) top view.

the axial flow along the vortex axis, and a departure from axial symmetry downstream of the topology change. This provides a natural division of the structure of the rib vortex into two distinct regions on the vortex axis: where the topology is stable focus/stretching and where it is unstable focus/contracting. At the later times considered, there is a third structurally distinct region downstream of the two described above. In this region, the spiralling of the vortex core is due to a vortex-vortex interaction between the streamwise rib vortex and the vortical flow in the main spanwise roller region which has been drawn up and stretched by two counter-rotating adjacent rib vortices.

Although vortex breakdown is beginning to take place at the times considered, it does not appear to be having much effect on the rest of the flow. There is no sudden core expansion, recirculation zone, or intense mixing, phenomena normally associated with large-scale vortex breakdown flows. Certainly the vortex-vortex interaction dominates the flowfield in region III. However, vortex breakdown in small-scale flows may play a role in defining a length scale for vortical structures. In the rib vortex, the region in which the enstrophy is largest compared with the mean flow is bounded by the topology change, a change which can be attributed to vortex breakdown in the rib vortex. In small scale flows, viscous dissipation and interactions with other similar structures have previously been regarded as the two mechanisms whereby a finite length is imposed on a vortex. Vortex breakdown, essentially an inviscid phenomenon, should be considered the third.

It would be interesting to follow the evolution of this flow further in time to determine whether the vortex breakdown develops further into a well defined recirculation zone or if a further pairing of the main rollers occurs before this eventuates.

Acknowledgements

We would like to thank Mike Rogers, Bob Moser, Julio Soria, Brian Cantwell and Rolf Sondergaard for discussions during the 1992 CTR Summer Program and Bruce Fairlie for his comments.

REFERENCES

- BERNAL, L. P. & ROSHKO, A. 1986 Streamwise vortex structure in plane mixing layers. *J. Fluid Mech.* **170**, 499-525.
- BROWN, G. L. & LOPEZ, J. M. 1990 Axisymmetric vortex breakdown. Part 2. Physical Mechanisms. *J. Fluid Mech.* **221**, 553-576.
- CHEN, J. H., CHONG, M. S., SORIA, J., SONDERGAARD, R., PERRY, A. E., ROGERS, M., MOSER, R. & CANTWELL, B. J. 1990 A study of the topology of dissipating motions in direct numerical simulations of time-developing compressible and incompressible mixing layers. *Proceedings of the Center for Turbulence Research Summer Program 1990*. Stanford Univ./NASA Ames.
- CHONG, M. S., PERRY, A. E. & CANTWELL, B. J. 1990 A general classification of three-dimensional flow fields. *Phys. Fluids A*, **2**, 765-777.

- CORCOS, G. M. 1988 The role of cartoons in turbulence. In *Perspectives in Fluid Mechanics* (ed. D. E. Coles) Lecture Notes in Physics, vol. 320, pp. 48-65. (Springer).
- DRESSELHAUS, E. & TABOR, M. 1991 The kinematics of stretching and alignment of material elements in general flow fields. *J. Fluid Mech.* **236**, 415-444.
- JIMÉNEZ, J. 1992 Kinematic alignment effects in turbulent flows. *Phys. Fluids A*. **4**, 652-654.
- KELSO, R. 1992 PhD Thesis, University of Melbourne, Australia.
- MOSER, R. & ROGERS, M. 1992 The three-dimensional evolution of a plane mixing layer: pairing and transition to turbulence. *J. Fluid Mech.*, submitted for publication.
- ORSZAG, S. A. 1991 Otto Laporte lecture, 44th meeting APSDFD, Scottsdale AZ.
- PERRY, A. E. & FAIRLIE, B. D. 1974 Critical points in flow patterns. *Adv. Geophys.* **18**, 299-315.
- SHE, Z.-S., JACKSON, E. & ORSZAG, S. A. 1990 Intermittent vortex structures in homogeneous isotropic turbulence. *Nature*. **344**, 226-228.
- YATES, L. A. & CHAPMAN, G. T. 1992 Streamlines, vorticity lines, and vortices around three-dimensional bodies. *AIAA Journal*. **30**, 1819-1826.

445353 510-34

189670 165
N94-140755

Direct simulation of polymer drag reduction in free shear flows and vortex dipoles

By P. Orlandi¹ G.M. Homsy² and J. Azaiez²

One of the most efficient techniques for drag reduction is the injection of polymers near a wall which can achieve a reduction in drag up to 80%. Several experimental observations tend to indicate that polymers modify the turbulence structures within the buffer layer and show that the changes consist of a weakening of the strength of the streamwise vortices. In this paper, we investigate the effects of viscoelasticity on two different types of flows: the vortex dipole impinging walls to model streamwise vortices in a turbulent boundary layer and the mixing layer that represents free shear flows. For this purpose, we examined three different rheological models: the Oldroyd-B model, the Jeffrey's corotational model, and the FENE-P model.

1 Introduction

Evidence of drag reduction both by passive and active control has been observed experimentally, but a clear explanation of the mechanisms responsible for this reduction has not been given, mainly because the experimental observations cannot describe all the details of the flow. In the literature, there is a large number of papers devoted to the experimental study of the wall layer structures in drag reducing flows. This literature is summarized in the review article of Tiederman (1989). The main conclusion that we can draw from these papers is that drag reduction is due to modifications of the wall layer structures, particularly in the buffer region, the most active region in wall bounded flows. From flow visualizations, Oldaker and Tiederman (1977) concluded that the polymer solution inhibits the formation of low speed streaks and that, when these are formed, their spacing in wall coordinates increases with polymer concentration.

In the last decade, direct simulations of wall bounded flows have been a very useful tool for a deeper understanding of turbulence structures and their role in wall friction. Free shear flows of viscoelastic fluids on the other hand, have not received as much attention as bounded flows did, and to our knowledge, only few and inconclusive experiments have been conducted.

Due to the lack of a universal constitutive equation that describes most common viscoelastic behaviors, numerical studies of non-Newtonian fluids have been limited to special types of polymeric solutions in simple flows. In spite of these limitations, many results showing important effects of viscoelasticity for different types of flows have been reported (Tiederman(1989)). In a previous paper (Orlandi 1991), a

1 Università di Roma, "La Sapienza"

2 Stanford University

heuristic relation between the polymer stresses and the flow properties in a channel flow was used to investigate how the flow structures change in a situation where drag reduction was achieved. The model was not tensorial invariant and was not related to the molecular structure of the polymers.

In this paper, we wish to initiate a systematic study of the effects of polymers on the flow structures using rheological models based on transport equations for the stresses of the polymers. In particular, we studied the case of vortex dipole in the presence of walls. A vortex dipole models the streamwise vortices in the buffer region of a turbulent channel, which are responsible for turbulence production and turbulent drag. This was shown numerically in a quasi two-dimensional simulation by Orlandi and Jimenez (1991). We have also examined the case of the roll-up of a two-dimensional mixing layer. Our interest in the mixing layer problem was motivated by the results of linear stability analysis reported by Azaiez and Homsy (1992). This analysis shows that, in a special limit of the elasticity number, viscoelasticity reduces the instability of the flow.

We considered three viscoelastic models: the Jeffrey's corotational model, the Oldroyd-B model, and the FENE-P model which describes the rheological properties of dilute polymeric solutions. The flows governed by these rheological models are characterized by three dimensionless numbers: The Reynolds number, Re , the Weissenberg number, We , a dimensionless measure of the elasticity of the fluid and the coefficient $K = \frac{\eta_S}{\eta_S + \eta_P}$, a ratio of the solvent viscosity η_S and the polymeric contribution to the shear viscosity, η_P . In the case of the FENE-P model, a third parameter, b , related to the nature of the spring used to model the macromolecule, is introduced.

The first interesting physical aspect that comes out of the study of these three models is that the formation of small scales is enhanced and that these small scales are rapidly dissipated. This unexpected phenomenon needs an experimental confirmation, and we hope that in the near future two-dimensional experiments will be performed in order to both understand in details the behavior of dilute polymeric solutions and validate the results of our two-dimensional viscoelastic simulations.

While for the mixing layer we obtained results in a quite large range of the Weissenberg number, only results at small Weissenberg numbers could be obtained for dipoles impinging walls because of the special flow topology: with the FENE-P model, the polymeric stresses reached very large values at the stagnation point, and the calculations were diverging for We of order 1. At smaller values of We , the calculations did not differ from the Newtonian case because the flow stresses were able to overcome any possible polymeric effect.

2 Physical and numerical model

We used a vorticity-streamfunction formulation for the Cauchy's momentum equation. This equation is closed through evolution equations relating the stress tensor to the shear rate tensor. In all the subsequent analysis, the stress tensor is written as the sum of two stresses.

$$\tau_{ij} = \eta(K\dot{\gamma}_{ij} + (1 - K)a_{ij}) \quad (1)$$

We fixed $K = 0.5$.

The first term in Eq.(1) reflects the contribution of the Newtonian solvent and is proportional to the shear rate tensor $\dot{\gamma}$, the second one represents the polymeric contribution and is proportional to the tensor a . The tensor a satisfies different evolution equations corresponding to the various rheological models we are examining.

Eq.(1) leads to the following vorticity equation

$$\frac{\partial \omega}{\partial t} = -J(\omega, \psi) + \frac{k}{Re} \nabla \omega + \frac{1-k}{Re} \left(\frac{\partial a_{12}}{\partial x_1^2} - \frac{\partial a_{12}}{\partial x_2^2} - \frac{\partial a_{11} - a_{22}}{\partial x_1 \partial x_2} \right) \quad (2)$$

where the nonlinear terms have been expressed as a Jacobian. The streamfunction is evaluated from the Poisson's equation $\nabla^2 \psi = -\omega$.

In the case of the mixing layer, we imposed periodic conditions in the streamwise direction. In the transverse direction, free slip conditions are imposed in the finite difference code while periodic conditions are imposed for the spectral code. In the case of the spectral code, the domain was made large enough in the transverse direction to ensure that all functions go to zero at the periphery of the domain. Non-slip conditions are imposed at the wall for the vortex dipole.

The stresses are governed by a set of partial differential equations which constitute the rheological model. We have considered several models: the first one is the Jeffrey's corotational model which is obtained by formulating the equations of state in a frame translating with the fluid and rotating with the local angular velocity of the fluid. The equation describing this model is:

$$a_{ij} + We \frac{\tilde{D}a_{ij}}{\tilde{D}t} = \dot{\gamma}_{ij} \quad (3)$$

where $We = \frac{U\lambda}{\delta}$ is the Weissenberg number.

$$\frac{\tilde{D}a_{ij}}{\tilde{D}t} = \frac{Da_{ij}}{Dt} + \omega_{ik}a_{kj} + \omega_{jk}a_{ik} \quad (4)$$

is the Jaumann derivative.

The rheological equation for the Oldroyd-B model is:

$$a_{ij} + We \frac{\delta a_{ij}}{\delta t} = \dot{\gamma}_{ij} \quad (5)$$

The upper convective derivative $\frac{\delta a_{ij}}{\delta t}$ is related to the Jaumann derivative through the relation:

$$\frac{\delta a_{ij}}{\delta t} = \frac{\tilde{D}a_{ij}}{\tilde{D}t} + \frac{1}{2}(a_{ik}\dot{\gamma}_{kj} + \dot{\gamma}_{ik}a_{kj}) \quad (6)$$

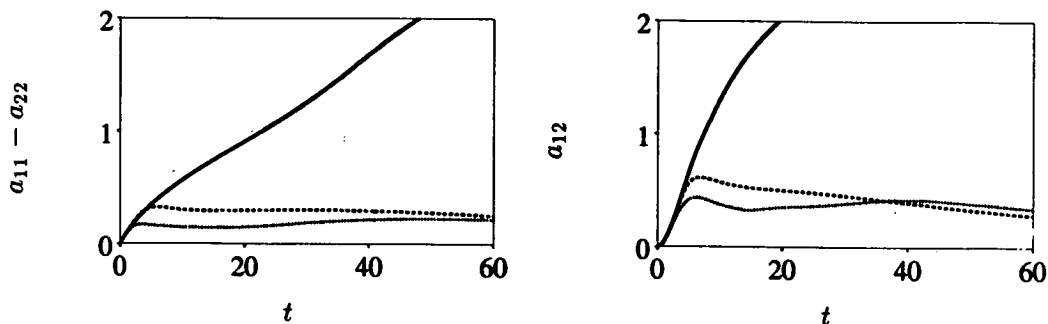


FIGURE 1. Time evolution of the polymeric stresses at $We = 5$. — Oldroyd; ... Jeffreys; ---- FENE-P

To the contrary of what is observed for the Jeffrey's model, the Oldroyd-B model has a very large dependence on the Weissenberg number as will be discussed in the next paragraph. We found that at certain values of We , the stresses grow indefinitely in time and the growth rate is flow dependent.

The Oldroyd-B model gives a steady state elongational viscosity that goes to infinity at a finite elongational rate. This unlikely behavior results because the Hookean dumbbell model permits infinite extension. In order to avoid this unrealistic behavior, a Warner law is used instead of the Hook law leading to the FENE-P model. This model is described by Mackay and Petrie (1989) and the rheological equation is:

$$a_{ij}Z + We \frac{\delta a_{ij}}{\delta t} = \dot{\gamma}_{ij} + \frac{D \ln Z}{Dt} (\mathbf{I} + a_{ij} We) \quad (7)$$

where $Z = 1 + \frac{n}{b} (1 + \frac{We}{n} a_{ii})$, $n = 2$ for a two dimensional flow. In order to facilitate the numerical solution of Eq.(7), $\frac{D \ln Z}{Dt}$ was derived from the transport equation for a_{ii} .

The set of governing equations have been discretized by a finite difference scheme second order accurate in space and in time. The main characteristics of the numerical method is that it discretizes $J(\omega, \psi)$ by the Arakawa scheme which conserves energy, enstrophy, and skew symmetry in the inviscid limit. The polymer contribution to the stresses have been located at different grid positions with a_{11} and a_{22} at the center of the cell and a_{12} at the same location of ω and ψ . This choice allows a very compact formulation of the right hand side of Eq. (2) and leads to the solution without imposing boundary conditions for a_{11} and a_{22} . On the other hand, a_{12} has been taken equal to zero both on free-slip and no-slip walls. The stream function has been solved directly by using the Fourier transform in the periodic direction. Numerical simulations have been performed on the CRAY YMP84 at NASA Ames and the CPU required for 1000 time steps on a 128×128 grid was 150 seconds.

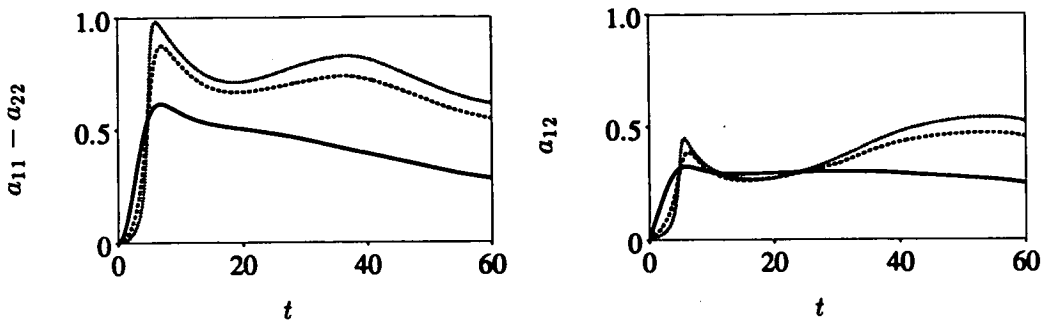


FIGURE 2. Time evolution of the polymeric stresses at $b = 5$. — $We = 5$; ---- $We = 20$; ... $We = 50$

3 Results

1 Mixing layer

The mixing layer simulations have been performed in order to study the effects of viscoelasticity on the vorticity field. Numerical simulation using a pseudospectral method were performed in order to compare with the finite difference results. The good comparison between finite difference and pseudospectral simulations will be presented elsewhere.

The initial base state is given by a hyperbolic tangent velocity profile on which we superposed a \cos perturbation on the stream function with the maximum at the centerline $y = 0$. The most unstable wave number, $\alpha = 0.44$, has been used in all the simulations. The extension of the domain in the streamwise direction is set to $\frac{2\pi}{\alpha}\delta$ with δ the momentum thickness of the mixing layer. The vertical extension has been heuristically fixed equal to 8δ . The Reynolds number is defined as $Re = \frac{\delta u_0}{\nu}$ where $u_0 = (U_1 - U_2)/2$. U_1 and U_2 are the free-stream velocities.

The growth of the maximum value of $(a_{11} - a_{22})$ and of a_{12} obtained for the three viscoelastic models are shown in Fig. 1. At $We = 5$, the stresses are smaller for the Jeffrey's corotational model than for the other two models; as a consequence, the vorticity field does not differ appreciably from the Newtonian case. In the case of the Oldroyd-B model, the stresses grew rapidly due to the unrealistic characteristic of this model that allows the macromolecules to extend infinitely.

We suspected that the divergence of the codes for the Oldroyd-B model at high We to result from some numerical instability. By refining the mesh and varying the time step for both the finite difference and the pseudospectral codes, we found that, at the same values of We , the solution was always diverging at the same point in time. We have shown that the divergence was caused by the change of sign of the eigenvalues of the system of nonlinear equations. The change of sign occurred at certain values of We , and this value is flow dependent.

In the case of the FENE-P model, the dependence of the flow on the Weissenberg number and on the parameter b has been studied by performing different simulations

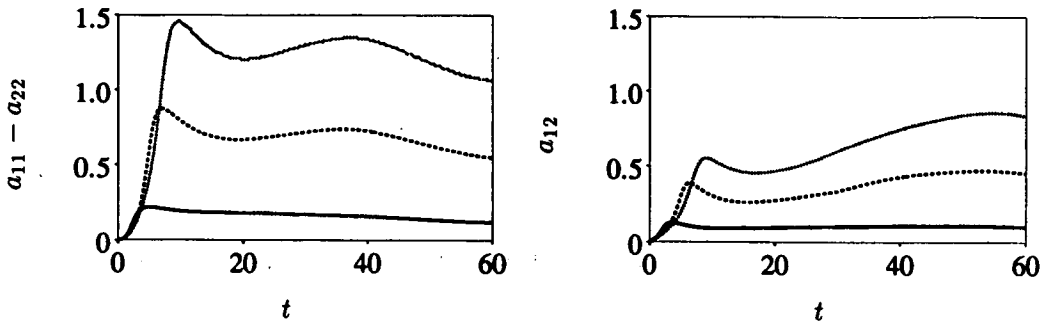


FIGURE 3. Time evolution of the polymeric stresses at $We = 20$. — $b = 1$; ---- $b = 5$; ... $b = 10$

for the mixing layer at $Re = 100$. Fig. 2 shows how the polymeric contribution to the stresses depend on We at $b = 5$. The simulations at $We = 5$ and $We = 20$ were performed on a 128×128 grid. With this grid, at $We = 50$, the high values of the stresses produced wiggles in the vorticity field at $t \approx 40$; these wiggles partially persisted with a grid twice finer and disappeared with a 384×384 grid. Fig. 2 also shows that the effect of the Weissenberg number on a_{12} are large at later times and that large variations of the maximum value of $(a_{11} - a_{22})$ occur at low rather than at high We values. Fig. 2 shows also that by increasing the Weissenberg number from $We = 20$ to $We = 50$, the variations are less important than those obtained by taking the We from 1 to 20.

Fig. 3 shows the dependence on the parameter b . We notice that the maxima are more dependent on b than on We and that the maximum values are higher than those observed in Fig. 2. This behavior is consistent with the fact that for very large values of b the Oldroyd-B model is recovered.

A clear picture of the evolution of the flow is obtained from the analysis of the vorticity and of the stress field. Vorticity contour plots at three different times and for three different We values are presented in Fig. 4. We remark that at low We , the flow does not differ from the Newtonian case while at higher We , more noticeable changes appear in the structure of the mixing layer. Very interesting is the occurrence of intense gradients in the braids. These gradients are convected in the roll-up region and persist for a longer time, producing a faster and more intense roll-up as shown at $We = 50$.

$a_{11} - a_{22}$ is the other quantity contributing to the modification of the vorticity field and can be measured experimentally. Fig. 5 shows a large increase of its maximum value when We goes from $We = 1$ to $We = 20$. On the other hand, when the Weissenberg number increases from $We = 20$ to $We = 50$, the value does not change significantly, then we can expect minor changes in the vorticity field. From Fig. 4 and Fig. 5 we can draw a first conclusion that the effect of the Weissenberg number is to concentrate the modifications by polymers at small scales. From contour plots of vorticity and $a_{11} - a_{22}$, not reported in this paper, we have observed that by increasing b , high peak values are produced and are localized in

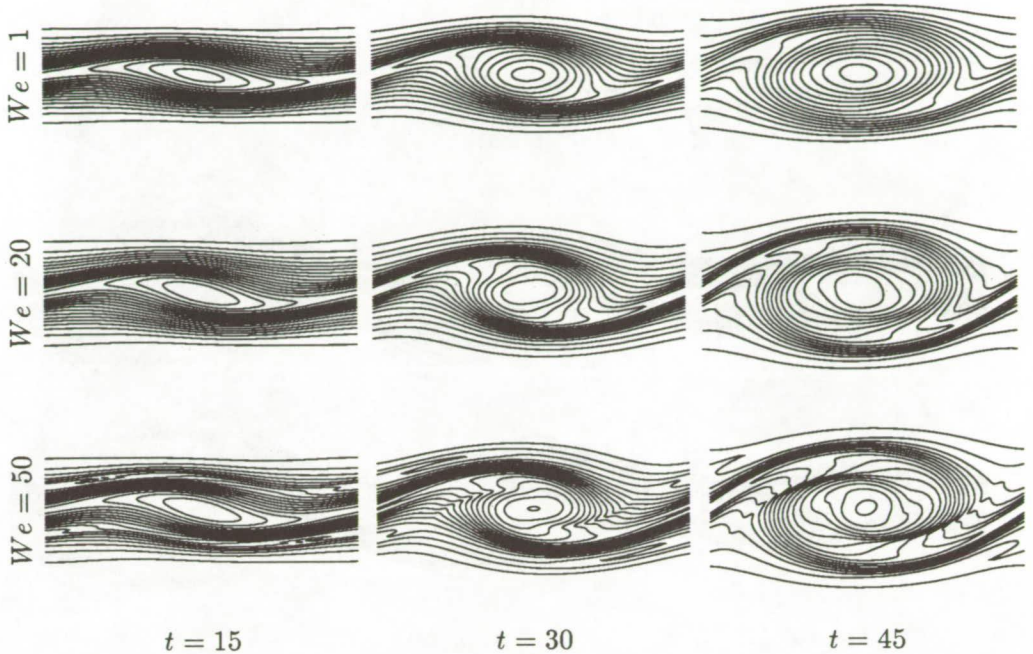


FIGURE 4. Vorticity contour plots. $b=5$.

wider regions, and thus weaker effects on the mixing layer roll-up are observed.

At this stage of the work and without having any experimental observations with which to compare our results, we do not wish to go into a deeper analysis of the flow to understand the mechanisms responsible for this rapid transfer of energy from the large scales to the smaller scales. We think that the results we obtained will be of more interest if they can be checked through experimental studies. The comparison between numerical and experimental predictions will help in understanding the physics behind the effects of viscoelasticity on the structure of the flow.

2 Vortex dipole impinging walls

This two-dimensional flow has been considered because it represents the stream-wise vortices in a turbulent boundary layer, which are responsible of turbulent drag and turbulence production. In the present two-dimensional simulation, we have introduced a Lamb dipole rather than a single vortical structure because the dipole moves towards the wall by self-induction while a single vortex must be advected towards the wall by an external field. As a first case, we have considered the interaction with a free-slip wall to investigate the distributions of the polymeric contribution to the stresses generated at the moment of the impact. We expect that, at the stagnation point, a large increase of the polymeric stresses is obtained since this is a point where strong elongations of the polymers molecule occur. This large increase of the polymers stresses is the cause of the difficulty to perform simulations at high Weissenberg numbers.

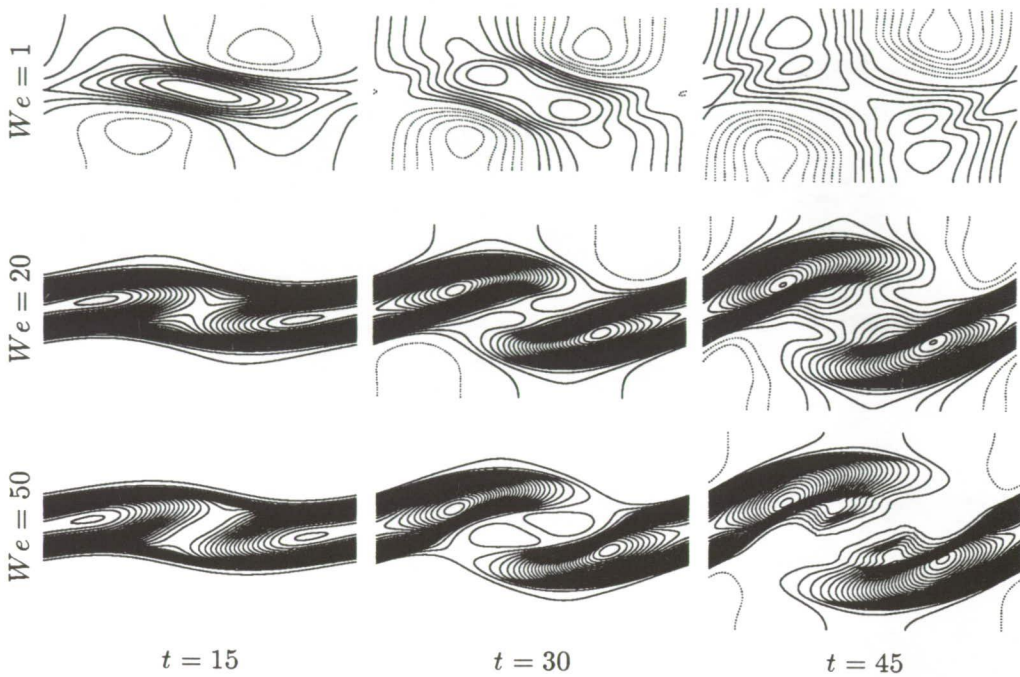


FIGURE 5. $a_{11} - a_{22}$ contour plots. $b=5$.

The simulations were performed on a 192×192 grid points in a domain extending in the horizontal and in the vertical directions 4 dipoles radii. Solutions with the FENE-P model were obtained only for $We \leq 3$ and $b \leq 1$ at $Re = \frac{U_d a}{\nu} = 50$ (U_d is the translation velocity of the dipole, a is the dipole radius). The simulations were performed both with free-slip and no-slip walls. In the case of the dipole impinging a free-slip wall, the vorticity field, at the moment of the impact, is shown in Fig. 6. Similarly to what has been observed in the mixing layer, this figure shows that $a_{11} - a_{22}$ increases more than a_{12} ; the maximum values are reached in the region of maximum normal stress and low vorticity. Although large polymeric stresses are obtained, the dipole does not change their shape appreciably, and this could be a consequence of the fact that dipolar structures are very stable to large perturbations.

When the dipole impinges a non-slip wall, Fig. 7 shows that the vorticity field does not depend strongly on the Weissenberg number. There is, however, a slight decrease of the magnitude of the vorticity level as compared to the Newtonian case, but this decrease is not sufficient to change the type of vortex rebound. We did not perform a systematic study of the We effects.

4 Conclusion

This preliminary study testing different viscoelastic models allowed us to predict the effects of the introduction of polymers on the flow structure. By comparing

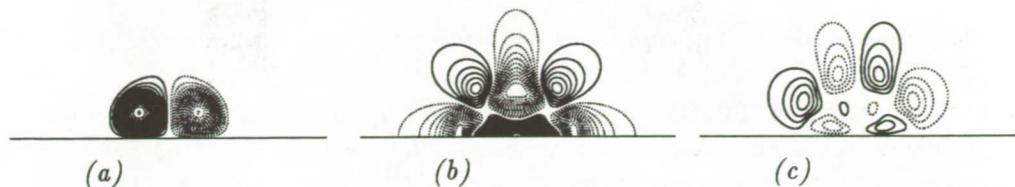


FIGURE 6. Contour plots of (a) vorticity, (b) $a_{11} - a_{22}$ and (c) a_{12} for dipole impinging a free-slip wall at $Re = 50$, $We = 2$ and $b = .4$.

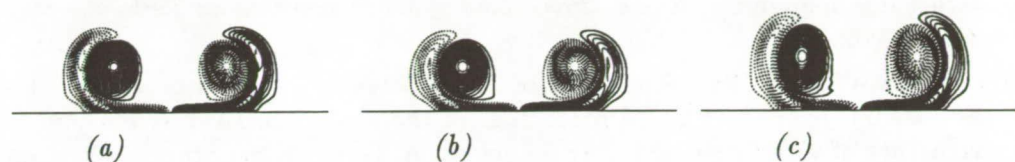


FIGURE 7. Vorticity Contour plots (a) newtonian, (b) $We = .5, b = 1$. and (c) $We = 3, b = 1$. for dipole impinging a non-slip wall at $Re = 50$.

the solutions obtained by the finite difference scheme and those obtained by a pseudospectral method, we have shown that the solutions did not diverge in time for numerical reasons. Two-dimensional simulations revealed that the cause of the exponential growth in the Oldroyd-B model at certain We is caused by a change in the sign of the eigenvalues of the a_{11} stress equation.

Using the FENE-P model, we were able to conduct numerical simulations at reasonably high Weissenberg numbers. In the case of the mixing layer, we noticed some changes in the structures of the roll-up. This is an interesting phenomenon since, in a space developing mixing layer just after the splitter plate, the initial instability could influence the growth of the mixing layer. The present simulations show the large potential in using polymers for the control and possibly the modification of the structures of the mixing layer. We hope to pursue this study by examining the effects of polymers on vortex stretching and streamwise vortices in the mixing layer. In the case of the vortex dipole, the changes on the vorticity field are negligible.

We believe that the results reported in this study should be pursued by more detailed simulations and by experimental studies that will help in understanding the mechanisms responsible for the changes observed in the case of the mixing layer with the FENE-P model. We hope that the present study will stimulate more interest in non-Newtonian flows among both theoreticians and experimentalists.

REFERENCES

- AZAIÉZ J., & HOMSY G. M. 1992 Linear stability of free shear flows of viscoelastic liquids. Submitted to *J. Fluid Mech.*
- LUMLEY J. L. 1971 Applicability of the Oldroyd constitutive equations to flow of dilute polymer solutions. *Phys. of Fluids*. **14**, 2282-2284
- MACKAY, M. E. & PETRIE, S. J. 1989 Estimates of apparent elongational viscosity using the fibre spinning and pure methods calculations for a FENE-P

- dumbbell model and comparisons with published data. *Rheological Acta.* **28**, 281-293
- OLDAKER, D. K. & TIEDERMAN W. G. 1977 Spatial structures of the viscous sublayer in a drag-reducing channel flows. *Phys. Fluids.* **20**, S133-S144
- ORLANDI, P. 1991 A tentative approach to the direct simulation of drag reduction by polymers. *Bulletin of the American Physical Society.* **36**(10), 2709
- ORLANDI, P. & JIMENEZ, J. 1991 A model for bursting of near wall vortical structures in boundary layers. *Proceeding of 8th Symposium on Turbulent Shear Flows*, Munchen.
- TIEDERMAN W. G. 1989 The effect of dilute polymer solutions on viscous drag and turbulence structure. Proceedings of the second IUTAM symposium on structure of turbulence and drag reduction. A. Gyr (editor) Springer-Verlag.

445354
ORIGINAL CONTAINS 511-34
COLOR ILLUSTRATION 789671
175
N94-14756

Estimation of the vortex length scale and intensity from two-dimensional samples

By D. L. Reuss¹ AND W. P. Cheng,²

A method is proposed for estimating flow features that influence flame wrinkling in reciprocating internal combustion engines, where traditional statistical measures of turbulence are suspect. Candidate methods were tested in a computed channel flow where traditional turbulence measures are valid and performance can be rationally evaluated.

Two concepts are tested. First, spatial filtering is applied to the two-dimensional velocity distribution and found to reveal structures corresponding to the vorticity field. Decreasing the spatial-frequency cutoff of the filter locally changes the character and size of the flow structures that are revealed by the filter. Second, vortex length scale and intensity is estimated by computing the ensemble-average velocity distribution conditionally sampled on the vorticity peaks. The resulting conditionally sampled "average vortex" has a peak velocity less than half the rms velocity and a size approximately equal to the two-point-correlation integral-length scale.

1. Introduction

The existence of turbulence is central to the operation of reciprocating internal-combustion (RIC) engines. In particular, turbulence controls the burning rates (and thus the efficiency and engine speed range) in homogeneous charge engines by controlling flame wrinkling and in stratified charge engines by controlling mixing rates. However, considerable controversy exists concerning the definition and measurement of the turbulence properties in RIC engines. The purpose of this work is to explore new ways of estimating the turbulence properties that affect flame wrinkling in a way that will overcome the problems of defining turbulence.

1.1 Turbulent flow in RIC engines

The flow field in the engine cylinder is first formed during the intake stroke as the air enters the engine cylinder through the annular gap between the inlet volume and the cylinder head. The flow is driven by the piston moving from top to bottom dead center. This forms very large scale motions (on the order of the cylinder diameter) often referred to as the "mean" flow. A strong swirling flow (similar to a single tornado filling the cylinder) is an example of the simplest mean flow that can be formed. The flow is then compressed as the piston moves up. Measurements and computations both suggest that the turbulent kinetic energy generated by the valve jets has largely decayed by top dead center, TDC. The turbulent kinetic energy that

1 General Motors Research & Environmental Staff, Warren, MI

remains near TDC (when combustion begins) is generated mostly by the breakdown of the large-scale mean-flow structures. As the engine cycle continues, the flow is further distorted during combustion by the expansion of hot product gases and by the piston motion during the expansion stroke. Finally, the burnt gases are expelled through the exhaust valve by the piston motion during the exhaust stroke.

The problem in defining RIC engine turbulence is rooted in what will be referred to here as "traditional turbulence theory", in particular, the traditional Eulerian point of view where the turbulent velocity, $u(t)$, is measured at a fixed point as a function of time. The Reynolds decomposition is invoked,

$$u = \bar{u} + u', \quad (1)$$

where \bar{u} is the steady (or at least slowly varying) mean and u' is the fluctuating component. For the Reynolds decomposition to be valid, it is implicit that the temporal (and spatial) variations in \bar{u} occur over times (and distances) that are large compared to those associated with variations in u' . Further, the traditional flow is statistically stationary so that temporal averaging can be performed where local homogeneity exists and spatial averaging can be performed where directional homogeneity exists.

Extending these traditional concepts to RIC engines is difficult at best (Arcoumanis & Whitelaw 1987, le Coz 1992, Fansler & French 1988, Fransler 1993, Fraser & Bracco 1988, Glover 1986, Rask 1981 & 1984). The velocity distribution of the largest structures associated with the "mean flow" is not steady, and the structures' spatial scales change due to dissipation and volume changes forced by the piston. Thus, simple temporal averaging cannot be used. Instead, the Eulerian velocity is conditionally sampled at each crank-angle during the engine cycle (eg. at each 720 degrees of a four-stroke-cycle engine or 360 degrees in a two-stroke-cycle engine) and ensemble averaged over many cycles. The fluctuations about this mean that would traditionally be viewed as turbulence are not statistically stationary during the cycle, and there is no clear separation of the spatial and temporal scales of the ensemble mean velocity and turbulence. There is no local or directional homogeneity for temporal or spatial averaging.

Further complicating the interpretation of RIC engine turbulence is the fact that cyclic variability in the mean flow contributes to measured fluctuations about the ensemble-mean velocity. Consider the swirling flow example above, but with no small scale random fluctuations normally associated with turbulence (ie. a laminar tornado). Let the center of the swirl (the point of zero velocity) randomly precess about the geometric center of the engine cylinder. Here the cyclic variability would be the phase variation in the position of the swirl center from cycle to cycle. That is, a fixed velocity probe might be precisely at the swirl center at a specific crank angle during one cycle and thus measure zero velocity, yet be near but outside the swirl center at the same crank angle during the next cycle and thus measure some finite velocity. By ensemble averaging many cycles at the same position and crank angle, a fluctuating velocity component is measured about the ensemble mean velocity. Whereas cyclic variability of the swirling flow would be expected to convect the flame

to different positions on different cycles, it would not contribute to flame wrinkling to control the burning rate as turbulence does. Further, this fluctuating velocity does not correspond to the traditional concepts of fluctuations that contribute to the dissipation of turbulent kinetic energy. In reality, the flow actually does contain small-scale random turbulent structures and thus the measured velocity fluctuation in eqn. 1, u' , is a sum of both the cyclic variability and the turbulence fluctuation. Consequently, estimates of the turbulence intensity, and thus kinetic energy, using u' will be overestimated, and turbulence length-scale estimates using two-point correlations will be incorrect.

In an attempt to separate the cyclic variability of the mean flow from the turbulence (Fansler & French 1988, Fraser & Bracco 1988), the instantaneous velocity has been separated as follows,

$$u = \langle u \rangle + u' \quad (2)$$

$$= \langle u \rangle + \tilde{u} + u'' \quad (3)$$

$$u = \langle U \rangle + u'' \quad (4)$$

where $\langle u \rangle$ is the ensemble mean, u' is the fluctuation about $\langle u \rangle$, \tilde{u} is the cyclic fluctuation, u'' is the turbulence fluctuation, and $\langle U \rangle$ is the cycle resolved mean. In practice, \tilde{u} and u'' are the low- and high-pass filtered components of u' , respectively, where an engine-speed-dependent cutoff frequency between 100 and 500 Hz is typically assigned (Rask 1981 & 1984).

The content of the cyclic fluctuations and turbulence fluctuations is dependent on this cutoff frequency and is technically incorrect if, as expected, the energy spectra (temporal and spatial scales) of \tilde{u} and u'' overlap.

In summary, the problem defining turbulence in RIC engines is that it has an unsteady mean with cycle-to-cycle variability, the temporal and spatial scales of the mean flow and turbulence fluctuations overlap, and in general the flow is inhomogeneous and anisotropic in all directions. Although velocity measurements have been used to illustrate the problem, the question of separating cyclic variability from turbulence is equally important in CFD modeling of in-cylinder combustion since single time- and length-scale models (usually $k - \epsilon$ model) are currently used in practical engineering calculations.

1.2 A nontraditional approach

The previous discussion has centered on temporal measurements made at a single position in space, as this has been the only measure available in RIC engines using either hot-wire or laser Doppler anemometry. However, it is now possible to measure two-dimensional velocities over an extended region at one instant in time using particle image velocimetry, PIV (Reuss, *et al.* 1989, and Reuss, *et al.* 1990). Two-dimensional spatial filtering techniques have been applied to this data to reveal velocity structures on the order of the turbulent integral-length scale that were not apparent in the instantaneous data. Further, vorticity and strain-rate distributions computed from the measured instantaneous-velocity gradients (not filtered) show a strong correspondence to the velocity structures revealed by spatial filtering. These

results stimulated the notion that spatial filtering of the velocity distribution or the use of the vorticity and strain-rate distributions might offer a means to separate the turbulence velocity fluctuations (expected to affect flame wrinkling and turbulence dissipation) from the cyclic fluctuations and ensemble-mean velocities.

The use of the filtered-velocity, vorticity, or strain-rate distributions to define turbulence tacitly assumes that the turbulence is made up of coherent structures. The concept of coherent structures in turbulence is not new (Hussain 1986). The existence and topological mapping of the coherent structures in three-dimensional direct numerical-simulations of turbulent flows has been under study for some time (Hunt, *et al.* 1988, Adrian & Moin 1988, Chong, *et al.* 1990, Chen, *et al.* 1990, and Kim & Hussain 1992). Topological mapping is an important tool to help understand the physical mechanisms that produce turbulent dissipation, mixing, and flame wrinkling. However, engineering calculations and measurements in the foreseeable future will require that the turbulence be characterized by statistical sampling of the velocity. The concept that turbulent flow is made up of coherent structures rather than totally random velocity fluctuations does not conflict with the traditional view. Sampling at one point as a function of time involves sampling of the coherent structures as they randomly pass by the sampling point. Thus, the existence of temporal and spatial correlations in turbulent measurements is consistent with the existence of coherent structures.

The ultimate goal is to explore a means for sampling the coherent structures that will provide a measure of the turbulence properties that contribute to flame wrinkling and turbulence dissipation and will also provide a rational separation of the mean flow and turbulence in RIC engines. As a first step, this study focuses on vortices or "eddy zones" as labeled by Hunt *et al.* (1988). In particular, an attempt is made to quantify the scale and intensity of the velocity associated with an "average vortex" by conditionally sampling the instantaneous velocity distribution at the position of each local maximum in the vorticity distribution. This approach is justified because the vorticity computed from the instantaneous flow reveals all vortices (rotational flow regions) found in the high-pass filtered velocity, and, even in the RIC engine flows (Reuss, *et al.* 1989, and Reuss, *et al.* 1990), the mean flow vorticity is negligible compared to the vorticity associated with the turbulent structures. Therefore, the conditional sampling is a filter-independent means to identify the position of the vortex structures. Both scale and intensity of the velocity associated with the average vortex are quantified (rather than the vorticity alone) because: one, it is the velocity that is required for closure in most engineering models, and two, the scale and the energy spectrum of the velocity is known to peak at low wave numbers while the energy spectrum of the vorticity is expected to follow that of the dissipation and therefore peak at high wave numbers (see discussions in Reuss, *et al.* 1989, and Tennekes & Lumley 1972).

It is recognized that vortex structures are by no means the only structures as indicated in the topological mappings of Hunt *et al.* (1988) and Chong *et al.* (1990). Further, it is recognized that the strain rate is associated with the turbulence dissipation and flame stretching. However, vortices are dominant structures in both

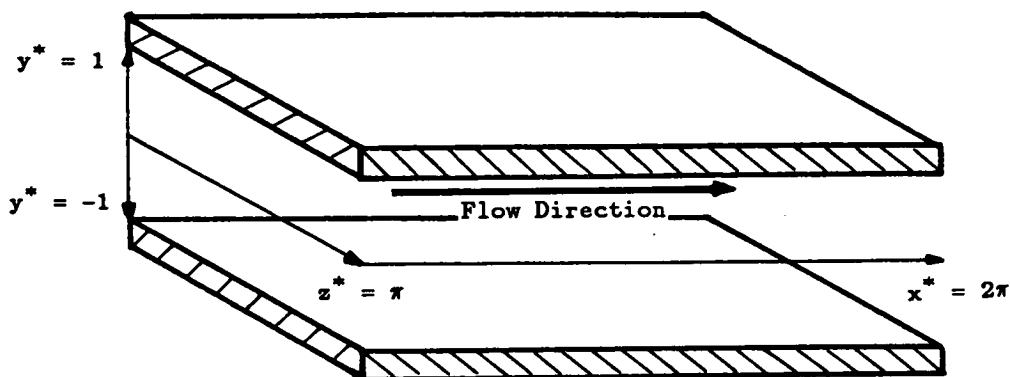


FIGURE 1. Schematic defining the channel coordinates and flow direction.

free shear and near wall flows (Chong, *et al.* 1990 and Smith, *et al.* 1991), strongly correlated with the dissipation (Chen, *et al.* 1990), and believed to be important in flame wrinkling and quenching (Poinso, *et al.* 1990 & Rutland 1989). Both filtering and conditional sampling are used to separate the vortex velocity from the instantaneous velocity in a two-dimensional sample of a computed, three-dimensional, steady channel flow. First, the high-pass-filtered velocity distributions with different cutoff frequencies are compared to reveal the content of different spatial scales. The filtered velocity distributions are compared with the vorticity distribution to reveal the correspondence between the two. Second, the instantaneous velocity is conditionally sampled on the peaks in the vorticity distribution and ensemble averaged to yield the vorticity and velocity of the “average vortex”. The strategy here is to test these two methods in a fully resolved flow where traditional measures are also valid before applying them to RIC engine data. A description of and justification for these two methods is given in Sections 3 and 4.

2. The computed channel flow

The flow geometry and coordinate direction of the computed channel flow are illustrated in Fig. 1. The channel flow is similar to that described by Kim, *et al.* (1987) but with a high Reynolds number, $(Re)_c = 7860$, where $(Re)_c$ is based on the channel half-width, δ , and the centerline velocity \bar{u}_c and $(Re)_\tau = 395$ is based on δ and the wall shear velocity, $u_\tau = [\nu(du/dy)_{\text{wall}}]^{1/2}$. The computational mesh spacing is $\Delta x^+ \approx 10$ and $\Delta z^+ \approx 6^\dagger$ over the domain $0 \leq x^* < 2\pi$ and $0 \leq z^* < 2\pi$, respectively. In the y direction (normal to the wall), a nonuniform mesh is used

[†] Here superscript + indicates nondimensionalization by wall shear units, and superscript * by the channel thickness, eg. $x^+ = xu_\tau/\nu = x^*Re)_\tau$ and $x^* = x/\delta$.

where $y_j^* = [(j - 1)\pi / (N - 1)]$, $j = 1 \dots 193$, over the domain $-1 < y^* \leq 1$ ($y^* = 0$ at the center). The governing equations and spectral solution method are detailed in Kim, *et al.* (1987).

The velocity was sampled in the $x - z$ plane (parallel to the wall) at the center of the channel for the last computational-time step. Thus the turbulence is expected to be statistically homogeneous in both directions. All three velocity components and nine gradient tensor components are available at each mesh point. However, only the in-plane velocities, u and w , and out of plane vorticity, ω_z were used since these will be the only components available when ultimately applied to PIV measurements. Strain rates were not considered.

A summary of the statistical properties of this flow are given in Table 1. The first column gives results from statistics taken over many realizations of this flow, while the second column gives statistics computed for the particular $x - z$ plane used in this study, which is the last realization from the calculation. The integral-length scales were found from the two-point-correlation functions by choosing the x^* or z^* separation at the e^{-1} point in the correlation function. It should be noted that the longitudinal-correlation function in the z^* direction (used to determine $L_{ww})_z$) asymptotically approaches approximately 0.13 rather than zero as it should. This indicates that a residual mean (or at least a very large-scale) velocity must exist in the z^* direction, which also appeared in \bar{w} for this realization. There also appears to be a discrepancy in the value of w_{rms} computed in this final realization and that averaged over many realizations.

3. Turbulence structures from spatial filtering

Spatial filtering of the two-dimensional, instantaneous-velocity distribution is a means to separate large and small scale structures, ie.

$$u(x, z) = u_l(x, z) + u_h(x, z) \quad (5)$$

where u_l and u_h are the low- and high-pass filtered velocity distributions corresponding to the large and small scale structures, respectively. This decomposition has been used for analysis of computed (Hunt, *et al.* 1988) and experimental data (Reuss, *et al.* 1989, and Reuss, *et al.* 1990). Further, Germano (1992) recently treated the filtered Navier-Stokes equations rigorously, relating the filtered velocity to the interpretation of Large Eddy Simulations results.

3.1 Computing the filtered-velocity distribution

In this study, u_l was computed from u and u_h was then determined from eqn. 5. u_l can be computed in a manner analogous to temporal signal processing by taking the two-dimensional, spatial Fourier transform of u , setting to zero all Fourier components above a desired spatial-frequency cutoff, and inverse transforming back to the real-space domain (Reuss, *et al.*, 1989). However, here the low-pass filtering was performed in the real-space domain by computing the two-dimensional local-average velocity at each mesh point as in Reuss, *et al.* (1990). This is accomplished by convolution of the instantaneous velocity distribution with an axisymmetric Gaussian kernel,

Table 1. Statistical properties of the channel flow for the centerline $x - z$ plane using many realizations or the last realization, which was studied here.

Label		Averaging Many	Plane(s) Last
Velocity	\bar{u}^+	20.004	19.76
	u_{rms}	0.805	0.809
	\bar{w}^+	—	0.098
	w_{rms}	0.671	0.595
Vorticity	$\bar{\omega}$	—	1.E-13
	u_{rms}	—	10.9
Integral- Length Scale*	$L_{uu})_x$	0.34	—
	$L_{ww})_x$	0.21	—
	$L_{uu})_z$	0.18	—
	$L_{ww})_z$	0.24	—

* Determined as the $1/e$ point of the one-dimensional, two-point, spatial autocorrelation.

$$g(x, z) = \exp[-(x^2 + z^2)/2A^2] \quad (6)$$

where A sets the cutoff frequency of the filter by adjusting the radius, d_{cf} , at which $w(x, z) = e - 2$. The kernel was evaluated to values of x^* and z^* that were twice that of the diameter of d_{cf} . The spatial frequency content of the low-pass filtered velocity is, therefore, a Gaussian-weighted, local average. This local averaging is equivalent to a windowed Fourier transform filter using the Fourier transform pair of the Gaussian kernel (itself Gaussian)

$$G(k_x, k_z) = (2\pi A^2)^{1/2} \exp[-\pi^2 A^2 (k_x^2 + k_z^2)/4] \quad (7)$$

for the spatial-frequency cutoff, where k_x and k_z are the spatial frequencies in the x and z directions, respectively. Local averaging is considerably simpler than the Fourier transform method for flame studies (its ultimate use) where the position

of the unburned gas boundary is arbitrary, discontinuous, and multivalued in both directions (Reuss, *et al.* 1990).

The use of the spatial average also suggests a more physical interpretation of the high-pass-filtered velocity. In particular, in the limit of a very large filter, $d_{cf} \rightarrow \infty$, the low-pass velocity is the spatial-mean velocity, which should be equal to the temporal mean for the $x - z$ plane. Thus the high-pass velocity is the velocity measured by an observer moving at the mean velocity at every point in the flow. As d_{cf} is decreased the velocity of the observer varies from the mean and approaches the instantaneous value at each point. Thus, in the limit $d_{cf} \rightarrow 0$, the observer is moving at the instantaneous velocity at each point and the high-pass velocity is zero everywhere.

3.2 Filtered-velocity results

The instantaneous and high-pass-filtered velocities for $d_{cf} = 0.74$ are shown in Figs. 2a and 2c for a sub-region of the $x - z$ plane at the center of the channel. The vector scale numbers indicate the magnitude of the vector scale used in each plot relative to those in of the instantaneous velocity distribution plot (Fig. 2a); e.g, a vector in Fig. 2b has a magnitude 0.3 times that of a vector of equal length in Fig. 2a. Comparison of these two figures demonstrates the ability of the filtering to reveal structures in the flow that one would normally associate with turbulence. In particular, "eddy zones" (vortices) and "streaming zones" (directed flows between the vortices as defined by Hunt *et al.* 1988) are readily apparent, and the size of these structures is on the order of the integral length scales listed in Table 1. Also shown in these figures is the vorticity distribution computed from the instantaneous velocity-gradient distribution. The red and blue patches indicate regions of positive vorticity (counter-clockwise rotation) and negative vorticity (clockwise rotation), respectively. As in the previous studies (Reuss, *et al.* 1989, and Reuss, *et al.* 1990) there is a direct correspondence between the velocity vortex in the high-pass-filtered velocity distributions and the regions of high vorticity, both in sign and position.

The existence of flow structures observable in the high-pass-filtered velocity distributions for $d_{cf} > 0.74$ was not as sensitive to the filter cutoff frequency as for the RIC engine data in Reuss, *et al.* (1989). This can be seen by comparing Fig. 2b, which was derived by subtracting the mean velocity ($d_{cf} \rightarrow \infty$), from the instantaneous velocity, and Fig. 2c where $d_{cf} = 0.74$. Although there are differences in the magnitude (note the vector scales used for each plot) and direction of the velocity vectors, the same flow structures are revealed. This is expected because in the channel flow there are no mean-velocity gradients in the $x - z$ plane as in the RIC engine of Reuss, *et al.* (1989) and hence, the scales of the mean flow and turbulence in this channel flow are widely separated. However, for higher frequency-cutoff filters, $d_{cf} < 0.74$, new structures did appear while the old structures remained (albeit with altered velocity vectors). Note the two regions around $(x, z) = (3.1, 1.55)$ and $(x, z) = (3.2, 1.15)$ in Figs. 2c and 2d. For $d_{cf} = 0.74$, these two regions of the flow structures appear as streaming zones, whereas for $d_{cf} = 0.1$ smaller-scale less-intense vortices appeared. These smaller vortices cannot be disregarded as unimportant, since the peak vorticity in these two regions is -16 and

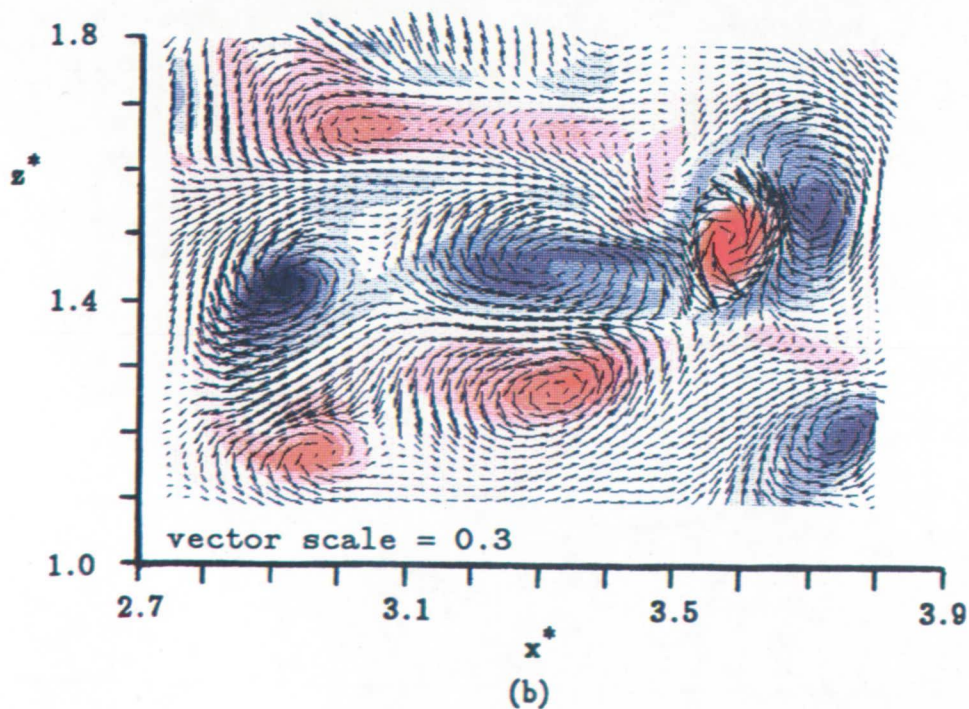
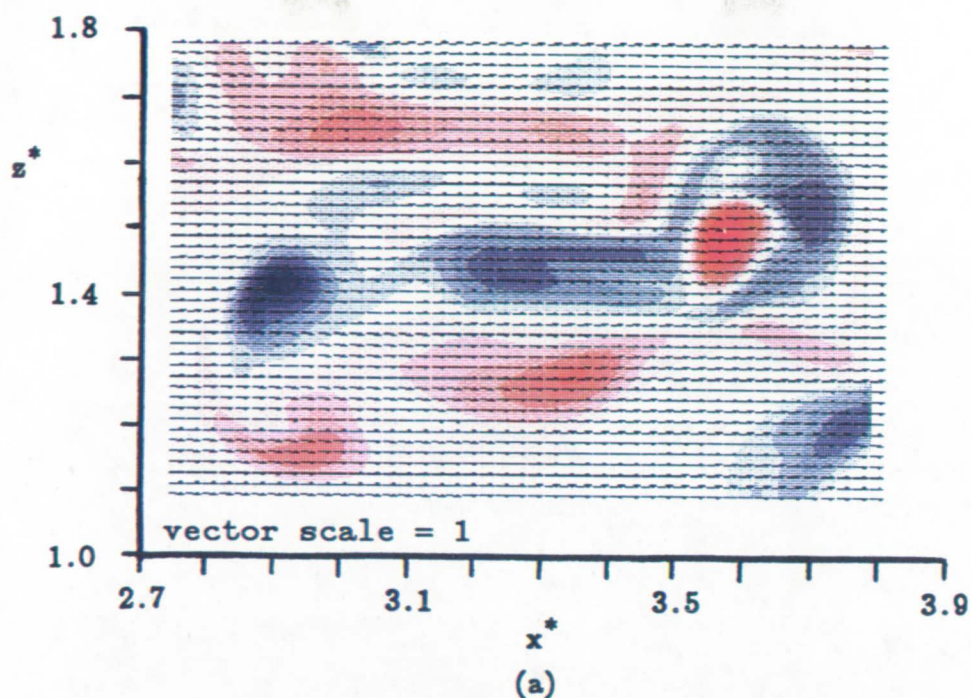


FIGURE 2 A AND B. Composite of the vorticity contours and velocity distributions for a subregion of the $x - z$ plane at $y^* = 0$. The white areas of the contours indicate regions of near zero vorticity. (a) Instantaneous velocity, (b) Mean velocity subtracted, $d_{cf} = \infty$.

Vortex length scale and intensity

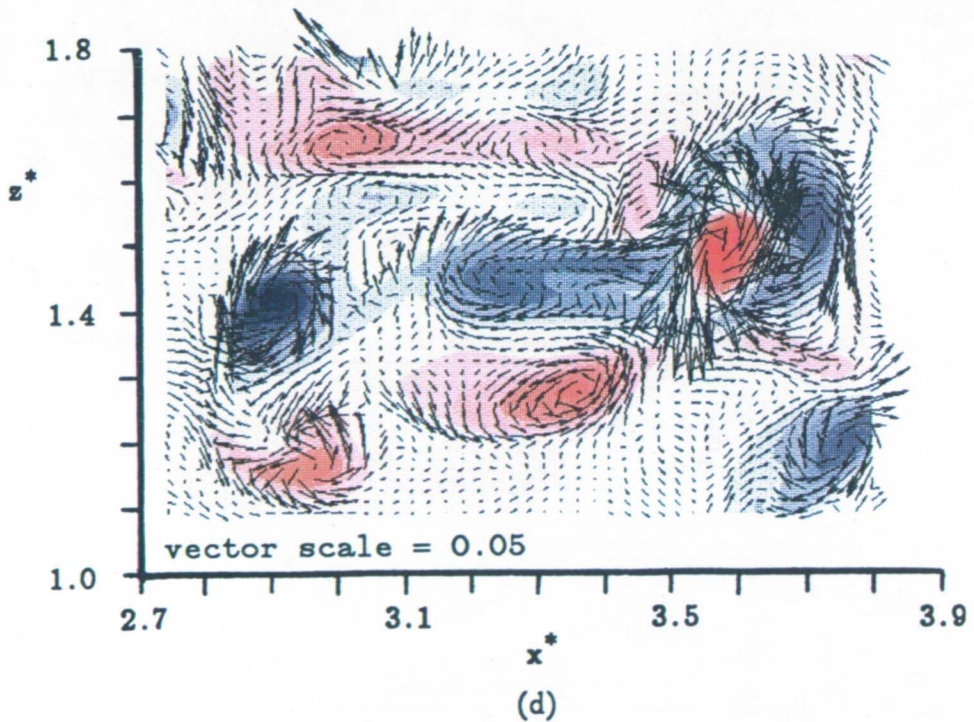
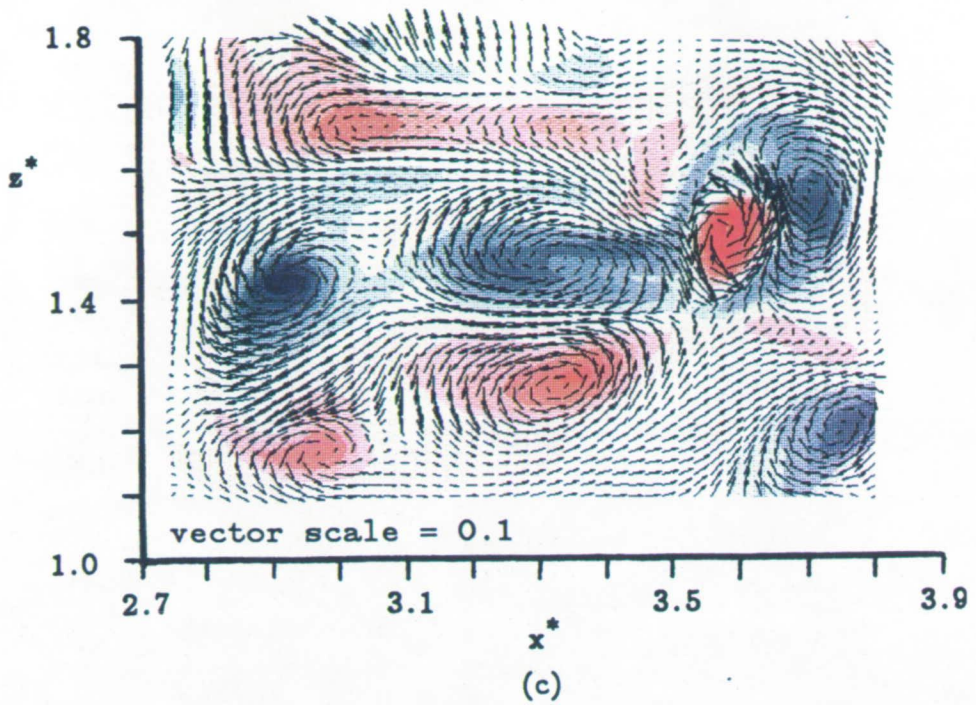


FIGURE 2 C AND D. Composite of the vorticity contours and velocity distributions for a subregion of the $x-z$ plane at $y^* = 0$. The white areas of the contours indicate regions of near zero vorticity. (c) High-pass filtered velocity with $d_{cf} = 0.74$ (d) High-pass filtered velocity with $d_{cf} = 0.1$.

+12, respectively. This is on the order of $\omega_{rms} = 10.9$ and vortices with this level of vorticity did appear with the $d_{cf} = 0.74$ filter in other regions of the $x - z$ plane. Thus, the filter cutoff can be adjusted to reveal vortices of different scales, but can miss some if applied at too low a cutoff frequency.

3.3 Discussion of the filtered-velocity results

The results of the previous section have two important implications about the usefulness of filtering. First the results demonstrated that filtering would in fact isolate vortices in the velocity distribution and on different scales, thus revealing in this channel flow the same types of flow structures observed in direct-numerical simulations of homogeneous stationary turbulence (Hunt, et al. 1988). It is tempting to contrive a method to quantify the scale and intensity of the vortices using the high-pass-filtered velocity distributions. However, even here where the mean and turbulence scales are clearly separated, both the existence of the vortex structures and the magnitude and direction of the associated vectors are dependent on the cutoff frequency. In particular, if the cutoff frequency is too low (d_{cf} large), small scale structures may be missed. If the cutoff frequency is increased (d_{cf} decreased) to assure that the smallest scale structures are revealed, the magnitude of the velocity vectors (and, therefore, any measure of the turbulence intensity) will be too low. Consequently, any quantitative measure of the scale and intensity based on the filtered velocity would be dependent on the choice of the filter cutoff frequency and does not offer a viable solution to the problems of the RIC engine. The second important finding is that the patches of vorticity, computed from the unfiltered (instantaneous) velocity distribution, identified all vortices (in the original contour plots) even though some did not appear in the filtered velocity distribution until a sufficiently high frequency cutoff was used. This suggests that the vorticity could provide a filter-independent detector of the existence of a vortex.

4. The velocity scale and intensity of the average vortex

To quantify the scale and intensity of the vortices, the instantaneous velocity distribution of the entire $x - z$ plane was conditionally sampled at the (x, z) location of the peak vorticity within each vorticity patch in the $x - z$ plane. A vorticity patch was defined as a local region with vorticity of like sign (eg. the blue and red patches in Fig. 2), and the (x, z) position selected at the peak vorticity within that patch. In some cases two peaks existed within each patch, in which case both were identified, eg. (3.05,1.55) and (3.35,1.55). Vortex detection by the vorticity peak is, in principle, a variation of the method of Hunt, et al. (1988) where "eddy zones" were defined by two criteria: one, the irrotational straining is small compared to the vorticity, and two, simultaneously the (local) pressure tends to a minimum somewhere in the zone. Their approach was not used here since it requires both the three-dimensional deformation tensor and the pressure distribution, which are not available from measurements. Although the simpler approach used here is less formal, it is not necessarily less rigorous or less valid for identification of vortices. The velocity distribution in Fig. 4 of Hunt, et al. (1988) shows regions of rotating flow structures that were not detected as eddy zones by the above criterion, as well

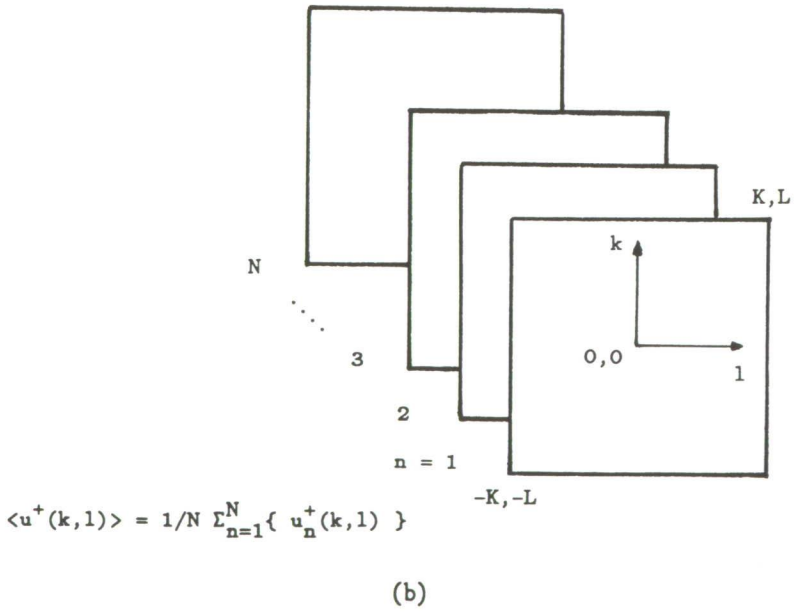
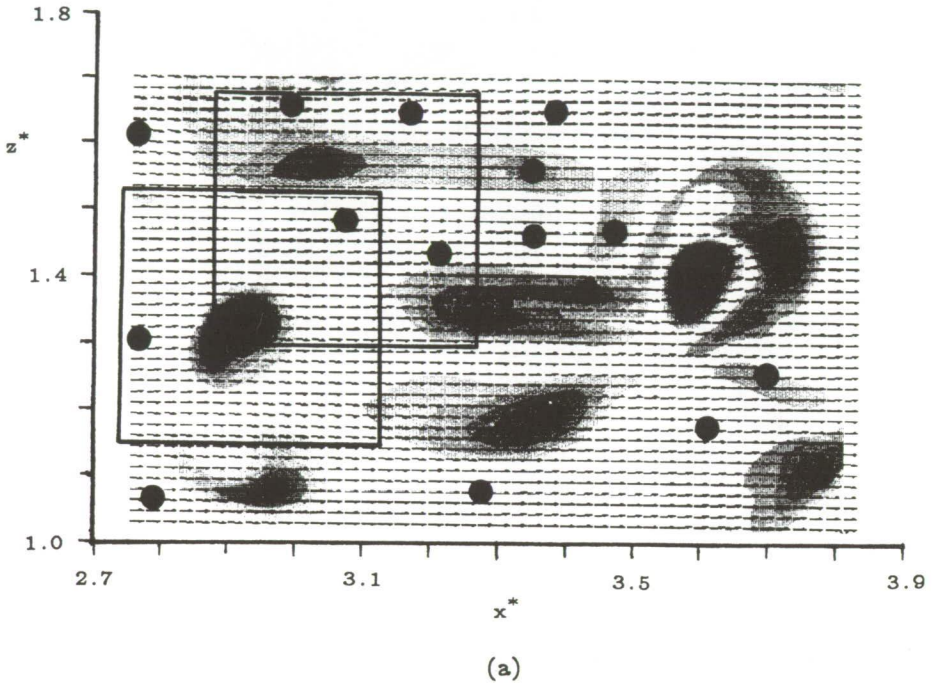


FIGURE 3. Schematic representation of (a) two conditional sampling windows (not to scale) and (b) ensemble averaging.

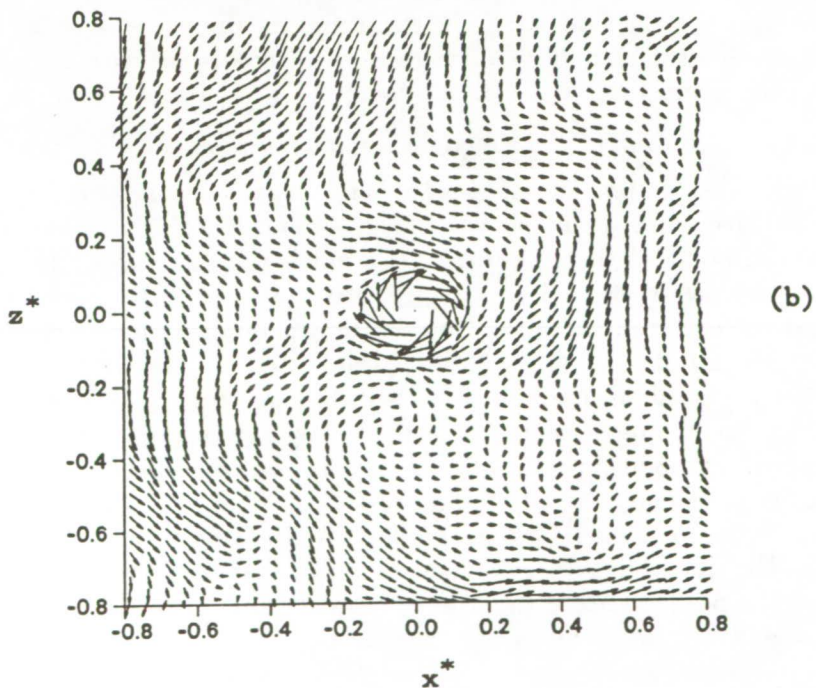
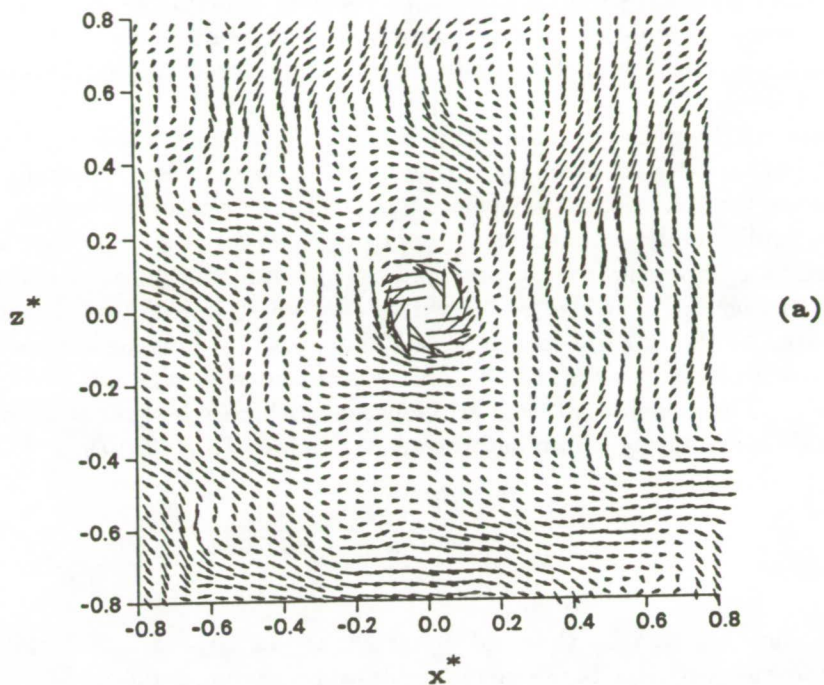


FIGURE 4. Velocity distribution of (a) the average positive vortex and (b) the average negative vortex.

as the converse. By contrast, all regions with vorticity above 10 percent of the rms value were detected regardless of the dissipation or pressure fields, and there was excellent agreement between the vorticity patches and the rotating structures in the velocity field.

The position of the peak vorticity within each vorticity patch was found manually with the aid of an interactive image processor. The dots in Fig. 3a indicate the positions of the vorticity peaks in the subregion. The instantaneous velocity distribution was conditionally sampled at these positions as follows. A square window was centered at each vorticity peak position, $\omega_p(i, j)$ and overlaid on the x, z mesh as depicted in Fig. 3a. The size of the window ($x^* = z^* = 1.6$) was chosen to be large compared to the integral length scale. The u^+ , and w^+ , values at each point of the window grid, (k, l) , were stored. This was repeated at all $N = 597$ vorticity peak positions. The velocities at each grid location within each of the windows were then ensemble averaged by summing over all N windows (Fig. 3b) as

$$\langle u^+(k, l) \rangle = \frac{1}{N} \sum_{n=1}^N [(u^+(k, l) | k = 1 = 0 @ \pm \omega_p(i, j))] \quad (8)$$

where the vertical bar signifies the conditional average and ω_p indicates conditioning on plus and minus vorticity. Thus two ensemble averages were computed resulting in both an average-positive and an average-negative vortex. The quantities $\langle w^+(k, l) \rangle$ and $\langle \omega(k, l) \rangle$ were averaged in a like manner. Near the edges of the $x - z$ plane the window overlaps the boundary. In these regions the value of N at each k, l mesh point outside the boundary is decreased to be consistent with the number of samples at each point.

4.2 Conditional-sampling results and discussion

The velocity distribution of the positive and negative, conditionally sampled, ensemble-averaged windows are shown in Fig. 4a and b. $\langle u^+(0, 0) \rangle$ has been subtracted at each point so that the observer is moving at the same velocity as the center of the average vortex. The strong positive (and negative, respectively) rotation about the center of the ensemble-average windows is immediately apparent. The velocity magnitudes, u^+ and w^+ , along the x^* and z^* axes are plotted in Figs. 5a and 6a for the positive ensemble-averaged window. Only the values for the average positive vortex are presented here as the average negative vortex plots are approximately equal but opposite in sign. Again, the rotation is apparent in the lateral velocity components $u^+(0, z^*)$ and $w^+(x^*, 0)$. The peak lateral velocities of the average vortex were small, ≈ 0.3 , compared to the statistical fluctuation value $\omega_{rms} = 0.6$. The ensemble-average vorticity along the axes is shown in Figs. 5b, and 6b as well. The peak values of the average-positive and average-negative vortices were $\langle \omega_p \rangle = \pm 18$ and the mean average vorticity,

$$\overline{\langle \omega \rangle} = \int_a^b \omega(x, 0) dx^* \quad (9)$$

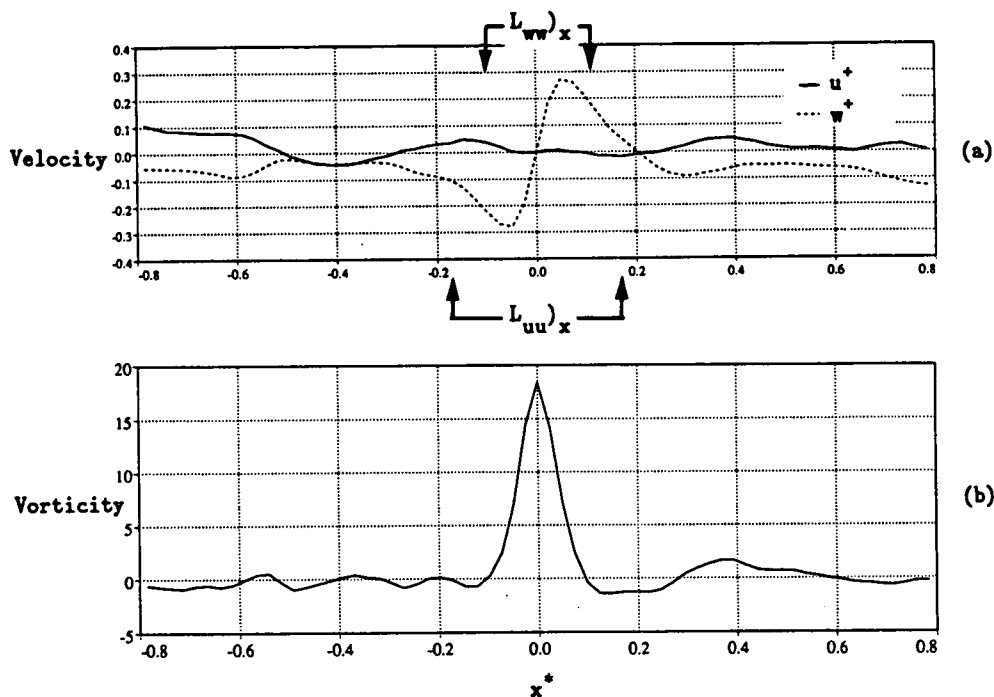


FIGURE 5. (a) The velocity, $u^+(x^*, 0)$ and $w^+(x^*, 0)$, and (b) vorticity, $\omega(x^*, 0)$, along the x^* axis for the average positive vortex in Fig. 4a.

was approximately 7.9, where a and b were the zero crossings of the center vorticity peak. These values bracket the traditional statistical rms of the vorticity over the $x-z$ plane, $\omega_{rms} = 10.9$.

It was surprising that there was so much structured flow outside the immediate vicinity of the center vortex. In particular, on average there are streaming regions (Hunt, *et al.*) outside the center vortex with velocities as large as 1/3 the peak velocity in the vortex. In general, the streaming regions adjacent to the center vortex are directed with its rotation; however, the vorticity in the streaming regions is relatively small (cf. Figs. 5b and 6b). The existence of streaming flows outside the center vortex may be reasonable since this is observed in the composites of the vorticity and high-pass filtered distributions (cf. Fig. 2). In particular, observation of any given vortex structure reveals that it is surrounded by neighboring (adjacent) vortices, separated by a distance approximately equal to the size of the vorticity patches, with streaming flows between them. If one assumes that over many conditionally sampled vortex peaks the neighboring vortices are randomly distributed azimuthally, then the neighboring vortex structures would be expected to average

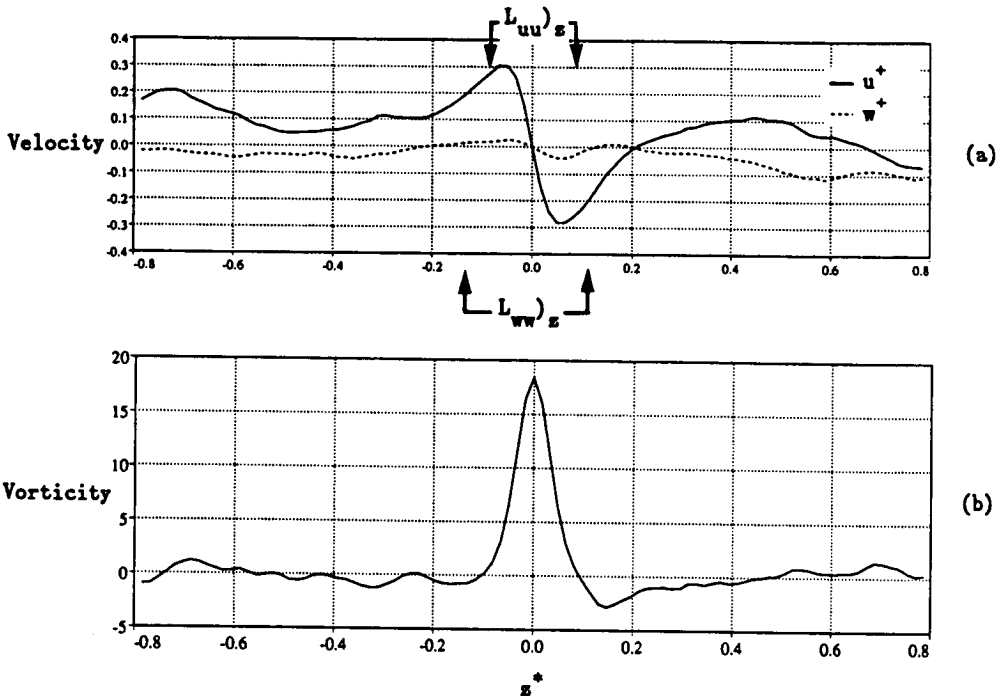


FIGURE 6. (a) The velocity, $u^+(0, z^*)$ and $w^+(0, z^*)$, and (b) vorticity, $\omega(0, z^*)$, along the z^* axis for the average positive vortex in Fig. 4a.

to zero with a large enough sample while average-steaming regions might remain. However, it is still surprising that the streaming regions exist at distances from the center vortex that are large compared to the size of the center vortex.

Most surprising was the fact that the center positive (negative) vortex is paired with an adjacent negative (positive) vortex in the positive (negative) z^* direction. The peak tangential velocity of the negative (positive) paired vortex (ie. u at $z^* \approx +0.3$ in Fig. 6a) is about 1/3 that of the peak tangential velocity of the center vortex, and the peak vorticity is about 1/7 (cf. Fig. 6b). The existence of this pair is surprising because the z^* direction should be statistically homogeneous, and it is not obvious why vortex pairs would preferentially couple with the positive vortex to the $-z^*$ side of the negative vortex. The existence of the structure and in particular the paired vortex outside the center vortex may be: one, an indication that the sample size was too small, or two, another manifestation of the flow properties in the z^* direction that resulted in the unexpected statistical properties discussed in Section 2.

The spatial scale of the vorticity associated with the average vortex is expected

to be smaller than that of the velocity as noted earlier, and this is clearly true of the average vortex since the spatial extent of the vorticity is approximately 1/2 the spatial extent of the velocity distributions in Figs. 5 and 6. To quantitatively compare the scale of the average-vortex velocity distribution with two point correlation is difficult as there is no rigorous means available. However, the lateral and longitudinal length scales in the x^* and z^* directions are indicated on the top and bottom Figs. 5a and 6a. There are no well defined structures in the longitudinal velocities, $u^+(x^*, 0)$ and $w^+(0, z^*)$. The spatial extent of the lateral velocity components, $u^+(0, z^*)$ and $w^+(x^*, 0)$, is on the order of the longitudinal and lateral-integral-length scales, $L_{uu}z$ and $L_{ww}x$. However, neither the differences between the lateral- and longitudinal-integral-length scales nor the anisotropy of the length scales between the x^* and z^* directions is obvious in the conditionally sampled data.

5. Conclusions

The spatial filtering and conditional sampling of the instantaneous velocity distribution were used to identify and quantify the vorticity structures in a computed channel flow. The spatial filtering revealed the vortices in the velocity distribution but required the application of different filter-cutoff frequencies to identify vortices of all scales. By contrast, conditional sampling the instantaneous, two-dimensional, velocity distribution at the vorticity-peak positions is a means to separate the vorticity structures associated with turbulence in a way that is independent of the cutoff frequency associated with filtering. The properties of the average-positive and average-negative vortices studied here are on the order of the traditional single-point time-averaged measures but do not provide an alternative for quantifying those values.

The average-positive and average-negative vorticity distributions are equal and opposite in value and are, therefore, consistent with the traditional-statistical-mean value of zero. However, the peak-average-vorticity, $\langle \omega_p \rangle = \pm 18$, and mean average vorticity, $\overline{\langle \omega \rangle} = 7.9$, differ from but bracket the traditional statistical value, $\omega_{\text{rms}} = 10.9$. A rigorous derivation of the correspondence between the traditional and conditionally-sampled values might resolve this difference. The peak velocity associated with the average vorticity was half the traditional rms velocity fluctuation. The spatial extent of the velocity distributions were on the order of the traditional lateral-length scales and somewhat smaller than the streamwise longitudinal length scales. This suggests that the vorticity structures are within the size of the structures sampled in two-point correlations but are themselves insufficient to explain either the full extent of the scale or the anisotropy measured by the two-point correlations. Larger structures must coexist and/or structures outside but adjacent to the average vortex must contribute to the two point correlations.

Acknowledgements

Support was provided by The Center for Turbulence Research and General Motors Research and Environmental Staff. We would like to thank Prof. Hugh Blackburn,

Dr. Todd D. Fansler, Dr. John Kim, and Minami Yoda for their help and consultation. A special thank you is extended to Prof. Brian D. Cantwell for his guidance during the summer program.

REFERENCES

- ADRIAN, R. J. & MOIN, P. 1988 Stochastic Estimation of Organized Turbulent Structure: Homogeneous Shear Flow. *J. Fluid. Mech.* **190**, 531.
- ARCOUMANIS AND WHITELAW, J. H., 1987 Fluid Mechanics of Internal Combustion Engines - A Review. *Proc. I. Mech. E.* **201C**, 57.
- CHEN, J. H., CHONG, M. S., SORIA, J., SONDERGAARD, R., PERRY, A. E., ROGERS, M., MOSER, R., & CANTWELL, B. J. 1990 A Study of the Topology of Dissipating Motions in Direct Numerical Simulations of Time-Developing Compressible and Incompressible Mixing Layers. In *Report CTR-S90, Proceedings of the 1990 Summer Program, Center for Turbulence Research, Stanford University & NASA Ames.*
- CHONG, M. S., PERRY, A. E., & CANTWELL, B. J. 1990 A General Classification of Three-Dimensional Flow Fields. *Phys. Fluids A* . **2(5)**.
- FANSLER, T. D., AND FRENCH, D. T. 1988 Cycle-Resolved Laser-Velocimetry Measurements in a Reentrant-Bowl-in-Piston Engine. *SAE Paper 880377*.
- FANSLER, T.D. 1993 Turbulence Production and Relaxation in Bowl-In- Piston Engines. Submitted to 1993 SAE International Congress.
- FRASER, R. A., AND BRACCO, F. V. 1988 Cycle-Resolved LDV Integral Length-Scale Measurements in an I. C. Engine. *SAE Paper 880021*.
- GERMANO, M. 1992 Turbulence: The Filtering Approach. *J. Fluid. Mech.* **238**, 325.
- GLOVER, A. R. 1986 Towards Bias-Free Estimates of Turbulence in Engines. *Third International Symposium on Applications of Laser Anemometry to Fluid Mechanics*. Lisbon, Portugal.
- HUNT, J. C. R., WRAY, A. A., & MOIN, P. 1988 Eddies, Streams, and Convergence Zones in Turbulent Flows. *Init Report CTR-S88, Proceedings of the 1988 Summer Program, Center for Turbulence Research, Stanford University & NASA Ames.*
- HUSSAIN, A. K. M. F. 1986 Coherent Structures and Turbulence. *J. Fluid. Mech.* **173**, 303.
- KIM, J., AND HUSSAIN, A. K. M. F. 1992 Propagation Velocity and Space-Time Correlation of Perturbations in Turbulent Channel Flow. *NASA Tech. Mem.* TM 103932.
- KIM, J., MOIN, P., & MOSER, R. 1987 Turbulence Statistics in Fully Developed Channel Flow at Low Reynolds Number. *J. Fluid Mech.* **177**, 133.
- LE COZ, J. F. 1992 Cycle-to-Cycle Correlations Between Flow Field and Combustion Initiation in an S. I. Engine. *SAE Paper 920517*.

- POINSOT, T., VEYNANTE, D., & CANDEL, S. 1990 Diagrams of Premixed Turbulent Combustion Based on Direct Simulation. *29rd Symposium (International) on Combustion*. The Combustion Institute, Pittsburgh, 613.
- RASK, R. B. 1981 Comparison of Window, Smoothed-Ensemble, and Cycle-by-Cycle Data Reduction Techniques for Laser Doppler Anemometry Measurements of In-Cylinder Velocity. In *Fluid Mechanics of Combustion Systems*, T. Morel, R. P. Lohmann & J. M. Rackley, ed., ASME, NY.
- RASK, R. B. 1984 Laser Doppler Anemometry Measurements of Mean Velocity and Turbulence in Internal Combustion Engines. In *Intl. Conf. on Applic. of Lasers and Electro-Optics*, Boston, Nov. 12-15, Also available at GM Research and Environmental Staff, Publication GMR-4839, October 3, 1984.
- REUSS, D. L., ADRIAN, R. J., LANDRETH, C. C., FRENCH, D. T., & FANSLER, T. D. 1989 Instantaneous Planar Measurements of Velocity and Large-Scale Vorticity and Strain Rate in an Engine Using Particle Image Velocimetry. *SAE Paper 890616*.
- REUSS, D. L., BARDSLEY, M., FELTON, P. G., LANDRETH, C. C., & ADRIAN, R. J. 1990 Velocity, Vorticity and Strain-Rate Ahead of a Flame Measured in an Engine Using Particle Image Velocimetry. *SAE Paper 900053*.
- RUTLAND, C. J., FERZIGER, J. H., & CANTWELL, B. J. 1989 Effects of Strain, Vorticity, and Turbulence on Premixed Flames. Ph. D Thesis, Stanford University.
- SMITH, C. R., WALKER, J. D. A., HAIDARI, A. H., & SOBRUN, U. 1991 On the dynamics of Near-Wall Turbulence. *Phil. Trans. R. Soc. Lond. A*. **336**, 131.
- TENNEKES, H., AND LUMLEY, J. L. 1972 *A first Course in Turbulence* MIT Press, Cambridge, Massachusetts, Chapt. 8.3, 262.

III. Compressible flow and modeling

A long-term objective of the CTR is to advance the state of turbulence modeling, particularly for compressible flows. The six papers in this section provide several important new ideas towards this end.

Cambon, Coleman, and Mansour used the DNS database for one-dimensional axial compression to guide the development of a rapid distortion theory (RDT) for compressible flows subjected to compressions. They showed that the controlling parameter for compressibility effects is the ratio of the distortion time scale to the acoustic time scale. In the case where the acoustic time scale is slow compared to the distortion time scale, "pressure released RDT" applies, in which the pressure fluctuations can be neglected. In this regime, the growth rate of the turbulent kinetic energy can be higher than the rate when the flow is nearly incompressible. This is different from the homogeneous shear case where compressibility effects are found to reduce the energy growth rate. Finally, they used the RDT and DNS results to suggest improvements in turbulence models for compressible flows.

Blaisdell and Zeman used Blaisdell's DNS for homogeneous turbulence to make further examinations of Zeman's model for the extra rate of turbulent energy dissipation due to turbulent dilatations arising from regions containing eddy shocklets. They show how acoustic waves can be focused in the turbulence to form such shocklets and that the Zeman model works well for turbulent Mach numbers less than 0.3. Their work raises unanswered questions about the model at higher Mach numbers, suggesting need for further study.

Vandromme and Zeman explored the applicability to boundary layer flows of a model for the pressure dilatational term developed by Zeman and Coleman by reference to DNS for rapid axial compressions. The flow considered was a supersonic compression corner flow with an extended separated region, where a considerable improvement over standard $k-\epsilon$ modeling was obtained.

Papamoschou and Lele studied the pressure field induced by a small isolated vortex in a compressible shear layer using DNS in a convected frame tied to the disturbance vortex. The idea was to examine the zone of influence of the disturbance with increasing convective Mach number M_c . They showed that this influence extends to the edges of the shear layer, although the zone of influence in the streamwise direction is strongly reduced with increasing M_c .

Kevlahan, Mahesh, and Lee used DNS to study the interaction of a weak shock front with strong isotropic turbulence. This included solving the equation for a propagating surface (the shock wave) and comparisons of the results with the DNS predictions. For 2D turbulence, the agreement was very good. In 3D turbulence, the alignment of the vorticity vector with the intermediate eigenvector of the strain-rate tensor, found in other DNS, occurred upstream of the shock and was strongly intensified by the shock. In addition, they found a more significant tendency for velocity to align with vorticity than has been observed in incompressible DNS.

Durbin and Yang studied a proposed transport equation for the eddy viscosity in wall bounded flows. The relatively simple model, which does not incorporate wall-proximity damping functions, is intended for use in complex turbulent flows. Comparisons with DNS and experiments for various boundary layer flows show good agreement. The model eliminates several of the problems of standard $k-\epsilon$ models and shows considerable promise for use in generalized practical engineering calculations.

Together these six contributions include a number of important new ideas that their authors and others at Stanford and NASA/Ames are working to include in operational turbulence models. Thus, these contributions will be extremely helpful in CTR's development of improved turbulence models for compressible flows.

W. C. Reynolds

445356 5/2-34

189672 199

N94-14757

Rapid distortion analysis and direct simulation of compressible homogeneous turbulence at finite Mach number

By C. Cambon,¹ G. N. Coleman² AND N. N. Mansour³

The effect of rapid mean compression on compressible turbulence at a range of turbulent Mach numbers is investigated. Rapid distortion theory (RDT) and direct numerical simulation results for the case of axial (one-dimensional) compression are used to illustrate the existence of two distinct rapid compression regimes. These regimes are set by the relationships between the timescales of the mean distortion, the turbulence, and the speed of sound. A general RDT formulation is developed and is proposed as a means of improving turbulence models for compressible flows.

1. Introduction

This paper focuses upon the behavior of homogeneous compressible turbulence under the influence of rapid axial (one-dimensional) mean compression. The motivation for this study is a need to cast light upon the physics of compressible turbulent flows and to improve compressible turbulence models. Our approach is to use both direct numerical simulations (DNS) and rapid distortion theory (RDT). The RDT developed in this paper is for general (those that preserve homogeneity) mean deformations; the resulting insight is then used to suggest improvements to compressible turbulence models that are applied to rapidly compressed flows.

Earlier RDT studies of homogeneous compressible turbulence have been limited to either isotropic compressions (Blaisdell 1992, private communication) or the vanishing turbulent Mach number limit (Durbin & Zeman 1992, hereafter referred to as DZ); the present investigation, therefore, attempts a more general treatment in that non-isotropic compressions and finite Mach numbers are considered. Some of our main conclusions confirm and extend those found in the recent study of shock-turbulence interactions by Jacquin & Cambon (1992).

An overview of our findings follows. The RDT analysis predicts that the crucial parameter for turbulence subjected to rapid compression is the ratio of the mean deformation rate, D , to the inverse sonic timescale L/a , where L is a turbulent lengthscale and a is the sound speed. This parameter, DL/a , hereinafter denoted as Δm (after DZ), is equivalent to the product of the inverse of the turbulent timescale, the deformation rate, and the turbulent Mach number, M_t ; it defines for the dilatational part of the velocity field two distinct limits: the "pseudo-acoustical"

1 CNRS, Ecole Centrale de Lyon

2 Center for Turbulence Research

3 NASA Ames Research Center

(nearly solenoidal) regime given by $\Delta m \ll 1$ (that studied by DZ) and the so-called "pressure-released" regime with $\Delta m \gg 1$. The term "pressure-released" is chosen because when Δm is large, the sonic and turbulent timescales are both much larger than D^{-1} and, therefore, correlations involving the fluctuating pressure and velocity fields are negligible during a rapid distortion. The behavior of the solenoidal velocity field, according to the RDT analysis, is unaffected by the dilatational field when the mean flow is irrotational, and is thus independent of Δm for axial compressions. Its history is, therefore, identical to that predicted for compression of purely solenoidal turbulence. In the following, we confirm these RDT predictions by comparison with DNS results.

The DNS results also show that for moderate values of Δm , all the double-velocity correlations involving the dilatational part of the turbulent velocity field remain weak with respect to the pure-solenoidal correlations and are in this sense similar to the pure solenoidal case, even for moderate compressibility. Only the $\Delta m \gg 1$ case is characterized by a strong amplification of the dilatational correlations.

The moderate Δm results are at first glance in conflict with recent studies of axially compressed turbulence (e.g., DZ, Zeman & Coleman 1992) which find unexpectedly large pressure-dilatation correlations in the nearly solenoidal flow. This led us to investigate the behavior of the pressure field, which has two roles for a rapid compression. On one hand, it modifies the production term in the turbulent kinetic energy equation by changing the Reynolds stress anisotropy through the classic pressure-strain rate correlation (via Π_{11} for an axial compression in the x_1 direction). On the other hand, the pressure is directly involved in the kinetic energy equation through the pressure-dilatation term, $\Pi = \Pi_{ii}/2$. The magnitude of Π_{11} is found to be larger than that of Π in all cases considered in this paper for a wide range of Mach numbers and large (but finite) compression speeds.

Both the pressure variance and pressure-dilatation correlation from the DNS are found to increase with Mach number (and, therefore, with Δm at a fixed mean distortion-to-turbulent timescale ratio) *with respect to their initial values*. However, when Π is compared to *the production term* in the turbulent kinetic energy transport equation, it is much smaller and has, in fact, less relative importance with increasing M_t . This reduced relative importance of the pressure field with increasing compressibility is a key result of this paper and is the basis of much of what follows. Between the $\Delta m \rightarrow 0$ and $\Delta m \rightarrow \infty$ extremes (where the pressure-dilatation correlation is identically zero), Π must reach a maximum; from the DNS results, it appears that this maximum occurs near the $\Delta m \rightarrow 0$ limit at a small but finite value.

In the next section, the RDT analysis is developed for compressible homogeneous turbulence; in §3, the theory is applied to the case of axial compression, and separate analytic expressions for the relevant dilatational and solenoidal correlations for both the $\Delta m \ll 1$ and $\Delta m \gg 1$ extremes are presented and compared to DNS results. The findings suggest that it would be appropriate for turbulence models to "interpolate" between the two extremes in order to accurately capture the M_t dependence during a rapid axial compression. We propose two methods for doing so

in §4, which deals with the role of, and closures for, the pressure-strain rate correlation. Section 5 considers the implications of this study for isotropically compressed and sheared flows, and §6 contains a recap of the main results and our conclusions.

2. A rapid distortion analysis for compressible homogeneous turbulence

2.1. General considerations

Blaisdell *et al.* (1991, hereafter referred to as BMR) observed that the “intrinsic compressibility” (the non-zero divergence) of the turbulent field often tends to reduce the amplification of turbulent kinetic energy produced by a mean velocity gradient, such as a bulk compression or mean shear, with respect to the pure solenoidal case. This effect depends on at least three different timescales and on the initial turbulent field. These are the mean distortion timescale,

$$\tau_D^{-1} = (U_{i,j}U_{j,i})^{1/2} \quad (1)$$

(where $U_{i,j}$ is the mean velocity gradient), the “turbulent decay” or “turn-over” time,

$$\tau_t^{-1} = q/L \quad (2)$$

(where $q^2/2$ is the turbulent kinetic energy and L is a lengthscale of the energy containing eddies), and the timescale linked to the sonic speed,

$$\tau_a^{-1} = a/L. \quad (3)$$

The compression speed, $r = \tau_t/\tau_D$, is the only relevant parameter for modeling homogeneous incompressible turbulence (at least for large Reynolds number). However, when intrinsic compressibility is considered, the ratio of the two latter timescales, which amounts to a turbulent Mach number $M_t = \tau_a/\tau_t$, must also be accounted for. The magnitude of the reduction of the kinetic energy amplification mentioned above is, therefore, not necessarily universal, given the multi-timescale and initial-value nature of the problem. In fact, RDT studies of inhomogeneous flows even go so far as to predict an *increase* with M_t of the kinetic energy amplification for turbulence under rapid (but finite) compression; these studies by Debiève *et al.* (1982, hereafter referred to as DGG) and Jacquin & Cambon (1992) are discussed in a following subsection, where the general RDT equations are presented and the reasons for the apparent growth rate versus M_t discrepancy are given. This analysis is based on an extended Craya-Herring decomposition (Cambon 1982, 1990; Cambon *et al.* 1985), which is shown to facilitate a separate investigation of the solenoidal and dilatational histories and provides a useful comparison to other approaches (e.g., BMR and DZ).

Some of the earlier RDT studies have apparently over-estimated the role of the pressure-dilatation term, attempting to force an increased damping due to compressibility of the kinetic energy growth rate. We hope to clarify the situation here by separately considering various terms in one-point closure equations and thus use RDT as a tool for improving a model’s representation of those terms. While the RDT is not a model in and of itself, by improving the accuracy of crucial terms, we expect that it will in turn also improve the overall accuracy of the model.

2.2. Definitions and background

To investigate the influence of the mean flow upon the turbulence, it is convenient to use a coordinate system x_i that deforms with the mean deformation. We accordingly define the Lagrangian displacement tensor F_{ij} (Eringen 1967) via

$$dx_i = \frac{\partial x_i}{\partial t} dt + \frac{\partial x_i}{\partial X_j} dX_j = U_i dt + F_{ij} dX_j, \quad (4)$$

where $x_i(\mathbf{X}, t)$ is the position at time t of a fluid particle moving with the mean flow, which has the position X_i at the initial time $t = 0$. Representing the substantial time derivative by a superimposed dot, one has

$$\dot{F}_{ij} = \frac{\partial \dot{x}_i}{\partial X_j} = \frac{\partial \dot{x}_i}{\partial x_l} \frac{\partial x_l}{\partial X_j} = U_{i,l} F_{lj} \quad \text{with} \quad F_{ij}(\mathbf{X}, t = 0, 0) = \delta_{ij} \quad (5a)$$

where

$$\dot{(\)} = (\),_t + U_j \frac{\partial (\)}{\partial x_j} \quad (5b)$$

is the substantial derivative; we shall also have occasion to use the symbol $\mathcal{D}(\)/Dt$ to denote the substantial derivative. Unless stated otherwise, the dependent variables are assumed to be decomposed into Reynolds averaged and fluctuating components, as $U_i + u_i$, where capital letters, overbars, and angle-brackets are all used interchangeably to denote Reynolds- (ensemble) averaged quantities, and either lowercase or primed variables are used to denote fluctuating quantities. Note that \mathbf{F} is a function of the stationary coordinate \mathbf{X} , the time t , and is parameterized by the time (in units of t) at which the tensor is orthonormal (hence the third argument in (5a)). For flows under mean compression, the determinant of \mathbf{F} has special significance since it is equal to the volumetric ratio J .

When the mean velocity field is irrotational, the analyses proposed (over a hundred years ago!) by Cauchy, Weber, or Kelvin for the total (mean plus fluctuating) vorticity can be used to give solutions for the fluctuating vorticity ($\omega_i = \epsilon_{ijk} u_{k,j}$) and velocity fields:

$$\omega_i(\mathbf{x}, t) = \frac{1}{J} F_{ij}(\mathbf{X}, t, 0) \omega_j(\mathbf{X}, 0) \quad (6)$$

$$u_i(\mathbf{x}, t) = F_{ji}^{-1}(\mathbf{X}, t, 0) u_j(\mathbf{X}, 0) + \phi_{,i}. \quad (7)$$

These solutions, which ultimately derive from the linearized Euler equations, remain approximately valid for moderately inhomogeneous flows (recall the spatial dependence of \mathbf{F}). Eq. (6) is the classic solution of the linearized Helmholtz equation when the mean vorticity-fluctuating velocity term is zero (that is, for an irrotational mean flow). When this term is not zero, simple solutions in physical space are not possible. Eq. (7) (also valid only for irrotational mean flows), an expression which has been extensively used by Goldstein (1978), contains the scalar potential ϕ , which is directly connected to the fluctuating pressure and can be calculated once certain assumptions are made (e.g., that the fluctuating velocity field is solenoidal or that

the dilatational field is nearly acoustic). The term ϕ is not the scalar potential arising from the Helmholtz decomposition (which we will denote φ in the following) because the " F_{ji}^{-1} " term in (7) contains contributions from both the solenoidal and dilatational velocity field.

DGG's RDT solution of the Lagrangian transport equation for the Reynolds stress tensor for the case of shock wave-turbulence interaction reads

$$\langle u_i u_j \rangle(t^+) = F_{mi}^{-1}(t^+, t^-) \langle u_m u_n \rangle(t^-) F_{nj}^{-1}(t^+, t^-), \quad (8)$$

where t^- and t^+ refer to positions upstream and downstream of the shock, respectively, following a mean streamline through the shock. The shock is considered as a pure discontinuity of the mean streamwise velocity. In other words, it is an external streamwise compression of infinite rate, and the associated tensor \mathbf{F} does not depend on the history of the velocity gradient, but is completely characterized by the mean density jump or mean volumetric ratio $J = \text{Det}(\mathbf{F})$, with $F_{ij} = J \delta_{i1} \delta_{j1}$ through the shock. The ratio J is linked to the upstream Mach number M_0 via

$$J = \frac{2 + (\gamma - 1)M_0^2}{(\gamma + 1)M_0^2} \quad (9)$$

where γ is the ratio of specific heats, and use has been made of the classic Rankine-Hugoniot relations for the mean (frozen) field. A comparison of equations (7) and (8) shows that this approach *ignores* the effect of pressure (which is mediated by ϕ in (7)); the response of the pressure fluctuations with a *finite* characteristic time even for the so-called "rapid" term is neglected compared to an *infinite* compression rate). Another idealization in the analysis of DGG, also pointed out by Lee *et al.* (1992), is that the distortion (curvature and unsteadiness) of the shock surface by the impinging turbulent structure is ignored. The latter issue, initially addressed by Ribner(1953), is not considered by the present paper. We investigate instead the role of the pressure field in a simpler homogeneous framework by explicitly defining and formalizing the range of validity of the "pressure released" regime that is implicit in the Debiève analysis. This paper has much in common with the recent analysis of the shock wave flow performed by Jacquin & Cambon (1992), in which the pressure-released limit was first explicitly advocated.

Equation (7) shows that an irrotational deformation of a purely solenoidal velocity field is given by

$$u_i(\mathbf{x}, t) = u_i^s(\mathbf{x}, t) = (F_{ji}^{-1}(\mathbf{X}, t, 0)u_j(\mathbf{X}, 0))^s, \quad (10)$$

where to maintain $u_{i,i} = 0$ we have,

$$\phi_{,i} = - (F_{ji}^{-1}(\mathbf{X}, t, 0)u_j(\mathbf{X}, 0))^d \quad (11)$$

(where the s and d superscripts (and later subscripts) are understood to respectively refer to the solenoidal and dilatational contributions). The latter equation is an integral form of the Poisson equation for the fluctuating pressure,

$$\nabla^2 \phi = - (F_{ji}^{-1}u_j)_{,i}. \quad (12)$$

For the solenoidal case, the pressure "kills off" the dilatational contribution, resulting in the lower limit of the kinetic energy growth rate caused by the mean compression. Conversely, in the pressure-released regime, the u_i^d contribution in Eq. (11) is no longer "removed" by the pressure, producing an extra contribution to the solenoidal energy, which is unaffected by the dilatation field and again grows in accordance with Eq. (10); in other words, the compressibility leads to an increase in the kinetic energy growth rate.

From this point hence, the RDT analysis will be continued under the assumption of flow homogeneity and make use of a spectral formalism; the Fourier wave-space proves to be invaluable for obtaining tractable RDT solutions. Beginning with Eq. (6), we shall use the Fourier space to extract the solenoidal velocity from the vorticity, as was done by Batchelor & Proudman (1954). Instead of solving a Poisson equation in physical space, we use a simple geometric wave-space projection to invoke the Helmholtz decomposition.

2.3. The mean flow

Before turning to the turbulent fields, however, we restrict the types of mean deformations that are admitted by this analysis to those that preserve the homogeneity of the flow. In incompressible turbulence, the constraint of maintaining homogeneous statistical properties leads to two conditions: the mean velocity gradient $U_{i,j}$ must be uniform in space, and the mean flow must be a particular solution of the Navier-Stokes equations. The last condition amounts to an irrotational mean acceleration,

$$\nabla \times \Gamma = 0, \quad (13)$$

or that

$$\dot{U}_{i,j} + U_{i,l}U_{l,j}$$

is symmetric, where

$$\Gamma_i = (\dot{U}_{i,j} + U_{i,l}U_{l,j})x_j = \ddot{F}_{ij}(t,0)X_j. \quad (14)$$

Compressibility introduces a new condition. The linearization of the momentum equation displays two acceleration terms. The first one is the product of mean density and the fluctuating acceleration and leads to the same constraint mentioned above. The second term is the product of density fluctuation ρ' by the mean acceleration Γ and is typically nonhomogeneous (as can be seen by the spatial dependence in (14)). This term can be removed, and homogeneity preserved, by neglecting the density fluctuation with respect to the mean density. Such an approximation (which is consistent with "compressed" turbulence at low Mach number) will be not used in this paper. Instead, we admit only mean flows without convective acceleration. From eqs. (5) and (14) we see that this requires

$$F_{ij}(t,0) = \delta_{ij} + A_{ij}t, \quad (15a)$$

or

$$U_{i,j}(t) = A_{il}F_{lj}^{-1} = A_{il}(\delta_{lj} + A_{lj}t)^{-1}. \quad (15b)$$

Eq. (15) is valid for an arbitrary constant (not necessarily symmetric) matrix \mathbf{A} for arbitrary times, provided that the determinant of \mathbf{F} , J , remains positive. Special cases of (15) have been given previously, for example, for pure strain and shear (BMR). A good approximation for the mean pressure P as a function of J can be derived from the isentropic relations. (While the isentropic relations are not strictly valid when M_t is nonzero, DNS of finite M_t turbulence under mean compression have shown that the deviation from the isentropic prediction is relatively small: for example, in Case C1DV discussed below – a rapid axial compression for initial $M_t = 0.3$ – the mean pressure at $J = \bar{\rho}(0)/\bar{\rho} = 1/5$ is within 6 percent of the isentropic value.)

2.4. The fluctuating flow

The linearized Euler equations (with $\rho'\Gamma_i = 0$) in the deforming coordinate system are

$$\dot{u}_i + U_{i,j}u_j = -\frac{p_{,i}}{\bar{\rho}} \tag{16}$$

with $\bar{\rho} = \bar{\rho}(t) = \bar{\rho}(0)/J(t)$ (recall that the dot superscript denotes a *substantial* derivative, see Eq. (5)). The linearized equations for the fluctuating pressure p and entropy s read (see DZ)

$$\begin{aligned} \left(\frac{\dot{p}}{\gamma P} \right) &= -u_{i,i} \\ \dot{s} &= 0, \end{aligned} \tag{17}$$

where $P = \bar{\rho}RT$. An investigation of the coupling between solenoidal and dilatational contributions to the fluctuating velocity field is conveniently done by transforming the variables in (the deformed coordinate) \mathbf{x} into (three-dimensional) Fourier space, which we indicate either by a caret symbol or the notation “ $\widehat{\mathcal{F}}(\cdot)$.” The classic Helmholtz decomposition is given first in physical and then in spectral space as follows:

$$v_i(\mathbf{x}, t) = \epsilon_{ijl}\psi_{l,j} + \varphi_{,i} \tag{18}$$

$$\widehat{v}_i(\mathbf{k}, t) = (\delta_{ij} - \frac{k_i k_j}{k^2})\widehat{v}_j + \frac{k_i k_j}{k^2}\widehat{v}_j, \tag{19}$$

for any vector field \mathbf{v} . The two terms on the right-hand sides correspond to \mathbf{v}^s and \mathbf{v}^d , which are defined in physical space by the vector ψ_i and the scalar potential φ . The corresponding spectral space decomposition into $\widehat{\mathbf{v}}^s$ and $\widehat{\mathbf{v}}^d$ is given by the projection operators in (19), which separate the (single-component) dilatational contribution parallel to the wavevector \mathbf{k} from the (two-component) solenoidal contribution in the plane normal to \mathbf{k} . Equations (16) and (17) are easily Fourier-transformed; only the advection term requires particular caution:

$$\widehat{\dot{u}}_i = \widehat{\mathcal{F}}(u_{i,t} + U_{j,l}x_l u_{i,j}),$$

so

$$\widehat{\dot{u}}_i = \widehat{u}_{i,t} - U_{l,i}\widehat{u}_i - U_{j,l}k_j \frac{\partial \widehat{u}_i}{\partial k_l}.$$

The first and the last terms in the right-hand side of the latter equation are collectively treated as a derivative along characteristic curves, which plays the same role as the mean trajectories in physical space. This derivative will, therefore, also be represented by a superimposed dot so that

$$\dot{k}_i + U_{j,i}k_j = 0, \quad \text{with solution} \quad k_i = F_{ji}^{-1}(t, 0)K_j. \quad (20)$$

The analogy with physical space is complete, since

$$\dot{x}_i - U_{i,j}x_j = 0, \quad \text{with solution} \quad x_i = F_{ij}(t, 0)X_j. \quad (21)$$

The initial \mathbf{k} value, \mathbf{K} , plays the same role in wave space as the Lagrangian coordinate \mathbf{X} does in physical space. Pure kinematic distortion by advection in physical and spectral space are linked by a wave conservation law

$$\exp(ik_jx_j) = \exp(iK_jX_j),$$

where $i^2 = -1$. Accordingly, one has

$$\widehat{\mathcal{F}}(\dot{u}_i) = \dot{\hat{u}}_i - U_{l,i}\hat{u}_l \quad (22)$$

and equation (16) becomes

$$\dot{\hat{u}}_i - U_{l,i}\hat{u}_l + U_{i,j}\hat{u}_j = -ik_i \frac{\widehat{p}}{\rho}. \quad (23)$$

In the latter equation, the projection operators in (19) can be used to separate solenoidal and dilatational contributions. We prefer to use a slightly different method by specifying a special frame for the solenoidal mode, according to an extended Craya-Herring decomposition (Cambon 1990). An orthonormal frame of reference ($\mathbf{e}^{(1)}, \mathbf{e}^{(2)}, \mathbf{e}^{(3)}$) attached to the wavevector is used with the last vector being parallel to \mathbf{k} ($\mathbf{e}_i^{(3)} = k_i/k$, where k is the wavevector modulus). In this local frame, the Fourier transform of the velocity fluctuation reads

$$\hat{u}_i(\mathbf{k}, t) = \widehat{\varphi}^{(1)}(\mathbf{k}, t)e_i^{(1)}(\mathbf{k}) + \widehat{\varphi}^{(2)}(\mathbf{k}, t)e_i^{(2)}(\mathbf{k}) + \widehat{\varphi}^{(3)}(\mathbf{k}, t)e_i^{(3)}(\mathbf{k}). \quad (24)$$

The two first terms give exactly \hat{u}_i^s , and the latter gives \hat{u}_i^d , with a minimal number of components and conservation of all the tensorial properties (invariants) due to the orthonormal properties of the local frame. Classic descriptions in terms of vorticity and divergence are easily recovered as

$$\widehat{\omega}_i = ik(\widehat{\varphi}^{(1)}e_i^{(2)} - \widehat{\varphi}^{(2)}e_i^{(1)}) \quad (25a)$$

and

$$\widehat{d} \equiv \hat{u}_{i,i} = ik\widehat{\varphi}^{(3)}. \quad (25b)$$

In order to remove the uncertainty regarding the azimuthal position of the solenoidal coordinates with respect to $\mathbf{e}^{(3)}$, the $(\mathbf{e}^{(1)}, \mathbf{e}^{(2)})$ plane is defined by choosing a fixed spherical coordinate polar axis \mathbf{n} , after Herring (1974). (Craya(1958) implicitly used $n_i = \delta_{i3}$ and addressed only covariance matrices of the velocity field and thus limited the generality of his approach.) We set

$$\mathbf{e}^{(1)} = \frac{\mathbf{k} \times \mathbf{n}}{|\mathbf{k} \times \mathbf{n}|} \quad \text{and} \quad \mathbf{e}^{(2)} = \mathbf{e}^{(3)} \times \mathbf{e}^{(1)}. \quad (26)$$

Striking simplifications can be made by choosing the polar axis according to the symmetries of the mean flow (if any) or the statistical properties of the fluctuating field, retaining the full generality of the method. The equations in the local frame can be made nearly independent of the choice of \mathbf{n} by using the ‘‘helical modes’’ $(\mathbf{e}_i^{(2)} - i\mathbf{e}_i^{(1)}, \mathbf{e}_i^{(2)} + i\mathbf{e}_i^{(1)})$ (which are also eigenmodes of the plane rotation matrix around \mathbf{k} and of the ‘‘curl’’ operator) as the basis set (see Greenspan 1968, Cambon & Jacquin 1989, Waleffe 1992). Substituting (24) into (23) leads to the linear system of equations for the three components of \hat{u}_i in the local Craya-Herring frame, with:

$$\dot{\hat{\varphi}}^{(\alpha)} - U_{l,l}\hat{\varphi}^{(\alpha)} + m_{\alpha\beta}\hat{\varphi}^{(\beta)} + m_{\alpha 3}\hat{\varphi}^{(3)} = 0 \quad (27)$$

$$\dot{\hat{\varphi}}^{(3)} - U_{l,l}\hat{\varphi}^{(3)} + m_{33}\hat{\varphi}^{(3)} + m_{3\alpha}\hat{\varphi}^{(\alpha)} + ik\frac{\hat{p}}{\rho} = 0. \quad (28)$$

Greek indices (indicating solenoidal space) take only the value 1 or 2, whereas the Latin indices range from 1 to 3 (and as in physical space, the Einstein summation convention is assumed). Calculation of the matrix m_{ij} is straightforward; remembering to account for the rotation due to the time derivative of the local frame at fixed \mathbf{K} using eqs. (20) and (26), the elements are

$$m_{\alpha\beta} = \dot{e}_i^{(\alpha)}U_{i,j}e_j^{(\beta)} - \dot{e}_i^{(\beta)}e_i^{(\alpha)} = e_i^{(\alpha)}U_{i,j}e_j^{(\beta)} - \epsilon_{\alpha\beta 3}R_E, \quad (29a)$$

$$m_{\alpha 3} = e_i^{(\alpha)}U_{i,j}e_j^{(3)} - \dot{e}_i^{(\alpha)}e_i^{(3)} = e_i^{(\alpha)}(U_{i,j} - U_{j,i})e_j^{(3)}, \quad (29b)$$

$$m_{3\alpha} = e_i^{(3)}U_{i,j}e_j^{(\alpha)} - \dot{e}_i^{(3)}e_i^{(\alpha)} = 2e_i^{(3)}U_{i,j}e_j^{(\alpha)}, \quad (29c)$$

$$m_{33} = e_i^{(3)}U_{i,j}e_j^{(3)}. \quad (29d)$$

The rotation term R_E is $e_i^{(2)}U_{i,j}e_j^{(1)}$ if the polar axis is chosen as one of the eigenvectors of the mean gradient matrix; its general expression is available in Cambon *et al.* (1985). The last equation relevant to our study is that which governs the pressure:

$$\left(\frac{\dot{\hat{p}}}{\gamma P}\right) - U_{l,l}\left(\frac{\hat{p}}{\gamma P}\right) = -\hat{d} = -ik\hat{\varphi}^{(3)}. \quad (30)$$

Without mean distortion, eqs. (28) and (30) correspond to a pure acoustic regime, where energy is exchanged between dilatational velocity and pressure at a frequency

ak . (The sonic speed a is easily reintroduced using the isentropic relation $a^2 = \gamma RT = \gamma P/\bar{\rho}$.) On the other hand, the (exact) balance between the two last terms in Eq. (28) is the equivalent in physical space of the Poisson equation for p in the pure solenoidal flow. The solenoidal contribution to velocity is seen to be completely uncoupled from the dilatational field if $m_{\alpha 3}$ is zero. This is valid for *any* irrotational compressing mean flow, *but not for pure shear*, as has been stressed by BMR. Finally, we note that the coupling of the solenoidal and dilatational fields is mediated by $m_{3\alpha}$. This term is zero for spherical compression but must be considered for any anisotropic straining process (except for very specific wavevectors given by the particular deformation). An investigation of the timescales in (28) introduces the parameter $R_a(k) \equiv (\tau_D)^{-1}/ak$, for which Δm is an averaged approximation in physical space. For very low values of this parameter, the incompressible limit is recovered, the dilatational mode $\varphi^{(3)}$ tends to zero, and the sonic speed a approaches infinity; both $k\hat{p}/\bar{\rho}$ (which tends to the solenoidal solution to the Poisson equation) and its time derivative (which from (30) is observed to be proportional to $a^2\varphi^{(3)}$) tend to finite non-zero values without inconsistency. At moderate $R_a(k)$, a pseudo-acoustic regime is recovered, which deviates from the pure incompressible ($u_{i,i} = 0$, $p = p_s$) case since the time variation of the $m_{3\alpha}$ term in (28) can be neglected and a WKB approximation can be used to predict the oscillating behavior of \hat{d} (Sabel'nikov 1975 and DZ). (This oscillating behavior will be revisited in §5.) For large values of $R_a(k)$, the pressure term in Eq. (28) can be neglected compared to the other terms, and the "pressure released" regime is obtained. We note that use of the solenoidal Poisson equation to approximate the total pressure variance (i.e. setting $p = p_s$) and then using (30) to estimate the pressure-dilatation term, a method followed by DZ, can lead to some inconsistencies. If $p = p^s$ holds, the dilatational mode is directly given by a simplification of (28) (equating the first three terms to zero), and the solution is

$$\hat{\varphi}^{(3)}(\mathbf{k}, t) = J \frac{k}{K} \hat{\varphi}^{(3)}(\mathbf{K}, 0). \quad (31)$$

The potential inconsistency is that this solution for q_d^2 is not necessarily the same as that found from Eq. (30). In (31), the dilatational part of the kinetic energy depends only upon its initial value; for a mean compression, $q_d^2(t) = \mathcal{F}(J(t))q_d^2(0)$, where $\mathcal{F}(J)$ depends on the type of compression. In contrast, the DZ method amounts to connecting both \hat{p} and $\hat{\varphi}^{(3)}$ to the initial value of the solenoidal modes, $\hat{\varphi}^{(\alpha)}(\mathbf{K}, 0)$, so that the dilatational part of the kinetic energy depends only on the *solenoidal* initial data: $q_d^2(t) = \mathcal{F}_{DZ}(J(t))(\Delta m)^4 q_s^2(0)$ (where $\mathcal{F}_{DZ}(J) \neq \mathcal{F}(J)$ and again depends upon the compression type).

An approach which avoids this ambiguity and allows the classification of other relevant limits is available by introducing integrating factors into (28) and (30) so that

$$y = J^{-1} \frac{\hat{\varphi}^{(3)}}{k} \quad \text{and} \quad z = J^{-1} \frac{\hat{p}}{\bar{\rho}a^2} \quad (32)$$

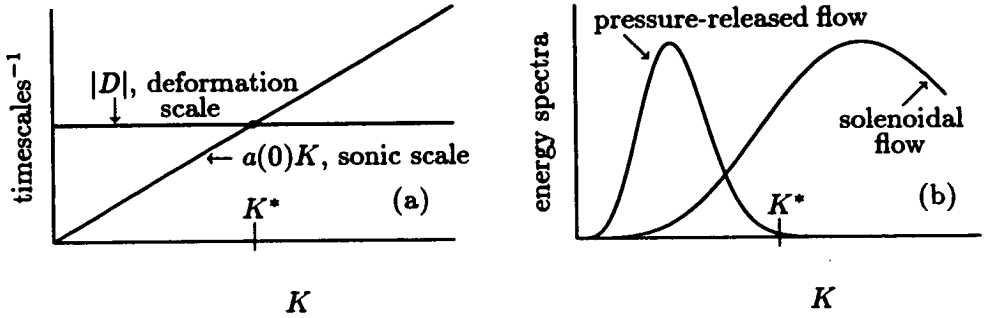


FIGURE 1. Solenoidal and pressure-release regimes.

satisfy the simpler equations:

$$\frac{\mathcal{D}(\dot{y}/a^2)}{\mathcal{D}t} + k^2 y = iz^s \tag{33}$$

$$\frac{\mathcal{D}(\dot{z}/k^2)}{\mathcal{D}t} + a^2 z = a^2 z^s, \tag{34}$$

where $z^s = J^{-1} \hat{p}_s / \bar{\rho} a^2 = i(J^{-1}/ka^2) m_{3\alpha} \hat{\varphi}^{(\alpha)}$. The left-hand sides of both (33) and (34) are linked only to the dynamics of the solenoidal field and thus decoupled from the dilatational and pressure terms for irrotational mean deformations.

We are now in a position to distinguish the different regimes implied by equations (33) and (34):

- I. The incompressible limit, with $a^2 \rightarrow \infty$, which corresponds to a vanishing value of all the time-derivatives in both equations; hence, z^s and $y \rightarrow 0$, and $z = z^s$ (i.e. $p = p_s$) and $y = 0$ are consistent limits in this case.
- II. The acoustic regime, recovered when $k^2 y \gg iz^s$.
- III. The regime studied by Durbin & Zeman, where the pressure-dilatation correlation is given by the solenoidal pressure variance, which corresponds to $k^2 y = iz^s$ in (33) and $z = z^s$ in (34); these equalities hold only if the time-derivative of the solenoidal term (right-hand side of (33)) is much larger than the time-derivative of the dilatational term (first term on the left-hand side of (33)).
- IV. The pressure-released limit, corresponding to $k^2 y \ll iz^s$ in (33), which leads to the condition

$$\overline{u_{i,i}^2} \ll (\Delta m)^4 \frac{q_s^2}{L^2}$$

(with L a lengthscale of the energy containing turbulence) required for the pressure-released regime to be valid. We mention in passing that if one assumes that the ratio λ of the dilatational to solenoidal kinetic energy is proportional to M_t^2 , the above inequality suggests that an alternative to Δm as the parameter that defines the pressure-released regime is the quantity $\Delta m M_t^{-1/2} = r M_t^{1/2}$. In spite of this, the DNS results presented below indicate that the pressure-released limit seems to be adequately parameterized by Δm alone.

Complete solutions of the system of linear equations (28) and (30) are required for intermediate values of $R_a(k)$. The method described in Cambon (1982) of extending the Townsend (1976) approach can also be used for the general (homogeneous) case; an overview of the scheme follows, which we plan to follow in future work. A linear transfer function \mathbf{g} , which generates the general solution of the system of equations as

$$\widehat{\varphi}^{(i)}(\mathbf{k}, t) = g_{ij} \left(\mathbf{e}^{(3)}, K/K_0, R_a(K_0), a_0 K_0 t \right) \widehat{\varphi}^{(j)}(\mathbf{K}, 0),$$

is computed by solving (numerically in general) (20), (27), (28), and (30) for a set of arbitrary simple initial data ($\widehat{\varphi}_0^{(i)} = \delta_{i1}, = \delta_{i2}, \text{etc.} \dots$). (For convenience, the subscript can be taken to vary from 1 to 4 in order to represent the pressure fluctuation with $\widehat{\varphi}^{(4)} = \widehat{p}/\bar{\rho}a$.) All the relevant one-point correlations can then be obtained by integrating over spectral space products of linear transfer functions and initial spectra. The initial spectra such as

$$\langle \widehat{\varphi}^{(i)*}(\mathbf{P}, 0) \widehat{\varphi}^{(j)}(\mathbf{K}, 0) \rangle = \frac{E^{(ij)}(K)}{4\pi K^2} \delta(\mathbf{K} - \mathbf{P})$$

can be generated by invoking isotropy and assuming acoustic equilibrium (Sarkar *et al.* 1989) and certain relationships between the dilatational spectra (Bataille, *et al.* 1992). Note that the delta function δ amounts to a factor $\delta_{nm}(\Lambda(0)/2\pi)^3$ if discrete Fourier modes ($P = n, K = m$) are chosen using periodic boxes of size Λ , as is done in DNS. For both the continuous and discrete case, the mean compression must be taken into account when computing correlations and integrating over wave space, using either

$$\delta(\mathbf{k} - \mathbf{p}) = \delta(\mathbf{K} - \mathbf{P})J(t)$$

or $\Lambda^3(t)/\Lambda^3(0) = J$ and $d^3\mathbf{k} = dk_1 dk_2 dk_3 = J^{-1} d^3\mathbf{K}$. For the solenoidal field certain results can be obtained analytically, as is demonstrated below for the case of axial compression, since g_{ij}^2 depends only on the orientation of the wave vector, and not on the modulus; integrations over wave space needed to derive the velocity correlations can thus be separated into the product of two one-dimensional integrals, one of which defines (independently of initial spectra shape) the initial kinetic energy. Evaluation of the non-solenoidal correlations is not as straightforward since the components of the linear transfer matrix that involve the dilatation depend on both the direction $e_i^{(3)} = k_i/k$ of the wavevector \mathbf{k} (as for the solenoidal case) and on its modulus. Accordingly, amplification coefficients like the functions \mathcal{F} and \mathcal{F}_{DZ} mentioned above in general require numerical integration. This complication is a symptom of the wave number dependence of the sonic timescale in spectral space $(a(0)K)^{-1}$, symbolically shown in Figure 1a; since the deformation scale D^{-1} is the same for all wave numbers, above a critical value K^* , the sonic is the shorter of the two timescales. For a given energy spectrum with peak at K_0 so that Δm is characterized by $R_a(K_0)$, the rapid distortion behavior depends on K/K_0 . The largest structures ($K < K_0$) will, therefore, naturally tend toward the pressure-released extreme and the smallest ($K > K_0$) toward the solenoidal limit.

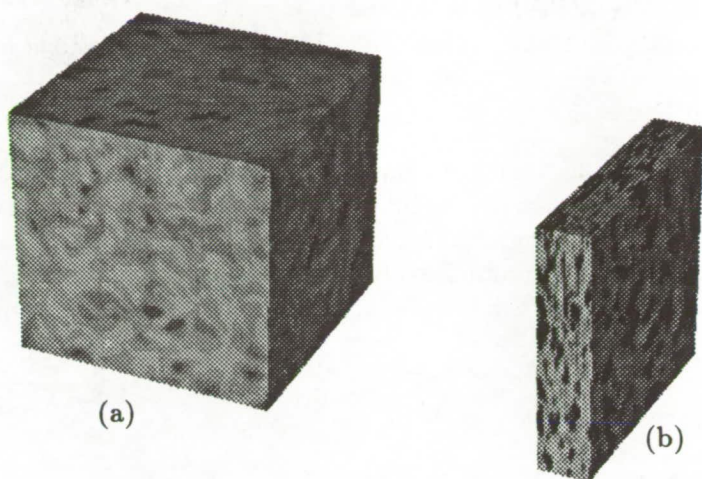


FIGURE 2. Contours of turbulent Mach number (a) before and (b) after axial compression (Case C1DW).

When K_0 falls well below K^* , the entire flow is within the pressure-released regime, and $\Delta m \gg 1$; when $K_0 \gg K^*$, the $\Delta m \rightarrow 0$ limit is valid (see Figure 1b).

In the next section, the analysis is applied to the special case of axial compression, and DNS results are used to verify the relevance of Δm as a critical parameter.

3. RDT and DNS of axially compressed flow

Both the RDT and DNS impose upon isotropic compressible turbulence the axial deformation that satisfies the homogeneity condition (15) so that the single nonzero mean velocity gradient component is

$$U_{1,1} = \frac{D_0}{1 + D_0 t} = D_0 J^{-1} \quad \text{and} \quad F_{11} = J. \quad (35)$$

For $D_0 \equiv D(0) < 0$, this straining can be maintained for a finite time for as long as the flow volume is nonzero. Here we consider mean density ratios (equal to J^{-1}) that vary from 1 to 5; see Figure 2. Before describing the various DNS runs, which is done in §§3.2, in the next subsection we specify the RDT correlations relevant to one point modeling of the axial compression.

3.1. Rapid distortion analysis for axial compression

For the case of axial compression, the Craya-Herring-Cambon coordinates given in §2 reduce to $e_1^{(3)} = \cos \theta$, $e_1^{(2)} = -\sin \theta$, where $\theta = (\mathbf{k}, \mathbf{n})$ if the polar axis is chosen along the compression direction so that $e_1^{(1)} = 0$ (see Cambon & Jacquin (1989) for other axisymmetric RDT applications). The RDT solutions for the solenoidal field are then

$$\hat{\varphi}^{(1)}(\mathbf{k}, t) = J \hat{\varphi}^{(1)}(\mathbf{K}, 0) \quad \text{and} \quad \hat{\varphi}^{(2)}(\mathbf{k}, t) = \frac{K}{k} \hat{\varphi}^{(2)}(\mathbf{K}, 0), \quad (36)$$

with $k_1 = K_1 J^{-1}$, $k_2 = K_2$, $k_3 = K_3$, $\cos \theta = k_1/k = \xi J^{-1}/(1 + C^2 \xi^2)^{1/2}$, $k^2 = 1 + C^2 \xi^2$, $C^2 = J^{-1} - 1$ and $\xi = K_1/K$. The double correlations are calculated using

$$\langle \hat{u}_i^* \hat{u}_i \rangle = \langle \hat{\varphi}^{(i)*} \hat{\varphi}^{(i)} \rangle \quad \text{and} \quad \hat{u}_1 = -\hat{\varphi}^{(2)} \sin \theta + \hat{\varphi}^{(3)} \cos \theta. \quad (37)$$

Assuming isotropic initial data, both the solenoidal and pressure-released analytical RDT predictions can be obtained by integrating either over ξ or directly in physical space, with the results being unaffected by the initial spectral shape. The axial compression correlations are tabulated below, using as super- or subscripts "s" and "p", respectively, to denote the solenoidal and pressure-released limiting cases.

Turbulent kinetic energy:

$$\frac{q_s^2(t)}{q_s^2(0)} = A_s(J), \quad (38a)$$

$$\frac{q^2(t)}{q^2(0)} = A_p(J). \quad (38b)$$

Compression-direction Reynold stress component:

$$\frac{\langle u_1^s u_1^s \rangle(t)}{q_s^2(0)} = B_s(J), \quad (39a)$$

$$\frac{\langle u_1 u_1 \rangle(t)}{q^2(0)} = B_p(J). \quad (39b)$$

Compression-direction solenoidal-dilatational cross-correlation:

$$\langle u_1^s u_1^d \rangle(t) = 0, \quad (40a)$$

$$\frac{\langle u_1^s u_1^d \rangle(t)}{q_s^2(0)} = C_p(J). \quad (40b)$$

Structure dimensionality tensor (Reynolds 1990; see also (47) and (48)):

$$\frac{D_{11}^s(t)}{q_s^2(0)} = D_s(J) = B_s(J), \quad (41a)$$

$$\frac{D_{11}(t)}{q^2(0)} = D_p(J). \quad (41b)$$

Compression-direction component of the pressure-strain rate correlation:

$$\frac{\Pi_{11}^s(t)}{q_s^2(0)} = DE_s(J), \quad (42a)$$

$$\Pi_{11} = E_p(J) = 0. \quad (42b)$$

The pressure-dilatation term Π is identically zero for both limits. In terms of the inverse compression ratio J with $C^2 \equiv J^{-2} - 1$, we have for the $J < 1$ case:

$$A_s = \frac{1}{2} \left(1 + J^{-2} \frac{\tan^{-1} C}{C} \right) \quad (43a)$$

$$A_p = \frac{2 + J^{-2}}{3} \quad (43b)$$

$$B_s = \frac{J^{-2}}{2C^2} \left(\frac{1}{2} + \frac{C^2 - 1}{2} \frac{\tan^{-1} C}{C} \right) \quad (43c)$$

$$B_p = \frac{J^{-2}}{3} \quad (43d)$$

$$C_p = \frac{J^{-2}}{2C^2} \left(-1 + J^{-2} \frac{\tan^{-1} C}{C} \right) - B_s \quad (43e)$$

$$D_p = \frac{J^{-2}}{C^2} \left(1 - \frac{\tan^{-1} C}{C} \right) \left(\frac{2 + J^{-2}}{3} \right) \quad (43f)$$

$$E_s = \frac{1}{2C^4} \left(C^2 + 3 + (C^2 - 3)J^{-2} \frac{\tan^{-1} C}{C} \right). \quad (43g)$$

The solenoidal amplification functions turn out to be nearly linear in J^{-1} , whereas the pressure-released expressions are nearly parabolic. The quantities A_s and B_s , previously derived by Ribner (1953), and the new expressions D_s and E_s are almost the same as those found for incompressible axisymmetric strain (of arbitrary history), with, for example, the Reynolds stress tensor $R_{ij}^s = \langle u_i^s u_j^s \rangle = J^{-2/3} R_{ij}^*(J)$, where \mathbf{R}^* is the RDT solution for the trace-free part of the mean deformation. Functions A_p and B_p are obtained by simply ignoring the pressure terms during the integration of the equations for the one-point correlations in the rapid axial compression limit, which are:

$$\frac{1}{2} \dot{q}^2 = -DR_{11} + \Pi, \quad (44)$$

$$\dot{R}_{11} = -2DR_{11} + \Pi_{11}, \quad (45)$$

where $R_{ij} = \langle u_i u_j \rangle$, and $\Pi = \Pi_{ii}/2 = \langle pu_{i,i} \rangle / \bar{\rho}$.

For moderate compressibility, we find from the DNS results that the role of Π_{11} , which reduces the anisotropy ($b_{11} = R_{11}/q^2 - 1/3$) in (44) and, therefore, *indirectly* reduces the production term in the kinetic energy equation, is more important than the *direct* role of Π . For future reference, we now put forth some useful results concerning the anisotropy tensor $b_{ij} = \langle u_i u_j \rangle / q^2 - \frac{1}{3} \delta_{ij}$, and a recommended general decomposition for the Reynolds stress:

$$R_{ij} = q_s^2 \left(\frac{\delta_{ij}}{3} + b_{ij}^{e(s)} + b_{ij}^{z(s)} \right) + \langle u_i^s u_j^d \rangle + \langle u_i^d u_j^s \rangle + q_d^2 \left(\frac{\delta_{ij}}{3} + b_{ij}^{e(d)} \right), \quad (46)$$

where the solenoidal deviator b_{ij}^s is split into a part reflecting the directional dependence (superscript e) and the "polarization" (subscript z) (Cambon *et al.* 1992). This decomposition can be recovered using the "structure tensors" introduced by Reynolds (1990) (see also BMR) via

$$D_{ij}^s = \langle \psi_{i,l} \psi_{l,j} \rangle = \int 2 \frac{k_i k_j}{k^2} e^s(\mathbf{k}, t) d^3 \mathbf{k} = q_s^2 \left(\frac{\delta_{ij}}{3} - 2b_{ij}^{e(s)} \right) \quad (47a)$$

$$C_{ij}^s = \langle \psi_{i,l} \psi_{j,l} \rangle = \int \frac{e_{ij}^s(\mathbf{k}, t)}{k^2} d^3 \mathbf{k} = q_s^2 \left(\frac{\delta_{ij}}{3} + b_{ij}^{e(s)} - b_{ij}^{z(s)} \right) \quad (47b)$$

$$D_{ij}^d = \langle \varphi_{i,l} \varphi_{l,j} \rangle = \int 2 \frac{k_i k_j}{k^2} e^d(\mathbf{k}, t) d^3 \mathbf{k} = q_d^2 \left(\frac{\delta_{ij}}{3} + b_{ij}^{e(d)} \right). \quad (48)$$

To show the equivalence of the two approaches we first note that the tensors in (47) and (48) are formally defined using the vector ψ_i or scalar φ potential functions according to the Helmholtz decomposition (18) in physical space. The three-dimensional spectra are then defined (the second equality in (47) and (48)), with e^s , e^d and e_{ij}^s being associated with respectively $\frac{1}{2} \langle \hat{u}_i^s \hat{u}_i^s \rangle = \frac{1}{2} \langle \hat{\varphi}^{(\alpha)} \hat{\varphi}^{(\alpha)} \rangle$, $\frac{1}{2} \langle \hat{u}_i^d \hat{u}_i^d \rangle = \frac{1}{2} \langle \hat{\varphi}^{(3)} \hat{\varphi}^{(3)} \rangle$, and $\langle \hat{\omega}_i \hat{\omega}_j \rangle$. Finally, the directional-polarization anisotropy tensors are specified (the third equality) so that the two approaches are reconciled.

In the notation of Reynolds (1990), D_{ij}^s reflects the "dimensionality" of the solenoidal field, which is close to the directional anisotropy, whereas C_{ij}^s is associated with the "componentality" of the turbulence. Only the dimensionality, or directional anisotropy, is needed for the dilatational velocity field since $D_{ij}^d = \langle u_i^d u_j^d \rangle$ (BMR). This reflects the single-component character of u_i^d , in contrast to the two-component structure of the solenoidal field. We finally note that the above tensors are not all independent; for example, C_{ij}^s can be derived from the other tensors using (46)–(48), or equivalently the equation found by Reynolds (1992):

$$\langle u_i^s u_j^s \rangle + D_{ij}^s + C_{ij}^s = q_s^2 \delta_{ij}.$$

It is hoped that the above general expressions will be useful in future attempts to model compressible flows. For the present, however, we narrow our approach as we use DNS results to test a few aspects of the rapid distortion analysis.

3.2. Comparison to DNS of rapid axial compression

The DNS results were obtained using a pseudo-spectral method to solve the compressible Navier-Stokes equations over a homogeneous domain in coordinates that move with the mean deformation (Rogallo 1981, BMR, Coleman & Mansour 1991). As mentioned previously, the mean density ratio, $J^{-1} = \bar{\rho}(t)/\bar{\rho}(0)$ varies from 1 to 5 during the compression. The runs use for initial conditions compressible isotropic turbulence at various turbulent Mach numbers that have evolved from velocity fields, with finite dilatational components, that are in near acoustic equilibrium; these initial fields are generated by running the code with no mean straining until they develop realistic triple-velocity correlations and dilatational energy for

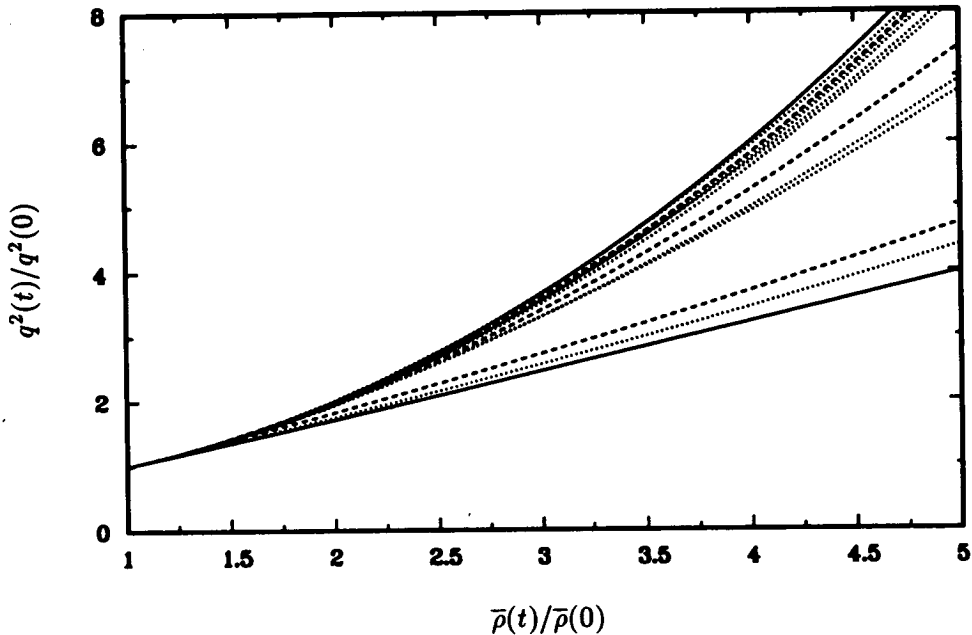


FIGURE 3. Turbulent kinetic energy histories: —, lower, Eq. (38a); —, upper, Eq. (38b); ·····, DNS with initial Δm ranging from 0.3 (lower) to from 3.0–8.0 (upper); ----, DNS Cases: lower, C1DJ ($M_t, \Delta m$) $_{t=0} = (0.03, 0.3)$; upper, C1DV (0.1, 7); middle, C1DW (0.3, 1).

the given M_t . (Note that BMR have found that compressible isotropic turbulence strongly depends upon *all* the initial conditions for the dilatational field, not just M_t , which implies that had we begun the precomputation with, for example, a purely solenoidal field, the levels of dilatational energy in the developed flow might be significantly different than those found here.) The initial turbulent Mach number for the runs varies from 0.03 to 0.44, the initial nondimensional compression speed $r = |D|q^2/\epsilon$ ranges from 50 to 800 (and $|D|/\langle\omega_i\omega_i\rangle^{1/2}$ from 2 to 88), and the initial values of $\Delta m = M_t|D|/\langle\omega_i\omega_i\rangle^{1/2}$ fall between 0.26 and 7. A ratio of constant specific heats $\gamma = 5/3$ and temperature dependent viscosity $\mu = T^{0.72}$ is assumed. All the runs used 96^3 grid points and were generated on the Intel Hypercube/i860 at the NASA Ames Numerical Aerodynamic Simulation program.

Results for the total (solenoidal and dilatational) turbulent kinetic energy will first be presented. In Figure 3, the DNS histories for $\langle\rho u_i u_i\rangle/\bar{\rho}$ are plotted against the mean density ratio $J^{-1} = \bar{\rho}(t)/\bar{\rho}(0)$. (Because it is convenient in the code to solve for momentum rather than velocity, all of the DNS results presented approximate velocity correlations by using density weighted averages. We find for our purposes

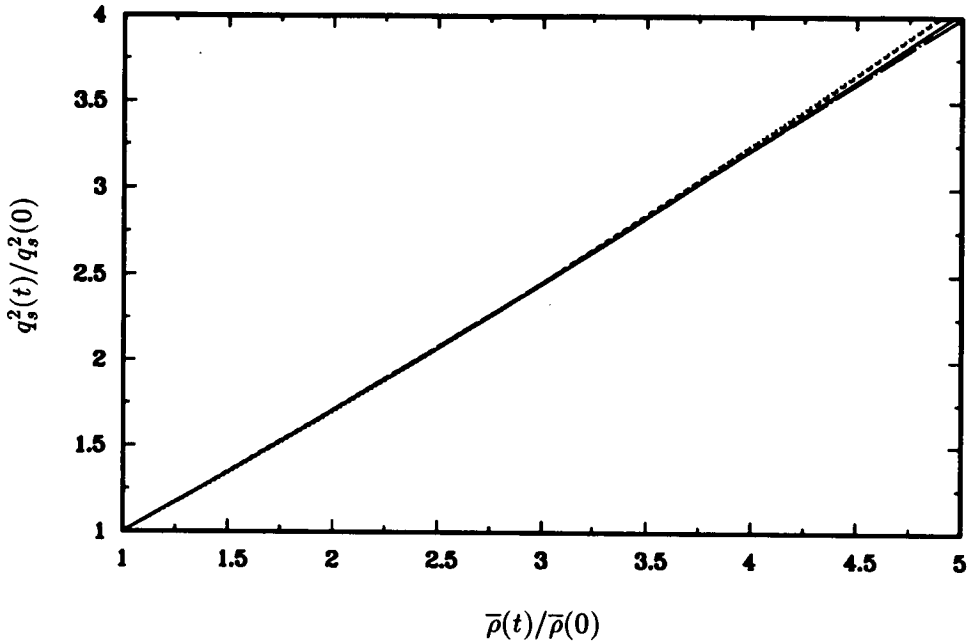


FIGURE 4. Solenoidal turbulent kinetic energy histories: —, C1DJ ($M_t, \Delta m$) _{$t=0$} = (0.03, 0.3); ----, C1DV (0.1, 7); , C1DW (0.3, 1); — — —, Eq. (38a).

that the uncertainty introduced by comparing the DNS Favre averages to the RDT Reynolds averages is unimportant.) These curves strongly support the validity of the RDT analysis presented above in that all the DNS results lie between the lower solenoidal (“ A_s ”) and upper pressure-releases (“ A_p ”) RDT limits and that rate of energy amplification scales almost monotonically with the initial value of Δm , which varies from 0.3 for the lower (dotted) curve to from 3 to 8 for the upper (dotted) curves. Three runs will be examined further, those represented by the dashed curves in Figure 3. Cases C1DJ, C1DV, and C1DW have initial M_t equal to 0.03, 0.1, and 0.3, respectively, but the compression rates are such that the corresponding order for Δm is 0.3, 7, and 1. At the end of the compression the ($M_t, \Delta m$) values for C1DJ, C1DV, and C1DW are respectively (0.03, 13), (0.2, 79), and (0.4, 6).

Figure 4 confirms that Eq. (38a) is an excellent approximation for q_s^2 for the three cases considered and that the solenoidal field is, in fact, unaffected by the dilatational field, as predicted by the RDT. Both contributions to the kinetic energy are shown in Figure 5. We see that the dilatational energy is most important at the end of the compression, when the pressure-released regime dominates. The initial values of the dilatational-to-solenoidal energy ratio λ_0 for the various runs is also apparent.

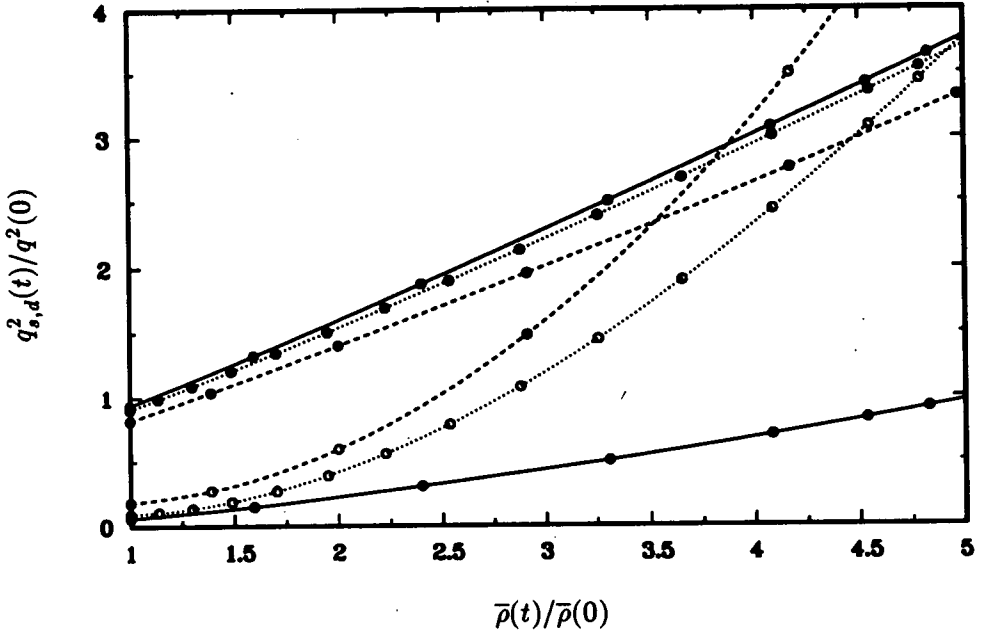


FIGURE 5. Solenoidal and dilatational turbulent kinetic energy histories: \bullet , solenoidal; \circ , dilatational; —, C1DJ ($M_t, \Delta m)_{t=0} = (0.03, 0.3)$; ----, C1DV (0.1,7); , C1DW (0.3,1).

These results suggest the following model for the Mach number dependence of the kinetic energy behavior during a rapid axial compression:

$$q_s^2(t) = A_s(J)q_s^2(0) \quad (49a)$$

$$q_d^2(t) = A_p(J)q_d^2(0) + (A_p^+(J) - A_s^+(J))q_s^2(0), \quad (49b)$$

where the “interpolation functions” A_p^+ and A_s^+ are assumed to vary monotonically with Δm , increasing from zero to maxima of A_p and A_s , respectively. Similar agreement with DNS data is found for the other correlations given in (43). The results for $\langle u_1^s u_1^s \rangle$ and $\langle u_1^d u_1^d \rangle$ are presented on Figure 6, where the DNS and RDT histories closely correspond. The slight overamplification of the DNS result compared to the analytical $\langle u_1^s u_1^s \rangle / q_s^2 = B_s / A_s$ ratio becomes more pronounced with increasing Δm . For the dilatational curves in Figure 6, $\langle u_1^d u_1^d \rangle / q_d^2$, we find the expected trend with Δm , since they are closest to the analytical pressure-released expression (the “chain-dash” curve) when Δm is largest. An analog to (49) is therefore proposed as a model for the dilatational Reynolds stress:

$$\frac{\langle u_1^d u_1^d \rangle}{q_d^2} = \frac{B_p(J)\lambda_0 + B_p^+(J) - B_s^+(J)}{A_p(J)\lambda_0 + A_p^+(J) - A_s^+(J)}, \quad (50)$$

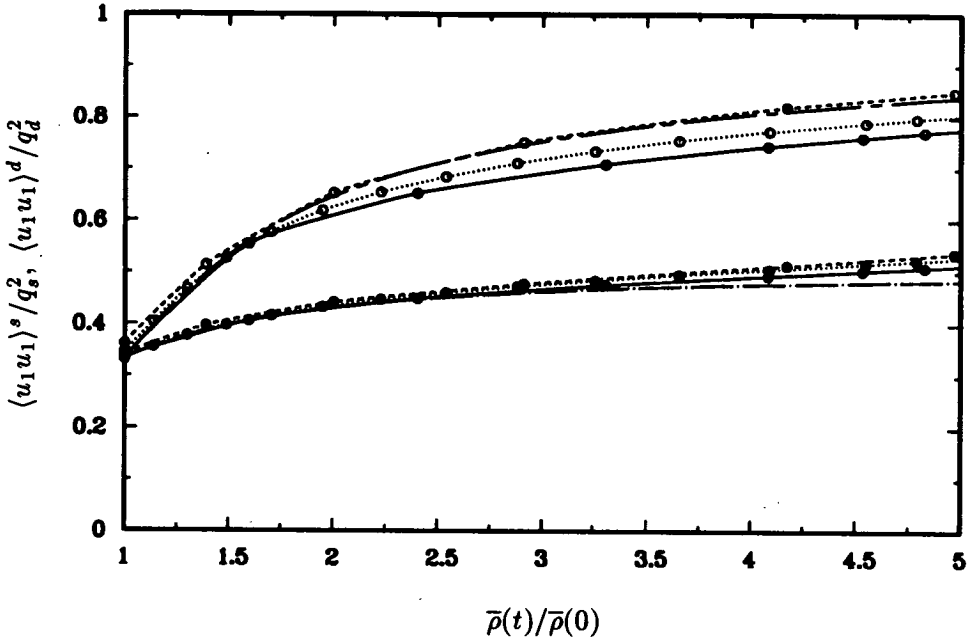


FIGURE 6. Histories of the anisotropy of solenoidal and dilatational turbulent kinetic energy: ●, solenoidal; ○, dilatational; —, C1DJ $(M_t, \Delta m)_{t=0} = (0.03, 0.3)$; ----, C1DV (0.1,7); ·····, C1DW (0.3,1); — — —, Eqs. (38a), (39a); — · —, Eqs. (38a, b), (39a, b), using $\lambda_0 = 0.22$ from Run C1DV.

where λ_0 is the initial ratio of the dilatational to solenoidal kinetic energy (which in practice might be neglected). The curves in Figure 6 suggest that the ratio $(B_p^+ - B_s^+) / (B_p - B_s)$ is smaller than the same ratio of "A" functions.

Another anisotropy measure is investigated in Figure 7, where the structure tensors are presented. Recall that $D_{11}^d = \langle u_1^d u_1^d \rangle$. The fact that $D_s = B_s$ in (41a) confirms that $b_{ij}^{e(s)} = -\frac{1}{2}b_{ij}^s$ and $b_{ij}^{z(s)} = \frac{3}{2}b_{ij}^s$ is a good approximation for axisymmetric strain, as suggested by studies of non-isotropic initial data under rapid rotation (Reynolds 1990, Cambon *et al.* 1992, Mansour *et al.* 1991). Rapid rotation was shown to damp $b_{ij}^{z(s)}$ and, therefore, to reveal the initial anisotropy of $b_{ij}^{e(s)}$ as the asymptotic limit reached after several revolution times. In axisymmetric turbulence, D_{11}/q^2 can be interpreted as an angular coefficient $\cos^2 \alpha$, as implied by the integrands in (47) and (48), which reveals the conical structure of the spectral region that contains energy (around the symmetry axis). For example, a value of 1/3 for this coefficient suggests no angular dependence (directional isotropy), whereas a value between 0 and 1/3 suggests a relative concentration of spectral energy in the plane normal to the symmetry axis. Unfortunately, the situation is

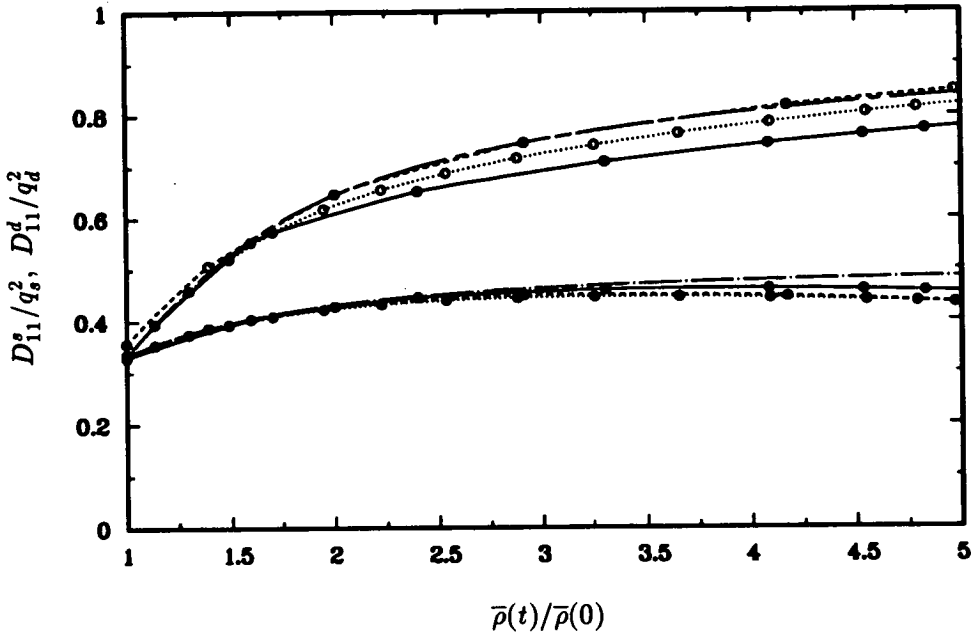


FIGURE 7. Structure tensor histories: \bullet , solenoidal; \circ , dilatational; —, C1DJ $(M_t, \Delta m)_{t=0} = (0.03, 0.3)$; ----, C1DV (0.1,7); , C1DW (0.3,1); —·—, Eqs. (38a), (41a); — — —, Eqs. (38a, b), (39a, b), using $\lambda_0 = 0.22$ from Run C1DV.

more complex in the presence of a mean distortion, which causes a variation in direction of the time-dependent wavevector; in the pressure-released case, the angular distribution of spectral energy is unchanged with respect to (isotropic) initial data, but the wavevector tends to be aligned with the symmetry (compression) direction (see (36)) so that $\cos^2 \alpha$ increases and tends to 1. On the other hand, in the pure solenoidal limit, the relative concentration of spectral energy in the plane normal to the compression direction opposes the tendency induced by the wavevector motion so that a slower (as compared to the pressure-released case), but still positive, net increase of the anisotropy is obtained. Note that the solenoidal ratio of D_{11}^s/q_s^2 given by the DNS is found to be slightly lower than the RDT analytical prediction.

The cross-correlation $\langle u_1^s u_1^d \rangle / \langle u_1^s u_1^s \rangle$ is plotted in Figure 8 and compared to the RDT expression $C_p(J)/B_s(J)$ from (39a) and (40b). The results suggest that for modeling purposes it might be advantageous to use an effective “saturated” volumetric ratio J^+ in place of J and define C_p^+ , an interpolating function for the cross-correlation, according to

$$\frac{C_p^+(J)}{B_s^+(J)} = \frac{C_p(J^+)}{B_s(J^+)}, \tag{51a}$$

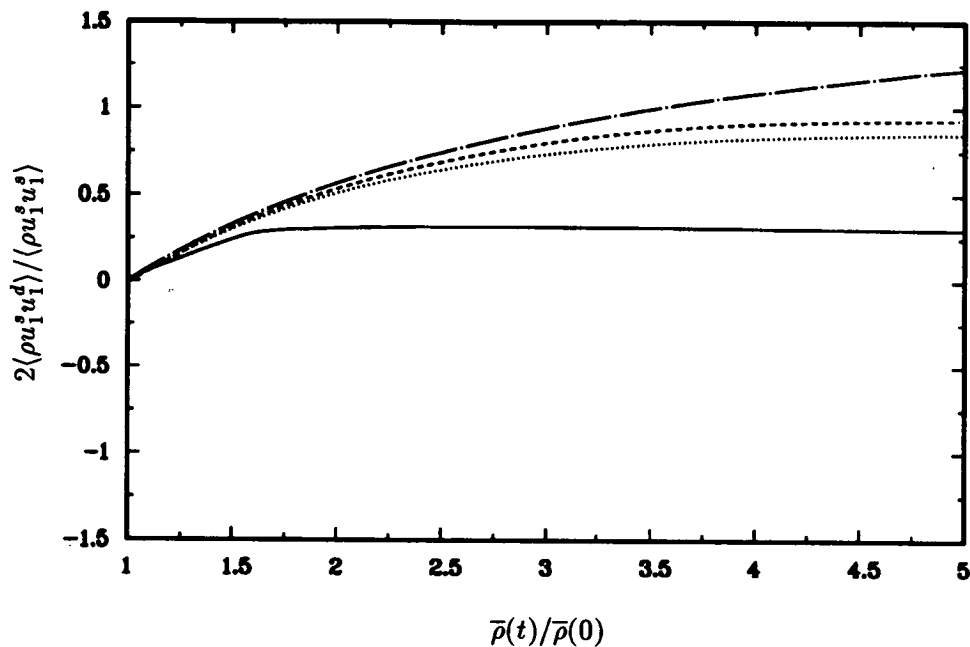


FIGURE 8. Histories of the compression-direction component of the dilatational-solenoidal Reynolds stress correlation: —, C1DJ ($M_t, \Delta m)_{t=0} = (0.03, 0.3)$; ----, C1DV (0.1, 7); , C1DW (0.3, 1); —·—, Eqs. (39a), (40b).

and use the model

$$\langle u_1^s u_1^d \rangle = C_p(J^+) q_s^2(0). \quad (51b)$$

The parameter J^+ would tend toward the actual J in the pressure-released limit and approach unity in the solenoidal limit. The role of pressure will be discussed further in §4; for now, we observe in Figures 9 and 10 the dramatic increase of both pressure variance and pressure-dilatation terms caused by the compression. The amplification increases with the initial turbulent Mach number, which at first seems to conflict with the idea of a pressure released limit. The paradox disappears, however, if the pressure-dilatation term is no longer nondimensionalised by initial values (as is done in Figures 9 and 10), but rather scaled by a term proportional to the kinetic energy production. DNS results for Π/Dq^2 are presented on Fig. 11. The magnitude of this term is found to decrease with increasing Δm for the three cases considered. This implies a non-monotonic variation with Δm for this term (since it is identically zero in the solenoidal limit) with a maximum reached at low compressibility. It can be noticed that increasing values of Π/Dq^2 are found at large J^{-1} for the intermediate Δm case (C1DW), which we expect cannot be explained by RDT. This illustrates that the requirements for a compression to be

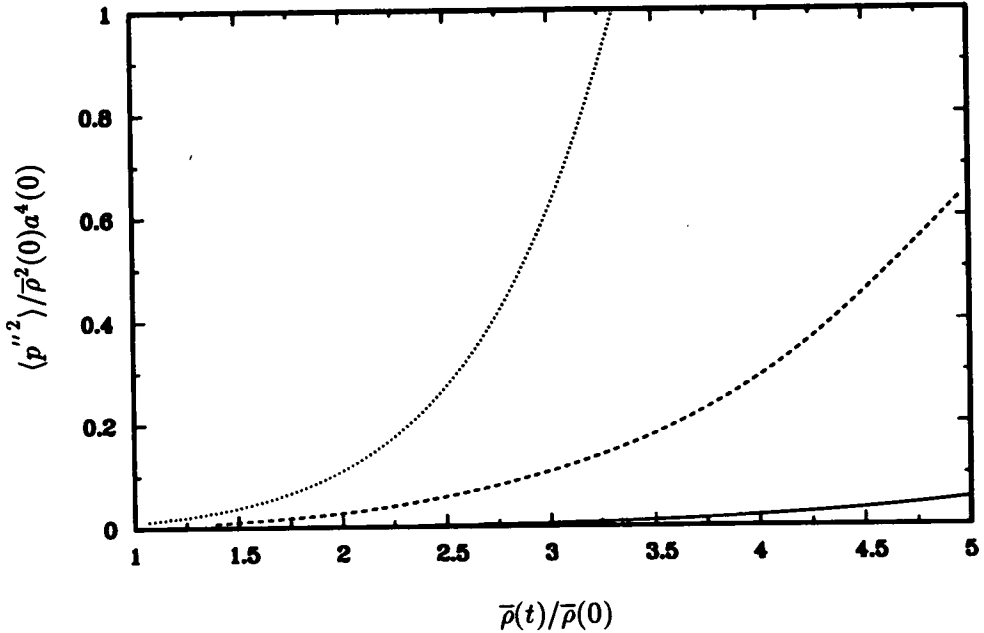


FIGURE 9. Pressure variance histories: —, C1DJ $(M_t, \Delta m)_{t=0} = (0.03, 0.3)$; ----, C1DV (0.1,7); , C1DW (0.3,1).

rapid enough for RDT to be valid are more difficult to meet when the flow is intrinsically compressible, a fact also stressed by Zeman & Coleman (1992). The term Π_{11}/Dq^2 linked to the compression-direction component of the pressure-strain rate correlations is shown in Figure 12. The solenoidal RDT expression, $E_s(J)/A_s(J)$, from (38a) and (42a) is plotted and is found to give an upper limit to the DNS curves. These results suggest a monotonic decrease of Π_{11}/Dq^2 with increasing Δm . Moreover, comparisons of the order of magnitude for both terms on Figures 11 and 12 (noting the different scales of the two plots) show that the compression-direction component of the pressure-strain rate is dominant compared to its trace (pressure-dilatation term) in all cases. This confirms that the reduction of amplification of turbulent kinetic energy with respect to the pressure-released case (where only the “production” effects are present) is mainly due to Π_{11} , through reduction of anisotropy, as in the pure solenoidal case.

4. Towards a pressure-strain rate model

Equations for Π_{11} and Π , valid for the rapid mean compression case, can be derived from eqs. (44) and (45), using eqs. (49) and (50) to model q^2 and $\langle u_1 u_1 \rangle$.

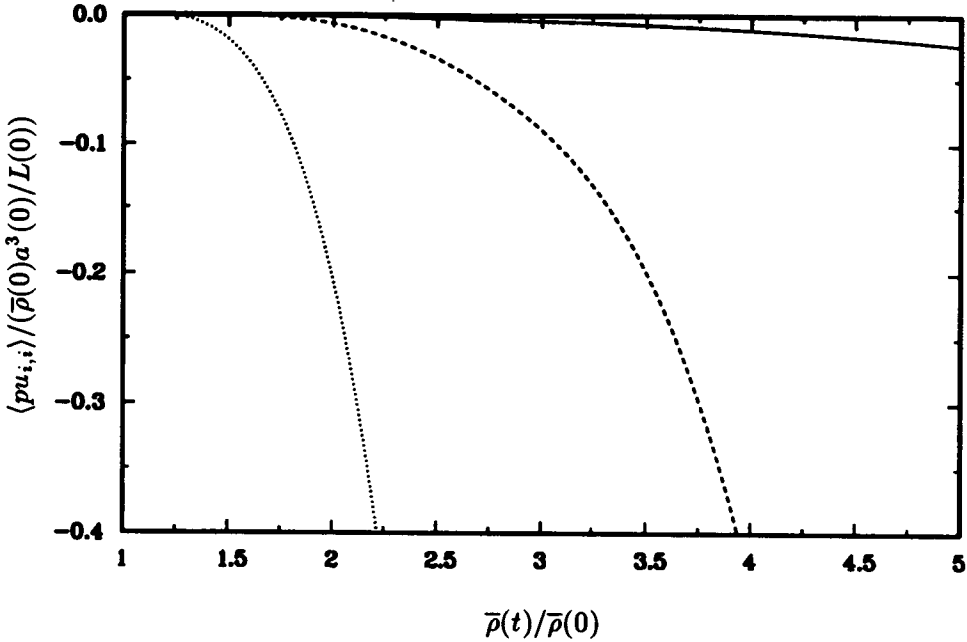


FIGURE 10. Pressure-dilatation correlation histories: —, C1DJ $(M_t, \Delta m)_{t=0} = (0.03, 0.3)$; ----, C1DV $(0.1, 7)$; ·····, C1DW $(0.3, 1)$.

The result is

$$\begin{aligned} \Pi_{11} &= J^{-2} \frac{d}{dt} (J^2 R_{11}) \\ &= J^{-2} \frac{d}{dt} (J^2 (B_s + B_p^+ - B_s^+) q_s^2(0) + J^2 B_p q_d^2(0)) \\ &= D E_s q_s^2(0) + J^{-2} \frac{d}{dt} (J^2 (B_p^+ - B_s^+)) q_s^2(0), \end{aligned} \quad (52)$$

and

$$\begin{aligned} \Pi &= \left(\frac{1}{2} (\dot{A}_s + \dot{A}_p^+ - \dot{A}_s^+) + D (B_s + B_p^+ - B_s^+) \right) q_s^2(0) \\ &= \left(\frac{1}{2} (\dot{A}_p^+ - \dot{A}_s^+) + D (B_p^+ - B_s^+) \right) q_s^2(0). \end{aligned} \quad (53)$$

To obtain the above, the relations

$$J^{-2} \frac{d}{dt} (J^2 B_s) = E_s; \quad \frac{d}{dt} (J^2 B_p) = 0; \quad \frac{1}{2} \dot{A}_s + D B_s = 0; \quad \frac{1}{2} \dot{A}_p + D B_p = 0, \quad (54)$$

have also been used.

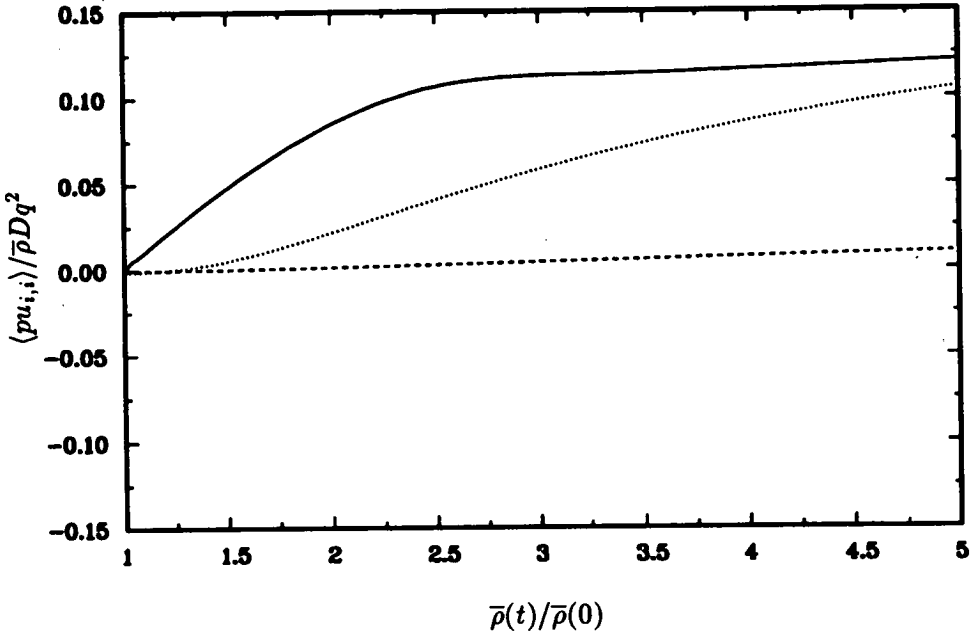


FIGURE 11. Rescaled pressure-dilatation correlation histories: —, C1DJ ($M_t, \Delta m)_{t=0} = (0.03, 0.3)$; ----, C1DV (0.1,7); , C1DW (0.3,1).

4.1 Proposals for Second-Order Modeling

Two simple ideas for constructing the Eq. (52) and (53) “interpolation” functions (denoted by a superscript “+”) are proposed:

1. Using two functions of Δm , passing monotonically from 0 to 1 so that $A_p^+ - A_s^+ = f_1(A_p - A_s)$ and $B_p^+ - B_s^+ = f_2(B_p - B_s)$; if the time-variation of the interpolation functions is neglected, this leads to the model

$$\Pi_{11} = \Pi_{11}^+(1 - f_2) \tag{55a}$$

$$\Pi = (f_2 - f_1)D(B_p - B_s)q_s^2(0). \tag{55b}$$

Note that $f_2 > f_1$ is consistent with the sign of Π found in the DNS results and with the interpretation of dilatational energy histories in Figure 5.

2. Using a “saturated” volumetric ratio J^+ instead of the actual J in the evaluation of the interpolation functions with + superscripts, so that $A^+(J) = A(J^+)$. The equation for J^+ would be

$$j^+ = U_{i,i}J^+ - C_{J^+} \frac{a}{L}(J^+ - 1), \tag{55c}$$

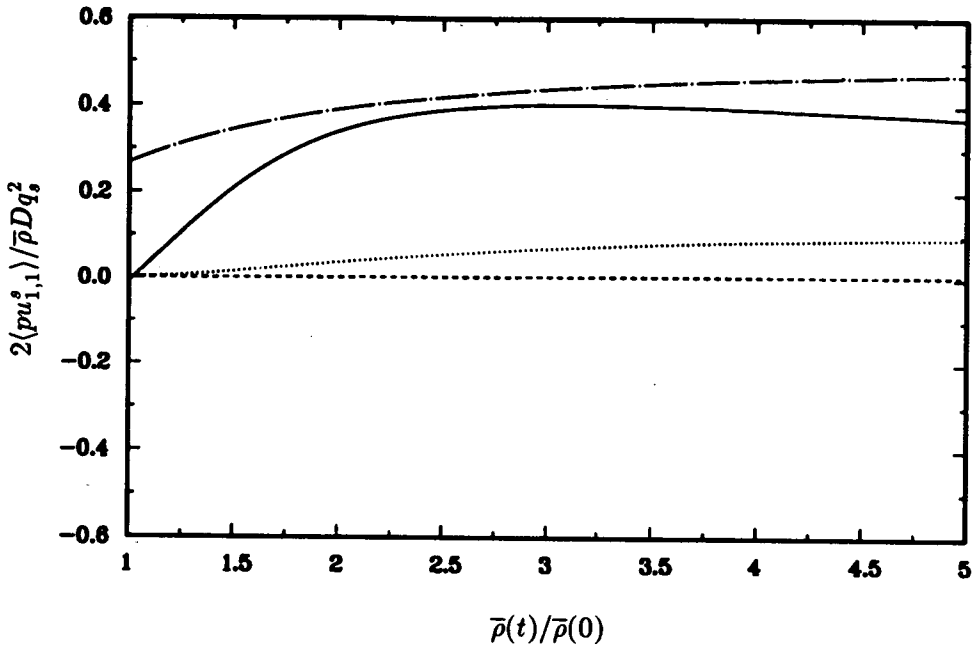


FIGURE 12. Histories of correlation of pressure and compression-direction velocity gradient: —, C1DJ ($M_t, \Delta m)_{t=0} = (0.03, 0.3)$; ----, C1DV (0.1,7); , C1DW (0.3,1); —·—, Eqs. (38a) and (42a).

where C_{J^+} is a modeling constant. The sonic timescale-damping term would allow J^+ to saturate close to unity as the regime of the flow approaches the solenoidal limit.

4.2 Testing a Second-Order Model

From our analysis of the three DNS cases, we find that they are in the regime where the production and the rapid redistribution terms are dominant. The contribution of the pressure-dilatation is about 10% of the production in the worst case. This leads us in our attempt to model the DNS results to adopt the first proposal of the previous subsection, and consider a linear (in b_{ij}) model for the solenoidal rapid part (see Shih *et al.*, 1990) of the redistribution term, taking $1 - f_2$ (see Eq. (55a)) to be an exponential function of Δm . The mean and Reynolds-stress equations reduce to:

$$\bar{\rho}_{,t} = -U_{i,i}\bar{\rho}, \quad U_{i,j} = \frac{D_0}{1 + D_0 t} \delta_{i1} \delta_{j1}, \quad T_{,t} = -(\gamma - 1)TU_{i,i},$$

$$R_{ij,t} = -R_{ik}U_{j,k} - R_{jk}U_{i,k} + \Phi_{ij} \exp(-\Delta m / C_{\Delta m}),$$

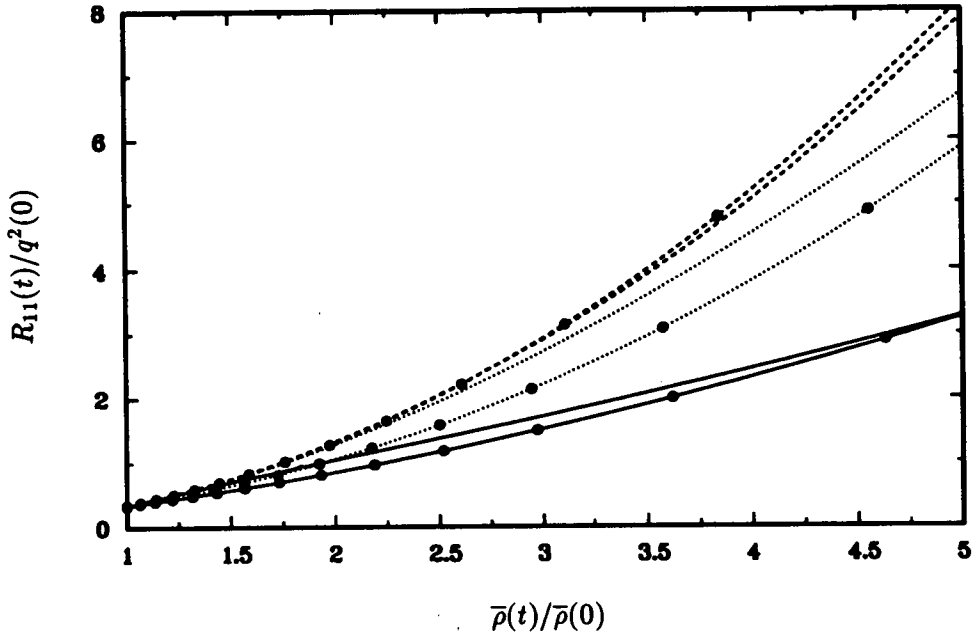


FIGURE 13. Reynolds stress history, compression-direction component: —, C1DJ ($M_t, \Delta m)_{t=0} = (0.03, 0.3)$; ----, C1DV (0.1,7); , C1DW (0.3,1); •, Eq. (55d); no symbols, DNS.

with

$$\begin{aligned} \frac{\Phi_{ij}}{\frac{1}{2}q^2} = & \frac{4}{5}S_{ij}^* + \frac{48\alpha - 60}{35} (S_{ik}^*b_{kj} + S_{jk}^*b_{ki} - \frac{2}{3}S_{mn}^*b_{mn}\delta_{ij}) \\ & + \frac{60 - 16\alpha}{15} (\Omega_{ki}b_{kj} + \Omega_{kj}b_{ki}), \end{aligned} \quad (55d)$$

where $\Delta m = \sqrt{S_{ij}S_{ji}}M_tq^2/\epsilon$ and we have set $\alpha = 2.523$ (to be consistent with the model of Launder *et al.* (1975)), and $C_{\Delta m} = 40$. The quantity $\Omega_{ij} = (U_{i,j} - U_{j,i})/2$ is the mean rotation tensor.

The development of the axial component of the Reynolds stress, R_{11} , as predicted by the above model for the three cases considered is shown in figure 13. We find that this simple model, where the effects of the redistributive term diminish when M_t increases, compares well with the DNS data. The development of the turbulent kinetic energy (see Fig. 14) is also well reproduced, indicating that the effects of the pressure-dilatation are, in fact, weak compared to the production term. No attempt was made to optimize the constant $C_{\Delta m}$ since the pressure-dilatation term was neglected. This term does play a role in the development of the flow, and $C_{\Delta m}$ should be optimized in conjunction with a model for the pressure dilatation term.

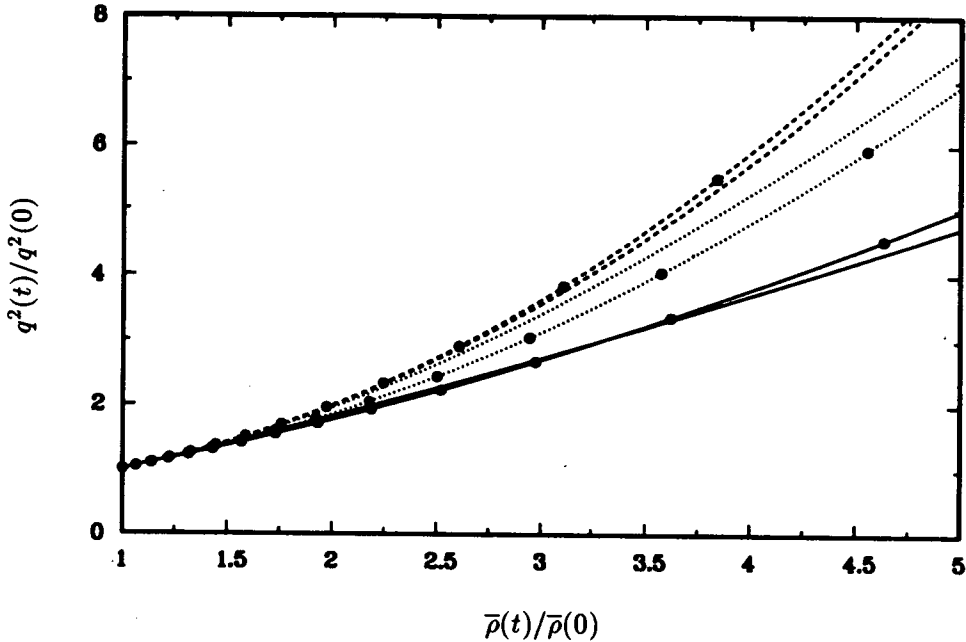


FIGURE 14. Turbulent kinetic energy history: —, C1DJ ($M_t, \Delta m)_{t=0} = (0.03, 0.3)$; ----, C1DV (0.1,7); , C1DW (0.3,1); •, Eq. (55d); no symbols, DNS.

5. Spherical compression and pure shear revisited

5.1. Isotropic spherical compression

In the presence of a mean spherical compression, with

$$U_{i,j} = D\delta_{ij}, \quad D = \frac{D_0}{1 + D_0 t} = D_0 J^{-1/3} \quad F_{ij} = J^{1/3} \delta_{ij} \quad \text{and} \quad k_i = K_i J^{-1/3}, \quad (56)$$

the coupling term $m_{3\alpha}$ in (27) and (28) has zero value. The evolution of the solenoidal kinetic energy is then easily found to be given by the amplification coefficient $J^{-2/3}$. For the dilatational field, eqs. (33) and (34) remain of interest now with their right-hand sides equal to zero (since $\hat{p}^s \sim m_{3\alpha}$). Even in the absence of the right-hand sides, a WKB analysis of the equations would not in general be appropriate because the timescale variation of a^2 and k^2 is not necessarily small with respect to the expected frequency ak of the oscillating system (depending on the value of Δm). Blaisdell (1992, private communication) has recently found a solution free of WKB assumptions; its validity is restricted to values of γ close to $5/3$, but a general analytical solution is possible (work in progress). If $\gamma = 5/3$, k^2 and a^2 have the same $J^{-2/3}$ time dependence, so simple solutions in terms of $\exp(\pm ia(0)k(t)t)$, where $k(t)$ varies as in (56), can be obtained for y and z . The

history of q_d^2 can then be derived from the initial (uncompressed) dilatational field. Assuming that acoustic equilibrium holds for the initial conditions, one can write

$$q_d^2(t) = J^{-2/3} q_d^2(0), \quad (57)$$

which is the same variation found for the solenoidal energy. The acoustic equilibrium assumption is realistic but perhaps not necessary; the initial balance between kinetic dilatational energy and potential (pressure) energy allows oscillating terms to be dropped, but the same final result could also be reached after a certain elapsed time because of the damping behavior of integrals such as

$$\int F(K) \exp(2ia(0)KJ^{-1/3}t) dK,$$

where F is defined by the initial energy spectra and is nonzero only for flows out of acoustic equilibrium. (This behavior is similar to that found for the case of rapid rotation.)

The above considerations show that an oscillating regime, more general than the pure acoustic one, is not inconsistent with the pressure-released limit and that the latter can be used to derive the same relationship (57) found via the acoustic equilibrium assumption. We thus find that the spherically compressed flow lends support to the general approach advocated in this paper.

5.2. Pure plane shear

The case of shear flow is particularly interesting because all the coupling terms, most notably $m_{\alpha 3}$ and $m_{3\alpha}$, are present. The crucial parameter in the absence of compression ($J = 1$) is the shear $S = dU_1/dx_2$. Under this deformation, eqs. (27), (33) and (34) become

$$\dot{\hat{\varphi}}^{(1)} + S \frac{k_3}{k} \hat{\varphi}^{(2)} = S \left(\frac{k_3 k_2}{(k_1^2 + k_3^2)^{1/2}} \right) y \quad (58a)$$

$$\frac{D}{Dt} (k \hat{\varphi}^{(2)}) = -S \left(\frac{k_1}{(k_1^2 + k_3^2)^{1/2}} \right) k^2 y \quad (58b)$$

$$\ddot{y} + a_0^2 k^2 y + S^2 \frac{k_1^2}{k^2} y = S^2 \frac{D}{D(S t)} \left(\frac{k_1 (k_1^2 + k_3^2)^{1/2}}{k^3} \right) k \hat{\varphi}^{(2)}, \quad (59)$$

with

$$U_{i,j} = S \delta_{i1} \delta_{j2}, \quad k_1 = K_1, \quad k_2 = K_2 - K_1 S t \quad \text{and} \quad k_3 = K_3.$$

Here the polar axis is chosen to be in the gradient direction ($n_i = \delta_{i2}$). The two solenoidal $\hat{\varphi}^{(1)}$ and $\hat{\varphi}^{(2)}$ components are very close to the set $(\omega_2, \nabla^2 u_2)$ used in linear stability analyses for decoupling, for example, the Orr-Sommerfeld equations for parallel flows (cf. Waleffe 1990). Even in the pure solenoidal case (where $y = \hat{\varphi}^{(3)}/k = 0$), the present approach appears to be more tractable than are classic RDT approaches (Townsend 1976). Unlike for a purely irrotational mean deformation,

the presence of the new coupling terms (mediated by $m_{13} = -Sk_2k_3/kk_{13}$, $m_{23} = Sk_3/k_{13}$ in the above equations) makes the solenoidal field no longer independent of the dilatational component. In addition, this coupling introduces the new term $S^2(k_1^2/k^2)y$ in Eq. (59). The pressure-released approximation amounts to neglecting $a_0^2k^2y$ compared *both* to this new term and to the solenoidal right-hand side in (59). The $\Delta m \gg 1$ regime then implies that (in physical space),

$$u_1 = u_1(0) - St u_2(0), \quad u_2 = u_2(0) \quad \text{and} \quad u_3 = u_3(0),$$

and leads to quadratic amplification, with respect to St , of the kinetic energy (which is more rapid than the nearly linear amplification obtained by numerically integrating the solenoidal RDT solution for $\frac{1}{2}(\widehat{\varphi}^{(1)*}\widehat{\varphi}^{(1)} + \widehat{\varphi}^{(2)*}\widehat{\varphi}^{(2)})$ over \mathbf{k} -space). Note that the inviscid *solenoidal* RDT solution for the vertical velocity component is given by $\mathcal{D}(\nabla^2 u_2)/\mathcal{D}t = 0$ in physical space (corresponding to Eq. (58) with $y = 0$) so that a rapid decay of u_2 is found. On the other hand, u_2 is conserved in the pressure-released inviscid RDT limit.

6. Recap and conclusions

The objective of this analysis has been to develop a rapid distortion theory for homogeneous compressible turbulence at finite Mach number and then use that theory to explore some issues related to one-point compressible turbulence models. We have applied the analysis to the case of axial compression and found that DNS results confirm the RDT prediction of two distinct flow regimes, one for vanishingly small turbulent Mach number and the other for flows with negligible sonic and turbulent timescale variations compared to the mean distortion. The latter is referred to as the pressure-released regime (since the fluctuating pressure field can be neglected in the RDT for this limit) and is defined by large values of the product of M_t and the ratio of the turbulent to mean deformation timescales. For large values of this parameter, we find that the intrinsic compressibility of the turbulence is responsible for an *increase* in the growth rate of kinetic energy with increasing M_t , an effect exactly opposite to that usually attributed to the compressibility. It would seem that the reduction in kinetic energy growth rate due to compressibility observed in previous compressible homogeneous DNS studies can be attributed to “slow” terms with nonlinear and dissipative origin, such as the “extra” dilatational dissipation associated by Zeman (1990) with eddy “shocklets.” In the future, we plan to perform systematic comparisons between compressible RDT (from numerical solutions obtained by the method presented in §§2.4) and existing DNS to allow an accurate differentiation between the “rapid” and “slow” terms, which are found to have opposite trends with respect to the effect of compressibility on the kinetic energy growth rate.

For the axial compression, analytic expressions for the correlations associated with one-point closures for both the solenoidal and pressure-released limits have been given. These expressions have been used to propose methods of interpolating between the two limiting RDT cases in models for the pressure-strain rate correlation, Π_{ij} and thus account for finite Mach number effects.

All the DNS results were obtained using the facilities of the Numerical Aerodynamic Simulation program. This work was partially supported by the Laboratoire de Mécanique des Fluides et d'Acoustique, Ecole Centrale de Lyon.

REFERENCES

- BATAILLE, F., BERTOGLIO J. P. & MARION, J. D. 1992 Spectral study of weakly compressible isotropic turbulence. To appear in *C. R. Académie des Sciences*, Paris.
- BATCHELOR, G. K. & PROUDMAN, I. 1954 The effect of rapid distortion on a fluid in turbulent motion. *Q. J. Mech. Appl. Math.* **7**, 83.
- BLAISDELL, G. A., MANSOUR N. N. & REYNOLDS, W. C. 1991 Numerical simulation of compressible homogeneous turbulence. Department of Mechanical Engineering, Stanford University, Thermosciences Division Report TF-50.
- CAMBON, C. 1982 Etude spectrale d'un champ turbulent incompressible soumis à des effets couplés de déformation et de rotation imposés extérieurement. *thèse d'Etat*. Université Claude-Bernard-Lyon I.
- CAMBON, C. 1990 Single and double point modeling of homogeneous turbulence. *CTR Annual Research Briefs*. Stanford University/NASA Ames.
- CAMBON, C., TEISSÈDRE, C. & JEANDEL, D. 1985 Etude d'effets couplés de déformation et de rotation sur une turbulence homogène. *J. Méc. Théor. Appl.* **4**, 629.
- CAMBON, C. & JACQUIN, L. 1989 Spectral approach to non-isotropic turbulence subjected to rotation. *J. Fluid Mech.* **202**, 295.
- CAMBON, C., JACQUIN, L. & LUBRANO, J. L. 1992 Toward a new Reynolds stress model for rotating turbulent flows. *Phys. Fluids A.* **4**(4), 812.
- COLEMAN, G. N. & MANSOUR, N. N. 1991 Modeling the rapid spherical compression of isotropic turbulence. *Phys. Fluids A.* **3**(9), 2255.
- CRAYA, A. 1958 Contribution à l'analyse de la turbulence associée à des vitesses moyennes P.S.T. No. 345.
- DEBIÈVE, J. F., GOUIN H. & GAVIGLIO J. 1982 Evolution of the Reynolds stress tensor in a shock wave turbulence interaction. *Indian J. Tech.* **20**, 90.
- DURBIN, P. A. & ZEMAN, O. 1992 Rapid distortion theory for homogeneous compressed turbulence with application to modeling. To appear in *J. Fluid Mech.*
- ERINGEN, A. C. 1967 *Mechanics of Continua*, Wiley.
- GOLDSTEIN, M. E. 1978 Unsteady vortical and entropic distortions of potential flows round arbitrary obstacles. *J. Fluid Mech.* **89**, 433.
- GREENSPAN, H. P. 1968 *The Theory of Rotating Fluids*, Cambridge University Press.

- HERRING, J. R. 1974 Approach of axisymmetric turbulence to isotropy. *Phys. Fluids*. **17**, 859.
- JACQUIN, L. & CAMBON, C. 1992 Turbulence amplification by a shock wave and rapid distortion theory. submitted to *Phys. Fluids A*.
- LAUNDER, B. E., REECE, G. J. & RODI, W. 1975 Progress in the development of a Reynolds-stress turbulence closure. *J. Fluid Mech.* **68**, 537.
- LEE, S., LELE, S. K. & MOIN, P. 1992 Interaction of isotropic turbulence with a shock wave. Department of Mechanical Engineering, Stanford University, Thermosciences Division Report TF-52.
- MANSOUR N. N., SHIH T-H. & REYNOLDS, W. C. 1991 The effects of rotation on initially anisotropic homogeneous flows. *Phys. Fluids A*. **10**, 2421.
- REYNOLDS, W. C. 1990 Towards a structure-based turbulence model. Special workshop for turbulence modelers, CTR summer program.
- REYNOLDS, W. C. 1992 Towards a structure-based turbulence modeling. *Studies in Turbulence*. Editors Gatski *et al.* (Springer-Verlag, New York) **76**.
- RIBNER, H. S. 1953 Convection of a pattern of vorticity through a shock wave. NACA Report 1164.
- ROGALLO, R. S. 1981 Numerical experiments in homogeneous turbulence. NASA TM 81315.
- SABEL'NIKOV, V. A. 1975 Pressure fluctuations generated by uniform distortion of homogeneous turbulence. *Fluid Mech. Soviet Res.* **4**, 46.
- SARKAR, S., ERLEBACHER, G., HUSSAINI, Y. M. & KREISS, H. O. 1989 The analysis and modeling of dilatational terms in compressible turbulence. *ICASE Report 89-79*.
- TOWNSEND, A. A. 1976 *The Structure of Homogeneous Turbulence*, Cambridge University Press.
- WALEFFE, F. 1990 On the origin of the streak spacing in turbulent shear flows. *CTR Annual Research Briefs*. Stanford, Univ./NASA Ames, 159.
- WALEFFE, F. 1992 Inertial transfers in the helical decomposition. Submitted to *Phys. Fluids A*.
- ZEMAN, O. 1990 Dilatational dissipation: the concept and application in modeling compressible mixing layers. *Phys. Fluids A*. **2**, 178.
- ZEMAN, O. & COLEMAN, G. N. 1992 Compressible turbulence subjected to shear and rapid compression. *Eight Symposium on Turbulent Shear Flows*, Munich. Springer-Verlag.

445358 513-34
Pg 16 189673

N94-14758

Investigation of the dilatational dissipation in compressible homogeneous shear flow

By G. A. Blaisdell¹ AND O. Zeman²

The dilatational dissipation rate within compressible homogeneous turbulent shear flow is studied using data from direct numerical simulations. It is found that the dilatational dissipation rate is mainly associated with large scale acoustic waves. Eddy shocklets are observed; however, they have little contribution to the average dissipation rate. A mechanism for the generation of eddy shocklets is shown to be the focusing of acoustic waves. Turbulence models for the dilatational dissipation rate are compared with data from the simulations. It is found that the formulation of Zeman (1990) used by Viegas & Rubesin (1991) to calculate a compressible mixing layer agrees well with the numerical simulation results for turbulent Mach numbers less than 0.3. However, it is also found that, for the Mach number range occurring in mixing layers, the model does not accurately represent the theory upon which it is based.

1. Introduction

Compressibility effects on turbulence are important in several applications including hypersonic and supersonic boundary layers, scramjet and ramjet engines, and internal combustion engines. The accurate and reliable prediction of such flows requires improvements be made to current turbulence models. Our goal is to better understand compressible turbulence and to make improvements to turbulence models for compressible flows. The approach used is to examine results from direct numerical simulations (DNS) of compressible homogeneous turbulent shear flow.

Direct numerical simulations of compressible homogeneous turbulent shear flow by Blaisdell *et al.* (1991) and Sarkar *et al.* (1991a) have shown that the growth rate of turbulent kinetic energy is reduced compared to the incompressible case. The reduction in the growth rate has been attributed to two additional compressibility terms occurring in the turbulent kinetic energy equation — the dilatational dissipation rate and the pressure-dilatation correlation. The dilatational dissipation rate is an additional dissipation due to the divergence of the velocity, while the pressure-dilatation correlation represents a reversible transfer of energy between internal and kinetic energy. Turbulence models for both of these terms have been proposed by Zeman (1990, 1991) and by Sarkar *et al.* (1991b, 1992). In the current investigation only the dilatational dissipation rate is considered.

1 Purdue University

2 Center for Turbulence Research

The basis for the models of Zeman (1990) and Sarkar *et al.* (1991b) are very different. Sarkar's model is based on the idea of acoustic equilibrium while Zeman's model is based on the existence of eddy shocklets. The direct numerical simulations of Blaisdell *et al.* show the existence of eddy shocklets, which are regions of strong local dilatational dissipation rate. In spite of this, Sarkar's model was found to agree better with the DNS data than Zeman's model. However, a comparison by Viegas and Rubesin (1991) of the two models applied to a compressible mixing layer showed that Zeman's model performed better in predicting the reduction in growth rate with increasing convective Mach number. Therefore, we seem to have contradictory evidence on the relative merits of the two models. It will be shown that the reason for the differences in the comparisons is that the model formulations considered are different.

The objectives of the present work are to shed some light on the apparent discrepancy in the relative performance of the two turbulence models and to better understand the dilatational dissipation in compressible homogeneous shear flow. We begin by examining the formulation of Zeman's model.

2. Model formulations for the dilatational dissipation rate

In both the models of Zeman (1990) and Sarkar *et al.* (1991), the dissipation rate in a compressible flow is written as

$$\varepsilon = \varepsilon_s + \varepsilon_d = \varepsilon_s(1 + \varepsilon_d/\varepsilon_s) \quad (1)$$

where ε_s is the solenoidal dissipation rate and ε_d is the dilatational dissipation rate. For homogeneous turbulence the solenoidal dissipation rate is given by $\varepsilon_s = \overline{\tilde{\mu}\omega'_i\omega'_i}$, where ω'_i is the fluctuating vorticity. This is the same as the dissipation rate in an incompressible flow. The dilatational dissipation rate is $\varepsilon_d = (4/3)\overline{\tilde{\mu}d'd'}$ where $d' = \partial u'_i/\partial x_i$ is the divergence of velocity (also called the dilatation). Both Zeman and Sarkar *et al.* have suggested modeling ε_s in the same manner that the dissipation is modeled in incompressible flows while accounting for compressibility effects through the ratio $\varepsilon_d/\varepsilon_s$. This strategy is supported by examination of the turbulent kinetic energy budget in the simulations of Blaisdell *et al.* (1991).

The model of Sarkar *et al.* is based on the idea of acoustic equilibrium between kinetic and internal energy and assumes a certain variation of the pressure variance with turbulent Mach number. The model is

$$\varepsilon_d/\varepsilon_s = c_s M_T^2 \quad (2)$$

where $M_T = q/\tilde{a}$ is the turbulent Mach number, $q = \sqrt{\overline{\rho u'_i u'_i}}/\bar{\rho}$ is the turbulent velocity scale using the Favre fluctuating velocity, and $\tilde{a} = \sqrt{\gamma R \tilde{T}}$ is the speed of sound based on the Favre averaged temperature. The model constant $c_s = 1.0$.

The model of Zeman (1990) is based on the existence of eddy shocklets and is formulated in terms of the probability density function (PDF) of the fluctuating

Mach number. An expression for the dilatational dissipation is given in equation (7) of Zeman (1990) which is then put in the form

$$\varepsilon_d/\varepsilon_s = c_z F(M_t^*) . \quad (3)$$

Zeman uses a turbulent Mach number, M_T^* , which is based on sonic conditions. The sonic temperature is given by $T^* = T_0[2/(\gamma + 1)]$ where T_0 is the stagnation temperature. Zeman argues that T_0 can be replaced by the Favre averaged static temperature, \tilde{T} . Then the turbulent Mach number used by Zeman can be related to that used by Sarkar *et al.* by

$$M_T^* = \frac{q}{\sqrt{\gamma RT^*}} = \sqrt{\frac{\gamma + 1}{2}} \frac{q}{\sqrt{\gamma R\tilde{T}}} = \sqrt{\frac{\gamma + 1}{2}} M_T . \quad (4)$$

For the case of a diatomic gas, $\gamma = 1.4$ and $M_T^* = 1.10M_T$. (Throughout the current paper use is made of M_T and M_T^* as well as M_{rms} . These are referred to as the turbulent Mach number, the turbulent Mach number based on sonic conditions, and the *rms* Mach number respectively. Data from the DNS show that M_T and M_{rms} differ by less than 1% and, therefore, can be used interchangeably.)

In determining $F(M_T^*)$, the form of the PDF varies depending on the flow considered. A form appropriate for homogeneous turbulence is given in equation (5) of Zeman (1991). This is the form used in the comparison of Blaisdell *et al.* (1991). The comparison of $\varepsilon_d/\varepsilon_s$ is shown in figure 1. The DNS results are indicated by the symbols. For a given initial *rms* Mach number, $\varepsilon_d/\varepsilon_s$ develops to become independent of its initial value, and the asymptotic values are the ones that should be compared to the model. The model results are shown by the dotted curve. In comparison to the DNS results, the model predicts too fast an increase with turbulent Mach number, and it underpredicts the values at low M_t . The model of Sarkar *et al.* (1991b) is also shown in figure 1. It matches the DNS data fairly well. On the basis of this comparison, one would conclude that Sarkar's model is better.

For compressible mixing layers, Zeman (1990) uses a PDF parameterized by the kurtosis of the fluctuating Mach number, K , as shown in equation (6) of that paper. Different values of K give different relations for $F(M_t^*)$, as shown in figure 2 of Zeman (1990). Rather than choose a particular value of K for performing calculations, Zeman (1990) offers a curve fit as follows

$$F(M_t^*) = \begin{cases} 1 - \exp\{-[(M_t^* - 0.1)/0.6]^2\}, & \text{if } M_t^* > 0.1; \\ 0, & \text{if } M_t^* \leq 0.1. \end{cases} \quad (5)$$

This is the form used by Zeman (1990) and by Viegas & Rubesin (1991) to calculate the compressible mixing layer. It was found to give good results for the reduction in the growth rate with convective Mach number. Even though this formulation was developed for the mixing layer, it is interesting to compare it with the homogeneous shear flow DNS data. This is also shown in figure 1. The above formula fits the

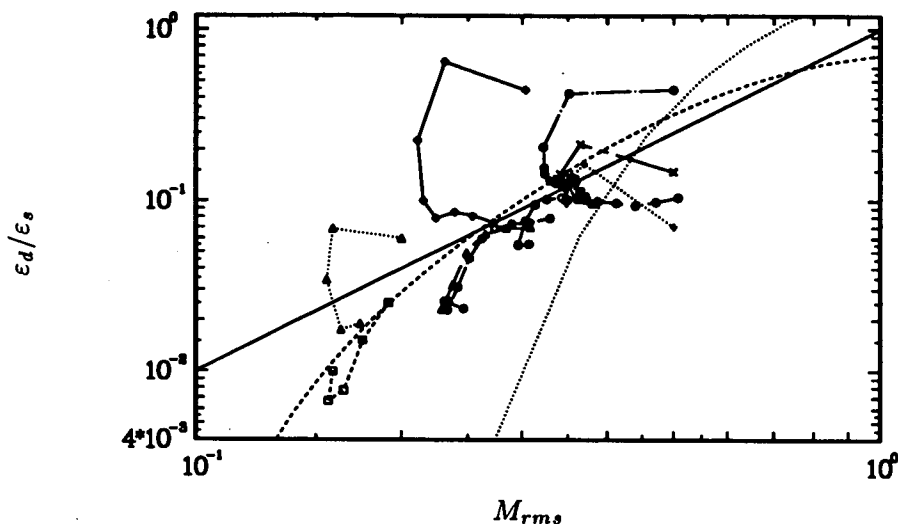


FIGURE 1. Dissipation ratio, $\varepsilon_d/\varepsilon_s$, as a function of M_{rms} . DNS data, symbols; model of Sarkar *et al.*, —; theoretical formulation of Zeman (1991),; approximate relation of Zeman (1990) given by equation (5), ----.

DNS data very well, especially at lower values of M_{rms} . This result is surprising in light of the previous comparison made with the DNS data.

In order to clarify the situation we need to examine the theory developed by Zeman (1990, 1991) more closely. There are some acknowledged errors in the form of the PDFs given in Zeman (1990, 1991), and so the development of the theory will be outlined and appropriate corrections made.

Based on scaling arguments, Zeman arrives at equation (5) of Zeman (1990) which can be rewritten as

$$\varepsilon'_d = \left(\frac{q^3}{L}\right) \frac{1}{M_T^{*3}} \left(\frac{(m_1^{*2} - 1)}{m_1^*}\right)^3. \quad (6)$$

This relation gives the contribution to the dilatational dissipation rate from an eddy shocklet structure where $m_1^* = \sqrt{u'_i u'_i}/a^*$ is the instantaneous Mach number on the upstream side of the shock. The Mach number used by Zeman is based on the speed of sound at sonic conditions, $a^* = \sqrt{\gamma RT^*}$. The average dilatational dissipation is obtained from a distribution of eddy shocklet structures, and, therefore, one needs to integrate this expression with the PDF of m_1^* .

Zeman has proposed two forms of the PDF depending on the flow. For homogeneous turbulence, in which case the velocity fluctuations are nearly Gaussian, the proposed PDF is given in equation (5) of Zeman (1991). Results using this PDF are shown in figure 1, and, as discussed above, they do not agree with the DNS data. In order to check whether the disagreement is due to differences between the actual PDF and the model PDF, the PDF of the fluctuating Mach number was taken directly from the simulations. However, the results did not agree with those of the DNS. This suggests that the basic theory does not apply to the flow

conditions considered in the DNS.

For inhomogeneous flows, such as mixing layers, in which the PDF of the velocity fluctuations are non-Gaussian, Zeman (1990) suggests using a Gram-Charlier expansion in which the kurtosis, K , appears as a parameter. The PDF given in equation (6) of Zeman (1990) contains a typographical error. It is also missing a factor of σ and is, therefore, unnormalized. The normalized PDF, put in terms of the Mach number, is

$$p(m^*, K) = \frac{1}{\sqrt{2\pi}\sigma} \left\{ 1 + \frac{(K-3)}{4!} \left[3 - 6 \left(\frac{m^*}{\sigma} \right)^2 + \left(\frac{m^*}{\sigma} \right)^4 \right] \right\} \exp \left(-\frac{m^{*2}}{2\sigma^2} \right) \quad (7)$$

where the variance $\sigma = M_T^*$.

Zeman obtains the average dilatational dissipation rate by integrating the expression in equation (6) with the PDF of m^* . This formulation, given in equation (7) of Zeman (1990), has a factor of $1/M_T^{*4}$ which is correct for the unnormalized PDF. If the PDF is normalized, then the dilatational dissipation rate is given by

$$\varepsilon_d \propto \frac{q^3}{L} \left[\frac{1}{M_T^{*3}} \int_1^\infty \left(\frac{m^{*2} - 1}{m^*} \right)^3 p(m^*) dm^* \right]. \quad (8)$$

Relating q^3/L to ε_s gives the form shown in equation (3) where $F(M_T^*)$ is the term in the brackets in equation (8) above.

Zeman (1990) used the non-Gaussian PDF given in equation (7) to produce $F(M_T^*)$ for a range of values of the kurtosis K . These results are shown in figure 2 of Zeman (1990). The curve fit given in equation (5) is supposed to correspond roughly to the theoretical predictions with K between 6 and 8. Comparing values of $F(M_T^*)$ from equation (5) with those from the figure, this seems to be the case for most of the range of M_T^* ; however, for values of $M_T^* < 0.5$ there are some significant differences. Differences in this range are important because the calculations of a compressible mixing layer done by Zeman (1990) show that M_T^* is limited to values less than 0.5.

In order to make a detailed comparison, the function $F(M_T^*)$ calculated using the PDF from equation (7) is shown in figure 2(a) for values of $K = 4, 6, 8, 10$, along with the model given by equation (5). The curves shown in figure 2(a) do not exactly match those in figure 2 of Zeman (1990). The curves in figure 2(a) are somewhat lower than the corresponding curves from Zeman (1990), but the shapes of the curves are the same. The differences in the curves seem to be greater for higher values of K . The reason for the differences may be the approximations used to evaluate the integral in equation (8). It is believed that the curves in the current paper are accurate.

The model curve shown in figure 2(a) has the same basic S-shape as the theoretical curves, and it lies between the curves for $K = 6$ and $K = 8$ for a large range of Mach numbers; but, in the range $M_T^* < 0.5$, the model curve deviates significantly from the theoretical curves. This is shown in detail in figure 2(b). The model gives

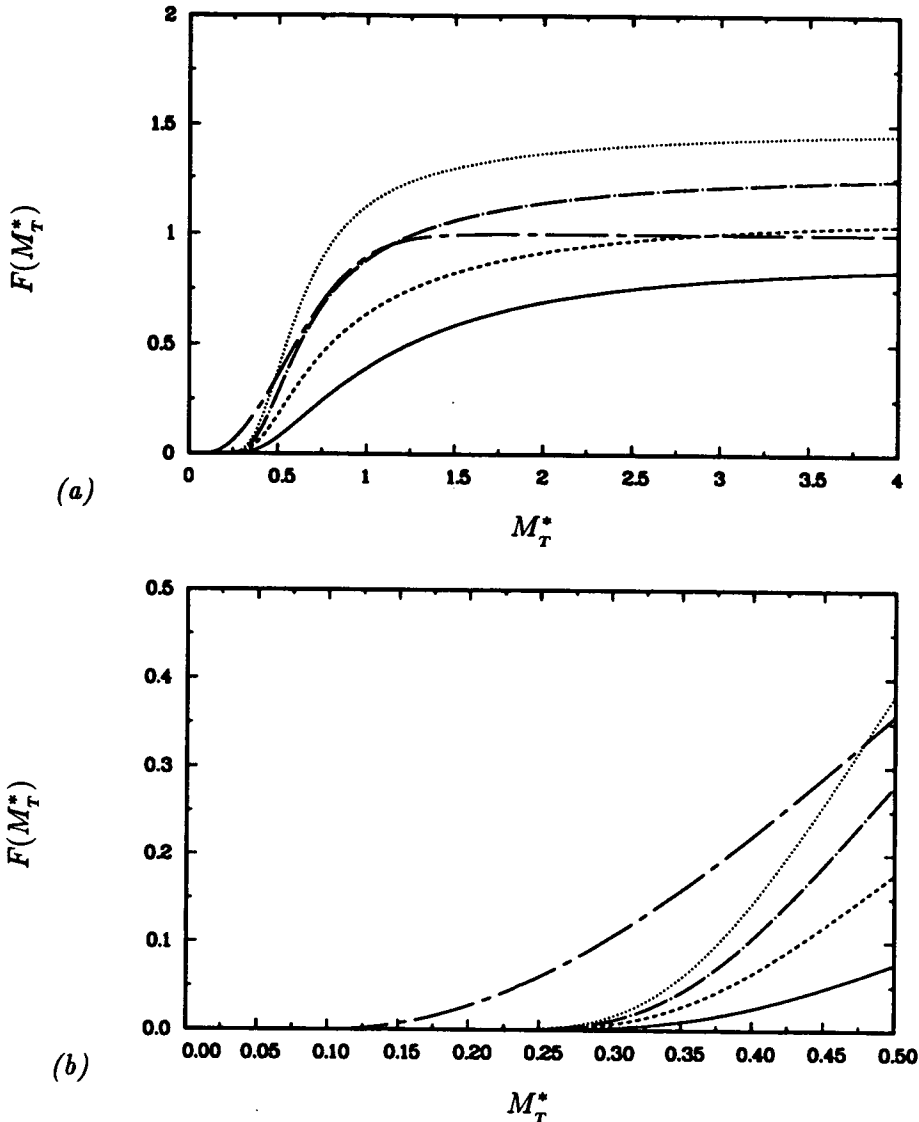


FIGURE 2. Dissipation function $F(M_T^*)$ for various values of K , (a) for a wide range of Mach numbers, (b) for $M_T^* < 0.5$. $K = 4$, —; $K = 6$, ---; $K = 8$, - · - ·; $K = 10$, ·····; approximate relation from equation (5), - - - -.

much higher values for $F(M_T^*)$ than what the theory predicts. The differences are especially great at lower values of M_T^* . The implication of the comparison shown in figure 2(b) is that, in the range of Mach numbers where the model is used, the model does not represent the theory upon which it is based. This does not mean that the model is not useful — it has been used to give the correct decrease in mixing layer thickness with increasing convective Mach number. However, the model must be viewed correctly as an empirical fit rather than having a fundamental theoretical

basis. The eddy shocklet dissipation theory developed by Zeman (1990) may still be valid under flow conditions different than those discussed here.

Returning to the comparison done by Viegas & Rubesin, one can understand the relative performance of the models of Zeman and Sarkar *et al.* in the compressible mixing layer by comparing the values predicted for $\varepsilon_d/\varepsilon_s$. From figure 4 of Zeman (1990), compressibility effects become important for convective Mach numbers above 0.5, and, from figure 5 of that paper, this corresponds to $M_T^* > 0.3$. From figure 1 of the current paper, Zeman's model gives a greater value of $\varepsilon_d/\varepsilon_s$ than Sarkar's model in the range $0.25 < M_{rms} < 0.75$. So, in the range of Mach numbers where compressibility effects are important, Zeman's model predicts a higher dissipation rate than Sarkar's model. Therefore, while Zeman's model gives the correct growth rate, Sarkar's model predicts too large a growth rate. However, it should be pointed out that the comparison of Viegas & Rubesin only included as extra compressibility terms the dilatational dissipation rate and neglected the pressure-dilatation and the inhomogeneous term arising from the pressure-velocity correlation. Also, the mixing layer may have compressibility effects that reduce the production rate. These additional effects have been lumped into the evaluation of the dilatational dissipation rate models.

Let us now examine how the DNS data fits into the evaluation of the models. From figure 1, Zeman's model agrees very well with the DNS data at the lower values of M_{rms} , while Sarkar's model overpredicts the dissipation rate in this range. The differences in the models for low turbulent Mach numbers are not significant for the mixing layer; however, there may be other flows, such as boundary layers, where these differences are important. For $M_{rms} > 0.3$, there are large differences between the DNS data and the models. The value of $\varepsilon_d/\varepsilon_s$ from the DNS becomes roughly constant at 0.09 for $M_{rms} > 0.3$. This trend is not predicted by either model. Since Zeman's model agrees with the experimental results on mixing layers, there are most likely physical differences in the mechanism of the dilatational dissipation rate between mixing layers and homogeneous shear flow. The dilatational dissipation within homogeneous turbulent shear flow is examined in more detail in the next section.

3. Cause of the dilatational dissipation in homogeneous shear flow

In Blaisdell *et al.* (1992), flow fields from DNS of compressible homogeneous turbulence were examined in order to see the effects of compressibility. Eddy shocklets were found, which are regions of high local dilatational dissipation rate. However, these structures do not necessarily contribute significantly to the average dilatational dissipation rate because they are also highly intermittent. Nonetheless, it was believed that eddy shocklets are important to the dynamics of the dilatational dissipation rate. Also, a mechanism for the generation of eddy shocklets was suggested in which streamwise vortical structures cause high speed and low speed fluid to come into contact, creating a compression that leads to the shock. In the current work, the question of the importance of eddy shocklets to the dilatational dissipation rate is reexamined, and, by using flow visualization of the temporal evolution of

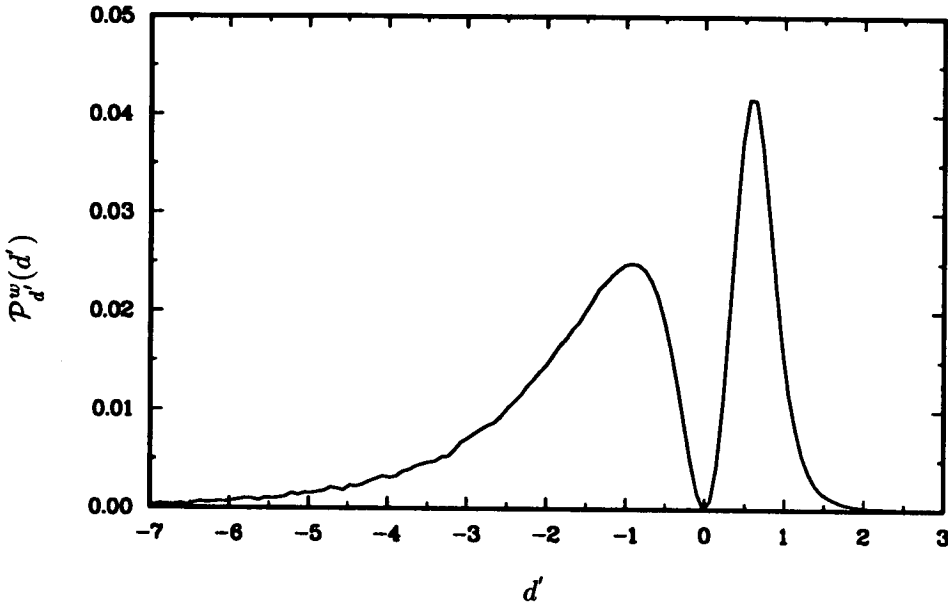


FIGURE 3. Weighted PDF of the dilatation for simulation scb192 at $St = 12$.

the turbulence, a different mechanism for the generation of eddy shocklets is shown to occur.

The nature of the dilatational dissipation rate can best be found by identifying the regions of the flow that contribute the most to the dilatational dissipation rate and seeing how these regions evolve in time. In Blaisdell *et al.* (1992), the flow field from simulation scb192 was examined at the nondimensional time $St = 12$. In the current study, we consider the time evolution of the turbulence using flow fields from the same simulation for times between $St = 11$ and 12.

In order to determine which regions of the flow contribute most significantly to the dilatational dissipation rate, use is made of a weighted PDF of the dilatation formed by Blaisdell *et al.* which is defined by

$$\mathcal{P}_{d'}^w(d') = \frac{d'^2 \mathcal{P}_{d'}(d')}{\int_{-\infty}^{\infty} d'^2 \mathcal{P}_{d'}(d') dd'} \quad (9)$$

where $\mathcal{P}_{d'}(d')$ is the PDF of the dilatation. Figure 3 shows $\mathcal{P}_{d'}^w(d')$ for simulation scb192 at $St = 12$. The integral of $\mathcal{P}_{d'}^w(d')$ gives the fraction of the dilatational dissipation due to a specific range of values of the dilatation. More of the dilatational dissipation rate comes from negative values of the dilatation, which correspond to compression zones, than from positive values, which correspond to expansion zones. This is consistent with the negative skewness of the dilatation and the fact that the second law of thermodynamics precludes expansion shocks. There are two peak values of $\mathcal{P}_{d'}^w(d')$, one negative at $d' = -0.93$ and one positive at $d' = 0.56$. We will examine the regions where the negative peak values occur since they are associated with compression zones and will give us insight into the formation of eddy shocklets.

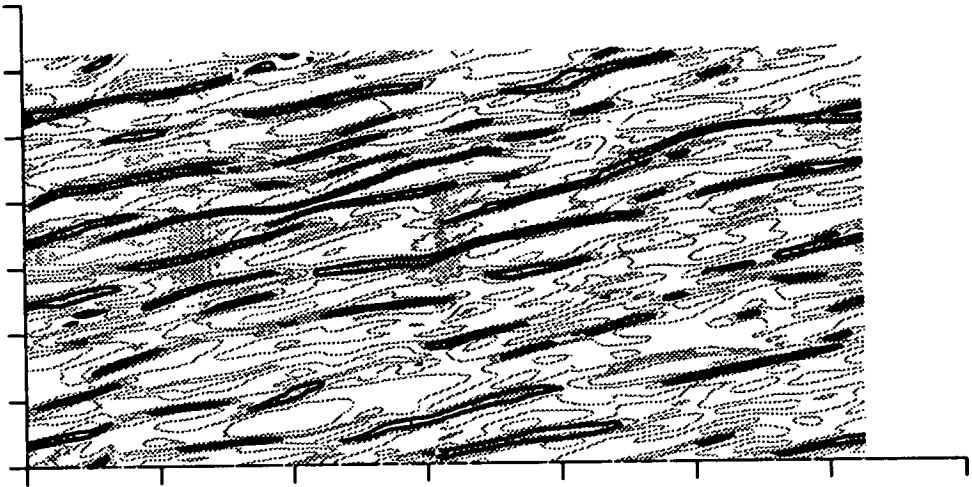


FIGURE 4. Contours of divergence of velocity in an x - y plane for simulation scb192 at $St = 12$. The highlighted contour corresponds to the negative peak in \mathcal{P}_d^w .

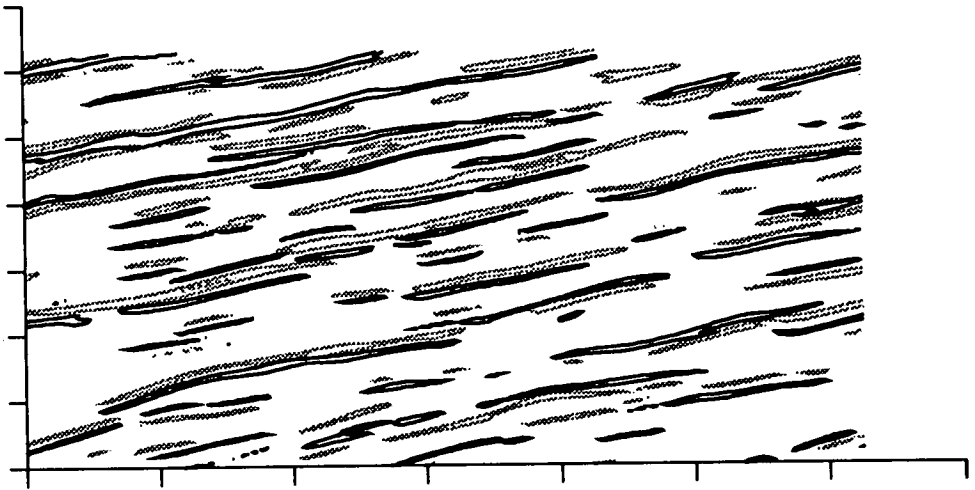


FIGURE 5. The highlighted contour of divergence of velocity at $St = 11.01$ (dark) and $St = 11.26$ (light).

Figure 4 shows contours of the dilatation in an x - y plane for simulation scb192 at $St = 12$. The mean velocity is in the x direction, and the mean velocity gradient is in the y direction. The contour with the peak value of $\mathcal{P}_d^w(d')$ for negative d' is highlighted. The view shown is chosen so that the strongest eddy shocklet (measured by the most negative dilatation) occurs in the center of the frame. The highlighted contour occurs on the periphery of the eddy shocklet but also throughout the rest of the flow field. The regions which contribute most significantly to the dilatational dissipation rate are long and thin and lie at a small positive angle to the direction of the mean flow.

Considerable insight is gained by observing the temporal evolution of these regions. Figure 5 shows the same highlighted contour at two different times, $St = 11.01$ and $St = 11.26$. For this view, the effect of the mean velocity was removed so that any motion observed occurs relative to the mean flow. It is apparent that the regions which contribute to the dilatation propagate as waves. Thus it appears that these regions are associated with large scale acoustic waves.

Next consider the dilatation in a spanwise, z - y plane. Figure 6 shows the spanwise plane at $St = 12$ which cuts through the strongest part of the eddy shocklet shown in figure 4. The same contour of the dilatation is highlighted. The regions that contribute to the dilatational dissipation rate are for the most part broad and thin. This view together with those shown in figures 4 and 5 gives the impression that these regions are portions of plane waves.

Again, it is useful to observe the temporal evolution of the regions that contribute the most to the dilatational dissipation rate. Figure 7 shows a sequence of the highlighted d' contour superposed on contours of streamwise vorticity for times between $St = 11$ and 12. The highlighted contours propagate as plane waves as shown before.

In figure 6, the eddy shocklet occurs about three quarters of the way across the plane (in z) and half way up (in y) at the base of the V-shaped highlighted contour. It is fairly narrow in the spanwise direction. The formation of the eddy shocklet can be observed by following the highlighted contour in figure 7(a) which lies somewhat below the location of that pointed out in figure 6 and which extends about a third of the way across the computational domain. As the contour propagates upward, it is distorted. It is believed that this distortion is due mainly to the vortical part of the turbulence, which is the reason for including contours of streamwise vorticity in figure 7. Shaded contours show positive streamwise vorticity, while dashed contours show negative streamwise vorticity. The particular contour of interest gets distorted as it passes what appears to be a pair of counter rotating streamwise vortices. Once the contour is distorted, it becomes focused and forms a cusp which is where the eddy shocklet occurs. Thus, the eddy shocklet is formed by a focused acoustic wave.

We have seen that the dilatational dissipation within homogeneous shear flow is associated mainly with large scale acoustic waves. Eddy shocklets do form, but, because they are highly intermittent, they do not contribute significantly to the dissipation.

The view shown in figure 4 with the highlighted contours lying at a shallow angle suggests that the regions which contribute the most to the dilatational dissipation may be due to the kinematic tilting of acoustic waves by the mean velocity field. Tilted acoustic waves would have increased dissipation compared to that of simple acoustic waves. This mechanism could be investigated by flow visualization, but this was not done.

The possible tilting of acoustic waves points out one of the differences between homogeneous flows and inhomogeneous flows such as mixing layers. In homogeneous shear flow, the shear continually acts on the turbulence, and any acoustic waves will feel the effect of the shear as long as they exist. In a mixing layer, acoustic waves

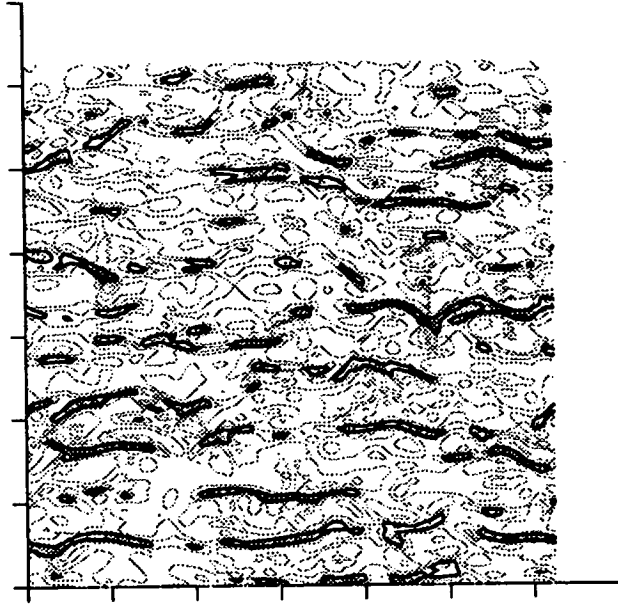


FIGURE 6. Contours of divergence of velocity in a z - y plane in simulation scb192 at $St = 12$. The highlighted contour corresponds to the negative peak in \mathcal{P}_d^w .

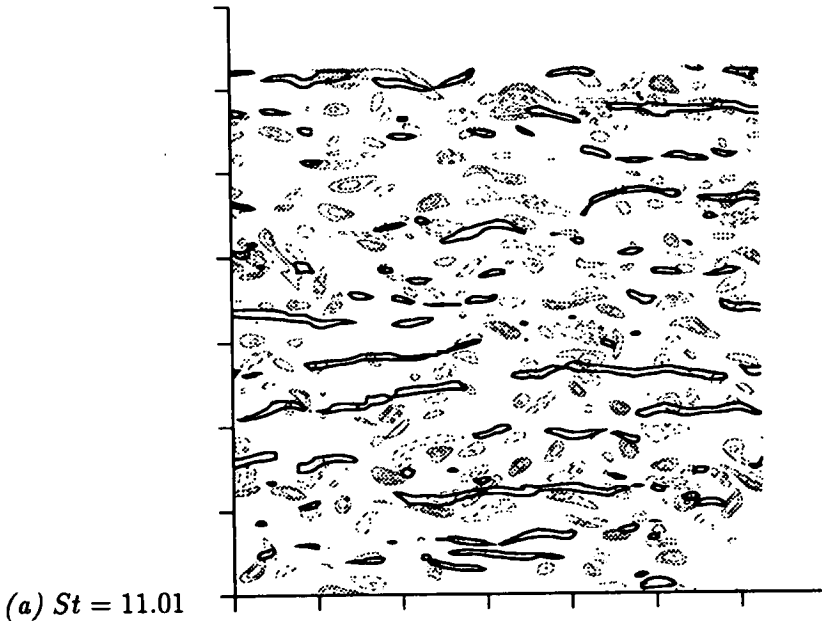


FIGURE 7. Sequence of views showing the highlighted contours of divergence of velocity superposed on contours of streamwise vorticity (shaded contours, positive ω_x ; dashed contours, negative ω_x). (a) $St = 11.01$, (b) $St = 11.26$, (c) $St = 11.50$, (d) $St = 11.75$, (e) $St = 12$.

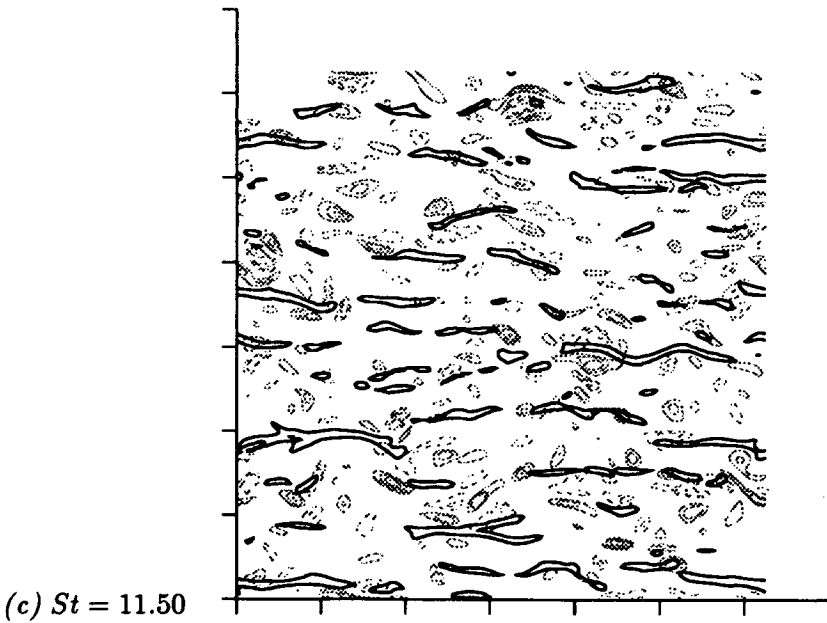
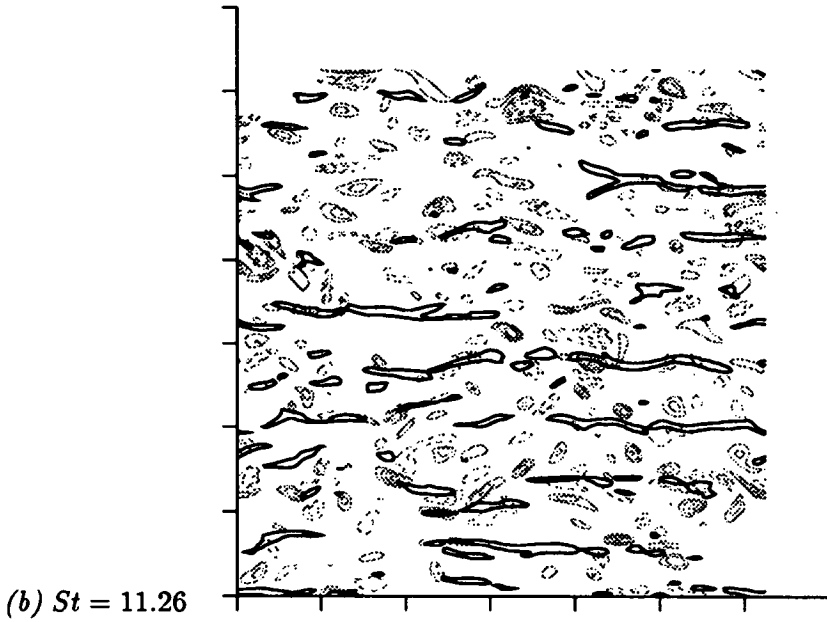


FIGURE 7. (continued).

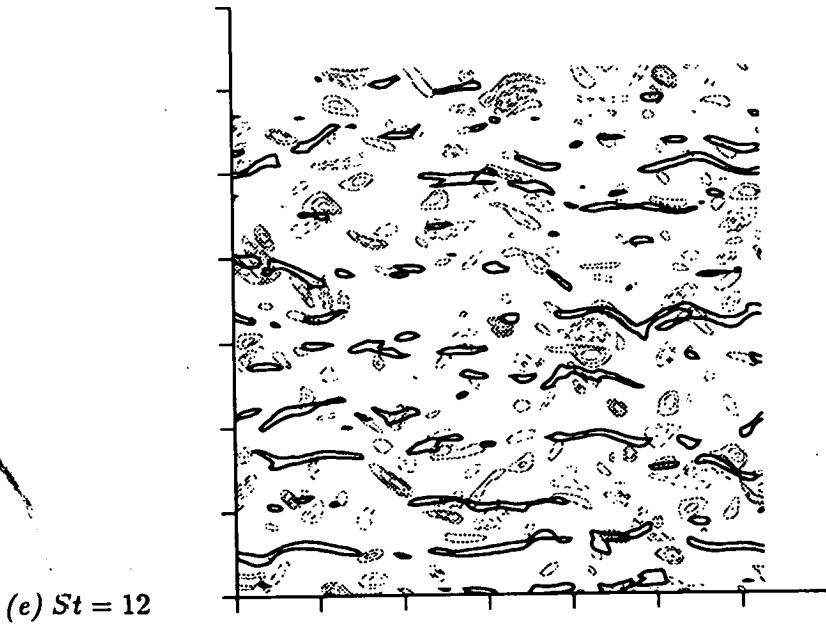
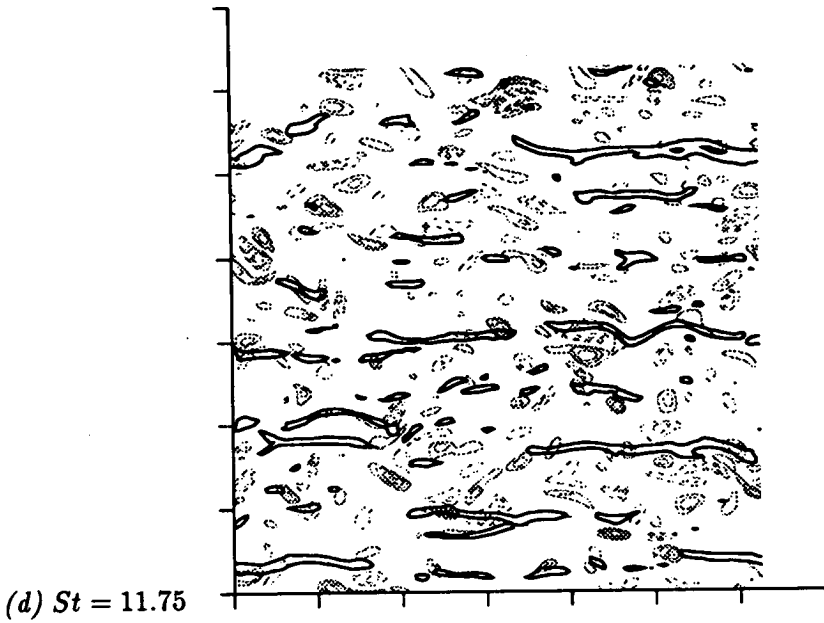


FIGURE 7. (continued).

ORIGINAL PAGE IS
OF POOR QUALITY

have the chance to propagate to the freestreams. The mean shear in a mixing layer will act on acoustic waves, but the interaction will only be significant if the time scale of the mean shear is small compared to time scale for an acoustic wave to propagate out of the layer. The propagation of acoustic waves to the freestream represents a loss of turbulent kinetic energy which is separate from the dilatational dissipation. Perhaps compressible turbulence models should be formulated to account for the separate mechanisms.

4. Conclusions

The dilatational dissipation within compressible homogeneous turbulent shear flow has been investigated using data and flow visualizations from direct numerical simulations. It is found that the dilatational dissipation rate is associated with large scale acoustic waves. Eddy shocklets, which are regions of large local dilatational dissipation, are observed; however, they occur too infrequently to contribute significantly to the average dilatational dissipation rate. A mechanism for the formation of eddy shocklets is shown to be the focusing of large scale acoustic waves.

The turbulence models for the dilatational dissipation rate of Zeman (1990, 1991) and Sarkar *et al.* (1991) were investigated. The model of Sarkar *et al.* agrees well with the DNS data for values of the turbulent Mach number less than 0.3. Some confusion arose concerning the formulation of Zeman's model. It was found that an approximate relation used for the case of mixing layers does not accurately represent the theory upon which the model is based. The theoretical formulation does not agree with the DNS data, while the approximate relation shows very good agreement for turbulent Mach numbers less than 0.3. For turbulent Mach numbers above 0.3, there are large differences between the DNS data and the models. Since Zeman's model was developed for a mixing layer and works well for that case, the differences between the DNS data and the models may be due to the differences in the physical nature of compressible homogeneous shear flow and a compressible mixing layer.

REFERENCES

- BLAISDELL, G. A., MANSOUR, N. N., & REYNOLDS, W. C. 1991 Numerical simulations of compressible homogeneous turbulence. *Report TF-50*. Mechanical Engineering, Stanford University.
- BLAISDELL, G. A., MANSOUR, N. N., & REYNOLDS, W. C. 1992 Compressibility effects on the growth and structure of homogeneous turbulent shear flow. Submitted to *J. Fluid Mech.*
- SARKAR, S., ERLEBACHER, G., & HUSSAINI, M. Y. 1991a Direct simulation of compressible turbulence in a shear flow. *Theoret. Comput. Fluid Dynamics*, **2**, 291-305.
- SARKAR, S., ERLEBACHER, G., HUSSAINI, M. Y., & KREISS, H. O. 1991b The analysis and modelling of dilatational terms in compressible turbulence. *J. Fluid Mech.*, **227**, 473-493.

- SARKAR, S. 1992 The pressure-dilatation correlation in compressible flows. Submitted to *Phys. Fluids A*.
- VIEGAS J. R. & RUBESIN, M. W. 1991 A comparative study of several corrections to turbulence models applied to high-speed shear layers. *AIAA paper 91-1783*.
- ZEMAN O. 1990 Dilatation dissipation: The concept and application in modeling compressible mixing layers. *Phys. Fluids A*, **2**, 178-188.
- ZEMAN O. 1991 On the decay of compressible isotropic turbulence. *Phys. Fluids A*, **3**, 951-955.

514-34 445359
189674 247
N94-124759

Response of a supersonic boundary layer to a compression corner

By D. Vandromme¹ AND O. Zeman²

On the basis of direct numerical simulations of rapidly compressed turbulence, Zeman and Coleman (1991) have developed a model to represent rapid directional compression contribution to the pressure dilatation term in the turbulent kinetic energy equation. The model has been implemented in the CFD code for simulation of supersonic compression corner flow with an extended separated region. The computational results have shown a significant improvement with respect to the baseline solution given by the standard $k - \epsilon$ turbulence model which does not contain any compressibility corrections.

1. Introduction

One of the critical problems in the field of compressible fluid dynamics is the response of turbulence to compressibility effects. Pioneering works in this area of research appeared in early 70's; the contribution of Wilcox & Alber (1972), Oh (1974), and Rubesin (1976) attempted to elucidate the modeling problem of the supersonic mixing layer by solving a transport equation for the turbulent kinetic energy. Later, Vandromme (1983) made an extension in the framework of a two-equation turbulence model by including compressibility effects in the dissipation equation. A detailed review of other extensions of incompressible models to high speed flows is in Vandromme (1991).

In recent years, progress has been made in understanding the compressibility effect on turbulence thanks principally to advances in direct numerical simulations (DNS) of 3D compressible turbulence (Feireisen et al. 1981, Blaisdell et al. 1991, Coleman & Mansour 1991, Lee 1991, Erlebacher et al. 1990). New theory models have been developed for the terms in the Reynolds stress equations, containing explicit compressibility effects: dilatation dissipation $\epsilon_d \propto \nu \overline{(u_{j,j})^2}$ and the pressure-dilatation correlation $\overline{pu_{j,j}}$ (Zeman, 1990, 1991a,b; Sarkar et al. 1991; Taulbee and VanOsdol 1991; Zeman and Coleman 1991; Durbin and Zeman 1992). In spite of the theoretical progress, the treatment of turbulence in supersonic flow codes is still inadequate. The principal reason for this is the lack of experiments to validate the variety of new modeling assumptions; furthermore, the new model are often fairly complex and difficult to implement in the compressible flow codes.

The present work is primarily concerned with the testing of novel modeling ideas which concern the effect of the so-called rapid compression (or volume deformation)

1 CNRS, INSA of Rouen, France

2 Center for Turbulence Research

on turbulence dynamics in a flow configuration of practical interest: a supersonic turbulent boundary layer (TBL) subjected to distortion through a compression corner. The qualifier *rapid* signifies that the rate of compression given by the mean flow divergence $\nabla \cdot \mathbf{U}$ is rapid with respect to the large eddy turnover time scale $\tau \propto k/\epsilon$ (see the following section for notation); i.e., $\nabla \cdot \mathbf{U}\tau \gg 1$. The condition of rapid compression is satisfied when turbulence passes through a shock or sequence of shocks near the corner. An engineering example of turbulence compression is a flow within the combustion chamber of a piston engine. However, here the condition of rapid compression is not satisfied since in the piston engine $\nabla \cdot \mathbf{U}\tau \approx 1$. The combustion chamber flow problem has been addressed from a modeling point of view by various investigators, and their work has led mainly to modification of the (solenoidal) dissipation equation to account for the compression effect on the turbulence scales (see e.g. Reynolds, 1980, Morel & Mansour, 1982).

The process of the rapid compression of (homogeneous) turbulence has been simulated by a DNS method developed by Coleman and Mansour (1991). Here, the turbulence could be subjected to both spherical (isotropic) or one-dimensional (1D) compression with the initial value of $\nabla \cdot \mathbf{U}\tau$ as high as 50 and initial $M_t = 0.05 - 0.44$. Thanks to these DNS results, Zeman (1991) and Zeman and Coleman (1991) were able to identify the directional rapid compression effect on the pressure dilatation term $\overline{p u_{j,j}}$: when turbulence was subjected to spherical compression $\overline{p u_{j,j}}$ remained virtually zero (w.r.t. ϵ); however, during 1D rapid compression, $\overline{p u_{j,j}}$ grew very large and negative, causing a significant drain on the turbulent kinetic energy k . Surprisingly, this process was more effective for initially low M_t ($= 0.05$). By now, physical and theoretical understanding of this phenomena has been achieved through the rapid distortion theory (Durbin and Zeman, 1992), and a realistic model for the rapid compression contribution to $\overline{p u_{j,j}}$ has been developed by Zeman and Coleman (1991).

The report is organized as follows: the turbulence modeling equations and the corresponding model expressions are described in the next section; Section 3 describes the main features of the numerical method which has been used for the solution of the Reynolds averaged Navier-Stokes (RANS) equations, including the new modeling ideas, when applied to the supersonic boundary layer submitted to a sudden compression along a 24-degree wedge (Section 4). In section 5, the results obtained for that specific test case are discussed.

2. Turbulence model

Considering a generic form of the classical two equation turbulence ($k - \epsilon$) model, the transport equation can be written as:

$$\frac{D\bar{k}}{Dt} - \text{Diffusion} = \underbrace{-\bar{\rho} \widetilde{v_\alpha^n v_\beta^n} \frac{\partial \widetilde{v_\alpha^n}}{\partial x_\beta}}_{\text{Production}} - \underbrace{\bar{\rho} \left(\widetilde{\epsilon} + 2\nu \left(\frac{\partial \sqrt{k}}{\partial x_n} \right)^2 \right)}_{\text{Destruction}} - \underbrace{\overline{v_\alpha^n} \frac{\partial \bar{p}}{\partial x_\alpha} + \overline{p' \frac{\partial v_\alpha^n}{\partial x_\alpha}}}_{\text{Compressibility}}$$

$$\frac{D\bar{\epsilon}}{Dt} - \text{Diffusion} = \underbrace{-C_{\epsilon 1} \frac{\epsilon}{k} \bar{\rho} \widetilde{v_\alpha^n v_\beta^n} \frac{\partial \widetilde{v_\alpha^n}}{\partial x_\beta}}_{\text{Production}} - \underbrace{-C_{\epsilon 2} \frac{\epsilon}{k} \bar{\rho} \widetilde{\epsilon} + 2\mu_t \frac{\mu}{\bar{\rho}} \left(\frac{\partial^2 \widetilde{v_{t\alpha}^n}}{\partial x_n^2} \right)^2}_{\text{Destruction}}$$

with all source terms in the RHS. The source terms include the low turbulent Reynolds number treatment proposed by Jones & Launder (1972). Subscripts *ta* and *no* stand here for tangential and normal components with respect to the solid wall.

The various options in order to account for compressibility effects concern either the ϵ or the k equation. The first correction, which is supported by DNS results of 1D or spherical strain, has been suggested by Reynolds (1980) based on the behavior of decaying isotropic turbulence submitted to a mean strain. Thus the various contributions to the production of dissipation can be subjected to different constants. That yields that, in ϵ -equation:

$$\text{Production} = C_{\epsilon 1} \frac{\epsilon}{k} 2\nu_t S_{\alpha\beta} - C'_{\epsilon 1} \frac{\epsilon}{k} \frac{2}{3} \nu_t \delta_{\alpha\beta} \frac{\partial \tilde{v}_\alpha}{\partial x_\beta} \frac{\partial \tilde{v}_\gamma}{\partial x_\gamma} - C''_{\epsilon 1} \frac{\epsilon}{k} \frac{2}{3} k \delta_{\alpha\beta} \frac{\partial \tilde{v}_\alpha}{\partial x_\beta}$$

in which the $C_{\epsilon 1}$ constants take the following values (Reynolds, 1980):

$$C_{\epsilon 1} = 1.45; \quad C'_{\epsilon 1} = 1.45; \quad C''_{\epsilon 1} = 3.50$$

The compressibility contributions in the turbulent kinetic energy equation are detailed in the following. They are the dilatational contribution to the dissipation, a proper model for the density-velocity correlations, and the pressure-dilatation term.

2.1. Dilatation dissipation parameterization

The first idea is based on the assumption that, for sufficiently high turbulent Mach number values, shocklets exist, at least statistically, and can be responsible for an extra amount of dissipation induced by the bulk deformation in the flow. Zeman (1990) proposed a model for this extra dissipation based on the splitting between the solenoidal and dilatational parts of the strain tensor, which can be written as:

$$\epsilon_d = \epsilon_s F(M_t, K) \quad (1)$$

in which $M_t = \sqrt{2k/a^2}$ is the rms (turbulent) Mach number, $F(M_t, K)$ is an integral functional of the pdf $p(m_t, K)$ of fluctuating Mach number $m_t = \sqrt{u_j u_j}/a$, and $K = \overline{m_t^4}/(\overline{m_t^2})^2$ is the kurtosis of the m_t -distribution, which characterizes the departure from Gaussianity (intermittency) of m_t .

For the purpose of numerical computation, the function F is approximated as

$$F(M_t, K) = C_d \left(1 - \exp\left\{-\left(\frac{M_t - M_{t0}}{\sigma_M}\right)^2\right\}\right) \quad (2)$$

$$F(M_t) = 0, \quad \text{if } M_t \leq M_{t0}$$

where the quantities C_d , M_{t0} , and σ_M are functions of K . For values of M_t lower than the threshold of 0.2, the function $F(M_t, K)$ is set to zero, which is consistent with the results of DNS (Lee *et al.* 1991).

In adiabatic turbulent boundary layers, M_t appears to be below this threshold level for $M_e \leq 5$. However, this is not so in hypersonic TBL's with wall cooling or in the vicinity of a separation bubble in compression corner flow.

2.2. Pressure-dilatation correlation $\overline{p u_{j,j}} \equiv \overline{p\theta}$

In TBL flows, two important contributions to $\overline{p\theta}$ have been identified and modeled: the density-gradient and rapid-compression contributions.

Relying on the balance of the transport equation for the pressure fluctuations and assuming that the gradient flux law is valid for the transport of density fluctuations in the framework of a thin layer approximation, Zeman (1993) suggested the following model for the mean density gradient contribution:

$$(\overline{p\theta})_\rho = f_\rho(M_t)\tau k a^2 \left(\frac{\partial \bar{p}}{\partial x_2} \frac{1}{\bar{p}}\right)^2 \quad (3)$$

Here, $\tau = k/\epsilon_s$ is a (vortical) turbulent time scale, and the function $f_\rho \rightarrow M_t^2$ as $M_t \rightarrow 0$. The above contribution is positive and reflects the process of conversion of the potential (pressure) to kinetic energies. Although this contribution is indispensable in the mode equations for preservation of the proper (Van-Driest) scaling in the constant stress layer, it has not been used in the present validation tests.

A model for the rapid compression contribution to $\overline{p u_{j,j}}$ has been first proposed by Zeman (1991b) and Zeman and Coleman (1991) in the form:

$$(\overline{p\theta})_R = -c_{d1}\bar{p}\frac{(\overline{p^2})^{1/2}}{\bar{p}M_t^2}k\tau\{(S_{ij}^*)^2 + c_{d2}b_{ik}S_{kj}^*S_{ij}^*\} \quad (4)$$

The model reflects the sensitivity to the directionality of compression strain and is bilinear in the (trace-free) strain rate tensor $S_{ij}^* = \frac{1}{2}(U_{i,j} + U_{j,i} - \frac{2}{3}\delta_{ij}\nabla\cdot\mathbf{U})$; b_{ij} is the anisotropy tensor associated with the Reynolds stresses, and $\overline{p^2}$ is the fluctuation pressure variance. The above expression yields results agreeing with the DNS data for both 1D and 3D rapid compression; however, it requires an addi-

tional equation for $\overline{p^2}$ (for details see Zeman and Coleman (1991)). In the present $k-\epsilon$ model, because b_{ij} and $\overline{p^2}$ are not accessible at this level of closure, we set $\frac{(\overline{p^2})^{1/2}}{\bar{p}M_t^2} \approx 1$ and used a simpler version

$$(\overline{p\theta})_R = -c_{d1}\bar{p}k\tau(S_{ij}^*)^2. \quad (5)$$

As discussed in the previous section, the rapid compression contribution to $\overline{p\theta}$ is expected to be very important in shock/turbulence interactions.

3. Numerical method

The numerical method is a predictor-corrector scheme developed initially by MacCormack. To the basic explicit version, various improvements have been added in order to make the code more accurate and robust as well as more efficient. These improvements, which have been described in MacCormack (1985) and Vandromme (1991), are mainly:

- Finite volume discretization
- Flux vector splitting

- Implicit approximation
- Line Gauss-Seidel relaxation
- Energy coupling with the turbulence
- Implicit treatment of the source terms

Performance of this code is remarkable. Although it allows the treatment of complex geometries, large values for the integration time step can be used (which would correspond to a CFL number above 10^6 for the Euler equations). Furthermore, special treatment of the source terms of the turbulence equations in the implicit part eliminates the stiffness of the equations during the transient preceding the convergence to steady state.

The set of RANS equations, completed with a two equation turbulence model, takes the following form:

$$\frac{\partial U}{\partial t} + \frac{\partial F}{\partial x} + \frac{\partial G}{\partial y} = H$$

in which the vectors U , F , G and H are defined as:

$$U = \begin{bmatrix} \bar{\rho} \\ \bar{\rho}\tilde{u} \\ \bar{\rho}\tilde{v} \\ \bar{\rho}\tilde{E} \\ \bar{\rho}k \\ \bar{\rho}\epsilon \end{bmatrix} \quad F = \begin{bmatrix} \bar{\rho}\tilde{u} \\ \bar{\rho}\tilde{u}^2 + \bar{p} + \frac{2}{3}\bar{\rho}k + \sigma_{xx} \\ \bar{\rho}\tilde{u}\tilde{v} + \tau_{xy} \\ \bar{\rho}\tilde{u}\tilde{E} + (\bar{p} + \frac{2}{3}\bar{\rho}k + \sigma_{xx})\tilde{u} + \tau_{xy}\tilde{v} - Q_x \\ \bar{\rho}\tilde{u}k - (\mu + \frac{\mu_t}{\sigma_k})\frac{\partial k}{\partial x} \\ \bar{\rho}\tilde{u}\epsilon - (\mu + \frac{\mu_t}{\sigma_\epsilon})\frac{\partial \epsilon}{\partial x} \end{bmatrix}$$

$$G = \begin{bmatrix} \bar{\rho}\tilde{v} \\ \bar{\rho}\tilde{u}\tilde{v} + \tau_{yx} \\ \bar{\rho}\tilde{v}^2 + \bar{p} + \frac{2}{3}\bar{\rho}k + \sigma_{yy} \\ \bar{\rho}\tilde{v}\tilde{E} + (\bar{p} + \frac{2}{3}\bar{\rho}k + \sigma_{yy})\tilde{v} + \tau_{yx}\tilde{u} - Q_y \\ \bar{\rho}\tilde{v}k - (\mu + \frac{\mu_t}{\sigma_k})\frac{\partial k}{\partial y} \\ \bar{\rho}\tilde{v}\epsilon - (\mu + \frac{\mu_t}{\sigma_\epsilon})\frac{\partial \epsilon}{\partial y} \end{bmatrix} \quad H = \begin{bmatrix} 0 \\ 0 \\ 0 \\ 0 \\ H_k \\ H_\epsilon \end{bmatrix}$$

Define the jacobian matrices as:

$$A = \frac{\partial F}{\partial U}; \quad B = \frac{\partial G}{\partial U}; \quad C = \frac{\partial H}{\partial U}$$

This implicit approximation can be solved either by a factorate approximation method or by a relaxation scheme:

$$(I + \Delta t \frac{\partial A^\bullet}{\partial x} + \Delta t \frac{\partial B^\bullet}{\partial y} - \Delta t \cdot C) \delta U^{(n+1)} = \Delta U^{(n)}$$

$$\delta U^{(n+1)} = \Delta t \frac{\partial U^{(n+1)}}{\partial t}; \quad \Delta U^{(n+1)} = \Delta t \frac{\partial U^{(n)}}{\partial t}$$

in which the source terms can be imbedded on the diagonal terms or a separate factorization can be performed for the sources. Inversion of the implicit source

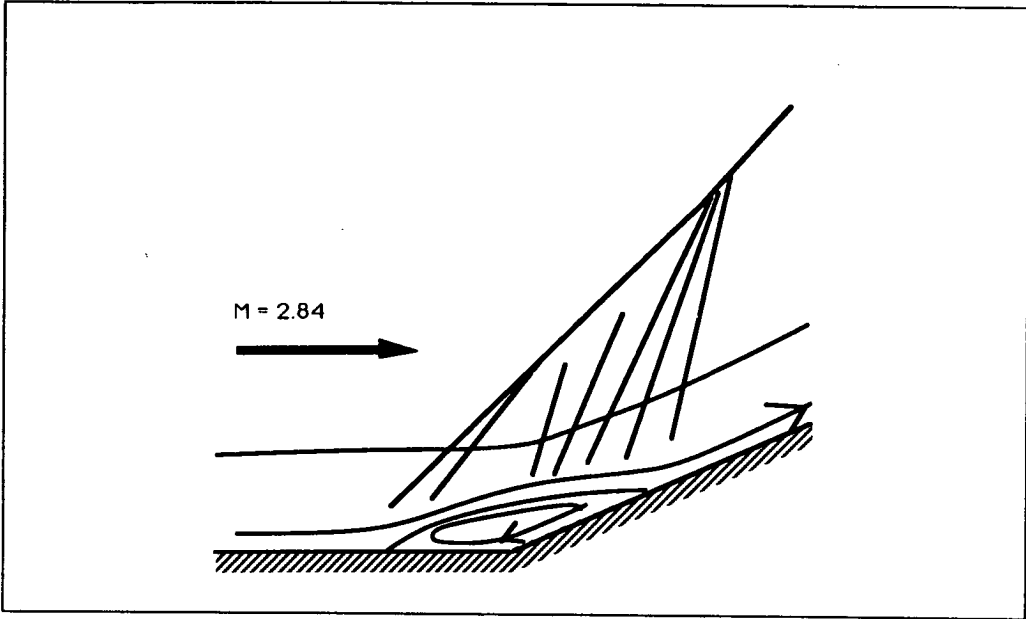


FIGURE 1. Flow Sketch.

operator is based on the knowledge of the analytical or the numerical form of the jacobian matrices. The standard solution procedure is to run line Gauss-Seidel in the streamwise direction (usually a backward-forward sweep), whereas the cross-wise lines are solved in a direct mode with a classical block-tridiagonal algorithm. When using the relaxation scheme, after application of the flux vector splitting, the resulting implicit approximation has one of the following form:

$$a_{i,j}\delta U_{i-1,j}^n + b_{i,j}\delta U_{i,j}^{n+1} + c_{i,j}\delta U_{i+1,j}^{n+1} + d_{i,j}\delta U_{i,j-1}^{n+1} + e_{i,j}\delta U_{i,j+1}^{n+1} = f_{i,j}\delta U_{i,j}^n + H_{i,j}^n$$

in a backward sweep, or

$$a_{i,j}\delta U_{i-1,j}^{n+1} + b_{i,j}\delta U_{i,j}^{n+1} + c_{i,j}\delta U_{i+1,j}^n + d_{i,j}\delta U_{i,j-1}^{n+1} + e_{i,j}\delta U_{i,j+1}^{n+1} = f_{i,j}\delta U_{i,j}^n + H_{i,j}^n$$

in a forward sweep. $H_{i,j}^n$ is the explicit source terms, and the $b_{i,j}$ coefficient contribute also to the implicit source treatment.

Independently, the sign of the sources is used to discriminate between stable and unstable implicit approximations (Vandromme, 1991). For stable cases, unlimited time step values can be used; nevertheless, experience shows that the turbulence equations (especially the dissipation equation) never do reach a "machine-zero" type of convergence.

4. Flow description

The main flow features are described with the sketch in Figure 1. A supersonic equilibrium boundary layer experiences a sudden deviation of 24 degrees. That deviation causes an oblique shock wave which induces a strong flow separation in

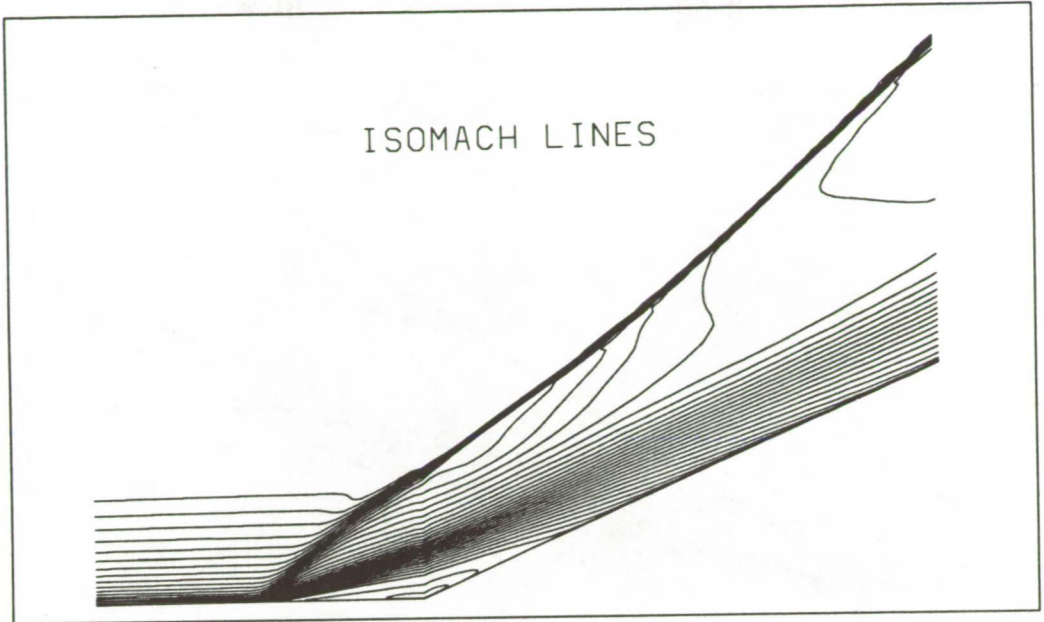


FIGURE 2. Isomach lines (basic solution).

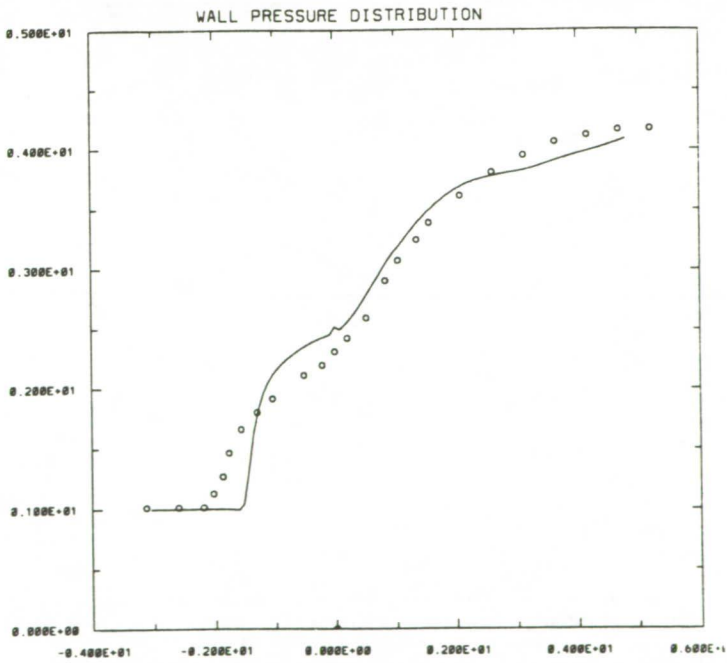


FIGURE 3. Wall pressure. (solid line = basic solution, symbols = experiments)

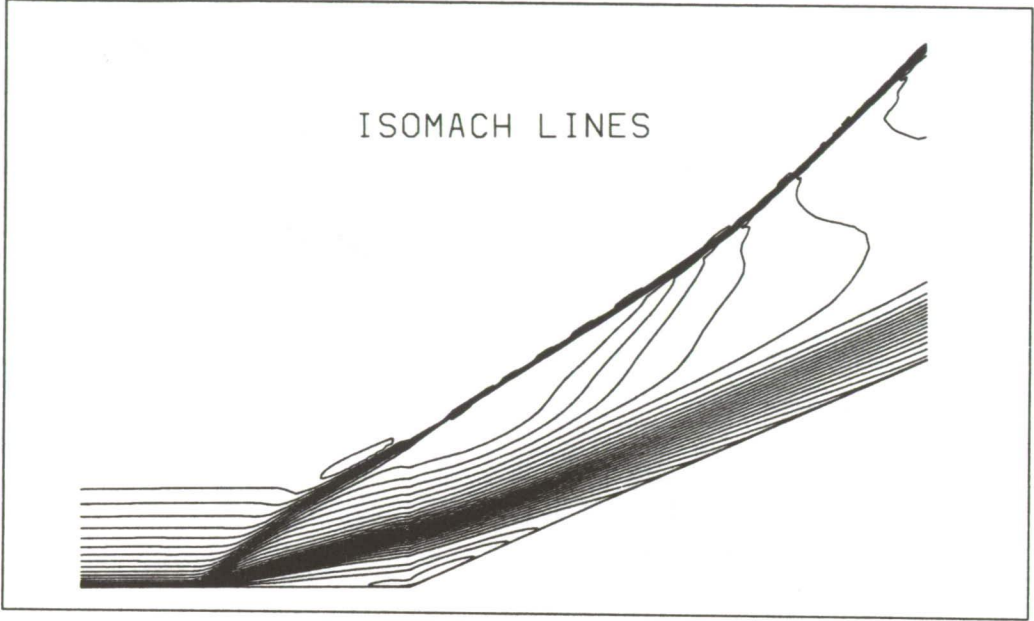


FIGURE 4. Isomach lines (with compressibility correction).

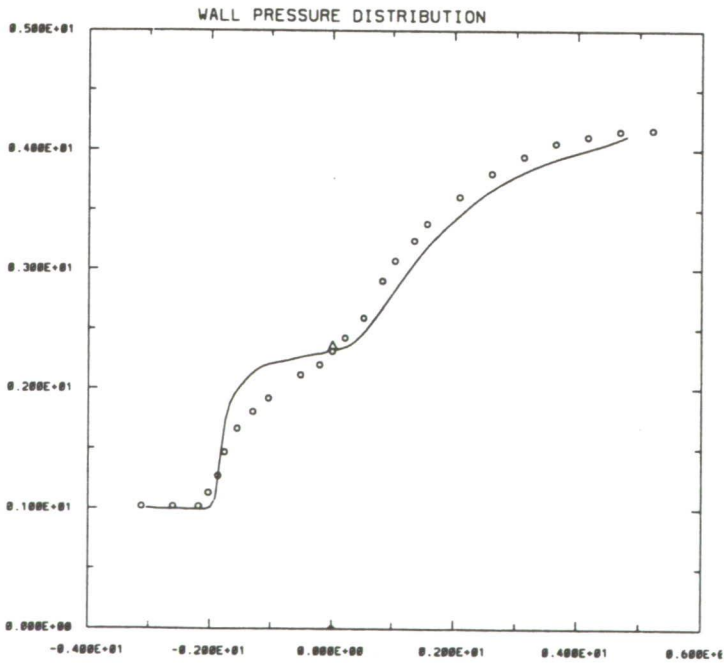


FIGURE 5. Wall pressure (solid line = with compressibility correction, symbols = experiments).

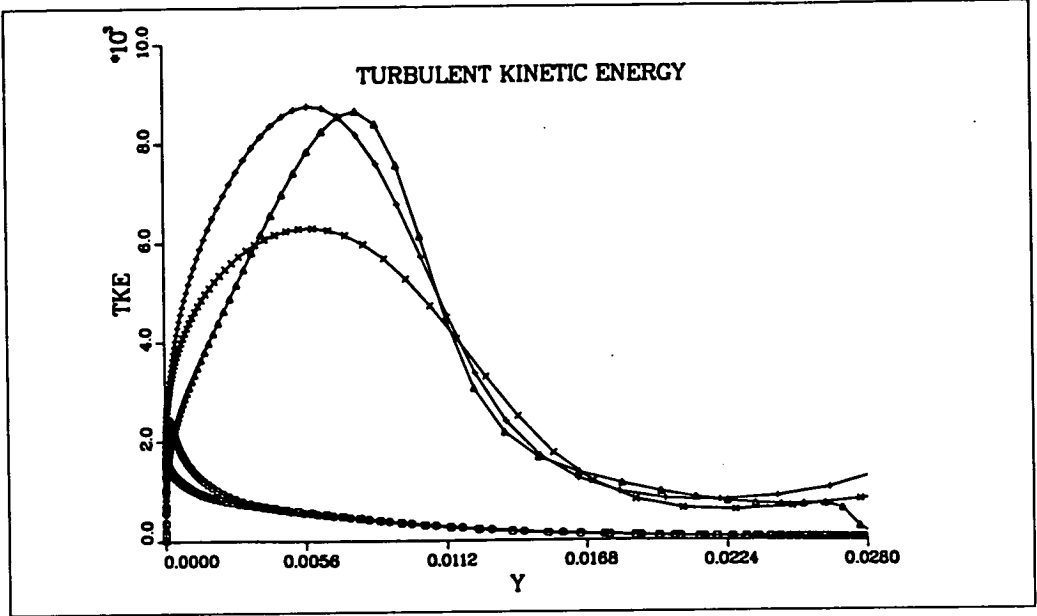


FIGURE 6. TKE profiles (basic solution).

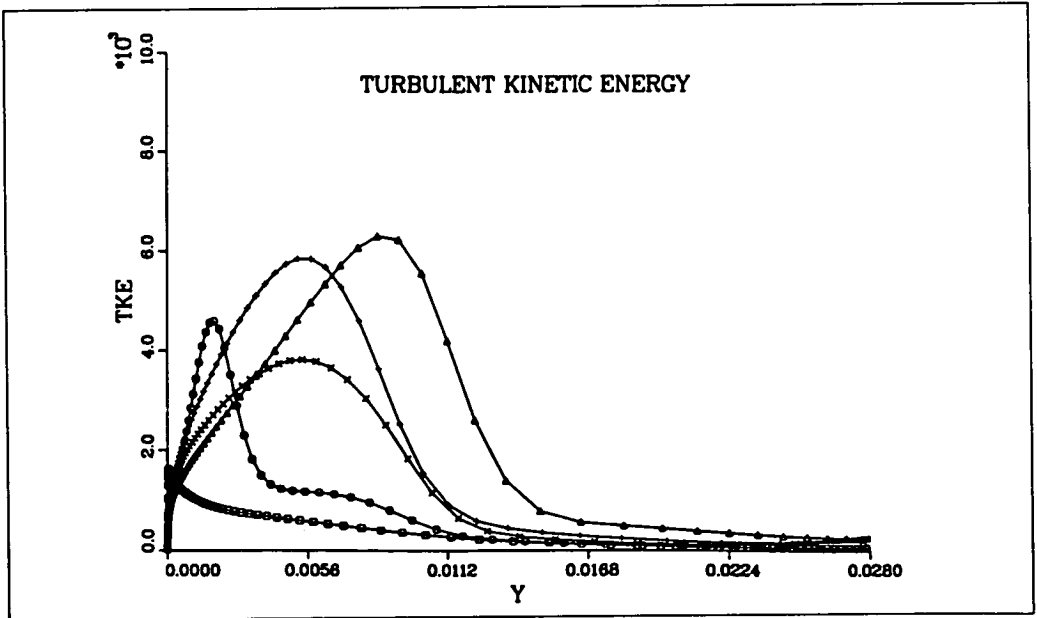


FIGURE 7. TKE profiles (with compressibility correction).

the wedge region. The separation point is at the foot of the shock, upstream of the wedge. The slight curvature of the streamlines above the separation bubble induces a weak expansion fan. Then, at the reattachment, the Mach lines focus again on the main shock and change its slope in the inviscid region. The flow conditions are as follows:

$$\begin{array}{llll} M_\infty = 2.84 & C_f = 11.5 \cdot 10^{-4} & P_t = 6.9 \cdot 10^5 \text{ Pa} & T_t = 270 \text{ K} \\ \delta = 2.6 \cdot 10^{-2} \text{ m} & \delta^* = 6.4 \cdot 10^{-3} \text{ m} & \theta = 1.3 \cdot 10^{-3} \text{ m} & Re = 1.78 \cdot 10^6 \end{array}$$

Experiments have been conducted at Princeton Gas Dynamics Laboratory (Settles *et al.* 1976, 1979). Similar flows have been studied with different ramp angles. i.e. 8° , 16° , and 20° . In this work, only the 24° has been considered because of the importance of the separated region related to the turbulence field.

A striking feature of this type of separated flow is the strong dependence of the separated region on the incoming turbulence within the boundary layer and on the changes occurring across the shock wave. In order to validate the changes due to the proposed compressibility corrections, all calculations have been made first with a basic model (which is the classical Jones-Launder $k - \epsilon$ model), and then the code was rerun with the compressibility corrections in (1) and (5) added to the basic model.

5. Results

The following results have been obtained during the course of the summer program. The basic solution is shown in Figures 2, 3, and 6. Figure 2 shows the distribution of isomach lines in the interaction region, and Figure 3 shows the wall pressure distribution compared to the experimental values (symbols). Figure 6 depicts profiles of turbulent kinetic energy (TKE) at successive streamwise locations beginning with an unperturbed boundary layer just upstream of the separation zone. Figures 4, 5, and 7 show the effect of inclusion of the compressibility contributions in (1), (2), and (5) in the code.

Comparing Figures 4 and 5 with the corresponding basic solution in Figures 2 and 3, it is evident that the compressibility corrections visibly improve the prediction of the extent of the separation zone. Comparing Figures 6 and 7, we observe that the compressibility corrections cause a marked reduction of overall TKE levels.

6. Conclusions

- The principal purpose of this project was to test the effect of compressibility corrections on computations of compression corner flow. These corrections consisted of i) a dilatation dissipation model representing additional dissipation of TKE due to eddy shocklets, and ii) a model for rapid compression contribution to the pressure dilation term.
- The suggested models have been implemented in a compressible R.A.N.S. solver, and computations with and without the compressibility corrections have been performed.

- A significant improvement has been gained in the prediction of a supersonic boundary layer interaction with an extended separation zone. The principal contributor of the improvement was the rapid compression term which becomes a large TKE sink in the vicinity of the shock regions. As expected, the dilatation dissipation effect was insignificant for this test case with the free stream Mach number $M_\infty < 3$. Dilation dissipation (due to shocklets) does become significant in hypersonic boundary layers with wall cooling (Zeman 1993).
- Overall, the new compressibility corrections are expected to play a much more dominant role in higher Mach number flows, for which further validation work is desired.

REFERENCES

- BLAISDELL G, MANSOUR N. N. & REYNOLDS W. C. 1991 Numerical simulations of compressible turbulence. Mechanical Engineering Dept. *Rept. TF-50*, Stanford University.
- COLEMAN G. N. & MANSOUR N. N. 1991 Direct simulation of homogeneous compressible turbulence under isotropic mean compression. In *Proceedings of the Eighth Symposium on Turbulent Shear Flows*, Technical University, Munich.
- DURBIN P. A. & ZEMAN O. 1992 Rapid distortion theory for homogeneous compressed turbulence with application to modeling. *J. Fluid Mech.* **242**, 349-370.
- ERLEBACHER G., HUSSAINI M. Y., KREISS H. O. & SARKAR S. 1990 The analysis and simulation of compressible turbulence. *Theor. Comput. Fluid Dynamics.* **2**, 73-95.
- JONES W. P. & LAUNDER B. E. 1972 The prediction of laminarization with a two-equation model of turbulence. *Int. J. Heat Mass Transfer.* **15**, 301-314.
- LEE S. 1991 Direct numerical simulations of compressible turbulence. PhD thesis, Mechanical Engineering Dept., Stanford University.
- LEE S., LELE S. K. & MOIN P. 1991 Direct numerical simulation and analysis of shock turbulence interaction. AIAA Paper 91-0523.
- MACCORMACK R. W. 1985 Current Status of the Numerical Solutions of the Navier-Stokes Equations. AIAA paper 85-00032.
- MOREL T. & MANSOUR N. N. 1982 Modeling of turbulence in internal combustion engines. S.A.E. paper, n° 820040.
- OH Y. H. 1974 Analysis of two dimensional free turbulent mixing. AIAA Paper 74-594.
- REYNOLDS W. C. 1980 Modeling of fluid motions in engines: An introductory overview. *Symp. on Combustion Modeling in Reciprocating Engines*. Plenum Press. 41-66.
- RUBESIN M. W. 1976 A one-equation model of turbulence for use with the compressible Navier-Stokes equations. *NASA TM X-73*. 128.

- SARKAR S., ERLEBACHER G., HUSSAINI M. Y. & KREISS H. O. 1991 The analysis and modeling of dilatational terms in compressible turbulence. *J. Fluid Mech.* **63**, 121.
- SETTLES G. S., VAS I. E. & BOGDONOFF S. M. 1976 Details of a shock separated turbulent boundary layer at a compression corner. *AIAA Journal.* **14**, 1709-1715.
- SETTLES G. S., FITZPATRICK T. J. & BOGDONOFF S. M. 1979 Detailed study of attached and separated compression corner flow fields in high Reynolds number supersonic flows. *AIAA J.* **17**.
- TAULBEE D. & VANOSDOL J. 1991 Modelling turbulent compressible flows: the mass fluctuating velocity and square density. AIAA paper 91-0524.
- VANDROMME D. 1983 Contribution à la modélisation et la prédiction d'écoulements turbulents à masse volumique variable. Thèse d'Etat. Université de Lille, France.
- VANDROMME D. 1991 Turbulence modelling for compressible flows. Von Karman Institute Lecture Serie, Rhode Saint Genèse, Belgium.
- WILCOX D. C. & ALBER I. E. 1972 A turbulence model for high speed flows. *Proceedings of the 1972 Heat Transfer and Fluid Mechanics Institute.* Stanford University Press, 231-252.
- ZEMAN O. 1990 Dilatation dissipation: The concept and application in modeling compressible mixing layer. *Phys. Fluids.* **A 2**, 178.
- ZEMAN O. 1991a On the decay of compressible isotropic turbulence. *Phys. Fluids.* **A 3**, 951.
- ZEMAN O. 1991b The role of pressure-dilatation correlation in rapidly compressed turbulence. *CTR Annual Research Briefs 1991.* Stanford Univ./NASA Ames, 105-117.
- ZEMAN O. & COLEMAN G. N. 1991 Compressible turbulence subjected to shear and rapid compression. *Proceedings of the Eight Symposium on Turbulent Shear Flows.* Springer Verlag.
- ZEMAN O. 1993 A new model for super/hypersonic turbulent boundary layers. AIAA Paper 93-0897.

Vortex-induced disturbance field in a compressible shear layer

By D. Papamoschou¹ AND S. K. Lele²

The disturbance field induced by a small isolated vortex in a compressible shear layer is studied using direct simulation in a convected frame. The convective Mach number, M_c , is varied from 0.1 to 1.25. The vorticity perturbation is rapidly sheared by the mean velocity gradient. The resulting disturbance pressure field is observed to decrease both in magnitude and extent with increasing M_c , becoming a narrow transverse zone for $M_c > 0.8$. A similar trend is seen for the perturbation velocity magnitude and for the Reynolds shear stress. By varying the vortex size, we verified that the decrease in perturbation levels is due to the mean-flow Mach number and not the Mach number across the vortex. At high M_c , the vortex still communicates with the edges of the shear layer, although communication in the mean-flow direction is strongly inhibited. The growth rate of perturbation kinetic energy declines with M_c primarily due to the reduction in shear stress. For $M_c \geq 0.6$, the pressure dilatation also contributes to the decrease of growth rates. Calculation of the perturbation field induced by a vortex doublet revealed the same trends as in the single-vortex case, illustrating the insensitivity of the Mach-number effect to the specific form of initial conditions.

1. Introduction

It is well known that the Mach number has a powerful effect to suppress the instability and growth of free shear flows. Landau¹ first showed that the vortex sheet becomes stable when the relative Mach number exceeds a critical value ($\sqrt{2}$ for the equal-density case). Early linear analyses (Lin 1953, Gropengiesser 1970, Blumen *et al.* 1975) and single-stream experiments (Sirieix & Solignac 1966) discovered that the growth rates of compressible, finite-thickness shear layers decrease sharply with increasing Mach number. Recent linear analyses (Ragab & Wu 1988, Zhuang *et al.* 1990), computations (Sandham & Reynolds 1989, Lele 1989), and two-stream experiments (Chinzei *et al.* 1986, Papamoschou & Roshko 1988, Samimy & Elliott 1990, Goebel & Dutton 1991) covering a larger range of conditions confirmed the above trends. The experiments, in particular, showed that at high Mach numbers the turbulent shear-layer growth rate decreases to as little as one fifth of the incompressible value. The perturbation levels of velocity decline in a similar fashion (Samimy & Elliott, Goebel & Dutton). Despite these recent gains in the field of

¹ University of California, Irvine

² Stanford University

compressible turbulence, the fundamental physical reason for the stabilizing effect of Mach number remains elusive.

While compressible shear flows typically contain density gradients, density effects alone are not responsible for the large reduction in growth rates. Brown & Roshko (1974) showed that the growth rate of the subsonic, variable-density shear layer changed only by about 50% when the density ratio was varied by a factor of 50. There is, therefore, a large effect associated with the Mach number itself. An exclusive property of Mach number is the ability to cut off communication between parts of the flow, a well-known phenomenon in supersonic flow.

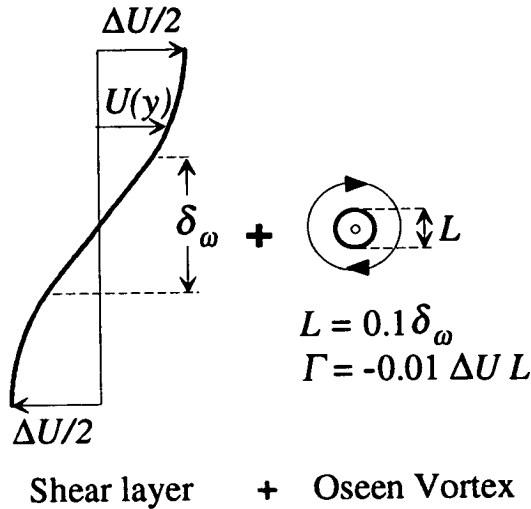
Morkovin (1987) stresses that upstream and cross-flow communication is essential for instabilities at supersonic and hypersonic speeds. His point is primarily based on Mack's (1984) linear stability analysis, where it is shown that the most unstable waves are those whose phase speed is subsonic relative to the free-stream velocity. Morkovin suggests the existence of zones of influence, defined by Mach cones, outside which a disturbance is not felt. The concept of reduced communication at high Mach number has been incorporated into recent turbulence models. Breidenthal's (1990) sonic-eddy model is based on the assumption that turbulent eddies whose rotational Mach number is greater than unity do not participate in fluid entrainment, while those with rotational Mach number of unity or less engulf fluid like incompressible eddies. The mixing-length model of Kim (1991) for a supersonic shear layer assumes that disturbances do not penetrate outside a region bounded by relative sonic velocities.

Morkovin's concept and the models by Breidenthal and by Kim, while conceptually useful, do not explain the fact that stabilization starts at low subsonic values of the Mach number and is practically complete when the velocity difference between the center and the edge of the shear layer becomes sonic (see references above). Furthermore, the fact that the relative velocity is supersonic does not prove that information will not propagate outside the region bounded by the sonic velocity. To address the problem in a more quantitative, although still idealized fashion, Papamoschou (1991) used ray theory to study the acoustic field of a monopole placed inside a shear layer. It was shown that the influence of the monopole diminishes with increasing Mach number but that a low level of communication still exists at supersonic relative speeds. Still, the connection between communication and instability remained a speculative one.

In this study, we explore the link between acoustic field and disturbance motion by direct numerical simulation of a simple instability problem: the impulse response of a shear layer to a localized vorticity perturbation and the change of that response with increasing Mach number. Specifically, we examine the unsteady process by which the shearing of a single vortex, placed in the center of the shear layer, produces velocity, pressure and density fluctuations in the surrounding flow field. Since vortical interactions among eddies are an essential ingredient of turbulence, our simplified problem may serve as a building block for understanding the effect of Mach number on the more complex vortical interactions in realistic shear flows.

2. Initial conditions

The computation is two dimensional, inviscid and temporal, with periodic boundary conditions in the mean-flow direction and non-reflecting boundary conditions in the y -direction. At time $t = 0$, the flow field consists of the shear layer, described by a hyperbolic-tangent velocity profile $U(y)$, with velocity difference ΔU and vorticity thickness $\delta_\omega = 0.1$, and an Oseen vortex (Fig.1).



papamos/fig1.ps [1] FIGURE 1. Initial conditions.

The Oseen vortex is a solution to the flow with zero shear and has a tangential velocity

$$v_\theta = \frac{\Gamma}{2\pi r} [1 - e^{-\alpha r^2/L^2}], \tag{1}$$

where Γ is the circulation, L is the vortex size, and $\alpha = 1.256431$ is chosen such that $v_\theta = v_{\theta,max}$ at $r = L$. The corresponding pressure distribution, derived by the radial momentum equation under the assumption of homentropic flow, is

$$\frac{p}{p_\infty} = \left[1 - \frac{(\gamma - 1)\Gamma^2}{4a_\infty^2 \pi^2 r^2} f(\alpha r^2/L^2) \right]^{\frac{\gamma}{\gamma-1}} \tag{2}$$

where

$$f(x) = \frac{1}{2} - e^{-x} + \frac{1}{2} e^{-2x} + x Ei(-2x) - x Ei(-x)$$

with $Ei(x)$ the exponential-integral function and ∞ denoting the unperturbed conditions.

The circulation of the Oseen vortex is fixed here at $\Gamma = 0.01\Delta UL$. Unless otherwise stated, the size of the vortex is $L = 0.1\delta_\omega$. The speed of sound a is constant throughout the flow field. The convective Mach number is

$$M_c = \frac{\Delta U}{2a}$$

with ΔU the velocity difference across the layer. To increase M_c , the velocity difference remains constant and the speed of sound decreases. The M_c range covered here is from 0.1 to 1.25.

For finite shear, the Oseen vortex is no longer a solution to the flow field. As a result, the flow tries to adjust to the new condition by generating an acoustic wave which propagates in all directions and becomes distorted by the mean Mach number gradient. Behind the acoustic wave, a disturbance field is established whose pattern evolves slowly with time. The disturbance velocity field is $\mathbf{u} = (u, v)$ and the pressure perturbation is p .

The computation is advanced in increments of *acoustic time* t whose non dimensional version is $t_a = ta/\delta\omega$. The corresponding *shearing time* is

$$t_s = tS = t_a \frac{\Delta U}{a} = 2t_a M_c$$

where $S = \Delta U/\delta\omega$ is the maximum shear. At fixed t_s , a particle at the edge of the shear layer has traveled the same distance, hence the flow has been sheared by the same amount, regardless of the value of M_c . Comparisons among the flow fields at various M_c 's will be made at fixed shearing time.

3. Computational Details

The computations were carried out in a domain of size 2 in the mean-flow direction (x) and of size 0.5 in the transverse direction (y). The disturbance vortex was placed at the center of the domain which was discretized by a non-uniform mesh in both directions. In the computations reported in this paper, the mesh contained 200 points in x (with a maximum mesh stretching of 3.2) and 50 points in y (with a maximum mesh stretching of 3.2). Near the vortex the mesh size was 0.0026 in both x and y . Spatial derivatives were evaluated using the sixth-order compact finite differences (Lele 1989, 1992), and third-order compact storage Runge-Kutta scheme was used for time advancement. Periodic boundary conditions in x and "non-reflecting" boundary conditions in y were employed. To make the initial conditions compatible with the periodicity in x , the method of images was used (with two images taken outside each x -boundary). To suppress the spurious generation of 2δ error waves in regions of mesh stretching, compact filtering scheme designed to remove only the near 2δ waves (Lele 1992) was applied to the fields being integrated every 20 time steps. It was verified that the applied filtering produced no significant change in the well-resolved physical disturbances.

4. Results and Discussion

We first present the time evolution of several quantities at $M_c = 0.4$. Fig. 2 shows the vorticity deformation due to the mean velocity gradient. At late times, vorticity is concentrated in a narrow, almost horizontal layer. Even though only the evolution at $M_c = 0.4$ is presented, the vortex shearing seen in Fig. 2 is practically the same for the full range of M_c 's covered here. The corresponding evolution in kinematic Reynolds shear stress $-uv$ is depicted in Fig. 3. At $t_s = 0$, the round

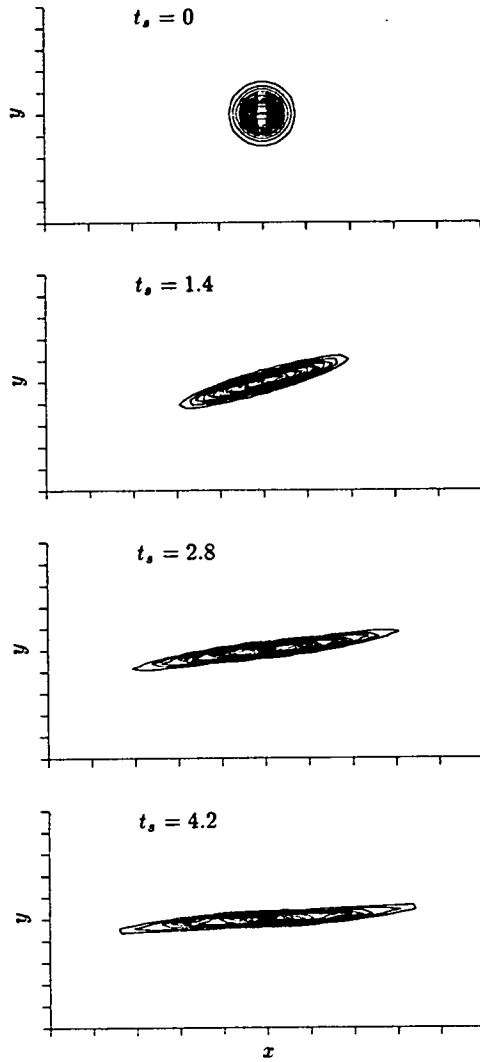


FIGURE 2. Iso-contours of disturbance vorticity $\omega L/\Delta U$ for $M_c = 0.4$. Contour levels: Minimum=-0.075; Maximum=-0.005; Increment=0.005. x -increment=0.02; y -increment=0.01.

vortex has equal amounts of positive and negative shear stress. As time progresses, the negative part vanishes while the positive part occupies a larger part of the flow field. The time development of the divergence is seen in Fig. 4, where the expanding wavefront is evident. As mentioned earlier, the wavefront arises from the reaction of the flow to the initial conditions. Partial reflection of the wave front from the upper and lower boundaries is due to numerical error associated with the boundary conditions.

We now present the Mach number effect on the disturbance field at fixed t_s . Fig.

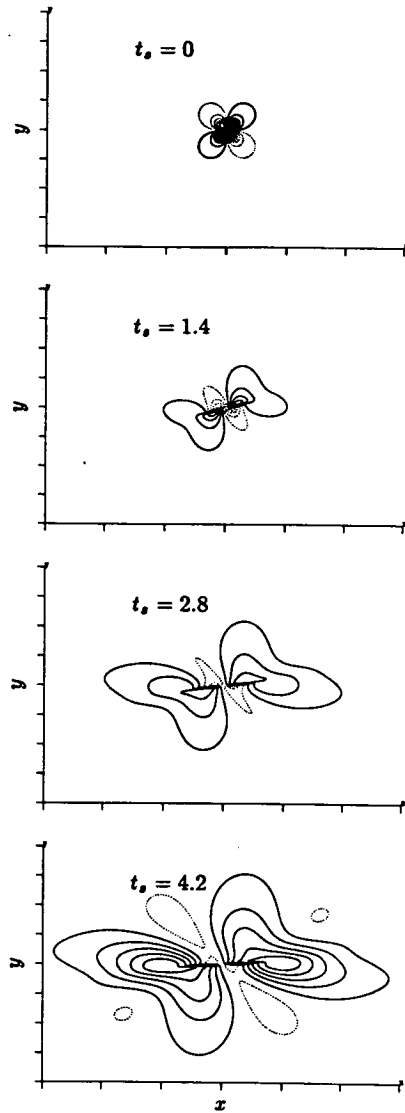


FIGURE 3. Iso-contours of Reynolds shear stress $-uv/(\Delta U)^2$ for $M_c = 0.4$. Contour levels: Maximum = $26E-5$; Minimum = $-26E-5$; Increment = $3E-5$. x -increment = 0.1 ; y -increment = 0.05 .

5 depicts the magnitude of the pressure perturbation at four different M_c 's. The extent and magnitude of the field decrease rapidly with increasing Mach number. At $M_c = 1.25$, the pressure field is reduced to a narrow transverse zone. The same trend is seen for the disturbance-velocity magnitude, shown in Fig. 6, and for the shear stress, shown in Fig. 7. Comparison of Figs. 5 and 7 shows that the decline

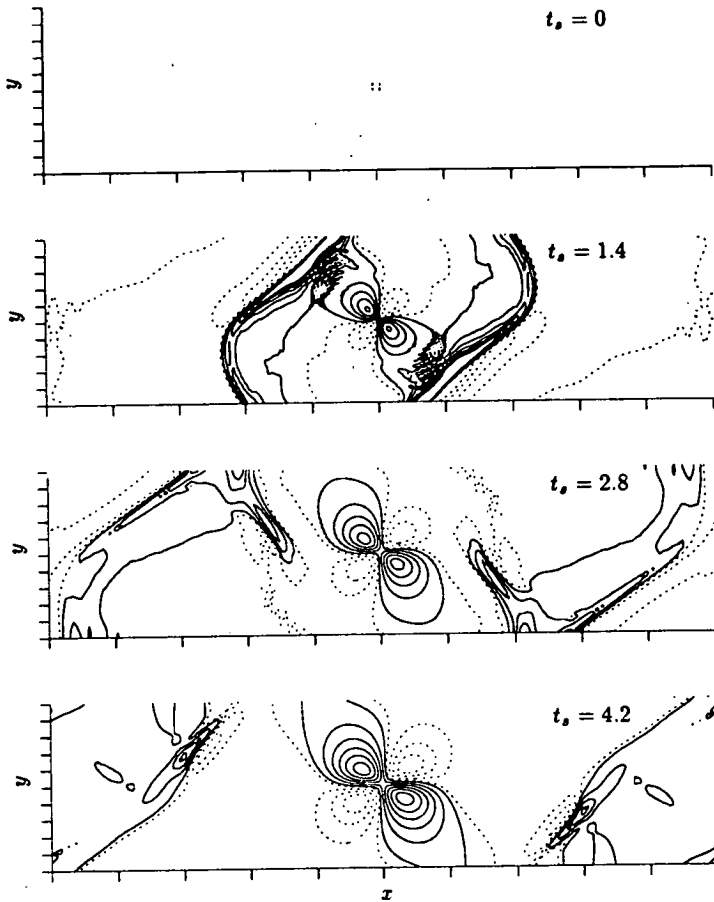


FIGURE 4. Iso-contours of divergence $\nabla \cdot \mathbf{u} L/\Delta U$ for $M_c = 0.4$. Contour levels: Maximum=0.025; Minimum=-0.017; Increment=0.004. x -increment=0.2; y -increment=0.05.

in magnitude and extent of the p and $-uv$ fields is very similar.

The pressure pattern seen in Fig. 5 reveals some very noteworthy effects of compressibility on the vortex influence. Evidently, at high M_c , the influence of the vortex does not propagate in x but stays confined within a narrow, transverse region. Interestingly, the vortex still communicates to edges of the shear layer, even when the relative velocity is supersonic. This implies that the turbulence models mentioned in the Introduction, which assume that all interactions occur within the a layer bounded by sonic velocities (Breidenthal 1990, Kim 1991), are overly idealized. The lack of communication in the x -direction may explain the lack of vortex pairing and shear-layer roll up at high M_c .

We now examine the source term for the transverse component of the kinetic energy $\frac{1}{2}v^2$, namely $-v\partial p/\partial y$. Note that generation of $\frac{1}{2}v^2$ does not involve the mean shear, thus is directly related to the pressure field. Fig 8 shows the source

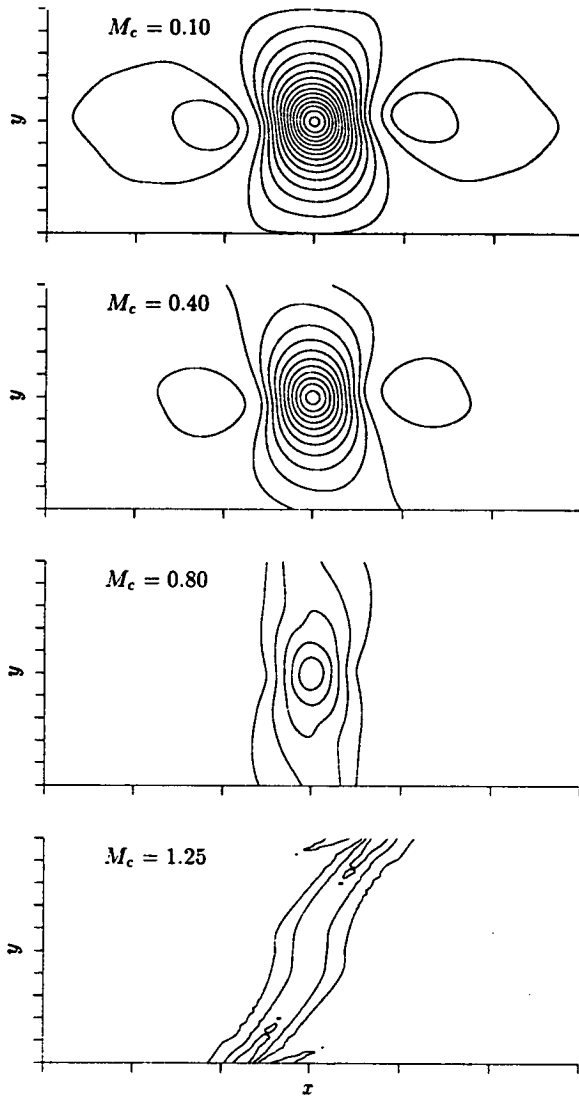


FIGURE 5. Iso-contours of pressure disturbance magnitude $|p|/(\rho_\infty \Delta U^2)$ at $t_s = 4.2$. Contour levels: Maximum=0.032; Minimum=0.002; Increment=0.002. x -increment=0.2; y -increment=0.05.

term dramatically decreasing with increasing M_c , practically vanishing at $M_c = 0.8$. At $M_c = 1.25$, the radiative nature of the flow, coupled with boundary-condition errors, make this term reappear in roughly-equal negative and positive amounts, so its integrated contribution is near-zero. The decline of $-v\partial p/\partial y$, and the resulting reduction in $|v|$, are the direct result of the reorientation of the pressure field due to the Mach number. Since $|u|$ and $|v|$ are of the same order, the shear stress $-uv$ is also reduced, as seen in Fig. 7. The lower $-uv$, in turn, causes a decrease in the growth rate of the overall fluctuation kinetic energy, which will be shown later.

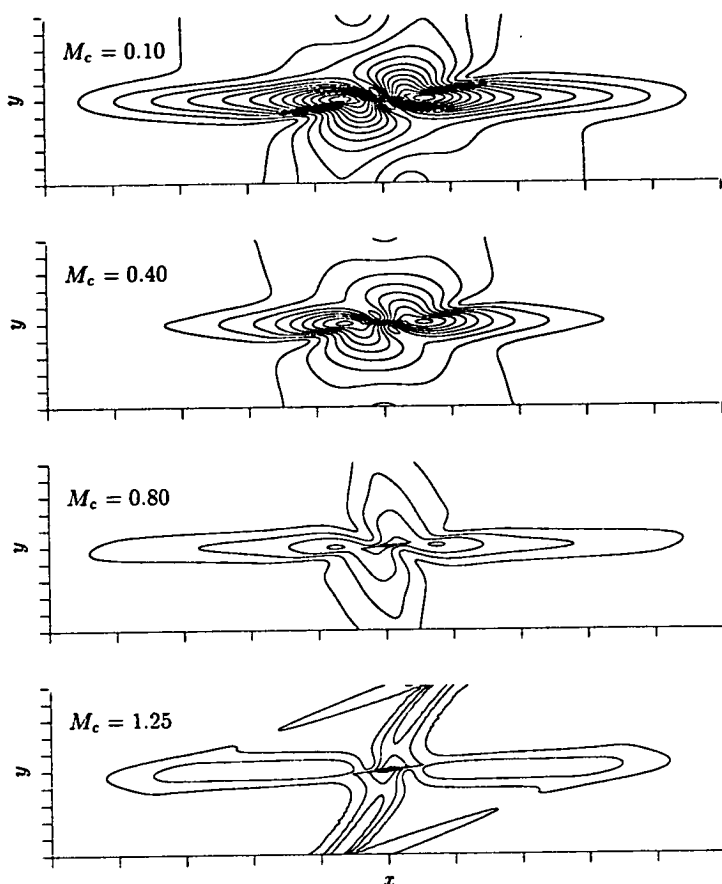


FIGURE 6. Iso-contours of disturbance velocity magnitude $|u|/\Delta U$ at $t_s = 4.2$. Contour levels: Maximum=0.028; Minimum=0.002; Increment=0.002. x -increment=0.2; y -increment=0.05.

The same mechanism has been observed to reduce the kinetic-energy growth rate in compressible homogeneous sheared turbulence (Blaisdell *et al.* 1991).

To verify that the observed trends are due to the mean-flow Mach number and not due to the Mach number $M_L = M_c L / \delta_\omega$ across the vortex, we varied M_L by changing the vortex size, keeping the circulation fixed, and compared the resulting disturbance fields. Fig. 9 offers two such comparisons: at $M_c = 0.4$, M_L changed from 0.04 to 0.08, while at $M_c = 0.8$, M_L changed from 0.08 to 0.04. If M_L were the critical parameter, one would expect similarity between the fields at $M_L = 0.04$ and between the fields at $M_L = 0.08$. This is clearly not the case, and, even though details near the vortex core change with size, the overall extent and magnitude of the fields depend only on M_c .

A quantity of great interest in any instability problem is the fluctuation kinetic energy $k = \frac{1}{2} \mathbf{u} \cdot \mathbf{u}$ and its generation terms. For our inviscid, two-dimensional flow,

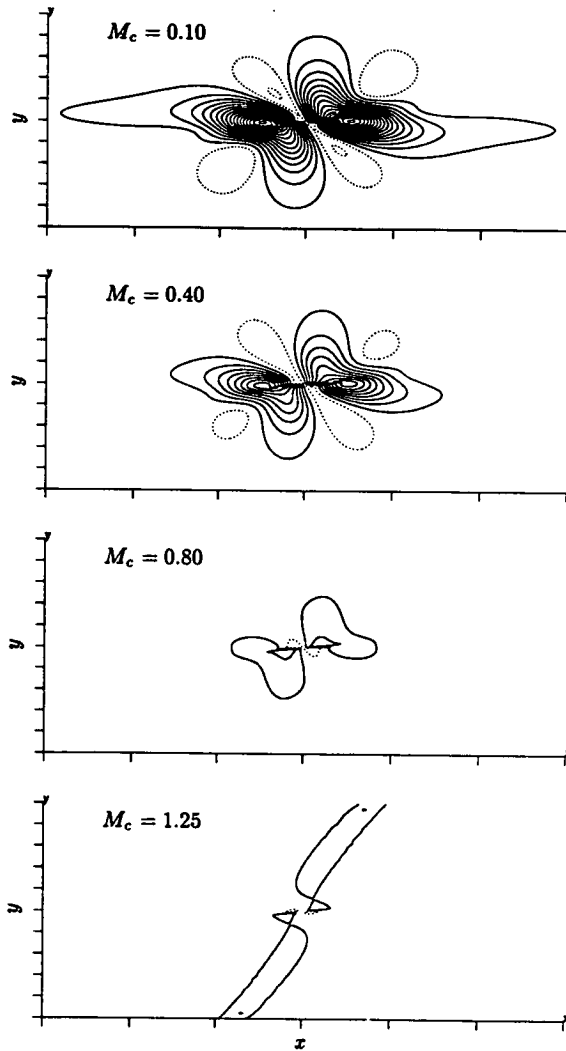


FIGURE 7. Iso-contours of Reynolds shear stress $-uv/(\Delta U)^2$ at $t_s = 4.2$. Contour levels: Maximum= $33E-5$; Minimum= $-5E-5$; Increment= $2E-5$. Negative values are denoted by dotted lines. x -increment= 0.2 ; y -increment= 0.05 .

the instantaneous k is described by

$$\frac{\partial k}{\partial t} + U \frac{\partial k}{\partial x} = -uv \frac{dU}{dy} + p \nabla \cdot \mathbf{u} - \nabla \cdot (p\mathbf{u}) - \nabla \cdot (k\mathbf{u}) \tag{3}$$

The terms on the right-hand side are called production due to shear stress, pressure dilatation, pressure transport, and kinetic-energy transport. We examine the time evolution of the quantities in Eq. 3, integrated in space over our computational domain.

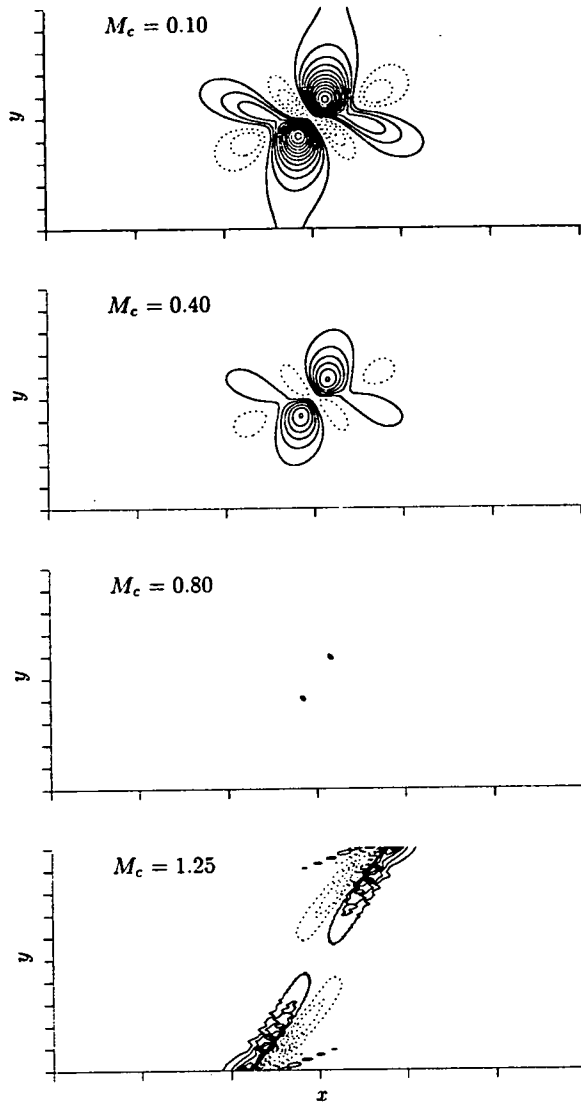


FIGURE 8. Iso-contours of $(v\partial p/\partial y)/\rho_\infty\Delta U^3$ at $t_s = 4.2$. Contour levels: Maximum=0.0026; Minimum=-0.0022; Increment=0.0002. Negative values are denoted by dotted lines. x -increment=0.2; y -increment=0.05.

The growth of the disturbance kinetic energy versus time for different M_c 's is seen in Fig. 10(a). As expected, the higher M_c 's produce significantly lower growth rates. At early times, the growth rate of the $M_c = 1.25$ case slightly exceeds that of the $M_c = 0.8$ case. This is probably due to the longer presence of the wavefront in the computational domain at $M_c = 1.25$. Recall that M_c is increased by lowering the speed of sound, thus the wavefront and its velocity perturbation take longer time to propagate outwards at high M_c . By late times, however, the $M_c = 1.25$ growth rate is seen to saturate and decline below the $M_c = 0.8$ curve. Figure 10(b) shows

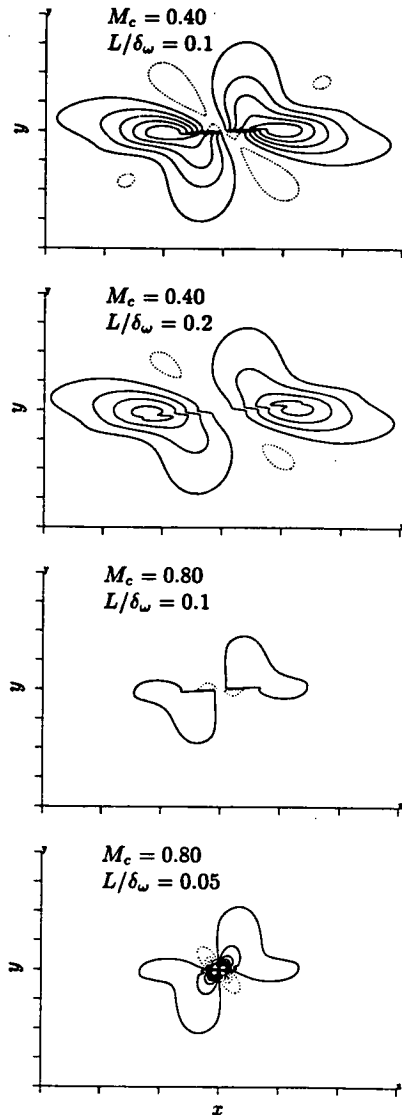


FIGURE 9. Iso-contours of Reynolds shear stress $-uv/(\Delta U)^2$ at $t_s = 4.2$ for variable initial vortex size L . Contour levels: Maximum= $26E-5$; Minimum= $-26E-5$; Increment= $3E-5$. Negative values are denoted by dotted lines. x -increment= 0.1 ; y -increment= 0.05 .

the production due to shear stress, which also declines rapidly with increasing M_c . The pressure dilatation term, seen in Fig 10(c), is much lower than the production term for $M_c = 0.1$ and 0.4 , but becomes comparable at the higher M_c 's. Thus, the decline in growth rates, most of which occurs at subsonic M_c , is primarily due to

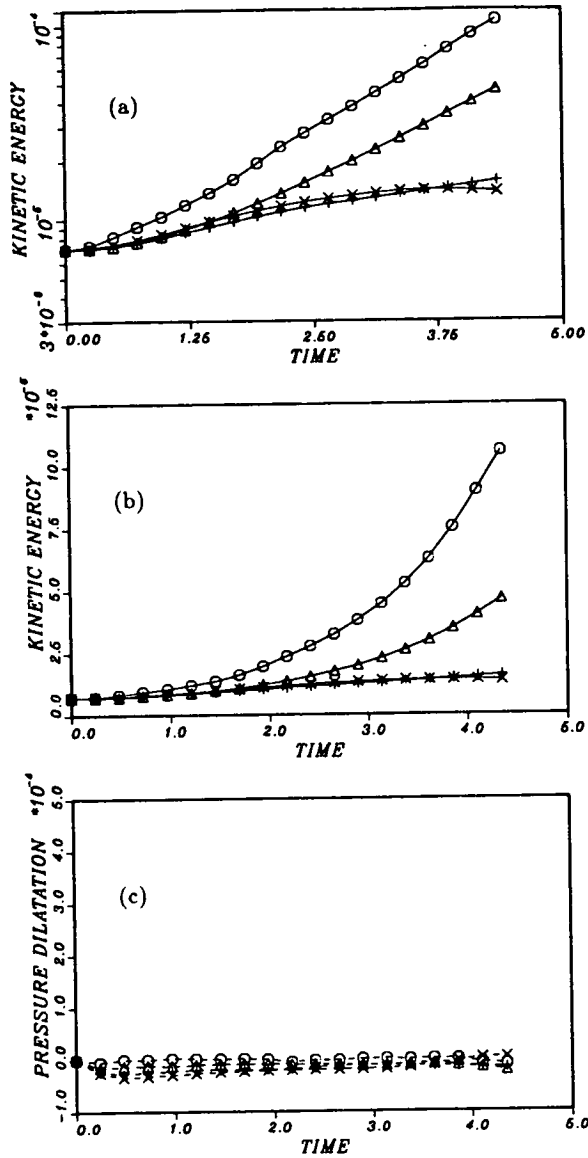


FIGURE 10. Evolution of spatially-integrated quantities versus t_s for variable M_c : (a) perturbation kinetic energy; (b) production due to shear stress; (c) pressure dilatation. $\circ M_c = 0.1$; $\triangle M_c = 0.4$; $+ M_c = 0.8$; $\times M_c = 1.25$.

the reduction in shear stress. The pressure dilatation term becomes significant at high-subsonic and supersonic M_c and makes the overall generation of kinetic energy even smaller. The pressure transport and kinetic-energy transport terms were found to be negligible compared to the previous two terms.

To test the sensitivity of the Mach-number effect on initial conditions, we replaced

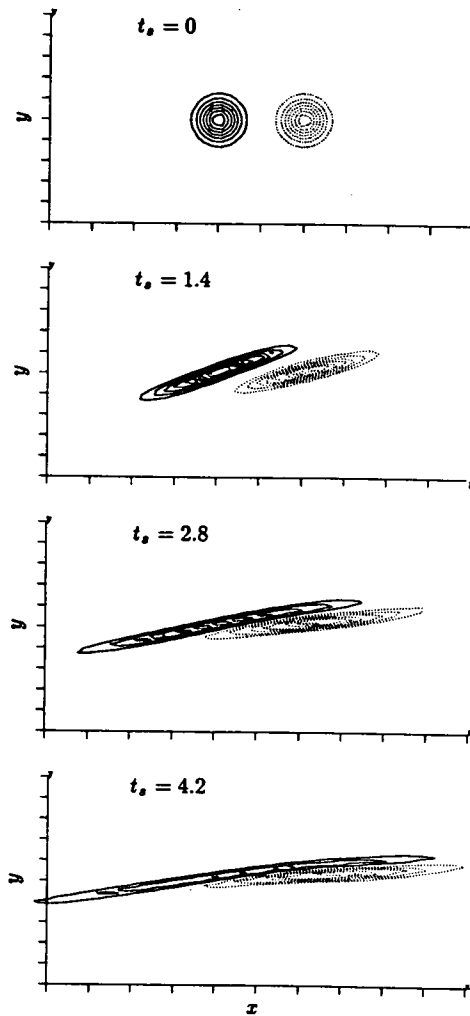


FIGURE 11. Iso-contours of dipole disturbance vorticity $\omega L/\Delta U$ for $M_c = 0.4$. Contour levels: Minimum=-0.07; Maximum=0.07; Increment=0.01. Negative values are denoted by dotted lines. x -increment=0.02; y -increment=0.01.

the single vortex by a vortex dipole. The dipole vortices have the same circulation and size as the previous single vortex, and are separated by a distance $4L$. The shearing of the dipole versus t_s is shown in Fig. 11. At late times, the positive vorticity is stretched a little more than the negative one, probably because of the interaction between the two vorticity regions. The Reynolds shear stress versus M_c is depicted in Fig. 12, where its magnitude and extent are seen to shrink rapidly with increasing M_c , as in the single-vortex case. Additionally, we reversed the circulation of the single vortex, producing a counter-clockwise motion. The magnitude and extent of perturbation fields remained identical to those of the clockwise vortex.

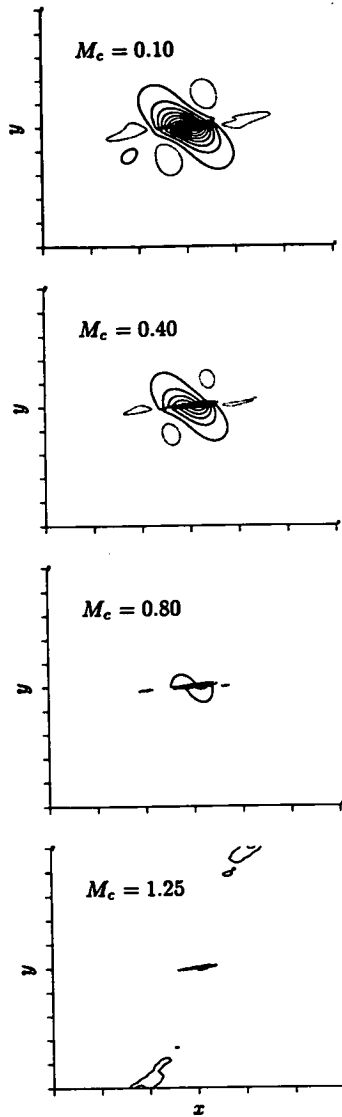


FIGURE 12. Iso-contours of dipole Reynolds shear stress $-uv/(\Delta U)^2$ at $t_s = 4.2$. Contour levels: Maximum= $21E-5$; Minimum= $-5E-5$; Increment= $2E-5$. Negative values are denoted by dotted lines. x -increment= 0.1 ; y -increment= 0.05 .

Evidently, the precise form of the initial condition does not affect the stabilizing influence of the mean-flow Mach number.

To illustrate the robustness of the high- M_c features observed here, we make qualitative comparisons among pressure fields at $M_c = 1.25$ generated by three different

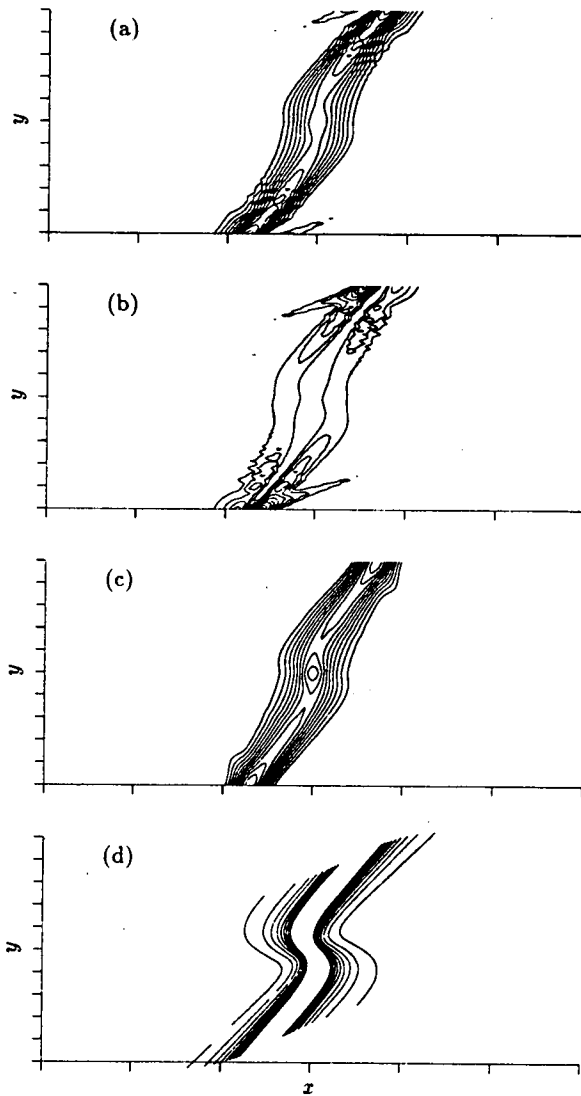


FIGURE 13. Qualitative comparison of $M_c = 1.25$ pressure disturbance fields. Direct simulation:(a) vortex monopole; (b) vortex dipole; (c) acoustic monopole. Geometric acoustics theory:(d) acoustic monopole. x -increment=0.2; y -increment=0.05.

initial conditions. In Fig. 13, the pressure-disturbance fields for (a) a single vortex, (b) a vortex dipole, and (c) an acoustic monopole are displayed. The acoustic monopole has an initial-pressure field same as in the single Oseen vortex, but the vorticity is now zero. All three features look very similar, which once again shows their dominance by the mean-flow Mach number and their independence from details of the initial condition. Fig. 13(d) depicts the field of an acoustic monopole, computed by the simple energy-invariance method of geometric acoustics (for details

see Ref. 19). Even though geometric-acoustics theory is only applicable to high-frequency sources, the calculated pressure field resembles very much those computed by direct numerical simulation.

5. Conclusions

The disturbance field generated by the shearing of a vortex placed in the center of a compressible shear layer has been studied by means of direct numerical simulation. The magnitude and extent of the induced pressure and velocity fields diminish rapidly with increasing convective Mach number M_c , with most of the decrease occurring at subsonic values of M_c . At $M_c > 0.8$, the influence of the vortex is reduced to a zone of narrow streamwise extent. The vortex still communicates to the edges of the shear layer, although communication in the mean-flow direction is practically cut off. Perturbation kinetic-energy growth rates decrease with increasing M_c , primarily due to reduction of the Reynolds shear stress. Pressure dilatation contributes to the decline in growth rates for $M_c > 0.6$. The trends observed here are insensitive to the specific form of the initial disturbance and are a result of the mean-flow Mach number.

REFERENCES

- BREIDENTHAL, R. 1990 The sonic eddy-A model for compressible turbulence. *AIAA-90-0495*.
- BLAISDELL, G. A., MANSOUR, N. N. & REYNOLDS, W. C. 1991 Numerical simulations of compressible homogeneous turbulence, Report No. TF-50, Dept. of Mech. Engrg., Stanford University.
- BLUMEN, W., DRAZIN, P. G., & BILLINGS, D. F. 1975 Shear layer instability of an inviscid compressible fluid. Part 2. *J. Fluid Mech.* **71**, 305-316.
- BROWN, G. L. & ROSHKO, A. 1974 On density effects and large-scale structures in turbulent mixing layers. *J. Fluid Mech.* **64**, 775-781.
- CHINZEI, N., MASUYA, G., KOMURO, G., MURAKAMI, T. & KUDOU, K. 1986 Spreading of two-stream supersonic mixing layers. *Phys. Fluids.* **29**, 1345-1347.
- GOEBEL, S. G. & DUTTON, J. C. 1991 Experimental study of compressible turbulent mixing layers. *AIAA J.* **29**, 538-546.
- GROPENGIESSER, H. 1970 Study of the stability of boundary layers in compressible fluids *NASA TT-F-12*, 786.
- KIM, S. C. 1990 New mixing length model for supersonic shear layers. *AIAA J.* **28**, 1999-2000.
- LANDAU, L. 1944 Stability of tangential discontinuities in compressible fluid. *Dokl. Akad. Nauk. SSSR.* **44**, 139-141.
- LELE, S. K. 1989 Direct numerical simulation of compressible shear flows. *AIAA-89-0374*.

- LELE, S. K. 1992 Compact finite difference schemes with spectral-like resolution, to appear in *Computational Physics*.
- LIN, C. C. 1953 On the stability of the laminar region between two parallel streams in a gas. *NACA Report TN 2887*.
- MACK, L. M. 1984 Boundary-layer linear stability theory. *AGARD Report R-709*.
- MORKOVIN, M. V. 1987 Transition at hypersonic speeds. *NASA-CR-178315, ICASE Interim Report 1*.
- PAPAMOSCHOU, D. & ROSHKO, A. 1988 The turbulent compressible shear layer: an experimental study. *J. Fluid Mech.* **197**, 453-477.
- PAPAMOSCHOU, D. 1991 Effect of Mach number on communication between regions of a shear layer. *Eighth Symp. Turb. Shear Flows*.
- RAGAB, S. A. & WU, J. L. 1988 Instabilities in turbulent free shear layers formed by two supersonic streams. *AIAA-88-0038*.
- SAMIMY, M. & ELLIOTT, G. S. 1990 Effects of compressibility on the characteristics of free shear layers. *AIAA J.* **28**, 439-445.
- SANDHAM, N. & REYNOLDS, W. 1990 The compressible mixing layer: linear theory and direct simulation. *AIAA J.* **28**, 618-624.
- SIRIEIX, M. & SOLIGNAC, J. L. 1966 Contribution a l'etude experimentale de la couche de melange turbulent isobare d'un ecoulement supersonique. *Symposium on Separated Flow, AGARD Conf. Proc.* **4**, 241-270.
- ZHUANG, M., KUBOTA, T. & DIMOTAKIS, P. E. 1990 Instability of inviscid, compressible shear layers. *AIAA J.* **28**, 1728-1733.

445361

516-34

189676 277
 N94-A14761

Evolution of the shock front and turbulence structures in the shock/turbulence interaction

By N. Kevlahan¹, K. Mahesh² AND S. Lee³

The interaction of a weak shock front with isotropic turbulence has been investigated using Direct Numerical Simulation (DNS). Two problems were considered: the ability of the field equation (the equation for a propagating surface) to model the shock and a quantitative study of the evolution of turbulence structure using the database generated by Lee *et al.* (1992).

Field equation model predictions for front shape have been compared with DNS results; good agreement is found for shock wave interaction with 2D turbulence and for a single steady vorticity wave. In the interaction of 3D isotropic turbulence with a normal shock, strong alignment of vorticity with the intermediate eigenvector of the rate of strain tensor ($S_{ij}^* = S_{ij} - 1/3\delta_{ij}S_{kk}$) is seen to develop upstream of the shock and to be further amplified on passage through the shock. Vorticity tends to align at 90° to the largest eigenvector, but there is no preferred alignment with the smallest eigenvector. Upstream of the shock, the alignments continue to develop even after the velocity derivative skewness saturates. There is a significant tendency, which increases with time throughout the computational domain, for velocity to align with vorticity. The alignment between velocity and vorticity is strongest in eddy regions and weakest in convergence regions.

1. Introduction

The subject of this investigation is the interaction of a weak shock (mean upstream Mach number, $M_1 = 1.05 - 1.20$) with relatively strong turbulence ($M_t = 0.07 - 0.40$ where M_t is the fluctuation Mach number defined as q/\bar{c} ; q is a velocity scale of the turbulence and \bar{c} is the mean sound speed). The interaction of shock waves with turbulence has been studied analytically (using the Linear Interaction Analysis) by many authors (eg. Ribner 1954, McKenzie & Westphal 1968, Anyiwo & Bushnell 1982). Experimental investigations have recently been carried out by Jacquin *et al.* (1991), Honkan & Andreopoulos (1990) and Hesselink & Sturtevant (1988). Numerical simulations of the shock turbulence interaction have been performed by Rotman (1991) and Lee *et al.* (1992).

We study shock/turbulence interaction as simulated by Lee *et al.* (1992). In the simulation the reference frame is fixed with respect to the mean shock position; the mean flow approaches the shock supersonically ($M_1 > 1$) and exits subsonically. Shock wave structure is resolved by the Navier-Stokes equations without

1 University of Cambridge

2 Stanford University

3 Center for Turbulence Research

using shock-fitting or shock-capturing techniques. Inflow turbulence is generated with a prescribed energy spectrum ($E(k) \propto k^4 \exp(-k^2)$) and is then allowed to evolve naturally as the flow approaches the shock front. The turbulence should be fully developed by the time it reaches the shock wave, and this is verified by making sure that the velocity derivative skewness stabilizes well upstream of the shock. Pressure and density are kept constant in the inflow plane. The simulation uses a $193 \times 64 \times 64$ grid and the Reynolds number based on the Taylor microscale, Re_λ , is 16.7.0. The study is divided into two parts: the effect of the turbulence on the shock (shock front evolution), and the effect of the shock on the turbulence (turbulence structure evolution).

In the first part of this study we test a new model for shock front/turbulence interaction based on a field equation approach where the front is treated as a surface which propagates normal to itself and is distorted by the turbulent velocity field. This model not only gives the instantaneous position and shape of the front, but can also be used to close the Rankine-Hugoniot equations for a curved front. Once the Rankine-Hugoniot equations have been closed, the turbulence quantities downstream of the shock can be calculated. In the weak shock/relatively strong turbulence regime considered here, the shock may become significantly distorted (however, it will still remain identifiable). Because of this strong deformation, the evolution of the shock front will not be well predicted by linear theories such as the Linear Interaction Analysis (LIA) which assume that the shock merely copies the shape of the distorting velocity field but at a different amplitude. The field equation, being nonlinear, can be used in such cases of large shock front distortion. The field equation approach has the advantages of simplicity and ease of numerical implementation. One important practical application of the field equation approach would be its inclusion in DNS to avoid having to numerically resolve the shock wave structure. Removing this restriction would greatly increase the maximum Mach number that can be reached using DNS. The field equation model is validated by comparing the shape and position of the shock front predicted by the field equation with two-dimensional DNS results under the same conditions. The field equation model is described in more detail in §2 below.

The second part of this investigation is a quantitative study of turbulence structure evolution. In this part, we analyze turbulence structure in planes (parallel to the mean shock) upstream and downstream of the shock. We are interested both in general aspects of turbulence structure and its development and in the effect of the rapid compression on the turbulence structure as it passes through the shock. To characterize turbulence structure we consider three dynamically important properties of the flow: (i) the angle between the vorticity and the shock normal, (ii) the angle between the vorticity and the eigenvectors of the strain rate tensor, (iii) the angle between the velocity and vorticity vectors. The flow is also divided into four classes of structure (eddies, shear, convergence, and streaming) based on local values of the rate of strain and rate of rotation tensors. Since we are interested in turbulence evolution, in all cases the instantaneous mean (computed by averaging over homogeneous directions) is subtracted before any analysis is performed.

2. Modeling shock front evolution

2.1. The field equation model

In this section we describe the validation of the field equation model applied to shock/turbulence interaction by comparison with DNS.

The field or G-equation model has been introduced by Kerstein *et al.* (1988) as a model for the propagation of a zero-thickness, constant-density premixed flame through a homogeneous turbulent flow. In this model a continuous scalar $G(x, y, t) = x - g(x, y, t)$ is convected by the flow with the surface $G(x, y, t) = 0$ corresponding to the position of the physical flame front. The flame propagates at a speed u_F normal to itself and is at the same time advected by the turbulent flow (\mathbf{u}) as described by equation (1) below.

$$\frac{\partial G}{\partial t} + \mathbf{u} \cdot \nabla G = u_F |\nabla G| \quad (1)$$

In general, u_F will be a function of the shape of the front, the local straining, and the history of the distortion (in the case of the flame front u_F is modeled as a function of local strain and curvature—the flame stretch).

The aim of this study is to determine whether the field equation model can be usefully applied to the propagation of a shock front through a turbulent flow. Initially, we take the simplest two-dimensional form of the model where u_F is taken as a constant: the laminar propagation speed of the front. If it is assumed that the front does not curl over on itself (as is assumed in the usual derivation of the Rankine-Hugoniot conditions for a curved front), then equation (1) for the propagation of the front may be re-written in terms of $g(y, t)$ as

$$\frac{\partial g}{\partial t} = u_F(1 + g_y^2)^{1/2} + u - v g_y \quad (2)$$

where u and v are, respectively, the x - and y -components of the turbulent velocity field (in a frame fixed in the mean shock, the mean shock speed must be subtracted from u), and the initial condition is that $g(y, 0) = 0$. Once equation (2) has been solved, $g_x(y, t)$ and $g_y(y, t)$ may be substituted into the Rankine-Hugoniot equations for a curved shock,

$$g_x[\rho] + g_y[\rho V] = [\rho U] \quad (3a)$$

$$g_x[\rho U] + g_y[\rho UV] = [\rho U^2 + P] \quad (3b)$$

$$g_x[\rho V] + g_y[\rho V^2 + P] = [\rho UV] \quad (3c)$$

$$g_x[\rho E] + g_y[V(\rho E + P)] = [U(\rho E + P)] \quad (3d)$$

to obtain the changes of turbulence quantities downstream of the shock front. In equations (3a-d), [] indicates the difference of the quantity in the brackets across the front and E is the internal energy ($= P/(\gamma - 1) + (U^2 + V^2)/2$ for an ideal gas). Equations 3(a-d) represent, respectively, conservation of mass, x -momentum,

y -momentum, and total energy across the shock front. The above conditions can be combined to give a further condition: the tangential component of velocity is continuous across the front. Equations (3a-d) can be solved for the turbulence (fluctuating) quantities u_2 , v_2 , P_2 , and ρ_2 downstream of the shock in terms of $g_t(y, t)$ and $g_y(y, t)$ and the upstream quantities:

$$u_2 = \{g_y^3(\gamma + 1)u_1v_1 + g_y^2[2v_1^2 - (\gamma + 1)u_1^2 + (\gamma + 1)u_1g_t - 2\gamma P_1/\rho_1] + g_y[(\gamma - 3)u_1v_1 + 4v_1g_t] + (1 - \gamma)u_1^2 + (\gamma - 3)u_1g_t - 2\gamma P_1/\rho_1 + 2g_t^2\} / \{(\gamma + 1)[g_y^3v_1 + (1 + g_y^2)(g_t - u_1) + g_yv_1]\} \quad (4a)$$

$$v_2 = v_1 + g_y(u_1 - u_2) \quad (4b)$$

$$P_2 = P_1 + \rho_1[u_1^2 - g_yu_1v_1 - g_tu_1 + u_2(g_yv_1 + g_t - u_1)] \quad (4c)$$

$$\rho_2 = \frac{\rho_1(g_yv_1 + g_t - u_1)}{[g_y^2u_1 + g_yv_1 + g_t - u_2(1 + g_y^2)]} \quad (4d)$$

Note that equations (4a-d) are *exact* solutions for the downstream quantities; no approximations or additional assumptions have been made in their derivation.

So we see that the field equation model for shock front evolution (2) provides a nonlinear closure to the Rankine-Hugoniot equations for a curved shock (3a-d) which allows us to obtain the changes in turbulence quantities across the shock (equations 4a-d). Because the closure is nonlinear and because we have made no linearizing assumptions in solving the Rankine-Hugoniot equations, this field equation/Rankine-Hugoniot model will be able to treat large deformations of the shock front and to predict nonlinear amplification effects of turbulence quantities across the front. LIA theory cannot be applied in the case of large deformation and will not be able to predict any nonlinear amplification. Shock dynamics theory is mathematically complicated and awkward to use in the case of fully developed turbulence.

The assumption of constant u_F is in a sense equivalent to the geometrical acoustics limit of shock dynamics. In both cases, the rays of an initially curved front in a uniform flow (eg. in the shock focusing experiments of Sturtevant & Kulikarny (1976)) will eventually cross, leading to a cusp-shaped front. The field equation (2) for the propagation of the front is not, however, the same as the eikonal equation for geometrical acoustics: $g_t^2 = c^2g_y^2$. That the field equation model is a better physical model than the eikonal equation for geometrical acoustics can be seen by working out the second order perturbation solution to the exact Rankine-Hugoniot equations (3a-d) for the evolution of the shock front.

The Rankine-Hugoniot equations for a curved front may be closed to second order by assuming that the flow downstream of the front is isentropic. The assumption of isentropy is very good for weak shocks: changes in entropy are of third order in the pressure jump across the shock. This leads to the following relation between pressure and density fluctuations:

$$p = \gamma \frac{P}{R} \rho \left(1 + \frac{1}{2}(\gamma - 1) \frac{\rho}{R} \right), \quad (5)$$

where upper case indicates mean quantities and lower case indicates fluctuating quantities. Combining equations (3a-d) with equation (5) closes the Rankine-Hugoniot equations to second order. Performing a perturbation expansion to second order in the $O(\epsilon)$ quantities u , v , P , ρ , g_t , and g_y on finds the following second-order solution for the evolution of the shock front:

$$g_t^2 + g_t(F_1 - 2u_1) = F_1 u_1 - u_1^2 + F_2 g_y v_1 + F_3 g_y^2 \quad (6)$$

where the F_i 's are coefficients that depend on mean flow quantities. From equation (5), letting $g_t = \epsilon g_{1t} + \epsilon^2 g_{2t} + O(\epsilon^3)$, $g_y = \epsilon g_{1y} + \epsilon^2 g_{2y} + O(\epsilon^3)$, $u_1 = \epsilon u_1$, $v_1 = \epsilon v_1$ the first-order solution is

$$g_{1t} = u_1, \quad (7)$$

and the second-order solution is

$$g_{2t} = \frac{F_3}{F_1} g_{1y}^2 + \frac{F_2}{F_1} g_{1y} v_1. \quad (8)$$

Now, a similar second-order perturbation expansion for the field equation (2) yields the following solutions:

$$g_{1t} = u_1 \quad (9)$$

and,

$$g_{2t} = \frac{1}{2} u_F g_{1y}^2 - g_{1y} v_1. \quad (10)$$

Thus, we see that the field equation gives essentially the same behavior as the solution of the full Rankine-Hugoniot equations, at least to second order. Note that the Rankine-Hugoniot equations do not have a closed-form analytical solution.

Nonlinear shock dynamics theory allows the shock propagation velocity to vary in proportion to the inverse square root of ray tube areas. This leads to higher propagation speeds in concave regions and lower speeds in convex regions of the front, thus reducing the tendency to form cusp. The assumption of constant u_F should be good until the constant u_F equation predicts cusp formation. In practice, when the front is distorted by a turbulent flow it will never distort to the extent of forming cusps, so the assumption of constant u_F is well justified. In the case of very weak shocks/strong turbulence, some variation of u_F (perhaps a dependence on shock curvature) should be included in the model.

2.2. Validating the field equation model

The field equation model is validated by comparing its predictions of front evolution with DNS. Since our interest is in nearly incompressible turbulence interacting with the shock, we consider the interaction of vorticity waves with the shock. Three cases are considered in order of increasing complexity (see Figure 1). First, the interaction of a shock with a single steady vorticity wave (one sine wave $u = A \sin ky$ at normal incidence to the shock), next, the interaction of a shock with a single

c-4

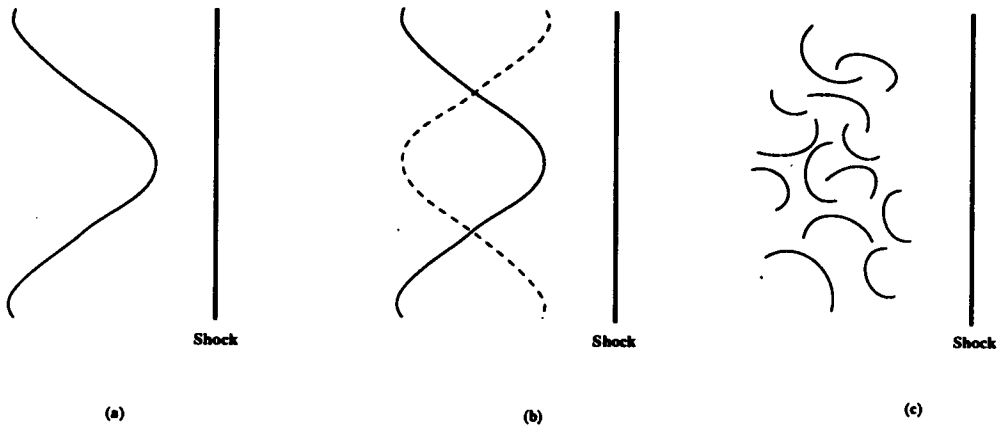


FIGURE 1. The three cases considered. (a) Steady, single mode, $u = A \sin ky$, (b) unsteady, single mode, $u = A \sin ky \cos \omega t$. $\tau_{\text{turb.}}/\tau_{\text{shock}} \sim 1$, (c) unsteady, many modes, 'full turbulence'. $\tau_{\text{turb.}}/\tau_{\text{shock}} \gg 1$.

unsteady mode, and finally, the interaction of a shock with 2D turbulence (many unsteady modes at various angles of incidence).

In the second case, the time for the shock to pass through the 'turbulence' is of the same order as the time-scale of the 'turbulence', while in the third case, the time for the shock to pass through an eddy is much less than the turnover time of the eddy.

In the first case, the prediction of the field equation is calculated from its third-order perturbation expansion solution:

$$\begin{aligned} \phi(\eta, \tau) = & \tau + \epsilon \tau \sin \eta + \frac{1}{6} \epsilon^2 \tau^3 \cos^2 \eta \\ & - \frac{1}{15} \epsilon^3 \tau^5 \sin \eta \cos^2 \eta + O(\epsilon^4). \end{aligned} \quad (11)$$

Where non-dimensional quantities $\epsilon = u/u_F$, $\eta = ky$, $\tau = u_F t k$, $\phi = kg$. Note that a *secularity* in time appears in (11): the perturbation expansion will break down when

$$\tau_c = \epsilon^{-1/2} \quad (12)$$

or,

$$t_c = (k^2 u_F u)^{-1/2}. \quad (13)$$

This is the time one expects the front to form *cusps* (places where the curvature becomes infinite). The simple version of the field equation with constant u_F is valid until t_c .

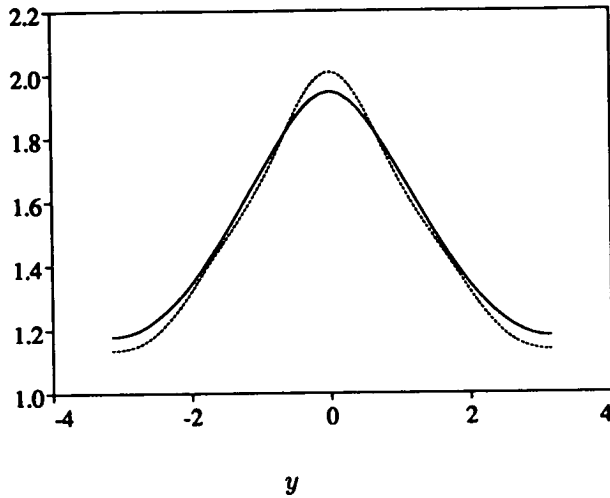


FIGURE 2. Comparison of front shape in DNS with field equation prediction. Comparison is made just before cusp formation (the worst time of agreement). — DNS, ---- Field equation

For the second case, the field equation is solved numerically using a Fourier spectral method; for the third case, the field equation with a viscous term $\epsilon \nabla^2 G$ for numerical stability is incorporated into the code of Lee *et al.* (1992). In all three cases, the position of the shock in the DNS is found from the pressure half-rise point.

In the first case, the agreement between the field equation and DNS was very good until the time predicted by the field equation for cusp formation. Both the curvature and front shape agreed well (see Figure 2). After the 'cusp' formed the DNS showed the formation of two secondary shocks which increased in strength and extent over time, while the original shock decreased in strength (see Figure 3). The post-cusp multi-shock DNS results are similar to what was seen in the shock-focusing experiments of Sturtevant & Kulkarny (1976).

The agreement in the second case is very poor: both the shape and magnitude of the distortion predicted by the field equation do not match the DNS results. We believe this discrepancy is due to the larger deviation of u_F from its assumed constant value in this case.

In the case of 2D turbulence ($M_1 = 1.2$, $M_t = 0.07$), the agreement of the field equation prediction with DNS is very good, even over periods as long as three eddy turnover times ($\tau_{turb.} = \lambda/u'$). The correlation between the displacement and slope of the field equation predictions and DNS is always over 80%, and mostly above 90% (see Figure 4). The RMS error of the field equation predictions for displacement and slope are also relatively low: generally less than 50% (see Figure 4). The fact that the field equation model works well in the case of turbulence and the steady vorticity wave, but not for the unsteady wave, indicates that the shock sees the turbulence as

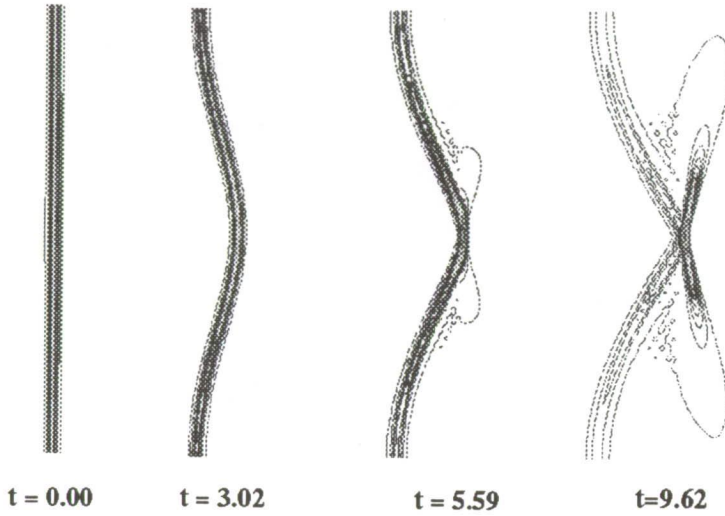


FIGURE 3. Evolution of front shape in DNS. Quantity plotted is dilatation. Note the cusp-like shape at $t=5.59$ and the formation of strong secondary shocks by $t=9.62$

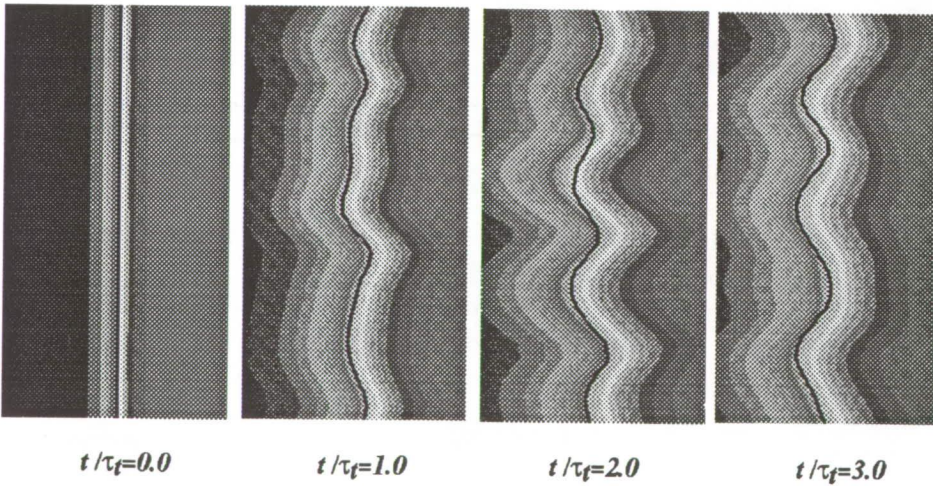


FIGURE 4. Comparison between instantaneous shock position in DNS and field equation prediction over time. The dark line is the DNS prediction.

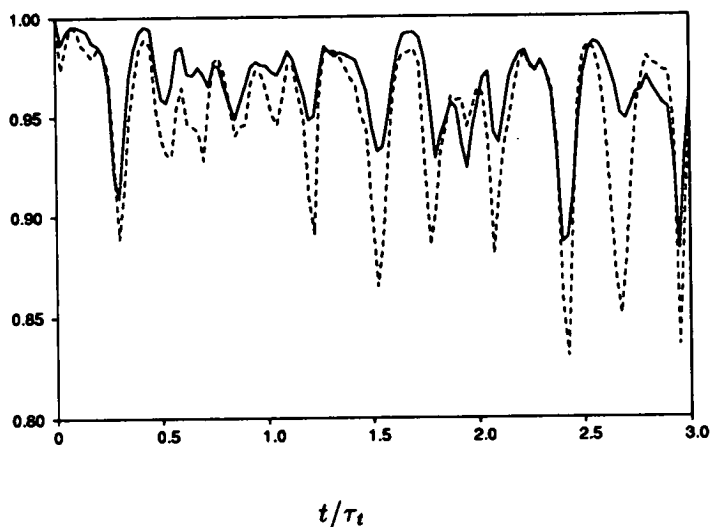


FIGURE 5A. Correlation between DNS and field equation of instantaneous shock position in 2D shock/turbulence interaction — Displacement, ---- Slope

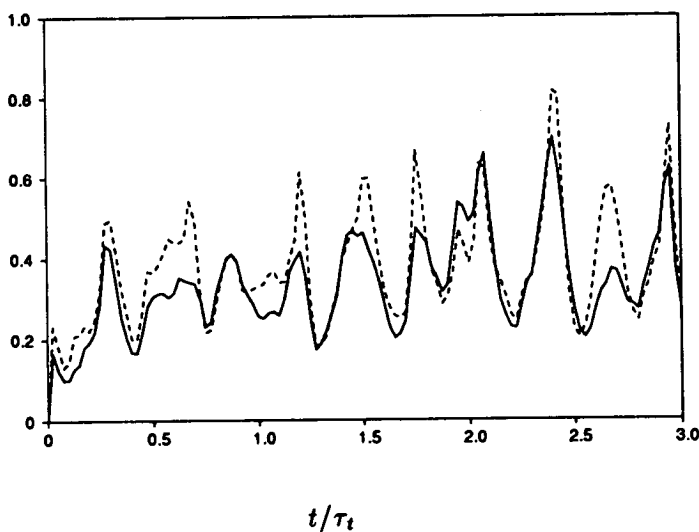


FIGURE 5B. RMS error in the field equation prediction of instantaneous shock position in 2D shock/turbulence interaction — Displacement, ---- Slope

frozen. Hence, the case of turbulence corresponds to the steady case (the turbulence time scale is about 1/100 the shock passage time) and the agreement of the field equation model with DNS is good. Note that presence of multiple modes at various angles of incidence does not seem to affect the validity of the field equation model.

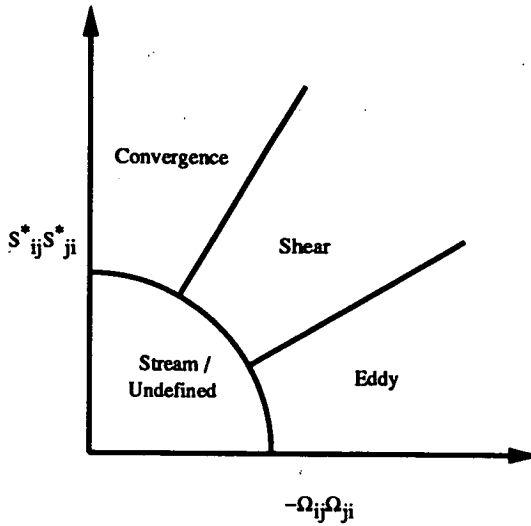


FIGURE 6. Schematic of the way the $S_{ij}^*S_{ji}^*$ - $-\Omega_{ij}\Omega_{ji}$ plane is divided into four characteristic structures.

3. Evolution of turbulence structure

In this section, we use the database of Lee *et al.* (1992) to study the evolution of turbulence structure in 3D isotropic turbulence/normal shock interaction. The results presented correspond to case *C* for which $M_1 = 1.2$, $M_t = 0.095$, and $Re_\lambda = 11.9$ upstream of the shock. The following three quantities were investigated: (i) the angle between the vorticity vector (ω) and the shock-normal, (ii) the angle between ω and the eigenvectors of the trace-free strain rate tensor defined as,

$$S_{ij}^* = \frac{1}{2} \left(\frac{\partial u_i}{\partial x_j} + \frac{\partial u_j}{\partial x_i} \right) - \frac{1}{3} \delta_{ij} \frac{\partial u_k}{\partial x_k}, \quad (14)$$

and (iii) the angle between the velocity and vorticity vectors.

The angle between ω and the eigenvectors of the rate of strain is indicative of the type of turbulence structure. Recent DNS of homogeneous, isotropic turbulence (eg. Ashurst *et al.* 1987, Vincent & Meneguzzi 1991) show that the vorticity vector aligns with the *intermediate* eigenvector of the strain rate tensor. The angle between the velocity and vorticity gives the balance between helicity density (their dot product, believed to be related to coherent large scale structures) and the nonlinear transfer of energy between scales (a function of their cross product). Some DNS (eg. Pelz *et al.* 1985 and She *et al.* 1991) show a tendency for the velocity and vorticity to align (a reduction in nonlinearity), while others (eg. Rogers & Moin 1987) see little preferential alignment.

We also compute the ratio of eigenvalues of S_{ij}^* ($\alpha : \beta : \gamma$) and the relative numbers of 'cigar' ($\alpha\beta\gamma > 0$) and 'pancake' ($\alpha\beta\gamma < 0$) regions (see Kevlahan (1992)). In addition, we classify the flow (see Figure 6) into four structures (convergence, shear, eddy, and streaming) based on $(S_{ij}^*S_{ji}^*)$ and the $(-\Omega_{ij}\Omega_{ji})$ (where Ω_{ij} is the rotation

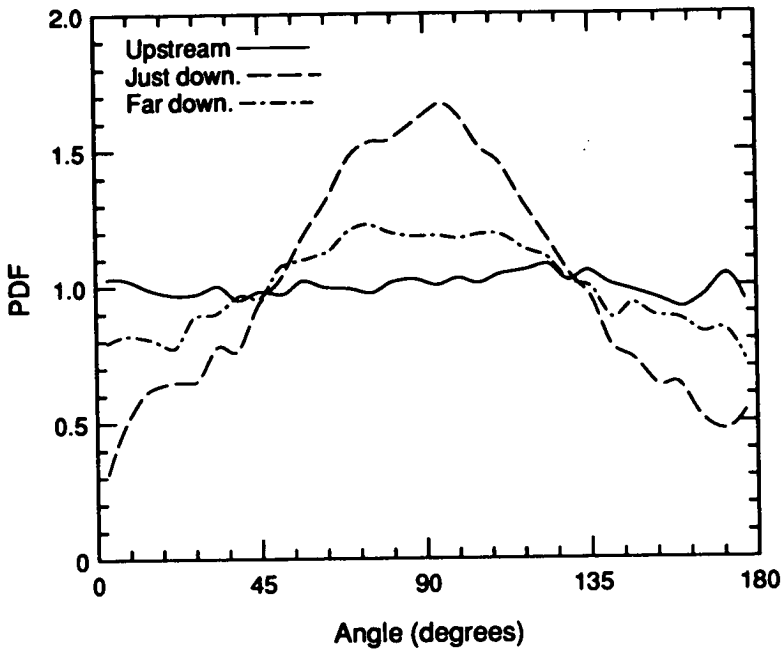


FIGURE 7. PDF of the angle between vorticity and the shock normal upstream of the shock (plane 72), just downstream of the shock (plane 111), far downstream (plane 174). The PDFs have been normalized by dividing by the sine of the angle and scaled so that 1.0 corresponds to a flat distribution. Note the persistence of the alignment far downstream where the flow is essentially incompressible.

rate tensor). Structures are further classified as incompressible, compressed, or expanded based on the value of $S_{kk}^2 / (S^{*2} + \Omega^2)$ (if greater than 5% the region is classified as compressible) and S_{kk} (less than zero, compressed; greater than zero, expanded).

According to this structural classification, convergence regions are places of high irrotational straining, shear regions are places of approximately equal rotational and irrotational straining, eddies are regions of high rotational straining, and stream regions are places where both the rotational and irrotational strains are small but the kinetic energy is large.

The quantities described above are calculated in planes parallel to the mean shock and averaged over ten realizations and homogeneous directions. The instantaneous means over the plane are subtracted from each quantity before they are analyzed. This eliminates the mean flow distortion and allows us to concentrate on the behavior of the turbulence itself. The PDFs of angles are normalized by the sine of the angle so that vectors isotropically distributed will lead to a flat distribution (if vectors are distributed isotropically over a sphere then the number of vectors at any angle to the 'north pole' is proportional to the sine of the angle).

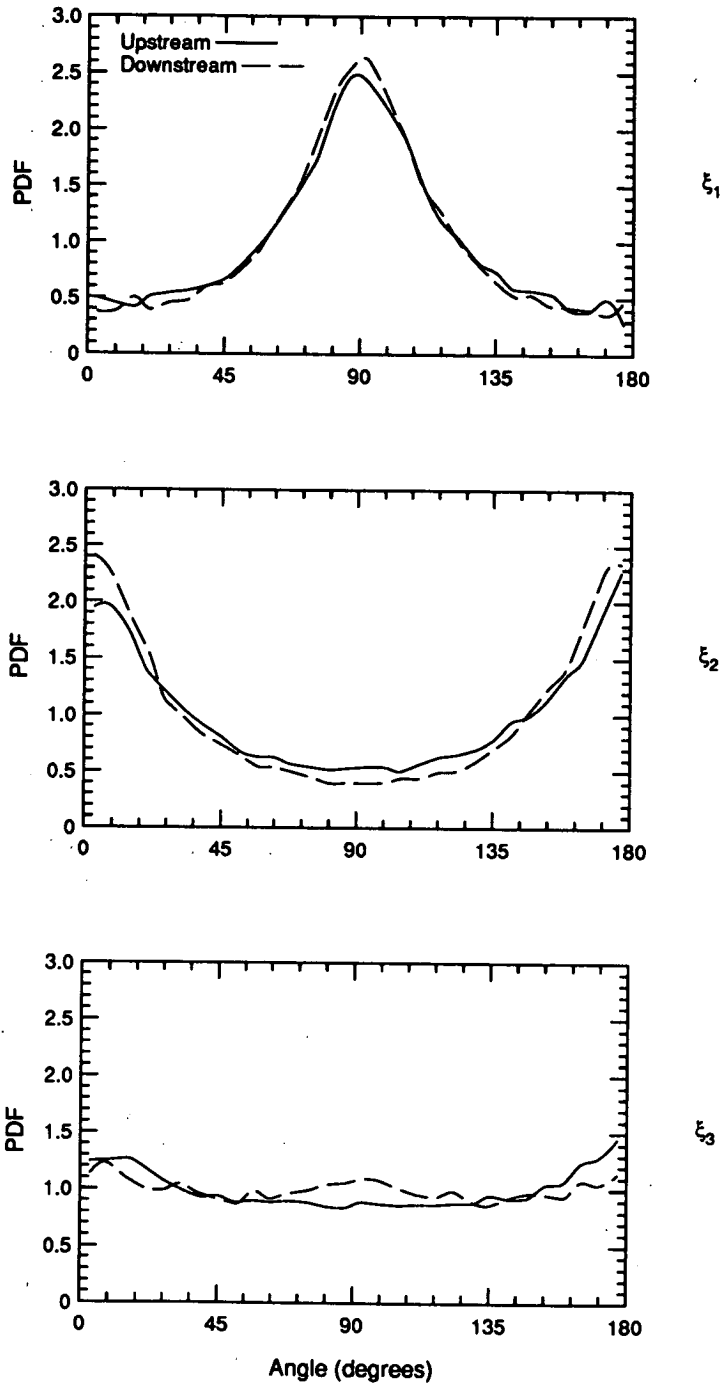


FIGURE 8. PDFs of the angle between the vorticity vector and the three eigenvectors of the rate of strain tensor upstream and downstream of the shock. Note the amplification of the alignments by the shock. The PDFs have been normalized by dividing by the sine of the angle and scaled so that 1.0 corresponds to a flat distribution. (a) Angle with largest eigenvector, (b) angle with middle eigenvector, (c) angle with smallest eigenvector.

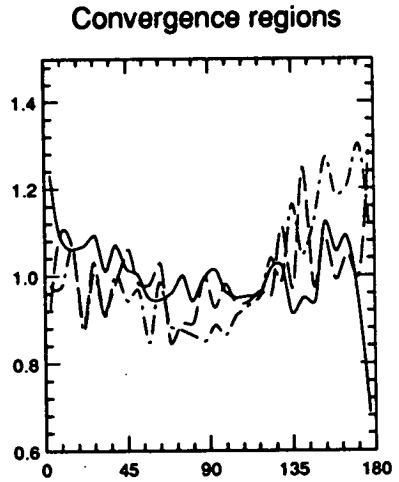
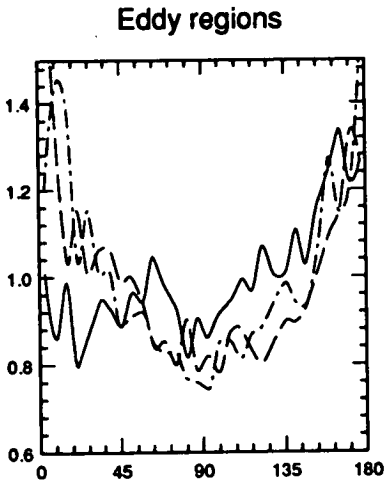
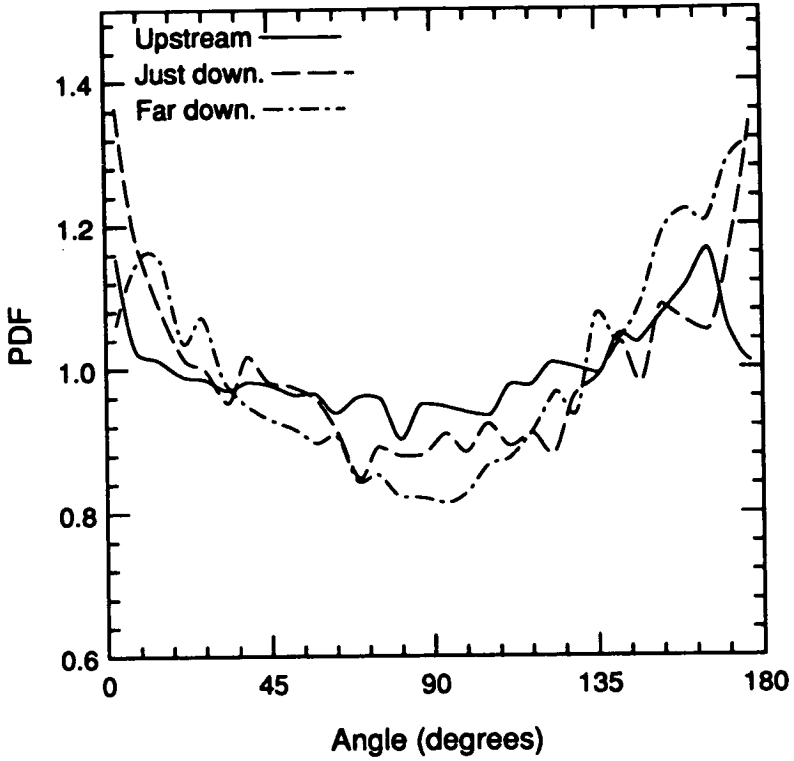


FIGURE 9. Angle between the vorticity and velocity vectors. Note the significant tendency for the vorticity and velocity vectors to align. (a) Overall, (b) in eddy regions, (c) in convergence regions.

3.1. Turbulence structure results

The eigenvalues of S_{ij}^* are in the ratio 4 : 1 : -5 and are unchanged up and downstream of the shock except in the vicinity of the shock itself where the middle eigenvalue increases leading to the ratio 2 : 1 : -3. These results are similar to the ratio 3 : 1 : -4 found by Chen *et al.* (1990) for isotropic incompressible flows. The flow is divided into pancake and cigar regions in the ratio 3 : 1 both upstream and downstream of the shock. The flow is composed of 27% convergence, 39% shear, 23% eddies, and 4% streams (7% undefined). This distribution is constant up and downstream of the shock. In the vicinity of the shock, the distribution changes to 33% convergence, 26% shear, 11% eddies, and 8% streams (22% undefined). In the vicinity of the shock, 82% of structures are compressible, and of these half are expanded and half are compressed. Eddies and shear regions are primarily *expanded* structures, while convergence regions are primarily *compressed*.

The vorticity vector preferentially aligns parallel to shock surface downstream of the shock with a probability 1.7 times as much as in a flat distribution (see Figure 7). This is a well known effect of the compression in the shock normal direction which amplifies the vorticity parallel to the shock and leaves vorticity normal to the shock unchanged.

Upstream of the shock where the turbulence is isotropic, we observe a very strong tendency for ω to align with ξ_2 (the middle eigenvector of S_{ij}^*) and to align at 90° to ξ_1 (the largest eigenvector of S_{ij}^*) (see Figure 8). Alignment of the vorticity with ξ_2 and at 90° to ξ_1 is 2.5 times more likely than in a flat distribution. The PDF of the angle between ω and ξ_3 is approximately flat. These alignments saturate before the turbulence interacts with the shock. The alignments are further amplified on passage through the shock, which is consistent with the Rapid Distortion Analysis of Kevlahan (1992). An interesting point regarding the flow upstream of the shock is that this alignment continues to develop *after* the velocity derivative skewness has saturated. This may suggest that skewness saturation may not be the best indicator that the turbulence is fully developed (evidently some structural evolution continues even after the skewness has stabilized).

We observe a significant tendency for the velocity and vorticity vectors to align (see Figure 9). This tendency increases as the flow moves through the computational domain. Alignment (or anti-alignment) far downstream is about 1.35 times as likely as in flat distribution. This alignment is strongest in eddy regions (1.48 times as likely) and weakest in convergence regions (about 1.05 times as likely). This indicates that the primary cause of the increase in helicity density (or decrease in nonlinearity) is vortical rather than irrotational straining. There also seems to be a tendency towards asymmetry upstream of the shock (eddies tend to antialign), although this may not be significant. These results are somewhat stronger than those of Rogers & Moin (1987) who find at most only a 20% deviation from a flat distribution. This discrepancy may be due to the differences in the flows (ours is slightly compressible and theirs is incompressible) or because our Reynolds number is relatively low (about 25) and they find that the reduction in nonlinearity decreases as Reynolds number increases.

4. Conclusions

Field equation model predictions for front shape have been compared with DNS results, and agreement is very good for 2D turbulence ($M_1^U = 1.20$, $M_t = 0.07$) and for a single steady vorticity wave. The field equation approach shows promise as a way of modeling the shock/turbulence interaction.

The eigenvalues of S_{ij}^* in the developed turbulence are in the ratio 4 : 1 : -5, except in the vicinity of the shock where they are in the ratio 2 : 1 : -3. The ratio of pancake to cigar type straining regions is in the ratio 3 : 1.

In the vicinity of the shock, 82% of structures are compressible and of these half are expanded and half are compressed. Eddies and shear regions are primarily *expanded* structures, while convergence regions are primarily *compressed* downstream of the shock.

Strong alignment of vorticity with the intermediate eigenvector of the trace-free strain rate tensor is seen upstream of the shock and further amplifies on passage through the shock. Vorticity tends to align at 90° to the largest eigenvector, but there is no preferred alignment with the smallest eigenvector. The alignments continue to develop upstream even after the skewness saturates. This suggests that skewness may not be the best indicator of fully developed isotropic turbulence.

It is interesting to note that our results on the alignment of vorticity with ξ_2 and the ratio of the eigenvalues are sometimes thought to be the result of turbulent structures such as long vortex tubes (eg. Jiménez 1992), and yet our Reynolds number is too low for these tubes to have formed.

There is a significant tendency for velocity to align with vorticity. This tendency continues to increase with time throughout the computational domain. The alignment between velocity and vorticity is strongest in eddy regions and weakest in convergence regions.

REFERENCES

- ANYIWO, J. C. & BUSHNELL, D. M. 1982 Turbulence amplification in shock-wave boundary-layer interaction. *AIAA J.* **20**(7), 893-899.
- ASHURST, W. T., KERSTEIN, A. R., KERR, R. M. & GIBSON, C. H. 1987. Alignment of vorticity and scalar gradients with strain rate in simulated Navier-Stokes turbulence. *Phys. Fluids* **30**(8), 2343-2353.
- CHEN, J. H., CHONG, M. S., SORIA, J., SONDERGAARD, R., PERRY, A. E., ROGERS, M., MOSER, R., & CANTWELL, B. J. 1990 A study of the topology of dissipating motions in direct numerical simulations of time-developing compressible and incompressible mixing layers. In *Studying turbulence using numerical simulation databases - III, Proceedings of the 1990 summer program*. Stanford: CTR.
- HESELINK, L. & STURTEVANT, B. 1988 Propagation of weak shocks through a random medium. *J. Fluid Mech.* **196**, 513-553.
- HONKAN, A. & ANDREOPOULOS, J. 1990 Experiments in a shock wave/homogeneous turbulence interaction. *AIAA Paper*, No. 90-1647.

- JACQUIN, L., BLIN, E. & GEFFROY, P. 1991 Experiments on free turbulence/shock wave interaction. *Eighth Symposium on turbulent shear flows*, Munich, September 9-11, 1991.
- JIMÉNEZ, J. 1992 Kinematic alignment effects in turbulent flows. *Phys. Fluids A*. 4(4), 652-654.
- KERSTEIN, A. R., ASHURST, W. T. & WILLIAMS, F. A. 1988 Field equation for interface propagation in a unsteady homogeneous flow field. *Phys. Rev. A*. 37, 2728.
- KEVLAHAN, N. 1992 Rapid distortion of turbulent structures. In *Proceedings of the fourth European turbulence conference*. To appear.
- LEE, S., MOIN, P., & LELE, S. K. 1992 The interaction of isotropic turbulence with a shock wave. *Report No. TF-52*. Thermosciences Division, Department of Mechanical Engineering, Stanford University.
- MCKENZIE, J. F. & WESTPHAL, K. O. 1968 Interaction of linear waves with oblique shock waves. *Phys. Fluids*. 11(11), 2350-2362.
- RIBNER, H. S. 1954 Convection of a pattern of vorticity through a shock wave.. *NACA TN-2864*.
- ROGERS, M. M. & MOIN, P. 1987 Helicity fluctuations in incompressible turbulent flows. *Phys. Fluids A*. 30(9), 2662-2671.
- SHE, Z., JACKSON, E. & ORSZAG, S. A. 1991 Structure and dynamics of homogeneous turbulence: models and simulations. *Proc. R. Soc. Lond. A*. 434, 101-124.
- STURTEVANT, B. & KULKARNY, V. A. 1976 The focusing of weak shock waves. *J. Fluid Mech.* 73(4), 651-671.
- VINCENT, A. & MENEGUZZI, M. 1991 The spatial structure and statistical properties of homogeneous turbulence. *J. Fluid Mech.* 225, 1-20.
- WHITHAM, G. B. 1957 A new approach to problems of shock dynamics. Part I. Two-dimensional problems. *J. Fluid Mech.* 2, 145-171.
- ZANG, T. A. & BUSHNELL, D. M. 1984 Numerical computation of turbulence amplification in shock-wave interactions. *AIAA J.* 22(1), 13-21.

445363 517-34

189677

293

N 94-1A 762

A transport equation for eddy viscosity

By P. A. Durbin¹ AND Z. Yang²

A transport equation for eddy viscosity is proposed for wall bounded turbulent flows. The proposed model reduces to a quasi-homogeneous form far from surfaces. Near to a surface, the nonhomogeneous effect of the wall is modeled by an elliptic relaxation model. All the model terms are expressed in local variables and are coordinate independent; the model is intended to be used in complex flows. Turbulent channel flow and turbulent boundary layer flows with/without pressure gradient are calculated using the present model. Comparisons between model calculations and direct numerical simulation or experimental data show good agreement.

1. Introduction

Algebraic turbulence models (Baldwin-Lomax 1978, Cebeci-Smith 1974) have been used extensively in calculations of aerodynamic flows. These algebraic models are easy to implement numerically and give accurate predictions for simple flows, such as that over an airfoil with an attached boundary layer; however, they are inadequate when used for more complex flows, such as that over an airfoil with separation. In addition, these models contain nonlocal parameters in their formulations. The interpretation of these parameters becomes ambiguous in complex geometries. Higher order turbulence models have been proposed to overcome deficiencies of these algebraic models, the most popular among these being the $k - \epsilon$ model. The empirical constants in the $k - \epsilon$ model have been optimized in a variety of simple shear flows, giving what is commonly referred to as the Standard $k - \epsilon$ model (Launder and Spalding 1974, Rodi 1980).

The Standard $k - \epsilon$ model was devised for turbulence far away from boundaries. For near wall turbulence, the model either has been used in conjunction with wall functions or has been modified by damping functions and other near wall terms to give the so called near wall version of the $k - \epsilon$ model. This fixed up model can be integrated down to the wall.

In the wall function approach, one assumes the existence of a universal wall layer, which is not valid in many complex flows. In the damping function approach, the results depend on the damping functions used—a wide variety of which have been proposed. These damping functions themselves must be assumed to be of a universal form.

It is also found that for near wall flows the $k - \epsilon$ model is numerically stiff: it requires many grid points near the wall to get a grid independent solution. This

1 Center for Turbulence Research

2 ICOMP/NASA Lewis Research Center

numerical stiffness makes the model rather unappealing for aerodynamic computations. The numerical stiffness of the $k - \epsilon$ model is partly due to the rapid variation of ϵ (and to a less extent k) near the wall.

The eddy viscosity, ν_t , varies much more gradually near the wall. This observation suggests that an equation for the eddy viscosity might be less stiff; this was one motivation for the work of Baldwin and Barth (1990) and Spalart and Allmaras (1992). In these papers, a transport equation for eddy viscosity of the type originally proposed by Nee and Kovaszny (1968) was formulated and solved in conjunction with the mean field equations. Wall effects were introduced in these models by damping functions, in which the distance to the wall y enters as a parameter. This wall distance y is not a local property; its definition may be ambiguous for flows in complex geometry—corner flow for example. Also, the damping functions are assumed to be universal, which does not seem valid in flows with strong adverse pressure gradients and separation.

Modeling of near wall turbulence is very important for engineering calculation because the near wall portion of the boundary layer contributes substantially to the total momentum and heat transfer. In the near wall region, the turbulence is strongly inhomogeneous and strongly anisotropic. Recently, Durbin (1991) introduced the method of elliptic relaxation to model the blocking effect of the wall on the turbulence. In this method, the behavior of the near wall turbulence is given by the solution of an (elliptic) differential equation rather than by prescribed algebraic expressions. Geometric information enters through the boundary conditions enforced at the wall. Thus, it is hoped that this formulation can handle flows in complex geometry. This approach also has the appeal that it is coordinate independent.

In the present work, we propose a new transport model for the eddy viscosity. Far away from the wall, the model is based on the quasi-homogeneous approximation; near the surface, the wall effect is introduced via an elliptic relaxation equation. The structure of the paper is as follows: the proposed model is presented in section 2; in section 3, we show calculations of turbulent channel flow and turbulent boundary layer flows with and without pressure gradient; section 4 concludes the paper.

2. The proposed model

2.1 The eddy viscosity

In the framework of the eddy viscosity model, the unknown Reynolds stress $-\overline{u_i u_j}$ in the mean momentum equation is assumed to be related to the mean velocity field by

$$-\overline{u_i u_j} = 2\nu_t S_{ij} - \frac{2}{3}k\delta_{ij} \quad (1)$$

where S_{ij} is the strain rate of the mean field and ν_t is the eddy viscosity. The last term in (1), containing the turbulent kinetic energy k , can be absorbed into the mean pressure. Thus, only the eddy viscosity needs to be modeled.

We propose that the general form of a transport equation for the eddy viscosity be

$$\frac{D}{Dt}\nu_t = \nabla \cdot \left[\left(\nu + \frac{\nu_t}{\sigma} \right) \nabla \nu_t \right] + \Phi \quad (2)$$

where the turbulent self transport is assumed to be analogous to the laminar diffusion and Φ is a source term representing the *combined effect* of production and dissipation of ν_t . Our objective is to propose a model for Φ which is valid for both near wall and free shear layers. The justification for using a scalar eddy viscosity, as in (1), is that our attention is on thin shear layers, in which transport is predominantly transverse to the shear.

2.2 Model for flow away from the wall

Far from the solid surface, the inhomogeneity of a turbulence field is relatively weak. The model for Φ could then be found by expanding about the homogeneous state. This quasi-homogeneous case is considered first.

For homogeneous shear flow, if ν_t is much larger than ν , the only variables that can enter the problem are the eddy viscosity ν_t and the shear rate S . (The shear rate S will be defined here via the rate of strain tensor of the mean field: $S = 2(S_{ij}S_{ji})^{1/2}$.) From dimensional reasoning, we have

$$\Phi = \Phi(S, \nu_t) = c_1 S \nu_t \quad (3)$$

where c_1 is a model constant. Experimental results for homogeneous shear flow give $c_1 \approx 0.12$.

In general, the flow is not homogeneous. Flow inhomogeneity can be represented by $|\nabla \nu_t|$ and by $|\nabla S|$, which are measures of the inhomogeneity of the turbulence field and of the mean field, respectively. If the inhomogeneity is weak, expansion about the homogeneous state suggests the form

$$\Phi = c_1 S \nu_t - c_2 |\nabla \nu_t|^2 - c_3 \frac{\nu_t^2}{L_\nu^2}, \quad (4)$$

where the length scale L_ν is given by

$$L_\nu^{-2} = \left(\frac{|\nabla S|}{S} \right)^2. \quad (5)$$

Other terms, such as $|\nabla \nu_t| \nu_t / L_\nu$ might be considered; (4) is analogous to the forms selected by Baldwin and Barth (1990) and Spalart and Almaras (1992). The model (4) allows inhomogeneities in both the turbulent field and the mean field to contribute to 'dissipation' of the eddy viscosity.

2.3 Model for near wall turbulence

Eq (4) is based on an expansion near the homogeneous state. The expansion is valid only for weak inhomogeneity. In the near wall region the flow changes very rapidly to adjust to the boundary condition at the wall; thus, the flow field is strongly inhomogeneous, and the expansion about the homogeneous state is not expected to be valid. (Direct application of equation (2) with Φ given by equation (4) to turbulent channel flow at $Re_\tau = 395$ leads to a value of the skin friction coefficient too high by about 30%.) In the present work, this strong inhomogeneity

is modeled by the elliptic relaxation model first proposed by Durbin (1991) for Reynolds stress closures.

In the Reynolds stress transport equation, the velocity-pressure gradient correlation term is a good candidate for this type of relaxation because pressure is elliptic in nature. In the transport equation for the eddy viscosity, the pressure term does not appear explicitly; which term should be operated on by elliptic relaxation is questionable. An examination of the transport equation for $-\overline{uv}/S$ in simple shear flows reveals that there are two origins for the elliptic relaxation: the velocity-pressure gradient correlation and the representation of v^2 in terms of \overline{uv} . The combination of these two effects suggests, in the case of the eddy viscosity transport model, that we write $c_1 = c_{11} - c_{12}$ and introduce the elliptic relaxation such that the transport equation appears as

$$\frac{D}{Dt}\nu_t = \nabla \cdot \left[\left(\nu + \frac{\nu_t}{\sigma} \right) \nabla \nu_t \right] + P_\nu - c_{12}S\nu_t - c_3 \frac{\nu_t^2}{L_p^2} \quad (6)$$

where P_ν is the quantity subject to relaxation. It is governed by the elliptic equation

$$L_p^2 \nabla^2 P_\nu - P_\nu = -(c_{11}S\nu_t - c_2 |\nabla \nu_t|^2). \quad (7)$$

In (7), L_p is the blocking length scale and is given by

$$L_p^2 = c_p^2 \max \left(\frac{\nu_t}{S}, c_i^2 \frac{\nu}{S} \right). \quad (8)$$

The first term in the 'max' function represents the turbulent length scale, which is appropriate away from the wall; the second term is chosen very close to the wall, where the appropriate length is the Kolmogorov scale. The switching from one length scale to the other is controlled by the value of c_i and the total length scale is controlled by c_p .

2.4 Modification near $S = 0$

Equations (5) and (8) give expressions for the length scales. These estimates break down when $S = 0$. $S = 0$ can occur at the edge of a boundary layer or inside a turbulent field, for example at the centerline of channel flow. A revision to the length scale formulation is needed to accommodate these cases. The singularity will be removed by the following modification:

$$L_\nu^2 = \left(\frac{S}{|\nabla S|} \right)^2 + \left(\frac{|\nabla \nu_t|}{S} \right)^2 \quad (9)$$

$$L_p^2 = \min \left[L_\nu^2, c_p^2 \max \left(\frac{\nu_t}{S}, c_i^2 \frac{\nu}{S} \right) \right]. \quad (10)$$

Over most of the flow field, the first term on the right hand sides of (9) and (10) is much larger than the second term. The modification only affects the region near $S = 0$.

In the course of developing and testing the model during the summer program, another modification to L_ν was inadvertently introduced: in the outermost portion of boundary layers, L_ν became constant. The algorithm was to make L_ν be independent of y when $\partial\nu_t/\partial y < 0$. ν_t decreases when y/δ_{99} is greater than ~ 0.9 . In future work, this restriction will be removed; it is an effective way to avoid the difficulty of specifying L_ν in the free-stream, but its applicability is restricted to attached boundary layers.

2.5 Boundary conditions

Equations (6) and (7), together with the length scales given by (9) and (10), are the eddy viscosity model we are proposing for wall bounded turbulent flows. They form a fourth order system of equations, and, consequently, four boundary conditions are needed. These conditions are as follows: On a solid surface

$$\nu_t = \hat{n} \cdot \nabla \nu_t = 0, \tag{11}$$

where \hat{n} is the surface normal; at a symmetry plane, the center line of a channel for example,

$$\nu'_t = P'_\nu = 0, \tag{12}$$

where the prime denotes the derivative normal to the symmetry plane; at the freestream edge of a boundary layer or shear layer

$$\nu'_t = P_\nu = 0. \tag{13}$$

The prime in (13) represents differentiation normal to the edge of the boundary layer. In some situations, (13) might be replaced by a condition prescribing properties of free-stream turbulence if it is present.

2.6 Model constants

There are seven empirical constants in the present model. They are σ , c_{11} , c_{12} , c_2 , c_3 , c_p , c_l . c_{11} and c_{12} are related by

$$c_{11} - c_{12} = c_1.$$

$c_1 \approx 0.12$ was determined by experiments on homogeneous shear flow.

Another relation among the constants is found by requiring that the model give the right behavior in the logarithmic region of a boundary layer. This imposes the constraint

$$\frac{1}{\sigma} + \frac{c_1}{\kappa^2} - c_2 = \frac{c_3}{1 + \kappa^4}$$

where κ is the Von Kármán constant; we take $\kappa = 0.41$.

The constant σ in the turbulent diffusion term should be about 1 and the value of c_p , which marks the switching from the Kolmogorov length scale to the turbulent length scale, should be about 3.5. All the other constants are chosen by comparing with direct numerical simulation data for turbulent channel flow at $Re_\tau = 395$ and

with experimental data for a zero pressure gradient, flat plate boundary. The values of the constants selected in this study are

$$\sigma = 1.3, c_{11} = 0.4, c_{12} = 0.28, c_2 = 1.3, c_3 = 0.2, c_p = 3.5, c_l = 1.6. \quad (14)$$

The constants listed above represent a preliminary choice: they are subject to adjustment in the course of further model development.

3. Results and discussions

Turbulent channel flows at different Reynolds numbers and turbulent boundary layers with and without pressure gradient were calculated using the present model. An implicit finite difference scheme was used to solve the momentum equation and the turbulence equations. For the present cases, the equations are parabolic and a marching scheme was used. The finite difference equations for ν_t and P_ν were solved as a coupled, block tridiagonal system. Variable grid spacing was used, with densest spacing near the wall. The total number of grid points was set to 105, which is large enough for the results to be grid independent.

Two dimensional, fully developed channel flow is attractive for model testing because it is statistically steady and nonhomogeneous in only one direction. Solutions can be found very efficiently, yet the effects of the wall on turbulent shear flow are still present. Computations were carried out for 2D fully developed turbulent channel flows at $Re_\tau = 180$ and $Re_\tau = 395$, for which DNS data are available (J. Kim, private communication). Figure 1 shows profiles of the mean velocity at these two Reynolds numbers along with DNS data. Both the dependent variable and the independent variables are represented in wall units. The predictions are in reasonable agreement with the data.

The second example calculated is the turbulent boundary layer with zero pressure gradient. The zero pressure gradient boundary layer on a flat plate has a self-similar profile (in the outer portion of the boundary layer, when scaled on outer variables). Thus, arbitrary profiles could be used as the initial conditions, and the solution should develop into its similarity form. Figure 2 shows velocity profiles scaled by the free stream velocity and the boundary layer thickness at $Re_\theta = 3195$ and $Re_\theta = 5473$, respectively. The experimental data is from Coles and Hirst (1968). It is found that indeed the velocity develops into a similarity profile, which serves as a good check for the present model. Figure 3 contains a conventional log-linear plot of the mean velocity profile. The agreement with the data is excellent except in the viscous sublayer, where the model profile is a bit low.

From an engineering point of view, the skin friction is of great interest. The skin friction coefficient as a function of Re_θ is shown in figure 4, along with experimental data (Coles and Hirst 1968). It is seen that the model gives a good prediction of C_f . The growth of the boundary layer in this range of Reynolds number is illustrated by figure 5, which shows displacement thickness as a function of Re_θ . δ_* is normalized by the boundary layer thickness at $Re_\theta = 1000$. The model gives a slight overprediction of the boundary layer growth rate.

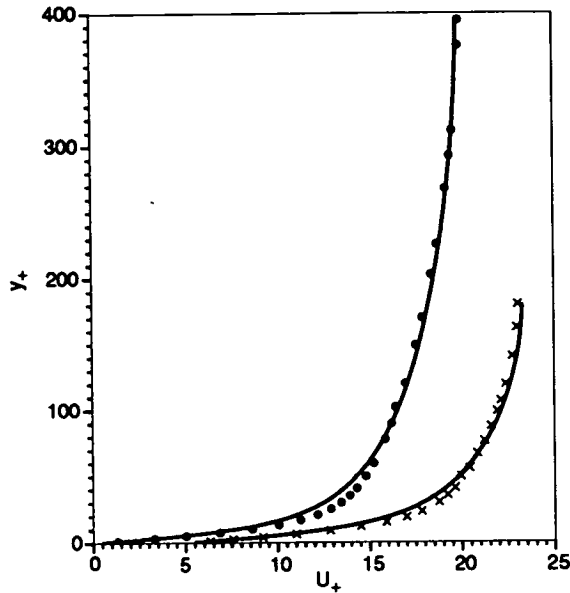


FIGURE 1. Mean velocity profiles in channel flow. ●, $Re_\tau = 395$; ×, $Re_\tau = 180$. The lower Reynolds number profile is offset 5 units for clarity.

Next we calculate the development of a turbulent boundary layer in a pressure gradient. The test case chosen is the Samuel and Joubert (1974) experiment on a boundary layer developing into an increasingly adverse pressure gradient. This boundary layer is not self-similar. During the 1981-82 Stanford Conference on Complex Turbulent Flows, it was found that this flow is very difficult to predict; since then, it has become a standard test case for turbulence models.

The initial condition for the computation was set in the following manner: We assume that the turbulent boundary layer develops under zero pressure gradient up to a point, x , say, at which the pressure gradient (which is known from the experiment) is applied. The position x , is determined so that at the first point of the working section of wind tunnel, where the experimental data begin, the predicted values of Re_θ and C_f agree with those of the experiment.

The predicted development of the boundary layer is shown in figure 6 along with the experimental data. The variation of the skin friction coefficient with x and the growth of the boundary layer thickness are predicted very well. The velocity profiles at $x = 1.87\text{ m}$ and $x = 2.55\text{ m}$ are shown in figure 7. The agreement with the experimental data is again found to be reasonable.

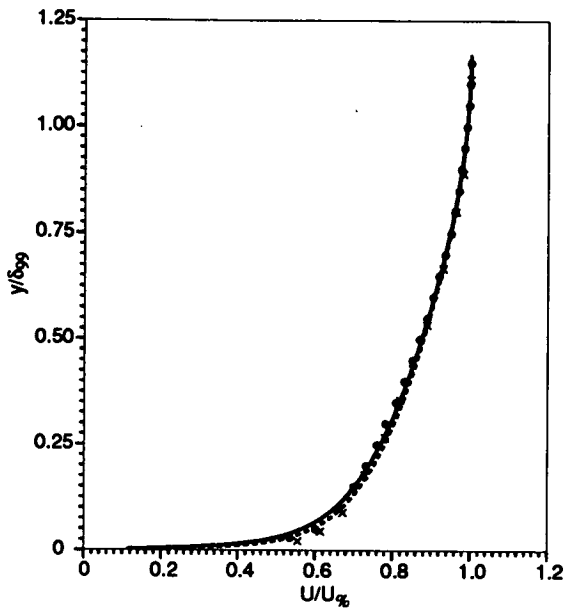


FIGURE 2. Similarity form of mean velocity profiles in zero pressure gradient boundary layer. \bullet (—), $Re_\theta = 3195$; \times (--), $Re_\theta = 5473$.

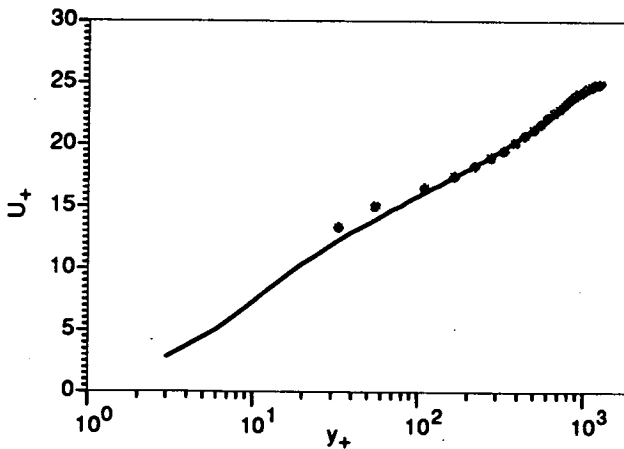


FIGURE 3. Log-linear plot of mean velocity profile in zero pressure gradient boundary layer.

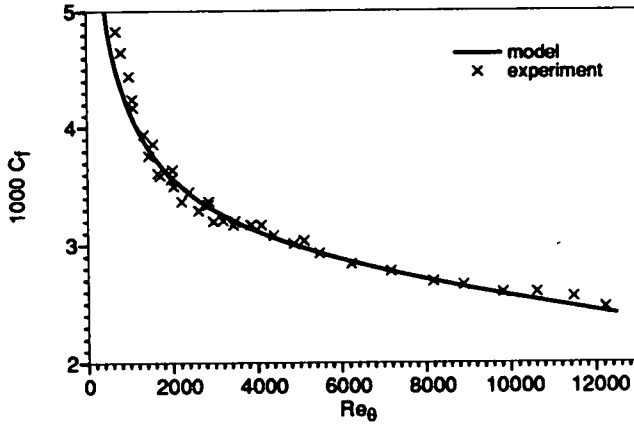


FIGURE 4. Skin friction coefficient versus momentum thickness Reynolds number for zero pressure gradient boundary layer.

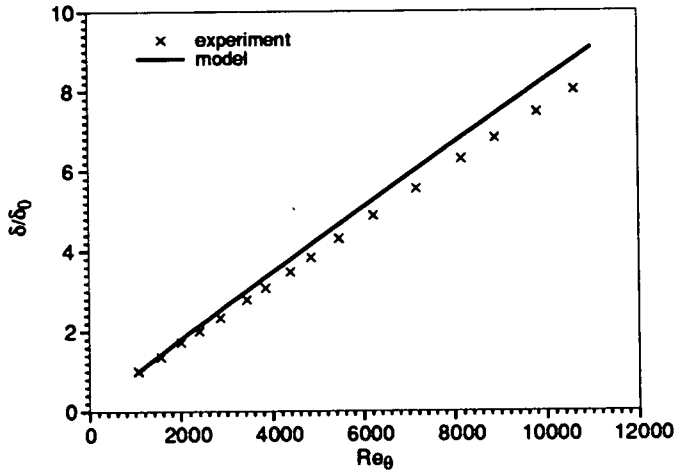


FIGURE 5. Boundary layer thickness versus Reynolds number for zero pressure gradient boundary layer.

4. Conclusions

We have presented a transport equation for eddy viscosity for wall bounded flows. Away from the wall, the proposed model reduces to a quasi-homogeneous model. The near wall effect is represented by an elliptic relaxation equation. Since geometrical information comes through the location where the boundary conditions are enforced while the model itself is free from the boundary information, the proposed

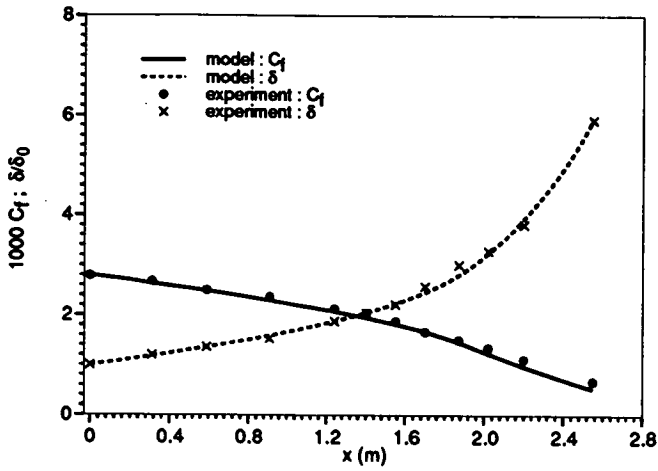


FIGURE 6. Skin friction coefficient and displacement thickness in the Samuel and Joubert boundary layer.

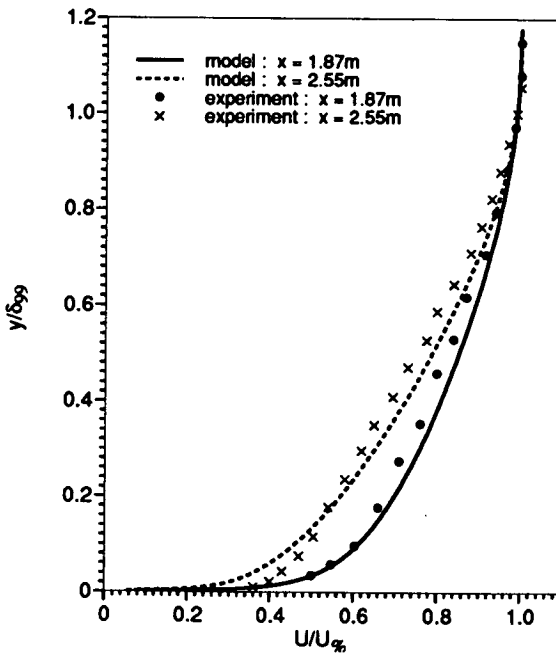


FIGURE 7. Mean velocity profiles at $x = 1.87\text{ m}$ and 2.55 m in the Samuel and Joubert boundary layer.

model has the potential to handle flows in complex geometry. All the quantities used in the model are local properties and are coordinate independent; the model is also Galilean invariant.

Channel flow at two Reynolds numbers and flat plate turbulent boundary layers with zero and adverse pressure gradients were calculated using the present model. The comparison with the DNS and experimental data were found to be quite promising.

Acknowledgement

Z. Y. would like to express his sincere thanks to Dr. T. Lund of CTR for his help during the Summer Program.

REFERENCES

- BALDWIN, B. S. & BARTH, T. J. 1990 A one-equation turbulence transport model for high Reynolds number wall-bounded flows. *NASA TM 102847*.
- BALDWIN, B. S. & LOMAX, H. 1978 Thin layer approximation and algebraic model for separated turbulent flows. *AIAA-78-256*.
- CEBECI, T. & SMITH, A. M. O. 1974 *Analysis of turbulent boundary layers*. Academic Press.
- COLES, D. E. & HIRST, E. A., eds. 1968 *Computation of turbulent boundary layers*, AFOSR-IFP-Stanford conference.
- DURBIN, P. A. 1991 Near-wall turbulence closure modeling without 'damping functions'. *Theoret. Comp. Fluid Dynamics*. **3**, 1-13.
- LAUNDER, B. E. & SPALDING, D. B. 1974 The Numerical Computation of Turbulent Flow. *Computer Methods in Applied Mechanics and Engineering*. **3**, 269-289.
- NEE, V. W. & KOVASZNAY, L. S. G. 1968 The calculation of incompressible turbulent boundary layers by a simple theory. *Computation of turbulent boundary layers*, AFOSR-IFP-Stanford conference. 300-319.
- RODI, W. 1980 *Turbulence Models and Their Application in Hydraulics*. Book Pub. of International Association for Hydraulic Research, Delft, the Netherlands.
- SAMUEL, A. E. & JOUBERT, P. N. 1974 A boundary layer developing in an increasingly adverse pressure gradient. *J. Fluid Mech.* **66**, 481-505.
- SPALART, P. R. & ALLMARAS, S. R. 1992 A one-equation turbulence model for aerodynamic flows. *AIAA-92-0439*.

omit

IV. The combustion group

The combustion group conducted six projects. Three projects were related to premixed and three to non-premixed combustion. The invited participants were: Mr. M. Baum (Ecole Centrale Paris), Dr. J. H. Chen (Sandia National Laboratories); Prof. R. O. Fox (Kansas State University), Dr. D. C. Haworth (General Motors Research Laboratories), Prof. J. C. Hill (Iowa State University), Prof. S. Mahalingam (University of Colorado), Dr. T. Poinso (Institut de Mécanique des Fluides de Toulouse), Prof. I. K. Puri (University of Illinois). The local participants were: Dr. R. D. Moser and Dr. M. M. Rogers from NASA Ames Research Center, and Dr. F. Gao, Dr. A. Trouvé, and Dr. L. Vervisch from the Center for Turbulence Research.

The broad scientific objectives of this group were similar to those of the CTR 1990 Summer Program: understanding of fundamental phenomena controlling turbulent combustion and application to modeling. However, the tools used in 1992 have covered a wider range: 2D or 3D, variable or constant density, simple or complex chemistry formulations for Direct Numerical Simulation (DNS) of turbulent combustion have been used. Recent progress in numerical analysis and code development have allowed us to use tools which were well adapted to the physical problems considered by each group.

The first three projects were aimed at increasing our understanding of turbulent premixed flames.

Poinso & Haworth studied the interaction between a turbulent flame and a cold wall. Flame quenching distances as well as wall heat fluxes were measured from 2D simulations. The characteristics of flamelets reaching the wall (curvature, flame speed, quenching times) were used to build a 'law-of-the-wall' model for turbulent combustion. A simplified version of this model was derived and may be implemented in any flamelet model for turbulent premixed combustion.

A new 3D variable-density code was used by Trouvé & Poinso to investigate the modeling of the evolution equation for the flame surface density. This analysis shows the limits of present flamelet models and suggests how the exact evolution equation for reactive surfaces may be closed to provide a suitable model. The effect of the Lewis number was evidenced and its influence on source or consumption terms for the flame surface density was demonstrated.

The first objective of the work by Baum, *et al.* was to prove the feasibility of DNS with complex chemistry and the potential of this approach for pollution studies. A second goal was to check whether the DNS results previously obtained with single-step chemistry are modified by accounting for more realistic chemical schemes. The project was based on a new 2D code where a DNS technique was coupled to CHEMKIN and TRANSPORT, the SANDIA packages for reacting flows with complex chemistry. Using this tool, it was possible to investigate the structure

of H₂-O₂ turbulent flames with the Warnatz scheme (9 species - 19 reactions). This project also provides the first analysis of the effects of stretch and curvature on flames with realistic chemistry.

The first project of Chen *et al.* was related to the effects of finite rate chemistry and differential diffusion on the structure of turbulent non-premixed flames. 3D variable-density simulations were performed over a range of conditions corresponding to fast and slow chemistry. This project provided new insights on the validity of the flamelet assumption as well as on the effects of transient regimes and small scales on the inner structure of the flame zone.

Chen *et al.* investigated one of the classical assumptions used to model turbulent non-premixed flames, *i.e.* single-step chemistry. Single-step and two-step chemical schemes were compared using 2D variable-density simulations of a non-premixed flame in isotropic turbulent flow. An important result was that extinction limits appear to be quite different: while single-step chemistry lead to multiple local extinctions, two-step chemistry feature more robust flames which do not quench.

DNS of a single-step chemical reaction with non-premixed reactants in forced isotropic turbulence were used by Fox *et al.* to obtain joint pdf's and other statistical information to parameterize and test a Fokker-Planck turbulent mixing model. The simulations were performed using a constant density, 3D spectral code developed by Moser and Rogers. Physical features as well as various statistics of the reacting scalars and their gradients were examined and compared to the model.

This Summer Program has brought many new and original results. The activity on non-premixed combustion was more intense than during previous programs and opened new perspectives for modeling for those flames. The demonstration that DNS of reacting flows was possible while taking into account complex chemistry or the presence of walls also opens new fields of investigations.

Modeling was one of our first objectives in this work. A fundamental aspect of the 1992 work is the impact and the power of DNS to answer certain critical questions for turbulent combustion models. We believe that DNS of reacting flows is now reaching a point where individual terms in combustion models may be estimated from DNS (as done by Trouvé & Poinso) and that this possibility will change the way we construct models in the next few years.

Thierry J. Poinso

DNS and modeling of the interaction between turbulent premixed flames and walls

By T. J. Poinsot¹ AND D. C. Haworth²

The interaction between turbulent premixed flames and walls is studied using a two-dimensional full Navier-Stokes solver with simple chemistry. The effects of wall distance on the local and global flame structure are investigated. Quenching distances and maximum wall heat fluxes during quenching are computed in laminar cases and are found to be comparable to experimental and analytical results. For turbulent cases, it is shown that quenching distances and maximum heat fluxes remain of the same order as for laminar flames. Based on simulation results, a 'law-of-the-wall' model is derived to describe the interaction between a turbulent premixed flame and a wall. This model is constructed to provide reasonable behavior of flame surface density near a wall under the assumption that flame-wall interaction takes place at scales smaller than the computational mesh. It can be implemented in conjunction with any of several recent flamelet models based on a modeled surface density equation, with no additional constraints on mesh size or time step.

1. Introduction

The understanding and modeling of turbulent phenomena that occur near walls is a formidable task. Even in the absence of chemical reaction, building 'law-of-the-wall' models or low-Reynolds-number models is an ongoing research subject and no satisfactory practical solution is yet available for general use in engineering codes. The situation is even more difficult when a flame is present. Combustion is strongly influenced by the presence of walls which may cause flame fronts to quench, for example. Moreover, the flame has a significant effect on the flow in the vicinity of the wall as well as on the heat flux to the wall. For these reasons, modeling of flame-wall interactions in turbulent situations is an important issue. Still, few experimental or modeling results have been reported, and most present models for turbulent premixed combustion do not use any specific corrections for near-wall effects. At best this may result in errors in the prediction of the reaction rate and of the wall heat fluxes and temperatures. In some cases, the absence of any reasonable approximation of the wall effects leads to numerical difficulties and to the use of ad-hoc numerical corrections to obtain solutions. These corrections are based on pragmatic rather than on physical grounds. Our objective here is to explore the flame-wall interaction mechanisms at a fundamental level using direct numerical simulations (DNS). The understanding thus obtained provides a sound

1 C. N. R. S., Institut de Mecanique des Fluides de Toulouse, France

2 General Motors Research & Environmental Staff, Warren, MI

basis for a model which can be viewed as a law-of-the-wall approach for turbulent premixed combustion.

2. Flame-wall interaction in laminar flows

Before considering turbulent cases, it is useful to consider results obtained on wall quenching of laminar flames (Jarosinski 1986, Huang *et al.* 1986). For these flows, two important quantities have been introduced: the minimum distance between the flame and the wall δ_Q and the maximum heat flux Φ_Q through the wall during the interaction with the flame. Most authors normalize the wall distance y by a characteristic flame thickness $d = \lambda_1/(\rho_1 c_p s_l^0)$ and define the local Peclet number to be $P_e = y/d$ (Here a subscript '1' refers to reference properties in the fresh gases). Therefore, the quenching distance is often expressed by its Peclet number P_{eQ} : $P_{eQ} = \delta_Q/d$ (Huang *et al.* 1986, Vosen *et al.* 1984, Lu *et al.* 1990). The wall heat flux may be normalized by the laminar reference 'flame power' (heat release) to yield $\phi = \Phi_Q/(\rho_1 Y_F^1 s_l^0 \Delta H)$ where ρ_1 and Y_F^1 designate the fresh-gas density and fuel mass fraction, s_l^0 is the unstretched laminar flame speed, and ΔH is the heat of reaction ($Y_F^1 \Delta H = c_p(T_2 - T_1)$ if T_1 is the temperature of the fresh gases and T_2 is the adiabatic flame temperature). These two quantities may be correlated in laminar flows. If one assumes that at quenching, the wall heat flux Φ_Q is due to heat conduction in the gas layer of thickness δ_Q , one can write

$$\Phi_Q \simeq \lambda \frac{T_2 - T_w}{\delta_Q}, \quad (1)$$

where λ is the gas thermal conductivity and T_w is the wall temperature. From Eq. (1), we obtain a relation which is expected to hold when the wall heat transfer is dominated by diffusion:

$$\phi = \frac{T_2 - T_w}{T_2 - T_1} \frac{1}{P_{eQ}}. \quad (2)$$

Three typical situations have been studied in the past (Figure 1):

1. Head-on quenching

When a flame front reaches a cold wall ($T_w = T_1$) at a normal angle, head-on quenching (HOQ) occurs (Figure 1a). This case has been studied numerically and experimentally (Huang *et al.* 1986, Jarosinski 1986, Vosen *et al.* 1984). Results suggest that quenching occurs for Peclet numbers of the order of three. Heat flux measurements indicate values of ϕ of the order of 0.34, which is consistent with the value predicted by Eq. (2) with $P_{eQ} \approx 3$. In terms of simple physics, this result suggests that a flame stops propagating towards the wall when the heat losses to the wall are equal to about one-third of the nominal flame power. The fact that ϕ is almost constant for different fuels (Huang *et al.* 1986) suggests that the problem is thermally controlled and that simple chemistry may be used to compute this phenomenon.

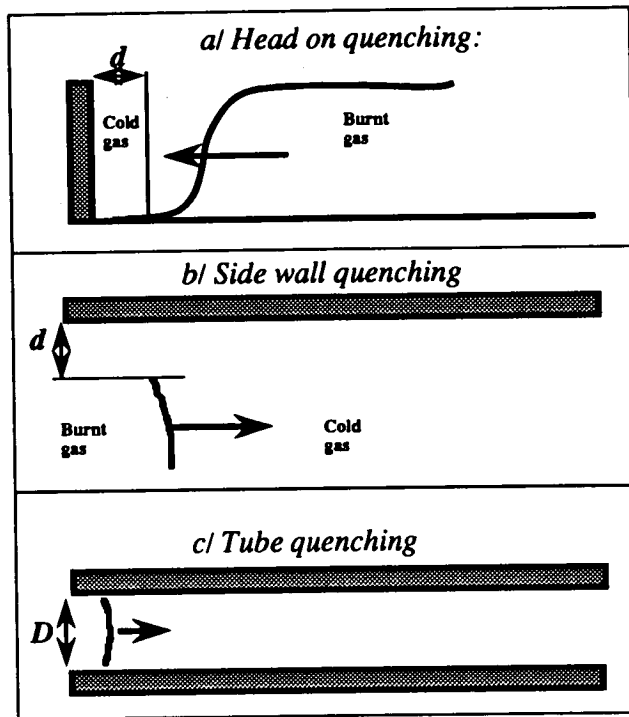


FIGURE 1. Configurations for flame-wall interaction studies in laminar flows.

2. Side-wall quenching

When a flame propagates parallel to a wall, the situation is different. Only localized quenching of the flame near the wall occurs (Figure 1b). This situation has been studied theoretically by Von Karman & Millan (1953) and Makhviladze & Melikov (1991), and experimentally by Lu *et al.* (1990) and Clendening *et al.* (1981). Peclet numbers in this case are of the order of seven suggesting values for ϕ of about 0.16 (Eq. (2)). Asymptotic theories of non-adiabatic flames also may be used to predict the quenching distance (Williams 1985): these predict the same order of magnitude for Pe_Q .

3. Tube quenching

Total flame quenching may occur in a tube if its diameter is sufficiently small (Lewis & Von Elbe 1987, Jarosinski 1986, Fairchild *et al.* 1984) (Figure 1c). This phenomenon is exploited, for example, in the design of flame arrestors: these are ensembles of tubes with diameters smaller than the quenching distance so that a flame cannot propagate through them. Peclet numbers in this case are based on the tube diameter and are of the order of 50 (Aly & Hermance 1981). We will not consider this configuration here since in most practical situations, the dimensions of the system (e.g., the size of the combustor chamber) are too large to induce total quenching.

3. Numerical method and configuration

To study numerically how a laminar or a turbulent flame interacts with a cold wall we have utilized a DNS code developed at Stanford (Poinsoot *et al.* 1991, Poinsoot & Lele 1992). Since this code has been described elsewhere, we will recall only its principal features here. We consider a compressible viscous reacting flow. The chemical reaction is represented by a single-step mechanism, R (reactants) \rightarrow P (products) where the reaction rate \dot{w}_R is expressed as,

$$\dot{w}_R = B\rho Y_R \exp\left(-\frac{T_a}{T}\right). \quad (3)$$

This can be interpreted as a binary reaction where one of the reactants (Y_R) is always deficient. Following Williams (1985) we cast this expression in the form,

$$\dot{w}_R = \Lambda\rho Y_R \exp\left(\frac{-\beta(1-\Theta)}{1-\alpha(1-\Theta)}\right). \quad (4)$$

Here Θ is the reduced temperature $\Theta = (T - T_1)/(T_2 - T_1)$, and T_2 is the adiabatic flame temperature. The activation temperature is T_a and the coefficients Λ , α , and β are, respectively, the reduced pre-exponential factor, the temperature factor, and the reduced activation energy,

$$\Lambda = B \exp(-\beta/\alpha), \quad \alpha = (T_2 - T_1)/T_2, \quad \text{and} \quad \beta = \alpha T_a/T_2. \quad (5)$$

Fluid properties follow the equations,

$$\rho = \rho_1(pT_1/p_1T), \quad \mu = \mu_1(T/T_1)^b,$$

$$Le = \lambda/\rho Dc_p = \text{constant}, \quad Pr = \mu c_p/\lambda = \text{constant}, \quad (6)$$

where μ , λ , and D are molecular diffusivities of momentum, internal energy, and species, respectively, and b is a constant. Using these assumptions and a Cartesian frame of reference, the conservation equations for compressible flows are solved using a high-order finite difference scheme (Lele 1992).

The calculations are initialized with reactants on one side of the computational domain and products on the other; these are separated by a laminar premixed flame. The wall is located on the reactant side of the domain (Figure 1a). All velocity components are zero on the wall and the wall temperature is imposed. For all the cases shown here, the wall temperature is equal to the fresh gas temperature, T_1 . On lateral boundaries, periodic conditions are enforced. On the right-hand side of the domain, non-reflecting boundary conditions are used (Poinsoot & Lele 1992).

The initial velocity field (turbulence spectrum) and spatial distribution of reactant mass fraction are specified at $t = 0$: the system is then allowed to evolve in time. The initially planar flame is convected and strained by the turbulence while the combustion influences the fluid mechanics through dilatation and temperature-dependent properties (Eq. (6)). After some time (typically 5 to 20 flame times in these computations), the flame reaches the wall and begins to interact with it.

4. Diagnostics

In the present case, we are especially interested in the effect of the wall on the flame structure. Postprocessing of the two-dimensional computed fields (snapshots at fixed times) begins by defining a flame front as an isocontour of temperature T . Once the flame front has been located, the local normal and local flame curvature are readily computed; curvature is taken to be positive for flame elements that are concave towards the products and conversely for elements concave towards reactants. One-dimensional cuts normal to the flame are taken: it is these profiles that define the local 'structure' of the turbulent flame. We compare the local turbulent flame profiles with the steady one-dimensional laminar flame profile for the same chemistry and fluid properties. Of particular interest is the distribution along the flame of the normalized local flame speed ('flamelet speed') s_n defined by $s_n = \int \dot{w} dn / s_l^0$, that is, the integral of the reaction rate profile in a direction locally normal to the flame.

The fixed chemical parameters used for this study are summarized in Table I. The flame speed and thickness are normalized respectively by the sound speed c and by the reference length $d = \lambda_1 / (\rho_1 c_p s_l^0)$. The flame thermal thickness δ_l^0 is based on the maximum temperature gradient: $\delta_l^0 = (T_2 - T_1) / \text{Max}(\frac{\partial T}{\partial n})$.

Table I. Fixed parameters for DNS of flame-wall interaction.

α	β	Λ	b	Pr	Le	s_l^0/c	δ_l^0/d
0.75	8.00	146.	0.76	0.75	1.0	0.016	3.8

5. DNS of the interaction between a laminar flame and a wall

To check the accuracy of the model, laminar runs were performed first. Figure 2 presents time variations of the flame distance to the wall as well as the flame power $\rho_1 s_n c_p (T_2 - T_1)$ and the normalized wall heat flux ϕ . There time has been normalized by the flame time $t_F = \delta_l^0 / s_l^0$ and y is the distance from the wall. The values obtained from DNS for this case are $P_e Q = 3.4$ and $\phi = 0.36$. These values are in good agreement with experimental data (Lu *et al.* 1990, Vosen *et al.* 1984) and with the simple model given by Eq. (2). Although total quenching occurs at $P_e Q = 3.4$, the flame senses the presence of the wall before this time: the flame speed s_n begins to decrease when the wall distance is less than a distance δ_T given by $P_e = \delta_T / d \approx 8$. Therefore, two zones are necessary to describe the near-wall region:

(i) The 'quenching' zone stretches from the wall to a local Peclet number y/d of about 3.5 ($0 < y < \delta_Q$). In this zone, no reaction ever takes place.

(ii) The 'influence' zone goes from the wall to a Peclet number y/d of about 8 ($0 < y < \delta_T$). Any flame entering the influence region will start sensing the wall and will eventually get quenched. The time t_Q needed for the flame to quench after it enters the influence zone is of the order of two flame times, $t_Q = 2t_F = 2\delta_l^0 / s_l^0$.

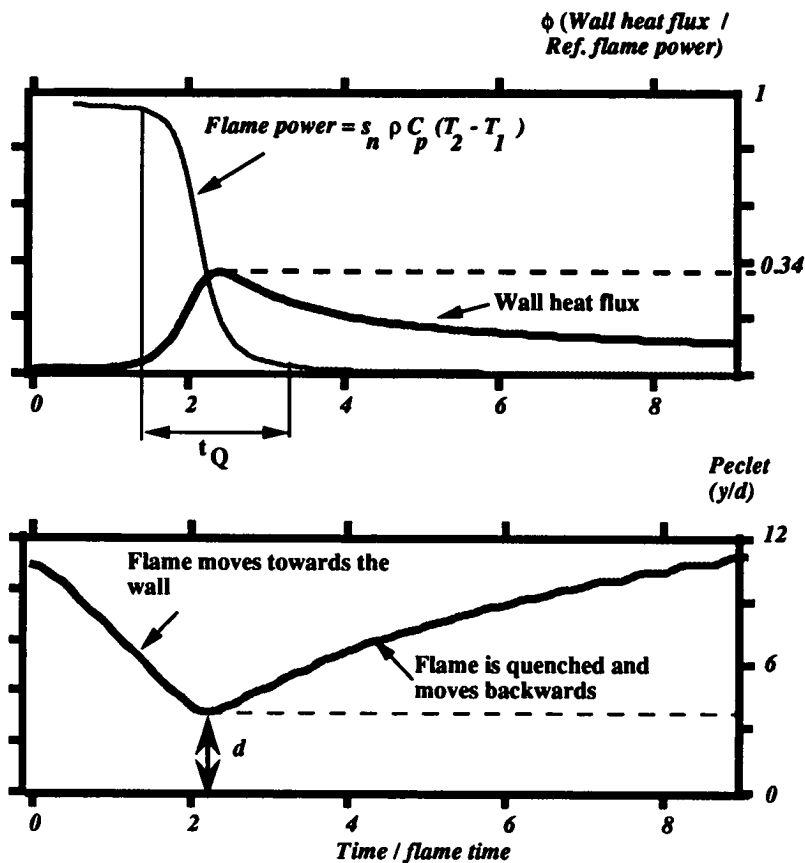


FIGURE 2. Numerical results for a laminar flame-wall interaction.

6. DNS of the interaction between a turbulent flame and a wall

The interaction between the wall and a turbulent flame front is characterized by three effects:

(i) A local thermal effect, by which heat losses to the wall affect the flame structure and result in local quenching.

(ii) A geometrical effect which limits the spatial extent of the flame brush and reduces the flame-brush size in the vicinity of the wall.

(iii) A laminarization effect which is an indirect effect of the wall on the flame. The wall affects the structure of the turbulence and leads to laminarization immediately adjacent to the wall. This induces a strong decrease of the turbulent stretch and thereby a decrease of the flame area.

Preferential species diffusion is beyond the scope of the present simple-chemistry investigation.

The structure of turbulence near the wall is clearly an important issue in the latter two questions. The configuration studied here corresponds to the 'shear-free' boundary layer in which turbulence with no mean shear interacts with a wall. This

may be realized experimentally in a wind tunnel, for example, using walls that move at the mean flow speed. The shear-free boundary layer has been studied experimentally by Thomas & Hancock (1977) and Uzkan & Reynolds (1967), theoretically by Hunt & Graham (1978), and numerically by Biringen & Reynolds (1981). The flow structure can be summarized as follows. Starting from initially isotropic homogeneous turbulence, the wall induces a perturbation zone whose thickness increases with time. In this zone, viscous effects are important, and the turbulence is damped. Moreover, by imposing zero normal velocities, the wall increases velocity perturbations in planes parallel to the wall (at sufficiently high Reynolds numbers). The role of this near-wall turbulence structure on flame evolution is difficult to quantify in the present simulations. We will concentrate instead on the thermal effects.

The parameters for the simulations reported here are summarized in Table II. There u' is the rms turbulence velocity, L_i is the length scale of the most energetic vortices in the initial turbulence spectrum, and l is the turbulence integral scale based on two-point velocity correlations. The initial turbulence field was chosen to produce small-scale turbulence near the wall and to impose zero velocity fluctuations at the wall. More sophisticated (three-dimensional) approaches will be necessary to produce more general results.

Table II. Initial conditions for DNS of turbulent flame-wall interaction.

<i>Case</i>	u'/s_i^0	L_i/δ_i^0	l/δ_i^0	$Re_l = u'l/\nu$	$Re_L = u'L_i/\nu$
2D3	6.25	8.9	2.85	90	280
2D4	6.25	4.5	1.43	45	140
2D6	6.25	1.9	0.64	19	60

Figures 3 and 4 present snapshots at one instant in time of reaction rate and vorticity fields during the interaction between the turbulent flame and the wall. Time has been normalized by the flame time $t_F = \delta_i^0/s_i^0$, and the maximum value of the vorticity modulus is normalized by the characteristic flame strain s_i^0/δ_i^0 . The structure of the vorticity field is affected both by the flame (viscosity in the burnt gases dissipates vorticity rapidly) and by the wall (the normal velocity component close to the wall goes to zero while the parallel component increases). Vortex pairs appear to play a dominant role. In Figures 3 and 4, for example, one vortex pair attracts a part of the flame front towards the wall while another pair pushes a different part of the flame away from the wall (sequence $t/t_F = 4.4$ to $t/t_F = 6.6$). This is confirmed by Figure 5 which presents the time evolution of the minimum and maximum wall distances in terms of Peclet numbers. When the first flame element touches the wall at time $t/t_F \simeq 6$, the most distant element is moving away from the flame front. This ejection of flame elements away from the flame

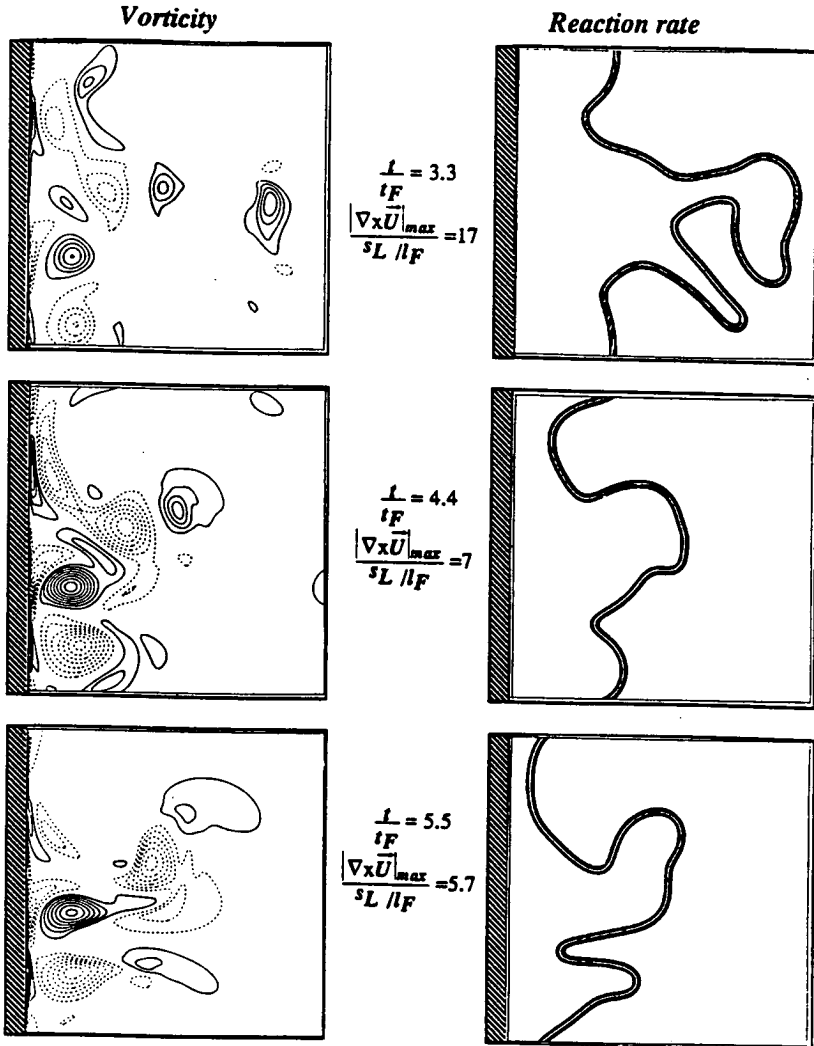


FIGURE 3. Vorticity and reaction rate contours for a turbulent flame-wall interaction (Case 2D4). Solid lines denote clockwise vorticity, dashed lines denote counterclockwise.

front may induce local counter-gradient turbulent diffusion of flame surface density which might be important in modeling.

As far as the thermal effect is concerned, results obtained during this simulation and during other simulations of the same type lead to a simple result (Figure 6): the maximum local heat flux to the wall corresponds within 10 percent to the laminar heat flux ($\phi = 0.36$), and the quenching distance δ_Q is equal to the value obtained in laminar cases ($P_{eQ} = 3.4$). Although the initial conditions used for these simulations lead to large velocity perturbations near the wall, the heat flux to the wall appears to be controlled mainly by heat diffusion, and the local instantaneous maximum

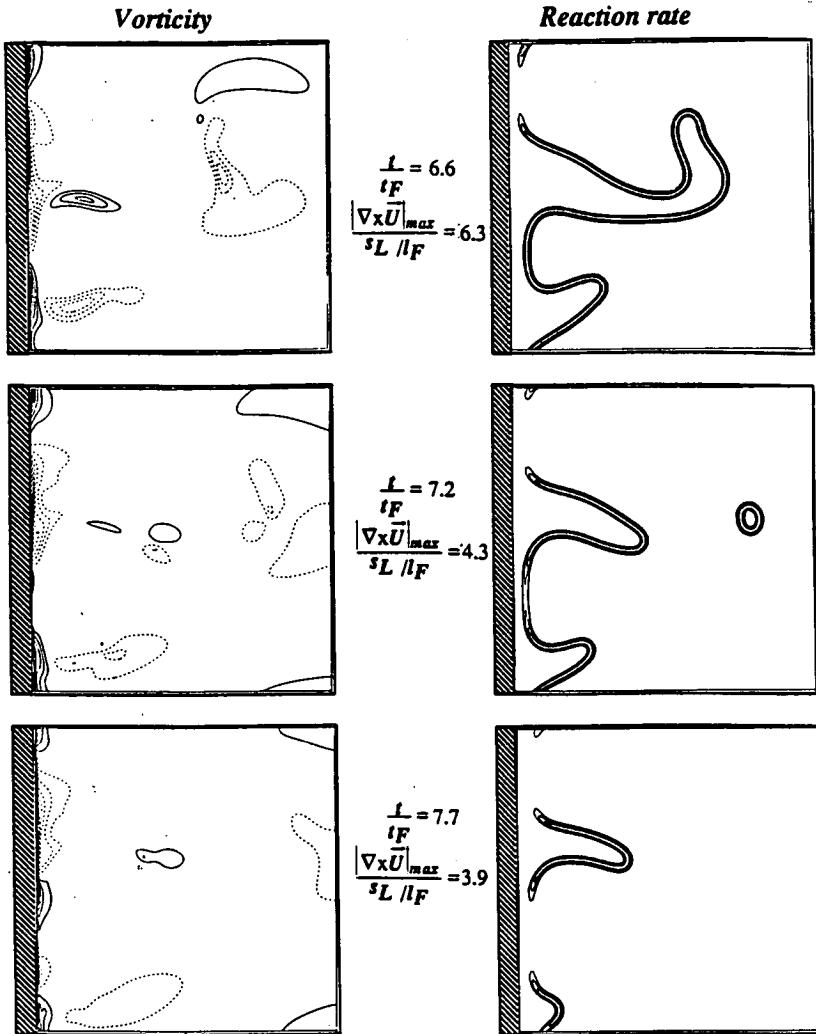


FIGURE 4. Vorticity and reaction rate contours for a turbulent flame-wall interaction (Case 2D4, continued).

heat flux obtained during quenching is the same as for the laminar cases.

Figure 7 presents a scatter plot of normalized flamelet speed s_n versus distance to the wall. This plot exhibits different behaviors for different flame elements ('flamelets') as they approach the wall. No flame elements approach closer than the laminar quenching distance δ_Q to the wall, and the minimum Peclet number is equal to about 3.5. Branch 1 corresponds to flames reaching the wall at normal angles (head-on quenching): these follow the curve (solid line) predicted by the laminar HOQ computation (Section 5), quenching at a Peclet of close to 3.5. Branch 2 corresponds to flamelets which disappear at Peclet numbers of about 7. Examination of DNS fields for these points suggest that these flamelets are propagating

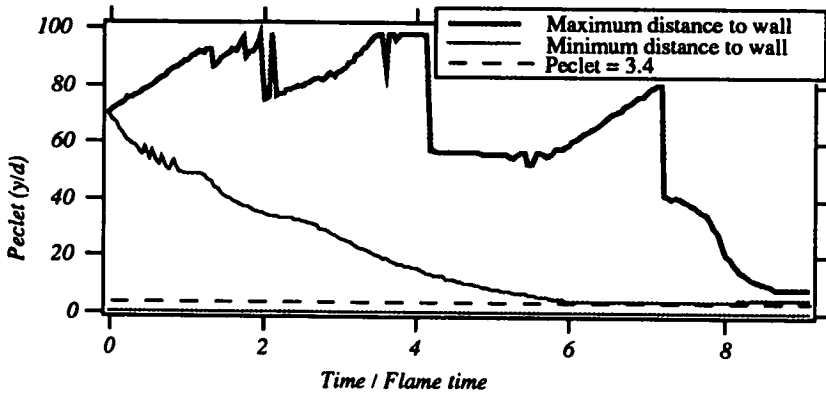


FIGURE 5. Maximum and minimum (over all computational cells adjacent to the wall) flame-wall distances for Case 2D4.

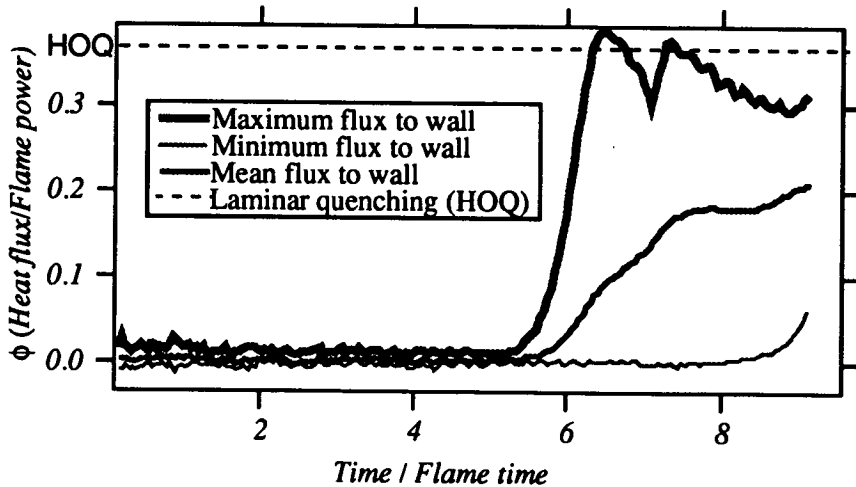


FIGURE 6. Minimum, maximum, and mean (over all computational cells adjacent to the wall) wall heat fluxes for Case 2D4.

parallel to the wall and not towards the wall, thus corresponding to the side-wall quenching situations described in Section 2. Branch 3 corresponds to flamelets which burn faster (accelerate) as they approach the wall, but subsequently quench on reaching a Peclet of about 3.5. At this point, no explanation for Branch 3 is proposed. The number of flamelets following Branch 2 is small compared to the other branches: most flamelets reach the wall at a normal angle. This is confirmed

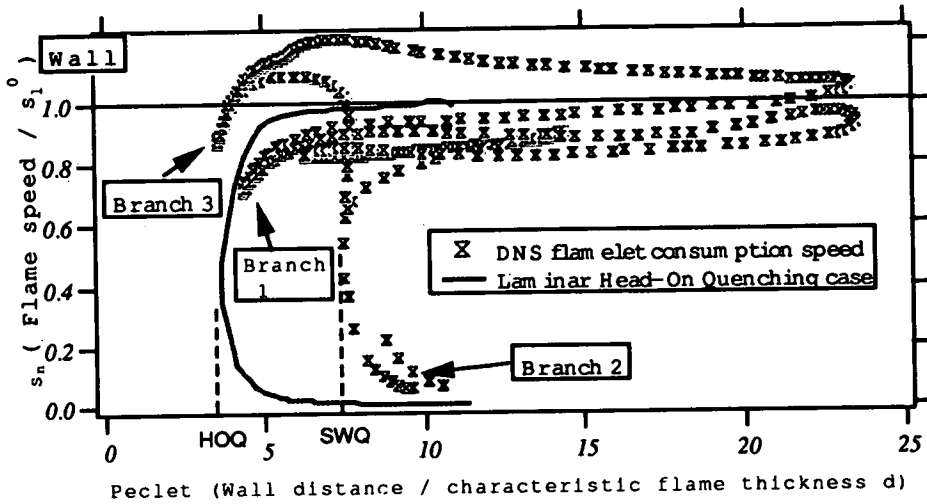


FIGURE 7. Flamelet consumption rate s_n versus wall distance at time $t/t_F = 4$ (Case 2D6).

by the distributions of flame curvature presented in Figure 8. While the flame is still far from the wall ($t/t_F = 0.5$), the mean curvature conditioned on distance to the wall is almost symmetrical about zero. As the flame brush approaches the wall ($t/t_F = 4$), flamelets flatten and curvature diminishes. Furthermore, positive values of curvature are clipped more strongly than negative values indicating that flamelets are predominantly concave towards the fresh gases and that most of them will reach the wall at close to a normal incidence angle.

The distance at which flamelets begin to sense the presence of the wall (i.e., where their local flamelet speed begins to drop) is given by a Peclet number of the order of 10 (Figure 7), close to that found for the laminar simulations. Although the existence of the three different branches suggests a more complex pattern than simple head-on quenching, it appears that an influence zone may be defined for turbulent cases whose thickness (in Peclet number) is something close to 10.

It appears that both the quenching zone thickness (δ_Q) and the influence zone thicknesses (δ_T) have similar values for turbulent and laminar premixed flames. This has some important consequences. Consider, for example, a reacting boundary layer. Invoking the usual normalizations, we denote by a superscript $+$ a wall-units-scaled value: $y^+ = yu_\tau/\nu$, where u_τ is the friction velocity and ν is the kinematic viscosity. The edge of the quenching zone is located at $\delta_Q^+ = u_\tau\delta_Q/\nu = (Pe_Q/Pr)(u_\tau/s_1^0)$. For most practical situations, u_τ (1 to 5 m/s) is of the order of the flame speed s_1^0 (0.3 to 1.5 m/s) so that δ_Q^+ is of the order of 1 to 10. That means that the quenching zone is located inside the viscous layer. Flamelets travelling from the free stream towards the wall first encounter laminar flow in the viscous

region and only *later* are quenched. This result will be used in the modeling of the flame-wall interaction (Section 7).

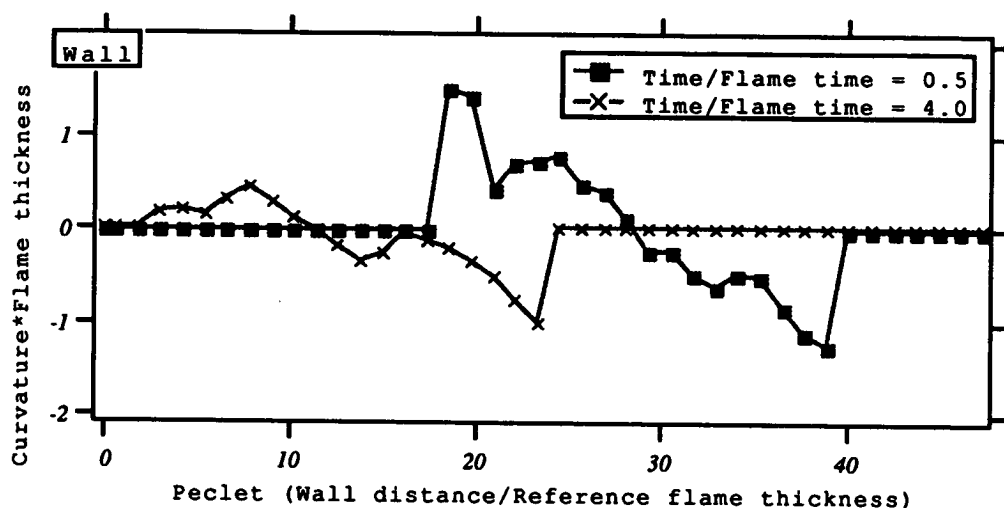


FIGURE 8. Mean curvature (conditioned on wall distance) for a flame far from the wall ($t/t_F = 0.5$) and a flame reaching the wall ($t/t_F = 4$) (Case 2D6).

7. A law-of-the-wall for turbulent premixed combustion

From the previous results, it is possible to construct law-of-the-wall models for premixed turbulent flames which we will designate here as 'FIST' models (Flame Interacting with Surface and Turbulence). This model will be derived in the framework of flamelet models: the dependent variable which will be modeled is the flame surface density (surface-to-volume ratio) Σ as defined by Pope (1988). Implementation is discussed in the context of a finite-volume method, although the concept may be applied to other numerical approaches.

We consider a generic flamelet model in which the flame surface density Σ evolves according to,

$$\frac{\partial \Sigma}{\partial t} + \frac{\partial \overline{U}_i \Sigma}{\partial x_i} = \frac{\partial \mathcal{F}_i}{\partial x_i} + S - D - D_Q. \quad (7)$$

This equation includes transport, turbulent diffusion (\mathcal{F}_i), and source (S) and consumption terms (D , D_Q). With the exception of the D_Q term which represents thermal quenching due to the wall, several recent flamelet models can be cast into this form (Cant *et al.* 1990, Candel *et al.* 1988, Boudier 1992, Cheng & Diringer 1991). The development of the present FIST model is independent of the exact

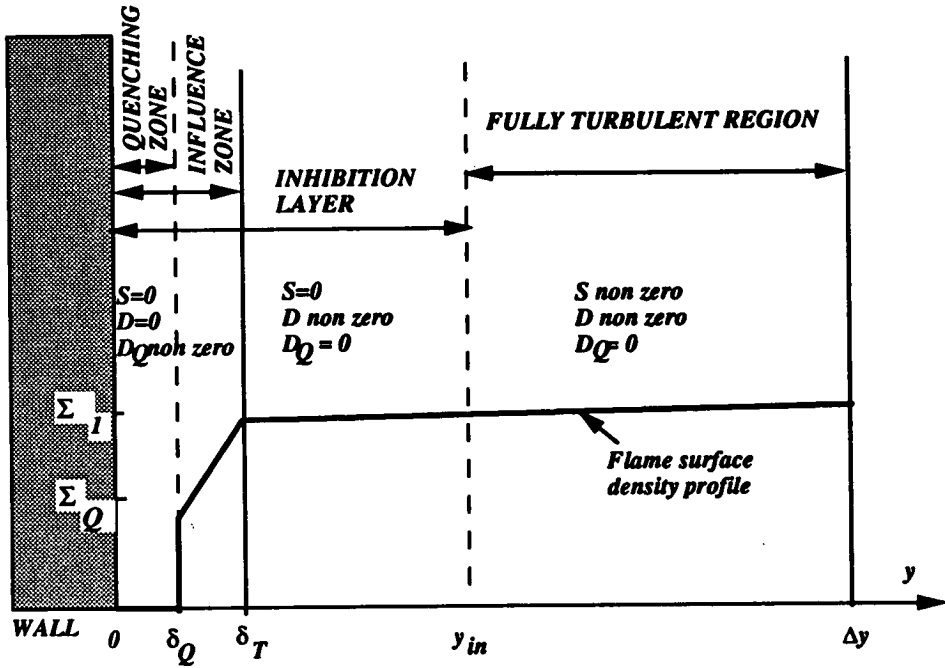


FIGURE 9. Principle of the FIST model (law-of-the-wall model for premixed turbulent combustion).

form of the S and D terms. The assumptions which will be used are the following (see Figure 9):

- We will consider a situation where a law-of-the-wall approach is used to describe near-wall turbulence since this is the case for most practical codes based on Reynolds-averaged mean equations.
- The computational cell size adjacent to the wall Δy is larger than the quenching zone and larger than the zone over which the wall modifies the free-stream turbulence structure (typically, in the case of a turbulent boundary layer, the first grid point is located at a y^+ larger than 200).
- Outside the quenching zone ($y > \delta_T$), no thermal quenching occurs as shown by DNS (see Section 6) so that $D_Q = 0$.
- Inside the quenching zone ($0 < y < \delta_T$), we need to estimate the characteristic time t_Q at which flamelets are quenched. For laminar cases, t_Q is of the order of two flame times as evidenced by DNS for laminar flames (see Section 5). Despite the existence of the three branches shown in Section 6, we will assume that all flamelets entering the influence zone in the turbulent case are quenched on a time

scale $t_Q = 2t_F$. Therefore, D_Q may be written as $D_Q = \Sigma_Q/t_Q$ where Σ_Q is the mean flame surface density in the quenching layer. This thermal quenching effect is supposed to be stronger than the usual consumption terms (due to mutual annihilation) in the Σ equation so that D may be set to zero. Since there is no turbulence inside the quenching layer (see Section 6) we will also assume that there are no source terms in this zone ($S = 0$).

– Inside an ‘inhibition zone’ which extends from $y = 0$ to $y^+ = y_{in}^+$, we assume that turbulence is affected strongly enough by the wall to reduce the flame stretch to zero. This assumption is not based on the present DNS but rather on the observation that turbulence must be strongly damped in this zone, therefore reducing the turbulent stretch.

– In the rest of the first computational cell ($y_{in}^+ < y^+ < \Delta y^+$), the normal form of the flamelet model is used.

– Finally, for the sake of clarity, we will consider a situation where the flow is homogeneous in planes parallel to the wall (i.e., Σ is a function of y only), and we will also neglect mean velocities normal to the wall. These last assumptions allow mean convective terms ($\frac{\partial \bar{U}_i \Sigma}{\partial x_i}$) to be neglected in the finite-volume expression of Eq. (7). This assumption is not restrictive, and is invoked only for convenience in writing the resulting modeled equations.

Under the previous assumptions, the equations of a FIST model may be derived by integrating Eq. (7) in two zones: the influence zone and the rest of the first computational cell. The mean flame surface densities in the influence zone and in the first computational cell, respectively, will be defined by: $\Sigma_Q = \frac{1}{\delta_T} \int_0^{\delta_T} \Sigma dy$, and $\Sigma_1 = \frac{1}{\Delta y - \delta_T} \int_{\delta_T}^{\Delta y} \Sigma dy$.

In the quenching zone, terms S and D are small compared to the thermal quenching effect. When Eq. (7) is integrated between $y = 0$ and $y = \delta_T$ with this assumption, the following conservation equation for Σ_Q is obtained:

$$\frac{\partial \Sigma_Q}{\partial t} = \frac{\mathcal{F}(y = \delta_T)}{\delta_T} - \frac{\Sigma_Q}{t_Q} \quad (8)$$

Integrating Eq. (7) between $y = \delta_T$ and $y = \Delta y$ provides an evolution equation for the average flame surface density Σ_1 in this zone:

$$\frac{\partial \Sigma_1}{\partial t} = \frac{1}{\Delta y - \delta_T} (\mathcal{F}(y = \Delta y) - \mathcal{F}(y = \delta_T)) + S \left(1 - \frac{y_{in}^+ - \delta_T}{\Delta y}\right) - D \quad (9)$$

Equations (8) and (9) form a closed set which provides the flame surface density in the quenching region (Σ_Q) and in the first computational cell (Σ_1). These two equations state that there is a sink mechanism for flame surface in the first computational cell: flamelets diffuse towards the quenching zone ($\mathcal{F}(y = \delta_T)$ term in Eq. (9)) and later get quenched in this zone on the time scale t_Q .

8. An equilibrium formulation for FIST models

Although Eqs. (8) and (9) may be solved under this form in finite-volume codes, it is interesting to propose a simpler model ‘Equilibrium FIST’ in which the flame

surface density in the quenching region Σ_Q may be eliminated. In the Equilibrium FIST model, four additional assumptions are invoked:

– The turbulent diffusion term \mathcal{F}_i is written as $\mathcal{F}_i = \frac{\nu_t}{S_c} \frac{\partial \Sigma}{\partial x_i}$ where ν_t is a turbulent diffusion coefficient and S_c is a turbulent Schmidt number.

– The flame surface-density profile inside the quenching zone is supposed to exhibit strong spatial variations compared to the profile outside this zone. Then the diffusion term $\mathcal{F}_y(y = \delta_T)$ may be estimated by $\mathcal{F}_y(y = \delta_T) = E \frac{\nu_t}{S_c} \frac{\Sigma_1 - \Sigma_Q}{\delta_T}$ where E is a model constant of order unity.

– The quenching zone is assumed to be in equilibrium, i.e., diffusion balances dissipation in Eq. (8). This allows us to derive an explicit expression for the flame surface density in the quenched region as a function of the flame surface density in the first cell Σ_1 :

$$\Sigma_Q = \Sigma_1 \frac{a_Q}{a_Q + 1} \quad \text{where} \quad a_Q = E \frac{\nu_t t_Q}{S_c \delta_T^2}. \quad (10)$$

The parameter a_Q is proportional to the turbulent diffusivity ν_t normalized by the quenching time and distance.†

– The size of the first cell is supposed to be sufficiently large compared to the quenching distance ($\Delta y \gg \delta_T$) to neglect δ_T in the RHS of Eq. (9).

Under these assumptions, the Equilibrium FIST model provides the following conservation equation for the flame surface density Σ_1 near a wall:

$$\frac{\partial \Sigma_1}{\partial t} = \frac{1}{\Delta y} \mathcal{F}(y = \Delta y) - \frac{\delta_T}{\Delta y} \frac{a_Q}{a_Q + 1} \frac{\Sigma_1}{t_Q} + S(1 - \frac{y_{in}^+}{\Delta y}) - D. \quad (11).$$

Wall corrections appear here only as an additional diffusion term towards the wall (second term on right-hand side of Eq. (11)) and as a correction of the turbulent stretch $S(1 - y_{in}^+/\Delta y)$. All other terms may be estimated by classical finite-volume methods. In this model, some constants may be set directly from the present DNS results: the influence distance is given by $\delta_T = P_e d = P_e \frac{\lambda_1}{\rho_1 c_p s_l^0}$ where the Peclet number should be of order 10 (Sections 5 and 6), and the quenching time scale t_Q is given by $t_Q = 2t_F = 2l_F^0/s_l^0$ (Section 5). The parameter y_{in}^+ has not been estimated from the present DNS results but might be determined by using a three-dimensional boundary-layer code. Reasonable estimates for this quantity are of the order of 50. The turbulent diffusivity ν_t appearing in the above formula may be estimated using standard expressions for this quantity near walls. Further improvements of the model may be based on an expression for ν_t which would take into account the counter-gradient diffusion of Σ mentioned in Section 6.

The simplicity of this formulation allows it to be used in conventional Reynolds-averaged multidimensional flow codes without additional constraints on time step

† By using an eddy-viscosity concept near the wall ($\nu_t = K u' \delta_T$), a_Q may be interpreted as a ratio between turbulence velocity near the wall and a characteristic quenching velocity ($a_Q = K \frac{E}{S_c} \frac{u'}{\delta_T/t_Q}$).

or grid size. Although the approach simplifies the actual physics of flame-wall interaction, it represents a significant improvement over approaches which fail to account explicitly for the influence of the wall on the turbulent flame. The Equilibrium FIST model accounts for turbulent diffusion of flamelets towards the wall and quenching on a time scale which is given by DNS. It also accounts in a crude way for the laminarization effect of the wall up to a distance given by y_{in}^+ .

9. Conclusions

Calculations of premixed laminar and turbulent flames interacting with isothermal walls have been reported. Quantitative results have been presented illustrating the influence of distance from the wall on the local and global flame structure. For laminar cases, the computed minimum distance between wall and flame (the 'quenching distance') and the maximum wall heat flux during quenching have been found to be comparable with available experimental and analytical results. For turbulent cases, it has been shown that quenching distances and maximum heat flux remain of the same order as for laminar flames. Correlations between wall distance and flame structure suggest that thermal effects are important only very close to the wall and that the wall acts as a strong sink term for flame surface density. Based on these DNS results, a model has been proposed to take into account the interaction between the turbulent flame and the wall. The equilibrium version of this model may be implemented in conventional finite-volume codes together with flamelet models based on modeled surface density equations. Further tests are necessary to assess its performance.

An important extension of the FIST model would be the development of a model for wall heat flux. Such a model could be based on the knowledge of the flame surface density in the quenching zone and on the correlations between wall heat flux and flame position. This issue will be addressed in future work.

REFERENCES

- ALY, S. L. & HERMANE, C. E. 1981 A two-dimensional theory of laminar flame quenching. *Combust. & Flame*. **40**, 173-185.
- BIRINGEN, S. & REYNOLDS, W. C. 1981 Large-eddy simulation of the shear-free turbulent boundary layer. *J. Fluid Mech.* **103**, 53-63.
- BOUDIER, P. 1992 Modelisation de la combustion turbulente dans un moteur piston. Ph.D. Thesis, Ecole Centrale, Paris.
- CANDEL, S. M., MAISTRET, E., DARABIHA, N., POINSOT, T., VEYNANTE, D. & LACAS, F. 1988 Experimental and numerical studies of turbulent ducted flames. *Marble Symposium, CALTECH*. 209-236.
- CANT, R. S., POPE, S. B. & BRAY, K. N. C. 1990 Modeling of flamelet surface to volume ratio in turbulent premixed combustion. *23rd Symp. (Intl.) on Combust.* The Combustion Institute, Pittsburgh, 809-815.
- CHENG, W. K. & DIRINGER, J. A. 1991 Numerical modeling of SI engine combustion with a flame sheet model. SAE Paper No. 910268.

- CLENDENING, J. C. W., SHACKLEFORD, W. & HILYARD, R. 1981 Raman scattering measurement in a side wall quench layer. *18th Symp. (Intl.) on Combust.* The Combustion Institute, Pittsburgh, 1583-1589.
- FAIRCHILD, P. W., FLEETER, R. D. & FENDELL, F. E. 1984 Raman spectroscopy measurement of flame quenching in a duct type crevice. *20th Symp. (Intl.) on Combust.* The Combustion Institute, Pittsburgh, 85-90.
- HUANG, W. M., VOSEN, S. R. & GREIF, R. 1986 Heat transfer during laminar flame quenching, effect of fuels. *21st Symp. (Intl.) on Combust.* The Combustion Institute, Pittsburgh, 1853-1860.
- HUNT, J. C. R. & GRAHAM, J. M. R. 1978 Free-stream turbulence near plane boundaries. *J. Fluid Mech.* **84**, 209-235.
- JAROSINSKI, J. 1986 A survey of recent studies on flame extinction. *Combust. Sci. & Technol.* **12**, 81-116.
- LELE, S. 1992 Compact finite difference schemes with spectral-like resolution. *J. Comput. Phys.* (to appear).
- LEWIS, B. & VON ELBE, G. 1987 *Combustion, Flames and Explosions of Gases.* Academic Press, New York.
- LU, J. H., EZENKOYE, O., GREIF, R. & SAWYER, F. 1990 Unsteady heat transfer during side wall quenching of a laminar flame. *23rd Symp. (Intl.) on Combust.* The Combustion Institute, Pittsburgh, 441-446.
- MAKHVILADZE, G. M. & MELIKOV, V. I. 1991 Flame propagation in a closed channel with cold side wall. *UDC.* **536.46**, 176-183. (*Fizika Goreniya i Vzryva* **2** 49-58, March-April 1991).
- POINSOT, T. & LELE, S. 1992 Boundary conditions for direct simulations of compressible viscous flows. *J. Comp. Phys.* **101**, 104-129.
- POINSOT, T., VEYNANTE, D. & CANDEL, S. 1991 Quenching processes and premixed turbulent combustion diagrams. *J. Fluid Mech.* **228**, 561-605.
- POPE, S. 1988 The evolution of surfaces in turbulence. *Intl. J. Engng. Sci.* **26**, 445-469.
- THOMAS, N. H. & HANCOCK, P. E. 1977 Grid turbulence near a moving wall. *J. Fluid Mech.* **82**, 481-496.
- UZKAN, T. & REYNOLDS, W. C. 1967 A shear-free turbulent boundary layer. *J. Fluid Mech.* **28**, 803-821.
- VON KARMAN, T. & MILLAN, G. 1953 Thermal theory of laminar flame front near cold wall. The Combustion Institute, Pittsburgh, 173-177.
- VOSEN, S. R., GREIF, R. & WESTBROOK, C. K. 1984 Unsteady heat transfer during laminar flame quenching. *20th Symp. (Intl.) on Combust.* The Combustion Institute, Pittsburgh, 76-83.
- WILLIAMS, F. A. 1985 *Combustion theory.* B. Cummings, Menlo Park, CA, 73-76.

The evolution equation for the flame surface density in turbulent premixed combustion

By A. Trouvé¹ AND T. Poinsot²

One central ingredient in flamelet models for turbulent premixed combustion is the flame surface density. This quantity conveys most of the effects of the turbulence on the rate of energy release and is obtained via a modeled transport equation, called the Σ -equation. Past theoretical work has produced a rigorous approach that leads to an exact, but unclosed, formulation for the turbulent Σ -equation (Section 1.2). In this exact Σ -equation, it appears that the dynamical properties of the flame surface density are determined by a single parameter, namely the turbulent flame stretch. Unfortunately, the flame surface density and the turbulent flame stretch are not available from experiments and, in the absence of experimental data, little is known on the validity of the closure assumptions used in current flamelet models. Direct Numerical Simulation (DNS) is the obvious, complementary approach to get basic information on these fundamental quantities. In the present work, three-dimensional DNS of premixed flames in isotropic turbulent flow is used to estimate the different terms appearing in the Σ -equation (Section 2.1). A new methodology is proposed to provide the source and sink terms for the flame surface density, resolved both temporally and spatially throughout the turbulent flame brush (Section 2.2). Using this methodology, the effects of the Lewis number on the rate of production of flame surface area are described in great detail and meaningful comparisons with flamelet models can be performed (Section 3). The analysis reveals in particular the tendency of the models to overpredict flame surface dissipation as well as their inability to reproduce variations due to thermo-diffusive phenomena. Thanks to the detailed information produced by a DNS-based analysis, this type of comparison not only underscores the shortcomings of current models but also suggests ways to improve them.

1. Introduction

1.1. The flamelet approach for turbulent premixed combustion

Premixed turbulent combustion is the propagation of a chemical reaction zone through a turbulent, molecularly mixed region of fuel and oxidizer. The turbulent flame is characterized by the topology of the region in which reaction occurs: front, pockets, or large volumes. Depending on the relative values of various chemical and turbulence scales, dimensional analysis reveals a range of premixed combustion

1 Center for Turbulence Research

2 C.N.R.S., Institut de Mécanique des Fluides de Toulouse, France

modes progressing from flamelets to distributed reaction zones to well-stirred reactors (Barrère 1974, Bray 1980, Borghi 1985, Peters 1986, Williams 1985, Poinso *et al.* 1990). These modes correspond to different topologies of the reaction zone and require different approaches for both understanding and modeling.

Experimental as well as theoretical evidence suggests that many technologically important flows occur in the flamelet burning mode. Flamelet combustion corresponds to chemical reaction occurring at fast time scales and short length scales relative to the turbulence. In this situation, the flame is confined to relatively thin layers within the turbulent flow field.

In the flamelet regime, it is convenient to describe the flame-flow interactions in terms of two basic ingredients: a flame speed that characterizes the flame structure and the flame front surface area. For instance, the mean reaction rate may be written as the product of the mean fuel consumption rate per unit flame surface area times the flame surface density:

$$\langle \dot{\omega}_R \rangle = (\rho_u Y_{R,u} \langle S_C \rangle_S) \langle \Sigma' \rangle, \quad (1)$$

where $\dot{\omega}_R$ is the mass of fuel consumed per unit time and per unit volume; ρ_u and $Y_{R,u}$ are respectively the density and the fuel mass fraction in the unburnt gas; S_C is the local integral of the reaction rate along the flame normal direction, $S_C = \int \dot{\omega}_R dn$, and characterizes the local combustion intensity; and Σ' is the flame surface area per unit volume. The flame surface density is defined as the expected value for Σ' : $\Sigma = \langle \Sigma' \rangle$.

In Eq.(1), the flamelet speed, $\langle S_C \rangle_S$, accounts for local variations of the reaction rate along the flame surface. Laminar flame theory indicates that the local flame structure is modified by flow divergence, usually characterized by the hydrodynamic strain rate acting in the flame tangent plane as well as by flame front curvature. Under certain conditions, these variations can become critical and lead to partial or total quenching of the flame. Recent studies, however, using Direct Numerical Simulations (DNS) suggest that quenching is a rather unlikely event for turbulent premixed flames (Poinso *et al.* 1990). In addition, although the local combustion intensity may exhibit large variations along the turbulent flame front, particularly for non-unity Lewis number flames, DNS suggest that these variations always tend to cancel in the mean (Haworth & Poinso 1992, Rutland & Trouvé 1991). In the simulations, the mean fuel consumption speed, \bar{S}_C , defined as the area-weighted, space-averaged value of S_C integrated along the turbulent flame surface, remain within 10% to 30% from the one-dimensional, laminar flame speed value, s_L .†

Thus, it appears that in the absence of quenching, the mean fuel consumption speed, \bar{S}_C , is only weakly sensitive to the flow field and the principle effect of turbulence is for the fluctuating velocity field to wrinkle the flame and greatly increase its surface area. This phenomenon accounts for most of the increase in the

† Note that \bar{S}_C is a space-averaged quantity and should not be confused with $\langle S_C \rangle_S$ which is an area-weighted ensemble-average as defined in section 1.2 and, therefore, depends on location within the turbulent flame brush (see Figure 7)

overall burning rate due to the turbulence and is represented in Eq.(1) through the flame surface density, Σ .

1.2. The evolution equation for the flame surface density, Σ

In current flamelet models, the flame surface density, Σ , is obtained via a modeled transport equation. This equation was first postulated by Marble & Broadwell (1977) based on phenomenological grounds. A more rigorous approach was later proposed by Pope (1988) and Candel & Poinso (1990) who derive an exact balance equation for the flame surface-to-volume ratio, Σ' :

$$\frac{\partial \Sigma'}{\partial t} + \nabla \cdot \dot{\mathbf{X}} \Sigma' = (\nabla \cdot \dot{\mathbf{X}} - \mathbf{nn} : \nabla \dot{\mathbf{X}}) \Sigma', \tag{2}$$

where $\dot{\mathbf{X}}$ is the displacement speed of the flame surface, given by the sum of the fluid velocity and the flame propagation speed in the normal direction: $\dot{\mathbf{X}} = \mathbf{u} + w\mathbf{n}$; \mathbf{n} is the unit vector normal to the flame surface; and where we use tensorial notations: $(\mathbf{nn} : \nabla \dot{\mathbf{X}}) = n_i n_j \frac{\partial \dot{X}_i}{\partial x_j}$.

The right-hand side of Eq.(2) can also be expressed in terms of flame stretch. The flame stretch, k , is defined as the rate of change of a Lagrangian flame surface element, δA :

$$k = \frac{d(\delta A)}{dt} = \frac{\partial(\delta A)}{\partial t} + \dot{\mathbf{X}} \cdot \nabla(\delta A) \tag{3}$$

A more useful expression for k is in terms of strain rate, flame curvature, and flame propagation speed (see for example Candel & Poinso 1990):

$$k = a_T + 2wk_m, \tag{4}$$

where a_T is the rate of strain acting in the flame tangent plane: $a_T = \nabla \cdot \mathbf{u} - \mathbf{nn} : \nabla \mathbf{u}$; and k_m is the flame surface curvature, as given by the divergence of the flame normal direction: $2k_m = \nabla \cdot \mathbf{n}$. In Eq.(4), positive curvature is chosen convex towards the reactants.

Using Eq.(4), the balance equation for the flame surface-to-volume ratio can be re-written as:

$$\frac{\partial \Sigma'}{\partial t} + \nabla \cdot \dot{\mathbf{X}} \Sigma' = k \Sigma' \tag{5}$$

When ensemble-averaged, this equation yields an exact balance equation for the flame surface density (Pope 1988, Cant *et al.* 1990):

$$\frac{\partial \Sigma}{\partial t} + \nabla \cdot \langle \dot{\mathbf{X}} \rangle_S \Sigma = \langle k \rangle_S \Sigma, \tag{6}$$

where the flame surface mean of any quantity Q is given by: $\langle Q \rangle_S = \langle Q \Sigma' \rangle / \langle \Sigma' \rangle = \langle Q \Sigma' \rangle / \Sigma$. Note that surface means are different from standard means; in particular, the surface mean of a quantity Q is different from the ensemble mean of Q conditioned on being at the flame location (see section 2.2).

Eq.(6) can be cast in various forms. For modeling purposes, it is useful to split the velocity vector into a mean component and a turbulent fluctuation: $\mathbf{u} = \langle \mathbf{U} \rangle + \mathbf{u}'$. We can then re-write Eq.(6) as follows:

$$\frac{\partial \Sigma}{\partial t} + \nabla \cdot \langle \mathbf{U} \rangle \Sigma + \nabla \cdot \langle \mathbf{u}' \rangle_S \Sigma + \nabla \cdot \langle w \mathbf{n} \rangle_S \Sigma = \langle a_T \rangle_S \Sigma + \langle A_T \rangle_S \Sigma + 2 \langle w k_m \rangle_S \Sigma, \quad (7)$$

where we use the following notations:

$$\begin{aligned} \langle a_T \rangle_S &= \langle \nabla \cdot \mathbf{u}' - \mathbf{nn} : \nabla \mathbf{u}' \rangle_S, \\ \langle A_T \rangle_S &= \nabla \cdot \langle \mathbf{U} \rangle - \langle \mathbf{nn} \rangle_S : \nabla \langle \mathbf{U} \rangle \end{aligned}$$

The three convective terms on the left-hand side of Eq.(7) are transport terms that correspond respectively to convection by the mean flow, turbulent diffusion, and flame propagation. The terms on the right-hand side of the equation are the source and sink terms for the flame surface density: $\langle a_T \rangle_S$ is the turbulent strain rate acting in the flame tangent plane, $\langle A_T \rangle_S$ is the strain rate due to the mean flow field, and $2 \langle w k_m \rangle_S$ is a term that accounts for the combined effects of flame curvature and flame propagation.

The principle effect of turbulence is to increase the flame surface area, and $\langle a_T \rangle_S$ is without ambiguity a source term in the equation for Σ . The effect of the mean flow field as measured by $\langle A_T \rangle_S$ is problem dependent; depending on the flow configuration, its sign can be positive or negative. We now focus attention on the last term in Eq.(7), referred to as the propagation term.

In many situations, flame propagation effects merely counteract the wrinkling due to the turbulence and the propagation term, $2 \langle w k_m \rangle_S$, is, therefore, expected to be negative. Consequently, this term is usually described as a sink term in flamelet models. There are some situations, however, where this description is clearly incorrect. Since the propagation term includes some of the effects associated with intrinsic flame instabilities†, this term must depend on the flame properties, thereby allowing for situations where its sign is positive and where the net effect corresponds to a production of flame surface.

The exact importance of laminar flame instabilities for turbulent combustion is an open subject. Recent evidence, however, both experimental (Abdel-Gayed *et al.* 1984, Wu *et al.* 1990, Goix & Sheperd 1992) and numerical (Ashurst *et al.* 1987, Haworth & Poinsot 1992, Rutland & Trouvé 1991), suggests that the role of the Lewis number has been underestimated in the past. For instance, current flamelet models fail to account for the effects of the Lewis number on the rate of production of flame surface. The objective of the present study is to determine how present formulations might be improved to incorporate such effects. The approach is to analyze the source and sink terms in the equation for the flame surface density, with particular emphasis on how the Lewis number can affect their balance. This is accomplished using DNS, as described in the next section.

† Using the terminology introduced to describe laminar flame instabilities, the propagation term represents the thermo-diffusive mechanism, while the strain term represents the hydrodynamic mechanism. These two instability mechanisms are coupled together and both account for Lewis number effects (Clavin 1985, Williams 1985)

2. Direct Numerical Simulation of turbulent premixed flames

2.1. Numerical method and configuration

We use DNS to analyze the different terms appearing in the equation for the flame surface density. The simulations are performed using a three-dimensional, compressible Navier-Stokes solver that fully resolves the turbulent flow field. Spatial derivatives are computed with a modified Padé scheme that is sixth-order accurate (Lele 1990). Solutions are advanced in time using a third-order Runge-Kutta method (Wray 1990). Boundary conditions are specified using the NSCBC method (Poinsot & Lele 1992). Because of the otherwise prohibitive computational cost, simulations are limited to simple but finite-rate reaction schemes. In this work, the chemistry model is a single step, irreversible chemical reaction where the reaction rate depends exponentially on temperature (Arrhenius kinetics):

$$\dot{\omega}_R = B\rho Y_R \exp\left(-\frac{T_a}{T}\right), \quad (8)$$

where T_a is the activation temperature and B is a constant that depends on the flame speed. This formulation corresponds to a binary reaction in which one of the reactants, Y_R , is strongly deficient as, for example, in fuel-lean combustion. Also, it is worth emphasizing that the simulations are not limited by the constant density assumption, and heat release effects are fully accounted for.

Following Williams (1985), we re-write the reaction rate as:

$$\dot{\omega}_R = \Lambda\rho Y_R \exp\left(\frac{-\beta(1-\Theta)}{1-\alpha(1-\Theta)}\right), \quad (9)$$

where Θ is the reduced temperature, $\Theta = (T - T_u)/(T_b - T_u)$; T_u is the temperature of the fresh reactants; T_b is the adiabatic flame temperature; and the coefficients Λ , α , and β are, respectively, the reduced pre-exponential factor, the heat release factor, and the reduced activation energy:

$$\Lambda = B \exp(-\beta/\alpha), \quad \alpha = (T_b - T_u)/T_b, \quad \text{and} \quad \beta = \alpha T_a/T_b \quad (10)$$

In the following, we use $\alpha = 0.75$ and $\beta = 8$.

Another important feature of the simulations is that transport coefficients are temperature dependent. These coefficients satisfy the following relations:

$$\mu = \mu_u(T/T_u)^b, \quad Le = \lambda/\rho Dc_p = \text{constant}, \quad Pr = \mu c_p/\lambda = \text{constant}, \quad (11)$$

where μ , λ , and D are the molecular diffusivities of, respectively, momentum, internal energy, and species mass, b is a constant, and Le and Pr are respectively the Lewis number and the Prandtl number. We use $b = 0.76$, $Pr = 0.75$. Simulations have been performed for different Lewis numbers, $Le = 0.8, 1.0$, and 1.2 .

The selected computational configuration corresponds to a premixed flame embedded in three-dimensional, decaying, isotropic turbulent flow. The left- and right-hand sides of the computational domain are inflow and outflow boundaries while

periodic boundary conditions are applied at lateral walls. The calculations are initialized with fresh reactants on one side of the domain and burnt products on the other side; the two are separated by a plane laminar flame. Isotropic turbulence is initially located in the flow of fresh reactants, its velocity field being specified according to a model spectrum. The turbulence is characterized by a Kolmogorov length scale smaller than the thermal thickness of the laminar flame, $\eta_k/\delta_T = 0.1$ where $\delta_T = (T_b - T_u)/(dT/dx)_{max}$, and a turbulence intensity that is much higher than the laminar flame speed, $u'/s_L = 10$. The initial turbulent Reynolds number, based on the Taylor microscale, is 50. The initial turbulent Reynolds number, based on the integral length scale, is 70. The grid resolution is 129^3 .

The simulations describe the wrinkling of the flame zone due to turbulent motions as well as the combustion feedback due to dilatation and temperature-dependent transport properties. Note that the turbulence is decaying in time, and conditions are non-stationary.

2.2. Diagnostics

All terms appearing in Eq.(7) may be obtained from the simulations. We now briefly describe how. The velocity vector and the velocity gradient tensor are readily obtained from the resolved flow field. To define flame-based quantities, we make use of concepts based on a thin flame picture. First, a progress variable, c , is introduced that is used to indicate location within the reaction zone, $c = 1 - Y_R$, where Y_R is the normalized fuel mass fraction. The progress variable varies monotonically through the flame from 0 in the reactants to 1 in the products. Constant progress variable surfaces may conveniently be used to define the flame front location: we use the surface $c = c_f = 0.8$. In addition, at any location on this surface, the local gradient of c defines the normal direction to the flame front:

$$\mathbf{n} = -\frac{\nabla c}{|\nabla c|}, \quad (12)$$

where \mathbf{n} points into the fresh reactants.

The propagation speed of the flame surface, w , is obtained from an expression analog to the well-known field equation (also called the G -equation). Let us first consider a point on the flame surface, $c = c_f$. The velocity, $\dot{\mathbf{X}}$, at which this point must move to remain on the surface is given by:

$$\frac{\partial c}{\partial t} + \dot{\mathbf{X}} \cdot \nabla c = 0, \quad (13)$$

which, using Eq.(12), implies that:

$$\dot{\mathbf{X}} \cdot \mathbf{n} = \frac{1}{|\nabla c|} \frac{\partial c}{\partial t}, \quad (14)$$

and which yields the following expression for the flame propagation speed:

$$w = \dot{\mathbf{X}} \cdot \mathbf{n} - \mathbf{u} \cdot \mathbf{n} = \frac{1}{|\nabla c|} \frac{Dc}{Dt}, \quad (15)$$

where quantities are estimated at the surface $c = c_f$. Since in the simulations we solve for a conservation equation for the fuel mass fraction, Y_R , and since by definition $c = 1 - Y_R$, the expression above can be readily obtained from the DNS data base.

The flame surface density, Σ , is a more subtle quantity. It includes both geometrical and statistical information. Following Pope (1990), the flame surface density is computed as the product of the expected value for the magnitude of the gradient of c , conditioned on being on the flame surface, times the probability of being on that surface:

$$\Sigma' = |\nabla c| \delta(c - c_f), \quad \text{and} \quad \Sigma = \langle \Sigma' \rangle = \langle |\nabla c| \mid c = c_f \rangle p(c_f), \quad (16)$$

where $p(c_f)$ is the probability of $c = c_f$.

We now turn to the averaging problem. In the simulations, the flame brush propagates along the x direction, and the problem remains homogeneous in the $y - z$ planes. Therefore, averaged quantities depend on x and time t only, and ensemble-averaging can be performed in the $y - z$ planes:

$$\langle Q \rangle(x, t) = \frac{1}{L_y L_z} \int Q(x, y, z, t) dy dz, \quad (17)$$

where L_y and L_z are the y and z dimensions of the computation domain. The accuracy of this expression depends on the size of the computational domain with respect to the turbulent length scales. In the simulations, the integral length scale of the turbulent flow field grows as the kinetic energy decays; this growth, however, is rather slow, and it was determined that the integral length scale remains at least 8 times smaller than L_y and L_z . Typically, in every $y - z$ plane within the turbulent flame brush, the statistical sample consists of approximately 10 fully independent flame events, and, although we recognize that the statistics are somewhat undersampled, reasonable accuracy is expected when estimating the first moments.

Conditional means are computed by integrating along the $c = c_f$ contour:

$$\langle Q \mid c = c_f \rangle(x, t) = \frac{\int_{c=c_f} Q dl}{\int_{c=c_f} dl} \quad (18)$$

Surface means are then obtained using the following relations:

$$\langle Q \rangle_s(x, t) = \frac{\langle Q \Sigma' \rangle}{\langle \Sigma' \rangle} = \frac{\langle Q |\nabla c| \mid c = c_f \rangle}{\langle |\nabla c| \mid c = c_f \rangle} = \frac{\int_{c=c_f} Q |\nabla c| dl}{\int_{c=c_f} |\nabla c| dl} \quad (19)$$

Clearly, surface means differ from conditional means.

The relations above provide a methodology to estimate the different means needed in our analysis. As shown in Eq.(16), the flame surface density, Σ , also requires

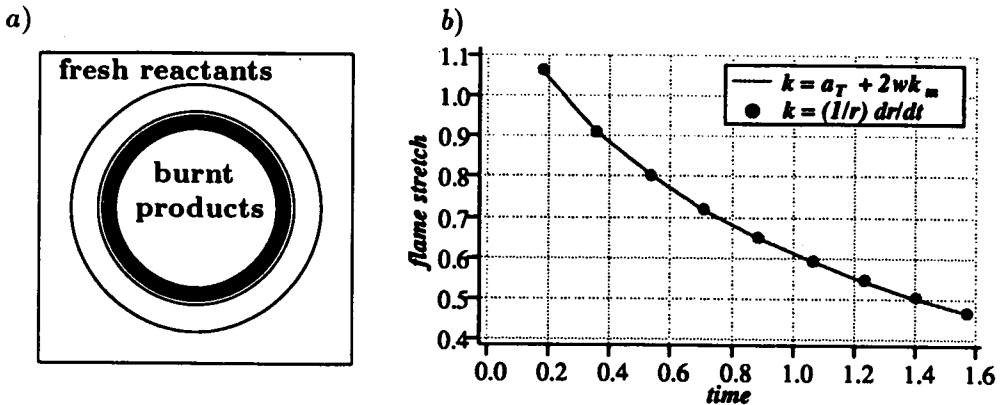


FIGURE 1. A test case for flame stretch: the problem of a cylindrical, freely-expanding, premixed laminar flame: a) temperature contours; b) flame stretch: solid line based on Eq.(4); symbols based on Eq.(22).

an estimate of the probability $p(c_f)$. Simple geometrical considerations lead to the following relation:

$$p(c_f) = \frac{1}{L_y L_z} \int_{c=c_f} \frac{dl}{\sqrt{(\frac{\partial c}{\partial y})^2 + (\frac{\partial c}{\partial z})^2}}, \quad (20)$$

and finally, Eqs.(16), (18) and (20) yield the following expression for Σ :

$$\Sigma = \frac{1}{L_y L_z} \int_{c=c_f} \frac{dl}{\sqrt{(\frac{\partial c}{\partial y})^2 + (\frac{\partial c}{\partial z})^2}} \frac{\int_{c=c_f} |\nabla c| dl}{\int_{c=c_f} dl} \quad (21)$$

Before applying these diagnostics to the turbulent flame simulations, we check the accuracy of our estimates for flame stretch and flame propagation speed using a model laminar flame problem as described in the next section.

2.3. Validation of DNS-based estimates for flame stretch

As seen in Eqs.(5) and (6), the flame stretch, k , is the single relevant parameter that determines the growth rate of flame surface area. Since this growth rate is locally exponential, it is important to obtain accurate estimates for k . In our analysis, the flame stretch is obtained using Eq.(4). The overall accuracy of our analysis thus depends on our ability to predict correctly strain rate, flame curvature, and flame propagation speed. To check the accuracy of our estimates, we performed simulations of a cylindrical, premixed laminar flame expanding freely into an initially quiescent medium (Figure 1a). In this model problem, the flame stretch can be directly measured from the growth of the flame radius:

$$k = \frac{1}{r_f} \frac{dr_f}{dt}, \quad (22)$$

where r_f designates the radius of the flame contour, $c = c_f$. Results based on this expression are compared with our DNS-based estimates in Figure 1b. The very

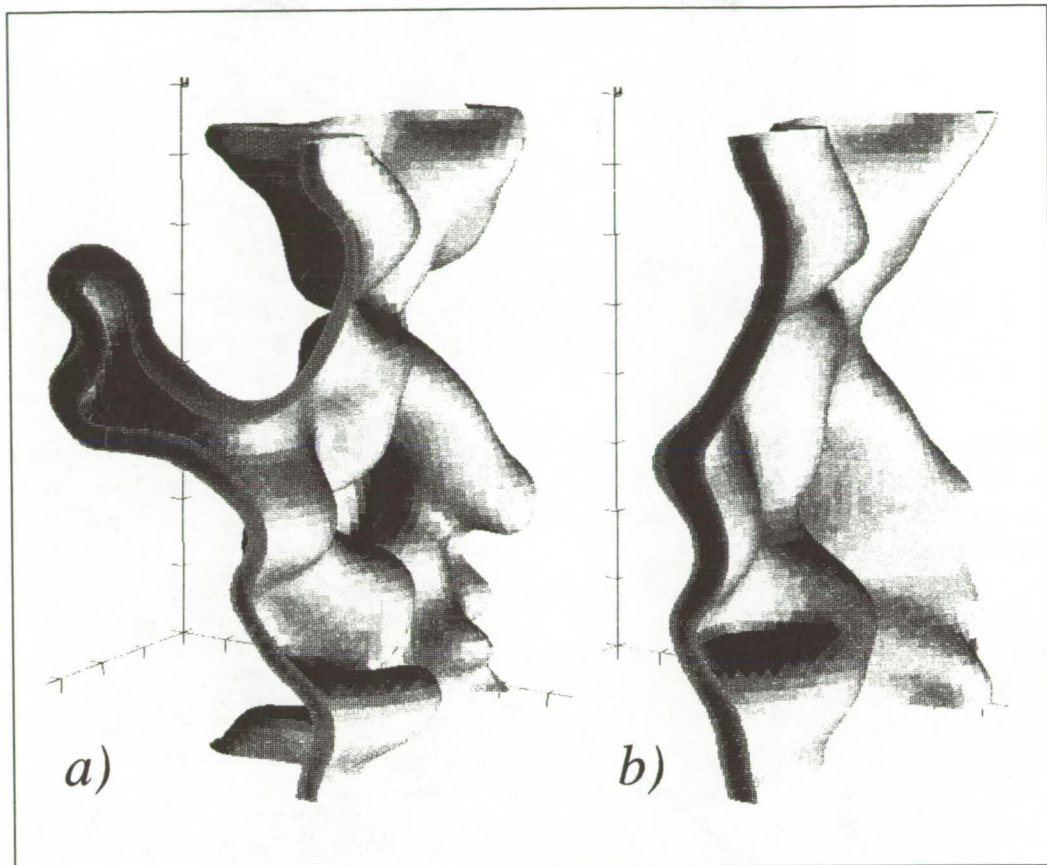


FIGURE 2. DNS of turbulent premixed flames in isotropic flow. Snapshots of the flame surface after 3.5 turbulent eddy turn-over time: a) $Le = 0.8$; b) $Le = 1.2$. The flow is from top-left (reactants) to bottom-right (products).

good agreement seen in Figure 1b demonstrates that the flame stretch as well as the flame propagation speed can be accurately monitored with our diagnostics.

3. Results and discussion

As described in the previous section, the present study uses three-dimensional, direct numerical simulations of turbulent premixed flames in isotropic flow. Three different cases have been studied that correspond to turbulent flames characterized by the same laminar thermal thickness, δ_T , the same laminar flame speed, s_L , embedded in the same initial turbulent flow field, but with different Lewis number, $Le = 0.8, 1.0$ and 1.2 (Figure 2).

3.1. The overall effect of the Lewis number

Figure 3 shows that the three cases exhibit large differences in the time history of the total reaction rate (space-averaged over the computational domain). After 4 turbulent eddy turn-over time, $t = 4\tau$, the $Le = 0.8$ flame burns more than twice as

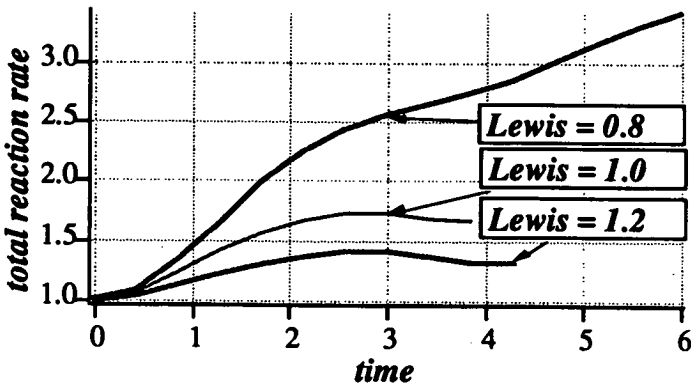


FIGURE 3. Lewis number effects on the overall combustion intensity. The total reaction rate is made non-dimensional by its initial value corresponding to a strain-free, plane laminar flame. Time is made non-dimensional by the initial, turbulent eddy turn-over time, τ .

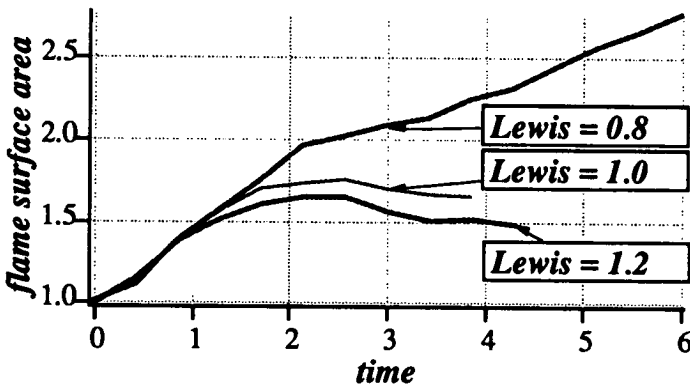


FIGURE 4. Lewis number effects on the relative increase of total flame surface area. Time is made non-dimensional by the turbulent eddy turn-over time, τ .

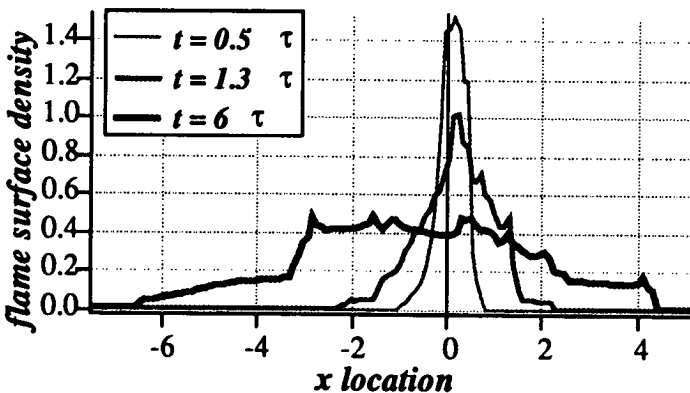


FIGURE 5. Time evolution of the flame surface density, Σ , through the turbulent flame brush (reactants on the left; products on the right). $Le = 0.8$. Σ and x are made non-dimensional by the laminar thermal thickness, δ_T . Time is measured in units of the turbulent eddy turn-over time, τ .

much as the $Le = 1.2$ flame. In agreement with the findings from previous studies (Ashurst *et al.* 1987, Haworth & Poinso 1992, Rutland & Trouvé 1991), the mean fuel consumption speed, \bar{S}_C , irrespective of the value of the Lewis number, is found to be only a weak function of the turbulence: at all times, departures of \bar{S}_C from the laminar value, s_L , remain within 20%. Thus, the principal effect of the Lewis number is to promote or inhibit the production of flame surface area.

The drastic effect of the Lewis number on flame surface production is displayed in Figure 4. For $Le = 1.0$ and $Le = 1.2$, the flame surface area initially increases, reaches a maximum, and then decreases in time. The increase occurs as the turbulence wrinkles the initially flat flame surface. The flame then adapts to its turbulent environment, and, as the turbulence decays, the flame surface becomes smoother and relaxes to its initial state. The $Le = 0.8$ flame exhibits a strikingly different behavior: the flame surface area keeps increasing in time without saturation. Although saturation might be expected at later times, our simulations are limited by the size of the computational domain and this subsequent phase cannot be observed. In any case, the simulations indicate that saturation will not occur on a time scale characteristic of the turbulence, and, in that sense, the flame can be said to be unstable.

The differences between the $Le = 0.8$ and $Le = 1.2$ flames are in fact so pronounced that they can easily be observed by comparing instantaneous snapshots of the flame surface (Figure 2). For instance, for $Le = 0.8$, fingers of burnt products are seen to propagate at a fast rate into the fresh reactants (Figure 2a). We believe this "fingering" is an important ingredient of the flame instability process. The "fingering" is not observed in the $Le = 1.0$ or $Le = 1.2$ flames (Figure 2b).

3.2. The source and sink terms in the equation for Σ

The effects of the Lewis number are now further studied by analyzing the structure of the terms appearing on the right-hand side of the equation for the flame surface density, Σ . As described in section 2.2, the analysis takes advantage of the fact that the problem is statistically one-dimensional and provides the source and sink terms for Σ as a function of time t and position x within the turbulent flame brush.

Figure 5 compares several Σ -profiles through the turbulent flame brush taken at different instants in the simulations. The Lewis number is 0.8. At $t = 0$, Σ is a delta function located at $x = 0$. As time evolves, the turbulent flame brush gets thicker and propagates deeper into the reactants. Accordingly, the Σ -profile spreads out and shifts towards negative values of x . In the simulations, this shift is rather weak but can clearly be seen at the latest times ($t = 6\tau$ in Figure 5). Note that the integral of Σ through the flame brush gives the relative increase of total flame surface area:

$$\int \Sigma(x, t) dx = \frac{S_V(t)}{L_y L_z}, \quad (23)$$

where $S_V(t)$ is the flame surface area within the computational domain of size V .

The main advantage of the present analysis is to distinguish between the leading edge and the rear edge of the turbulent flame brush. The geometry as well as the dynamics of the flame differ quite significantly from one end of the reaction zone

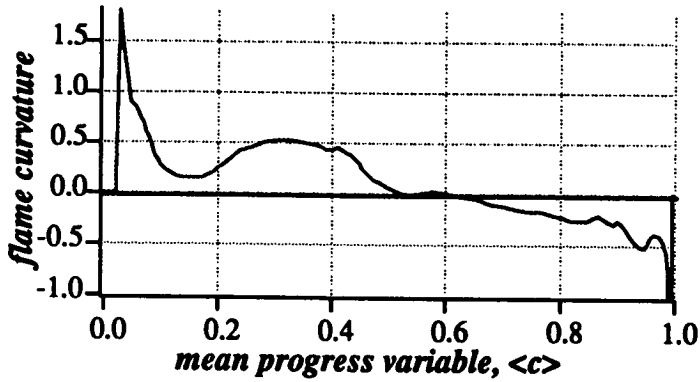


FIGURE 6. Variations of the mean flame curvature, $\langle k_m \rangle_S$, through the turbulent flame brush. $Le = 0.8$, $t = 4 \tau$. Flame curvature is made non-dimensional by the laminar thermal thickness, δ_T .

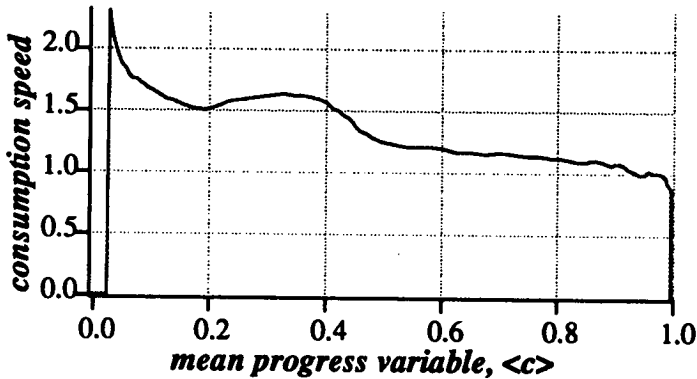


FIGURE 7. Variations of the mean fuel consumption speed, $\langle S_C \rangle_S$, through the turbulent flame brush. $Le = 0.8$, $t = 4 \tau$. S_C is made non-dimensional by the laminar flame speed, s_L .

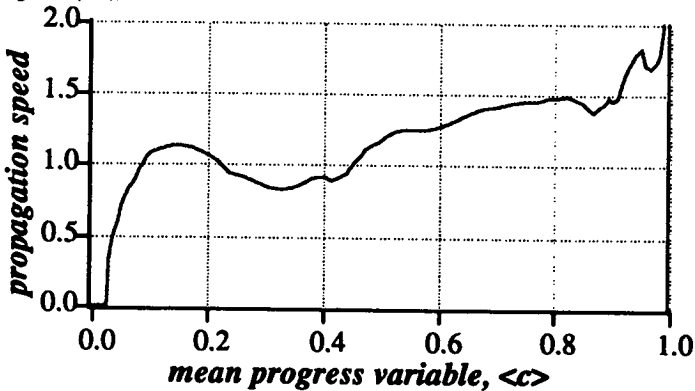


FIGURE 8. Variations of the mean flame propagation speed, $\langle w \rangle_S$, through the turbulent flame brush. $Le = 0.8$, $t = 4 \tau$. w is made non-dimensional by its value corresponding to a strain-free, plane laminar flame, $w = s_L \rho(c = 0) / \rho(c = c_f)$.

to the other as shown in Figures 6 to 12. For convenience, in Figures 6 to 12, x -location within the turbulent flame brush is indicated by the local mean progress variable, $\langle c \rangle$.

Figure 6 shows an instantaneous plot of the spatial variations of the mean flame curvature, $\langle k_m \rangle_S$, through the turbulent flame. The mean curvature goes from positive at the leading edge to negative at the rear edge of the turbulent flame. Since in non-unity Lewis number flames, the local combustion intensity, as measured by the reactant consumption speed S_C , depends strongly on the flame curvature, and since the dependence is quasi-linear (Haworth & Poinso 1992, Rutland & Trouvé 1991), it might be inferred from Figure 6 that the statistical distribution of S_C is non-homogeneous as well. Figure 7 shows that this is indeed the case. For $Le < 1$, $\langle S_C \rangle_S$ is a decreasing function of the mean progress variable, $\langle c \rangle$: the combustion intensity is higher at the leading edge than at the rear edge of the turbulent flame. For $Le > 1$, the trends are opposite: the combustion intensity is lower at the leading edge, close to $\langle c \rangle = 0$, than at the rear edge, close to $\langle c \rangle = 1$. For $Le = 1$, $\langle S_C \rangle_S$ remains approximately constant and equal to the laminar flame speed, s_L .

In the flamelet regime, a flame element can be characterized by two speeds: S_C , which is a chemical rate, and w , which is a kinematic quantity and gives the velocity of the flame front with respect to the flow field (Eq.(15)). For a strain-free, plane laminar flame these two speeds are the same and equal to s_L . As pointed out by Poinso *et al.* (1992), in the context of highly stretched flames, S_C and w can be significantly different. Figure 8 shows the variations of the mean flame propagation speed, $\langle w \rangle_S$, through the turbulent flame. $\langle w \rangle_S$ is an increasing function of the mean progress variable, $\langle c \rangle$. Comparison of Figures 7 and 8 indicate that, for $Le = 0.8$, the leading edge of the turbulent flame burns faster but propagates more slowly than the rear edge of the flame, which burns more slowly but propagates faster into the reactants.

It is worth emphasizing that the dynamical properties of the turbulent flame are not completely described by the knowledge of the distribution of the propagation speed, w , along the flame. To determine whether the flame surface will actually grow or contract, some information about the hydrodynamic flow field has to be included.† In other words, one needs to solve for the Σ -equation.

We now turn to the terms appearing on the right-hand side of the equation for Σ . While the strain term, $\langle a_T \rangle_S$, remains approximately constant through the turbulent flame (Figure 9), the propagation term, $2\langle wk_m \rangle_S$, exhibits strong variations and decreases from positive values on the unburnt side, close to $\langle c \rangle = 0$, to negative values on the burnt side, close to $\langle c \rangle = 1$ (Figure 10). The net effect on the surface growth rate is given by the flame stretch, $\langle k \rangle_S = \langle a_T \rangle_S + 2\langle wk_m \rangle_S$. Figures 9 and 10 indicate that both contributions to stretch have the same order of magnitude.

† This is best seen in the context of laminar flame instabilities, where the classical linear theory shows that the stability problem is not solved at the level of determining the Markstein length but also requires solving for a dispersion relation, which includes hydrodynamic effects (Clavin 1985, Williams 1985)

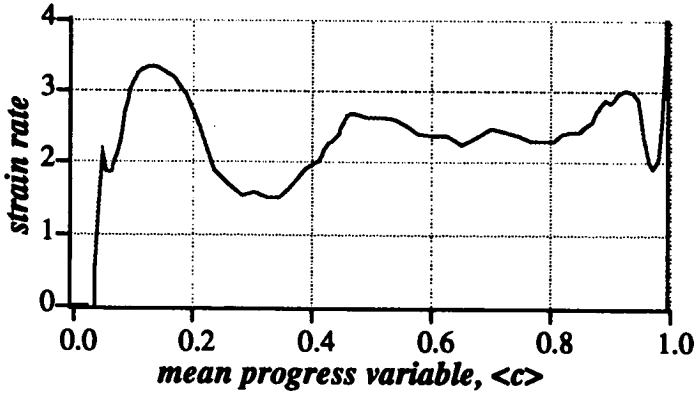


FIGURE 9. Variations of the mean strain rate, $\langle a_T \rangle_S$, through the turbulent flame brush. $Le = 0.8$, $t = 4 \tau$. Strain rate is made non-dimensional by the characteristic flame time, δ_T/s_L .

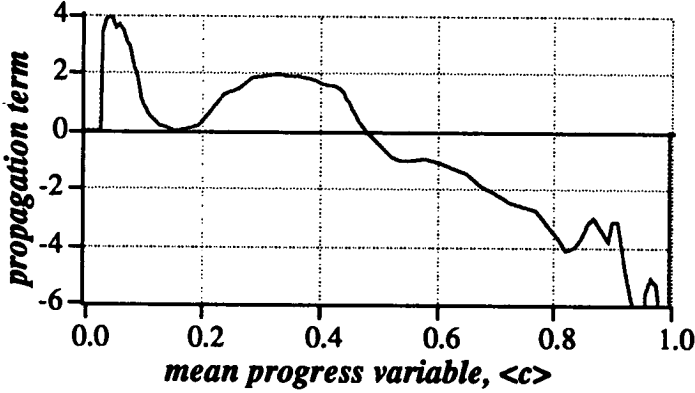


FIGURE 10. Variations of the mean propagation term, $2\langle wk_m \rangle_S$, through the turbulent flame brush. $Le = 0.8$, $t = 4 \tau$. wk_m is made non-dimensional by the characteristic flame time, δ_T/s_L .

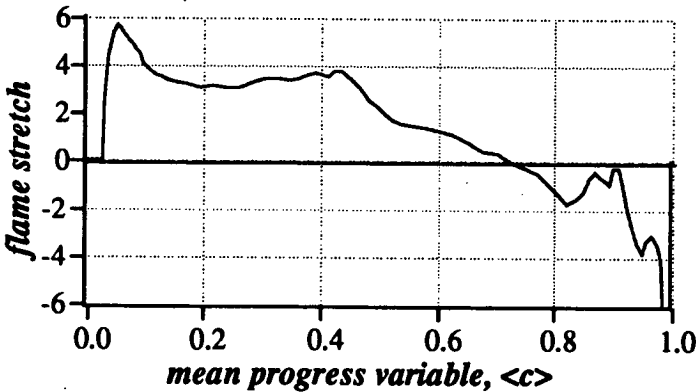


FIGURE 11. Variations of the mean flame stretch, $\langle k \rangle_S$, through the turbulent flame brush. $Le = 0.8$, $t = 4 \tau$. k is made non-dimensional by the characteristic flame time, δ_T/s_L .

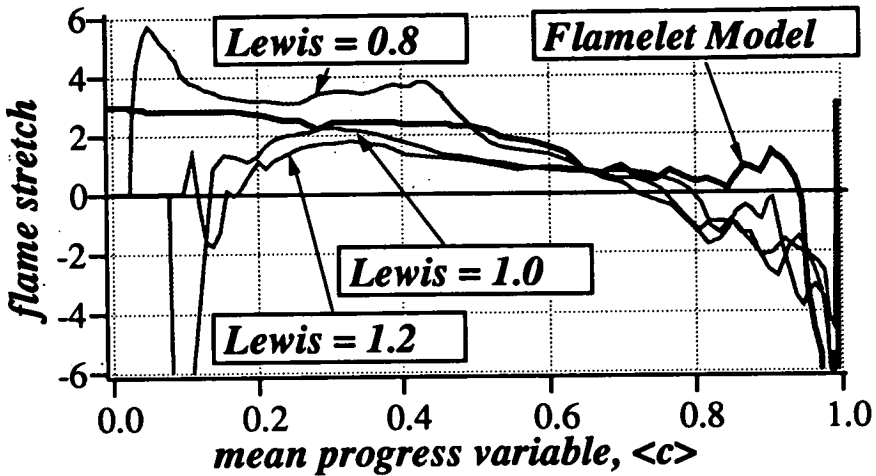


FIGURE 12. Lewis number effects on the variations of the mean flame stretch, $\langle k \rangle_S$, through the turbulent flame brush, and comparison with flamelet models. $t = 4 \tau$. k is made non-dimensional by the laminar flame time, δ_T/s_L .

Figure 11 presents the mean flame stretch profile through the turbulent reaction zone. At the leading edge, strain rate and flame propagation effects are locally cumulative and the overall balance is strongly positive. The leading edge of the turbulent flame is a region of strong production of flame surface area. On the contrary, the propagation term takes large negative values on the burnt side. In that region, strain rate and flame propagation effects are locally opposite, and the overall balance is negative. The rear edge of the turbulent flame thus appears as a region where flame surface area gets strongly dissipated.

Figure 11 spatially resolves the balance between production and dissipation of flame surface area. The net effect is given by defining a mean stretch, \bar{k} , space-averaged throughout the flame brush:

$$\bar{k} = \frac{d}{dt} \left(\frac{S_V(t)}{L_y L_z} \right) = \int \langle k \rangle_S \Sigma dx \quad (24)$$

\bar{k} gives the instantaneous rate of change of the flame surface area in the computational domain. If \bar{k} is positive, the flame surface grows; if negative, the flame surface contracts. The next section further discusses the effect of the Lewis number on the spatially-resolved flame stretch profile, as well as the resulting impact on the net mean flame stretch, \bar{k} , and presents some comparison with flamelet models.

3.3. Comparison of DNS results with flamelet models

Figure 12 compares the mean flame stretch profiles, $\langle k \rangle_S$, plotted for different Lewis numbers. In all cases, stretch takes large negative values on the burnt side, close to $\langle c \rangle = 1$. The effect of the Lewis number is not visible in that region. On the contrary, at the leading edge of the flame, there are large differences between

the different Lewis number cases. This suggests that the turbulent flame is most sensitive to Lewis number effects on the unburnt side, whereas it remains unaffected on the burnt side. Using Eq. (24), we can quantify the overall differences previously observed in Figure 4; we find (in units of the laminar flame time): $\bar{k} = 2.6$ for $Le = 0.8$, and the flame surface area is quickly growing; $\bar{k} \simeq 0.0$ for $Le = 1.0$ and $Le = 1.2$, and the flame surface area remains roughly constant.

Also plotted in Figure 12 is a comparison with flamelet models. Many current flamelet models use a transport equation for the flame surface density. Different formulations of this equation have been proposed in the literature (Marble & Broadwell 1977, Candel *et al.* 1990, Cant *et al.* 1990, Borghi 1990). For the sake of comparison, we use a closure assumption similar to the one proposed in the Coherent Flame Model by Marble & Broadwell (1977) and Candel *et al.* (1990). In this formulation, the turbulent flame stretch is written as:

$$k = \frac{\epsilon}{k_t} - s_L \frac{\Sigma}{\langle Y_R \rangle}, \quad (25)$$

where k_t is the turbulent kinetic energy and ϵ its dissipation; $\langle Y_R \rangle$ is the ensemble-averaged fuel mass fraction. The first term on the right-hand side of Eq.(25) represents straining due to the flow motions and is assumed to scale with the integral time scale of the turbulence; the second term is a disparition term associated with flame propagation and is assumed to scale with the laminar flame speed, s_L , and the flame surface density, Σ .

Figure 12 shows that this model is indeed able to reproduce qualitatively the spatial structure of the balance between production and dissipation of Σ , going from production at the leading edge of the turbulent flame to dissipation at the rear edge. However, the $1/\langle Y_R \rangle$ behavior of the disparition term leads to numerical difficulties on the burnt side of the flame. The model, therefore, overpredicts the dissipation of Σ , near $\langle c \rangle = 1$, and gives a negative mean flame stretch, $\bar{k} = -3.6$, in strong disagreement with the values reported above. In addition, the disparition term in Eq.(25) is always and everywhere negative and cannot account for the possible transition to unstable flame conditions as observed in the simulations.

4. Conclusion

Flamelet models constitute one of the most common approach for turbulent premixed combustion. In these models, the flame surface density is a central ingredient that conveys most of the effects of the turbulence on the rate of energy release. The flame surface density is usually obtained via a modeled transport equation, called the Σ -equation, first postulated by Marble & Broadwell (1977). Recent theoretical work, based on conservation equations for surfaces and volumes in a turbulent flow field, has produced a more rigorous approach that leads to an exact, but unclosed, formulation for the turbulent Σ -equation (Pope 1988, Candel & Poinso 1990). In this exact Σ -equation, it appears that the dynamical properties of the flame surface density are determined by a single parameter, namely the turbulent flame stretch. Unfortunately, the flame surface density and the turbulent flame stretch

are extremely difficult to measure and are simply not available from experiments. Therefore, little is known on the validity of the closure assumptions used in current formulations of flamelet models.

Direct Numerical Simulation (DNS) is the obvious, complementary approach to get basic information on these fundamental quantities. In the present work, three-dimensional DNS of premixed flames propagating in isotropic turbulent flow have been used to estimate the different terms appearing in the Σ -equation. A new methodology has been proposed to provide the source and sink terms for the flame surface density, estimated as a function of time and position within the turbulent flame brush. Using this methodology, the effects of the Lewis number on the rate of production of flame surface area are described in great detail. Principal findings are that: (1) the balance between production and dissipation of flame surface area is strongly non-homogeneous: the leading edge of the turbulent flame is a region of production of flame surface area, whereas the rear edge is a region where flame surface gets strongly dissipated; (2) the turbulent flame is most sensitive to Lewis number effects at the leading edge, whereas it remains unaffected on the burnt side. These results suggest that most of the important dynamical features of turbulent flames take place at the leading edge of the reaction zone.

Detailed comparisons with flamelet models were also performed. The analysis reveals the tendency of the models to overpredict flame surface dissipation as well as their inability to reproduce variations due to thermo-diffusive phenomena. Thanks to the detailed information produced by a DNS-based analysis, this type of comparison not only underscores the shortcomings of current models but also suggests ways to improve them. Future work will focus on the development of a new formulation of the Σ -equation that would incorporate thermo-diffusive mechanisms.

Acknowledgements

The authors acknowledge the fruitful interaction with other members of the combustion group during the 1992 CTR summer program. In particular, we thank Dr. Feng Gao for his many insights during the program. We also thank Prof. Stephen Pope and Prof. Forman Williams for their helpful comments and suggestions.

REFERENCES

- ABDEL-GAYED, R. G., BRADLEY, D., HAMID, M. N., & LAWES, M. 1984 Lewis number effects on turbulent burning velocity. *Twentieth Symp. (International) on Combust.* 505-512. The Combustion Institute.
- ASHURST, W. T., PETERS, N., & SMOOKE, M. D. 1987 Numerical simulation of turbulent flame structure with non-unity Lewis number. *Combust. Sci. Technol.* **53**, 339-375.
- BARRÈRE, M. 1974 Modèles de combustion turbulente. *Revue Générale de Thermique.* **148**, 295-308.
- BORGHİ, R. 1985 On the structure and morphology of turbulent premixed flames. *in Recent Advances in Aerospace Sciences.* Pergamon.

- BORGHI, R. 1990 Turbulent premixed combustion: further discussion on the scales of the fluctuations. *Combust. Flame*. **80**, 304-312.
- BRAY, K. N. C. 1980 Turbulent flows with premixed reactants. in *Topics in Applied Physics* **44**. Springer-Verlag.
- CANDEL, S. M., VEYNANTE, D., LACAS, F., MAISTRET, E., DARABIHA, N., & POINSOT, T. 1990 Coherent flame model: applications and recent extensions. in *Series on Advances in Mathematics for Applied Sciences*. World Scientific.
- CANDEL, S. M., & POINSOT, T. 1990 Flame stretch and the balance equation for the flame surface area. *Combust. Sci. Technol.* **70**, 1-15.
- CLAVIN, P., & GARCIA, P. 1983 The influence of temperature dependence of diffusivities on the dynamics of flame fronts. *J. Mécanique*. **2**, 245-263.
- CLAVIN, P. 1985 Dynamic behavior of premixed flame fronts in laminar and turbulent flows. *Prog. Energy Combust. Sci.* **11**, 1-59.
- CANT, R. S., POPE, S. B., & BRAY, K. N. C. 1990 Modelling of flamelet surface-to-volume ratio in turbulent premixed combustion. *Twenty-Third Symp. (International) on Combust.* 809-815. The Combustion Institute.
- GOIX, P. J., & SHEPERD, I. G. 1992 Lewis number effects on turbulent premixed flame structure. *Fall Meeting of the Western States Section*. The Combustion Institute.
- HAWORTH, D. C., & POINSOT, T. 1992 Numerical simulations of Lewis number effects in turbulent premixed flames. *J. Fluid Mech.* **244**, 405-436.
- LELE, S. K. 1990 Compact finite difference schemes with spectral-like resolution. *J. Comp. Phys.* (submitted for publication).
- MARBLE, F. E., & BROADWELL, J. E. 1977 The coherent flame model for turbulent chemical reactions. *Project Squid Technical Report*. TRW-9-PU.
- PETERS, N. 1986 Laminar flamelet concepts in turbulent combustion. *Twenty-First Symp. (International) on Combust.* 1231-1250. The Combustion Institute.
- POINSOT, T., VEYNANTE, D., & CANDEL, S. M. 1991 Quenching processes and premixed turbulent combustion diagrams. *J. Fluid Mech.* **228**, 561-605.
- POINSOT, T., ECHEKKI, T., & MUNGAL, M. G. 1992 A study of the laminar flame tip and implications for premixed turbulent combustion. *Combust. Sci. Technol.* **81**, 45-73.
- POINSOT, T., & LELE, S.K. 1992 Boundary conditions for direct simulations of compressible viscous flows. *J. Comp. Phys.* **101**, 104-129.
- POPE, S. B. 1988 Evolution of surfaces in turbulence. *International J. Engng. Sci.* **26**, 445-469.
- POPE, S. B. 1990 Computations of turbulent combustion: progress and challenges. *Twenty-Third Symp. (International) on Combust.* The Combustion Institute.

- RUTLAND, C. J., & TROUVÉ, A. 1991 Direct simulations of premixed turbulent flames with non-unity Lewis numbers. *Combust. Flame* (submitted for publication).
- WU, M. S., KWON, S., DRISCOLL, J. F., & FAETH, G. M. 1990 Turbulent premixed hydrogen/air flames at high reynolds numbers. *Combust. Sci. Technol.* **73**, 327-350.
- WILLIAMS, F. A. 1985 *Combustion theory*. 2nd ed., Benjamin Cummings.
- WRAY, A. A. 1990 Minimal storage time-advancement schemes for spectral methods. *J. Comp. Phys.* (submitted for publication).

Numerical simulations of turbulent premixed $H_2/O_2/N_2$ flames with complex chemistry

By M. Baum,¹ T. J. Poinsot,² AND D. C. Haworth³

Premixed stoichiometric $H_2/O_2/N_2$ flames propagating in two-dimensional turbulence have been studied using direct numerical simulation (simulations in which all fluid and thermochemical scales are fully resolved) including realistic chemical kinetics and molecular transport. Results are compared with earlier zero-chemistry (flame sheet) and one-step chemistry simulations. Consistent with the simpler models, the turbulent flame with realistic chemistry aligns preferentially with extensive strain rates in the tangent plane and flame curvature probability density functions are close to symmetric with near-zero means. By contrast to simple-chemistry results with non-unity Lewis numbers (ratio of thermal to species diffusivity), local flame structure does not correlate with curvature but rather with tangential strain rate. Turbulent straining results in substantial thinning of the flame relative to the steady unstrained laminar case. Heat release and H_2O_2 contours remain thin and connected ('flamelet-like') while species including H-atom and OH are more diffuse. Peak OH concentration occurs well behind the peak heat-release zone. This work suggests the feasibility of incorporating realistic chemistry into full turbulence simulations to address issues such as pollutant formation in hydrocarbon-air flames.

1. Introduction

Turbulent premixed combustion in practical devices is a complex phenomenon combining chemical kinetics, molecular transport, and hydrodynamic turbulence in difficult geometric configurations. Increasing regulative and competitive pressures demand improved physical understanding and predictive modeling capability for combustion phenomena including ignition, quenching, and pollutant formation. For example, many governments impose limits on emissions of oxides of nitrogen, carbon monoxide, and unburned hydrocarbons from gasoline-fueled spark-ignited automotive engines. Pending regulations in the United States seek further reductions in the allowable levels of these pollutants and provide for species differentiation in hydrocarbon emissions to account for the relative propensity of different components to promote ozone formation in the atmosphere. Many aspects of chemical kinetics (e.g. aromatic hydrocarbon chemistry, Westbrook 1991) are poorly understood even at a fundamental level and emissions models for engineering applications remain largely

1 Ecole Centrale, Paris

2 C.N.R.S., Institut de Mecanique des Fluides de Toulouse, France

3 General Motors Research & Environmental Staff, Warren, MI

empirical. Thus complex chemical kinetics in turbulent premixed combustion is a crucial topic for research and modeling.

Both experimental and numerical investigations of chemical kinetics influences in turbulent premixed combustion are complicated by the strong coupling of hydrodynamics with thermochemistry and by resolution requirements: hydrodynamic and thermochemical spatial and temporal scales span many orders of magnitude in premixed flames at high Reynolds and Damköhler numbers (the latter being the ratio of a characteristic flow time scale to chemical time scales). Thus direct numerical simulation (DNS) of practical turbulent premixed flames is impracticable at present and will remain so for the foreseeable future. (Here and in the following, 'DNS' is taken to mean simulations in which all scales of motion are fully resolved both spatially and temporally so that no turbulence modeling – explicit spatial or temporal filtering – is employed.) Idealized model problems are amenable to numerical analysis, and carefully designed numerical simulations are well suited to isolating specific phenomena and extracting fundamental physical understanding. However, one must remain wary in extrapolating results from idealized model problems to practical combustion systems.

Numerical combustion studies have tended to proceed along one of two parallel paths. Either detailed chemical kinetics models have been implemented in simple flow configurations (one-dimensional laminar, e.g. Warnatz 1981, Drake & Blint 1988; axisymmetric laminar, e.g. Smooke *et al.* 1990), or turbulence simulations have been performed with embedded simple-chemistry models (zero-chemistry or flame sheet, e.g. Kerstein *et al.* 1988, Girimaji & Pope 1992; zero-heat-release one-step Arrhenius, e.g. Rutland *et al.* 1990; one-step Arrhenius with heat release, e.g. Haworth & Poinsot 1992). The detailed chemistry scheme for methane-air oxidation employed by Xu & Smooke (1991) includes 26 species and 45 reactions. Solving the resulting stiff system of convection/diffusion/reaction equations for a laminar axisymmetric Bunsen burner flame requires on the order of 100 CPU hours using state-of-the-art numerical algorithms on a high-end workstation (~ 26 Mflops). This is the same order of computational resources as that required for DNS of *nonreacting* homogeneous isotropic turbulence at a Taylor-scale Reynolds number of $Re_\lambda \approx 90$ (Pope 1991).

The present research represents an attempt to bridge the two numerical approaches by coupling complex chemistry and full turbulence simulations. Here H_2-O_2 chemistry (inert N_2 diluent) has been modeled using a nine-species, 19-reactant scheme (Miller *et al.* 1982) including detailed molecular transport in two-dimensional isotropic turbulence. Specific goals are threefold. First, we wish to explore the feasibility of complex-chemistry DNS for future application to more complex thermochemical systems (e.g. hydrocarbon fuels). Ignition, quenching, and pollutant formation issues are of practical interest in such systems. Second, we will compare results obtained using the present detailed-chemistry scheme to those obtained earlier using simpler zero- and one-step chemistry models. In particular we are interested in statistics of strain rate, curvature, and local burning rate along the flame front and the robustness of flamelet models with realistic kinetics. Finally,

we will compare the local structure of the turbulent premixed flame with detailed kinetics to that of an unstrained laminar flame having the same thermochemical properties. Questions of interest include possible shifts in radicals relative to laminar profiles and which radical species might best be suited to marking the region of peak heat release in experiments.

2. Background: DNS of turbulent premixed combustion

DNS has proved to be a valuable tool in addressing fundamental physical questions and in the construction of models for turbulent premixed combustion. The past several years have seen DNS applied to a hierarchy of premixed systems of increasing complexity. Results of these simulations generally have been interpreted in the framework of the flamelet regime of combustion wherein a thin laminar-like reaction zone separates unburnt gas from hot burnt products. (In propagating-interface type models, this structure is imposed.) Roughly speaking, flamelet combustion corresponds to conditions where the largest chemical scales are small compared with the smallest hydrodynamic scales: however, it has proven to be a worthwhile framework in which to interpret results even in cases where turbulence microscales are smaller than the flame thickness (Haworth & Poinso 1992). Moreover, flamelet models are widely used as combustion 'submodels' in Reynolds-averaged computations of premixed turbulent combustion in engineering applications (e.g. El Tahry 1990, Boudier *et al.* 1992).

2.1. Propagating-interface (zero-chemistry) models

Analytic studies of the kinematics of a propagating surface in turbulent flow have resulted in relationships that provide a basis for flamelet models and for interpreting numerical simulation results. For example, the roles of hydrodynamic straining and flame curvature in modifying the area A of a propagating surface element are expressed in the relationship (Pope 1988, Candel & Poinso 1990),

$$\frac{1}{A} \frac{dA}{dt} = a_t + \frac{s_d}{\mathcal{R}} \quad (1)$$

Here a_t is the hydrodynamic strain rate in the plane tangent to the surface, s_d is the speed of advance of the propagating surface relative to the fresh gas, and \mathcal{R} is the radius of curvature ($\mathcal{R} < 0$ for surface elements propagating towards the center of curvature, e.g. concave towards reactants for the premixed flame). This relationship motivates attempts to isolate strain-rate from curvature effects in turbulent premixed combustion, even though the two are not completely independent (Pope 1988, Haworth & Poinso 1992).

Numerical simulations (DNS) incorporating propagating surface models have proceeded via a variety of front-tracking algorithms (reviewed in Oran & Boris 1987), field-equation approaches (Kerstein *et al.* 1988, Ashurst *et al.* 1988), and statistical ensembles of infinitesimal surface elements (Girimaji & Pope 1992). These zero-chemistry flame-sheet models have contributed significantly to our understanding of flame topology and have provided quantitative information on statistical correlations that is useful in the construction and calibration of models of turbulent

premixed combustion in the flamelet regime (e.g. Bray & Cant 1991). The influence of chemical kinetics effects in such models generally is felt only through the propagation speed, whose dependence on thermochemical and/or turbulence parameters must be prescribed.

2.2. Simple-chemistry models

Studies of the dynamic interactions between fluid flow and finite-rate chemistry in flamelet or non-flamelet regimes require that the flame structure be resolved. However, the addition of chemical length and time scales that are of the order of or smaller than the smallest turbulence scales implies that, for a given spatial and temporal resolution, a smaller range of hydrodynamic scales can be simulated compared to computations in which the flame has no internal structure. Two-dimensional vortex methods have been used to study interactions between turbulent fluid flow and finite-rate chemistry by a number of authors including Ashurst & Barr (1983), Ghoniem & Krishnan (1988), and Ashurst *et al.* (1987). Three-dimensional simulations including finite-rate chemistry (constant density, zero heat release, single-step Arrhenius chemistry) have been reported by Rutland *et al.* (1990): results included distributions of local burning rate over a range of Damköhler numbers. Further three-dimensional constant-density simulations been published by El Tahry *et al.* (1991) Rutland & Trouvé (1990) (a study of Lewis number effects) and by Cant *et al.* (1990) (a study of statistics relevant to the Bray-Moss-Libby model of turbulent premixed combustion).

The present work follows a number of two-dimensional simulations with variable fluid properties and heat release (Poinsot 1991; Poinsot *et al.* 1990, 1991, 1992; Meneveau & Poinsot 1990, Haworth & Poinsot 1992, Poinsot & Haworth 1992). Contributions of these studies include a characterization of the scales of turbulent motion that influence flame structure (Poinsot *et al.* 1990, 1991), investigations of flame quenching (Poinsot *et al.* 1991, Meneveau & Poinsot 1990), identification of Lewis number effects (Haworth & Poinsot 1992), a study of ignition and early flame-kernel growth (Poinsot 1991), and a model for flame-wall interactions (Poinsot & Haworth 1992). Compared to three-dimensional constant-property simulations, two-dimensional variable-density simulations allow a wider dynamic range of scales and full two-way fluid-chemistry coupling. Values of relevant dimensionless parameters in the present study are given in Section 3.

However, the dynamics of two-dimensional turbulence are not identical to those of three-dimensional turbulence (Batchelor 1953, Herring *et al.* 1974, Lesieur 1987). In particular, the vortex-stretching mechanism for the cascade of energy to progressively smaller scales of motion is absent in two dimensions and the smallest scales of motion do not follow the usual Kolmogorov scaling. Thus the statistics of small-scale quantities especially are expected to differ between two-dimensional and three-dimensional simulations. Partial justification for the appropriateness of two-dimensional studies of premixed flame structure can be found in three-dimensional results: the topology of a propagating surface in three-dimensional turbulence has been found to be primarily two-dimensional, particularly those surface elements having the highest curvatures (Ashurst 1990, Cant *et al.* 1990, Girimaji & Pope

1992). That is, a flame tends to be locally cylindrical rather than spherical in shape. Further *a posteriori* justification can be found in the two-dimensional results themselves, where many features in common with the three-dimensional findings have been noted (Haworth & Poinso 1992). Common results include: preferential alignment of the flame with extensive strain rates in the tangent plane; scaling of flame-area-averaged mean tangential strain rate with turbulence micro-timescales; and nearly symmetric pdf's of flame curvature having near-zero mean.

The present work follows most immediately the study of nonunity Lewis number effects ($Le =$ ratio of thermal to species diffusivity) in two-dimensional turbulent premixed combustion reported by Haworth & Poinso (1992). In addition to the results already discussed, it was found that for $Le = 1$, the local burning velocity of the turbulent flame is everywhere nearly identical to that of an undisturbed laminar flame; for nonunity Lewis numbers, the local burning velocity differs from that of the laminar flame and correlates strongly with the local flame curvature; curvature effects cancel out in the mean to leave the mean extensive tangential strain rate as the principal influence on the mean burning velocity of the turbulent flame; and thermodiffusive effects result in more flame area for $Le < 1$ than for $Le > 1$. It was further argued that these molecular transport effects should remain important at higher Reynolds numbers and for complex chemistry, provided that a single global deficient-reactant-based Lewis number can be defined. Here the simulations are extended from one-step chemistry with simple transport to realistic chemistry and transport, permitting a direct assessment of the second claim. We continue to adopt a flamelet viewpoint for diagnostics and analysis.

3. Problem definition

3.1. Governing equations and numerical methods

The set of equations solved is the compressible multi-species reacting flow equations comprising conservation of mass, linear momentum, energy, and N_s species mass fractions. In Cartesian tensor notation (no sum on Greek indices),

$$\frac{\partial \rho}{\partial t} + \frac{\partial \rho u_j}{\partial x_j} = 0, \quad (2)$$

$$\frac{\partial \rho u_i}{\partial t} + \frac{\partial \rho u_i u_j}{\partial x_j} = -\frac{\partial p}{\partial x_i} + \frac{\partial \tau_{ij}}{\partial x_j}, \quad (3)$$

$$\frac{\partial \rho e_t}{\partial t} + \frac{\partial (\rho e_t + p) u_j}{\partial x_j} = \frac{\partial (u_j \tau_{ij})}{\partial x_i} - \frac{\partial q_j}{\partial x_j}, \quad (4)$$

$$\frac{\partial \rho Y_\alpha}{\partial t} + \frac{\partial \rho Y_\alpha u_j}{\partial x_j} = -\frac{\partial \rho Y_\alpha V_{\alpha j}}{\partial x_j} + W_\alpha \dot{\omega}_\alpha. \quad (5)$$

Here u_i is the i^{th} component of the fluid velocity, e_t is the total energy density per unit mass, and Y_α , $\alpha = 1, \dots, N_s$, is the mass fraction of species α . The fluid mass density is ρ , p is the thermodynamic pressure, and τ_{ij} and q_j are, respectively, the

viscous stress tensor and the heat flux vector. The molar chemical production rate of species α is $\dot{\omega}_\alpha$ while W_α is its molecular weight. The variable $V_{\alpha j}$ is the diffusion velocity for species α .

The set of governing equations is closed with the ideal gas equation of state and constitutive relations,

$$p = \rho RT, \quad (6)$$

$$\tau_{ij} = \bar{\mu} \left(\frac{\partial u_i}{\partial x_j} + \frac{\partial u_j}{\partial x_i} - \frac{2}{3} \delta_{ij} \frac{\partial u_k}{\partial x_k} \right), \quad (7)$$

$$e_t = \frac{1}{2} u_k u_k + e, \quad (8)$$

$$e = \sum_{\alpha=1}^{N_s} h_\alpha Y_\alpha - \frac{p}{\rho}, \quad (9)$$

$$h_\alpha(T_1) = \Delta h_{f\alpha}^0 + \int_{T_0}^{T_1} C_{p\alpha}(T) dT, \quad (10)$$

$$q_j = -\bar{\lambda} \frac{\partial T}{\partial x_j} + \rho \sum_{\alpha=1}^{N_s} h_\alpha Y_\alpha V_{\alpha j}. \quad (11)$$

In these equations, $\bar{\mu}$ and $\bar{\lambda}$ are, respectively, the mean viscosity and thermal conductivity. The formation enthalpy of species α at the reference temperature T_0 is $\Delta h_{f\alpha}^0$, and h_α is the enthalpy of species α . (Here the reference state is $T_0 = 298.15$ K.)

Species molecular transport is modeled using Fick's law. An effective species diffusivity D_α is computed as follows:

$$D_\alpha = \frac{(1 - Y_\alpha)}{\sum_{\beta=1, \beta \neq \alpha}^{N_s} X_\beta / D_{\alpha\beta}}, \quad (12)$$

where $D_{\alpha\beta}$ are the binary diffusion coefficients and X_α is the mole fraction of species α . Diffusion coefficients are related to the diffusion velocity $V_{\alpha j}$ by,

$$V_{\alpha j} = -\frac{D_\alpha}{X_\alpha} X_{\alpha,j}. \quad (13)$$

The diffusion velocities resulting from Eqs. (12) and (13) do not, in general, satisfy conservation of mass. A correction velocity $V_{c j}$ is added such that the net diffusive flux is equal to zero,

$$\sum_{\alpha=1}^{N_s} Y_\alpha V_{\alpha j} = 0. \quad (14)$$

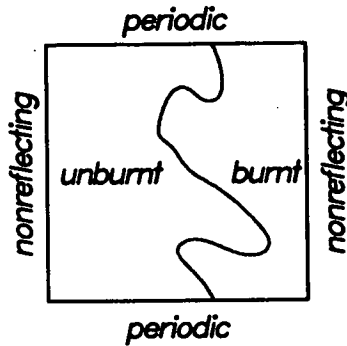


FIGURE 1. Schematic of computational domain: a premixed flame separates unburnt reactants from burnt products.

Finally, we have,

$$V_{\alpha j} = v_{\alpha j} + v_{c j} = -\frac{D_{\alpha}}{X_{\alpha}} X_{\alpha, j} + \frac{\sum_{\beta=1}^{N_s} Y_{\beta} (D_{\beta}/X_{\beta}) X_{\beta, j}}{\sum_{\beta=1}^{N_s} Y_{\beta}} \quad (15)$$

Species production rates are given by the Arrhenius law with (forward) rate constants $k_{f\alpha}$ of the form,

$$k_{f\alpha} = A_{\alpha} T^{\beta_{\alpha}} \exp(-E_{0\alpha}/R_0 T), \quad (16)$$

where R_0 is the universal gas constant. Hydrogen-oxygen kinetics has been modeled using the nine-species, 19-reaction scheme devised by Miller *et al.* (1982). Coefficients for this scheme are summarized in Table I. Fluid properties, molecular transport coefficients, and reaction source terms are computed using CHEMKIN and TRANSPORT (Kee *et al.* 1980, Kee *et al.* 1983).

Using these assumptions and a Cartesian frame of reference, the conservation equations are solved using a high-order finite-difference scheme (Lele 1992). The calculations are initialized with reactants on one side of the computational domain and products on the other; these are separated by a laminar premixed flame (Figure 1). The initial laminar profiles are themselves steady one-dimensional solutions to Eqs. (2)–(16). On lateral boundaries, periodic conditions are enforced while non-reflecting boundary conditions are used on inflow/outflow boundaries (Poinsot & Lele 1992). Isotropic two-dimensional turbulence is prescribed with a turbulence spectrum that is the same as that used in earlier studies (e.g. Haworth & Poinsot 1992). Two parameters suffice to define the initial energy spectrum: the rms turbulence velocity $u_p = u'(t=0)$ and the peak energy wavelength L_i . These and other relevant parameters are summarized in Table II.

Table I. Reaction mechanism rate coefficients in the form $k_f = AT^\beta \exp(-E_0/R_0T)$ (Eq. 16) (Miller *et al.* 1982). Units are moles, cubic centimeters, seconds, degrees K, and calories/mole. Species: H₂ O₂ OH O H H₂O HO₂ H₂O₂ N₂.

#	Reaction	A	β	E_0
R ₁	H ₂ + O ₂ \rightleftharpoons 2 OH	1.7×10^{13}	0.	47780
R ₂	H ₂ + OH \rightleftharpoons H ₂ O + H	1.17×10^9	1.3	3626
R ₃	H + O ₂ \rightleftharpoons OH + O	5.13×10^{16}	-0.816	16507
R ₄	O + H ₂ \rightleftharpoons OH + H	1.8×10^{10}	1.0	8826
R ₅	H + O ₂ + M \rightleftharpoons HO ₂ + M ^a	2.1×10^{18}	-1.0	0
R ₆	H + 2 O ₂ \rightleftharpoons HO ₂ + O ₂	6.7×10^{19}	-1.42	0
R ₇	H + O ₂ + N ₂ \rightleftharpoons HO ₂ + N ₂	6.7×10^{19}	-1.42	0
R ₈	OH + HO ₂ \rightleftharpoons H ₂ O + O ₂	5×10^{13}	0.	1000
R ₉	H + HO ₂ \rightleftharpoons 2 OH	2.5×10^{14}	0.	1900
R ₁₀	O + HO ₂ \rightleftharpoons O ₂ + OH	4.8×10^{13}	0.	1000
R ₁₁	2 OH \rightleftharpoons O + H ₂ O	6×10^8	1.3	0
R ₁₂	H ₂ + M \rightleftharpoons H + H + M ^b	2.23×10^{12}	0.5	92600
R ₁₃	O ₂ + M \rightleftharpoons O + O + M	1.85×10^{11}	0.5	95560
R ₁₄	H + OH + M \rightleftharpoons H ₂ O + M ^c	7.5×10^{23}	-2.6	0
R ₁₅	HO ₂ + H \rightleftharpoons H ₂ + O ₂	2.5×10^{13}	0.	700
R ₁₆	2 HO ₂ \rightleftharpoons H ₂ O ₂ + O ₂	2×10^{12}	0.	0
R ₁₇	H ₂ O ₂ + M \rightleftharpoons OH + OH + M	1.3×10^{17}	0.	45500
R ₁₈	H ₂ O ₂ + H \rightleftharpoons H ₂ + HO ₂	1.6×10^{12}	0.	3800
R ₁₉	H ₂ O ₂ + OH \rightleftharpoons H ₂ O + HO ₂	1.0×10^{13}	0.	1800

^a Third-body efficiencies: $k(\text{H}_2) = 3.3k(\text{Ar})$, $k(\text{H}_2\text{O}) = 21.0k(\text{Ar})$.

^b Third-body efficiencies: $k(\text{H}_2) = 3.0k(\text{Ar})$, $k(\text{H}) = 2.0k(\text{Ar})$, $k(\text{H}_2\text{O}) = 6.0k(\text{Ar})$.

^c Third-body efficiencies: $k(\text{H}_2\text{O}) = 20.0k(\text{Ar})$.

In Table II, a subscript 'u' refers to properties in the unburnt reactants. Key parameters are: the rms turbulence intensity u' , the turbulence integral length scale l based on two-point velocity correlations and timescale $\tau = l/u'$, and flame or chemical scales s_l^0 (the unstrained laminar flame speed), $\delta_l \equiv (T_b - T_u)/(dT/dx|_{max})$ (the laminar flame thickness), and $\tau_f = \delta_l/s_l^0$. The fuel mass equivalence ratio is Φ . There are $n_x \times n_y$ computational grid points in the $L_{box} \times L_{box}$ square computational domain.

The turbulence Reynolds numbers and ratio of rms turbulence intensity to laminar flame speed of Table II imply a regime of combustion where turbulence is intense compared to the laminar flame speed, and flames are thinner than the turbulence integral scale but are thicker than turbulence microscales. Turbulence and flame timescales are of the same order.

Table II. Initial parameters for two-dimensional simulations.

Case	Φ	T_u	p	s_l^0	δ_l	Re_{L_i} $= \frac{u_p L_i}{\nu}$	Re_l $= \frac{u' l}{\nu}$	u'/s_l^0	L_i/δ_l	l/δ_l	τ/τ_f	L_{box}	n_x $= n_y$
	[-]	[K]	[kPa]	[m/s]	[cm]	[-]	[-]	[-]	[-]	[-]	[-]	[cm]	[-]
1	1.0	800	101	19.5	0.044	2000	650	2.1	6.3	2.0	0.48	2.00	487
2	1.0	800	101	19.5	0.044	4000	1300	4.2	12.7	4.0	0.95	1.24	301

3.2. Diagnostics

Postprocessing of the two-dimensional computed fields (snapshots at fixed times) begins by defining a flame front as an isocontour of reactant mass fraction or temperature. Here we have used $Y_{O_2} = 0.22$, corresponding to the position of peak heat release in the laminar flame (Figure 2). Once the flame front has been located, the local normal and local curvature are readily computed. Curvatures concave towards the hot products are taken to be positive. One-dimensional cuts normal to the flame are taken: it is these profiles that define the local 'structure' of the turbulent flame. We compare the local turbulent flame profiles with the steady unstrained one-dimensional laminar flame profile for the same chemistry and fluid properties. Of particular interest is the distribution along the flame of the normalized local flame speed ('flamelet speed') s_n defined as the integral of the heat-release profile in a direction locally normal to the flame. The local heat-release rate \dot{w}_Q is defined by,

$$\dot{w}_Q = \sum_{\alpha=1}^{N_s} \dot{w}_\alpha \Delta h_{f\alpha}^0, \quad (17)$$

and the normalized flamelet speed is then,

$$s_n = \int \dot{w}_Q dn / s_{n0}. \quad (18)$$

A normalized flame length \mathcal{L}^* and turbulent flame speed s_T^* are defined as,

$$\mathcal{L}^* \equiv L_{flame}/L_{flame0}, \quad (19)$$

$$s_T^* \equiv \overline{\dot{w}_Q} / \overline{\dot{w}_{Q0}} = \langle s_n \rangle \mathcal{L}^*. \quad (20)$$

In Eqs. (18)–(20), the subscript '0' denotes the value for the unstrained planar laminar flame; overbars denote volume (area) averages while angled brackets are reserved for flame-area-weighted means (length-weighted in two spatial dimensions). A check of self-consistency is to verify the equality between s_T^* calculated in the two ways given in Eq. (20): they are found to agree to within a few percent in all cases.

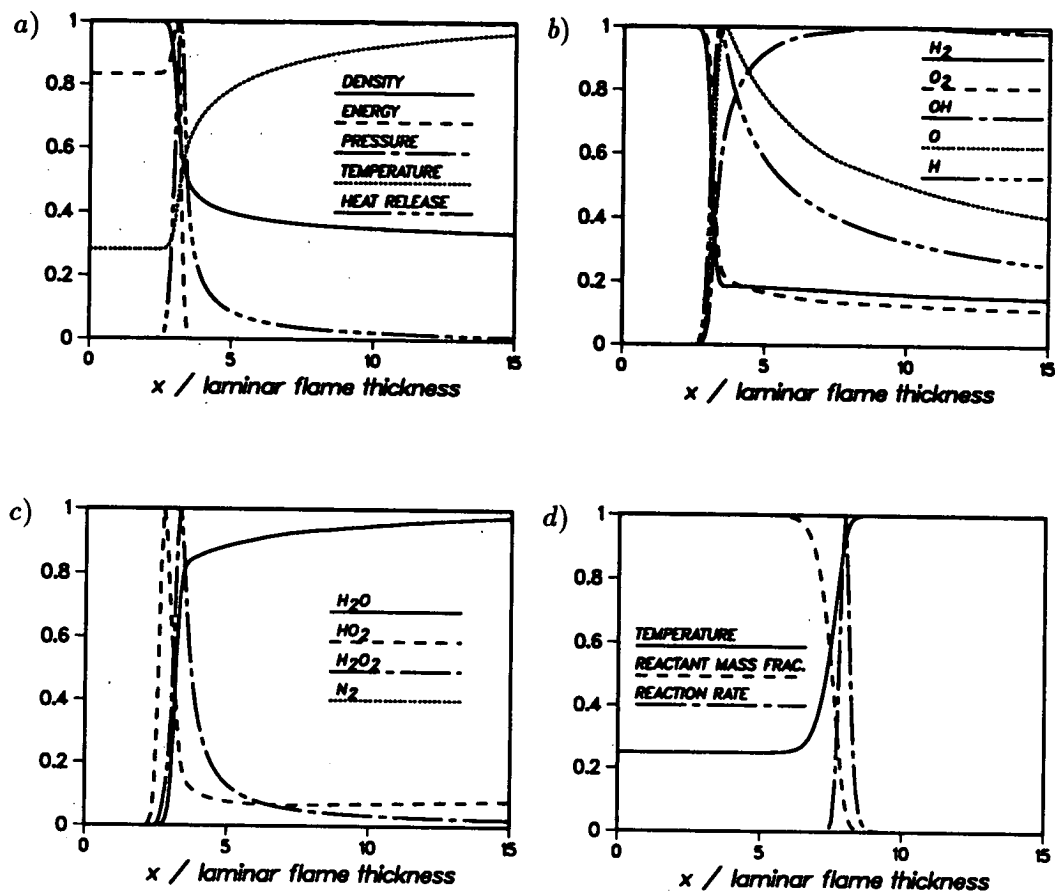


FIGURE 2. Normalized (by their maximum value) steady unstrained laminar flame profiles: a)–c) complex chemistry (Tables I and II); d) one-step chemistry $\dot{\omega} = \Lambda \rho Y \exp\left(\frac{-\beta(1-\Theta)}{1-\alpha(1-\Theta)}\right)$, $\Theta = (T - T_u)/(T_b - T_u)$, $\alpha = 0.75$, $\beta = 8.0$, $\Lambda = 146$ (Haworth & Poinso 1992).

4. Results

4.1. Laminar profiles

Profiles of the steady one-dimensional laminar solution are displayed in Figure 2a–c, where each quantity has been normalized by its maximum value. Corresponding profiles for the one-step Arrhenius scheme used in Haworth & Poinso (1992) are shown in Figure 2d. The abscissa is in units of the laminar flame thickness δ_l , which is of the order of the heat-release zone thickness. A striking difference between the simple- and complex-chemistry temperature and species profiles is the extended tails into the burnt gas for the complex chemistry case. One might anticipate difficulty in maintaining this structure in turbulent flames: even in cases where all turbulence scales are larger than δ_l , turbulence may still be able to modify the laminar flame structure on the burnt side. Other noteworthy features of these profiles include the significant ‘leakage’ of fuel and oxidizer into the products, high

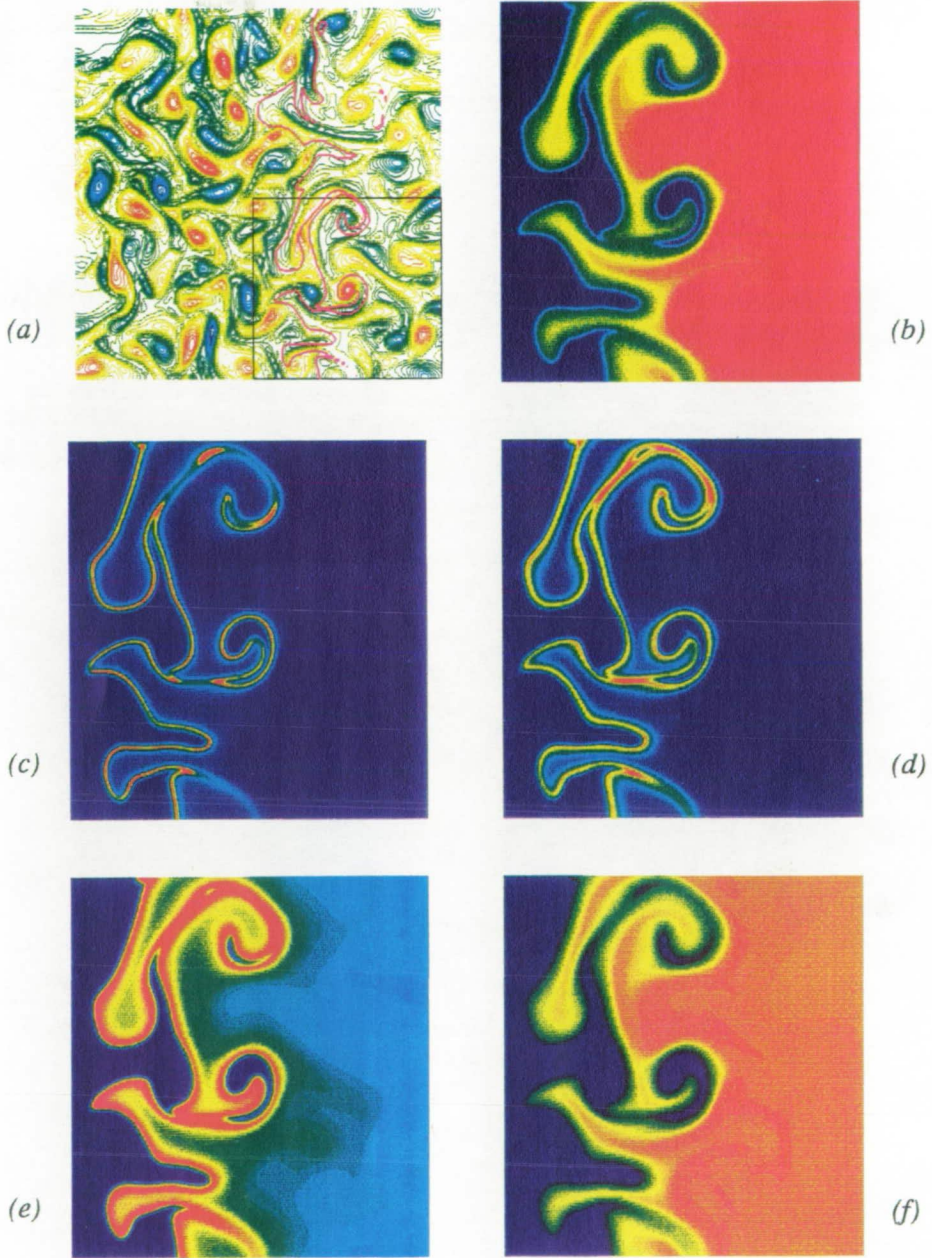


FIGURE 3. Computed fields at one instant of time, Case 1, time $t/\tau_f = 1.24$: a) vorticity contours with flame isocontour in magenta; b) temperature; c) heat release; d) H_2O_2 mass fraction; e) H mass fraction; f) OH mass fraction. Contour color scale ranges from blue (min) to red (max). In a), the full computational box is shown while b)–f) depict only the subdomain indicated by the black outline in a).

OH concentrations in the burnt gas, and locations of peak radical concentrations relative to peak heat release. The high product temperature (2840 K) is responsible for the high equilibrium H_2 , O_2 , and OH concentrations on the burnt side. Peak OH concentration occurs well behind the peak heat-release zone, while H- and O-atom, H_2 , O_2 , and HO_2 peak closer to the location of peak heat release.

4.2. Turbulent flame contours

Examples of computed fields at one instant of time for Case 1 at $t/\tau_f = 1.24$ are given in Figure 3 (unburnt gases are on the left, burnt products are on the right). The initially planar flame has been severely distorted by the turbulence by this time, even to the extent of tearing off pockets of fresh gas which are carried into the product side. Eventually these pockets of fresh gas are consumed for these adiabatic flames. Nevertheless, the structure of the underlying laminar flame remains readily recognizable. Heat release contours (Fig 3c) suggest a thin flamelet-like structure albeit with some islands of fresh gas burning enveloped by the hot products. Some radicals including H_2O_2 (Figure 3d) show similar behavior to the heat release: profiles remain thin and appear to mark the region of maximum heat release. On the other hand, H-atom levels (Figure 3e), while peaking close to the maximum heat-release zone, show a long diffuse tail on the burnt side, presumably a consequence of the high H diffusivity. Gradients in OH mass fraction are steep through the region of maximum heat release (Figure 3f) but peak OH occurs well behind the flame front and isocontours of high OH concentration do not remain connected on the burnt side. Most of these features might be anticipated from Figure 2a-c. Thus in the present case, OH does not serve as a good marker of the region of maximum heat release in the flame.

An example of the influence of turbulence parameters on flame structure is given in Figure 4. There the isocontour used to define the flame at one instant of time is plotted for Cases 1 and 2 at equal flame times $t/\tau_f = 0.36$ and at equal turbulence times $t/\tau_0 \approx 0.8$ ($\tau_0 = \tau(t=0)$). The smaller integral scale of Case 1 yields a more highly wrinkled flame that, as illustrated in Figure 3, even shows pockets in the burnt gas at later times. Case 2, by contrast, yields a flame with large-scale folding versus fine-scale wrinkling.

4.3. Statistics of flame curvature, strain rate, and flamelet speed

Statistics of tangential strain rate, flame curvature, and local flamelet speed are presented in Figs. 5-9. Probability density functions (pdf's) of flame tangential strain rate and flame curvature are given in Figs. 5 and 6, respectively. Figure 5 confirms the findings of several earlier studies using zero- and single-step chemistry models: the turbulent flame aligns preferentially with extensive strain rates in the tangent plane (Ashurst 1990, Girimaji & Pope 1992, El Tahry *et al.* 1991, Cant *et al.* 1990, Rutland *et al.* 1990). Figure 6 also is reminiscent of results found using simpler models (Haworth & Poinso 1992) and experiments (Lee *et al.* 1991): curvature pdf's are close to symmetric with near-zero mean curvature. While some skewing of the pdf's towards negative curvatures might be expected at low u'/s_f^0 (Rutland & Trouvé 1990, Becker *et al.* 1990), no such skewing is evident here. The

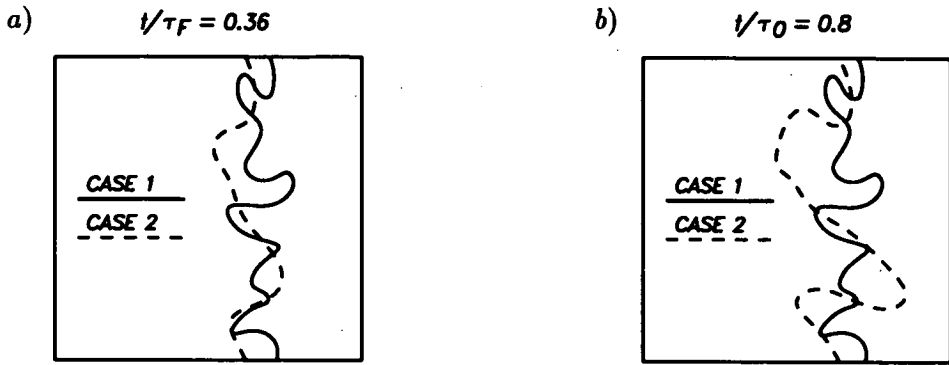


FIGURE 4. Isocontours $Y_{O_2} = 0.22$ for Cases 1 and 2 in a $1.24 \text{ cm} \times 1.24 \text{ cm}$ region: a) $t/\tau_f = 0.36$; b) $t/\tau_0 \approx 0.8$.

more highly wrinkled nature of the Case 1 flame is manifested in the broader tails (higher rms) of the curvature pdf for Case 1 versus Case 2.

Scatter plots of local flamelet speed s_n versus local tangential strain rate and local flame curvature are given in Figs. 7 and 8, respectively. Each point in these two figures corresponds to a point sampled uniformly along the isocontour defining the turbulent flame. While no correlation of local burning velocity with curvature is evident, the decrease in s_n with increasing tangential strain rate is surprisingly strong. In fact, this correlation develops over time in the computations: at time $t = 0$, the normalized flamelet speed s_n is everywhere equal to unity. The flame-area-averaged normalized mean flamelet speed $\langle s_n \rangle$ decreases with time (Figure 9). Figure 9b, for example, portrays the evolution from the initial delta function pdf of flamelet speed at time $t = 0$ for Case 2: both the mean value $\langle s_n \rangle$ and the value of s_n at which the pdf peaks decrease with time as the flame develops (Table III).

No statistically steady state is achieved in the duration of the present computations. While the mean consumption rate per unit area of flame $\langle s_n \rangle$ (Eq. 18) is significantly smaller than unity, the increase in flame area \mathcal{L}^* (Eq. 19) more than compensates to yield normalized turbulent flame speeds s_T^* (Eq. 20) that are greater than unity, as expected. The evolution of these global quantities with time is summarized in Table III.

Peak heat-release rates (not shown) remain within $\pm 5\%$ of the laminar value in all cases, suggesting that this reduction of local consumption rate $\langle s_n \rangle$ is primarily a flame thickness effect. These results are unexpected in view of the findings in Haworth & Poinso (1992) for simple chemistry. There it was found that, for nonunity Lewis numbers, curvature dominated the local flame structure, and a correlation between local burning velocity and local tangential strain rate was evident only for $Le = 1$. In no case was the straining sufficiently high to yield the extremely low values of $\langle s_n \rangle$ found here. While the fuel-based (H_2) Lewis number in the present case is clearly less than unity, no single global deficient-reactant-based Lewis number can be unambiguously defined for $\Phi = 1$ (Chelliah & Williams 1987). Arguments by

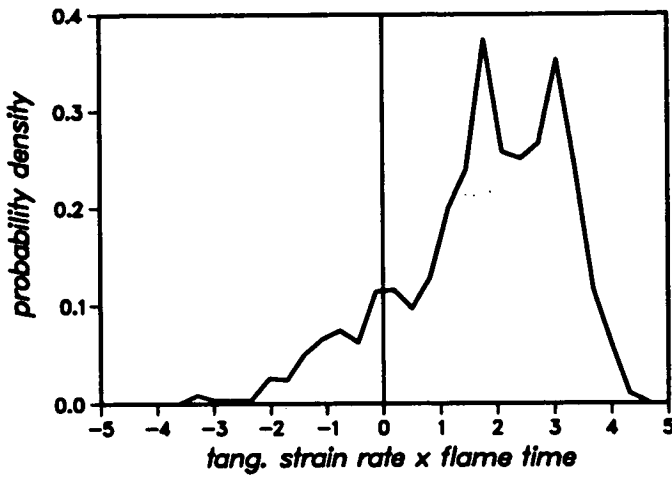


FIGURE 5. Pdf of normalized tangential strain rate, Case 1, $t/\tau_f = 0.36$: mean=1.816, rms=1.394.

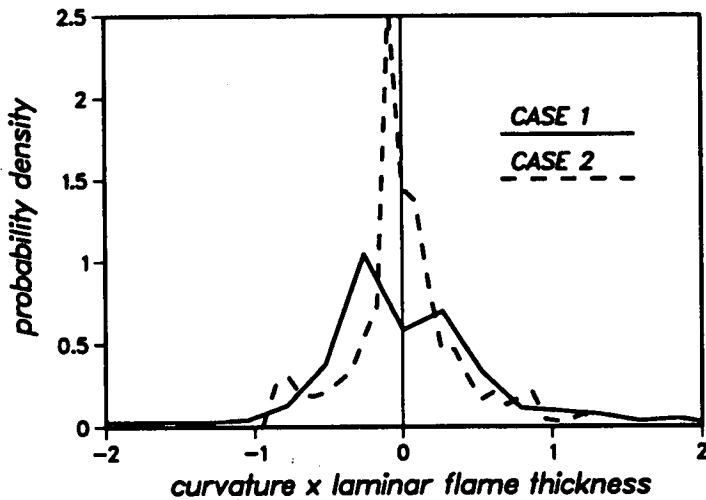


FIGURE 6. Pdf's of normalized flame curvature, $t/\tau_0 \approx 0.8$. Case 1: mean=0.0056, rms=0.82; Case 2: mean=0.0043, rms=0.35.

Joulin & Mitani (1981) suggest an equivalent Lewis number of somewhat less than unity for the present thermochemistry: however, the decreasing flamelet speed with increasing tangential strain rate of Figure 7 suggests that, if anything, the effective Lewis number may be greater than or equal to unity here.

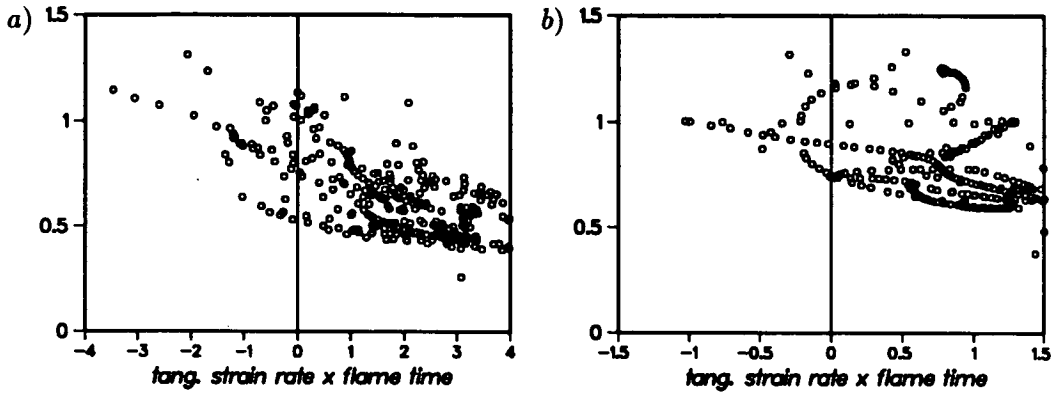


FIGURE 7. Scatter plots of normalized flamelet speed s_n (Eq. 18) versus normalized tangential strain rate at $t/\tau_0 \approx 0.8$: a) Case 1; b) Case 2.

Table III. Evolution with time of normalized flamelet speed $\langle s_n \rangle$ (Eq. 18), normalized flame area \mathcal{L}^* (Eq. 18), and normalized turbulent flame speed s_T^* (Eq. 20) for Case 2.

t/τ_0	$\langle s_n \rangle$	\mathcal{L}^*	s_T^*
0.0	1.00	1.00	1.00
0.23	0.96	1.10	1.06
0.36	0.91	1.24	1.13
0.80	0.75	1.86	1.40

4.4. Local flame structure

Profiles of heat-release rate and OH mass fraction along the local flame normal are overlaid on the corresponding laminar profiles in Figure 10 for Case 2 at two instants of time. The turbulent profiles have been uniformly sampled along the turbulent flame front; only nine or ten turbulent profiles are shown, for clarity. At the earlier time ($t/\tau_0 = 0.23$), local turbulent profiles collapse neatly onto the steady unstrained laminar contours. At later times ($t/\tau_0 = 0.80$), the collapse remains reasonable on the fresh-gas side while the turbulent profiles generally are shifted inwards towards the peak heat-release zone on the burnt-gas side. This appears to be a consequence of the net extensive tangential strain rates thinning the flame in the turbulent flow and reducing the local flamelet speed while peak heat release rate remains relatively unchanged.

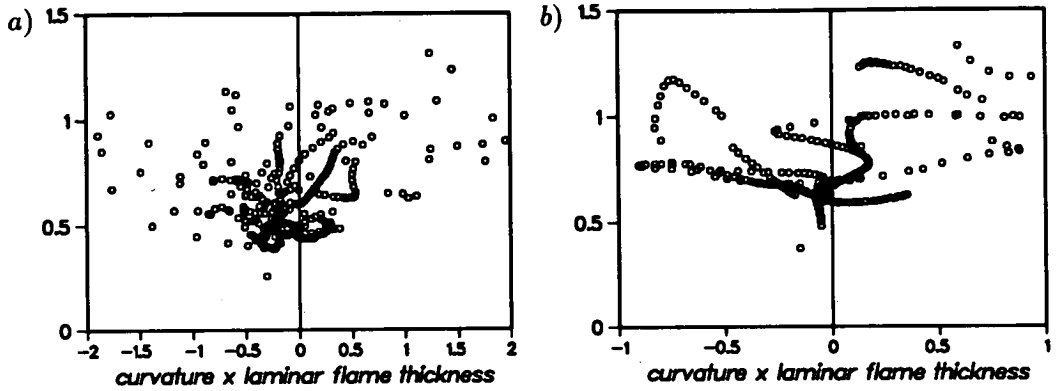


FIGURE 8. Scatter plots of normalized flamelet speed s_n (Eq. 18) versus normalized flame curvature at $t/\tau_0 \approx 0.8$: a) Case 1; b) Case 2.

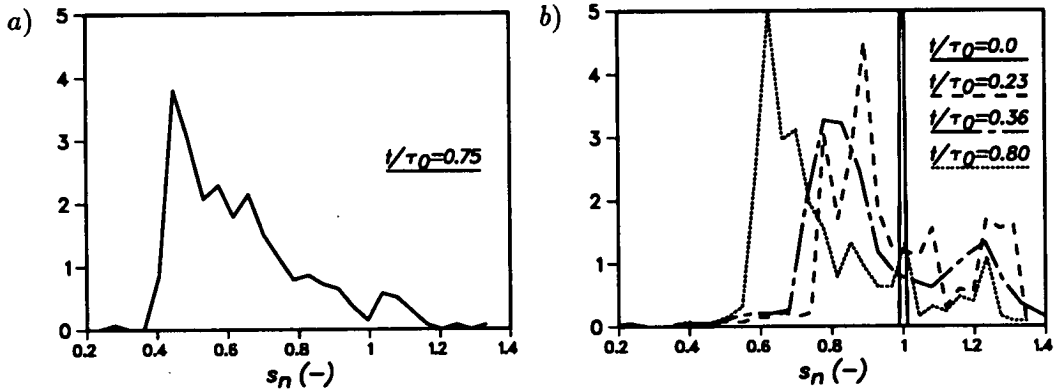


FIGURE 9. Pdf's of normalized flamelet speed s_n (Eq. 18): a) Case 1; b) Case 2.

5. Discussion

Predictive models of turbulent premixed combustion for engineering applications remain at an early stage of development. Key physical processes including ignition and early flame kernel development, complex hydrocarbon-air reaction kinetics, turbulence-chemistry interactions, and flame-wall interaction remain poorly understood even at a fundamental level. Direct numerical simulation has played an increasingly important role in recent years both in contributing to fundamental understanding and in providing guidance for modeling. Fundamental contributions of DNS include elucidation of flame topology and structure (Kerstein *et al.* 1988, Ashurst *et al.* 1988, Rutland & Trouve 1990, Ashurst 1990, Cant *et al.* 1990, Rutland *et al.* 1990, El Tahry *et al.* 1991, Girimaji & Pope 1992), a characterization of the scales of turbulent motion that influence flame structure (Poinsot *et al.* 1990, 1991), flame quenching (Poinsot *et al.* 1991, Meneveau & Poinsot 1990), and thermodiffusive (Lewis number) effects (Rutland & Trouvé 1990, Haworth & Poinsot 1992). Moreover, DNS results have been used to construct and to calibrate models for premixed flame propagation (Bray & Cant 1992), ignition and

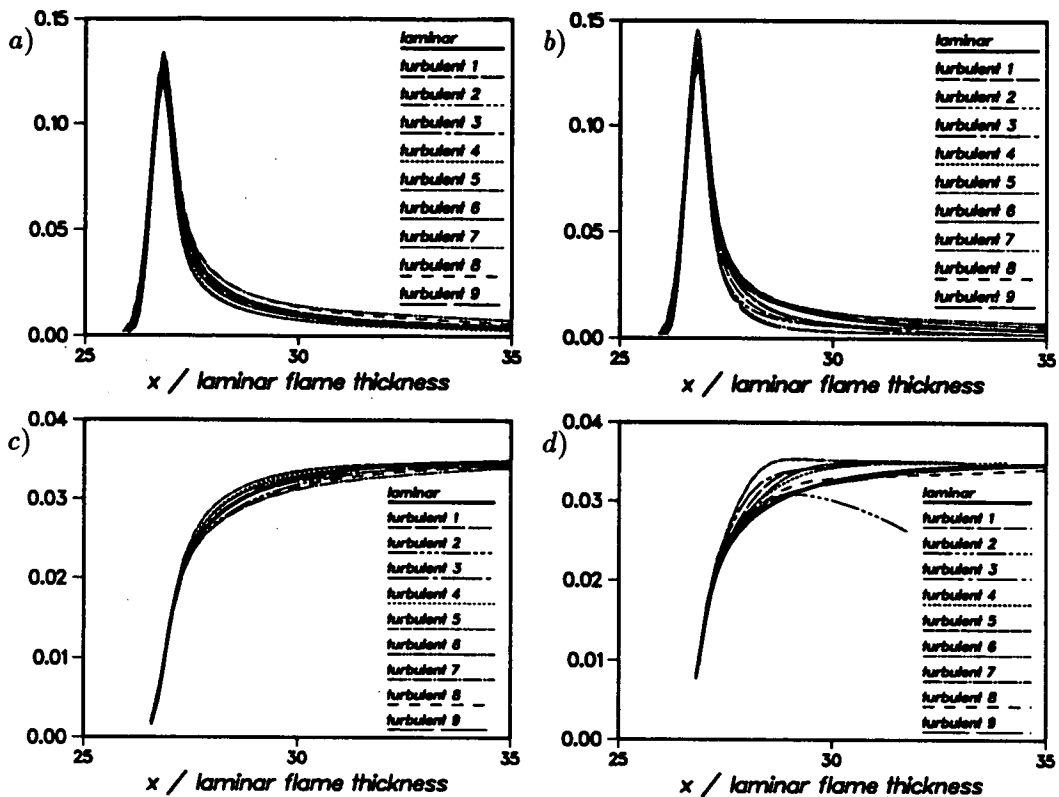


FIGURE 10. Unnormalized laminar and turbulent flame profiles for Case 2: a) heat-release rate, $t/\tau_0 = 0.23$; b) heat-release rate, $t/\tau_0 = 0.80$; c) OH mass fraction, $t/\tau_0 = 0.23$; d) OH mass fraction, $t/\tau_0 = 0.80$.

early flame-kernel growth (Poinso 1991), and flame-wall interactions (Poinso & Haworth 1992). These models can be incorporated into multidimensional Reynolds-averaged modeling approaches for engineering devices (e.g. Boudier *et al.* 1992).

The present simulations represent a first attempt to incorporate realistic chemical kinetics and transport into full turbulence simulations. Principle results are: 1) Realistic chemical kinetics and transport have been implemented successfully into full turbulence simulations. 2) Consistent with the simpler models, the complex-chemistry turbulent flame aligns preferentially with extensive strain rates in the tangent plane and flame curvature pdf's are close to symmetric with near-zero means. 3) By contrast to simple chemistry results with non-unity Lewis numbers, local flame structure does not correlate with local flame curvature but rather with local tangential strain rate. Turbulent straining results in substantial thinning of the flame relative to the steady unstrained laminar case. Peak heat-release rate remains close to the laminar value, but integrated heat release along the local flame normal is substantially lower in the turbulent flame. 4) Heat release and H_2O_2 contours remain thin and connected ('flamelet-like') while species including H-atom and OH are more diffuse. In particular, peak OH concentration occurs well behind the peak

heat-release zone.

The strong correlation of s_n with strain rate rather than with curvature (Figures 7 and 8) for the present computations suggests an effective Lewis number that is greater than or equal to unity. However, no amount of straining of the simple-chemistry flames in Haworth & Poinot (1992) resulted in the extreme thinning and decrease in $\langle s_n \rangle$ than has been observed here. For the present stoichiometric reactants, definition of a single deficient-reactant-based Lewis number is problematic (Joulin & Mitani 1981, Chelliah & Williams 1987). Computations with fuel-lean reactants may help to shed light on these results.

Present turbulence Reynolds numbers and the normalized turbulence intensity u'/s_l^0 (Table II) are typical of values found, for example, in reciprocating internal combustion (IC) engines at low engine speeds. The computed flames remain thick compared to the $l/\delta_l \approx 30$ typical of propane-air mixtures under standard IC-engine operating conditions (stoichiometric, $p = 5$ atm, $T_u = 600$ K, undiluted). However, l/δ_l can be as low as three for high T_u , low p , or high exhaust-gas dilution engine cases (Mantzaras *et al.* 1988; Blint, 1988, 1990). The present choice of initial turbulence spectrum (Haworth & Poinot 1992) results in too little energy at low wavenumbers compared with classic equilibrium turbulence: thus there is little dissipation in the hot post-flame gas in spite of the high temperature-induced viscosity there. Computations with a more realistic initial spectrum are planned.

The high adiabatic flame temperature (2840 K) for the present thermochemistry results in significant equilibrium levels of fuel and oxidizer in the burnt gas and in high equilibrium radical concentrations of OH, H-atom, and O-atom (Figure 2). Thus it is not surprising that OH serves as a poor marker of the heat-release zone for this flame. The H_2O_2 radical serves better in this regard computationally, but may be a poor choice in practice: peak H_2O_2 mass fraction in the present case is 0.000094 versus 0.0348 for OH. Moreover, the reaction-rate constants involving H_2O_2 in Table I are not well established. Nonstoichiometric and cooler reactants would result in lower temperatures and narrower OH radical profiles. In these cases, OH may better serve as a marker of the reaction zone consistent with the experimental observations of Becker *et al.* (1990), for example.

Further hydrogen-air work thus will include modifications to the initial turbulence spectrum, fuel-lean cases, runs to later times t/τ_f , and additional postprocessing to look at relative shifts in species mass fraction profiles relative to the steady laminar flame. Additional chemistry for NO_x production and extensions to pollutant formation in hydrocarbon-air systems are anticipated subjects for future investigations.

Acknowledgements

The authors acknowledge the fruitful interaction with other members of the combustion group during the 1992 summer program of the CTR. In particular, we thank our CTR host Dr. Arnaud Trouvé.

REFERENCES

- ASHURST, W. T. & BARR, P. K. 1983 Stochastic calculation of laminar wrinkled flame propagation via vortex dynamics. *Combust. Sci. & Technol.* **34**, 227–256.
- ASHURST, W. T., PETERS, N., & SMOOKE, M. D. 1987 Numerical simulation of turbulent flame structure with non-unity Lewis number. *Combust. Sci. & Technol.* **53**, 339–375.
- ASHURST, W. T., SHIVASHINSKY, G. I., & YAKHOT, V. 1988 Flame-front propagation in nonsteady hydrodynamic fields. *Combust. Sci. & Technol.* **62**, 273–284.
- ASHURST, W. T. 1990 Geometry of premixed flames in three-dimensional turbulence. In *Proc. 1990 Summer Program*, Center for Turbulence Research, Stanford University & NASA Ames, 245–253.
- BATCHELOR, G. K. 1953 *The theory of homogeneous turbulence*. Cambridge University Press.
- BECKER, H., MONKHOUSE, P. B., WOLFRUM, J., CANT, R. S., BRAY, K. N. C., MALY, R., PFISTER, W., STAHL, G., & WARNATZ, J. 1990 Investigation of extinction in unsteady flames in turbulent combustion by 2D-LIF of OH radicals and flamelet analysis. *23rd Symp. (Intl.) on Combust.* The Combustion Institute, Pittsburgh, 817–823.
- BLINT, R. J. 1988 Flammability limits for exhaust gas diluted flames. *22nd Symp. (Intl.) on Combust.* The Combustion Institute, Pittsburgh, 1547–1554.
- BLINT, R. J. 1990 Stretch in premixed laminar flames under IC engine conditions. *Combust. Sci. & Technol.* (to appear).
- BOUDIER, P., HENRIOT, S., POINSOT, T., & BARITAUD, T. 1992 A model for turbulent flame ignition and propagation in spark ignition engines. *24th Symp. (Intl.) on Combust.* The Combustion Institute, Pittsburgh, in press.
- BRAY, K. N. C. & CANT, R. S. 1991 Some applications of Kolmogorov's turbulence research in the field of combustion. *Proc. R. Soc. Lond. A.* **434**, 217–240.
- CANDEL, S. M. & POINSOT, T. J. 1990 Flame stretch and the balance equation for the flame area. *Combust. Sci. & Technol.* **70**, 1–15.
- CANT, R. S., RUTLAND, C. J., & TROUVÉ, A. 1990 Statistics for laminar flamelet modeling. In *Proc. 1990 Summer Program*, Center for Turbulence Research, Stanford University & NASA Ames, 271–279.
- CHELLIAH, H. K. & WILLIAMS, F. A. 1987 Asymptotic analysis of two-reactant flames with variable properties and Stefan–Maxwell transport. *Combust. Sci. & Technol.* **51**, 129–144.
- DRAKE, M. C. & BLINT, R. J. 1988 Structure of laminar opposed-flow diffusion flames with CO/H₂/N₂ fuel. *Combust. Sci. & Technol.* **61**, 187–224.
- EL TAHRY, S. H. 1990 A turbulence combustion model for premixed charge engines. *Combust. & Flame.* **79**, 122–140.

- EL TAHRY, S. H., RUTLAND, S. H., & FERZIGER, J. H. 1991 Structure and propagation speeds of turbulent premixed flames – a numerical study. *Combust. & Flame*. **83**, 155–173.
- GHONIEM, A. F. & KRISHNAN, A. 1988 Origin and manifestation of flow/com-bustion interactions in a premixed shear layer. *22nd Symp. (Intl.) on Combust.* The Combustion Institute, Pittsburgh, 665–675.
- GIRIMAJI, S. S. & POPE, S. B. 1992 Propagating surfaces in isotropic turbulence. *J. Fluid Mech.* **234**, 247–277.
- HAWORTH, D. C. & POINSOT, T. J. 1992 Numerical simulations of Lewis number effects in turbulent premixed flames. *J. Fluid Mech.* **244**, 405–436.
- HERRING, J. R., ORSZAG, S. A., KRAICHNAN, R. H., & FOX, D. G. 1974 Decay of two-dimensional homogeneous turbulence. *J. Fluid Mech.* **66**, 417–444.
- JOULIN, G. & MITANI, T. 1981 Linear stability analysis of two-reactant flames. *Combust. & Flame*. **40**, 235–246.
- KEE, R. J., MILLER, J. A., & JEFFERSON, T. H. 1980 CHEMKIN: a general-purpose, problem-independent, transportable, FORTRAN chemical-kinetics code package. SANDIA Report No. SAND80-8003.
- KEE, R. J., WARNATZ, J., & MILLER, J. A. 1983 A FORTRAN computer code package for the evaluation of gas-phase viscosities, conductivities, and diffusion coefficients. SANDIA Report No. SAND83-8209.
- KERSTEIN, A. R., ASHURST, W. T., & WILLIAMS, F. A. 1988 Field equations for interface propagation in an unsteady homogeneous flowfield. *Phys. Rev. A*. **37**, 2728–2731.
- LEE, T.-W., NORTH, G. L., & SANTAVICCA, D. A. 1991 Curvature and orientation statistics of turbulent premixed flame fronts. *Combust. Sci. & Technol.* (submitted for publication).
- LELE, S. 1992 Compact finite difference schemes with spectral-like resolution. *J. Comp. Phys.* (to appear).
- LESIEUR, M. 1987 *Turbulence in Fluids*. Martinus Nijhoff.
- MANTZARAS, J., FELTON, P. G., & BRACCO, F. V. 1988 Three-dimensional visualization of premixed-charge engine flames. SAE Paper No. 881635.
- MENEVEAU, C. & POINSOT, T. 1990 Stretching and quenching of flamelets in premixed turbulent combustion. *Combust. & Flame*. **86**, 311–332.
- MILLER, J. A., MITCHELL, R. E., SMOOKE, M. D. & KEE, R. J. 1982 Toward a comprehensive chemical kinetic mechanism for the oxidation of acetylene: comparison of model predictions with results from flame and shock tube experiments. *19th Symp. (Intl.) on Combust.* The Combustion Institute, Pittsburgh, 181–196.
- ORAN, E. S. & BORIS, J. P. 1987 *Numerical simulation of reactive flow*. Elsevier, New York, 416–431.

- POINSOT, T., VEYNANTE, D., & CANDEL, S. 1990 Diagrams of premixed turbulent combustion based on direct simulation. *23rd Symp. (Intl.) on Combust.* The Combustion Institute, Pittsburgh, 613-619.
- POINSOT, T. 1991 Flame ignition in a premixed turbulent flow. In *Center for Turbulence Research Annual Research Briefs*, Center for Turbulence Research, Stanford University & NASA Ames, 1-22.
- POINSOT, T., VEYNANTE, D., & CANDEL, S. 1991 Quenching processes and premixed turbulent combustion diagrams. *J. Fluid Mech.* **228**, 561-606.
- POINSOT, T., ECHEKKI, T., & MUNGAL, M. G. 1992 A study of the laminar flame tip and implications for premixed turbulent combustion. *Combust. Sci. & Technol.* **81**, 45-55.
- POINSOT, T. & LELE, S. 1992 Boundary conditions for direct simulations of compressible viscous flows. *J. Comp. Phys.* **101**, 104-129.
- POINSOT, T. J. & HAWORTH, D. C. 1992 Numerical simulations and modeling of the interaction between turbulent premixed flames and walls. In *Proc. 1992 Summer Program, Center for Turbulence Research, Stanford University & NASA Ames* (in press).
- POPE, S. B. 1988 Evolution of surfaces in turbulence. *Intl. J. Engng. Sci.* **26**, 445-469.
- POPE, S. B. 1991 Numerical issues in pdf methods. *Fourth International Conference on Numerical Combustion*, St. Petersburg, FL, December 2-4, 1991, 165.
- RUTLAND, C. J., FERZIGER, J. H., & EL TAHRY, S. H. 1990 Full numerical simulation and modeling of turbulent premixed flames. *23rd Symp. (Intl.) on Combust.* The Combustion Institute, Pittsburgh, 621-627.
- RUTLAND, C. & TROUVÉ, A. 1990 Premixed flame simulations for nonunity Lewis numbers. In *Proc. 1990 Summer Program, Center for Turbulence Research, Stanford University & NASA Ames*, 299-309.
- SMOOKE, M. D., LIN, P., LAM, J.K., & LONG, M. B. 1990 Computational and experimental study of a laminar axisymmetric methane-air diffusion flame. *23rd Symp. (Intl.) on Combust.* The Combustion Institute, Pittsburgh, 575-582.
- WARNATZ, J. 1981 Concentration-, pressure-, and temperature-dependence of the flame velocity in hydrogen-oxygen-nitrogen mixtures. *Combust. Sci. & Technol.* **26**, 203-213.
- WESTBROOK, C. 1991 *Engineering Foundation Meeting on Present and Future Engines for Automobiles*, Santa Barbara, CA, August 25-30, 1991.
- XU, Y. & SMOOKE, M. D. 1991 Primitive variable solution of a confined laminar diffusion flame using a detailed reaction mechanism. *Fourth International Conference on Numerical Combustion*, St. Petersburg, FL, December 2-4, 1991, 228-229.

445370 521-25
189681
p. 21

N94-14766

Effect of finite-rate chemistry and unequal Schmidt numbers on turbulent non-premixed flames modeled with single-step chemistry

By J. H. Chen¹, S. Mahalingam², I. K. Puri³ AND L. Vervisch⁴

The interaction between a quasi-laminar flame and a turbulent flowfield is investigated through direct numerical simulations (DNS) of reacting flow in two- and three-dimensional domains. Effects due to finite-rate chemistry are studied using a single-step global reaction A (fuel) + B (oxidizer) \rightarrow P (product), and by varying a global Damköhler number, as a result of which the turbulence-chemistry interaction in the flame is found to generate a wide variety of conditions, ranging from near-equilibrium to near-extinction. Differential diffusion effects are studied by changing the Schmidt number of one reactive species to one-half. It is observed that laminar flamelet response is followed within the turbulent flowfield, except in regions where transient effects seem to dominate.

1. Introduction

Due to the presence of kinetically influenced source terms in the species and energy equations, modeling of turbulent reacting flows is a complex and arduous task (Williams, 1985; Borghi, 1988). Classical approaches to turbulent combustion have generally sought to decouple the chemical kinetics from the fluid dynamics, such as in models involving the laminar flamelet concept (Williams, 1985; Peters, 1986), or the probability density function (pdf) approach which usually involves the hypothesis that mixing is unaffected by reactive processes (Kollmann, 1990).

The use of direct numerical simulations in investigations involving non-premixed flames, for a variety of circumstances that include extinction, is intrinsically attractive, since data is simultaneously available for the species concentrations, temperature, and flow dynamics. From this data, the determination of relevant quantities, both scalars and vectors, such as mixture fraction, scalar dissipation rate, reaction rate, strain rate, flame curvature, and stretch is straightforward and corresponds to a single-time/multiple-point experimental measurement of the same. As has been demonstrated for premixed flames (see Trouvé, 1991, Poinso *et al*, 1991), DNS results are expected to provide an insight into the flow processes as well as an

- 1 Combustion Research Facility, Sandia National Laboratories, Livermore, CA
- 2 Center for Combustion Research, University of Colorado, Boulder, CO
- 3 Department of Mechanical Engineering, University of Illinois, Chicago, IL
- 4 Center for Turbulence Research

aid in the development of appropriate models of flame phenomena associated with turbulent non-premixed flames.

In this study, the source terms due to chemistry in the governing equations are retained by simplifying the chemical kinetics to an overall global step. The rate of this global step is varied in order to investigate conditions that extend from strong (near equilibrium) chemistry to weak (near extinction) chemistry. Modeling chemistry in the form of a single-step global reaction has served as a strong tool in the analytical investigation of laminar reacting flows (cf. Williams, 1985) and is expected to retain that purpose in the investigation of turbulent non-premixed flames through direct numerical simulation. Through the global step, it is assumed that fuel and oxidizer, i.e., species A and B, meet in stoichiometric proportion to form a single product, namely P. The species A, B, and P are assumed to have equal diffusivities in one set of simulations; in another set, in order to investigate effects due to differential diffusion, A is assumed to diffuse two times faster than B and P.

2. Model problem

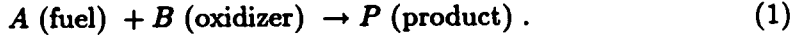
The model problem involves a quasi-laminar flame interacting with decaying homogeneous and isotropic turbulence in a "rectangle" (2-D) or "box" (3-D) containing fuel and oxidizer on either side. At an initial time, the reaction zone is laminar although it is surrounded by a specified turbulent flow field. As time progresses the flame becomes unsteady and assumes turbulent characteristics. Boundary conditions stipulated at the boundaries that lie latitudinally to the flame, i.e., across it, are periodic while those that lie longitudinally, i.e., parallel to the flame, are non-reflecting (Poinsot, Lele 1991). Therefore, depending on the scale of the problem, the simulated "rectangle" or "box" represents instantaneous measurements in a flowfield corresponding to similar flow conditions that are represented by equivalent values of the local Reynolds, Damköhler, and Schmidt numbers. For instance, in the present simulations the Reynolds number based on the Taylor length scale, Re_t , has an initial value of fifty, the Damköhler number, Da , is assigned several values ranging from slow to fast chemistry, and the Schmidt number, Sc , for a select reactive species is assumed to be either unity or one-half. Studies of hydrogen-argon jet flames (Dibble *et al.*, 1986; Magre & Dibble, 1988) indicate that the Reynolds number based on the velocity profile half-width increases from fifty to eighty along the jet axis. We recognize that this analogy is somewhat imprecise, since the velocity and length scales that are involved differ, but are hampered by the unavailability of simultaneously obtained data, the precise facet that makes direct numerical simulations attractive.

3. Methodology

A compressible direct simulation code developed by Trouvé (1991) is utilized in this investigation. The code is able to simulate a reacting flow, including effects due to variations in density and viscosity. Various aspects of the methodology that are specific to this study are described below.

3.1 Chemistry

The chemical reaction is represented by a single-step global mechanism, i.e.,



The reaction rate is in the familiar Arrhenius form, namely

$$\dot{w} = K\rho Y_A \rho Y_B \exp\left(-\frac{T_a}{T}\right), \quad (2)$$

which can be transformed such that (Williams, 1985),

$$\dot{w} = K\rho Y_A \rho Y_B \exp\left(\frac{-\beta(1-\Theta)}{1-\alpha(1-\Theta)}\right). \quad (3)$$

In the above equations, the symbol Θ is a reduced temperature, such that $\Theta = (T - T_o)/(T_f - T_o)$, T_f is the adiabatic flame temperature and T_o the ambient temperature; T_a denotes the activation temperature; K is a pre-exponential factor; α and β respectively denote a temperature factor and the dimensionless activation energy; and $K = K \exp(-\beta/\alpha)$. In the present study, databases have been generated for the case: $\beta = 8$, $\alpha = 0.8$; these values are close to the overall characteristics of methane air combustion.

3.2 Conservation equations

The equation of state is assumed to hold true in the flowfield, and without loss of generality, the fuel, oxidizer, and product are assumed to be of equal molecular weight. The dynamic viscosity μ is assumed to be a function of temperature, such that $\mu = \mu_o(T/T_o)^a$, the exponent a being assigned a value of 0.76. The thermal conductivity λ and mass diffusivities \mathcal{D}_A , \mathcal{D}_B that appear below are related to the dynamic viscosity through the Prandtl and Schmidt numbers, the subscripts A and B corresponding to the relevant species. The value of the Prandtl number is unity in the present simulations.

In a Cartesian frame of reference, the conservation equations are of the form:

$$\frac{\partial \rho}{\partial t} + \frac{\partial \rho u_i}{\partial x_i} = 0, \quad (4)$$

$$\frac{\partial \rho u_i}{\partial t} + \frac{\partial \rho u_i u_j}{\partial x_j} = -\frac{\partial p}{\partial x_i} + \frac{\partial \tau_{ij}}{\partial x_j}, \quad (5)$$

$$\frac{\partial \rho E}{\partial t} + \frac{\partial (\rho E + p) u_i}{\partial x_i} = \frac{\partial (u_j \tau_{ij})}{\partial x_i} + \frac{\partial}{\partial x_i} \left(\lambda \frac{\partial T}{\partial x_i} \right) + Q \dot{w}, \quad (6)$$

$$\frac{\partial \rho Y_A}{\partial t} + \frac{\partial \rho Y_A u_i}{\partial x_i} = \frac{\partial}{\partial x_i} \left(\rho \mathcal{D}_A \frac{\partial Y_A}{\partial x_i} \right) - \dot{w}. \quad (7)$$

$$\frac{\partial \rho Y_B}{\partial t} + \frac{\partial \rho Y_B u_i}{\partial x_i} = \frac{\partial}{\partial x_i} \left(\rho \mathcal{D}_B \frac{\partial Y_B}{\partial x_i} \right) - \dot{w}. \quad (8)$$

where

$$\rho E = \frac{1}{2} \rho \sum_{k=1}^3 u_k^2 + \frac{p}{\gamma - 1} \quad (9)$$

and

$$\tau_{ij} = \mu \left(\frac{\partial u_i}{\partial x_j} + \frac{\partial u_j}{\partial x_i} - \frac{2}{3} \delta_{ij} \frac{\partial u_k}{\partial x_k} \right). \quad (10)$$

In the above equations, the symbol ρ denotes the mass density, E the total energy, p the pressure, and Q the heat release per unit mass of fuel. The remaining symbols are associated with the usual quantities. The specific heat ratio, γ , is assumed to have a value of 1.4. The equations are made dimensionless by a reference length, L_o , the speed of sound, and reference values for the fuel and oxidizer mass fractions. In the manner discussed above, the temperature is converted into an appropriate reduced temperature. The equations are solved using a high-order finite difference scheme (Lele, 1989).

3.3. Turbulence and flame parameters studied

Through interaction with the turbulence, the initial laminar flame is strained by the vorticity, and both reactants and product are convected by it. The heat release interacts with the flow field within and outside the high reaction rate zone through effects that are due to dilatation and through variations of viscosity and diffusivities with temperature. Databases were generated for two- and three-dimensional flames for several conditions.

The initial turbulent kinetic energy spectrum function is given by:

$$E(k) = C_0 \frac{u_0^2}{k_0} \left(\frac{k}{k_0} \right)^4 \exp \left[-2 \left(\frac{k}{k_0} \right)^2 \right], \quad (11)$$

where k is the wavenumber, k_0 is the wavenumber corresponding to the most energetic eddies, and u_0 is the rms velocity. A spatial filter is used to reduce the velocity fluctuations within the initial laminar flame, thereby allowing the flame to be distorted by the turbulence prior to undergoing extinction. The initial Taylor Reynolds number based on the cold fluid viscosity is fifty. The ratio of the initial reaction zone thickness, δ_{fl} , to the Kolmogorov scale is the order of ten.

The initial global Damköhler number defined as:

$$Da = \frac{l_t}{u_0} \left[\frac{1}{\delta_{fl}} \int_{\delta_{fl}} \dot{w} dx \right] \quad (12)$$

is a ratio of the eddy turnover time to a characteristic chemical reaction time based on the heat release. The databases have been investigated for a time equal to 1.6 eddy turnover times.

3.4. Initial conditions

Initially, fuel and oxidizer exist on either side of a domain separated by a laminar non-premixed flame. The initial turbulence spectrum and velocity field are specified in the domain, after which the governing equations are advanced in time. The initial distribution of reactant and product concentration in the laminar flame is obtained from a one-dimensional computation, the result of which is displayed in Figure 1(a). The velocity profile across the flame is presented in Figure 1(b). Note that velocity increases monotonically across the flame. Effects due to dilatation are apparent in the reaction zone which can be identified from the species concentration profiles of Figure 1(a). The initial laminar flame obeys the conservation equations, and the physical properties of this flame are well known. As a check, the growth of the laminar flame is investigated with respect to time. The thickness of the flame, δ_{fl} , is determined to grow in proportion to the square root of time, t , a result that is presented in Figure 1(c).

4. Results and discussion

In order to analyze various characteristics of the flame-turbulence interaction, we describe the reacting flowfield globally, as well as specifically, in terms of the flame topology. In addition, field statistics are obtained in a manner relevant to model construction and validation. At this juncture, additional descriptions are introduced, namely for the mixture fraction and the scalar dissipation. The mixture fraction, Z , is given in the form :

$$Z = \frac{1}{2} (1 + Y_A - Y_B) \quad (13)$$

The fuel and oxidizer vanish at the stoichiometric surface when fast chemistry prevails, such that at this location $Z = Z_{st} = 0.5$ in the simulations. The mixture fraction is a conserved scalar when each of the species involved in the reacting flow has equal mass diffusivities and is, obviously, not conserved when the Schmidt number of any one of the species is changed as is done in some of the simulations. However, in order to make global comparisons between differing situations involving a variety of length and time scales, investigators have generally found it instructive to examine the global description of non-premixed flames with respect to the mixture fraction, even for those cases when this quantity is not conserved.

The scalar dissipation rate, χ , is related to the gradient of the mixture fraction and is given as :

$$\chi = 2D |\nabla Z|^2. \quad (14)$$

4.1. Global description

Postprocessing of the databases indicates that a global description of the two- and three-dimensional flames is essentially similar. Therefore, for sake of brevity, only the two-dimensional results are discussed in this subsection. Flames corresponding to high enough Damköhler numbers, i.e., greater than of order unity, burn vigorously, such that an equilibrium based description of the chemistry is adequate,

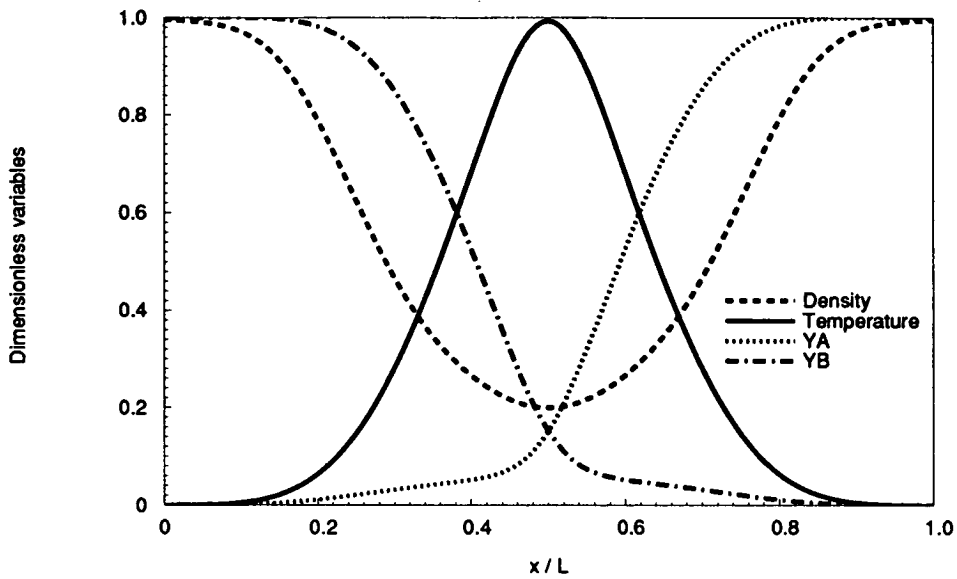


FIGURE 1(A). Species concentration profiles across the flame for a representative condition (1-D simulation, $Da = 1$).

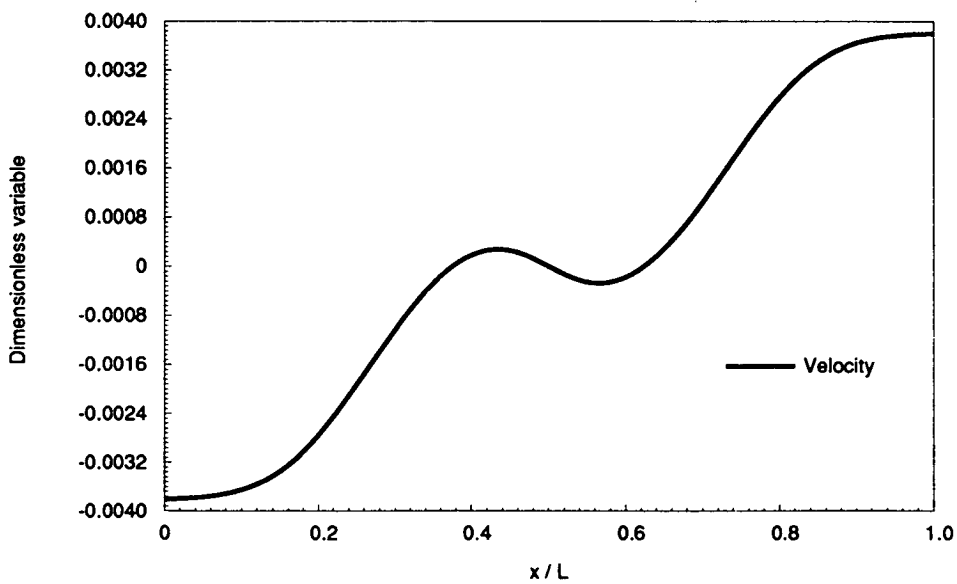


FIGURE 1(B). Velocity profile across the flame for a representative condition (1-D simulation, $Da = 1$).

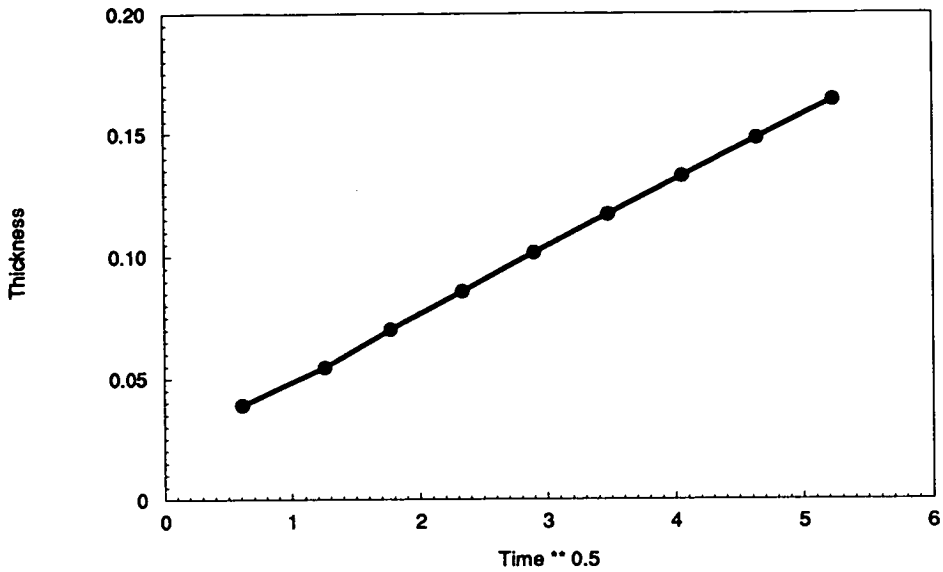


FIGURE 1(C). The growth of the laminar flame thickness with time for a representative condition (1-D simulation, $Da = 1$).

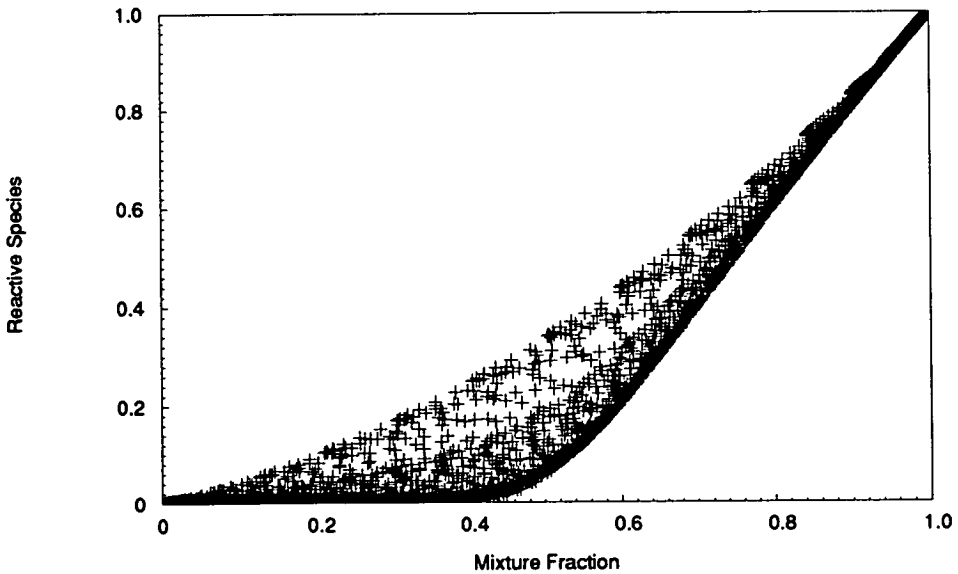


FIGURE 2(A). Distribution of the reactive species A (fuel) mass concentration with respect to the mixture fraction Z (2-D simulation, $Da = 1$).

whereas flames established at Da of $O(1)$ are close to extinction at conditions far from chemical equilibrium.

In Figure 2(a), we present the variation of the reactive species A (fuel) mass fraction with respect to the mixture fraction. The lower bound on the species concentration profile corresponds to those locations in the flame that experience "full" burning and the upper bound to those locations that are influenced by extinction and, hence, close to undergoing only mixing. The species distribution that lies between these two limits is due to turbulence-induced mixing, influencing both the fully burning and extinguished locations, and is, therefore, a transient response. We note that in the equilibrium (or fast-chemistry) limit, the reactive species would reach a negligible concentration at $Z = Z_{st}$, whereas in Figure 2, this location is shifted to the reactant B side, i.e., $Z \approx 0.39$, due to finite-rate chemistry effects.

The dissipation rate of the reactive species, χ_A , described in the form:

$$\chi_A = 2D |\nabla Y_A|^2, \quad (15)$$

is a quantity that represents the magnitude of the gradient of A . This dissipation rate is presented in Figure 2(b). Two regions are immediately evident, corresponding to the results of Figure 2(a), related to pure mixing (frozen flow) and fully burning situations. In the fully burning case, the dissipation rate is negligible for $Z < 0.39$ (Figure 2(c)), whereas for the situation corresponding to extinction (frozen flow), a finite bound appears in the Figure 2(b). Clearly, penetration of the species A (fuel) has taken place in the oxidizer side, thereby creating, at the very least, a partially premixed situation. Whether and under what conditions this premixing causes local re-ignition will be the focus of a subsequent study.

The global temperature profile of the $Da = O(1)$ flames is similarly distributed between the limits corresponding to fully burning and pure mixing situations. For flames corresponding to $Da > O(1)$, the maximum value of the reaction rate invariably occurs at the location of the peak temperature. However, as is clear from Figure 3, this situation is altered for the $Da = O(1)$ flames. We recall that the first-order reaction rate (cf. Equation (1)) simultaneously depends on the local fuel and oxidizer mass fractions and the local temperature. Due to turbulence-induced convection of species and local extinction, which causes penetration and premixing of the reactive species, a high reaction rate can exist at lower temperature locations where there is sufficient fuel and oxidizer concentration to sustain the chemical reaction. Therefore, in the presence of extinction, high values of the local instantaneous reaction rate are distributed over a range of temperatures below the peak temperature that is found in the flame. For cases corresponding to $Da = O(1)$, the smearing of the reaction rate in the domain is caused by higher levels of local vorticity.

Flames established at a low ($O(1)$) Damköhler number, i.e., those experiencing local extinction, also possess thicker reaction zones in both physical and mixture fraction space than those corresponding to higher Da values. In Figure 4(a), we present the reaction rate profile for a flame with Da of $O(1)$. The effect of extinction is apparent in the results presented in this figure since, at the stoichiometric location,

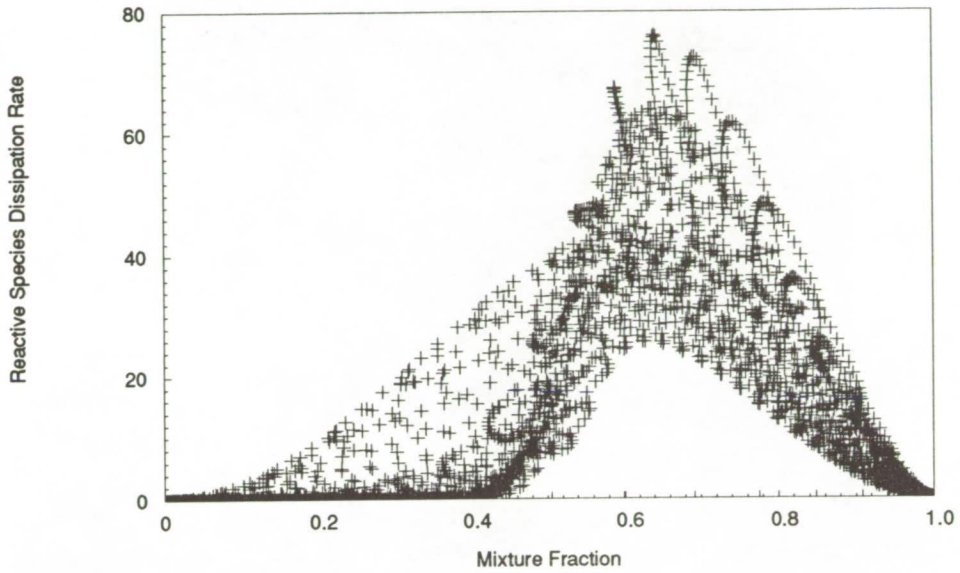


FIGURE 2(B). Distribution of the reactive species A (fuel) dissipation rate with respect to the mixture fraction Z (2-D simulation, $Da = 1$).

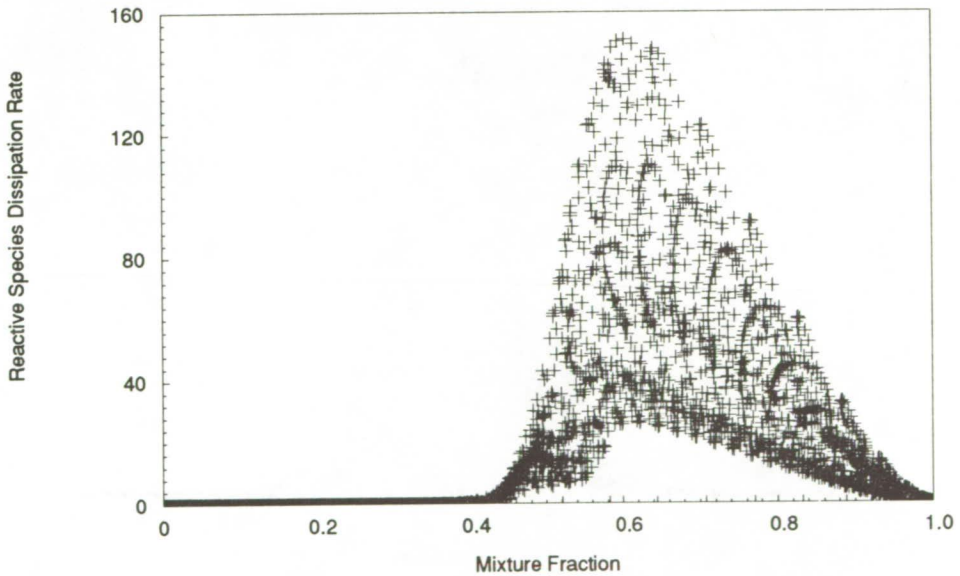


FIGURE 2(C). Distribution of the reactive species A (fuel) dissipation rate with respect to the mixture fraction Z (2-D simulation, $Da = 10$).

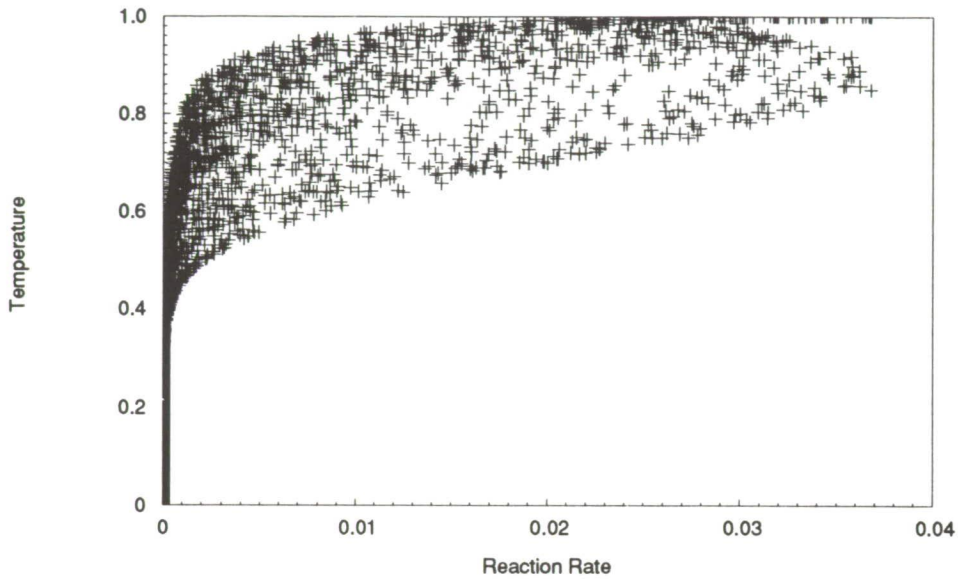


FIGURE 3. Distribution of the reaction rate \dot{w} with respect to the reduced temperature (2-D simulation, $Da = 1$).

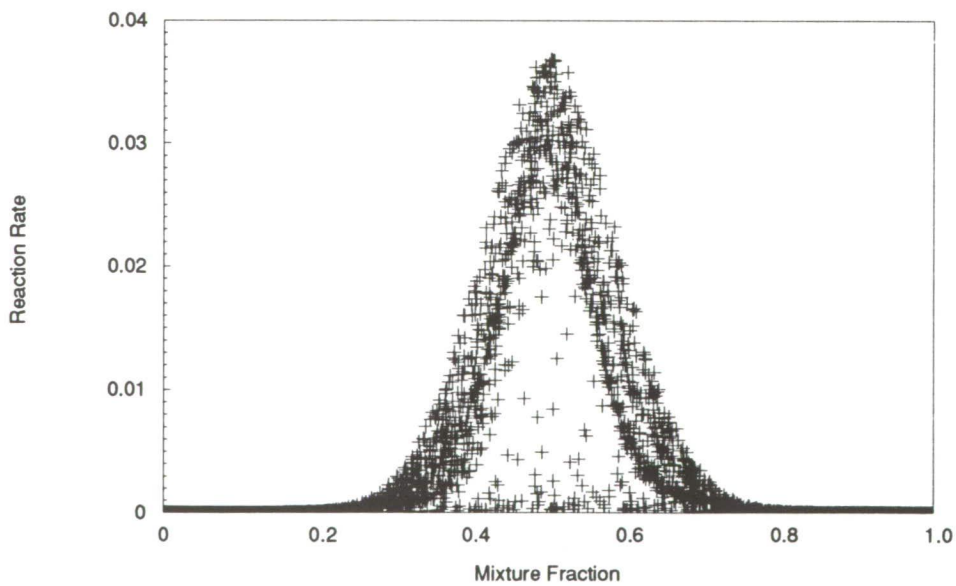


FIGURE 4(A). Distribution of the reaction rate \dot{w} with respect to the mixture fraction Z (2-D simulation, $Da = 1$).

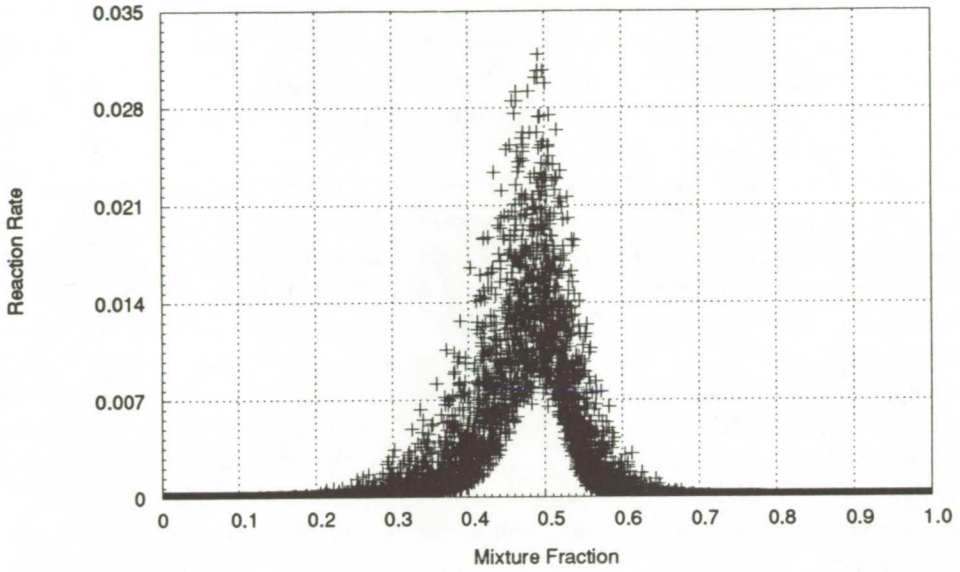


FIGURE 4(B). Distribution of the reaction rate \dot{w} with respect to the mixture fraction Z (3-D simulation, $Da = 2.5$, $Sc_A = 0.5$).

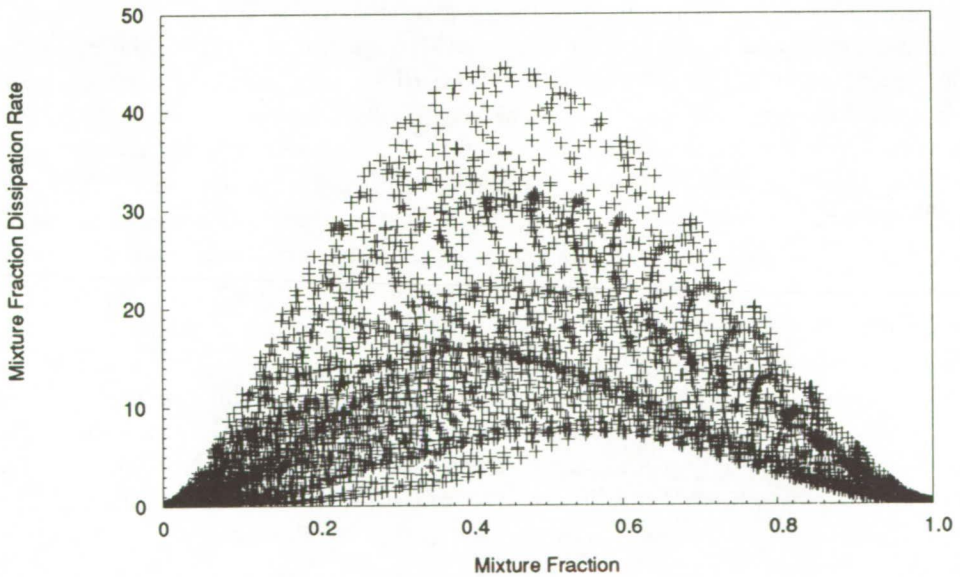


FIGURE 5(A). Distribution of the scalar dissipation rate, χ , with respect to the mixture fraction Z (2-D simulation, $Da = 1$).

C-5

there is both high and negligible reaction rate. Though the reaction rate reaches a maximum at the stoichiometric surface, Z_{st} , the reaction zone falls in a broad band around that location, spanning $Z \approx 0.3 - 0.7$. In contrast, the reaction zone corresponding to $Da = 10$, results for which are not displayed for sake of brevity, is thinner in both physical and Z -space (spanning $Z \approx 0.42 - 0.58$), with no evidence of local extinction, as is to be expected.

When the Schmidt number of the reactive species A (fuel) is decreased to a value of 0.5, the location of the peak reaction rate moves towards the "B-side" of the reaction zone since species A (fuel) diffuses faster than species B . Results for this situation are presented in Figure 4(b). We note that, for this case, the reaction zone is skewed and is broader on the "B-side". This is to be expected since reactant A , upon leakage through the reaction zone, will penetrate farther into for $Sc_B > Sc_A$. Conversely, the reaction zone on the "A-side" is thinner due to the inability of the species B to diffuse farther into A , after leaking through the reaction zone. The leakage of either reactant through the surface locating the maximum reaction rate is due to effects attributable to finite-rate chemistry. We note that when the Schmidt number of either reactant is different from unity, the mixture fraction is no longer a conserved scalar.

In accord with laminar flamelet theory, the scalar dissipation rate increases with the reaction rate and is somewhat symmetrically distributed about the stoichiometric surface. Results for χ are presented in Figure 5(a). The peak scalar dissipation rate in Figure 5(a) occurs on the oxidizer side, a phenomenon attributable to the slightly larger vorticity on that side (specified as part of the initial conditions) that causes more mixing and consequently larger gradients on that side. The χ profile lies within an envelope that appears to mark the response of a typical laminar-like flamelet. For instance, the inverse of the scalar dissipation rate after being appropriately normalized is indicative of a local Damköhler number (Peters, 1986). The instantaneous peak reaction rate associated with a laminar flamelet increases monotonically as this quantity is decreased, until abrupt extinction occurs (Williams, 1985). However, the classical hypothesis used in non-premixed flamelet modeling (Peters, 1986, Warnartzt and Rogg, 1986) that Z and χ are uncorrelated, appears to be invalid, when the combustion occurs in the flamelet regime.

In Figure 5(b), we present the effect of Schmidt number on the scalar dissipation rate. The scalar dissipation rate is skewed away from the species that has a higher diffusivity. The higher diffusivity of species A smooths its spatial gradients and, as discussed above, simultaneously moves the reaction zone into the "B-side". The results of Figure 5(b) suggest a means to lower the local value of the instantaneous scalar dissipation rate by systematically involving differential diffusion effects. This has been identified as a topic of further investigation by this group.

4.2. Flame topology

The reaction zone is observed to undergo local extinction as the Damköhler number is reduced due to an increase in the local scalar dissipation rate or due to vorticity-induced strain. The flame surface becomes interrupted, as is apparent

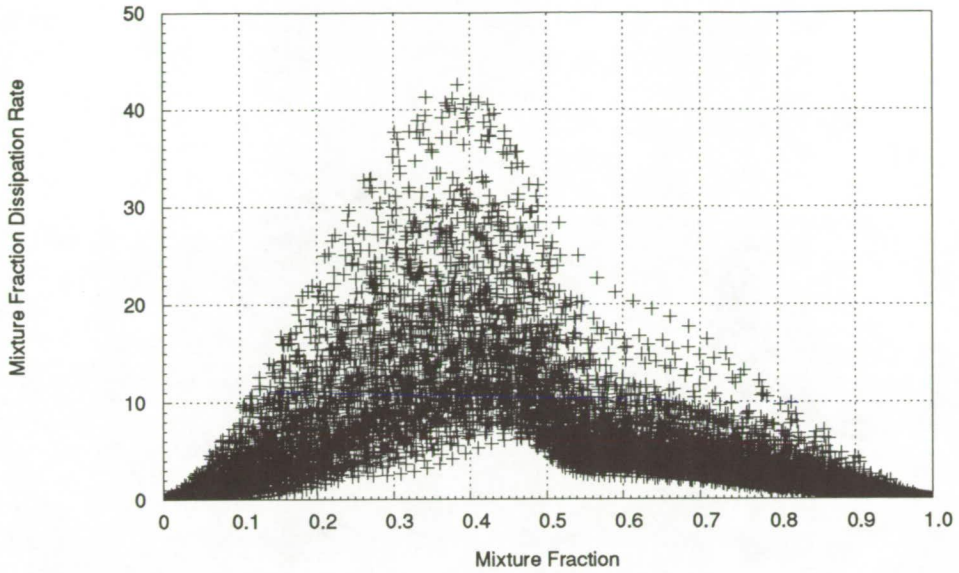


FIGURE 5(B). Distribution of the scalar dissipation rate χ with respect to the mixture fraction Z (3-D simulation, $Da = 2.5$, $Sc_A = 0.5$).

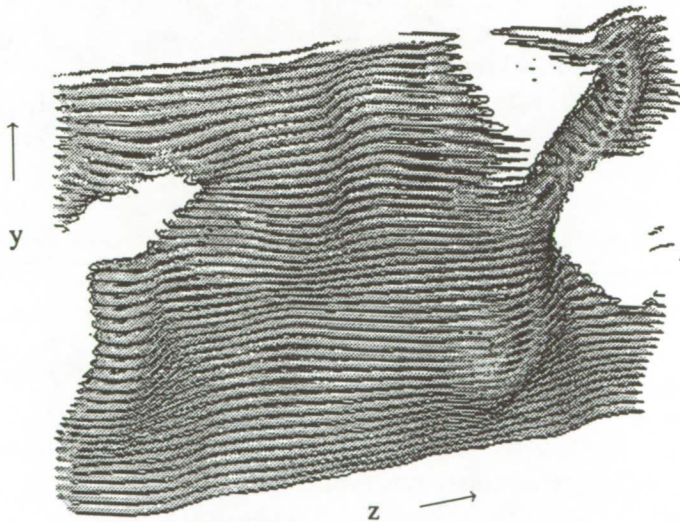


FIGURE 6. Distribution of the maximum reaction rate \dot{w} in the turbulent flowfield (Y-Z plane, 3-D simulation, $Da = 1$).

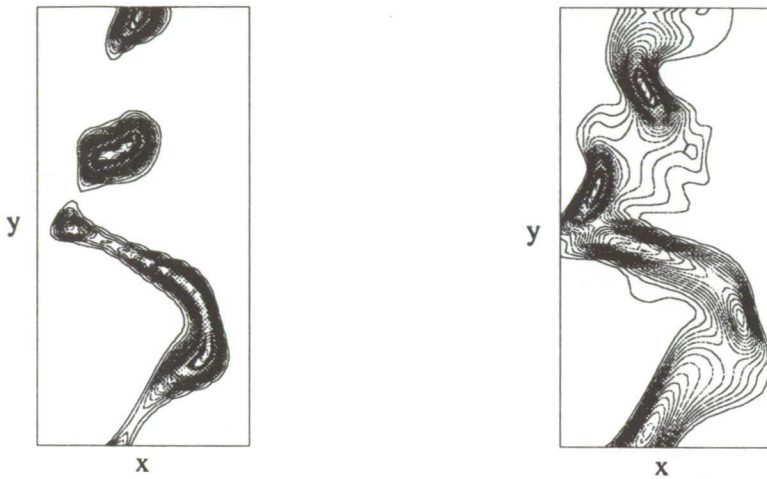


FIGURE 7(A) AND 7(B). On the left, distribution of the reaction rate; on the right, distribution of the scalar dissipation rate, at a specified z -location in the turbulent flowfield (3-D simulation, $Da = 1$)

from Figure 6. In this flame, “holes” occur where frozen flow, i.e., pure mixing, exists. In accord with laminar flamelet theory, the extinguished locations correspond to a high rate of the instantaneous scalar dissipation rate. This situation is clear in Figures 7(a) and 7(b), in which a flame is cut in the z -direction (corresponding to Figure 6) at a specified location and contours of the reaction and scalar dissipation rates are presented.

Extinction may also occur due to “flame-shortening” effects. This occurs when the product is not convected away at a rapid enough rate such that the reactive species are not present in a high enough concentration to sustain the chemical reaction. While we have observed the effect of flame-shortening in the two-dimensional databases, these effects are absent in the three-dimensional simulations, indicating the importance of including convection in a direction normal to (i.e. across) the reaction zone.

The flame presented in Figure 6 includes locations that are fully-burning and those that are close to extinction. We locate the stoichiometric surface and assume this to be the location of the peak reaction zone for the case corresponding to equal Schmidt numbers for all of the species (cf. Figure 4(a)). At this location, the scalar dissipation rate and the tangential strain rate are found to be well correlated as is apparent from Figure 8. Therefore, vorticity effects imply increasing tangential strain but also increased mixing and, consequently, larger gradients and dissipation rates. The extinguished locations in the flame presented in Figure 6 are a consequence of high local tangential strain rates.

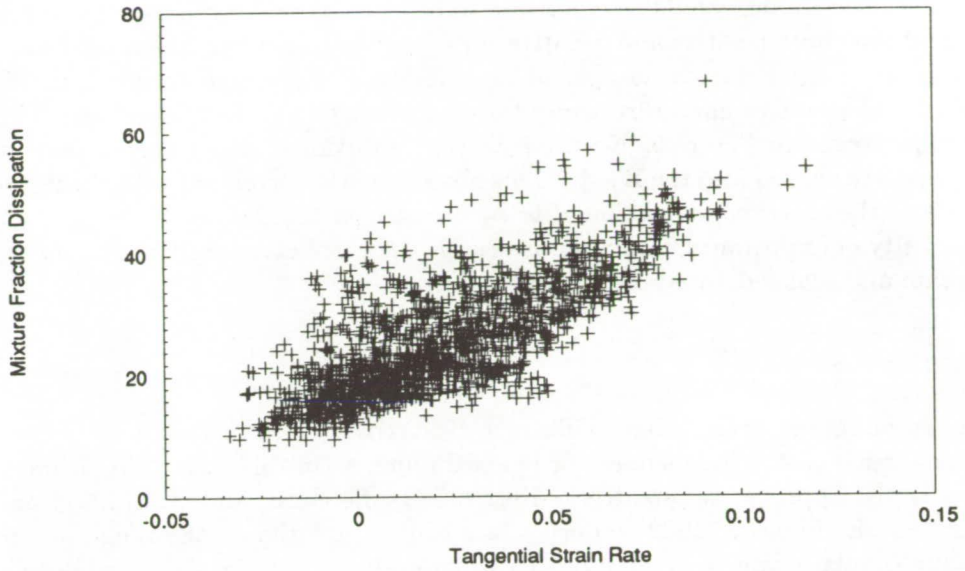


FIGURE 8. Correlation of the rate of strain tangential to the flame surface with the scalar dissipation rate, χ , along the flame surface (3-D simulation, $Da = 1$).

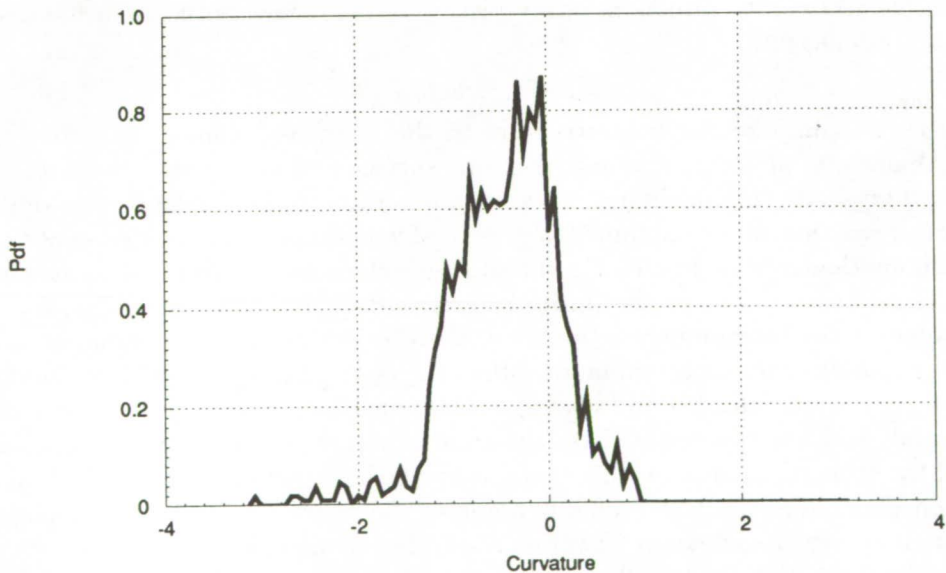


FIGURE 9. Probability density function of the curvature along the flame surface (3-D simulation, $Da = 2.5$, $Sc_A = 0.5$).

If the Schmidt number of all of the species is assigned a value of unity, the curvature of the three-dimensional flame is found to be symmetric, i.e., the stoichiometric surface exhibits both positive and negative curvature in an arbitrary reference frame. However, when the Schmidt number of the species *A* is changed to one-half, the probability of negative curvature along the stoichiometric surface increases. This result is presented in Figure 9. Negative curvature in this instance corresponds to flames that are curved into the B side. This observation is correlated with the figure 4(b), where the reaction zone is found to be broader on the B side.

A quantity of importance in mixing theories is the correlation coefficient between strain rate and scalar dissipation rate defined as:

$$\sigma = \frac{\langle \nabla Z \cdot e \cdot \nabla Z \rangle}{\langle e : e \rangle^{\frac{1}{2}} \langle \nabla Z \cdot \nabla Z \rangle},$$

where *e* is the rate of strain tensor. Gibson's (1968) theory for constant density flows predicts a value of -0.5 independent of Prandtl number (in this study, the Schmidt number is the appropriate quantity). Kerr (1985), Leonard, and Hill (1991) and Nomura and Elghobashi (1992) report values of this quantity in the range -0.4 to -0.5. Our simulations give a value of -0.6 when evaluated at the flame surface for *Da* = 1. The larger correlation is likely to be a result of dilatation associated with heat release in our computations. In Figure 10, the pdf of the magnitude of the cosine of the angle between the mixture fraction gradient and the principal strain rate directions at the flame surface is plotted. It is clear that the most probable alignment (Γ) is one in which the scalar gradient is aligned with the most compressive strain rate direction. This picture is consistent with the computed correlation coefficient.

4.3. Field Structure

In order to compare the field structure of the simulated flames with that of laminar flamelets, we locate the stoichiometric surface and postprocess the data in order to interpolate the maximum reaction rate normal to this surface. The value of the peak reaction rate so obtained is presented with respect to the inverse of the scalar dissipation rate in Figure 11; the plotted values are made nondimensional using the reference values of the initial laminar flame. It is apparent that, for a given value of the maximum reaction rate, there exists a maximum value of the scalar dissipation rate (or a minimum value of $1/(\chi/\chi_{lam})$). Chemical reaction at that rate is not sustained if the corresponding maximum scalar dissipation rate is exceeded, and must increase. This dynamic situation continues until a critical value of the scalar dissipation rate is reached at which extinction occurs. The lower bound on that curve is a trace corresponding to the response of a typical laminar flamelet. However, as is obvious from Figure 11, the reaction rate–scalar dissipation response in the 3-D turbulent flame need not follow the typical laminar flamelet trace, thereby indicating circumstances under which the classical flamelet approach is inadequate.

The flamelet approach assumes that the length scales involved with the strain rate are much smaller than the small scales in the turbulent flow such that the

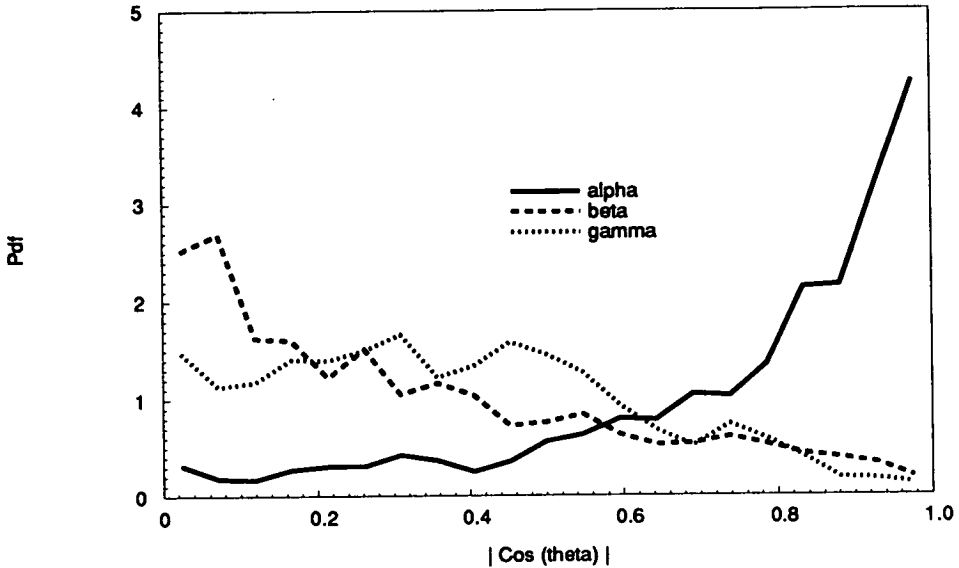


FIGURE 10. Pdf of the magnitude of the cosine of the angle between the scalar gradient and the principal strain directions (3-D simulation, $Da = 1$).

flame is strained by vorticity and convection in the outer flow. This circumstance holds true for the present simulations, in which it is apparent that vorticity does not penetrate the flame except at locations where extinction is observed. A contour map of the vorticity field is presented in Figure 12. In the high temperature region (where the reaction zone is located), the dynamic viscosity increases, which has the effect of locally damping the turbulence. If turbulence levels are high enough and the vorticity is not sufficiently decreased, extinction occurs (cf. Figure 7(a),(b) and 8). We speculate that deviation from the bounds indicated by laminar flamelet theory is due to a transient response involving finite rate chemistry, i.e., the peak value of the reaction rate lags changes to the local instantaneous scalar dissipation rate. The reason for this lag is due to the reaction rate being influenced not only by the local temperature but also by the local fuel and oxidizer mass fractions. The influence of extinction on the distribution of the reactive species is clear from Figures 2(a)–2(c). The effect of turbulence on the flame appears to be such that enhanced mixing convects more fuel (or oxidizer) to the reaction zone than in a purely diffusive situation or one corresponding to a typical laminar flamelet, thereby enhancing the local instantaneous reaction rate. The local temperature does not fall dramatically since the reactive species that is convected to the reaction zone comes from locations that are already hot (or at least warm). In Figure 13, the reactive species mass concentration at the reaction zone is presented for the case corresponding to Figure 11. The lower bound in this distribution is to be interpreted as that corresponding to the response of a laminar flamelet. It is obvious that higher

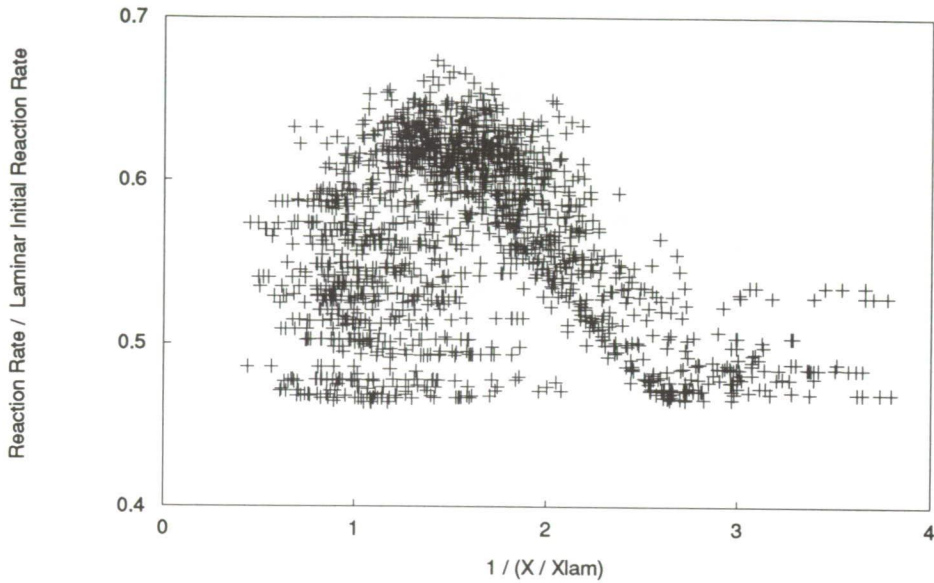


FIGURE 11. Distribution of the maximum reaction rate \dot{w} mass concentration with respect to the inverse scalar dissipation rate $1/(\chi/\chi_{lam})$ (3-D simulation, $Da = 1$).

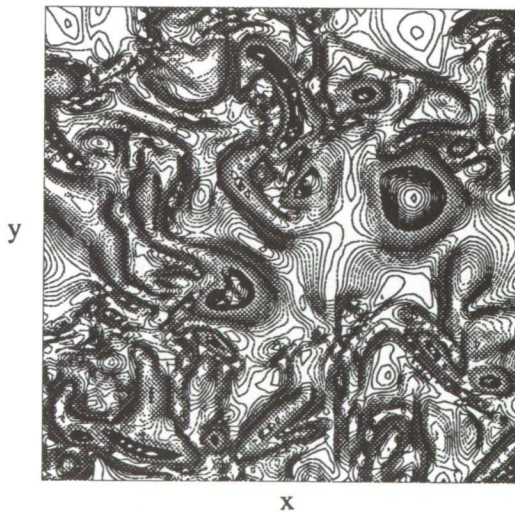


FIGURE 12. Distribution of the vorticity field in the turbulent flame (X-Y plane, 3-D simulation, $Da = 1$).

concentrations of reactive species are to be found than is proposed by flamelet theory. A systematic study of the seemingly transient effect induced by turbulent mixing has been identified as another topic of further investigation by this group.

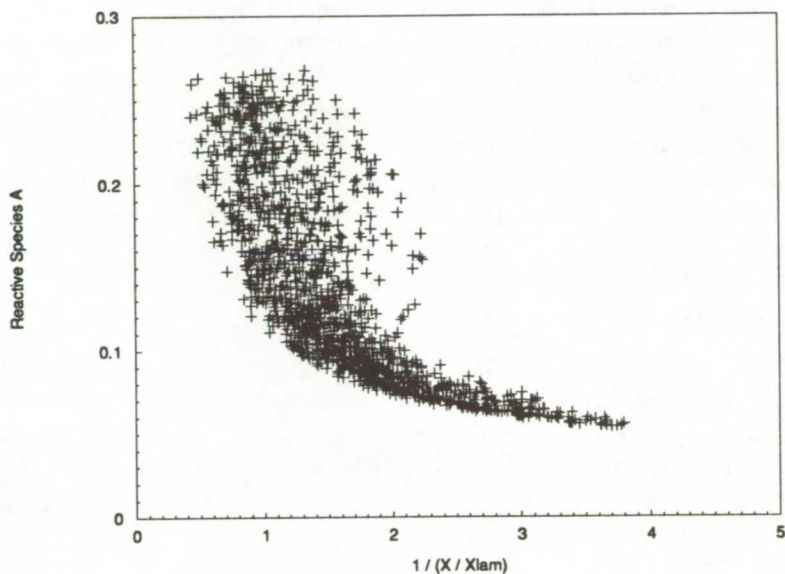


FIGURE 13. Distribution of the reactive species *A* mass concentration with respect to the inverse scalar dissipation rate $1 / (\chi / \chi_{lam})$ (3-D simulation, $Da = 1$).

5. Conclusions and perspectives

Direct numerical simulations databases obtained using a compressible, variable property code have been investigated in order to study turbulent non-premixed flames established in two- and three-dimensional configurations. The flame is assumed to react fuel and oxidizer to form product through a global single-step reaction. A laminar flame is established at an initial time after which it is allowed to interact with a turbulent flowfield. From the databases that were thus created, the global description, flame topology, and field statistics are computed. The effects due to unequal species diffusivities is examined by changing the Schmidt number of one reactant.

The flames are found to extinguish when the scalar dissipation rate in the reaction zone exceeds a critical value. This rate, in turn, is well correlated with the tangential strain rate experienced by the flame. Flames that experience local extinction along the flame surface are found to exhibit global characteristics that are intermediate between those pertaining to frozen flow and fully burning situations. The reaction zones of such flames are thicker in both physical and mixture fraction space. It is determined that the scalar dissipation rate profile can be skewed with respect to the stoichiometric surface by effects stemming from unequal vorticity on the two sides

of the flame and, also, due to effects of unequal diffusivity. Differential diffusion also skews the curvature of the flame surface such that the flames are curved into the species that diffuses at a slower rate.

The response of the quasi-laminar flame is bounded by the characteristics typical of a laminar flamelet although significant deviation from this behavior is also observed. In particular, convection of reactants into the reaction zone suggests that the reaction rate may lag the change in scalar dissipation rate (or tangential strain rate) at the stoichiometric surface.

Several topics which require further investigation have been identified during this study. These include a study of the effects due to differential diffusion, the role of reignition in locally extinguished flames, and the deviation of the behavior of quasi-laminar flames from a flamelet-like behavior due to transient turbulence-related effects.

Acknowledgements

The authors have benefited from discussions with the other members of the combustion group during the 1992 CTR summer program, in particular with Dr. Arnaud Trouvé and Dr. Thierry Poinsot. We also thank Prof. Forman Williams and Prof. Stephen Pope for their helpful comments and suggestions. J. H. Chen has been supported for this work by the Department of Energy's Office of Basic Energy Sciences, Division of Chemical Sciences.

REFERENCES

- BORGHI, R. 1988 Turbulent combustion modeling. *Prog. Energy Combust. Sci.* **14**, 245-292.
- DIBBLE, R. W., SCHEFER, R. W., CHEN, J.-Y., HARTMANN, V. KOLLMAN, W. 1986 Velocity and density measurements in a turbulent nonpremixed flame with comparison to numerical model predictions. *Paper WSS/CI 86-65, Western States Section of the Combustion Institute Spring Meeting, Banff, Canada.*
- GIBSON, C. H. 1968 Fine structure of scalar fields mixed by turbulence: I. Zero gradient points and minimal gradient surfaces. *Phys. Fluids.* **11**, 2305
- KERR, R. M. 1985 Higher-order derivative correlations and alignment of small-scale structures in isotropic numerical turbulence. *J. Fluid Mech.* **153**, 31
- KOLLMAN, W. 1990 The PDF approach to turbulent flow. *Theoret. Comput. Fluid Dynamics.* **1**, 249-285
- LELE, S. 1989 Direct numerical simulation of compressible free shear flows. *27th Aerospace Sciences Meeting, AIAA 89-0374*
- LEONARD A. D., HILL, J. C. 1988 Direct numerical simulation of a homogeneous turbulence reacting flow. *AIAA Paper No. AIAA-88-3624*
- MAGRE, P., DIBBLE, R. W. 1988 Finite chemical kinetic effects in a subsonic turbulent hydrogen flame. *Combust. Flame.* **73**, 195-206.

- NOMURA K. K., ELGHOBASHI 1992 Mixing characteristics of an inhomogeneous scalar in isotropic and homogeneous sheared turbulence. *Phys. Fluids*. A4 (3), March
- PETERS, N. 1986 Laminar flamelet concepts in turbulent combustion. *Twenty-First Symposium (International) on Combustion*. 1231-1250. The Combustion Institute.
- POINSOT T., VEYNANTE D., CANDEL S. 1991 Quenching processes and premixed turbulent combustion diagrams. *J. Fluid Mech.* 228, 561-606
- POINSOT, T., LELE, S. 1991 Boundary conditions for direct simulations of compressible viscous flows. *J. Comput. Phys.* 101, No 1, July 92
- TROUVE, A. 1991 Simulation of flame-turbulence interaction in premixed combustion. *Annual Research Briefs 1991*. CTR, Stanford U./NASA Ames.
- WARNARTZ, J., ROGG, B. 1986 Turbulent non premixed combustion in partially premixed flamelets detailed chemistry. *Twenty-First Symposium (International) on Combustion*. 1533-1541. The Combustion Institute.
- WILLIAMS, F. A. 1985 *Combustion Theory*. Benjamin/Cummings.

449372 522-25

189682

389

N⁹4-14767

Structure of turbulent non-premixed flames modeled with two-step chemistry

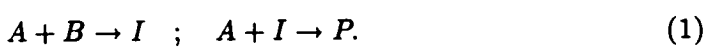
By J. H. Chen¹, S. Mahalingam², I. K. Puri³ AND L. Vervisch⁴

Direct numerical simulations of turbulent diffusion flames modeled with finite-rate, two-step chemistry, $A + B \rightarrow I$, $A + I \rightarrow P$, were carried out. A detailed analysis of the turbulent flame structure reveals the complex nature of the penetration of various reactive species across two reaction zones in mixture fraction space. Due to this two-zone structure, these flames were found to be robust, resisting extinction over the parameter ranges investigated. As in single-step computations, mixture fraction dissipation rate and the mixture fraction were found to be statistically correlated. Simulations involving unequal molecular diffusivities suggest that the small scale mixing process and, hence, the turbulent flame structure is sensitive to the Schmidt number.

1. Introduction

The development of turbulent combustion models that accurately reflect key physical phenomena is essential for many engineering applications. Modern laser-based diagnostics applied to simplified laboratory flows are providing valuable data that is essential for any model development. However, since chemical reactions in flames proceed by a series of elementary steps, it is extremely difficult to isolate the role played by individual species and individual reaction steps on turbulent flame structure. Thus the task of studying the two-way coupling between turbulence and combustion becomes formidable. Recently, direct numerical simulations (DNS) of turbulent non-premixed flames with simplified chemistry have proven to be useful in studying various aspects of the problem.

DNS of turbulent diffusion flames including complex geometry and full chemistry is neither feasible with present-day computers, nor is it desirable since the objectives of DNS are usually to study specific aspects of the full problem. It is in this spirit that we studied the influence of turbulence on the structure of non-premixed flames in which chemistry is modeled through the following two-step mechanism:



The stoichiometric coefficients are chosen so that the global step is identical to the one step mechanism discussed by Chen *et al* (1992). The mechanism and the

1 Combustion Research Facility, Sandia National Laboratories, Livermore, CA
2 Center for Combustion Research, University of Colorado, Boulder, CO
3 Department of Mechanical Engineering, University of Illinois, Chicago, IL
4 Center for Turbulence Research

388

parameters were chosen to model step1 as a radical production step in which the intermediate I is produced followed by a radical consumption step in which the intermediate I is consumed to form the product P . Step2 proceeds with a small activation energy and a large enthalpy of reaction compared with step1. Usually, the intermediate radical species I diffuses at a faster rate compared with the other species. Only Fickian diffusion is modeled. Such reaction mechanisms have been studied using large activation energy (for both steps) asymptotics by Margolis and Matkowsky (1982). They point out that the case wherein the radical species concentration has a non-zero peak is typical of multi-step flames. The selected reaction mechanism may also be used to model practical flames (such as hydrocarbon oxidation) using global parameters. Altering the molecular diffusivity of the intermediate species can lead to modifications to flame structure and a change in flame temperature. This latter effect could be significant in accurately predicting thermal NO_x formation in practical combustors (Law and Chung, 1984). Experimental measurements by Kerstein *et al* (1989) in nonreacting flows suggest that effects due to differential diffusion are not insignificant, and, hence, it is important to include them in models of chemically reacting flows. In reacting flows with significant heat release, these effects are likely to be amplified because of significant decrease in local Reynolds numbers due to an increase in kinematic viscosity with temperature.

The goal of this work is thus to obtain a good understanding of turbulent non-premixed flames modeled by a two-step mechanism, to identify the role of the intermediate species on flame structure, and to understand the significance of differential diffusion on flame structure.

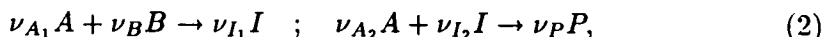
2. Model problem

The problem studied is the interaction of turbulence with an initially unstrained laminar diffusion flame. Computations to date have been performed over a two-dimensional square domain with 129×129 equi-spaced grid points. A laminar diffusion flame in which species A and B are present on either side of the flame (located at approximately $x = 0$) is initialized. Non-reflecting boundary conditions in x and periodic boundary conditions in y are imposed. The full compressible form of the equations of continuity, Navier-Stokes, energy, and species are solved using higher-order finite differencing schemes. The code used was developed by Trounev (1991) for 3D premixed flames and subsequently modified for non-premixed flames. The treatment of boundary conditions and the differencing scheme is based on the methodology of Poinso and Lele (1991). Fluid viscosity varies with temperature according to a power law with an exponent of 0.76.

2.1 Governing equations and parameters

The governing equations and non-dimensionalization are discussed by Chen *et al* (1992). In this subsection, the evolution equations of various species and the parameters associated with the two-step chemistry model are discussed.

The generalized chemical scheme is given by:



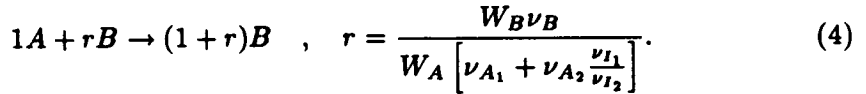
where the ν 's are the stoichiometric coefficients.

We define the following mass ratios:

$$r_{AB} = \frac{W_B \nu_B}{W_A \nu_{A_1}}, \quad r_{AI_1} = \frac{W_I \nu_{I_1}}{W_A \nu_{A_1}}, \quad r_{AI_2} = \frac{W_I \nu_{I_2}}{W_A \nu_{A_2}}, \quad r_{AP} = \frac{W_P \nu_P}{W_A \nu_{A_2}}, \quad (3)$$

where W_A , W_B , W_I , and W_P are the molecular weights of species A , B , I , and P respectively.

In terms of mass, the overall reaction is given by



Let q_1 and q_2 be the energy released per unit mass of species A consumed in step1 and step2 respectively, and let $\delta = q_2/q_1$. Then from the definition of the adiabatic flame temperature, one can show that the following equality, expressing global energy conservation, has to be satisfied:

$$q_1 [\epsilon + \delta(1 - \epsilon)] = \frac{1}{Y_{A,0}} [1 + \phi] c_p (T_f - T_0), \quad \epsilon = \frac{\nu_{A_1}}{\nu_{A_1} + \nu_{A_2} \frac{\nu_{I_1}}{\nu_{I_2}}}, \quad (5)$$

where T_f is the adiabatic flame temperature, $Y_{A,0}$ is the mass fraction of species A in the unmixed A stream, c_p is the specific heat, T_0 is the temperature of the unmixed A and B streams, and ϕ is the overall equivalence ratio defined as:

$$\phi = r \frac{Y_{A,0}}{Y_{B,0}}, \quad (6)$$

where $Y_{B,0}$ is the mass fraction of species B in the unmixed B stream. Continuity and Navier-Stokes equations are given in Chen *et al* (1992) and are not repeated here. The energy and species equations are:

$$\frac{\partial \rho E}{\partial t} + \frac{\partial (\rho E + p) u_i}{\partial x_i} = \frac{\partial (u_j \tau_{ij})}{\partial x_i} + \frac{\partial}{\partial x_i} \left(\lambda \frac{\partial T}{\partial x_i} \right) + q_1 \dot{w}_{A_1} + q_2 \dot{w}_{A_2}, \quad (7)$$

$$\frac{\partial \rho Y_A}{\partial t} + \frac{\partial \rho Y_A u_i}{\partial x_i} = \frac{\partial}{\partial x_i} \left(\rho D_A \frac{\partial Y_A}{\partial x_i} \right) - \dot{w}_{A_1} - \dot{w}_{A_2}, \quad (8)$$

$$\frac{\partial \rho Y_B}{\partial t} + \frac{\partial \rho Y_B u_i}{\partial x_i} = \frac{\partial}{\partial x_i} \left(\rho D_B \frac{\partial Y_B}{\partial x_i} \right) - r_{AB} \dot{w}_{A_1}, \quad (9)$$

$$\frac{\partial \rho Y_I}{\partial t} + \frac{\partial \rho Y_I u_i}{\partial x_i} = \frac{\partial}{\partial x_i} \left(\rho D_I \frac{\partial Y_I}{\partial x_i} \right) + r_{AI_1} \dot{w}_{A_1} - r_{AI_2} \dot{w}_{A_2}, \quad (10)$$

$$\frac{\partial \rho Y_P}{\partial t} + \frac{\partial \rho Y_P u_i}{\partial x_i} = \frac{\partial}{\partial x_i} \left(\rho D_P \frac{\partial Y_P}{\partial x_i} \right) + r_{AP} \dot{w}_{A_2}, \quad (11)$$

where

$$\rho E = \frac{\rho u_k u_k}{2} + \frac{p}{\gamma - 1}. \quad (12)$$

In the above equations, ρ denotes the fluid density, E denotes the total (internal plus kinetic) energy per unit mass, and γ is the specific heat ratio taken to be 1.4. The thermal conductivity λ and the molecular diffusivities \mathcal{D}_A , \mathcal{D}_B , \mathcal{D}_I , and \mathcal{D}_P are related to the dynamic viscosity μ through the Prandtl and species Schmidt numbers. The other symbols have the usual meaning as in the standard literature. The reaction rate terms \dot{w}_{A_1} and \dot{w}_{A_2} are given by the Arrhenius expressions:

$$\dot{w}_{A_1} = B_1 \rho Y_A \rho Y_B \exp\left(-\frac{T_{a_1}}{T}\right), \quad \text{and} \quad \dot{w}_{A_2} = B_2 \rho Y_A \rho Y_I \exp\left(-\frac{T_{a_2}}{T}\right), \quad (13)$$

or alternatively in the form:

$$\dot{w}_{A_1} = \mathbf{B}_1 \rho Y_A \rho Y_B \exp\left(\frac{-\beta_1(1-\tau)}{1-\alpha(1-\tau)}\right), \quad (14)$$

and

$$\dot{w}_{A_2} = \mathbf{B}_2 \rho Y_A \rho Y_I \exp\left(\frac{-\beta_2(1-\tau)}{1-\alpha(1-\tau)}\right), \quad (15)$$

where T_{a_1} and T_{a_2} are the activation temperatures associated with step1 and step2, τ is a nondimensional temperature defined as $\tau = (T - T_0)/(T_f - T_0)$ as given by Williams (1985), $\mathbf{B}_1 = B_1 \exp(-\beta_1/\alpha)$ and $\mathbf{B}_2 = B_2 \exp(-\beta_2/\alpha)$ are the pre-exponential factors, and α is a temperature factor defined as $\alpha = (T_f - T_0)/T_f$.

In the simulations reported here, the following values were chosen for the stoichiometric coefficients: $\nu_{A_1} = \nu_{A_2} = 1/2$, $\nu_B = \nu_I = \nu_P = 1$, so that the overall scheme corresponds to the one-step model used by Chen *et al* (1992). Values for other constants are: $\alpha = 0.8$, $\beta_1 = 8$, $\beta_2 = 2$, $\delta = 5$, consistent with the discussion in Section 1. The value of the Prandtl number is unity. The Schmidt numbers are $Sc_A = Sc_B = Sc_P = 1$. The Schmidt number of the intermediate species $Sc_I = 1$ unless otherwise noted.

2.2 Initial conditions and turbulence field

The generation of initial conditions corresponding to profiles associated with a one-dimensional, unstrained laminar diffusion flame was achieved by the following procedure: the flowfield is initialized with the solution to the one-step chemistry problem discussed by Chen *et al* (1992). The second reaction is turned "off" by setting $B_2 = 0$, and the product profile for the one-step model is used as the profile for species I . The equations are time-advanced, and, simultaneously, the pre-exponential coefficient B_2 is increased until the desired value is reached. Care is taken to ensure that the flame does not extinguish during this process. Once the pressure waves exit the domain, the flowfield is saved (after any required rescaling), and, from this point forward, the turbulence is allowed to interact with the flame.

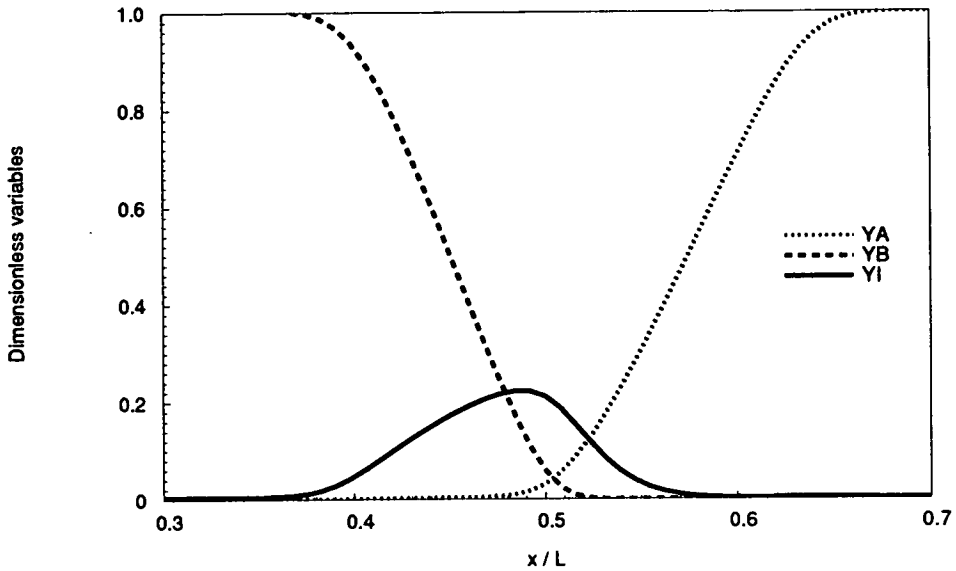


FIGURE 1. Species concentration profiles across the initial 1D laminar flame for a representative condition ($Da = 1$).

For details on the turbulence characteristics and definition of the global Damköhler number, Chen *et al* (1992) may be consulted. A plot of the species profiles of the laminar flame is presented in Figure 1. It is clear that the concentration of the intermediate is significant. Its peak value is a measure of the extent of physical separation between reaction zones associated with the production (step1) and consumption (step2) of the intermediate species.

3. Results and discussion

A quantity that is often used in descriptions of non-premixed flames is the mixture fraction, defined for our choice of stoichiometric coefficients, molecular weights, and unmixed stream concentrations as:

$$Z = \frac{2Y_A - Y_I - 2Y_B + 2}{4}, \quad (16)$$

such that in the unmixed *A* stream, $Z = 1$, and in the unmixed *B* stream, $Z = 0$. When all the molecular diffusion coefficients are equal, Z is a conserved scalar. In the limit of infinitely fast chemistry, at the flame $Y_A = Y_B = Y_I = 0$, giving $Z_{c1} = 1/2$, whereas if the second step is relatively slow compared to the first step, at the flame $Y_A = Y_B = 0$, $Y_I = 1$, giving $Z_{c2} = 1/4$. Thus these two limits of Z identify the locations of the reaction zones under these limiting cases. Finite rate chemistry will tend to cause a deviation from these two stoichiometric surface locations. Note that Z is not a conserved scalar when the diffusivities of the various

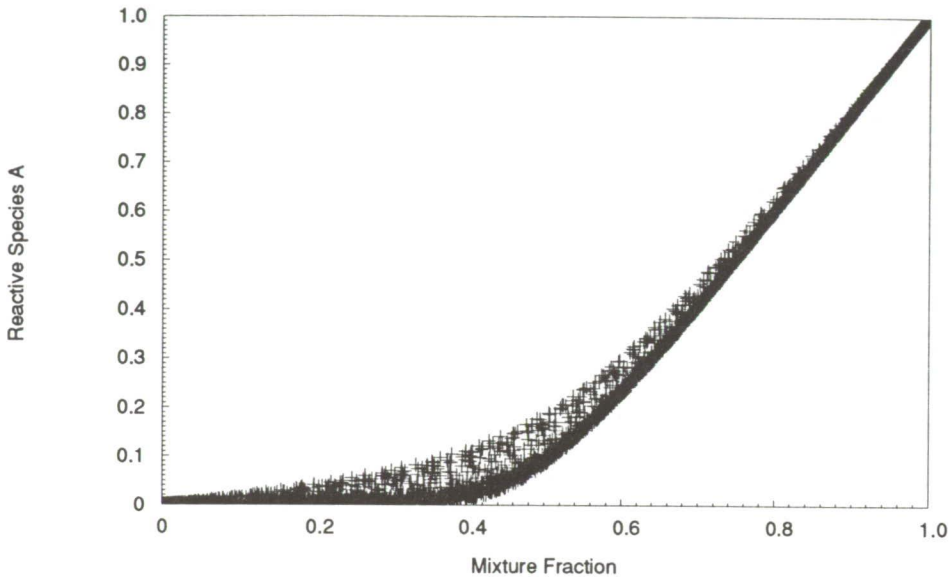


FIGURE 2(A). Distribution of species A mass fraction Y_A , versus mixture fraction Z ($Da = 1$).

species are not equal. In Figure 2(a), the mass fraction Y_A is plotted as a function of Z . It is clear that most of the data points lie close to the equilibrium line, represented by the lower boundary of the data points. The penetration of species A into the B regime is due to finite rate kinetics. The scatter in these data points is due to unsteady effects associated with the turbulence field. The variations of Y_B and Y_I and the reduced temperature τ are shown in Figures 2(b)-(d). These results are consistent with Figure 2(a). It is apparent from Figure 2(d) that no significant drop in temperature is seen, suggesting that extinction is not seen for the conditions of the present simulation.

Reaction rate profiles associated with steps 1 and 2, respectively, are presented in Figures 3(a)-(b). Several features may be readily observed. It is clear that reaction rates for steps 1 and 2 peak for $Z \approx 0.45$ and $Z \approx 0.58$, respectively. Since the mass fraction of species I is significant where reaction 1 occurs, it is apparent from the definition of Z that the shift would be towards lower values of Z . Reaction 2 occurs on the A side of the flame, where A is in excess, thus shifting the peak towards larger values of Z . For the parameters chosen, we have two reaction zones that are not completely segregated in mixture fraction (and physical) space. It is clear from these plots and the plot of reduced temperature (Figure 2(d)) that *no extinction* has occurred in either step. This is a significant observation since the global Damköhler number is comparable to the case for single-step chemistry for which extinction was observed (see Chen *et al*, 1992). An increase in the number of radical-like species and segregation of reaction zones apparently makes the flame

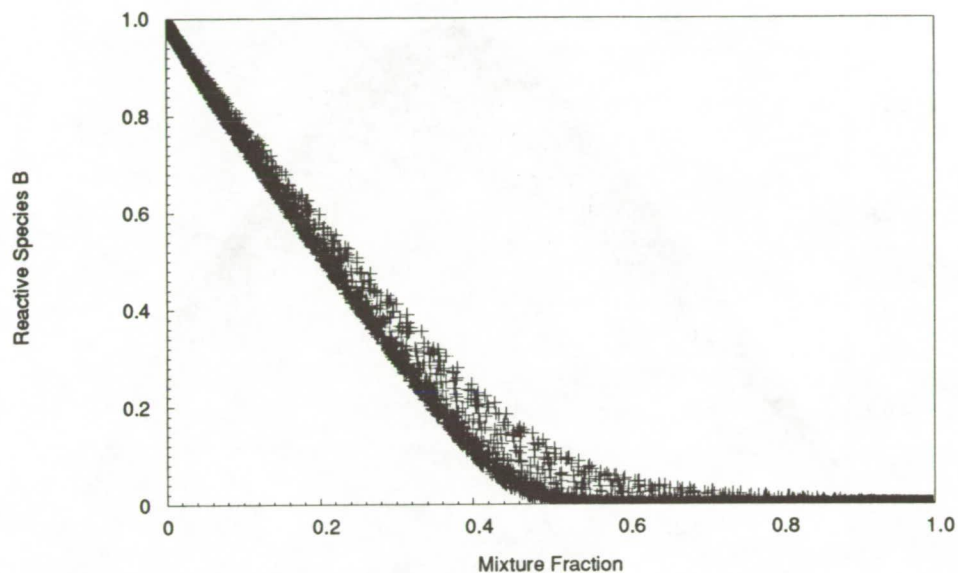


FIGURE 2(B). Distribution of species B mass fraction Y_B , versus mixture fraction ($Da = 1$).

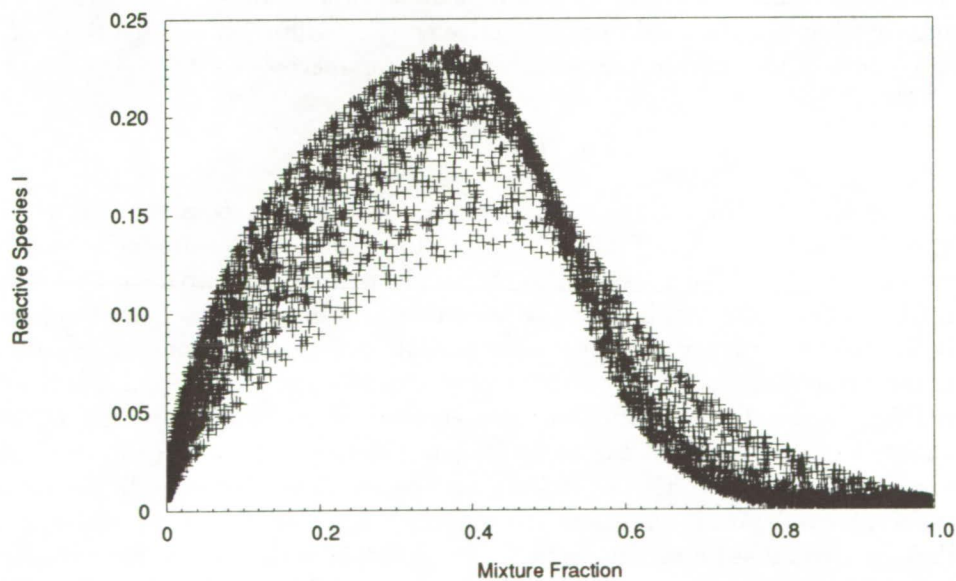


FIGURE 2(C). Distribution of intermediate species I mass fraction Y_I , versus mixture fraction ($Da = 1$).

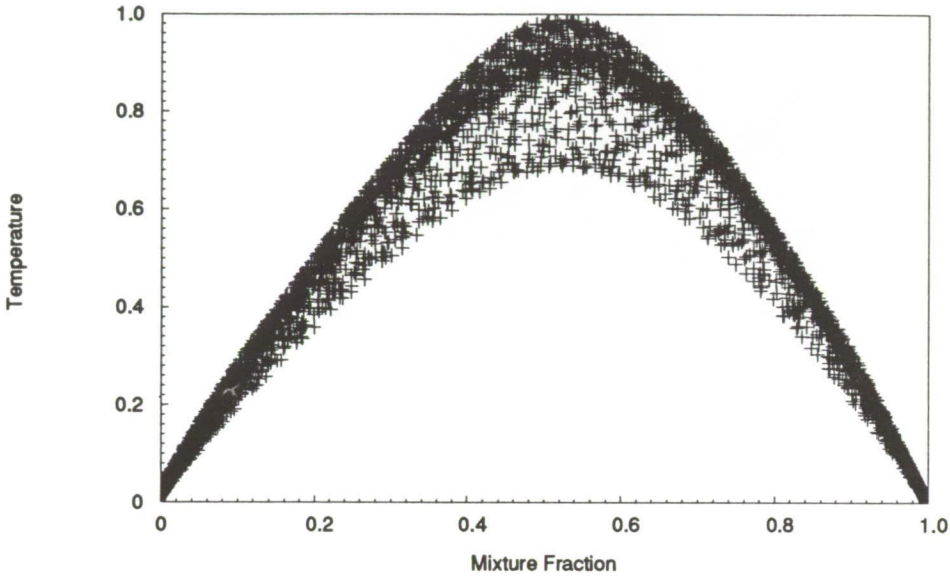


FIGURE 2(D). Distribution of reduced temperature τ versus mixture fraction ($Da = 1$).

less sensitive to extinction either by strain or flame shortening.

A quantity that may be used to characterize reaction-diffusion zones is the scalar dissipation rate of the appropriate scalar, defined for species A as:

$$\chi_A = 2D_A \nabla Y_A \cdot \nabla Y_A \quad (17)$$

In Figures 4(a)-(c), the scalar dissipation rates of scalars A , B , and the intermediate species I are plotted as functions of mixture fraction. Results for species A are very similar to that for species A in the single step case (compare with Figure 2(b) in Chen *et al*, 1992), with the peak occurring at a mixture fraction of approximately 0.7. Note, however, that there are no data points corresponding to frozen flow in the present case. This is consistent with the fact that no extinction was observed for the conditions simulated. Penetration of species A into the B side is apparent, but this is solely due to finite-rate kinetics. The scatter in the data points is due to unsteady effects. Results for species B complement those for A . Results for species I are interesting. If the second reaction were suppressed, it is clear that one would see a minimum in χ_I for $Z = 0.5$, with two symmetric peaks on either side, corresponding to locations where the molecular diffusion of species I would be highest. Note that since I is consumed by A in step2, the peak on the A side is enhanced, relative to the peak on the B side, with the minimum shifted to approximately $Z = 0.4$. This location corresponds to generation of species I by step 1.

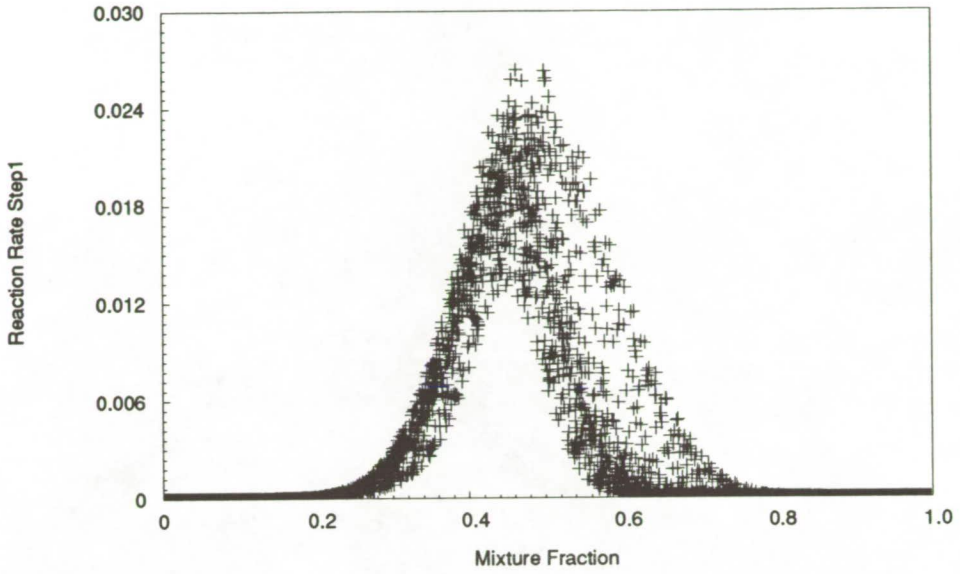


FIGURE 3(A). Distribution of reaction rate for step 1 versus mixture fraction ($Da = 1$).

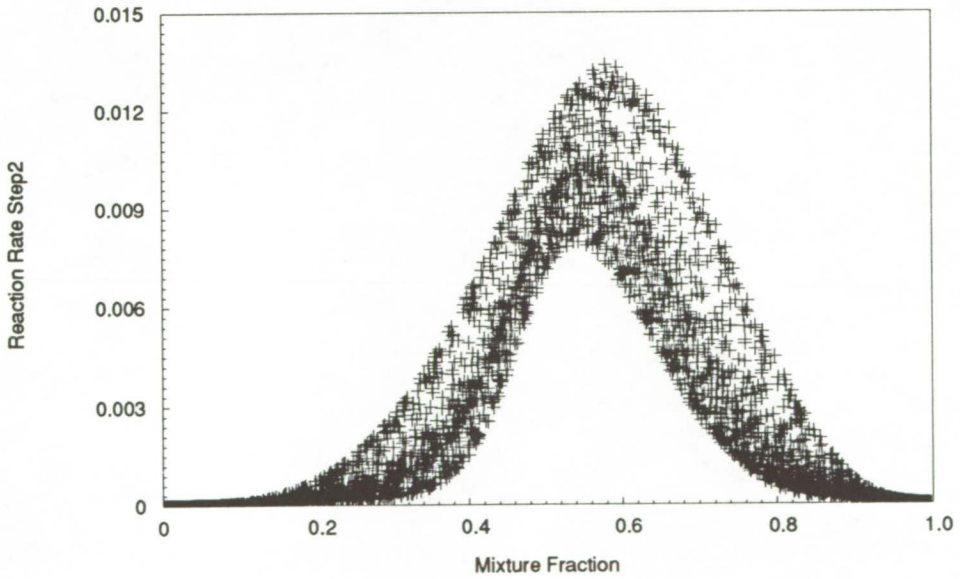


FIGURE 3(B). Distribution of reaction rate for step 2 versus mixture fraction ($Da = 1$).

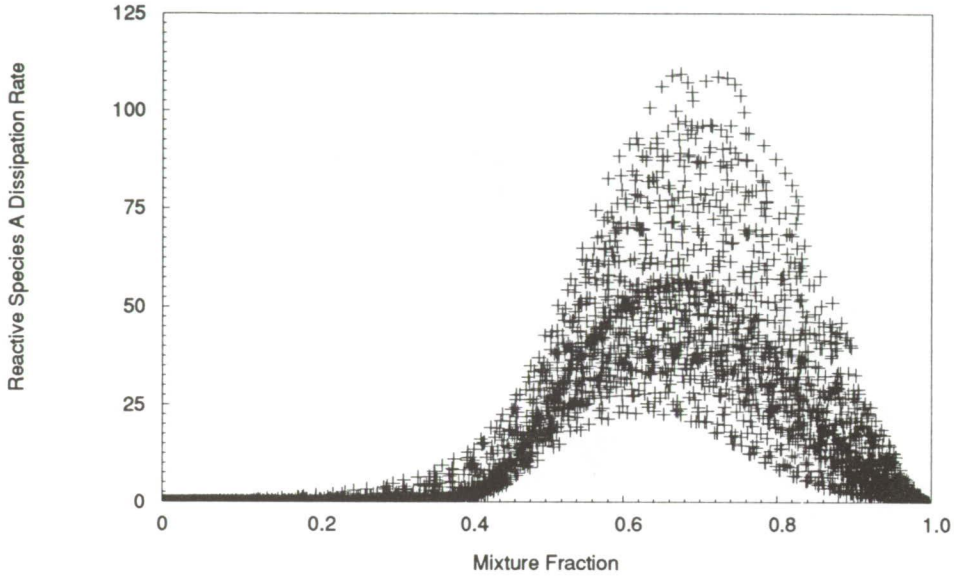


FIGURE 4(A). Distribution of dissipation rate of species *A* versus mixture fraction ($Da = 1$).

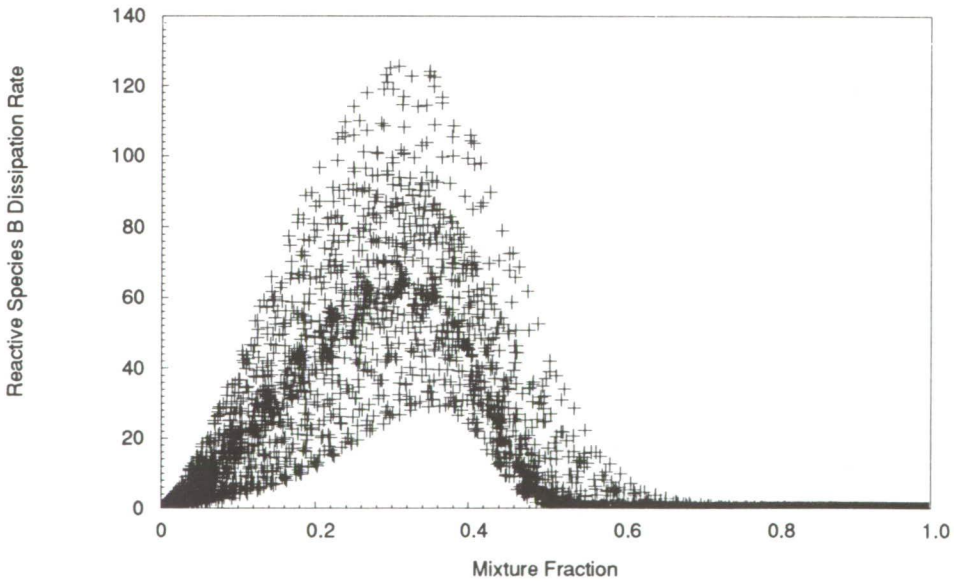


FIGURE 4(B). Distribution of dissipation rate of species *B* versus mixture fraction ($Da = 1$).

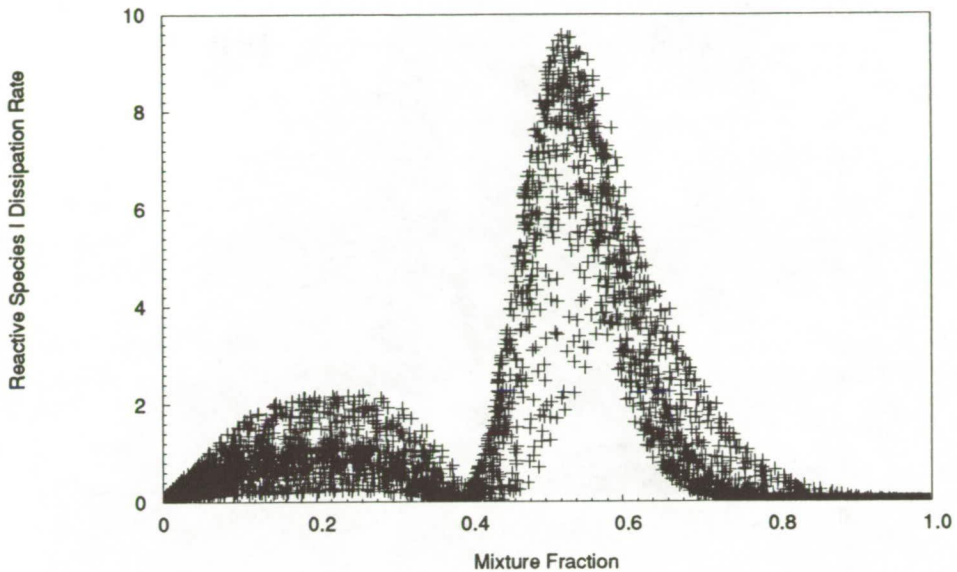


FIGURE 4(c). Distribution of dissipation rate of intermediate species I versus mixture fraction ($Da = 1$).

In Figure 5(a), the distribution of the scalar dissipation rate of the intermediate as a function of the mixture fraction for $Sc_I = 0.5$ is shown. It is clear that the rapidly diffusing intermediate species penetrates further into the A side (compare with Figure 4(c)). Instantaneous contour plots of χ_I in physical space for $Sc_I = 1$ and $Sc_I = 0.5$, shown in Figures 5(b)-(c), reveals that the dissipation zone is larger when the species diffusion coefficient is larger (ie., Sc_I lower). This result suggests that small scale mixing is sensitive to the molecular diffusion coefficient of the intermediate species even though turbulent diffusion is the more active process. It is clear that three dimensional results need to be examined before one can draw definitive conclusions.

In Figure 6, the mixture fraction dissipation rate χ defined as:

$$\chi = 2D\nabla Z \cdot \nabla Z, \quad (18)$$

is plotted as a function of mixture fraction.

This picture is qualitatively similar to the results for single step chemistry presented by Chen *et al* (1992), with the exception that no extinction is observed in the present case. It is clear that a correlation exists between χ and Z contrary to the assumptions made in laminar flamelet theories (Peters, 1986, Warnatz and Rogg, 1986).

4. Conclusions

From the first study of non-premixed flames modeled by a two-step reaction

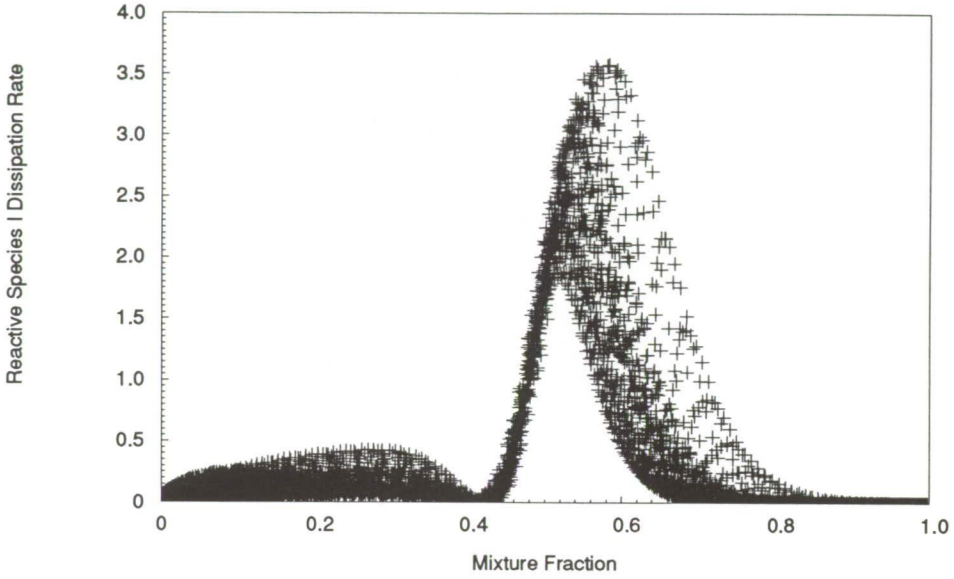


FIGURE 5(A). Distribution of dissipation rate of intermediate species I versus mixture fraction ($Sc_I = 0.5, Da = 1$).

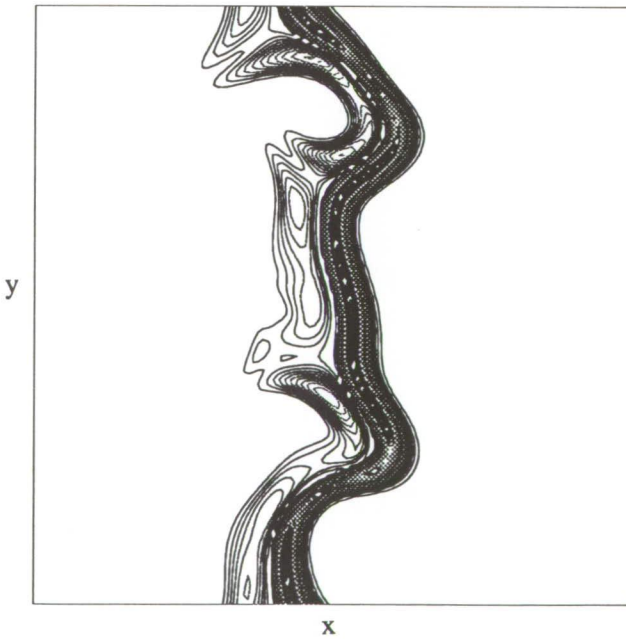


FIGURE 5(B). Intermediate species dissipation rate contours ($Sc_I = 1.0, Da = 1$).

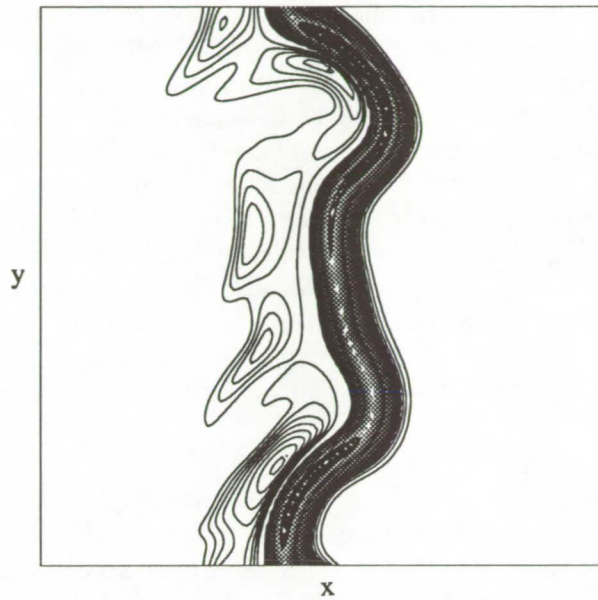


FIGURE 5(C). Intermediate species dissipation rate contours ($Sc_I = 0.5, Da = 1$).

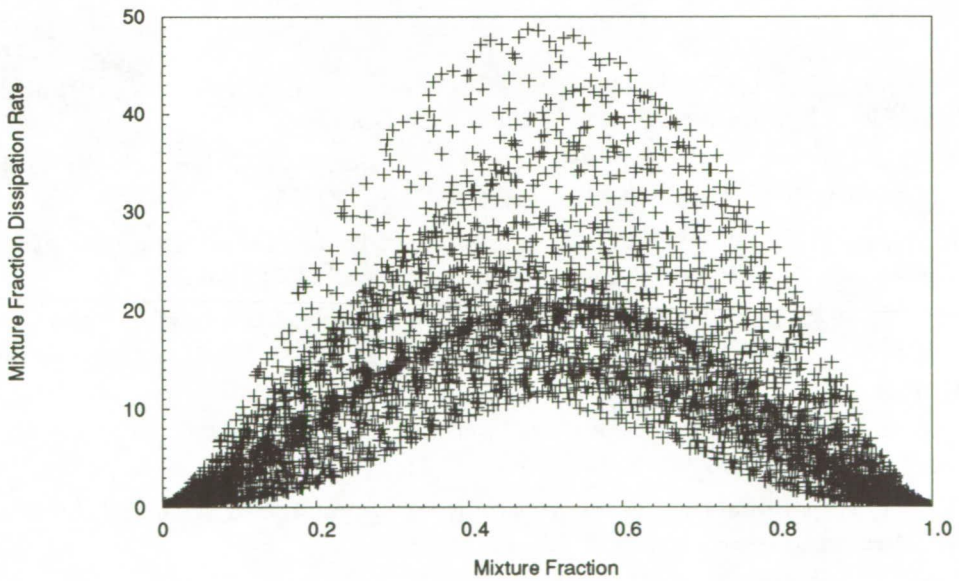


FIGURE 6. Distribution of the scalar dissipation rate χ with respect to the mixture fraction ($Da = 1$).

mechanism in a compressible, turbulent flow, two-dimensional databases were generated. Finite values of the intermediate species mass fraction arise as a result of a slight segregation of the reaction zones associated with the two steps. A consequence of the segregated reaction zones is that the flame is less susceptible to extinction compared to flames modeled with a single-step, having an equivalent overall reaction step. It was demonstrated that the assumption of statistical independence between the mixture fraction and its dissipation rate is a poor one, invalidating an important assumption made in flamelet models. It is expected that these results would hold for three-dimensional simulations currently in progress. Preliminary results from simulations in which the intermediate species diffuses at twice the rate compared to the other species suggest that the small scale mixing process and, hence, the turbulent flame structure is significantly influenced. Further examinations of the flame structure and flame response to turbulence are being carried out.

Acknowledgements

The authors have benefited from discussions with the other members of the combustion group during the 1992 CTR summer program, in particular with Dr. Arnaud Trouvé and Dr. Thierry Poinsot. We also thank Prof. Forman Williams and Prof. Stephen Pope for their helpful comments and suggestions. J. H. Chen has been supported for this work by the department of Energy's Office of Basic Energy Sciences, Division of Chemical Sciences.

REFERENCES

- KERSTEIN, A., DIBBLE R., LONG, M. 1989 Proceedings of the Seventh Turbulent Shear Flows Symposium, Stanford University, Stanford.
- LAW, C. K., CHUNG, S. H. 1982 Steady state diffusion flame structure with Lewis number variations. *Combust. Sci. and Tech.* **29**, 129-145.
- MARGOLIS, S. B., MATKOWSKY, B. J. 1982 Steady and pulsating modes of sequential flame propagation. *Combust. Sci. and Tech.* **27**, 193-213.
- PETERS, N. 1986 Laminar flamelet concepts in turbulent combustion. *Twenty-First Symposium (International) on Combustion*. 1231-1250. The Combustion Institute.
- POINSOT, T., LELE, S. 1991 Boundary conditions for direct simulations of compressible viscous flows. *J. Comput. Phys.* **101**, No 1, July 92
- TROUVE, A. 1991 Simulation of flame-turbulence interaction in premixed combustion. *Annual Research Briefs, CTR, Stanford U.*
- WARNATZ, J., ROGG, B. 1986 Turbulent non-premixed combustion in partially premixed flamelets detailed chemistry. *Twenty-First Symposium (International) on Combustion*. 1533-1541. The Combustion Institute.
- WILLIAMS, F. A. 1985 *Combustion Theory*, Benjamin/Cummings Publishing Company

445373 523-34

189683

403

N94-14768

Stochastic modeling of turbulent reacting flows

By R. O. Fox¹, J. C. Hill², F. Gao³, R. D. Moser⁴, AND M. M. Rogers⁴

Direct numerical simulations of a single-step irreversible chemical reaction with non-premixed reactants in forced isotropic turbulence at $R_\lambda = 63$, $Da = 4.0$, and $Sc = 0.7$ were made using 128^3 Fourier modes to obtain joint pdfs and other statistical information to parameterize and test a Fokker-Planck turbulent mixing model. Preliminary results indicate that the modeled gradient stretching term for an inert scalar is independent of the initial conditions of the scalar field. The conditional pdf of scalar gradient magnitudes is found to be a function of the scalar until the reaction is largely completed. Alignment of concentration gradients with local strain rate and other features of the flow were also investigated.

1. Introduction

Modern treatments of the theory of chemically reacting turbulent flows are often based on the probability density function (pdf) method, since in the pdf equations for the concentrations of the chemical species, the chemical reaction terms are closed in the statistical sense (O'Brien 1980, Pope, 1985). However, the mixing terms involving molecular diffusion are not closed, so statistical models are needed for these terms. The shortcomings of the commonly used coalescence-dispersion models and LMSE closures have been well-documented (Kosály & Givi, 1987, Leonard & Hill, 1991), and more recent closures such as the mapping closure (Chen *et al.* 1989, Pope 1991, Gao 1991) and the linear-eddy model (Kerstein 1991) are being investigated.

In the present study, the Fokker-Planck (FP) closure is applied to the joint scalar-scalar gradient pdf for a two-species, single-step, irreversible chemical reaction



of non-premixed reactants in forced, homogeneous isotropic turbulence. The mass conservation equation for the concentration of reactant A (ϕ_A) is

$$\frac{\partial \phi_A}{\partial t} + u_i \frac{\partial \phi_A}{\partial x_i} = D \frac{\partial^2 \phi_A}{\partial x_i \partial x_i} - S_A, \quad (2)$$

1 Kansas State University

2 Iowa State University

3 Center for Turbulence Research

4 NASA Ames Research Center

where $S_A = -k\phi_A\phi_B$ in the work described here (a similar equation described the concentration of species B). In the current development, it is assumed that the scalar diffusivity D is the same for both reactants and the product of reaction and that all physical properties are constant, including the finite reaction rate constant, k . The joint pdf's of the reactant concentrations and their gradients are used in the model discussed here to avoid problems common with closures based on pdfs of the reactant concentrations alone.

The joint pdf equation for the scalars ϕ_A and ϕ_B and their gradients ψ_A and ψ_B may be written

$$\begin{aligned} \frac{\partial P(\phi_A, \phi_B)}{\partial t} = & -\frac{\partial}{\partial \phi_A} [S_A P] - \frac{\partial}{\partial \phi_B} [S_B P] \\ & - D \frac{\partial^2}{\partial \phi_A^2} [\langle \psi_A^2 | \phi_A, \phi_B \rangle P] - D \frac{\partial^2}{\partial \phi_B^2} [\langle \psi_B^2 | \phi_A, \phi_B \rangle P] \\ & - 2D \frac{\partial^2}{\partial \phi_A \partial \phi_B} [\langle \psi_{A_i} \psi_{B_i} | \phi_A, \phi_B \rangle P] \end{aligned} \quad (3)$$

$$\begin{aligned} \frac{\partial P(\phi_A, \phi_B, \psi_A, \psi_B)}{\partial t} = & -\frac{\partial}{\partial \phi_A} [S_A P] - \frac{\partial}{\partial \phi_B} [S_B P] \\ & - \frac{\partial}{\partial \psi_{A_i}} \left[\frac{\partial S_A}{\partial \phi_A} \psi_{A_i} P \right] - \frac{\partial}{\partial \psi_{B_i}} \left[\frac{\partial S_B}{\partial \phi_B} \psi_{B_i} P \right] \\ & - \text{Molecular mixing terms} \\ & - \frac{\partial}{\partial \psi_{A_i}} [\langle d_{ij} | \phi_A, \phi_B, \psi_A, \psi_B \rangle \psi_{A_i} P] \\ & - \frac{\partial}{\partial \psi_{B_i}} [\langle d_{ij} | \phi_A, \phi_B, \psi_A, \psi_B \rangle \psi_{B_i} P] \end{aligned} \quad (4)$$

where $P(\)$ is the probability density function of its arguments and the arguments to P on the right hand side of each equation are the same as those appearing on the left, S_A and S_B are the reaction source terms (both equal to $-k\phi_A\phi_B$ in this work), $d_{ij} = \partial u_i / \partial x_j$ is the velocity derivative tensor, and the summation convention applies to repeated indices. Clearly, the reaction terms in the above equations are closed. In the traditional scalar pdf formulation involving only concentrations ϕ , the three mixing terms in (3) must be modeled. In the joint pdf formulation studied here, the modeling is postponed to the gradient pdf equation (4), wherein the three molecular mixing terms (not shown) must be modeled as well as the scalar gradient magnification terms, the last two terms in (4). In the development to follow, the FP model studied here is further simplified by considering only a passive progress variable ϕ rather than both reactant concentrations and by treating the diffusion/reaction zones between the two reactants as locally one-dimensional. Among other things, this allows us to consider the magnitude of the scalar gradient $|\psi|$ rather than the full gradient vector.

In this work, we compare the results of stochastic simulations with results from direct numerical simulations (DNS) and sample the DNS results to evaluate various

quantities that appear in the pdf equations. Also, the computed fields were probed for physical insights suggested from previous simulations at lower Reynolds number (Leonard *et al.* 1988 and Leonard & Hill 1988, 1990, 1992).

2. Approach

2.1. Direct numerical simulations

To provide data to check the FP model, a direct numerical simulation of stationary, isotropic turbulence with chemically reacting scalars was carried out using the Rogallo (1981) method with 128^3 Fourier modes and low-wavenumber negative viscosity to provide the forcing. The turbulence was allowed to evolve until it reached statistical equilibrium, at which time scalar fields for the reactant concentrations were initialized and the simulations were continued. Two sets of reacting scalar initial conditions were used in the simulation. Case I was begun from "blob" initial conditions in which the two reactants are segregated into three-dimensional "blobs" with thin diffusion zones between them. The distribution of blobs was determined from a passive scalar field using a method similar to that used by Eswaran & Pope (1988). However, in this case, we follow Leonard & Hill (1991) and use a passive scalar field that has evolved with the turbulence so that the initial blobs are correlated with the velocity field. Case II uses 'slab' conditions, in which the reactants A and B are segregated into "slabs" with two planar (x - z planes) diffusion zones between them in the periodic domain. In both cases, the overall (average) reactant concentrations were in stoichiometric proportions. The Damköhler number or dimensionless reaction rate coefficient was set at $Da \equiv kA_0q^2/\epsilon = 4.0$ where $q^2 \equiv \langle u_i u_i \rangle$ and ϵ is the dissipation rate of the turbulent kinetic energy $2\nu \langle e_{ij} e_{ij} \rangle$ (e_{ij} is the strain rate tensor). The Schmidt number Sc was 0.7 for all species. The simulations were carried out until $t\epsilon/q^2 = 0.968$. Figure 1 shows the reaction zones in the plane $z = 0$ at time $t\epsilon/q^2 = 0.968$ for the two cases, showing the nearly isotropic scalar field for the blob conditions and remnants of the initial dual reaction zones in the slab case.

Comprehensive diagnostics of the simulated fields were generated, including marginal, joint, and conditional pdf's of the concentrations of the reactants and the conserved scalar $\phi = \phi_A - \phi_B$, the magnitudes of their gradients, velocity field properties such as the vorticity and dissipation, and various correlations.

2.2. Gradient alignment analysis

An analysis of the alignment of the reactant concentration gradients was carried out to provide theoretical support for stochastic models and closures that assume one-dimensionality or alignment of scalar gradients in non-premixed systems (this includes flamelet models, conditional moment closures, and the linear eddy model as well as the model developed here). The approach taken was to use (2) to obtain an expression for the evolution of the cosine of the angle μ_{AB} between scalar gradient vectors ψ_A and ψ_B , where $\mu_{AB} = \psi_{Ai}\psi_{Bi}/(|\psi_A||\psi_B|)$. For cases in which $D\mu/Dt = 0$, a linear stability analysis was performed to determine the stability of this state. General results were obtained for arbitrary reaction rate functions $S(\phi)$,

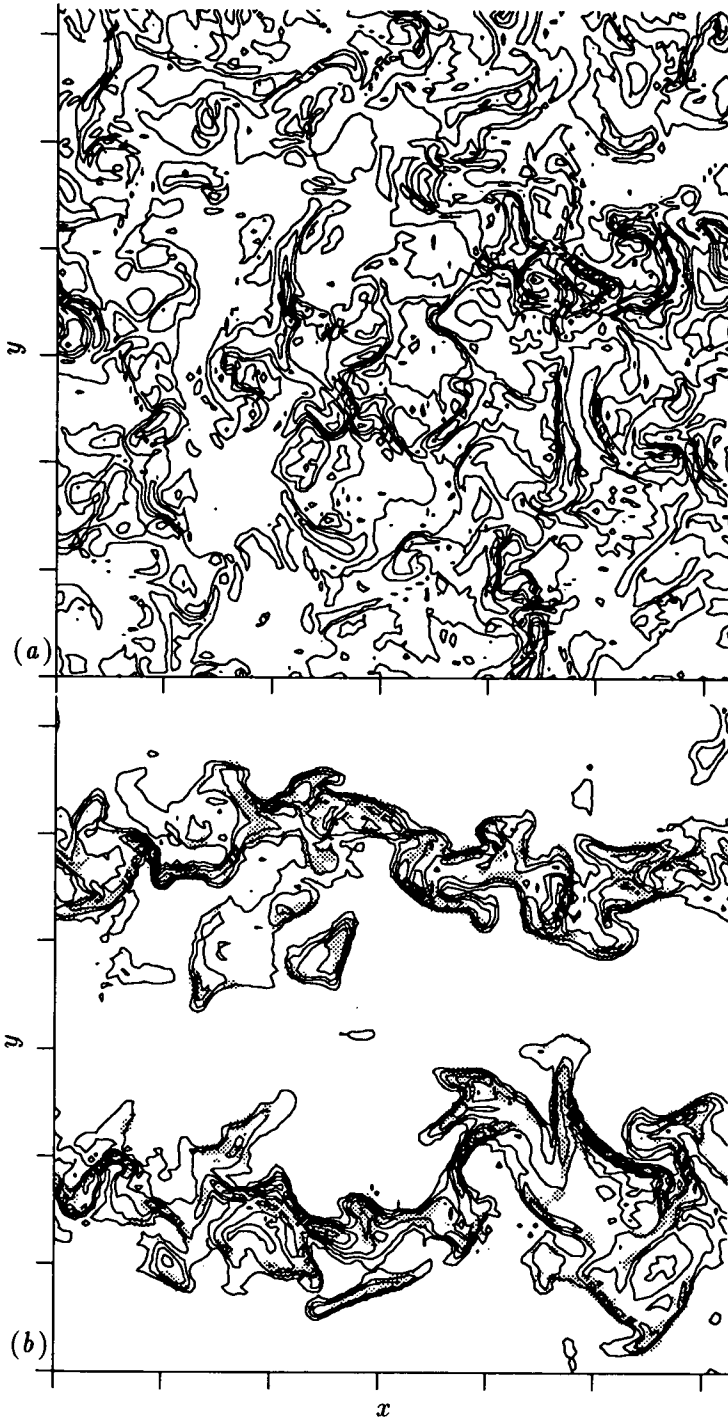


FIGURE 1. Scalar $\phi_A\phi_B$ (reaction rate over k) in an x - y plane at $t\epsilon/q^2 = 0.968$ for (a) blob initial conditions and (b) slab initial conditions. Contour increments are (a) 0.05 and (b) 0.1. Shaded areas indicate large values of the gradient amplification rate ($\psi_{Ai}e_{ij}\psi_{Bj} > 3.0\langle\psi_{Ai}e_{ij}\psi_{Bj}\rangle$).

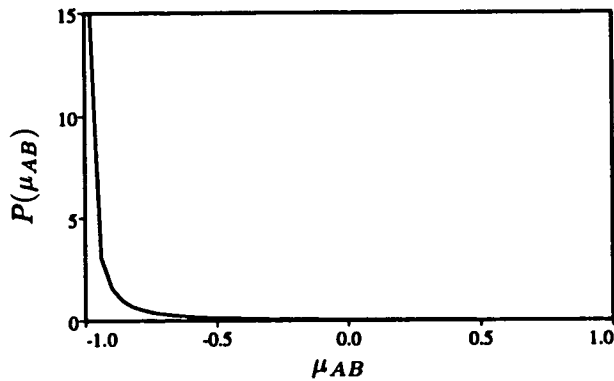


FIGURE 2. PDF of the cosine of the angle between ψ_A and ψ_B at $t\epsilon/q^2 = 0.497$ for the blob case ($\mu_{AB} = \psi_A \cdot \psi_B / (|\psi_A||\psi_B|)$).

including reversible reactions and the temperature-dependent kinetics. In addition, the alignment of reactant gradients with temperature gradient, the reaction product gradient, and the conserved scalar ($\phi_A - \phi_B$) gradient was considered. The results pertinent to this study are summarized here:

1. If $\mu_{AB}(t = 0) = -1$ (gradients initially aligned and opposed in the non-premixed system) then $\mu_{AB}(t)$ remains equal to -1 (aligned), independent of the reaction rate and of the presence of products of reaction (in the reversible case) including temperature, independent of the diffusivities D_A and D_B (which may differ), and independent of the strain rate e_{ij} , except as noted below.
2. A stability analysis of the case described in (1) above shows that in nonisothermal systems, the reactant concentration gradients can become misaligned, depending on the Zeldovich number and on the direction of the temperature gradient with respect to ψ_A .
3. If $\mu_{AB}(0) \neq -1$ (gradients initially misaligned) then the irreversible reaction (1) tends to align the gradients of ϕ_A and ϕ_B .
4. As the reaction rate constant k in (2) becomes large, the reactants become segregated such that $\mu = -1$ on the reaction surface and undefined elsewhere.
5. The alignment of a reacting and non-reacting scalar, say ϕ_A and ϕ , is preserved as in (1) above and is not influenced by the reaction rate even if gradients are initially misaligned.

Thus, in the simple non-premixed reaction case considered here, the initial scalar gradients are aligned ($\mu_{AB} = -1$), and remain aligned for all time. This theoretical result was confirmed in the direct numerical simulations by examining the pdf of μ_{AB} , which is approximately a delta functions at -1 (see figure 2).

2.3 Fokker-Planck closure

A Fokker-Planck (FP) molecular mixing closure was developed by Fox (1992a) to describe the evolution of the joint scalar, scalar gradient pdf in a system of reacting

one-dimensional, random-sized lamellae. Numerical (Fox, 1992b) and theoretical (Sokolov and Blumen, 1991a, 1991b) studies of diffusion in such systems have shown that the joint pdf evolves to a bivariate independent Gaussian pdf. However, if the scalar and scalar gradient are initially correlated, the correlation diminishes at a rate on the order of the scalar dissipation rate suggesting that the scalar and scalar gradient cannot be treated as independent random variables. Fox (1992b) has shown that the FP closure captures the form of the joint pdf and the decay rate of the correlation function for diffusion in random-sized lamellae in the absence of turbulent stretching, and suggested a modification to the closure to include the effect of the latter. In the following subsections, the application and extension of this model to the reacting system under consideration is presented.

2.3.1 A single inert scalar

In the following derivation for an inert scalar, the diffusion is assumed to be locally one-dimensional, so that only the magnitude of the scalar gradient is relevant. In §2.3.2, the alignment results of §2.2 will allow this treatment to be extended to the reacting multiple scalar case. For a scalar ϕ and its gradient ψ , the modified FP closure can be expressed in terms of a pair of stochastic differential equations:

$$d\phi = \kappa^2 A_\phi(\phi, \psi)dt + \kappa B_\phi(\phi, \psi)dW_\phi(t), \quad (5)$$

$$d\psi = \kappa^2 A_\psi(\phi, \psi)dt + C_{\omega^*} \omega^* \psi dt + \kappa B_\psi(\phi, \psi)dW_\psi(t), \quad (6)$$

where A_ϕ , B_ϕ , A_ψ , and B_ψ are functions determined as in Fox (1992a), $C_{\omega^*} \omega^* \psi$ is the gradient stretching term suggested by Fox (1992b), ω^* is the turbulence relaxation rate defined by Pope & Chen (1990) (see (9) below), and

$$\kappa^2 = D\langle\psi^2\rangle/\langle\phi^2\rangle = 6D/\lambda_\phi^2. \quad (7)$$

The turbulence relaxation rate, ω^* , is a random variable defined in terms of the (random) pseudo-dissipation rate,

$$\epsilon^*(x, t) = \nu \frac{\partial u_i}{\partial x_j} \frac{\partial u_i}{\partial x_j}, \quad (8)$$

and the (nonrandom) turbulent kinetic energy, $q^2/2 = \langle u_i u_i \rangle/2$, as

$$\omega^*(x, t) = 2\epsilon^*(x, t)/q^2(t). \quad (9)$$

Pope and Chen (1990) have proposed a stochastic differential equation for ω^* whose coefficients are independent of ϕ and ψ , and which yields a limiting log-normal pdf for ω^* . The gradient stretching constant, C_{ω^*} , is assumed to be independent of the initial conditions.

The FP model can be used to derive equations for the moments of the scalar and its gradient. In particular for an inert scalar in isotropic turbulence, the exact equations for the variance of the scalar is

$$\frac{d\langle\phi^2\rangle}{dt} = -2D\langle\psi^2\rangle, \quad (10)$$

and, from the model, the scalar gradient variance is

$$\frac{d\langle\psi^2\rangle}{dt} = -2C_\psi D \frac{\langle\psi^2\rangle^2}{\langle\phi^2\rangle} + 2C_{\omega^*} \langle\omega^* \psi^2\rangle, \quad (11)$$

where C_ψ is a parameter in the definition of the functions A_ψ and B_ψ in (6). In the absence of turbulence ($\omega^* = 0$), the above equations are closed and constitute a two-equation model for the scalar energy and its dissipation rate. For this case, Fox (1992b) has found that $C_\psi = 3$ gives a good fit to the random-sized lamellae data and is required by the limiting form of $\langle\phi^2\rangle/\langle\psi^2\rangle$ predicted by theory (Sokolov and Blumen, 1991a). Note that if ω^* and ψ are uncorrelated, or if ω^* is nonrandom as is often assumed in pdf modeling studies, then $\langle\omega^* \psi^2\rangle = \langle\omega^*\rangle\langle\psi^2\rangle$ and the equations are again closed. In particular, if $\langle\omega^*\rangle$ is time-independent, the long-time asymptotic behavior of the variances (characterized by constant $\langle\psi^2\rangle/\langle\phi^2\rangle$) can be determined as

$$\frac{d\langle\phi^2\rangle}{dt} \rightarrow -\frac{2C_{\omega^*}}{C_\psi - 1} \langle\omega^*\rangle\langle\phi^2\rangle. \quad (12)$$

Note that the scalar rms decreases exponentially in the limit of large t and the rate is independent of D . Other molecular mixing closures for the scalar pdf, such as the LMSE model (Pope, 1985) usually take

$$\frac{d\langle\phi^2\rangle}{dt} = -C_\phi \langle\omega^*\rangle\langle\phi^2\rangle \quad (13)$$

with $C_\phi = 2.0$.

The FP closure discussed above extends standard scalar mixing models in two ways: (1) it models the scalar dissipation rate instead of assuming that λ_ϕ is constant, and (2) it treats the turbulence relaxation rate as a random variable so that, for example, regions in the flow with large ω^* will be correlated with regions of large scalar gradient and hence with increased mixing and reaction. Direct numerical simulations indicate that these qualitative features are characteristic of turbulent reacting flows (see Leonard and Hill, 1991 and §3).

2.3.2 Multiple reacting scalars

In the FP closure, multiple reactive scalars are handled by first considering an inert scalar ϕ with gradient ψ , which are governed by the stochastic differential equations (5) and (6). Let ϕ_α and ψ_α , $\alpha = 1, \dots, N$, denote reactive scalars and their gradients, respectively, all with the same molecular diffusivity as ϕ , and with linearly dependent initial values; that is $\phi_\alpha(x, y, z, t = 0) = a_\alpha \phi(x, y, z, 0) + b_\alpha$, and $\psi_\alpha(x, y, z, 0) = a_\alpha \psi(x, y, z, 0)$. As discussed by Pope (1985), the molecular mixing model to be developed below must be linear in the scalars ϕ_α , so in the absence of source terms

$$\frac{\partial \phi_\alpha}{\partial t} = F(\phi, \psi) \phi_\alpha + G_i(\phi, \psi) \psi_{\alpha i} - \langle F(\phi, \psi) \phi_\alpha \rangle - \langle G_i(\phi, \psi) \psi_{\alpha i} \rangle, \quad (14)$$

where F and G_i are functions to be determined. Using the same arguments, it can be shown that a similar linearity property must hold for ϕ_α . Moreover, when the source term is zero, $\phi_\alpha(x, y, z, t) = a_\alpha\phi(x, y, z, t) + b_\alpha$ and $\psi_\alpha(x, y, z, t) = a_\alpha\psi(x, y, z, t)$ for all t . The scalars thus remain correlated for all time, implying that the same two Wiener processes (W_ϕ and W_ψ) that appear in (5) and (6) must also appear in the equations for ϕ_α and ψ_α (Fox, 1992a). Equivalently, the multiple reactive scalar model can be formulated in terms of $d\phi$ and $d\psi$ as follows.

Assume that a local one-to-one differentiable mapping exists between ϕ and ϕ_α , namely $\phi_\alpha = \Phi_\alpha(\phi, t)$. Differentiation then leads to an expression for the time-derivative of Φ_α :

$$\frac{\partial\Phi_\alpha}{\partial t} = D\psi^2 \frac{\partial^2\Phi_\alpha}{\partial\phi^2} + S_\alpha(\Phi_1, \dots, \Phi_N), \quad (15)$$

Given ϕ and ψ , (15) is closed; however, it cannot be conveniently solved using Monte Carlo methods.

It is interesting that the conditional moment closure (CMC) (Bilger 1991) employs a similar mapping equation:

$$\frac{\partial\Phi_\alpha}{\partial t} = D\langle\psi^2 | \phi\rangle \frac{\partial^2\Phi_\alpha}{\partial\phi^2} + S_\alpha(\Phi_1, \dots, \Phi_N), \quad (16)$$

where $D\langle\psi^2 | \phi\rangle$ is the conditional scalar dissipation rate of the inert scalar given ϕ . The CMC mapping equation is closed given ϕ and results in a joint pdf for ϕ and ϕ_α with a 1-dimensional support (it falls on a curve in (ϕ, ϕ_i) -space). However, in the current formulation, the support will, in general, be 2-dimensional since each value of ψ will result in a separate curve in (ϕ, ϕ_i) -space. Mell *et al.* (1992) have solved the CMC mapping equation numerically for the reaction $A + B \rightarrow P$ with $D\langle\psi^2 | \phi\rangle$ and the pdf of ϕ taken directly from DNS, and found good agreement with the joint pdf of ϕ and ϕ_A computed from the DNS data (the curve computed by CMC falls near the maximum of the joint pdf found by DNS). In addition, they found that the CMC results are insensitive to the functional form used for $D\langle\psi^2 | \phi\rangle$, which suggests that the source term may dominate the diffusion term in the mapping equation. We therefore hope that the crude model used for this term below will be adequate.

In order to apply a Monte Carlo method, $d\phi_\alpha$ is written in terms of its partial derivatives:

$$d\phi_\alpha = \frac{\partial\Phi_\alpha}{\partial\phi} d\phi + \frac{\partial\Phi_\alpha}{\partial t} dt, \quad (17)$$

or substituting (15)

$$d\phi_\alpha = \frac{\partial\Phi_\alpha}{\partial\phi} d\phi + D\psi^2 \left(\frac{\partial^2\Phi_\alpha}{\partial\phi^2} \right) dt + S_\alpha(\phi_1, \dots, \phi_N) dt. \quad (18)$$

In (18) the diffusion term (premultiplied by D) is zero if the source term is zero or linear. Also, if the source term is such that Φ_α is time invariant (e.g., an infinitely fast bimolecular reaction) the sum of the diffusion and source terms is zero. Otherwise it must be closed in terms of the ϕ , ψ , ϕ_α and ψ_α , and the closure must be

linear in ϕ_α and ψ_α as discussed above. The simplest closure hypothesis is to assume that this term is independent of the modeled variables, leading to the simplest model of the form (14):

$$d\phi_\alpha = \frac{\partial\Phi_\alpha}{\partial\phi} d\phi - \left\langle \frac{\partial\Phi_\alpha}{\partial\phi} d\phi \right\rangle + S_\alpha(\phi_1, \dots, \phi_N) dt. \quad (19)$$

The terms involving $\partial\Phi_\alpha/\partial\phi$ are closed in terms of ψ_α (see below).

To obtain a similar expression for $d\psi_{\alpha i}$, note that our assumed form for ϕ_α implies that

$$\psi_{\alpha i} = \frac{\partial\phi_\alpha}{\partial x_i} = \frac{\partial\Phi_\alpha}{\partial\phi} \psi_i \quad (20)$$

The total derivative of $\psi_{\alpha i}$ is thus

$$d\psi_{\alpha i} = \frac{\partial^2\Phi_\alpha}{\partial\phi^2} \psi_i d\phi + \frac{\partial\Phi_\alpha}{\partial\phi} d\psi_i + \frac{\partial^2\Phi_\alpha}{\partial t \partial\phi} \psi_i dt. \quad (21)$$

The time derivative term can be evaluated by differentiating (15) with respect to x_i to obtain

$$\psi_i \frac{\partial^2\Phi_\alpha}{\partial t \partial\phi} = D \frac{\partial^3\Phi_\alpha}{\partial\phi^3} \psi^2 \psi_i + D \frac{\partial^2\Phi_\alpha}{\partial\phi^2} \frac{\partial\psi^2}{\partial x_i} + \sum_\beta \frac{\partial S_\alpha}{\partial\phi_\beta} \frac{\partial\Phi_\beta}{\partial\phi} \psi_i \quad (22)$$

which when substituted into (21) yields

$$\begin{aligned} d\psi_{\alpha i} = & \frac{\partial^2\Phi_\alpha}{\partial\phi^2} \psi_i d\phi + \frac{\partial\Phi_\alpha}{\partial\phi} d\psi_i \\ & + D \frac{\partial^3\Phi_\alpha}{\partial\phi^3} \psi^2 \psi_i dt + D \frac{\partial^2\Phi_\alpha}{\partial\phi^2} \frac{\partial\psi^2}{\partial x_i} dt + \sum_\beta \frac{\partial S_\alpha}{\partial\phi_\beta} \frac{\partial\Phi_\beta}{\partial\phi} \psi_i dt \end{aligned} \quad (23)$$

Terms involving more than one derivative of Φ_α are not closed with respect to ϕ_α and ψ_α . The first term is modeled as zero, which is exact if S_i is zero or linear and the diffusion terms are modeled as in (19) yielding

$$d\psi_{\alpha i} = \frac{\partial\Phi_\alpha}{\partial\phi} d\psi_i - \left\langle \frac{\partial\Phi_\alpha}{\partial\phi} d\psi_i \right\rangle + \sum_\beta \frac{\partial S_\alpha}{\partial\phi_\beta} \frac{\partial\Phi_\beta}{\partial\phi} \psi_i dt \quad (24)$$

The functional form of $\psi_{\alpha i}$ in (20) implies that all the scalar gradients are aligned with the gradient of the inert scalar ϕ , in agreement with the analysis in §2.2. Therefore, it is not necessary to treat ψ_α and ψ as vectors. Without loss of generality we can let $\psi_\alpha = \psi_{\alpha i} \psi_i / |\psi|$ (the projection of ψ_α onto the ψ direction) and $\psi = |\psi|$. This is also consistent with the one-dimensional nature of the FP model for the inert scalar (equations (5) and (6)). It is also clear that $\partial\Phi_\alpha/\partial\phi = \psi_\alpha/\psi$. With these simplifications the final model equations for the evolution of ϕ_α and ψ_α are

$$\frac{\partial\phi_\alpha}{\partial t} = \frac{\psi_\alpha}{\psi} \frac{\partial\phi}{\partial t} - \left\langle \frac{\psi_\alpha}{\psi} \frac{\partial\phi}{\partial t} \right\rangle + S_\alpha(\phi_1, \dots, \phi_N) \quad (25)$$

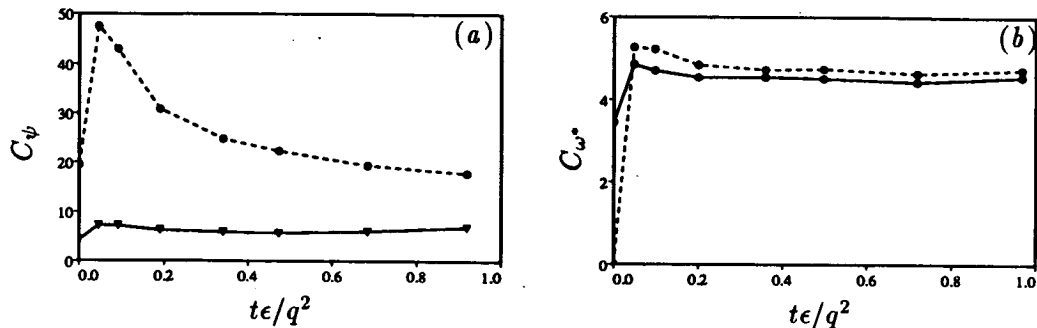


FIGURE 3. Evolution of the model constants (a) C_ψ and (b) C_{ω^*} in the direct numerical simulation for — blob initial conditions and ---- slab initial conditions.

$$\frac{\partial \psi_\alpha}{\partial t} = \left(\frac{1}{\psi} \frac{\partial \psi}{\partial t} \right) \psi_\alpha - \left(\frac{\psi_\alpha}{\psi} \frac{\partial \psi}{\partial t} \right) + \sum_\beta \frac{\partial S_\alpha}{\partial \phi_\beta} \psi_\beta, \quad (26)$$

which in the absence of source terms are linear as required.

Since the marginal pdfs of ψ and ψ_α are both symmetric about zero, the expected value of ψ obtained from (26) should be zero for all time. The FP closure for ψ_α is similar to the LMSE closure since, in the absence of source terms, $\partial \ln |\psi_\alpha| / \partial t = \partial \ln |\psi| / \partial t$. But since $\partial \ln |\psi| / \partial t$ is not constant, the two closures are not identical; in particular, with the FP closure the joint pdf of ϕ and ψ evolves to a bivariate Gaussian (Fox, 1992a).

The FP closure can be extended to scalars with nonequal molecular diffusivities by including a separate inert scalar with the same molecular diffusivity as each corresponding reactive scalar. The stochastic differential equations for the new inert scalars have the same form as Eqs. (5) and (6) except with κ^2 modified to include the correct molecular diffusivity. The same Wiener processes (W_ϕ and W_ψ) must appear in each pair of stochastic differential equations as discussed by Fox (1992a).

2.4 Evaluation of model constants

The FP closure has two “universal” constants C_ψ and C_{ω^*} whose values can be determined using DNS data. The exact equations for an inert scalar and the magnitude of its gradient in a three-dimensional flow are

$$\frac{D\phi}{Dt} = D\nabla^2 \phi, \quad (27)$$

$$\frac{D\psi^2}{Dt} = 2D\psi_i \frac{\partial^2 \psi_i}{\partial x_j \partial x_j} - 2\psi_i e_{ij} \psi_j, \quad (28)$$

where e_{ij} is the strain rate tensor. By comparing the expected value of (28) with (11) derived from the FP model, the model constants can be evaluated as

$$C_{\omega^*} = - \frac{\langle \psi_i e_{ij} \psi_j \rangle}{\langle \omega^* \psi^2 \rangle}, \quad (29)$$

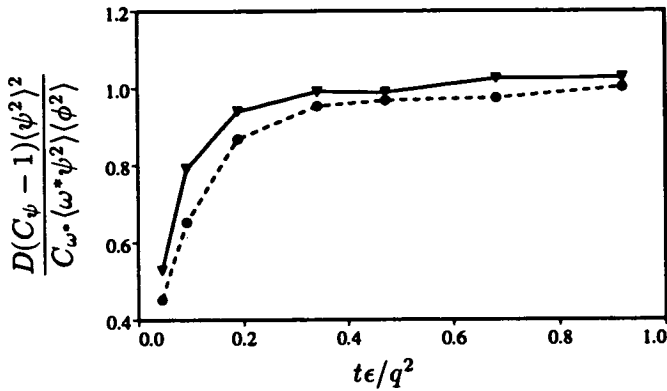


FIGURE 4. Evolution of $\frac{D(C_\psi - 1)\langle\psi^2\rangle^2}{C_{\omega^*}\langle\omega^*\psi^2\rangle\langle\phi^2\rangle}$ evaluated from DNS for — blob and ---- slab initial conditions.

and

$$C_\psi = -\frac{\langle\psi_i\nabla^2\psi_i\rangle\langle\phi^2\rangle}{\langle\psi^2\rangle^2}. \quad (30)$$

The model constants, evaluated from the direct numerical simulations using (29) and (30), are shown as functions of time in figure 3. It is clear from figure 3a that the gradient mixing constant, C_ψ , depends strongly on initial conditions. For the anisotropic slab initial conditions, C_ψ decreases steadily with time after an initial jump. On the other hand, for the isotropic blob initial conditions, $C_\psi \approx 6.7$ for all time. This difference is most likely due the difference in integral length scales of the scalar fields in the two cases. Integral length scale effects have not yet been incorporated into the FP closure, but have been shown to have a significant effect on the scalar dissipation rate (Eswaran and Pope, 1988; Eswaran and O'Brien, 1989; Kosály, 1989; Jiang and O'Brien, 1991). For the slab case, scalar integral length scales are initially infinite in two directions and decrease as the turbulent advection creates a more isotropic field. For the blob case, the integral length scale is approximately constant for all time. In contrast, the gradient stretching constant, C_{ω^*} , shown in figure 3b appears to be independent of initial conditions and approximately equal to 4.7 for all time.

An expression relating C_ψ and C_{ω^*} can be found from the limiting value of $\lambda_\phi^2 = 6\langle\phi^2\rangle/\langle\psi^2\rangle$. From Eqs. (10) and (11) for the FP model, the following relation is found for λ_ϕ^2 :

$$\frac{d\lambda_\phi^2}{dt} = 12D(C_\psi - 1) - 2C_{\omega^*}\frac{\langle\omega^*\psi^2\rangle}{\langle\psi^2\rangle}\lambda_\phi^2. \quad (31)$$

For statistically stationary ω^* , (31) has a single stable limiting solution:

$$\lambda_\phi^2/6 = \frac{\langle\phi^2\rangle}{\langle\psi^2\rangle} = \frac{D(C_\psi - 1)\langle\psi^2\rangle}{C_{\omega^*}\langle\omega^*\psi^2\rangle}. \quad (32)$$

Thus, if the model has asymptotic behavior consistent with the DNS, we should find that

$$\frac{D(C_\psi - 1)\langle\psi^2\rangle^2}{C_{\omega^*}\langle\omega^*\psi^2\rangle\langle\phi^2\rangle} \rightarrow 1 \quad (33)$$

for large t . The left side of (33) is plotted as a function of time in figure 4 for both the slab and blob cases. For both cases this quantity does indeed approach 1.

Mantel and Borghi (1991) have proposed a two-equation model for scalar energy, scalar dissipation similar in form to (10) and (11) but with $\langle\omega^*\rangle\langle\psi^2\rangle$ in place of $\langle\omega^*\psi^2\rangle$. In their model, the coefficients are defined in terms of a turbulence Reynolds number $Re_t = \sqrt{(q^2/2)}l_t/\nu$ so that, for large Re_t , $C_\psi = \beta_0\sqrt{Re_t}/2$, and $C_{\omega^*} = \alpha_0\sqrt{Re_t}/2$, with $\alpha_0 = 0.9$ and $\beta_0 = 1.25$ found by DNS (Borghi *et al.*, 1992). For $Re_t = 194$ of the present DNS simulations, these expressions yield $C_\psi = 8.7$ and $C_{\omega^*} = 6.3$. These estimates are both 30% larger than the values given above, implying that the ratio C_ψ/C_{ω^*} is similar. Since $C_\psi = 3$ in the limit where $Re_t = 0$ (Fox, 1992b), the Reynolds number dependence embodied in these large- Re_t relations may not be valid for these relatively low Reynolds number DNS computations. (Although the Re_t values for the DNS runs used to determine α_0 and β_0 have not yet appeared in the literature (Borghi *et al.*, 1992), they must be small due to the limitations of DNS.) This fact may explain some of the discrepancies between the two sets of values for the model constants.

2.5 Application to the single-step reaction

The FP closure described above has been used to generate joint pdfs of the reactant concentrations and their gradients for the 2-component, single-step reaction scheme (1) using a Monte Carlo simulation. For this reaction (25) and (26) yield:

$$d\phi_A = \frac{\psi_A}{\psi}d\phi - \left\langle\frac{\psi_A}{\psi}d\phi\right\rangle - k\phi_A\phi_B dt, \quad (34)$$

$$d\phi_B = \frac{\psi_B}{\psi}d\phi - \left\langle\frac{\psi_B}{\psi}d\phi\right\rangle - k\phi_A\phi_B dt, \quad (35)$$

$$d\psi_A = \frac{\psi_A}{\psi}d\psi - \left\langle\frac{\psi_A}{\psi}d\psi\right\rangle - k\phi_A\psi_B dt - k\phi_B\psi_A dt, \quad (36)$$

and

$$d\psi_B = \frac{\psi_B}{\psi}d\psi - \left\langle\frac{\psi_B}{\psi}d\psi\right\rangle - k\phi_A\psi_B dt - k\phi_B\psi_A dt. \quad (37)$$

The Monte Carlo algorithm uses fractional time-stepping to split the mixing and reaction steps into separate processes (Pope, 1985; Fox, 1992a). The expected values appearing in (34)–(37) are computed during the mixing step so that the mean values of the scalars and scalar gradients are constant during mixing. A constant turbulence relaxation rate, $\omega^* = \langle\omega^*\rangle$ was used in (6). The resulting joint pdf's are compared to the DNS results below.

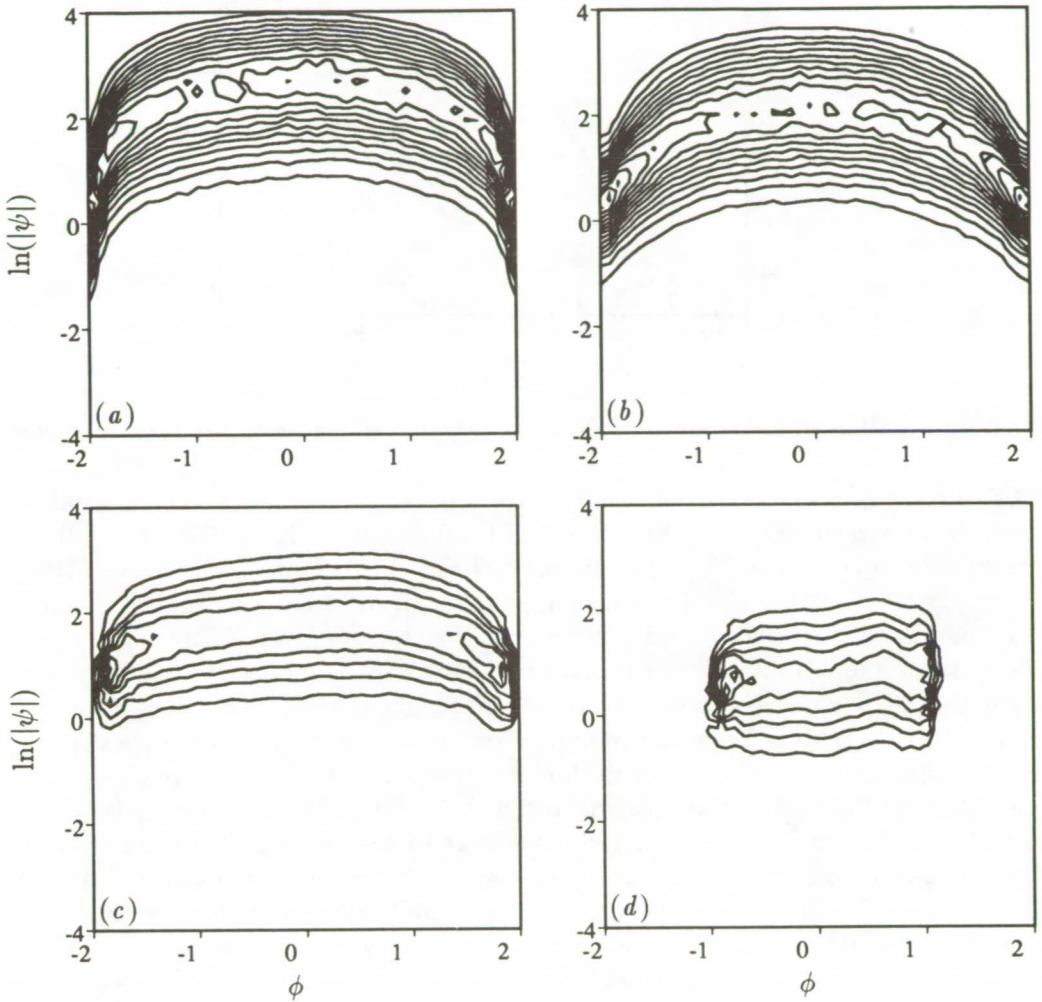


FIGURE 5. Conditional PDF of $\ln(|\psi|)$ given ϕ ($P(\ln(|\psi|) | \phi)$) for the direct numerical simulation with (a,b) slab initial conditions and (c,d) blob initial conditions at (a,c) $t\epsilon/q^2 = 0.497$ and (b,d) $t\epsilon/q^2 = 0.968$. At these times $\phi_{\text{rms}}/\phi_{\text{rms}}(t=0)$ is (a) 0.846, (b) 0.645, (c) 0.426, and (d) 0.172.

3. Results

3.1 Statistics of the inert scalar field

The DNS data have been used to compute a wide range of statistics involving the inert and reactive scalars and the magnitudes of their gradients. The marginal pdf $P(\phi)$ for the inert scalar is nearly identical in shape, at a given rms value, to those reported in previous DNS studies. The marginal pdf of the log of the magnitude of the inert scalar gradient, $P(\ln |\psi|)$, approaches a nearly Gaussian form, but with a slightly longer negative tail, in agreement with the DNS results of Eswaran and Pope (1988).

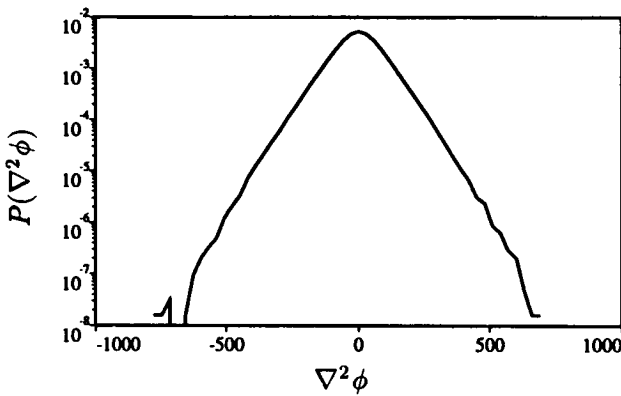


FIGURE 6. PDF of $\nabla^2\phi$ for the DNS with blob initial conditions at $t\epsilon/q^2 = 0.968$.

Of greater interest is the joint pdf of the inert or conserved scalar, ϕ , and its gradient, ψ , which has been the subject of both theory (Bilger, 1976; Fox, 1992a, 1992b; Gao and O'Brien, 1991; Meyers and O'Brien, 1981; Valiño and Dopazo, 1991) and experiments (Anselmet and Antonia, 1985). In most reactive mixing closures (e.g., the flamelet model), ϕ and ψ are assumed to be independent so that the joint pdf is separable, $P(\phi, \psi; t) = P(\phi; t)P(\psi; t)$. In order to check for independence using the DNS data, the conditional pdf of ψ given ϕ , defined by $P(\psi|\phi; t) = P(\phi, \psi; t)/P(\phi; t)$, has been computed. Note that if ϕ and ψ are independent, then $P(\psi|\phi; t) = P(\psi; t)$ and will thus be independent of ϕ . Examples of the computed conditional pdf are shown in figure 5. From figure 5a ($\phi_{\text{rms}}/\phi_{\text{rms}}(t=0) = 0.846$) it can be seen that near the start of the molecular mixing process, the scalar and scalar gradient are correlated. The correlation decays slowly so that in figure 5b ($\phi_{\text{rms}}/\phi_{\text{rms}}(0) = 0.645$) the conditional pdf continues to show a important ϕ -dependence. Not until the molecular mixing process is farther along ($\phi_{\text{rms}}/\phi_{\text{rms}}(0) = 0.172$) as shown in figure 5d does the conditional pdf appear to be independent of ϕ .

Another interesting pdf is that of the Laplacian of ϕ shown in figure 6 on a log-linear plot for $\phi_{\text{rms}}/\phi_{\text{rms}}(0) = 0.172$. As is clear from the form of the pdf, it is non-Gaussian with nearly exponential tails over 4 decades.

3.2 Statistics for inert scalar mixing

Statistics involving the scalar or scalar gradient and various turbulence quantities have been computed using the DNS data. For example, the scalar gradient-turbulence relaxation rate correlation function, defined by

$$\frac{\langle \omega^* \psi^2 \rangle}{\langle \omega^* \rangle \langle \psi^2 \rangle} - 1, \quad (38)$$

was found to be approximately time independent with values of 0.06 for the blob case and 0.15 for the slab case, indicating that ω^* and ψ^2 have a slight tendency to be simultaneously larger than their mean value. This tendency can be seen

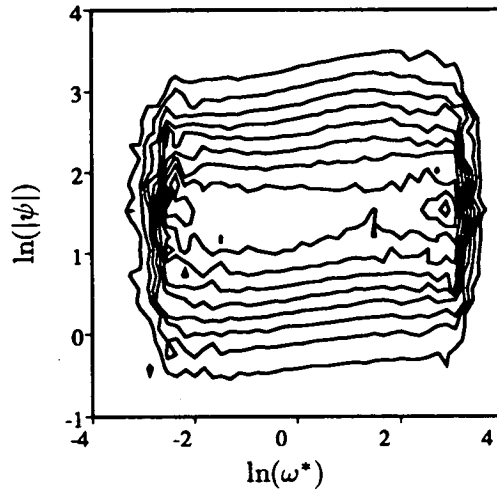


FIGURE 7. Conditional pdf of $\ln(|\psi|)$ given $\ln(\omega^*)$ for the DNS with slab initial conditions at $t\epsilon/q^2 = 0.968$.

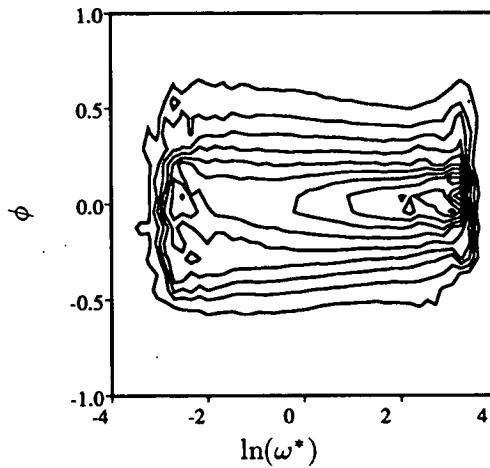


FIGURE 8. Conditional pdf of ϕ given $\ln(\omega^*)$ for the DNS with blob initial conditions at $t\epsilon/q^2 = 0.968$.

more clearly by examining the conditional pdf of $\ln(|\psi|)$ given $\ln(\omega^*)$ shown in figure 7 (slab case with $\phi_{\text{rms}}/\phi_{\text{rms}}(0) = 0.645$). From this figure it can be seen that the conditional pdf has a nearly constant shape but shifts upward as $\ln(\omega^*)$ increases. This behavior is consistent with the FP closure (6) wherein ω^* appears as a stretching (positive) term in the drift coefficient.

Similar conclusions can be drawn from the conditional pdf of ϕ given $\ln(\omega^*)$ shown in figure 8 for the blob case at $\phi_{\text{rms}}/\phi_{\text{rms}}(0) = 0.172$. There it can be seen that larger values of $\ln(\omega^*)$ lead to smaller conditional variances for ϕ . This is consistent with the model equations in that large $\ln(\omega^*)$ leads to large gradients and hence

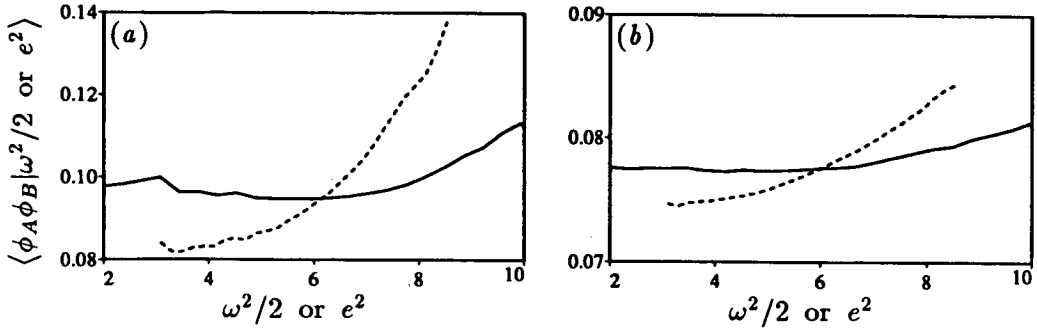


FIGURE 9. Conditional expectation of $\phi_A \phi_B$ (reaction rate over k) given — entropy (ω^2) and ---- dissipation (e^2) for (a) slab initial conditions and (b) blob initial conditions at $t\epsilon/q^2 = 0.968$.

faster scalar dissipation.

Finally, as noted by Pope and Chen (1990), the DNS simulations confirm that the log of the pseudo-dissipation rate of the turbulence, $\ln \epsilon^*$ is more nearly Gaussian than is the log of the true turbulence dissipation rate, $\ln \epsilon$. For example, the skewness and flatness of $\ln \epsilon^*$ are -0.06 and 3.05 , respectively, compared to -0.29 and 3.24 for $\ln \epsilon$ at $t\epsilon/q^2 = 0.968$

3.3 Statistics of reacting scalars

Some statistical quantities evaluated in previous simulations in decaying turbulence at lower Reynolds numbers (Leonard *et al.* 1988, Leonard & Hill 1988, 1990, 1992) and in a similar study for a non-reacting system (Nomura & Elgobashi 1992) were examined in order to determine the extent to which the present system exhibits the same physical behavior. For example, pdf's of the cosine between the directions of the reactant scalar gradients and the eigenvectors of the strain rate tensor, and plots of the eigenvectors superposed on reaction rate contours, show that there is considerable tendency for the most compressive eigenvector to align with the scalar gradients and to lie across the reaction zone. Furthermore, there is a similar but less pronounced tendency for the intermediate strain rate eigenvector to lie tangent to the reaction zones and isoscalar surfaces.

Figures 9 and 10 show the effect of certain kinematic quantities on the reaction rate, and *vice versa*, at $t=0.92$. In figure 9, for reaction rate conditioned on levels of strain and enstrophy, $\langle \phi_A \phi_B | e^2 \rangle$ and $\langle \phi_A \phi_B | \omega^2/2 \rangle$ where $e^2 = e_{ij}e_{ij}$, it is seen that strain has a marked effect on reaction rate, but the effect of vorticity is considerably less. The converse plot, figure 10 for strain and enstrophy conditioned on reaction rate, confirms the previous observation of Leonard & Hill (1990) that conditional averages of e^2 and $\omega^2/2$ are near their volume averages and each other, except for the regions of most intense reaction rate where the straining is very high and the enstrophy is appreciably less than the volume averaged value.

Regions where the gradient amplification term, $\langle \psi_{A_i} e_{ij} \psi_{B_j} \rangle$, is greater than $3.0 \langle \psi_{A_i} e_{ij} \psi_{B_j} \rangle$ are shaded in figure 1b. Clearly the largest values of this term are associated with peak values in the reaction rate, supporting earlier claims by

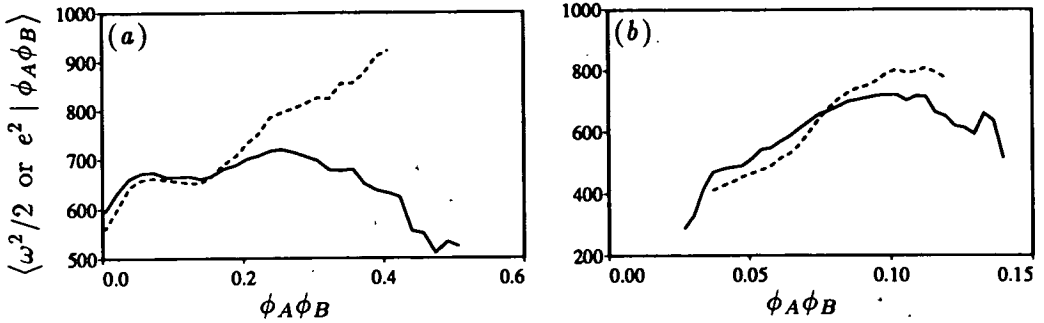


FIGURE 10. Conditional expectation of — entrophy (ω^2) and ---- dissipation (e^2) given $\phi_A \phi_B$ (reaction rate over k) for (a) slab initial conditions and (b) blob initial conditions at $t\epsilon/q^2 = 0.968$.

Leonard & Hill (1990, 1992) and underlining the importance of the modeled gradient amplification term in the FP model. Although not shown, the gradient amplification term seldom takes on negative values and since ψ_A and ψ_B tend to be aligned and opposing in the reaction zone, the compressive part of e_{ij} must dominate this term as expected.

Finally, various scalar gradient-strain rate correlation coefficients important in mixing studies were evaluated. One such quantity, $\langle \psi_{A_i} e_{ij} \psi_{B_j} \rangle / \langle \psi_{A_i} \psi_{B_i} \rangle \sqrt{e^2}$, approaches the value -0.45 for the slab case and -0.40 for the blob case; the same values are obtained for the conserved or inert scalar ϕ in these two cases. These values differ somewhat from the values -0.56 and -0.45 (-0.52 and -0.43 for the nonreacting scalars) found in decaying turbulence by Leonard & Hill (1990) and the value -0.5 found by Kerr (1985) for a nonreacting scalar in forced turbulence.

The joint pdf of the reacting scalars, ϕ_A and ϕ_B have also been computed using the DNS data and can be compared to the joint pdf found from the FP closure. For example, the joint pdf at $\phi_{rms}/\phi_{rms}(0) = 0.426$ is shown in figure 11 and that found using the FP closure for the same value of $\phi_{rms}/\phi_{rms}(0)$ in figure 12a. It can be seen that, despite the closure approximations needed to derive (19) and (24), the general shape of the pdf predicted by the FP closure corresponds closely to that found by DNS. In particular, the width of the curved region of significant probability is about the same in the DNS and the model. †

The comparisons between the pdfs of the modeled and DNS gradients (figures 11(b-d) and 12(b-d)) are not nearly as good, though the modeled gradients do have the correct order of magnitude. The strange bimodal structure of the gradient-gradient pdf (figure 12d) is presumably caused by one of the modeling assumptions used to derive equation (24).

† This can also be compared to the CMC model which predicts no scatter about the curve (Riley, 1992).

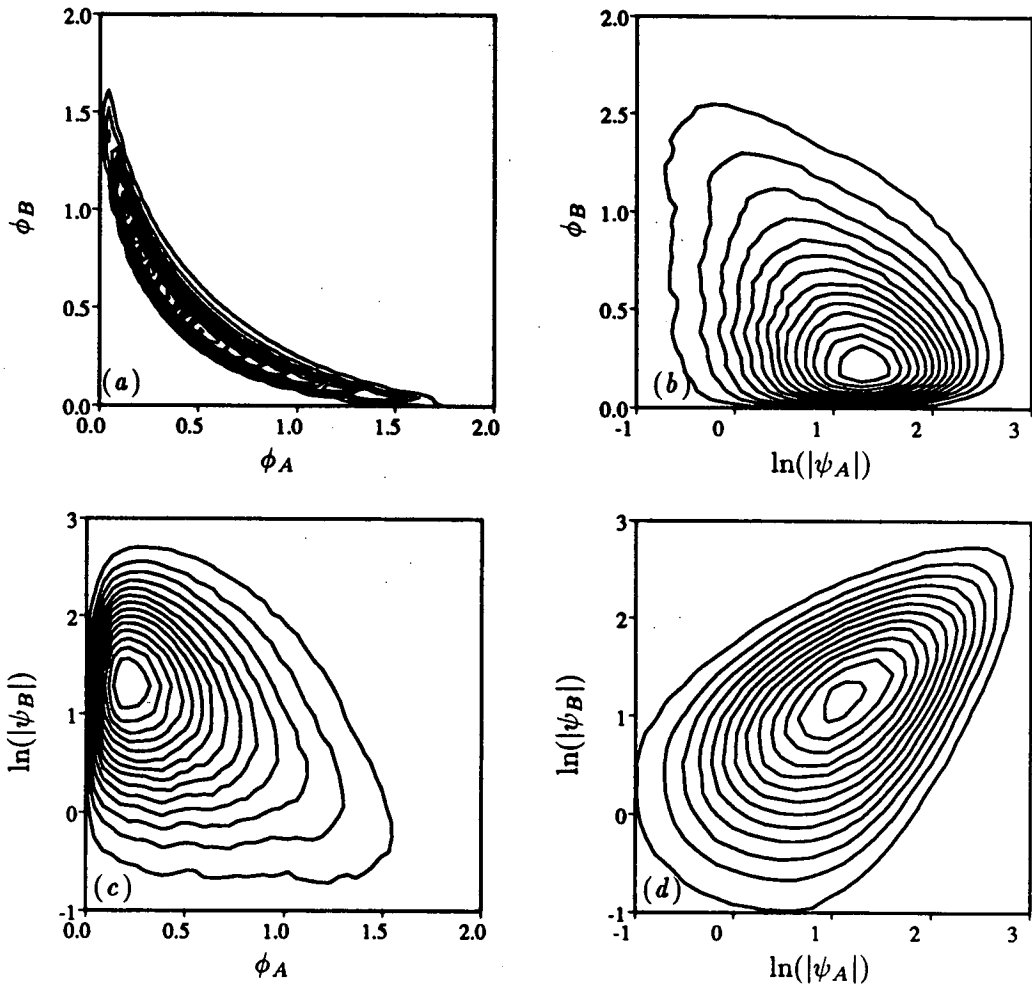


FIGURE 11. Joint pdf's of reactant concentrations and gradients from the DNS for blob initial conditions at $t\epsilon/q^2 = 0.497$.

4. Conclusions

Direct numerical simulations of a single-step chemical reaction between non-premixed reactants in forced isotropic turbulence were made for both "slab" and "blob" initial scalar reactant configurations. As found in previous simulations at lower Reynolds number, the amplification of concentration gradients in the reaction zone by the strain field was seen to be an important feature of these flows, in that regions of large local reaction rate are coincident with regions of large values of the gradient amplification factor.

An analysis of the alignment of various scalar gradients with each other provides some justification for treating the mixing process as locally one-dimensional as assumed in the Fokker-Planck model studied here and other closures.

Comparisons were made between predictions of the FP closure and results of

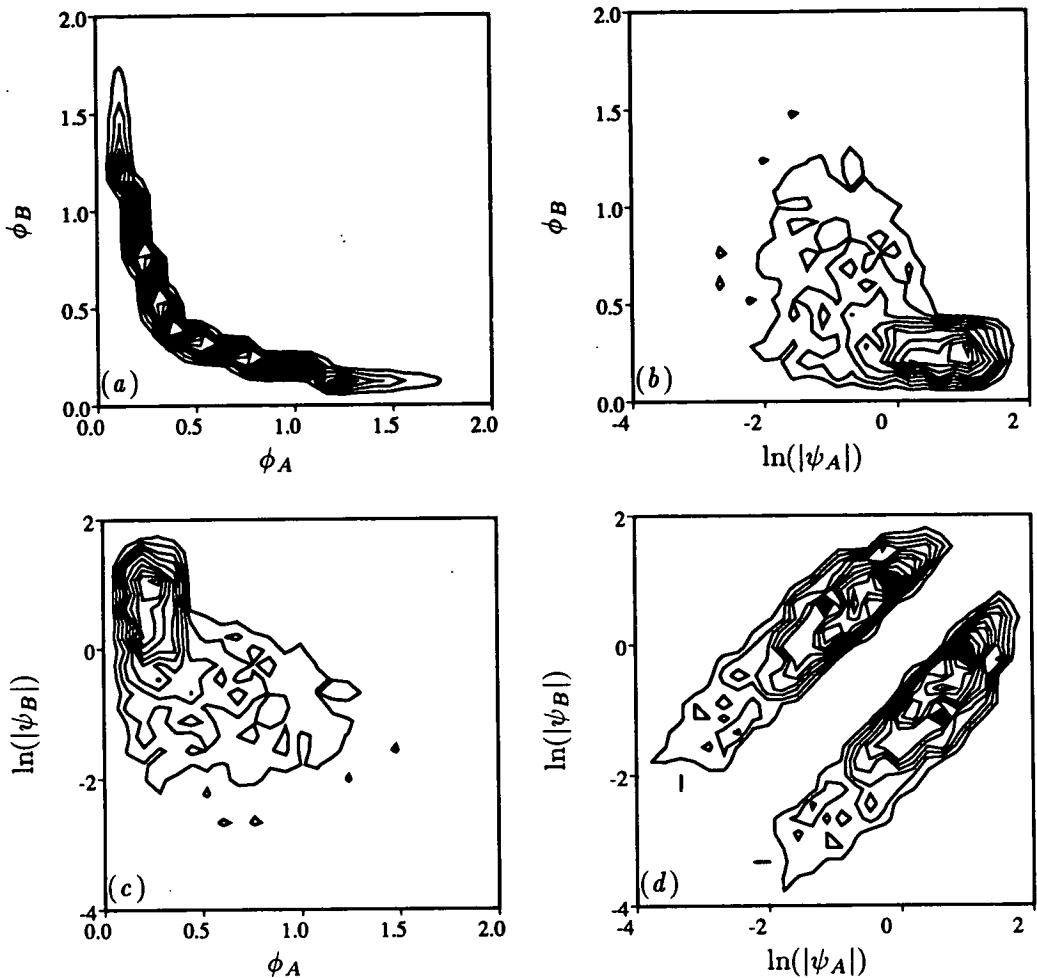


FIGURE 12. Joint pdf's of reactant concentrations and gradients from the FP model for the same conditions as in figure 11.

turbulence simulations. The closure's treatment of gradient stretching as a bilinear term in the model equation is generally supported by the DNS data. For example, the gradient stretching constant was found to be independent of initial conditions, and the DNS results for the joint pdf of the scalar gradient and the turbulence relaxation rate were found to be consistent with the model. Likewise, the closure's prediction for the joint pdf of the reactive scalars is very similar in shape to the DNS result. However, it was also found that for the non-isotropic initial scalar field the gradient mixing constant appearing in the closure is not constant as assumed, and that the closure's prediction for the form of the joint reactive scalar gradient pdf differs significantly from the DNS result. The former can most likely be accounted for in the closure by incorporating scalar integral length scale information, and the latter by modifying the closure assumptions used in deriving (24) from (23). In any

case, since it can be easily incorporated into existing Monte-Carlo simulation codes (Pope, 1985), the formulation of the FP closure in terms of a stochastic process offers a significant computational advantage over other closures that require the solution of a reaction-diffusion equation.

Acknowledgments

Authors ROF and JCH appreciate the generous support and use of the facilities provided by the Center for Turbulence Research. Portions of the work of ROF were supported by NSF Grant CTS-9158124. The authors appreciate the use of data from a high resolution simulation by R. S. Rogallo and A. A. Wray for forced, homogeneous turbulence, and also appreciate helpful dialogs with L. Vervisch, T. Poinso, A. Trouvé, and S. Mahalingam.

REFERENCES

- ANSELMET, F. & ANTONIA, R. A. 1985 Joint statistics between temperature and its dissipation in a turbulent jet. *Phys. Fluids*. **28**, 1048–1054.
- BILGER, R. W. 1976 Turbulent jet diffusion flames. *Prog. Energy Combust. Sci.* **1**, 87–109.
- BILGER, R. W. 1991 Conditional moment methods for turbulent reacting flows using Crocco variable conditions. *Charles Kolling Research Lab. TN F-99* (Dept. Mech. Eng., The Univ. of Sydney)
- BORGHI, R., DOPAZO, C., MANTEL, T. & PICART, A. 1992 The modeling of the scalar dissipation rate in turbulent mixing. (In preparation.)
- CHEN, H. C., CHEN, S., & KRAICHNAN, R. H. 1989 Probability distribution of a stochastically advected scalar field. *Phys. Rev. Lett.* **63**, 2657.
- ESWARAN, V. & O'BRIEN, E. E. 1989 Simulations of scalar mixing in grid turbulence using an eddy-damped closure model. *Phys. Fluids A*. **1**, 537–548.
- ESWARAN, V. & POPE, S. B. 1988 Direct numerical simulations of the turbulent mixing of a passive scalar. *Phys. Fluids*. **31**, 506–520.
- FOX, R. O. 1992a The Fokker-Planck closure for turbulent molecular mixing: passive scalars. *Phys. Fluids A*. **4**, 1230–1244.
- FOX, R. O. 1992b On the joint scalar, scalar gradient pdf in lamellar systems. *Phys. Fluids A* (submitted).
- GAO, F. 1991 Mapping closure and non-Gaussianity of the scalar probability density function in isotropic turbulence. *Phys. Fluids A*. **3**, 2438.
- GAO, F. & O'BRIEN, E. E. 1991 Joint probability density function of a scalar and its gradient in isotropic turbulence. *Phys. Fluids A*. **3**, 1625–1632.
- JIANG, T. L. & O'BRIEN, E. E. 1991 Simulation of scalar mixing by stationary isotropic turbulence. *Phys. Fluids A*. **3**, 1612–1624.
- KERR, R. M. 1985 Higher-order derivative correlations and the alignment of small-scale structures in isotropic numerical turbulence. *J. Fluid Mech.* **153**, 31–58.

- KERSTEIN, A. 1991 Linear-eddy modeling of turbulent transport, Part VI. Microstructure of diffusive scalar mixing fields. *J. Fluid Mech.* **231**, 361–394.
- KOSÁLY, G. 1989 Scalar mixing in isotropic turbulence. *Phys. Fluids A*, **1**, 758–760.
- KOSÁLY, G. & GIVI, P. 1987 *Combust. Flame.* **70**, 101.
- LEONARD, A. D. & HILL, J. C. 1988 Direct numerical simulation of turbulent flows with chemical reaction. *J. Sci. Comput.* **3**, 25–43.
- LEONARD, A. D. & HILL, J. C. 1990 Kinematics of the reaction zone in homogeneous turbulence. *Proc. 12th Sympos. Turb. (Rolla)*, submitted for publication.
- LEONARD, A. D. & HILL, J. C. 1991 Scalar dissipation and mixing in turbulent reacting flows. *Phys. Fluids A*, **3**, 1286–1299.
- LEONARD, A. D. & HILL, J. C. 1992 Mixing and chemical reaction in sheared and nonsheared homogeneous turbulence. *Fluid Mech. Research.* **10**, 273–297.
- LEONARD, A. D., HILL, J. C., MAHALINGAM, S., & FERZIGER, J. H. 1988 Analysis of homogeneous turbulent reacting flows. *Studying Turbulence Using Numerical Simulation Databases-II. Proceedings of the 1988 Summer Program* (Moin, P., Reynolds, W. C., & Kim, J., eds., Center for Turbulence Research Report CTR-S88,243–255).
- MANTEL, T. & BORGHI, R. 1991 A new model of premixed wrinkled flame propagation based on a scalar dissipation equation. (preprint).
- MELL, W. E., NIELSEN, V., KOSÁLY, G. & RILEY, J. J. 1992 Direct numerical simulation investigation of the conditional moment closure model for non-premixed turbulent reacting flows. *Combust. Sci. Tech.* (in press).
- MEYERS, R. E. & O'BRIEN, E. E. 1981 The joint pdf of a scalar and its gradient at a point in a turbulent fluid. *Combust. Sci. and Tech.* **26**, 123–134.
- NOMURA, K. K. & ELGOBASHI, S. E. 1992 Mixing characteristics of an inhomogeneous scalar in isotropic and homogeneous sheared turbulence. *Phys. Fluids A*, **4**, 606–625.
- O'BRIEN, E. E. 1980 The probability density function (pdf) approach to reacting turbulent flows. *Turbulent Reacting Flows* (Libby, P. A. and Williams, F. A., eds.) *Topics in Applied Physics.* **44**, Springer-Verlag, Heidelberg.
- POPE, S. B. 1985 PDF methods for turbulent reactive flows. *Prog. Energy Combust. Sci.* **11**, 119–192.
- POPE, S. B. & CHEN, Y. L. 1990 The velocity-dissipation probability density function model for turbulent flows. *Phys. Fluids A*, **2**, 1437–1449.
- POPE, S. B. 1991 Mapping closures for turbulent mixing and reaction. *Theor. Comput. Fluid. Dyn.* **2**, 255.
- RILEY, J. J. 1992 Investigation of closure models for turbulent reacting flows using direct numerical simulations. *13th Symp. on Turbulence*, Rolla, MO.

- ROGALLO, R. S. 1981 Numerical experiments in homogeneous turbulence. *NASA TM 81315*.
- SOKOLOV, I. M. & BLUMEN, A. 1991a Diffusion-controlled reactions in lamellar systems. *Phys. Rev. A.* **43**, 2714.
- SOKOLOV, I. M. & BLUMEN, A. 1991b Distribution of striation thicknesses in lamellar systems. *Phys. Rev. A.* **43**, 6545.
- VALIÑO, L. & DOPAZO, C. 1991 Joint statistics of scalars and their gradients in nearly homogeneous turbulence. *Advances in Turbulence.* **3** (Springer), 312–323.



Panel discussion on computational combustion

By J. C. Hill¹

A moderated panel discussion was held to gather opinions on the status of computational methods for turbulent combustion and to assess the role and usefulness of direct numerical simulations in fundamental studies of turbulent combustion and in the development of engineering predictive models. Panelists were F. A. Williams, S. B. Pope, and T. Poinso. It is clear that computational models are in need of considerable work for combusting flows and that DNS can be useful in their development, in which canonical or simple problems are computed fully to validate a model or answer questions about the pertinent physics of the problem.

1. Introduction

An increasing portion of the research projects at the first four CTR summer programs deals with reacting flows—two of 30 in 1987, one of 23 in 1988, five of 25 in 1990, and six of 23 in 1992 (Moin *et al.* 1987, 1988, 1990, 1992). Several of the studies involve direct numerical simulations of 2-D and 3-D reacting flows, some with Arrhenius kinetics and others for isothermal systems, some with volume generation from heat release (compressible codes) and others for isochoric motions, some with simple reaction kinetics and others for systems with complex chemistry. Most of the studies are motivated by questions dealing with turbulent combustion, although some do not deal with the combustion problem *per se* but with simpler problems in order to answer specific questions about reacting flows.

In support of these studies, a panel discussion was held to review the status of computational models for turbulent combustion. (See Table 1 for an outline of available types of computer models, noting those for which production codes are available.²) A particular focus of the panel was to determine to what extent direct simulations are useful in support of these models or for investigating the fundamental physics of these flows. Indeed, there is a variety of degrees of refinement for DNS of turbulent combustion (constant/variable density, infinitely fast/finite rate chemistry, single step/complex chemistry). Due to resolutions requirements, the more elaborate the approach is, the more restricted the simulations are in terms

¹ Iowa State University

² Table 1 was prepared by D. C. Haworth with the assistance of the following members of the reacting flows research group: M. Baum, J. H. Chen, R. O. Fox, F. Gao, J. C. Hill, S. Mahalingam, T. Poinso, I. K. Puri, D. Reuss, A. Trouvé, and L. Vervisch. The designation 'production code' indicates that computer models of that type are in common use by the gas turbine industry, IC engine companies, and parts of the chemical and petroleum processing industries in the opinions of the above group.

of Reynolds and Damköhler numbers. So it is useful to ask whether the best compromise might be found and, in particular, whether including more physics in the simulations does not result in tractable problems with characteristics far from the range of Reynolds and Damköhler numbers of interest. Consequently, it was felt desirable to step back and reflect on the situation.

The panel, moderated by W. C. Reynolds, consisted of the following members: F. A. Williams (University of California at San Diego), S. B. Pope (Cornell University), and T. Poinsot (CNRS, Institut de Mécanique des Fluides, Toulouse). The panelists delivered brief position statements (summarized in Section 2) and then responded to general questions in the discussion period (summarized in Section 3).

Table 1. Types of turbulent combustion models. ^a Listed in increasing order of complexity. "Production" codes are in use for models marked with an asterisk*.

	Turbulence Models	Combustion Models		
		Premixed	Diffusion	Premixed/diffusion
One-point, time- or ensemble-average	ℓ	Arrhenius*	Equilibrium*	EBU/Arrhenius*
	$k-\epsilon^*$	EBU*	EBU*	
	ASM	EBU/Arrhenius*	Simplified pdf*	
	RSM	Simplified pdf	Flamelet*	
	pdf	Flamelet*	Full pdf	
Spatial filter	LES	Arrhenius	Equilibrium	
	RVM	G-equation	Arrhenius	

^a Notations: ℓ denotes algebraic length models, ASM = algebraic stress model, RSM = Reynolds stress model, EBU = eddy breakup model, LES = large eddy simulation (with subgrid model), RVM = random vortex methods, Simplified pdf = assumed pdf methods, Equilibrium = fast chemistry assumption. Arrhenius models are usually based on mean concentrations and neglect turbulent fluctuations. There are various versions of EBU and flamelet models. The last column refers to situations such as in IC engines where flames are partially premixed and where both types of flames exist.

2. Position statements of the panelists

This section presents the basic ideas contained in the position statements of the panelists, as interpreted by J. C. Hill.

2.1 Models for computing turbulent combusting flows

(F. A. Williams, University of California at San Diego)

To provide some framework for discussion, F. A. Williams presented the following classification of the wide variety of computational models available for turbulent combusting flows (Liñán and Williams 1993): (1) 0-dimensional models (no turbulence), (2) moment methods including algebraic closures, k - ϵ (- g) models (KIVA, SPEED, FIRE, etc.), full second order models, (3) presumed pdf approximations using moments including BML and G-equation for premixed flames and mixture fraction for diffusion flames, (4) pdf evolution methods including C/D and LMSE closures, (5) extended perturbation methods including RNG and moment modeling of the G-equation, fractals, etc., (6) field methods not based on the conservation equations (age theories in CSTR's for example), and (7) DNS. There are a number of models in (1)–(6) that have resulted in production codes (*cf* Table 1), which have met with varying degrees of success; however, in category (7), only LES is possible for any practical problem, but it does not yet exist for combustion.

One of the overriding factors in selecting a model is the range of Da and Re in the problem at hand (See Fig. 2 in Williams 1985, which classifies the regimes). Other parameters are less important. Most models are for low to moderate Re_L , and (7) is currently only possible at low Re_L . No models seem to apply in the broken flamelet regime (high Re_L , moderate Da). To illustrate the difficulty of validating a model, experimental (laboratory) data for turbulent flame speed can vary over nearly an order of magnitude, and this is reflected by the more than half dozen commonly used expressions for the turbulent burning velocity S_t . Some theoretical estimates of S_t are clearly incorrect, and perhaps DNS can be of help, although extrapolation to high Re_L will be difficult.

2.2 Role of numerical simulation in the study of turbulent combustion

(S. B. Pope, Cornell University)

S. B. Pope makes the point that DNS of turbulent combustion cannot be done in the engineering context. For example, for a simple hydrocarbon–air reaction with 50 chemical species and 200 reactions with time scales differing by as much as a factor of 10^{10} , variable temperature and physical properties, and with the complex geometry of the combustor, DNS is not practicable with computer technology available now or in the near future. The way to proceed, however, is to use DNS to study phenomena in isolation by simplifying the problem until tractable, taking care to preserve the desired physics, and then using the results to develop statistical models which *can* be applied to practical problems, *i.e.* apply DNS to a model problem that contains an essence of the desired problem and which contains sufficient physics for the results to be useful (Pope 1990).

Examples were shown from S. B. Pope's own studies of the use of DNS in constant density, forced isotropic turbulence. These include the evaluation of the Reynolds number dependence of Lagrangian statistics of the velocity and acceleration fields

for a stochastic model suitable for engineering purposes (Yeung & Pope 1989), the evaluation of pdf's of mixture fraction (inert scalar field) in order to parameterize a mapping closure of mixing (Eswaran & Pope 1988, Pope 1991), and studies of the motion and curvature of material surfaces and stoichiometric surfaces (Pope *et al.* 1989, Yeung *et al.* 1990, Girimaji & Pope 1992) to determine characteristics needed for flamelet models; in the latter studies it was shown that curvatures become unbounded and that cusps form in finite times.

In summary, statistical models can be applied to practical problems and DNS cannot, but models applied to simple problems accessible to DNS are useful for testing their foundations. However, one needs to be careful of extrapolating Re- and Da- dependence.

2.3 Direct numerical simulations: one of the tools to study turbulent combustion

(T. Poinso, CNRS, Institut de Mécanique des Fluides de Toulouse)

T. Poinso presented several examples of the use of DNS to study turbulent premixed combustion. Applied to the flamelet approach, there is a three-fold computational problem: (1) the validity of the flamelet assumption has to be tested, then when this assumption is valid, it is necessary to compute (2) the flame surface density Σ and (3) the burning velocity or consumption rate per unit flame surface area, S_c . DNS computations have been made for 2-D and 3-D constant density and variable density flows, simple chemistry with Arrhenius kinetics and complex chemistry (including variable density in 2-D) (Rutland & Ferziger 1989, Cant *et al.* 1990, Poinso *et al.* 1991, Mahalingam 1989, Haworth & Poinso 1992); in terms of the parameters u'/u_{flame} and l_t/L_{flame} , DNS with chemistry is approaching the range of these parameters of practical interest, at least for some simple problems (Haworth & Poinso 1992). [Note: The latter point, particularly with regard to the IC modeling study mentioned in the next paragraph, was debated by the other panelists during the discussion period.]

Several features of the flamelet model have been examined by DNS; for example, it has been found that the flamelet structure is controlled not only by strain rate as assumed in the library approach, but also by flame curvature. In addition, strong effects of thermo-diffusive instabilities (Lewis number effects) on the flame surface evolution were found. Vortex-flame interaction studies have also been made to study quenching phenomena, and the results give further support to the flamelet model (Poinso *et al.* 1991). DNS has been used in models of premixed flames (Meneveau & Poinso 1991, Boudier *et al.* 1992, Bray & Cant 1991, Nicolleau *et al.* 1991) and has also inspired or followed new experiments on flame-vortex interactions, on the effect of Lewis number in turbulent jet flames, on flame speeds in curved flames, and on optical diagnostics (Roberts & Driscoll 1991, Poinso *et al.* 1991, Wu *et al.* 1991). DNS has also been used to develop a new model implemented in KIVA to predict ignition in spark-ignited engines and to accurately describe such important effects as flame behavior at the wall, combustion efficiency, and equivalence ratio (Boudier *et al.* 1992).

In summary, it was shown that DNS is useful in building models of turbulent combusting flows and is also useful in improving our understanding of combustion. Future work is needed on the theory, especially for non-premixed flames, and for the DNS of complex chemistry in 2-D, simple chemistry in 3-D, and for more efficient parallel codes.

3. Discussion

In addition to some technical issues not reported here, the following principle points were raised in response to the presentations of the panelists:

- The following simplifications are common for DNS of reacting flows: (a) cold flows (constant T and ρ , 3-D Navier-Stokes, *i.e.*, the passive scalar problem) vs. flows with variable temperature; (b) incompressible (either constant T or with Arrhenius rate but with constant ρ) vs. compressible (Arrhenius kinetics with heat release; *i.e.*, couple hydrodynamics, energy, and reaction); (c) 2-D vs. 3-D simulations; (d) equilibrium vs. finite rate chemistry; simple (single-step) kinetics vs. complex chemistry, model vs. 'real' chemistry; (e) Fickian diffusion vs. multicomponent diffusion; (f) decaying vs. forced turbulence; (g) premixed or nonpremixed vs. partially mixed systems. It is apparent that such simplifications are necessary to make some problems tractable, and that the simplification made depends on the problem, with care taken that the essential physical properties are preserved. For example, if interested in mixing terms, isothermal simulations might be acceptable, if interested in complex chemistry with widely different reaction rate constants, 2-D simulations might prove sufficient, etc. In general, it was thought best to do the simpler simulations first (*e.g.*, 2-D without full chemistry) and then add complications, but within the context of a model or the physics being examined. Care must be taken with the simplifications, however; for example, the reverse energy cascade in 2-D may have some unexpected influence on flame surface density.
- A good problem to attack by DNS would be to do the fluid mechanics for the broken-flamelet regime in the case of non-premixed combustion. Also, it was clear from the discussion that there is no universal agreement on the mechanism of flamelet extinction.
- The next generation of machines (T-flop) may be able to shift the focus in DNS away from the archetypal simple problems to more practical problems, but as suggested above, doing the simpler problems first increases understanding.
- The prospects for LES and SGM in a reacting environment are not very good because of domination by small scales at high Da , although the LEM of Kerstein (1991) may be useful. [However, its successes are mixed.] The concept of LES that tracks the flame was suggested by analogy with the RVM and with adaptive grid methods. [Note: This has been suggested by others (random surface model) but still requires a model of the reaction zone and thus DNS coupled with flamelet or other models as appropriate.]
- All of the discussion centered on single-phase systems (conventional flames) since features of computational models in that area are amenable to testing by laboratory experiments and to some extent by DNS. A future challenge for DNS and

for theories with the same level of rigor as used in some of the models discussed here or studied in this workshop are flows with particulates (soot and ash formation, condensation reactions, spray combustion), radiation, wet combustion, and complex geometries with recirculation or backmixing.

4. Conclusions

In summary, F. Williams gave an overview of the regimes of applicability of the different types of combustion models, pointing out their shortcomings and the limitations of DNS for practical problems as well as the overriding importance of Da and Re in considering models for practical problems. S. B. Pope presented the case that one cannot do DNS for practical combustion systems but can learn something from simple canonical problems used for model building. T. Poinsot pointed out the difficulties with length and time scales in turbulent combustion but claims that DNS in premixed systems can be used for some practical combustion problems and has been used to validate the flamelet model.

Although the panel members were not in complete agreement, it is clear that there is a need for additional work on computational models and that DNS—even simplified canonical problems—can be useful for model development and validation and also for answering specific questions about the physics that are not accessible in the laboratory.

Acknowledgment

The assistance of the combustion research group in preparing for the panel discussion is appreciated. Also, the panelists were kind enough to provide J. C. Hill with copies of material used in their presentations and to review Section 2 of this report. The facilities and support provided by the Center for Turbulence Research and its staff are also appreciated.

REFERENCES

- BOUDIER, P., HENRIOT, S., POINSOT, T. AND BARITAUD, T. 1992 A model for turbulent flame ignition and propagation in piston engines. *24th Symp. (Int.) on Combustion*. The Combustion Institute, Pittsburgh.
- BRAY, K. N. C. AND CANT, R. S. 1991 Some applications of Kolmogorov's turbulence research in the field of combustion. *Proc. Roy. Soc. A London* (A.N. Kolmogorov Special Issue).
- CANT, R. S., RUTLAND, C. & TROUVÉ, A. 1990 Statistics for laminar flamelet modeling, in Moin *et al.* (1990), pp. 271–279
- ESWARAN, V., & POPE, S. B. 1988 Direct numerical simulations of the turbulent mixing of a passive scalar. *Phys. Fluids*. **31**, 506–520.
- GIRIMAJI, S. S., & POPE, S. B. 1992 Propagating surfaces in isotropic turbulence. *J. Fluid Mech.* **234**, 247–277.
- HAWORTH, D. C. & POINSOT, T. J. 1992 Numerical simulations of Lewis number effects in turbulent premixed flames. *J. Fluid Mech.* **244**, 405–436.

- KERSTEIN, A. 1991 Linear-eddy modeling of turbulent transport, Part VI. Microstructure of diffusive scalar mixing fields. *J. Fluid Mech.* **231**, 361–394.
- LIÑÁN, A., & WILLIAMS, F. A. 1993 *Fundamental Aspects of Combustion*, Oxford University Press (in press).
- MAHALINGAM, S. 1989 Non-premixed combustion: full numerical simulation of a coflowing axisymmetric jet, inviscid and viscous stability analysis, Ph. D. dissertation (Stanford University).
- MENEVEAU, C. & POINSOT, T. 1991 Stretching and quenching of flamelets in premixed turbulent combustion. *Comb. Flame.* **86**, 311–332.
- MOIN, P., REYNOLDS, W. C., & KIM, J. (eds.) 1987 *Studying Turbulence Using Numerical Simulation Databases-I. Proceedings of the 1987 Summer Program*, Center for Turbulence Research Report CTR-S87.
- MOIN, P., REYNOLDS, W. C., & KIM, J. (eds.) 1988 *Studying Turbulence Using Numerical Simulation Databases-II. Proceedings of the 1988 Summer Program*, Center for Turbulence Research Report CTR-S88.
- MOIN, P., REYNOLDS, W. C., & KIM, J. (eds.) 1990 *Studying Turbulence Using Numerical Simulation Databases-III. Proceedings of the 1990 Summer Program*, Center for Turbulence Research Report CTR-S90.
- MOIN, P., REYNOLDS, W. C., & KIM, J. (eds.) 1992 *Studying Turbulence Using Numerical Simulation Databases-IV. Proceedings of the 1992 Summer Program*, Center for Turbulence Research Report CTR-S92.
- NICOLLEAU, F., BERTOGLIO, J. P. & MATHIEU, J. 1991 A contribution to turbulent combustion: premixed flames and material surfaces. *Revue de L'I.F.P.* **46**.
- POINSOT, T., ECHEKKI, T. & MUNGAL, M. G. 1991 A study of the laminar flame tip and implications for premixed turbulent combustion. *Comb. Sci. Technol.* **81**, 45.
- POINSOT, T., VEYNANTE, D. & CANDEL, S. 1991 Quenching processes and premixed turbulent combustion diagrams. *J. Fluid Mech.* **228**, 561–605.
- POPE, S. B. 1990 Computations of turbulent combustion: progress and challenges. *Twenty-third Sympos. (Int'l.) on Combustion*, pp. 591–612.
- POPE, S. B. 1991 Mapping closures for turbulent mixing and reaction. *Theor. Comput. Fluid Dyn.* **2**, 255.
- POPE, S. B., YEUNG, P. K., & GIRIMAJI, S. S. 1989 The curvature of material surfaces in isotropic turbulence. *Phys. Fluids A.* **1**, 2010–2018.
- ROBERTS, W. L. & DRISCOLL, J. F. 1991 A laminar vortex interacting with a premixed flame: measured formation of pockets of reactants. *Comb. Flame.* **87**, 245–256.
- RUTLAND, C. J. & FERZIGER, J. 1989 Interaction of a vortex and a premixed flame. *27th AIAA Aerospace Sciences Meeting* (AIAA Preprint # 89-0127).

- WILLIAMS, F. A. 1985 Turbulent combustion, pp. 97-131 in Buckmaster, J.D. (ed.), *The Mathematics of Combustion*, SIAM.
- WU, M. S., KWON, S., DRISCOLL, J. F. & FAETH, G. M. 1991 Preferential diffusion effects on the surface structure of turbulent premixed hydrogen/air flames. *Comb. Sci. Technol.* **78**, 69-96.
- YEUNG, P. K. & POPE, S. B. 1989 Lagrangian statistics from direct numerical simulations of isotropic turbulence. *J. Fluid Mech.* **207**, 531-586.
- YEUNG, P. K., GIRIMAJI, S. S., & POPE, S. B. 1990 Straining and scalar dissipation on material surfaces in turbulence: Implications for flamelets. *Combust. Flame.* **79**, 340-365.